ADVANCES IN ROBOT KINEMATICS

Advances in Robot Kinematics

Mechanisms and Motion

Edited by

JADRAN LENARČIČ
Jožef Stefan Institute
Ljubljana, Slovenia

and

B. ROTH
Stanford University
California, U.S.A.

Springer

A C.I.P. Catalogue record for this book is available from the Library of Congress.

ISBN-10 1-4020-4940-4 (HB)
ISBN-13 978-1-4020-4940-8 (HB)
ISBN-10 1-4020-4941-2 (e-book)
ISBN-13 978-1-4020-4941-5 (e-book)

Published by Springer,
P.O. Box 17, 3300 AA Dordrecht, The Netherlands.

www.springer.com

Printed on acid-free paper

Printed in the Netherlands.

Preface

This is the tenth book in the series of Advances in Robot Kinematics. Two were produced as workshop proceedings, Springer published one book in 1991 and since 1994 Kluwer published a book every two years without interruptions. These books deal with the theory and practice of robot kinematics and treat the motion of robots, in particular robot manipulators, without regard to how this motion is produced or controlled. Each book of Advances in Robot Kinematics reports the most recent research projects and presents many new discoveries.

The issues addressed in this book are fundamentally kinematic in nature, including synthesis, calibration, redundancy, force control, dexterity, inverse and forward kinematics, kinematic singularities, as well as over-constrained systems. Methods used include line geometry, quaternion algebra, screw algebra, and linear algebra. These methods are applied to both parallel and serial multi-degree-of-freedom systems. The results should interest researchers, teachers and students, in fields of engineering and mathematics related to robot theory, design, control and application.

All the contributions had been rigorously reviewed by independent reviewers and fifty three articles had been recommended for publication. They were introduced in seven chapters. The authors discussed their results at the tenth international symposium on Advances in Robot Kinematics which was held in June 2006 in Ljubljana, Slovenia. The symposium was organized by Jozef Stefan Institute, Ljubljana, under the patronage of IFToMM - International Federation for the Promotion of Mechanism and Machine Science.

We are grateful to the authors for their contributions and for their efficiency in preparing the manuscripts, and to the reviewers for their timely reviews and recommendations. We are also indebted to the personnel at Springer for their excellent technical and editorial support.

Jadran Lenarčič and Bernard Roth, editors

Contents

Methods in Kinematics

Properties of Mechanisms

Humanoids and Biomedicine

Analysis of Mechanisms

Workspace and Performance

Design of Mechanisms

Motion Synthesis and Mobility

Methods in Kinematics

WIRE-BASED TRACKING USING MUTUAL INFORMATION

Juan Andrade-Cetto
Computer Vision Center, UAB
Edifici O, Campus UAB, 08193 Bellaterra, Spain
cetto@cvc.uab.es

Federico Thomas
Institut de Robòtica i Informàtica Industrial, CSIC-UPC
Llorens Artigas 4-6, 08028 Barcelona, Spain
fthomas@iri.upc.edu

Abstract Wire-based tracking devices are an affordable alternative to costly tracking devices. They consist of a fixed base and a platform, attached to the moving object, connected by six wires whose tension is maintained along the tracked trajectory. One important shortcoming of this kind of devices is that they are forced to operate in reduced workspaces so as to avoid singular configurations. Singularities can be eliminated by adding more wires but this causes more wire interferences, and a higher force exerted on the moving object by the measuring device itself. This paper shows how, by introducing a rotating base, the number of wires can be reduced to three, and singularities can be avoided by using an active sensing strategy. This also permits reducing wire interference problems and the pulling force exerted by the device. The proposed sensing strategy minimizes the uncertainty in the location of the platform. Candidate motions of the rotating base are compared selected automatically based on mutual information scores.

Keywords: Tracking devices, Kalman filter, active sensing, mutual information, parallel manipulators

1. Introduction

Tracking devices, also called 6-degree-of-freedom (6-DOF) devices, are used for estimating the position and orientation of moving objects. Current tracking devices are based on electromagnetic, acoustic, mechanical, or optical technology. Tracking devices can be classified according to their characteristics, such as accuracy, resolution, cost, measurement range, portability, and calibration requirements. Laser tracking systems exhibit good accuracy, which can be less than $1\mu m$ if the system is well calibrated. Unfortunately, this kind of systems are very expensive, their

J. Lenarčič and B. Roth (eds.), Advances in Robot Kinematics, 3–14.

calibration procedure is time-consuming, and they are sensitive to the environment. Vision systems can reach an accuracy of $0.1mm$. They are low-cost portable devices but their calibration procedure can be complicated. Wire-based systems can reach an accuracy of $0.1mm$, they are also low cost portable devices but capable of measuring large displacements. Moreover, they exhibit a good compromise among accuracy, measurement range, cost and operability.

Wire-based tracking devices consist of a fixed base and a platform connected by six wires whose tension is maintained, while the platform is moved, by pulleys and spiral springs on the base, where a set of encoders give the length of the wires. They can be modelled as 6-DOF parallel manipulators because wires can be seen as extensible legs connecting the platform and the base by means of spherical and universal joints, respectively.

Dimension deviations due to fabrication tolerances, wire-length uncertainties, or wire slackness, may result in unacceptable performance of a wire-based tracking device. In general, the effects of all systematic errors can be eliminated by calibration. Some techniques for specific errors have already been proposed in the literature. For example, a method for compensating the cable guide outlet shape of wire encoders is detailed in Geng and Haynes, 1994, and a method for compensating the deflections caused by wire self-weights is described in Jeong et al., 1999. In this paper, we will only consider wire-length errors which cannot be compensated because of their random nature.

Another indirect source of error is the force exerted by the measuring device itself. Indeed, all commercial wire encoders are designed to keep a large string tension. This is necessary to ensure that the inertia of the mechanism does not result in a wire going slack during a rapid motion. If a low wire force is used, it would reduce the maximum speed of the object to be tracked without the wires going slack. On the contrary, if a high wire force is used, the trajectory of the object to be tracked could be altered by the measuring device. Hence, a trade-off between accuracy and speed arises.

The minimum number of points on a moving object to be tracked for pose measurements is three. Moreover, the maximum number of wires attached to a point is also three, otherwise the lengths of the wires will not be independent. This leads to only two possible configurations for the attachments on the moving object. The *3-2-1 configuration* was proposed in Geng and Haynes, 1994. The kinematics of this configuration was studied, for example, in Nanua and Waldron, 1990 and Hunt and Primrose, 1993. Its direct kinematics can be solved in closed-form by using three consecutive trilateration operations yielding 8 solutions, as

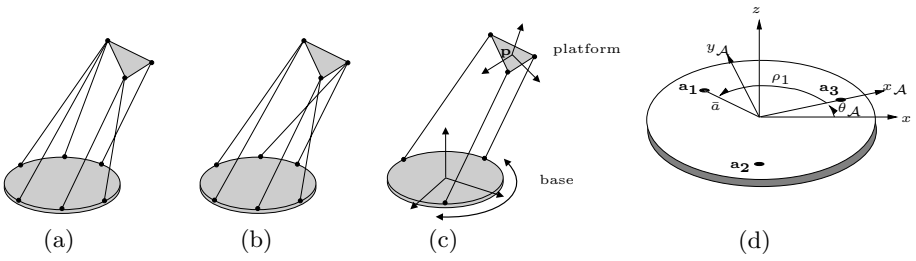

Figure 1. The main two configurations used for wire-based tracking devices: (a) the "3-2-1", (b) the "2-2-2", and (c) the proposed tracking device, with (d) the rotating base.

in Thomas et al., 2005. The *2-2-2 configuration* was first proposed in Jeong et al., 1999 for a wire-based tracking device. The kinematics of this configuration was studied, for example, in Griffis and Duffy, 1989, Nanua et al., 1990, and Parenti-Castelli and Innocenti, 1990 where it was shown that its forward kinematics has 16 solutions. In other words, there are up to 16 poses for the moving object compatible with a given set of wire lengths. These configurations can only be obtained by a numerical method. The two configurations above were compared, in terms of their sensitivity to wire-length errors, in Geng and Haynes, 1994. The conclusion was that they have similar properties.

This paper is organized as follows. Section 2 contains the mathematical model of our proposed 3-wire-based sensing device, while Section 3 derives the filtering strategy for tracking its pose. Given that this device has a moving part, Section 4 develops an information theoretic metric for choosing the best actions for controlling it. A strategy to prevent possible wire crossings is contemplated in Section 5. Section 6 is devoted to a set of examples demonstrating the viability of the proposed approach. Finally, concluding remarks are presented in Section 7.

2. Kinematics of the Proposed Sensor

In order to reduce cable interferences, singularities, and wire tension problems we choose to reduce the number of cables from six to three, and to have the base rotate on its center. Provided the tracked object motion is sufficiently slow, two measurements at different base orientations would be equivalent to a 2-2-2 configuration.

More elegantly, and to let the tracked object move at a faster speed, measurements can be integrated sequentially through a partially observable estimation framework. That is, a Kalman filter.

Consider the 3-wire parallel device in Figure 1(c). It is assumed that the platform configuration is free to move in any direction in $\mathbb{R}^3 \times SO(3)$. Let the pose of our tracking device be defined as the 14-dimensional array

$$\mathbf{x} = \begin{bmatrix} \mathbf{p} \\ \boldsymbol{\theta} \\ \mathbf{v} \\ \boldsymbol{\omega} \\ \theta_{\mathcal{A}} \\ \omega_{\mathcal{A}} \end{bmatrix} , \tag{1}$$

where $\mathbf{p} = (x, y, z)^\top$ is the position of the origin of a coordinate frame fixed to the platform, $\boldsymbol{\theta} = (\psi, \theta, \phi)^\top$ is the orientation of such coordinate frame expressed as yaw, pitch and roll angles, $\mathbf{v} = (v_x, v_y, v_z)^\top$ and $\boldsymbol{\omega} = (\omega_x, \omega_y, \omega_z)^\top$ are the translational and rotational velocities of $\mathbf{p}$, respectively; and $\theta_{\mathcal{A}}$ and $\omega_{\mathcal{A}}$ are the orientation and angular velocity of the rotating base.

Assume that the attaching points on the base $\mathbf{a}_i$, $i = 1, 2, 3$, are distributed on a circle of radius $\bar{a}$ as shown in Figure 1(d). Then, the coordinates of $\mathbf{a}_i$ can be expressed in terms of the platform rotation angle $\theta_{\mathcal{A}}$ as

$$\begin{bmatrix} a_{xi} \\ a_{yi} \\ a_{zi} \end{bmatrix} = \begin{bmatrix} \bar{a}\cos(\rho_i + \theta_{\mathcal{A}}) \\ \bar{a}\sin(\rho_i + \theta_{\mathcal{A}}) \\ 0 \end{bmatrix} . \tag{2}$$

Moreover, let $\mathbf{e}_i$ be the unit norm vector specifying the direction from $\mathbf{a}_i$ to the corresponding attaching point $\mathbf{b}_i$ in the platform; and let l_i be the length of the i-th wire, $i = 1, 2, 3$. The value of $\mathbf{b}_i$ is expressed in platform local coordinates, where $\mathcal{R}$ is the rotation matrix describing the absolute orientation of the platform. Then, the position of the wire attaching points in the platform, in global coordinates, are

$$\mathbf{b}'_i = \mathbf{a}_i + l_i \mathbf{e}_i = \mathbf{p} + \mathcal{R}\mathbf{b}_i . \tag{3}$$

3. State Estimation

We adopt a smooth unconstrained constant-velocity motion model, its pose altered only by zero-mean, normally distributed accelerations and staying the same on average. The Gaussian acceleration assumption means that large impulsive changes of direction are unlikely. In such model the prediction of the position and orientation of the platform at time t plus a time interval τ is given by

$$\begin{bmatrix} \mathbf{p}(t+\tau) \\ \boldsymbol{\theta}(t+\tau) \end{bmatrix} = \begin{bmatrix} \mathbf{p}(t) + \mathbf{v}(t)\tau + \delta\mathbf{a}(t)\tau^2/2 \\ \boldsymbol{\theta}(t) + \boldsymbol{\omega}(t)\tau + \delta\boldsymbol{\alpha}(t)\tau^2/2 \end{bmatrix} , \tag{4}$$

with $\delta\mathbf{a}$ and $\delta\boldsymbol{\alpha}$ zero mean white Gaussian translational and angular acceleration noises. Moreover, the adopted model for the translational and angular velocities of the platform is given by

$$\begin{bmatrix}\mathbf{v}(t+\tau)\\ \boldsymbol{\omega}(t+\tau)\end{bmatrix} = \begin{bmatrix}\mathbf{v}(t)+\delta\mathbf{a}(t)\tau\\ \boldsymbol{\omega}(t)+\delta\boldsymbol{\alpha}(t)\tau\end{bmatrix} . \tag{5}$$

By the same token, the adopted models for the orientation and angular velocity of the base are

$$\begin{bmatrix}\theta_{\mathcal{A}}(t+\tau)\\ \omega_{\mathcal{A}}(t+\tau)\end{bmatrix} = \begin{bmatrix}\theta_{\mathcal{A}}(t)+\omega_{\mathcal{A}}(t)\tau+(\alpha_{\mathcal{A}}(t)+\delta\alpha_{\mathcal{A}}(t))\tau^2/2\\ \omega_{\mathcal{A}}(t)+(\alpha_{\mathcal{A}}(t)+\delta\alpha_{\mathcal{A}}(t))\tau\end{bmatrix} , \tag{6}$$

in which the control signal modifying the base orientation is the acceleration impulse $\alpha_{\mathcal{A}}$.

Since in practice, the measured wire lengths, l_i, $i = 1, 2, 3$, will be corrupted by additive Gaussian noise, δz_i, we have that

$$z_i(t) = l_i(t) + \delta z_i(t) = \|\mathbf{p}(t) + \mathcal{R}(t)\mathbf{b}_i - \mathbf{a}_i(t)\| + \delta z_i(t) . \tag{7}$$

Lastly, the orientation of the moving base is measured by means of an encoder. Its model is simply

$$z_4(t) = \theta_A(t) + \delta z_4(t) . \tag{8}$$

Eqs. 4 and 5 constitute our motion prediction model $\mathbf{f}(\mathbf{x}, \alpha_{\mathcal{A}}, \delta\mathbf{x})$. Eqs. 7 and 8 complete our measurement prediction model $\mathbf{h}(\mathbf{x}, \delta\mathbf{z})$. Now, an Extended Kalman Filter can be used to propagate the platform pose and velocity estimates, as well as the base orientation estimates, and then, to refine these estimates through wire length measurements. To this end, $\delta\mathbf{x} \sim N(\mathbf{0}, \mathbf{Q})$, $\delta\mathbf{z} \sim N(\mathbf{0}, \mathbf{R})$, and our plant Jacobians with respect to the state $\mathbf{F} = \partial\mathbf{f}/\partial\mathbf{x}$, and to the noise $\mathbf{G} = \partial\mathbf{f}/\partial\delta\mathbf{x}$ become

$$\mathbf{F} = \begin{bmatrix}\mathbf{I} & & \tau\mathbf{I} & & & \\ & \mathbf{I} & & \tau\mathbf{I} & & \\ & & \mathbf{I} & & & \\ & & & \mathbf{I} & & \\ & & & & 1 & \tau \\ & & & & & 1\end{bmatrix} \quad \text{and} \quad \mathbf{G} = \begin{bmatrix}\frac{\tau^2\mathbf{I}}{2} & & \\ & \frac{\tau^2\mathbf{I}}{2} & \\ \tau\mathbf{I} & & \\ & \tau\mathbf{I} & \\ & & \frac{\tau^2}{2} \\ & & \tau\end{bmatrix} . \tag{9}$$

The measurement Jacobians $\mathbf{H} = \partial\mathbf{h}/\partial\mathbf{x}$ are simply

$$\mathbf{H}_i(t) = \begin{bmatrix}\mathbf{e}_i(t) & \mathbf{b}_i \times \mathbf{e}_i(t) & \mathbf{0} & \mathbf{0} & \frac{\partial\mathbf{h}_i}{\partial\theta_{\mathcal{A}}} & 0\end{bmatrix} , \tag{10}$$

with

$$\mathbf{e}_i(t) = \frac{\mathbf{p}(t) + \mathcal{R}(t)\mathbf{b}_i - \mathbf{a}_i(t)}{\|\mathbf{p}(t) + \mathcal{R}(t)\mathbf{b}_i - \mathbf{a}_i(t)\|} . \tag{11}$$

Then, by rewriting $\mathcal{R} = \begin{bmatrix} \mathbf{r}_1^\top \\ \mathbf{r}_2^\top \\ \mathbf{r}_3^\top \end{bmatrix}$, the term $\frac{\partial \mathbf{h}_i}{\partial \theta_\mathcal{A}}$ in $\mathbf{H}_i$ becomes

$$\begin{aligned} \frac{\partial \mathbf{h}_i}{\partial \theta_\mathcal{A}} &= 2\bar{a}((x(t) + \mathbf{r}_1(t)^\top \mathbf{b}_i)\sin(\theta_\mathcal{A}(t) + \rho_i) \\ &\quad -(y(t) + \mathbf{r}_2(t)^\top \mathbf{b}_i)\cos(\theta_\mathcal{A}(t) + \rho_i))/l_i(t)\,. \end{aligned} \tag{12}$$

Lastly,

$$\mathbf{H}_4(t) = \begin{bmatrix} \mathbf{0} & \mathbf{0} & \mathbf{0} & \mathbf{0} & 1 & 0 \end{bmatrix}. \tag{13}$$

For the sake of clarity, in the sequel, when needed, time dependencies will be placed as subscripts. Moreover, the term $t + \tau|t$ will be used to indicate an a prior estimate (before measurements are incorporated), and the terms $t|t$ and $t + \tau|t + \tau$ will represent posterior estimates (once measurements are taken into account). The prediction of the state and state covariance are given by

$$\mathbf{x}_{t+\tau|t} = \mathbf{f}(\mathbf{x}_{t|t}, \alpha_\mathcal{A}, \mathbf{0}) \tag{14}$$

$$\mathbf{P}_{t+\tau|t} = \mathbf{F}\mathbf{P}_{t|t}\mathbf{F}^\top + \mathbf{G}\mathbf{Q}\mathbf{G}^\top \tag{15}$$

and, the revision of the state estimate and state covariance are

$$\mathbf{x}_{t+\tau,t+\tau} = \mathbf{x}_{t+\tau|t} + \mathbf{K}(\mathbf{z}_{t+\tau} - \mathbf{h}(\mathbf{x}_{t+\tau|t}, \mathbf{0})) \tag{16}$$

$$\mathbf{P}_{t+\tau|t+\tau} = (\mathbf{I} - \mathbf{K}\mathbf{H})\mathbf{P}_{t+\tau|t} \tag{17}$$

with $\mathbf{I}$ the identity matrix, and $\mathbf{K} = \mathbf{P}_{t+\tau|t}\mathbf{H}^\top(\mathbf{H}\mathbf{P}_{t+\tau|t}\mathbf{H}^\top + \mathbf{R})^{-1}$ the usual Kalman gain.

4. Information Gain

This section builds from basic principles a metric for the expected information gain as a result of performing a given action, and develops from it, a strategy for controlling the base orientation. The aim is to rotate the base in the direction that most reduces the uncertainty in the entire pose state estimate, by using the information that should be *gained* from future wire measurements were such a move be made, but taking into account the information *lost* as a result of moving with uncertainty.

The essential idea is to use mutual information as a measurement of the statistical dependence between two random vectors, that is, the amount of information that one contains about the other. Consider the states $\mathbf{x}$, and the measurements $\mathbf{z}$. The mutual information of the

two continuous probability distributions $p(\mathbf{x})$ and $p(\mathbf{z})$ is defined as the information about $\mathbf{x}$ contained in $\mathbf{z}$, and is given by

$$I(\mathbf{x},\mathbf{z}) = \int_{\mathbf{x},\mathbf{z}} p(\mathbf{x},\mathbf{z}) \log \frac{p(\mathbf{x},\mathbf{z})}{p(\mathbf{x})p(\mathbf{z})} d\mathbf{x}d\mathbf{z}\,. \tag{18}$$

Note how mutual information measures the independence between the two vectors. It equals zero when they are independent, $p(\mathbf{x},\mathbf{z}) = p(\mathbf{x})p(\mathbf{z})$. Mutual information can also be seen as the relative entropy between the marginal density $p(\mathbf{x})$ and the conditional $p(\mathbf{x}|\mathbf{z})$

$$I(\mathbf{x},\mathbf{z}) = \int_{\mathbf{x},\mathbf{z}} p(\mathbf{x},\mathbf{z}) \log \frac{p(\mathbf{x}|\mathbf{z})}{p(\mathbf{x})} d\mathbf{x}d\mathbf{z}\,. \tag{19}$$

Given that our variables of interest can be described by multivariate Gaussian distributions, the parameters of the marginal density $p(\mathbf{x})$ are trivially the Kalman prior mean $\mathbf{x}_{t+\tau|t}$ and covariance $\mathbf{P}_{t+\tau|t}$. Moreover, the parameters of the conditional density $p(\mathbf{x}|\mathbf{z})$ come precisely from the Kalman update equations $\mathbf{x}_{t+\tau|t+\tau}$ and $\mathbf{P}_{t+\tau|t+\tau}$. Substituting the genaral form of the Gaussian distribution in Eq. 19, we can obtain a closed formula

$$I(\mathbf{x},\mathbf{z}) = \frac{1}{2}\left(\log|\mathbf{P}_{t+\tau|t}| - \log|\mathbf{P}_{t+\tau|t+\tau}|\right)\,. \tag{20}$$

Thus, in choosing a maximally mutually informative motion command, we are maximizing the difference between prior and posterior entropies (MacKay, 1992). In other words, we are choosing the motion command that most reduces the uncertainty of $\mathbf{x}$ due to the knowledge of $\mathbf{z}$.

The real-time requirements of the task preclude using an optimal control strategy to search for the base rotation command that ultimately maximizes our mutual information metric. Instead, we can only evaluate such metric for a discrete set of actions within the range of possible commands, and choose the best action from those. The set of possible actions is a discretization of a range of accelerations.

5. Preventing Wire Crossings

Providing the base with the ability to rotate has the added advantage of increasing the range of motion of the tracked platform; mainly, for rotations along the vertical axis. One of the main difficulties however, is in appropriately choosing base rotation commands so as to prevent wire crossings. Considering that wire end-point displacements are sufficiently small per sampling interval, the trajectory described by each

wire can be assumed to be circumscribed within a tetrahedron. One way to predict wire crossings is by checking whether the tetrahedra described by the current and posterior poses for each wire intersect each other; each tetrahedron described by the four attaching points $\{\mathbf{a}_{i,t|t}, \mathbf{a}_{i,t+\tau|t}, \mathbf{b}'_{i,t|t}, \mathbf{b}'_{i,t+\tau|t}\}$.

A very fast test of tetrahedra intersection is based on the Separating Axis Theorem described in the computer graphics literature (Ganovelli et al., 2003). The test consists on checking whether the plane lying on the face of one tetrahedron separates the two of them. If this is not the case, the test continues to find out if there exists a separating plane containing only one edge on one of the tetrahedra.

6. Implementation and Examples

6.1 Mechanical Considerations

In a cable extension transducer, commonly known as a string pot, the tension of the cable is guaranteed by a spring connected to its spool. Using a cable guide, the cable is allowed to move within a 20° cone, making it suitable for 3D motion applications. There are cable guides that permit 360° by 317° displacement cable orientation flexibility. Manufacturers of such sensors are Celesco Transducer Products Inc., SpaceAge Control Inc., Carlen Controls Inc., and several others.

String pots provide a long range $(0.04 - 40m)$, with typical accuracy of 0.02% of full scale. The maximum allowable cable velocity is about $7.2m/s$ and the maximum cable acceleration is about $200m/s^2$.

The usefulness of a tracking device depends on whether it can track the motion fast enough. This ability is determined by the lag, or latency, between the change of the position and orientation of the target being tracked and the report of the change to the computer. In virtual reality applications, lags above 50 milliseconds are perceptible to the user. In general, the lag for mechanical trackers is typically less than $5ms$.

6.2 Maximum Base Rotation Speed

The quality of the estimated pose is directly influenced by the velocity at which the base can rotate. To determine the range of motion velocities that can be tracked with our system, a tracking simulation was repeated limiting the base rotation velocity. A set of 20 runs was conducted, varying the maximum platform rotation speed from 0 to 1 rad/s, and with time steps of 0.01 s; the tracked object translating at a constant velocity of 0.2 m/s along the x axis, and rotating at $\frac{\pi}{10}$ rad/s about an axis perpendicular to the base. Figure 2 shows the average error of the pose

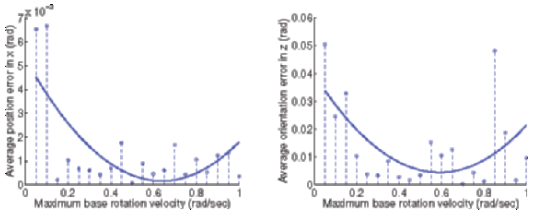

Figure 2. Average position and orientation recovery error as a function of the maximum platform rotation speed, and 2nd order curve fit.

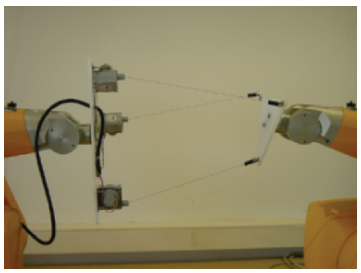

Figure 3. Wire sensing device. The rotating base is attached to the Staubli arm shown in the left side. The moving platform is attached to the arm shown to the right.

estimation as a function of the maximum base rotational velocity. The best pose estimations are achieved when the base rotates at twice the speed of the tracked object, approximately $\frac{\pi}{5}\ rad/s$ for this experiment.

6.3 Pure Rotations

A second experiment consisted in testing the tracking system under pure rotations along the vertical axis. The idea is to show that, whenever cable crossing allows it, the largest acceleration commands are selected. This is because prior and posterior entropy difference is maximized for largest possible configuration changes. The attaching points in both the base and the platform have been arranged to form equilateral triangles. Their coordinates can be found in Table 1, and refer to the frames shown in Figure 1. The actual testbench used is shown in Figure 6.3.

For this example, the object to be tracked rotated at $\frac{\pi}{10}\ rad/s$, whilst kept at a distance of 1 m from the base. The maximum base rotation speed was limited to $\frac{\pi}{5}\ rad/s$, and the limit for possible base acceleration command was set to 5 rad/sec^2. Figure 4(a) shows the evolution of the wire length measurements along the trajectory. Wire length sensors are modeled with additive Gaussian noise with zero mean and 1 mm standard deviation. Moreover, readings of the base orientation are also

Table 1. Coordinates of the attaching points (in meters) in their local coordinate frames.

	x	y	z		x	y	z
$\mathbf{a}_1$	0.3000,	0.0000,	0.0000	$\mathbf{b}_1$	0.1000,	0.0000,	0.0000
$\mathbf{a}_2$	−0.1500,	0.2598,	0.0000	$\mathbf{b}_2$	−0.0500,	0.0866,	0.0000
$\mathbf{a}_3$	−0.1500,	−0.2598,	0.0000	$\mathbf{b}_3$	−0.0500,	−0.0866,	0.0000

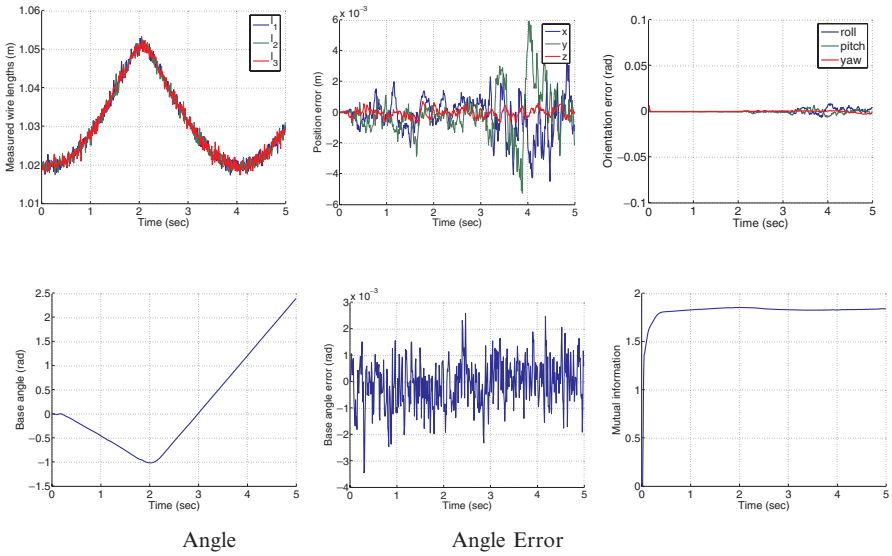

Figure 4. Wire tracking of pure rotations along an axis perpendicular to the base platform.

modeled with zero mean white additive Gaussian noise with 0.001 *rad* standard deviation. Figures 4(b) and 4(c) show the tracked object position and orientation recovery errors, respectively. The motion of the rotating base is depicted in Figures 4(d)-4(e), showing that commands for maximal platform rotation velocities are being selected from our mutual information metric (Figure 4(f)).

6.4 Compound Motions

In this last example, the tracked object moves back and forth in the three Cartesian components along a line from $(1, 1, 1)$ to $(2, 2, 2)$ meters, whilst rotating $\frac{\pi}{3}$ *rad* about its center in all raw, pitch and yaw components. This experiment shows that for compound motions it is more

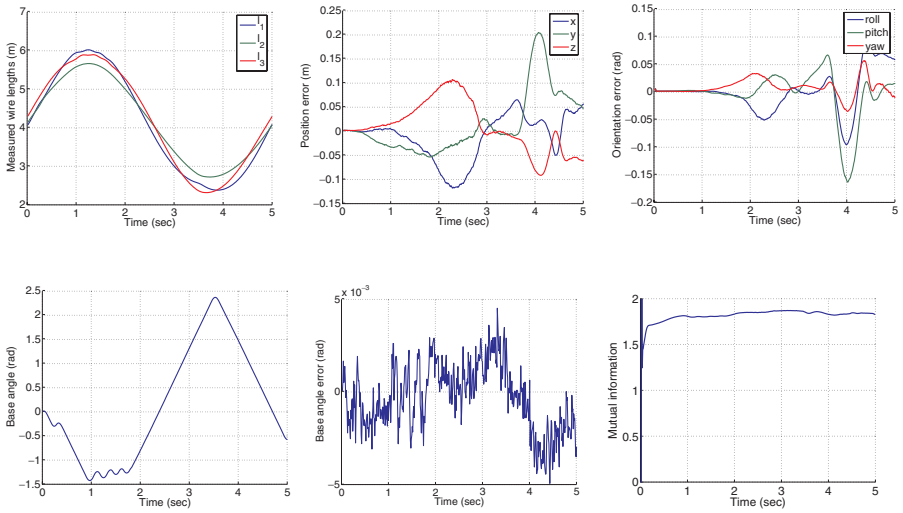

Figure 5. Wire tracking of compound motion.

difficult to disambiguate orientation error, while still doing a good job at tracking the correct object pose. Once more, the maximum base rotation speed was limited to $\frac{\pi}{5}$ rad/sec, and the limit for possible base acceleration command was set to 30 rad/sec^2. Figure 5(a) shows the evolution of wire length measurements for this example. The tracked object position and orientation errors is shown in Figures 5(b) and 5(c). The motion of the rotating base is depicted in Figures 5(d)-5(e). And, our mutual information action selection mechanism is shown in Figure 5(f).

7. Conclusion

An active sensing strategy for a wire tracking device has been presented. It has been shown how by allowing the sensor platform rotate about its center, a wider range of motions can be tracked by reducing the number of wires needed from 6 to 3. Moreover, platform rotation is performed so as to maximize the mutual information between poses and measurements, and at the same time, so as to prevent wire wrappings as far as possible.

Acknowledgements

J. Andrade-Cetto completed this work as a Juan de la Cierva Postdoctoral Fellow of the Spanish Ministry of Education and Science under project TIC2003-09291 and was also supported in part by projects DPI 2004-05414, and the EU PACO-PLUS project FP6-2004-IST-4-27657. F. Thomas was partially supported by the Spanish Ministry of Education and Science, project TIC2003-03396, and the Catalan Research Commission, through the Robotics and Control Group.

References

Bruynickx, H. (1999). Forward kinematics for hunt-primrose parallel manipulators. *Mechanism and Machine Theory*, 34:657–664.

Davison, A. (2005). Active search for real-time vision. In *Proceedings of the IEEE International Conference on Computer Vision*, pages 66–73, Beijing.

Ganovelli, F., Ponchio, F., and Rocchini, C. (2003). Fast tetrahedron-tetrahedron overlap algorithm. *ACM Journal of Graphics Tools*, 7(4).

Geng, Z.J. and Haynes, L.S. (1994). A 3-2-1 kinematic configuration of a Stewart platform and its application to six degree of freedom pose measurements. *Robotics and Computer-Integrated Manufacturing*, 11(1):23–34.

Griffis, M. and Duffy, J. (1989). A forward displacement analysis of a class of Stewart platforms. *Journal of Robotic Systems*, 6(6):703–720.

Hunt, K. and Primrose, E. (1993). Assembly configurations of some in-parallel-actuated manipulators. *Mechanism and Machine Theory*, 28(1):31–42.

Jeong, J., Kim, S., and Kwak, Y. (1999). Kinematics and workspace analysis of a parallel wire mechanism for measuring a robot pose. *Mechanism and Machine Theory*, 34(6):825–841.

MacKay, D.J.C. (1992). Information based objective functions for active data selection. *Neural Computation*, 4(4):589–603.

Merlet, J.P. (2006). *Parallel Robots*, volume 128 of *Solid Mechanics and its Applications*. Springer, New York, 2nd edition.

Nanua, P. and Waldron, K. (1990). Direct kinematics solution of a special parallel robot structure. In *Proceedings of the 8th CISM-IFToMM Symposium on Theory and Practice of Robots and Manipulators*, pages 134–142, Warsaw.

Nanua, P., Waldron, K., and Murthy, V. (1990). Direct kinematic solution of a Stewart platform. *IEEE Transactions on Robotics and Automation*, 6(4):438–444.

Parenti-Castelli, V. and Innocenti, C. (1990). Direct displacement analysis for some classes of spatial parallel machanisms. In *Proceedings of the 8th CISM-IFToMM Symposium on Theory and Practice of Robots and Manipulators*, pages 126–133, Warsaw.

Thomas, F., Ottaviano, E., Ros, L., and Ceccarelli, M. (2005). Performance analysis of a 3-2-1 pose estimation device. *IEEE Transactions on Robotics*, 21(3):288–297.

Vidal-Calleja, T., Davison, A., Andrade-Cetto, J., and Murray, D. (2006). Active control for single camera SLAM. In *Proceedings of the IEEE International Conference on Robotics and Automation*, Orlando. To appear.

THE CONTROL NUMBER AS INDEX FOR STEWART GOUGH PLATFORMS

G. Nawratil
Vienna University of Technology
Institute of Discrete Mathematics and Geometry
upuaut@controverse.net

Abstract Singular postures of Stewart Gough Platforms must be avoided because close to singularities they lose controllable degrees of freedom. Hence there is an interest in a distance measure between the instantaneous configuration and the nearest singularity. This article presents such a measure, which is invariant under Euclidean motions and similarities, which has a geometric meaning and can be computed in real-time. This measure ranging between 0 and 1 can serve as a performance index.

Keywords: Stewart Gough Platform, distance measure, perfomance index

1. Introduction

In *Section* 3 of this article we define a new measure, which allows to compare different postures of different nonredundant Stewart Gough Platforms (*SGP*s). Such a measure should assign to each configuration $\mathcal{K}$ a scalar $D(\mathcal{K})$ obeying the following six properties:

1. $D(\mathcal{K}) \geq 0$ for all $\mathcal{K}$ of the configuration space,
2. $D(\mathcal{K}) = 0$ if and only if $\mathcal{K}$ is singular,
3. $D(\mathcal{K})$ is invariant under Euclidean motions,
4. $D(\mathcal{K})$ is invariant under similarities,
5. $D(\mathcal{K})$ has a geometric meaning,
6. $D(\mathcal{K})$ is computable in real-time.

$\mathcal{K}$ is singular if and only if the six legs belong to a linear line complex (see Merlet, 1992) or, analytically seen, the determinant of the Jacobian

$$\mathcal{J}^T = \begin{pmatrix} \widehat{\mathbf{l}}_1 \|\mathbf{l}_1\|^{-1} & \vdots & \widehat{\mathbf{l}}_6 \|\mathbf{l}_6\|^{-1} \\ \mathbf{l}_1 \|\mathbf{l}_1\|^{-1} & \vdots & \mathbf{l}_6 \|\mathbf{l}_6\|^{-1} \end{pmatrix} \quad \text{with} \quad \begin{matrix} \mathbf{l}_i = \mathbf{P}_i - \mathbf{B}_i \quad \text{and} \\ \widehat{\mathbf{l}}_i = \mathbf{B}_i \times \mathbf{l}_i = \mathbf{P}_i \times \mathbf{l}_i \end{matrix} \tag{1}$$

vanishes, where $\mathbf{B}_i$ resp. $\mathbf{P}_i$ are the coordinates of the base resp. platform anchor points with respect to any fixed reference frame Σ_0 with origin O. Therefore the i^{th} row of $\mathcal{J}$ equals the normalized Plücker coordinates $\|\mathbf{l}_i\|^{-1}(\mathbf{l}_i, \widehat{\mathbf{l}}_i)$ of the carrier line $\mathcal{L}_i$ of the i^{th} leg oriented in the direction $\mathbf{B}_i\mathbf{P}_i$. We'll assume for the rest of this article that $\mathbf{B}_i \neq \mathbf{P}_i$ for $i = 1, .., 6$.

J. Lenarčič and B. Roth (eds.), Advances in Robot Kinematics, 15–22.

Kinematic meaning of the Jacobian. The velocity vector $\mathbf{v}(\mathbf{P}_i)$ of $\mathbf{P}_i$ due to the instantaneous screw (= twist) $\underline{\mathbf{q}} := (\mathbf{q}, \widehat{\mathbf{q}})$ of the platform Σ against Σ_0 can be decomposed in a component $\mathbf{v}_{\mathcal{L}}(\mathbf{P}_i)$ along the i^{th} leg $\mathcal{L}_i$ and in a component $\mathbf{v}_{\perp}(\mathbf{P}_i)$ orthogonal to it (see *Fig. 1*), thus

$$\mathbf{v}(\mathbf{P}_i) = \widehat{\mathbf{q}} + (\mathbf{q} \times \mathbf{P}_i) = \mathbf{v}_{\mathcal{L}}(\mathbf{P}_i) + \mathbf{v}_{\perp}(\mathbf{P}_i) \tag{2}$$

$$\text{with} \qquad \|\mathbf{v}_{\mathcal{L}}(\mathbf{P}_i)\| = \frac{\mathbf{l}_i}{\|\mathbf{l}_i\|} \cdot \mathbf{v}(\mathbf{P}_i) = \frac{\widehat{\mathbf{l}}_i}{\|\mathbf{l}_i\|} \cdot \mathbf{q} + \frac{\mathbf{l}_i}{\|\mathbf{l}_i\|} \cdot \widehat{\mathbf{q}} =: d_i. \tag{3}$$

Therefore the Jacobian $\mathcal{J}$ is the matrix of the linear mapping

$$\iota : \ \underline{\mathbf{q}} \mapsto \mathbf{d} = \mathcal{J}\,\underline{\mathbf{q}} \qquad \text{with} \qquad \mathbf{d} = (d_1, .., d_6)^T. \tag{4}$$

ι has at least a one-dimensional kernel ker_ι, if $\mathcal{K}$ is singular. Let $\underline{\mathbf{k}} \in ker_\iota$ and $\underline{\mathbf{k}} \neq \mathbf{o}$. Then also $\mu\underline{\mathbf{k}}$ with $\mu \in \mathbb{R}$ lies in ker_ι. Therefore we can say, that $\mathbf{v}(\mathbf{P}_i)$ can be arbitrarily large for vanishing translatory velocities in the six prismatic legs. The sole exeption is the case where $\mathbf{P}_i$ lies on the instantaneous screw axis (*isa*) and $\underline{\mathbf{k}}$ is an instantaneous rotation.

Review. In the following we analyze some of the in our opinion most important indices in view of the initially stated six properties.

The *manipulabilitiy* introduced by Yoshikawa, 1985 is not invariant under similarities, because for *SGP*s it equals $|det(\mathcal{J})|$. So Lee et al., 1998 used $|det(\mathcal{J})| \cdot |det(\mathcal{J})|_m^{-1}$ as index, where $|det(\mathcal{J})|_m$ denotes the maximum of $|det(\mathcal{J})|$ over the *SGP*'s configuration space. But the computation of $|det(\mathcal{J})|_m$ is a nonlinear task and was only done for planar *SGP*s with very special geometries. Only for these *SGP*s $|det(\mathcal{J})|_m$ can be interpreted geometrically as the volume of the framework.

Pottmann et al., 1998 introduced the concept of the *best fitting linear line complex* $\underline{\mathbf{c}}$ of $\mathcal{L}_1, .., \mathcal{L}_6$. The suggested index equals the square root of the minimum of $\sum d_i^2$ with respect to $\underline{\mathbf{c}}$ under the side condition $\mathbf{c}^T\mathbf{c} = 1$. The index is not invariant under similarities and it is not defined for instantaneous translations $\underline{\mathbf{c}}$. In order to close this gap, the authors proposed to minimize a further function, which yields a second value. But how should these two values be combined to a single number?

The *rigidity rate* introduced by Lang et al., 2001 is based on the idea, that a *SGP* at any position $\mathcal{K}$ permits a one-parametric self-motion within the group of Euclidean similarities $\mathcal{G}_7$. The angle $\varphi \in [0, \pi/2]$ between the tangent of the self-motion in $\mathcal{K}$ and the subgroup of Euclidean displacements serves as an index. But the choice of the invariant symmetric bilinear form in the tangent space of $\mathcal{G}_7$, which is necassary in order to define a measure in the sense of non-Euclidean geometry, is arbitrary. Although φ fulfills all six stated properties, its applicability is limited. This becomes manifest in the remark at the end of *Section* 5.

2. Preliminary Considerations

Now we take a closer look at the reciprocal of the *condition number* (cdn^{-1}) introduced by Salisbury and Craig, 1982, because it will be the starting point of our considerations. cdn^{-1} equals the ratio of the minimum $\widehat{\lambda}_-$ and the maximum $\widehat{\lambda}_+$ of the quadratic objective function

$$\widehat{\zeta}(\underline{\mathbf{q}}): \quad \underline{\mathbf{q}}^T \mathcal{I}_6 \, \underline{\mathbf{q}} = \omega^2 + \left[\widehat{\omega}^2 + \omega^2 \overline{Op}^2\right] \tag{5}$$

with p denoting the *isa*, ω the angular velocity and $\widehat{\omega}$ the translatory velocity of the screw $\underline{\mathbf{q}}$, under the quadratic side condition

$$\nu(\underline{\mathbf{q}}): \quad \mathbf{d}^T\mathbf{d} = \underline{\mathbf{q}}^T \mathcal{N} \, \underline{\mathbf{q}} = 1 \qquad \text{with} \qquad \mathcal{N} = \mathcal{J}^T\mathcal{J}. \tag{6}$$

Due to the linearity of ι in (4) the screw $\mu\underline{\mathbf{q}}$ corresponds to the μ-fold translatory velocity d_i in the six prismatic legs, and therefore the side condition $\nu(\underline{\mathbf{q}})$ is well defined. The weak point of this index is the objective function for the following reasons. First, it is not invariant under translations, because $\widehat{\zeta}(\underline{\mathbf{q}})$ depends on the choice of O. In practice O is not selected arbitrarily, but placed in the tool center point. But the real problem, which causes the variance of cdn^{-1} under similarities, occurs from the dimensional inhomogeneity of $\widehat{\zeta}(\underline{\mathbf{q}})$. To overcome this deficiency, different concepts (*e.g. characteristic length*, see Zanganeh and Angeles, 1997) were introduced, but they still weight the ratio of length and angle in a more or less arbitrary way. The inhomogeneity and the lacking invariance of $\widehat{\zeta}(\underline{\mathbf{q}})$ do not allow a geometric interpretetion of cdn^{-1} and they question its adequacy as a performance index for *SGP*s.

The conslusion of this considerations is, that we have to look for a new objective function $\zeta(\underline{\mathbf{q}})$ which meets our initially stated demands. But we want to add a further argument, which has the following motivation: The cdn^{-1} as well as the *manipulability* are also used to optimize the design of *SGP*s. But these two indices do not depend on the choice of $\mathbf{B}_i$ and $\mathbf{P}_i$ on $\mathcal{L}_i$ as long as $\mathbf{B}_i \neq \mathbf{P}_i$. Thus we require:

7. $D(\mathcal{K})$ depends on the geometry of the *SGP*, not only on the carrier lines $\mathcal{L}_1$,...,$\mathcal{L}_6$ of the six legs.

Pottmann et al., 1998 also presented a modified version of his method, namely the *line segment method*, which statisfies the 7^{th} demand but does not eliminate the other weak points. The *rigidity rate* is independent of the choice of the base anchor points and so it only takes the geometry of the platform into consideration. This raises the following problem: If we change the viewpoint and consider Σ as the unmoved base and Σ_0 as platform, we get another index for the same *SGP* configuration. So the instantaneous *rigidity* of the *SGP* depends on the viewpoint which is dissatisfying.

2.1 Uncontrollable Postures of *SGP*s

In practice configurations must be avoided, where minor variations of the leg lengths have uncontrollable large effects on the instantaneous displacement of the platform Σ. But how should the quantity of effects be measured in relation to the variation of the leg lengths? The boarder case of this uncontrollability is, if there exists an infinitesimal motion of Σ while all actuators are locked. In such a singular position the velocities of the platform points can be arbitrarily large, and therefore the posture is uncontrollable. The question is, which measurable parameter of the *SGP* indicates the circumstance of uncontrollability in a natural way and has a geometric meaning for the manipulator.

3. Idea and Definition of the Control Number *ctn*

Let's assume there is instantaneously a minor variation of the six leg lenghts and the *SGP* is not singular. So there exists a unique screw $\underline{\mathbf{q}}$ which describes the motion of Σ against Σ_0 according to (4). To meet our 7^{th} property, we consider the velocity $\mathbf{v}(\mathbf{P}_i)$ of $\mathbf{P}_i$ with respect to $\underline{\mathbf{q}}$. We are not interested in the instantaneous displacements of $\mathbf{P}_i$ in direction of the leg, because the leg length is an active joint which can be controlled totally. Therefore only the component $\mathbf{v}_\perp(\mathbf{P}_i)$ can be an indicator of uncontrollability. But $\mathbf{v}_\perp(\mathbf{P}_i)$ is no mechanical parameter of a *SGP* and therefore we look at the angular velociety $\omega_{\mathcal{B}_i}$ of the i^{th} passive base joint. This $\omega_{\mathcal{B}_i}$ is defined as (see Fig. 1)

$$\omega_{\mathcal{B}_i} := \frac{\|\mathbf{v}_\perp(\mathbf{P}_i)\|}{\|\mathbf{l}_i\|} \quad \Rightarrow \quad {\omega_{\mathcal{B}_i}}^2 = \frac{\|\mathbf{v}_\perp(\mathbf{P}_i)\|^2}{\|\mathbf{l}_i\|^2} = \frac{\|\mathbf{v}(\mathbf{P}_i)\|^2 - d_i^2}{\|\mathbf{l}_i\|^2} \tag{7}$$

according to (2) and (3) and so it is proportional to $\|\mathbf{v}_\perp(\mathbf{P}_i)\|$. But there also exists angular velocities $\omega_{\mathcal{P}_i}$ in the passive platform joints, which are defined analogously. The sole difference is that we regard the inverse motion of $\underline{\mathbf{q}}$. So we have to substitute $\mathbf{B}_i$ for $\mathbf{P}_i$ and $-\underline{\mathbf{q}}$ for $\underline{\mathbf{q}}$ in (2), (3) and (7). Obviously ${\omega_{\mathcal{B}_i}}^2$ and ${\omega_{\mathcal{P}_i}}^2$ are quadratic forms with the coordinates of $\underline{\mathbf{q}}$ as unkowns. Therefore we can rewrite them as

$${\omega_{\mathcal{B}_i}}^2 = \underline{\mathbf{q}}^T \mathcal{W}_{\mathcal{B}_i} \underline{\mathbf{q}} \quad \text{and} \quad {\omega_{\mathcal{P}_i}}^2 = \underline{\mathbf{q}}^T \mathcal{W}_{\mathcal{P}_i} \underline{\mathbf{q}}, \tag{8}$$

where $\mathcal{W}_{\mathcal{B}_i}$ and $\mathcal{W}_{\mathcal{P}_i}$ are symmetric 6×6 matrices.

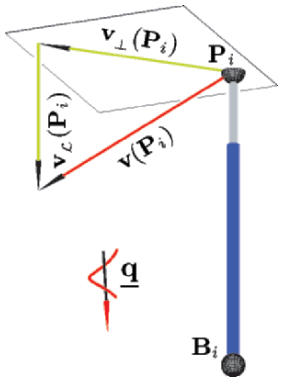

Figure 1. Defining $\omega_{\mathcal{B}_i}$

Now we define the new objective function $\zeta(\underline{\mathbf{q}})$ as

$$\zeta(\underline{\mathbf{q}}) = \sum_{i=1}^{6} {\omega_{\mathcal{B}_i}}^2 + {\omega_{\mathcal{P}_i}}^2 = \underline{\mathbf{q}}^T \mathcal{Z}\, \underline{\mathbf{q}} \quad \text{with} \quad \mathcal{Z} = \sum_{i=1}^{6} \mathcal{W}_{\mathcal{B}_i} + \mathcal{W}_{\mathcal{P}_i}. \tag{9}$$

Definition 1. *The control number of a SGP configuration $\mathcal{K}$ is defined as*

$$ctn(\mathcal{K}) := +\sqrt{\lambda_- / \lambda_+} \quad \text{with} \quad ctn(\mathcal{K}) \in [0,1]\,, \tag{10}$$

where λ_- resp. λ_+ is the minimum resp. maximum of the objective function $\zeta(\underline{\mathbf{q}})$ in (9) *under the side condition $\nu(\underline{\mathbf{q}})$ in* (6)*. $ctn(\mathcal{K}) = 0$ characterizes a singular configuration and a value of* 1 *an optimal one.*

4. Computation and Well-definedness of *ctn*

We solve the optimization problem in order to compute λ_- resp. λ_+ by introducing a Lagrange multiplier λ. Then the approach simplifies in consideration of $\nabla\zeta = 2\,\mathcal{Z}\,\underline{\mathbf{q}}$ and $\nabla\nu = 2\,\mathcal{N}\,\underline{\mathbf{q}}$, to the general eigenvalue problem $(\mathcal{Z} - \lambda\,\mathcal{N})\,\underline{\mathbf{q}} = \mathbf{o}$. This system of linear equations has a nontrivial solution, if and only if $|\mathcal{Z} - \lambda\,\mathcal{N}| = 0$. The degree of the characteristic polynomial in λ corresponds with $rank(\mathcal{J})$ because of $\mathcal{N} = \mathcal{J}^T\mathcal{J}$. Every general eigenvalue λ_i is linked with an general eigenvector $\underline{\mathbf{e}}_i$. The smallest λ_- and the largest λ_+ are the wanted extreme magnitudes because of

$$\mathcal{Z}\,\underline{\mathbf{e}}_i = \lambda_i\,\mathcal{N}\,\underline{\mathbf{e}}_i \quad \text{and} \quad \underline{\mathbf{e}}_i^T\,\mathcal{N}\,\underline{\mathbf{e}}_i = 1 \quad \Rightarrow \quad \zeta(\underline{\mathbf{e}}_i) = \lambda_i. \tag{11}$$

Theorem 1. *λ_- and λ_+ of* Def. *1 are the extreme general eingenvalues of $\mathcal{Z}$ with respect to $\mathcal{N}$. All roots λ_i of the characteristic polynomial $|\mathcal{Z} - \lambda\,\mathcal{N}| = 0$ are positive if and only if $rank(\mathcal{J}) = 6$.*

Proof: According to Hestenes, 1975 all λ_i's are real. Due to (11) all λ_i's are nonnegative. If $\underline{\mathbf{q}}$ is no pure translation ($\mathbf{q} \neq \mathbf{o}$), then all angular velocities in the passive joints would vanish if and only if the 12 anchor point lie on the *isa*. But such a configuration yields $rank(\mathcal{J}) = 1$. In the case of a pure translation, there would be no angular velocities in the passive joints if and only if the legs are parallel to the direction of the translation. But such a configuration yields $rank(\mathcal{J}) \leq 3$. □

Theorem 2. *The number of roots λ_i of the characteristic polynomial $|\mathcal{Z} - \lambda\,\mathcal{N}| = 0$ dropping to infinity equals the defect($\mathcal{J}$).*

Proof: All screws $\pm\mu\underline{\mathbf{q}} \in ker_\iota$ with $\mu \in \mathbb{R}$ cause arbitrarily large velocities $\mathbf{v}(\mathbf{P}_i) = \mathbf{v}_\perp(\mathbf{P}_i)$ resp. $\mathbf{v}(\mathbf{B}_i) = \mathbf{v}_\perp(\mathbf{B}_i)$ and therefore arbitrarily large $\omega_{\mathcal{B}_i}$ resp. $\omega_{\mathcal{P}_i}$. The proof follows by carring out $lim_{\mu\to\infty}$ and (11). □

Due to *Theorem 1* and *2* the *control number* is well defined. Therefore all initially stated seven properties are obviously fulfilled.

Remark. It does not make sense to define $\zeta(\underline{\mathbf{q}})$ only as $\sum {\omega_{\mathcal{B}_i}}^2$ (resp. $\sum {\omega_{\mathcal{P}_i}}^2$) for following reasons: First, the index would not fulfill our 7^{th} demand for the same reason as the *rigidity rate*. Second, the index would not fulfill our 2^{nd} demand, because there exist nonsingular *SGP* configurations, where the $\mathcal{L}_i$'s are the path tangents of $\mathbf{P}_i$ (resp. $\mathbf{B}_i$) with regard to $\underline{\mathbf{q}}$. Consequently we get $\zeta(\underline{\mathbf{q}}) = 0$ and the index would equal 0.

4.1 Instantaneous Motion near Singularities

According to Wolf and Shoham, 2003 the closest path normal complex of a helical motion (rotations and translations included) to $\mathcal{L}_1, .., \mathcal{L}_6$, described by its axis and pitch, provides additional information on the *SGP*'s instantaneous motion and understanding of the type of singularity when the *SGP* is at, or in the neighborhood of, a singular configuration. Since the *ctn* is a performance index as well as a distance measure, a small *ctn* indicates the closeness to a singularity. Due to *Theorem 2* and the continuity of the polynomial functions $|\mathcal{Z} - \lambda\mathcal{N}| = 0$, which arise if we move towards a singular position, we can say that the closest linear complex to $\mathcal{L}_1, .., \mathcal{L}_6$ equals the path normal complex of $\underline{\mathbf{e}}_+$ according to (11). Therefore this method additionally brings about a kind of best approximating linear line complex in the neighbourhood of singularities, and the calculation needs no case analysis like Pottmann's method.

5. Final Example

We consider a two parametric set $\mathcal{S}_\mathcal{K}$ of configurations $\mathcal{K}$, given by

$$\mathbf{B}_i = (\cos\alpha_i, \sin\alpha_i, -h)^T \quad \text{and} \quad \mathbf{P}_i = (\cos\beta_i, \sin\beta_i, h)^T \quad \text{with}$$

$$\alpha_1 = \beta_2 - \frac{\pi}{3} = -\alpha \qquad \alpha_3 = \beta_4 - \frac{\pi}{3} = \frac{2\pi}{3} - \alpha \qquad \alpha_5 = \beta_4 - \frac{\pi}{3} = \frac{4\pi}{3} - \alpha$$

$$\alpha_2 = \beta_1 + \frac{\pi}{3} = \alpha \qquad \alpha_4 = \beta_3 + \frac{\pi}{3} = \frac{2\pi}{3} + \alpha \qquad \alpha_6 = \beta_5 + \frac{\pi}{3} = \frac{4\pi}{3} + \alpha$$

where $\alpha \in [0, \frac{\pi}{6}]$ denotes the *design parameter* and $h \in \mathbb{R}^+$ the *posture parameter* of the *SGP*. All $\mathcal{K} \in \mathcal{S}_\mathcal{K}$ with $\alpha \neq \frac{\pi}{6}$ and $h \notin \{0, \infty\}$ are nonsingular. We study this example, because such manipulators are very relevant in practice as flight simulators. The matrix $\mathcal{Z} - \lambda\mathcal{N}$ can be manipulated by elementary row and column operations to the diagonal matrix $diag(\Delta_1, .., \Delta_6)$. Therefore the eigenvalues λ_i can be computed explicitly using $\Delta_i = 0$, whereas $\lambda_1 = \lambda_2$ and $\lambda_4 = \lambda_5$. $\mathcal{K}_+$ given by

$$h_+ = \frac{\gamma}{4} \approx 0.4, \quad \alpha_+ = -\arctan\left(\frac{\sqrt{5}\gamma - \sqrt{15}}{5}\right) \approx 4^\circ, \quad \gamma = \sqrt{2\sqrt{5} - 2} \quad (12)$$

has the maximal *ctn* of all $\mathcal{K} \in \mathcal{S}_\mathcal{K}$(see Figs. 2 and 3). For $\mathcal{K}_+$ determined by $\lambda_{1,2} = \lambda_{4,5}$ and $\lambda_3 = \lambda_6$ we get $ctn(\mathcal{K}_+) = \sqrt{2\sqrt{5} - 4} \approx 0.687$.

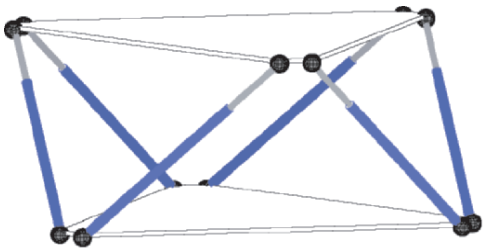

Figure 2. Axonometry of $\mathcal{K}_+$

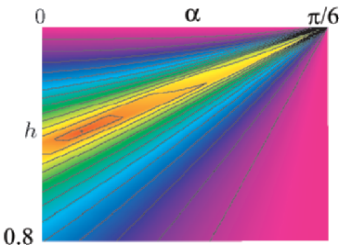

Figure 3. Contours of $ctn(\mathcal{S}_\mathcal{K})$

The *SGP* with α_+ also makes sense from the practical point of view, because contrary to the often propagandized 3-3 octahedral manipulator ($\alpha = 0$) no anchor points coincide. But coinciding anchor points are hard to manufacture. Therefore we take a closer look to this *SGP*. Fig. 5 illustrates the graph of *ctn* depending on h. Fig. 4 shows the contour lines of *ctn* when the platform is translated away from the central location parallel to the base plane. The difference between two neighbouring contour lines is 0.05, where the highest has the value of 0.65. Figs. 6, 7 and 8 illustrate the graphs of *ctn* dependig on the angle ω of the rotation of Σ about an axis parallel to x, z or y, respectively, through $(0, 0, h_+)$.

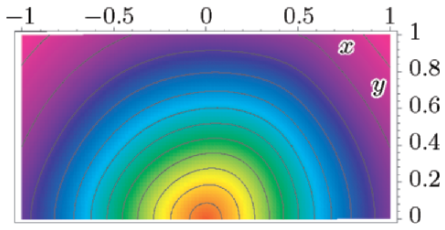

Figure 4. Translation of Σ in $z = h_+$

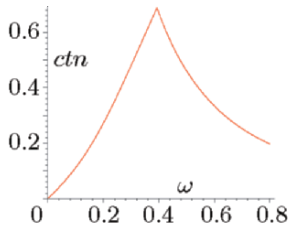

Figure 5. Variation of h

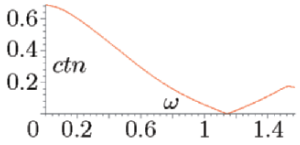

Figure 6. Rotation about a x-parallel

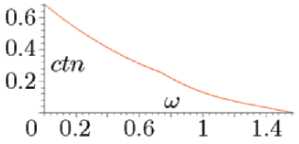

Figure 7. Rotation about a z-parallel

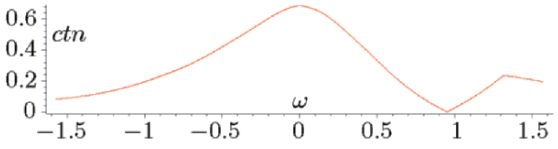

Figure 8. Rotation about a y-parallel

Remark. The *rigidity rate* of all nonsingular configurations of this set $\mathcal{S}_\mathcal{K}$ is constant at the maximal value of $\pi/2$. Only in singular positions it drops to zero. So if we approach a singularity of $\mathcal{S}_\mathcal{K}$ the value of the *rigidity rate* is constant $\pi/2$. Therefore this index is not recommendable for comparing different postures of different *SGP*s.

6. Conclusion

The presented index, called *control number* (*ctn*), allows to compare different postures of different *SGP*s, because it obeys the initially stated seven conditions. Therefore *ctn* can serve as a performance index as well as a distance measure to the closest singularity. This concept can also be modified for redundant *SGP*s and 3 dof RPR manipulators.

An article about optimal configurations $\mathcal{K}$ with $ctn(\mathcal{K}) = 1$ is in preparation. It can be proved, that such configurations do exist. New performance indices for 6R robots have been presented in Nawratil, 2006.

Acknowledgement

This is part of the author's PhD-thesis. The author expresses his sincere thanks to his supervisor Prof. H. Stachel for continuous support.

References

Hestenes, M.R. (1975), *Optimization theory*, New York, A Wiley publication.

Lang, J., Mick, S., and Röschel, O. (2001), The Rigidity Rate of Positions of Stewart-Gough Platforms, *Journal for Geometry and Graphics*, vol. 5, no. 2, pp. 121–132.

Lee, J., Duffy, J., and Hunt, H. (1998), A Practical Quality Index Based on the Octahedral Manipulator, *Int. J. of Robotics Research*, vol. 17, no. 10, pp. 1081–1090.

Merlet, J.-P. (1992), Singular Configurations of Parallel Manipulators and Grassmann Geometry, *Int. J. of Robotics Research*, vol. 8, no. 5, pp. 45–56.

Nawratil, G. (2006), New Performance Indices for 6R Robot Postures, *CD-Proc. of the 1st EuCoMeS* (M. Husty, H.P. Schröcker, eds.), 12pp., Obergurgl, Austria.

Pottmann, H., Peternell, M., and Ravani, B. (1998), Approximation in line space: applications in robot kinematics and surface reconstruction, *Advances in Robot Kinematics: Analysis & Control* (J. Lenarcic, M. Husty, eds.), pp. 403–412, Kluwer.

Salisbury, J.K. and Craig, J.J. (1982), Articulated Hands: Force Control and Kinematic Issues, *Int. J. of Robotics Research*, vol. 1, no. 1, pp. 4–17.

Wolf, A., and Shoham, M. (2003), Investigations of Parallel Manipulators Using Linear Complex Approximation, *Journal of Mechanical Design*, vol. 125, pp. 564–572.

Yoshikawa, T. (1985), Manipulability of Robotic Mechanisms, *Int. J. of Robotics Research*, vol. 4, no. 2, pp. 3–9.

Zanganeh, K.E., and Angeles, J. (1997), Kinematic Isotropy and the Optimum Design of Parallel Manipulators, *Int. J. of Robotics Research*, vol. 16, no. 2, pp. 185–197.

DETERMINING THE 3×3 ROTATION MATRICES THAT SATISFY THREE LINEAR EQUATIONS IN THE DIRECTION COSINES

Carlo Innocenti
DIMeC – University of Modena and Reggio Emilia – Italy
carlo.innocenti@unimore.it

Davide Paganelli
DIEM – University of Bologna – Italy
davide.paganelli@mail.ing.unibo.it

Abstract The paper presents a solution to all the spatial kinematics problems that require determination of the 3×3 rotation matrices whose nine direction cosines satisfy three linear equations. After having expressed the direction cosines in terms of the Rodrigues parameters, a classical elimination method to solve three quadratic equations in three unknowns is here extended to include all solutions at infinity. Therefore no admissible 3×3 rotation matrix is neglected even though it corresponds to a singularity of the Rodrigues parametrization of orientation. A case study exemplifies the new method.

Keywords: Rotation matrix, direction cosines, Rodrigues parameters

1. Introduction

A whole class of problems of spatial kinematics can be solved by determining all 3×3 rotation matrices whose nine direction cosines obey three given linear equations. Owing to the orthogonality constraints among the direction cosines, these problems are equivalent to solving a set of nine equations: three linear and six quadratic.

Rather than tackling right away the solution of such an equation set, it is computationally more efficient to replace, in each equation, all unknown direction cosines by their expressions in terms of the Rodrigues parameters. In doing so, all orthogonality constraints are implicitly fulfilled, whereas the former linear equations in the direction cosines turn into second-order equations in the Rodrigues parameters.

Unfortunately, the known algebraic elimination algorithms that solve a set of three quadratic equations – such as the Sylvester method – are

J. Lenarčič and B. Roth (eds.), Advances in Robot Kinematics, 23–32.

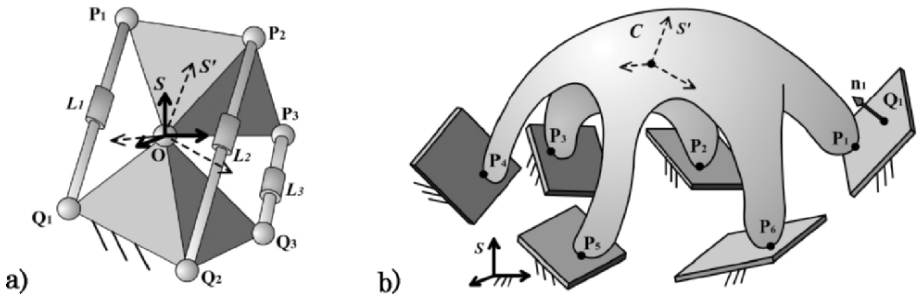

Figure 1. a) Fully-parallel spherical wrist;
b) rigid body supported at six points by six planes.

not always suitable to the case at hand. The reason is twofold: i) they are unable to find real solutions at infinity, which are here of interest too because infinite real Rodrigues parameters are associated to finite real 3×3 rotation matrices, and ii) in case one or more solutions at infinity exist, these algorithms might fail to determine even the finite solutions.

After exemplifying the recurrence in kinematics of the addressed three-equation set in the direction cosines, this paper presents an original procedure to find all real solutions of the equation set. The proposed procedure – based on the Rodrigues parametrization of orientation and presented with reference to the Sylvester algebraic elimination algorithm – is able to identify all real solutions in terms of Rodrigues parameters, both finite and at infinity. Therefore its adoption guarantees that no real 3×3 rotation matrix compatible with the original three linear equations is neglected.

A numerical example shows application of the proposed computational procedure to a case study.

2. The Relevance to Kinematics

A linear three-equation set in nine direction cosines is the unifying factor behind a number of seemingly different kinematics problems, such as those epitomized in Fig. 1. Although these problems have already been solved in the literature by *ad-hoc* algorithms, they could be also worked out by determining all 3×3 rotation matrices satisfying three linear conditions in the direction cosines. In this respect, the procedure proposed in this paper is a viable alternative to already-known solving methods.

Figure 1a shows a fully-parallel spherical wrist, whose direct kinematics aims at determining all possible orientations of the moving platform

for a given set of actuator lengths (Innocenti and Parenti-Castelli, 1993). If $\mathbf{v}_i$ and $\mathbf{w}_i$ are the coordinate vectors of points Q_i and P_i relative to the fixed (S) and movable (S') reference frames respectively, and $\mathbf{R}$ is the rotation matrix for transformation of coordinates from S' to S, then – by applying Carnot's theorem to triangle OQ_iP_i – the compatibility equations can be written as

$$\mathbf{v}_i^T \mathbf{v}_i + \mathbf{w}_i^T \mathbf{w}_i - 2\,\mathbf{v}_i^T \mathbf{R}\,\mathbf{w}_i = L_i^2 \quad (i = 1,..,3) \tag{1}$$

These equations are linear in the (unknown) elements of matrix $\mathbf{R}$.

Figure 1b refers to another kinematics problem, which consists in finding any possible positions of a rigid body C supported at six given points P_i (i=1,..,6) by six fixed planes (Innocenti, 1994; Wampler, 2006). The coordinate vector $\mathbf{w}_i$ of each point P_i is known with respect to a reference frame S' attached to C. Each supporting plane is defined with respect to the fixed frame S by the coordinate vector $\mathbf{v}_i$ of a point Q_i lying on the plane, together with the components in S of a unit vector $\mathbf{n}_i$ orthogonal to the plane. The unknown position of C with respect to S is parametrized through the coordinate vector $\mathbf{s}$ of the origin of S' with respect to S, together with the rotation matrix $\mathbf{R}$ for transformation of coordinates from S' to S. The compatibility equations can be written as:

$$\mathbf{n}_i^T \left[(\mathbf{s} + \mathbf{R}\,\mathbf{w}_i) - \mathbf{v}_i \right] = 0 \qquad (i = 1,..,6) \tag{2}$$

They are linear in both the elements of $\mathbf{R}$ and the components of $\mathbf{s}$. If there exist three supporting planes not parallel to the same line, three of these equations can be linearly solved for the components of vector $\mathbf{s}$, and their expressions inserted into the remaining three equations. Therefore a linear three-equation set that has the nine direction cosines of matrix $\mathbf{R}$ as only unknowns is obtained once more.

Other kinematics problems susceptible of being reduced to the same linear formulation as the one just exemplified are traceable in Gosselin et al., 1994, Husain and Waldron, 1994, Wohlhart, 1994, Callegari et al., 2004.

3. The Equations to be Solved

If r_{ij} $(i,j=1,2,3)$ is the ij^{th} element (direction cosine) of a rotation matrix $\mathbf{R}$ and $a_{ij,k}$, b_k $(i,j,k=1,..,3)$ are known quantities, the set of three linear equations that has to be solved for r_{ij} $(i,j=1,2,3)$ is

$$\sum_{i,j=1,..,3} a_{ij,k}\, r_{ij} = b_k \qquad (k = 1,..,3) \tag{3}$$

The expressions of r_{ij} in terms of the vector of Rodrigues parameters $\mathbf{p} = (p_1,p_2,p_3)^{\mathrm{T}}$ are concisely given by (Bottema and Roth, 1979)

$$\mathbf{R} = \frac{(1 - \mathbf{p}^{\mathrm{T}}\mathbf{p})\mathbf{I} + 2\tilde{\mathbf{p}} + 2\mathbf{p}\,\mathbf{p}^{\mathrm{T}}}{1 + \mathbf{p}^{\mathrm{T}}\mathbf{p}} \tag{4}$$

where $\tilde{\mathbf{p}}$ is the skew-symmetric matrix associated with vector $\mathbf{p}$, i.e., $\tilde{\mathbf{p}}\,\mathbf{e} = \mathbf{p} \times \mathbf{e}$ for any three-component vector $\mathbf{e}$. As is known, the vector $\mathbf{p}$ of Rodrigues parameters corresponds to a finite rotation of amplitude $\theta = 2\tan^{-1}\|\mathbf{p}\|$ about the axis defined by unit vector $\mathbf{u} = \mathbf{p}/\|\mathbf{p}\|$.

Unfortunately, the Rodrigues parametrization of orientation is singular for any half-a-turn rotation ($\theta = \pi$ rad) about any line because, in this instance, at least one of the components of $\mathbf{p}$ approaches infinity.

By considering Eq. (4), Eq. (3) can be re-written as:

$$\frac{1}{1+p_1^2+p_2^2+p_3^2}\left(\sum_{i,j=1,..,3;\, i\le j} A_{ij,k}\, p_i p_j + \sum_{i=1,..,3} B_{i,k}\, p_i + C_k\right) = 0 \qquad (k = 1,..,3) \tag{5}$$

where quantities $A_{ij,k}$, $B_{i,k}$, and C_k (i,j,k = 1,..,3; i ≤ j) are known because dependent on the given quantities $a_{ij,k}$ and b_k only.

Because the denominator of Eq. (5) does not vanish for any real vector $\mathbf{p}$, if $\mathbf{p}$ does not approach infinity Eq. (5) can be simplified as follows

$$\sum_{i,j=1,..,3;\, i\le j} A_{ij,k}\, p_i p_j + \sum_{i=1,..,3} B_{i,k}\, p_i + C_k = 0 \qquad (k = 1,..,3) \tag{6}$$

Conversely, in case the denominator of Eq. (5) approaches infinity, so does at least one of the components of $\mathbf{p}$. If both the numerator and the denominator of Eq. (5) are homogenized by replacing p_i with expression x_i/x_0 (i = 1,..,3), and subsequently multiplied by x_0^2, the resulting denominator is definitely different from zero (the real quantities x_0, x_1, x_2, and x_3 cannot vanish simultaneously). Finally, for $x_0 = 0$ (which means that at least one Rodrigues parameter approaches infinity), Eq. (5) becomes

$$\sum_{i,j=1,..,3;\, i\le j} A_{ij,k}\, x_i x_j = 0 \qquad (k = 1,..,3) \tag{7}$$

This is a set of three homogeneous quadratic equations in three unknowns, namely, the components of vector $\mathbf{x} = (x_1, x_2, x_3)^T$.

If the set of the non-vanishing vectors that satisfy Eq. (7) is partitioned into equivalence classes so that two solution vectors parallel one to the other belong to the same class, then each class corresponds to a vector $\mathbf{p}$ of Rodrigues parameters which satisfies Eq. (5) and has infinite magnitude.

Finding all real solutions of Eq. (5) – both finite and at infinity – has been thus reduced to determining all real finite solutions of Eq. (6), together with all equivalence classes of real solutions of Eq. (7). This implies that all real solutions of Eq. (6) – including those at infinity – need to be computed. Bezout's theorem (Semple and Roth, 1949) ensures that the maximum number of these solutions is eight.

4. The Solving Procedure

As will be proven further on, the existence of solutions at infinity might affect the search for the finite solutions. It is therefore convenient to compute the solutions at infinity first.

The Appendix at the end of the paper briefly summarizes the mathematical tools that will be taken advantage of in this section.

4.1 Solutions at Infinity

The solutions at infinity, if existent, can be found by identifying Eq. (7) with Eq. (1-A) of the Appendix. For the case at hand, Eq. (3-A) becomes

$$\mathbf{M}\begin{pmatrix} x_1^2 & x_2^2 & x_3^2 & x_1x_2 & x_1x_3 & x_2x_3 \end{pmatrix}^T = \mathbf{0} \tag{8}$$

where $\mathbf{M}$ is a 6×6 matrix that depends on coefficients $A_{ij,k}$ of Eq. (7) only.

In case the determinant of $\mathbf{M}$ is different from zero, there is only the trivial solution for Eq. (7), and no solution at infinity exists for Eq. (6).

Conversely, if the determinant of $\mathbf{M}$ vanishes, Eq. (7) has non-vanishing solutions. The number of equivalence classes of these solutions matches the number of solutions at infinity for Eq. (6). Determination of all solutions of Eq. (7) poses no hurdles and will not be detailed in this paper. Suffices it to say that, in the worst possible scenario, the classes of equivalence for the solutions of Eq. (7) can be found by solving a set of two quadratic equations in two unknowns.

4.2 Finite Solutions

In most cases, the finite solutions of Eq. (6) can be determined through the procedure described by Roth, 1993, and here briefly summarized. If (α,β,γ) is a permutation of indices (1,2,3), two of the three unknowns, say p_α and p_β, are first replaced in Eq. (6) by quantities y_α/y_0 and y_β/y_0. Following multiplication by y_0^2, the ensuing equation set is obtained:

$$\sum_{i,j=\alpha \text{ or } \beta;\, i\le j} A_{ij,k}\, y_i y_j + \sum_{i=\alpha \text{ or } \beta} \left[A_{\min(i,\gamma)\max(i,\gamma),k}\, p_\gamma + B_{i,k} \right] y_i y_0 + \left(A_{\gamma\gamma,k}\, p_\gamma^2 + B_{\gamma,k}\, p_\gamma + C_k \right) y_0^2 = 0 \qquad (k=1,..,3) \tag{9}$$

which is homogeneous with respect to unknowns y_0, y_α, and y_β.

If a triplet of values for p_α, p_β, and p_γ fulfils Eq. (6), Eq. (9) must be satisfied by the same value of p_γ together with a non-vanishing triplet of values for y_0, y_α, and y_β. By also taking into account the dependence on p_γ of the coefficients of the homogeneous system in Eq. (9), the solvability condition for Eq. (9) that corresponds to Eq. (3-A) turns into

$$\mathbf{N}(p_\gamma) \begin{pmatrix} y_0^2 & y_\alpha^2 & y_\beta^2 & y_0 y_\alpha & y_0 y_\beta & y_\alpha y_\beta \end{pmatrix}^T = \mathbf{0} \tag{10}$$

The solution of this linear set is meaningful only if the triplet (y_0, y_α, y_β) does not vanish, i.e., if the following condition is satisfied (see Eq. (4-A))

$$\det \mathbf{N}(p_\gamma) = 0 \tag{11}$$

This univariate polynomial equation in p_γ has degree not greater than eight (Roth, 1993). It is the outcome of elimination of unknowns p_α and p_β from Eq. (6). For every root of Eq. (11), the corresponding values of p_α and p_β can be easily found by Eq. (10) through linear determination of a non-vanishing triplet (y_0, y_α, y_β). Thus far is the outline of the procedure that has been presented – without investigating its singularities – in Roth, 1993.

It is worth noting that Eq. (11) is unable to yield solutions at infinity. Things keep manageable if an infinite p_γ satisfies Eq. (5) for some values of p_α and p_β, as Eq. (11) has a degree lower than eight and its roots convey information on finite solutions only. Regrettably, should an infinite solution to Eq. (5) exist for a finite p_γ (i.e., only p_α or p_β or both approach infinity) then Eq. (11) vanishes and the described elimination method becomes pointless.

This latter drawback can be explained by noticing that – for p_α or p_β approaching infinity – Eq. (10) should hold for $y_0 = 0$ and for some (not simultaneously vanishing) values of y_α and y_β, irrespective of the value of p_γ (the left-hand side of Eq. (9) does not depend on p_γ when $y_0 = 0$). Consequently, the determinant of 6×6 matrix $\mathbf{N}(p_\gamma)$ should vanish for any finite p_γ, which also means that Eq. (11) collapses into a useless identity.

If it is not possible to choose index γ so as to circumvent the just mentioned inconvenience, the classical elimination method is definitely unable to find any finite solution to Eq. (6). Even a different set of Rodrigues parameters consequent on a randomly-chosen offset rotation does not guarantee removal of the inconvenience.

4.3 Adding robustness

To overcome the drawback outlined at the end of the previous subsection, once the solutions at infinity of Eq. (6) have been computed (see subsection 4.1), and prior of attempting determination of the finite solutions, the vector $\mathbf{p}$ of Rodrigues parameters is replaced by vector $\mathbf{q} = (q_1, q_2, q_3)^{\mathrm{T}}$, related to the former by the ensuing relation

$$\mathbf{q} = \mathbf{L}\ \mathbf{p} \tag{12}$$

where $\mathbf{L}$ is a 3×3 non-singular constant matrix whose third row is not orthogonal to each non-vanishing vector $(x_1, x_2, x_3)^{\mathrm{T}}$ that solves Eq. (7).

By selecting $\gamma = 3$ and replacing q_1 and q_2 with quantities z_1/z_0 and z_2/z_0, Eq. (9) turns into

$$\begin{aligned} \sum_{i,j=1,2;\, i\le j} A'_{ij,k} z_i z_j + \sum_{i=1,2} \left(A'_{i3,k} q_3 + B'_{i,k} \right) z_i z_0 \\ + \left(A'_{33,k} q_3^2 + B'_{3,k} q_3 + C'_k \right) z_0^2 = 0 \qquad (k = 1,..,3) \end{aligned} \tag{13}$$

where coefficients $A'_{ij,k}$, $B'_{i,k}$, and C'_k, depend on the coefficients of Eq. (6) and on the chosen matrix $\mathbf{L}$. By applying the elimination procedure described in the previous subsection, the correspondent of Eq. (11) is

$$\det \mathbf{N}'(q_3) = 0 \tag{14}$$

which is a univariate polynomial equation in the unknown q_3.

Differently from Eq. (11), Eq. (14) does not lose trace of the finite solutions of Eq. (6), because any solution at infinity in terms of $\mathbf{p}$ involves a vector $\mathbf{q}$ whose third component, q_3, approaches infinity too.

5. Numerical Example

The ensuing linear equation set in the direction cosines is considered:

$$\begin{cases} r_{21} + r_{22} + r_{23} + 1 = 0 \\ r_{31} + r_{32} + r_{33} + 1 = 0 \\ r_{11} + r_{12} + r_{21} + 3r_{22} - r_{33} + 1 = 0 \end{cases}$$

In terms of homogenized Rodrigues parameters (x_1, x_2, x_3), these equations have three solutions at infinity, i.e., (1, −1,0), (0,1, −1), and (1,0,0). Since each Rodrigues parameter is finite for at least one solution at infinity, the change of variable in Eq. (12) is crucial. The third row of $\mathbf{L}$ is expressly chosen not normal to each of the three solutions at infinity. A possible expression for $\mathbf{L}$ is

$$\mathbf{L} = \begin{pmatrix} 1 & 0 & 0 \\ 0 & 1 & 0 \\ -1 & 1 & -1 \end{pmatrix}$$

Following the change of variables in Eq. (12), Eq. (14) yields

$$q_3^5 - 9q_3^4 + 54q_3^3 - 126q_3^2 + 57q_3 - 9 = 0$$

The only real root of this equation is $q_3 = 3$. Back-substitution of this root into the analogous of Eq. (10) completes determination of vector $\mathbf{q} = (-1,1,3)^T$. Next, Eq. (12) results into $\mathbf{p} = (-1,1,-1)^T$. The rotation matrices corresponding to the four real solutions – three at infinity in terms of Rodrigues parameters, and the other finite – are respectively (see Eq. 4):

$$\begin{pmatrix} 0 & -1 & 0 \\ -1 & 0 & 0 \\ 0 & 0 & -1 \end{pmatrix}, \quad \begin{pmatrix} -1 & 0 & 0 \\ 0 & 0 & -1 \\ 0 & -1 & 0 \end{pmatrix}, \quad \begin{pmatrix} 1 & 0 & 0 \\ 0 & -1 & 0 \\ 0 & 0 & -1 \end{pmatrix}, \quad \begin{pmatrix} 0 & 0 & 1 \\ -1 & 0 & 0 \\ 0 & -1 & 0 \end{pmatrix}.$$

6. Conclusions

This paper has presented a new procedure to find all 3×3 real rotation matrices satisfying three linear equations in the direction cosines. The proposed procedure is based on the Rodrigues parametrization of orientation and takes advantage of a classical algebraic elimination method in order to solve a set of three quadratic equations in three unknowns. To avoid neglecting any possible 3×3 rotation matrix, the classical

elimination method has been extended in the paper so that it keeps effective even in case one or more Rodrigues parameters approach infinity.

A numerical example has shown application of the proposed procedure to a case study.

References

Bottema, O., and Roth, B. (1979), *Theoretical Kinematics,* North-Holland Publishing Co., Amsterdam, NL.

Callegari M., Marzetti P., and Olivieri B. (2004), Kinematics of a Parallel Mechanism for the Generation of Spherical Motions, *On Advances in Robot Kinematics* (J. Lenarčič and C. Galletti (eds.)), Kluwer Academic Publishers, the Netherlands, pp. 449-458.

Gosselin, C.M., Sefrioui J., and Richard, M.J. (1994), On the Direct Kinematics of Spherical Three-Degree-of-Freedom Parallel Manipulators of General Architecture, *ASME Journal of Mechanical Design,* vol. 116, no. 2, pp. 594-598.

Husain, M., and Waldron, K.J. (1994), Direct Position Kinematics of the 3-1-1-1 Stewart Platforms, *ASME Journal of Mech. Design,* vol. 116, no. 4, pp. 1102-1107.

Innocenti, C. (1994), Direct Position Analysis in Analytical Form of the Parallel Manipulator That Features a Planar Platform Supported at Six Points by Six Planes, *Proc. of the 1994 Engineering Systems Design and Analysis Conference,* July 4-7, London, U.K., PD-Vol. 64-8.3, ASME, N.Y., pp. 803-808.

Innocenti, C., and Parenti-Castelli, V. (1993), Echelon Form Solution of Direct Kinematics for the General Fully-Parallel Spherical Wrist, *Mechanism and Machine Theory*, vol. 28, no. 4, pp. 553-561.

Roth, B. (1993), Computations in Kinematics, in *Computational Kinematics*, Kluwer Academic Publisher, the Netherlands, pp. 3-14.

Salmon, G. (1885), *Modern Higher Algebra,* Hodges, Figgis, and Co., Dublin.

Semple, J.G., and Roth, L. (1949), *Introduction to Algebraic Geometry,* Oxford University Press, London, UK.

Wampler, C.W. (2006), On a Rigid Body Subject to Point-Plane Constraints, *ASME Journal of Mechanical Design,* vol. 128, no. 1, pp. 151-158.

Wohlhart, K. (1994), Displacement Analysis of the General Spherical Stewart Platform, *Mechanism and Machine Theory,* vol. 29, no. 4, pp. 581-589.

Appendix

Let $\mathbf{f}(\mathbf{g})$ be an n-dimensional vector function that depends on an n-dimensional vector $\mathbf{g}$. If all components of $\mathbf{f}$ are homogeneous functions of the same degree in the components of $\mathbf{g}$, for any non-vanishing solution of the following homogenous system

$$\mathbf{f}(\mathbf{g}) = \mathbf{0} \tag{1-A}$$

the ensuing condition holds (Salmon, 1885)

$$\nabla D = \mathbf{0} \tag{2-A}$$

where D is the determinant of the Jacobian matrix of $\mathbf{f}$.

Sylvester (Salmon, 1885) has suggested the following procedure in order to assess whether a set of three second-order homogeneous equations in three unknowns has non-vanishing solutions:

i) compute the determinant D (which is a third-order homogeneous polynomial in the components g_i, i = 1,..,3, of vector $\mathbf{g}$);

ii) determine the gradient of D (its components are quadratic homogeneous polynomials in g_i, i = 1,..,3);

iii) consider Eqs. (1-A)-(2-A) as a set of six equations that are linear and homogeneous in the six monomials $g_i g_j$ (i,j = 1,..,3, i ≤ j)

$$\mathbf{H} \begin{pmatrix} g_1^2 & g_2^2 & g_3^2 & g_1 g_2 & g_1 g_3 & g_2 g_3 \end{pmatrix}^T = \mathbf{0} \tag{3-A}$$

where $\mathbf{H}$ is a 6×6 matrix whose elements are functions of the coefficients of Eq. (1-A).

The original set of three homogeneous quadratic equations has non-vanishing solutions if and only if the ensuing condition is satisfied

$$\det \mathbf{H} = 0 \tag{4-A}$$

A POLAR DECOMPOSITION BASED DISPLACEMENT METRIC FOR A FINITE REGION OF SE(N)

Pierre M. Larochelle
Robotics & Spatial Systems Lab
Department of Mechanical and Aerospace Engineering
Florida Institute of Technology
pierrel@fit.edu

Abstract An open research question is how to define a useful metric on SE(n) with respect to (1) the choice of coordinate frames and (2) the units used to measure linear and angular distances. A technique is presented for approximating elements of the special Euclidean group SE(n) with elements of the special orthogonal group SO(n+1). This technique is based on the polar decomposition (denoted as PD) of the homogeneous transform representation of the elements of SE(n). The embedding of the elements of SE(n) into SO(n+1) yields hyperdimensional rotations that approximate the rigid-body displacement. The bi-invariant metric on SO(n+1) is then used to measure the *distance* between any two spatial displacements. The result is a PD based metric on SE(n) that is left invariant. Such metrics have applications in motion synthesis, robot calibration, motion interpolation, and hybrid robot control.

Keywords: Displacement metrics, metrics on the special Euclidean group, rigid-body displacements

1. Introduction

Simply stated a metric measures the distance between two points in a set. There exist numerous useful metrics for defining the distance between two points in Euclidean space, however, defining similar metrics for determining the distance between two locations of a finite rigid body is still an area of ongoing research, see Kazerounian and Rastegar, 1992, Martinez and Duffy, 1995, Larochelle and McCarthy, 1995, Etzel and McCarthy, 1996, Gupta, 1997, Tse and Larochelle, 2000, Chirikjian, 1998, Belta and Kumar, 2002, and Eberharter and Ravani, 2004. In the cases of two locations of a finite rigid body in either SE(3) (spatial locations) or SE(2) (planar locations) any metric used to measure the distance between the locations yields a result which depends upon the chosen reference frames, see Bobrow and Park, 1995 and Martinez and Duffy, 1995. However, a metric that is independent of these choices,

J. Lenarčič and B. Roth (eds.), Advances in Robot Kinematics, 33–40.

referred to as being bi-invariant, is desirable. Interestingly, for the specific case of orienting a finite rigid body in SO(n) bi-invariant metrics do exist.

Larochelle and McCarthy, 1995 presented an algorithm for approximating displacements in SE(2) with spherical orientations in SO(3). By utilizing the bi-invariant metric of Ravani and Roth, 1983 they arrived at an approximate bi-invariant metric for planar locations in which the error induced by the spherical approximation is of the order $\frac{1}{\mathsf{R}^2}$, where R is the radius of the approximating sphere. Their algorithm for an approximately bi-invariant metric is based upon an algebraic formulation which utilizes Taylor series expansions of *sine*() and *cosine*() terms in homogeneous transforms, see McCarthy, 1983. Etzel and McCarthy, 1996 extended this work to spatial displacements by using orientations in $SO(4)$ to approximate locations in $SE(3)$. This paper presents an alternative approach for defining a metric on SE(n). Here, the underlying geometrical motivations are the same- to approximate displacements with hyperspherical rotations. However, an alternative approach for reaching the same goal is presented. The polar decomposition is utilized to yield hyperspherical orientations that approximate planar and spatial finite displacements.

2. The PD Based Embedding

This approach, analogous to the works reviewed above, also uses hyperdimensional rotations to approximate displacements. However, this technique uses products derived from the singular value decomposition (SVD) of the homogeneous transform to realize the embedding of SE(n-1) into SO(n). The general approach here is based upon preliminary work reported in Larochelle et al., 2004.

Consider the space of $(n \times n)$ matrices as shown in Fig. 1. Let $[T]$ be a $(n \times n)$ homogeneous transform that represents an element of SE(n-1). $[A]$ is the desired element of SO(n) nearest $[T]$ when it lies in a direction orthogonal to the tangent plane of SO(n) at $[A]$. The PD of $[T]$ is used to determine $[A]$ by the following methodology.

The following theorem, based upon related works by Hanson and Norris, 1981 provides the foundation for the embedding

Theorem 1. *Given any* $(n \times n)$ *matrix* $[T]$ *the closest element of SO(n) is given by:* $[A] = [U][V]^T$ *where* $[T] = [U][diag(s_1, s_2, \ldots, s_n)][V]^T$ *is the SVD of* $[T]$.

Shoemake and Duff, 1992 prove that matrix $[A]$ satisfies the following optimization problem: *Minimize:* $\|[A]-[T]\|_F^2$ subject to: $[A]^T[A]-[I] = [0]$, where $\|[A]-[T]\|_F^2 = \sum_{i,j}(a_{ij}-t_{ij})^2$ is used to denote the Frobenius

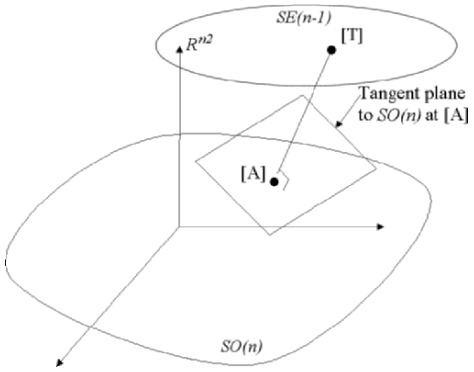

Figure 1. General Case: SE(n-1) ⇒ SO(n).

norm. Since $[A]$ minimizes the Frobenius norm in R^{n^2} it is the element of SO(n) that lies in a direction orthogonal to the tangent plane of SO(n) at $[R]$. Hence, $[A]$ is the closest element of SO(n) to $[T]$. Moreover, for full rank matrices the SVD is well defined and unique. Th. 1 is now restated with respect to the desired SVD based embedding of SE(n-1) into SO(n).

Theorem 2. *For $[T] \in$ SE(n-1) and $[U]$ & $[V]$ are elements of the SVD of $[T]$ such that $[T] = [U][diag(s_1, s_2, \ldots, s_{n-1})][V]^T$ if $[A] = [U][V]^T$ then $[A]$ is the unique element of SO(n) nearest $[T]$.*

Recall that $[T]$, the homogenous representation of SE(n), is full rank (McCarthy, 1990) and therefore $[A]$ exists, is well defined, and unique.

The polar decomposition is quite powerful and actually provides the foundation for the better known singular value decomposition. The polar decomposition theorem of Cauchy states that "a non-singular matrix equals an orthogonal matrix either pre or post multiplied by a positive definite symmetric matrix", see Halmos, 1958. With respect to our application, for $[T] \in$ SE(n-1) its PD is $[T] = [P][Q]$, where $[P]$ and $[Q]$ are $(n \times n)$ matrices such that $[P]$ is orthogonal and $[Q]$ is positive definite and symmetric. Recalling the properties of the SVD, the decomposition of $[T]$ yields $[U][\text{diag}(s_1, s_2, \ldots, s_{n-1})][V]^T$, where matrices $[U]$ and $[V]$ are orthogonal and matrix $[\text{diag}(s_1, s_2, \ldots, s_{n-1})]$ is positive definite and symmetric. Moreover, it is known that for full rank square matrices that the polar decomposition and the singular value decomposition are related by: $[P] = [U][V]^T$ and $[Q] = [V][\text{diag}(s_1, s_2, \ldots, s_{n-1})][V]^T$, Faddeeva,

1959. Hence, for $[A] = [U][V]^T$ it is known that $[A] = [P]$ and the PD yields the same element of SO(n). The result being the following theorem that serves as the basis for the PD based embedding.

Theorem 3. *If $[T] \in$ SE(n-1) and $[P]$ & $[Q]$ are the PD of $[T]$ such that $[T] = [P][Q]$ then $[P]$ is the unique element of SO(n) nearest $[T]$.*

2.1 The Characteristic Length & Metric

A characteristic length is employed to resolve the unit disparity between translations and rotations. Investigations on characteristic lengths appear in Angeles, 2005; Etzel and McCarthy, 1996; Larochelle and McCarthy, 1995; Kazerounian and Rastegar, 1992; Martinez and Duffy, 1995. The characteristic length used here is $\mathsf{R} = \frac{24L}{\pi}$ where L is the maximum translational component in the set of displacements at hand. This characteristic length is the radius of the hypersphere that approximates the translational terms by angular displacements that are ≤ 7.5(deg). It was shown in Larochelle, 1999 that this radius yields an effective balance between translational and rotational displacement terms. Note that the metric presented here is not dependent upon this particular choice of characteristic length.

It is important to recall that the PD based embedding of SE(n-1) into SO(n) is coordinate frame and unit dependent. However that this methodology embeds SE(n-1) into SO(n) and that a bi-invariant metric does exist on SO(n). One useful metric d on SO(n) can be defined using the Frobenius norm as,

$$d \;=\; \|[I] - [A_2][A_1]^T\|_F. \tag{1}$$

where $[A_1]$ and $[A_2]$ of elements of SO(n). It is straightforward to verify that this is a valid bi-invariant metric on SO(n), see Schilling and Lee, 1988.

2.2 A Finite Region of SE(3)

In order to yield a left invariant metric we build upon the work of Kazerounian and Rastegar, 1992 in which approximately bi-invariant metrics were defined for a prescribed finite rigid body. Here, to avoid cumbersome volume integrals over the body a unit point mass model for the moving body is used. Proceed by determining the center of mass $\vec{c}$ and the principal axes frame [PF] associated with the n prescribed locations where a unit point mass is located at the origin of each location:

$$\vec{c} \;=\; \frac{1}{n}\sum_{i=1}^{n} \vec{d}_i \tag{2}$$

where $\vec{d_i}$ is the translation vector associated with the i^{th} location (i.e. the origin of the i^{th} location with respect to the fixed frame). Next, define [PF] with origin at $\vec{c}$ and axes along the principal axes of the n point mass system by evaluating the inertia tensor [I] associated with the n point masses,

$$[\text{PF}] = \begin{bmatrix} \vec{v}_1 & \vec{v}_2 & \vec{v}_3 & \vec{c} \\ 0 & 0 & 0 & 1 \end{bmatrix} \tag{3}$$

where $\vec{v_i}$ are the principal axes associated with [I] Greenwood, 2003 and the directions $\vec{v_i}$ are chosen such that [PF] is a right-handed system. Note that the principal frame is not dependent on the orientations of the frames at hand. However, the metric is dependent on the orientations of the frames. For a set of n locations in a finite region of SE(3) the procedure is:

1 Determine [PF] associated with the n displacements.

2 Determine the relative displacements from [PF] to each of the n locations.

3 Determine the characteristic length R associated with the n relative displacements and scale the translation terms in each by $\frac{1}{\mathsf{R}}$.

4 Compute the elements of SO(4) associated with [PF] and each of the scaled relative displacements using the polar decomposition.

5 The magnitude of the i^{th} displacement is defined as the distance from [PF] to the i^{th} scaled relative displacement as computed via Eq. 1. The distance between any 2 of the n locations is similarly computed via the application of Eq. 1 to the scaled relative displacements embedded in SO(4).

Since $\vec{c}$ and [PF] are invariant with respect to both the choice of coordinate frames as well as the system of units (Greenwood, 2003) the relative displacements determined in step 2 are left invariant and it follows that the metric is also left invariant.

3. Case Study

Consider the 4 spatial locations in Table. 1 and shown in Fig. 2 along with the fixed reference frame [F] where the x-axes are shown in red, the y-axes in green, and the z-axes in blue. Their centroid is $\vec{c} = [0.7500\ 1.5000\ 0.4375]^T$. Next, the principal axes directions are

Table 1. Four Spatial Locations.

#	x	y	z	θ (deg)	ϕ (deg)	ψ (deg)	$\|\|[T]\|\|$
1	0.00	0.00	0.00	0.0	0.0	0.0	2.5281
2	0.00	1.00	0.25	15.0	15.0	0.0	2.5701
3	1.00	2.00	0.50	45.0	60.0	0.0	2.7953
4	2.00	3.00	1.00	45.0	80.0	0.0	2.8057

determined to define the principal frame,

$$[\mathrm{PF}] = \begin{bmatrix} -0.5692 & 0.8061 & -0.1617 & 0.75000 \\ -0.7807 & -0.5916 & -0.2012 & 1.5000 \\ -0.2578 & 0.0117 & 0.9661 & 0.4375 \\ 0 & 0 & 0 & 1 \end{bmatrix} \tag{4}$$

shown in Fig. 2. The characteristic length is $\mathsf{R} = \frac{24 \times 1.7108}{\pi} = 13.0695$ and the magnitudes of the displacements are listed in Table 1. Interestingly, the magnitude of the first displacement is not zero. This is because the relative displacement from the principal frame to the first location is non-identity and that the magnitudes of all displacements are computed with respect to the principal frame.

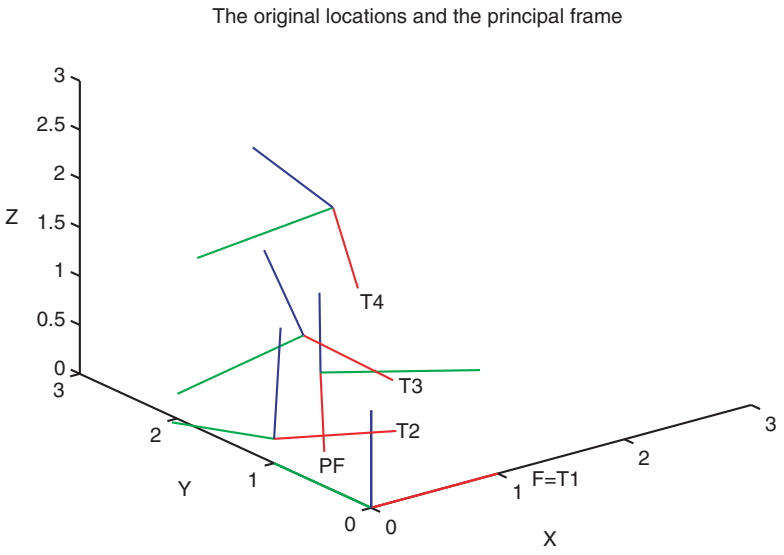

Figure 2. The 4 Spatial Locations.

4. Conclusions

We have presented a metric on SE(n). This metric is based on embedding SE(n) into SO(n+1) via the polar decomposition of the homogeneous transform representation of SE(n). It was shown that this method determines the element of SO(n+1) nearest the given element of SE(n). A bi-invariant metric on SO(n+1) is then used to measure the *distance* between any two spatial displacements SE(n). The results is a PD based metric on SE(n) that is left-invariant. Such metrics have applications in motion synthesis, robot calibration, motion interpolation, and hybrid robot control.

5. Acknowledgements

The contributions of Profs. Murray (U. Dayton) and Angeles (McGill U.) to this work are gratefully acknowledged. This material is based upon work supported by the National Science Foundation under Grants No. #0422705. Any opinions, findings, and conclusions or recommendations expressed in this material are those of the author(s) and do not necessarily reflect the views of the National Science Foundation.

References

Angeles, J., (2005), Is there a characteristic length of a rigid-body displacement, *Proc. of the 2005 International Workshop on Computational Kinematics*, Cassino, Italy.

Belta, C., and Kumar, V., (2002), An svd-based projection method for interpolation on SE(3), *IEEE Transactions on Robotics and Automation*, vol 18, no 3, pp. 334-345.

Bobrow, J.E., and Park, F.C., (1995), On computing exact gradients for rigid body guidance using screw parameters, *Proc. of the ASME Design Engineering Technical Conferences*, Boston, MA, USA.

Bodduluri, R.M.C., (1990), *Design and planned movement of multi-degree of freedom spatial mechanisms*, PhD Dissertation, University of California, Irvine.

Chirikjian, G.S., (1998), Convolution metrics for rigid body motion, *Proc. of the ASME Design Engineering Technical Conferences*, Atlanta, USA.

Eberharter, J., and Ravani, B., (2004), Local metrics for rigid body displacements, *ASME Journal of Mechanical Design*, vol. 126, pp. 805-812.

Etzel, K., and McCarthy, J.M., (1996), A metric for spatial displacements using biquaternions on SO(4), *Proc. of the IEEE International Conference on Robotics and Automation*, Minneapolis, USA.

McCarthy, J.M., (1990), *Computational Methods of Linear Algebra*, Dover Publishing.

Greenwood, D.T., (2003), *Advanced Dynamics*, Cambridge University Press.

Gupta, K.C., (1997), Measures of positional error for a rigid body, *ASME Journal of Mechanical Design*, vol. 119, pp. 346-349.

Halmos, P.R., (1990), *Finite Dimensional Vector Spaces*, Van Nostrand.

Hanson and Norris, (1981), Analysis of measurements based upon the singular value decomposition, *SIAM Journal of Scientific and Computations*, vol. 2, no. 3, pp. 308-313.

Kazerounian, K., and Rastegar, J., (1992), Object norms: A class of coordinate and metric independent norms for displacements, *Proc. of the ASME Design Engineering Technical Conferences*, Scotsdale, USA.

Larochelle, P. (1999), On the geometry of approximate bi-invariant projective displacement metrics, *Proc. of the World Congress on the Theory of Machines and Mechanisms*, Oulu, Finland.

Larochelle, P., Murray, A., and Angeles, J., (2004), SVD and PD Based Projection Metrics on SE(n), in Lenarčič, J. and Galletti, C. (editors), *On Advances in Robot Kinematics*, Kluwer Academic Publishers, pp. 13-22, 2004.

Larochelle, P., and McCarthy, J.M., (1995), Planar motion synthesis using an approximate bi-invariant metric, *ASME Journal of Mechanical Design*, vol. 117, no. 4, pp. 646-651.

Martinez, J.M.R., and Duffy, J., (1955), On the metrics of rigid body displacements for infinite and finite bodies, *ASME Journal of Mechanical Design*, vol. 117, pp. 41-47.

McCarthy, J.M., (1983), Planar and spatial rigid body motion as special cases of spherical and 3-spherical motion, *ASME Journal of Mechanisms, Transmissions, and Automation in Design*, vol. 105, pp. 569-575.

McCarthy, J.M., (1990), *An Introduction to Theoretical Kinematics*, MIT Press.

Ravani, B., and Roth, B., (1983), Motion synthesis using kinematic mappings, *ASME Journal of Mechanisms, Transmissions, and Automation in Design*, vol. 105, pp. 460-467.

Schilling, R.J., and Lee, H., (1988), *Engineering Analysis- a Vector Space Approach*, Wiley & Sons.

Shoemake, K., and Duff, T., (1992), Matrix animation and polar decomposition, *Proc. of Graphics Interface '92*, pp. 258-264.

Tse, D.M., Larochelle, P.M., (2000), Approximating spatial locations with spherical orientations for spherical mechanism design, *ASME Journal of Mechanical Design*, vol. 122, pp. 457-463.

ON THE REGULARITY OF THE INVERSE JACOBIAN OF PARALLEL ROBOTS

Jean-Pierre Merlet
INRIA
Sophia-Antipolis, France
Jean-Pierre.Merlet@sophia.inria.fr

Peter Donelan
Victoria University
Wellington, New-Zealand
Peter.Donelan@mcs.vuw.ac.nz

Abstract Checking the regularity of the inverse jacobian matrix of a parallel robot is an essential element for the safe use of this type of mechanism. Ideally such check should be made for all poses of the useful workspace of the robot or for any pose along a given trajectory and should take into account the uncertainties in the robot modeling and control. We propose various methods that facilitate this check. We exhibit especially a sufficient condition for the regularity that is directly related to the extreme poses that can be reached by the robot.

Keywords: Inverse jacobian, singularity, parallel robots

1. Introduction

Determining if a parallel robot may be in a singular configuration during its motion is a problem that is of high practical interest. Many papers have addressed first the determination of the inverse jacobian, denoted $\mathbf{J}^{-1}$, of such robots and then the analysis of the singularity condition that can be deduced from the singularity of this matrix. $\mathbf{J}^{-1}$ relates the joint velocities to the twist of the end-effector and is usually pose dependent. In a singularity the end-effector will exhibit non-zero velocities for some motion although the actuators are locked. The determinant of $\mathbf{J}^{-1}$ is usually complicated but for most parallel robots $\mathbf{J}^{-1}$ has as rows the Plücker vectors of well-defined lines. Consequently Grassmann geometry may be used to characterize the geometry of the singularity and to deduce simplified singularity conditions [Monsarrat 01; Merlet 89; Wolf 04]. It must be noted that even for robot with less than 6 d.o.f. it is necessary to consider the *full jacobian matrix* i.e. the matrix that involves the full twist of the end-effector. Indeed for a robot with n d.o.f.

J. Lenarčič and B. Roth (eds.), Advances in Robot Kinematics, 41–48.

the jacobian that relates the n d.o.f. velocities to the n actuated joint velocities may be not singular while $\mathbf{J}^{-1}$ is singular [Bonev 01].

A singularity detection algorithm should be able to determine the presence of a singularity within a motion variety with dimension 1 to n for a n d.o.f. robot. An important point is that the singularity detection should be *certified* i.e. the algorithm should provide a safe answer even if numerical round-off errors occur. This certification constraint usually rules out the use of an optimization procedure.

2. A Singularity Detection Scheme

This singularity detection problem has been addressed in [Merlet 01] where an efficient algorithm was exhibited. This algorithm proceeds along the following steps: symbolic computation is used to determine an analytical form of the determinant of $\mathbf{J}^{-1}$and its sign at a particular pose $\mathbf{X_1}$. Then an interval analysis based method [Jaulin 01; Moore 79], that takes round-off errors into account, allows one to determine if the motion variety includes a set of poses in which the determinant has a sign opposite to the one found at $\mathbf{X_1}$.

The main difficulty with this algorithm (apart of using efficiently interval analysis) is the calculation of the closed-form of the determinant as will be illustrated on a difficult example, the Gough platform.

2.1 The Inverse Jacobian of a Gough Platform

We define a reference frame $(O, \mathbf{x}, \mathbf{y}, \mathbf{z})$. The attachment points of the leg i on the base will be denoted by A_i. The attachment points on the platform will be denoted by B_i and it is well known that the coordinates of B_i in the reference frame can be obtained as function of the pose parameters. The inverse jacobian matrix is then constituted of the normalized Plücker vectors of the line associated to each leg:

$$\mathbf{J}^{-1} = ((\frac{\mathbf{A_iB_i}}{||\mathbf{A_iB_i}||} \quad \frac{\mathbf{OA_i} \times \mathbf{OB_i}}{||\mathbf{A_iB_i}||})) \tag{1}$$

Note that we may use the non normalized Plücker vector to define another matrix $\mathbf{M} = ((\mathbf{A_iB_i} \quad \mathbf{OA_i} \times \mathbf{OB_i}))$ with the property that the sign of $\mathbf{J}^{-1}$ is the same than those of $|\mathbf{M}|$. As $\mathbf{M}$ is simpler than $\mathbf{J}^{-1}$ it will be used for the singularity detection.

2.2 Evaluation of the Determinant

Being given a motion variety the pose parameters are functions of the variety parameters and thus the components of the inverse jacobian may be obtained as functions of the variety parameters. As mentioned earlier

a closed-form of the determinant is obtained by symbolic computation. It should be noted that this is not strictly necessary. Indeed being given ranges for the variety parameters interval arithmetic may used to determine ranges for each component of the inverse jacobian. We get then an *interval matrix* $\mathbf{J}_I^{-1}$ i.e. a matrix whose components are intervals. Classical method for the calculation of determinant may then be used to obtain an interval evaluation of the determinant but with a large overestimation of the minimum and maximum of the determinant. Indeed interval arithmetic is very sensitive to multiple occurrence of the same variable. Consider for example the matrix $\mathbf{A}$ whose determinant is xy and its interval version $\mathbf{A}_I$ when x and y lie in the range [1,2]

$$\mathbf{A} = \begin{pmatrix} x & x \\ y & 2y \end{pmatrix} \quad \mathbf{A}_I = \begin{pmatrix} [1,2] & [1,2] \\ [1,2] & [2,4] \end{pmatrix} \tag{2}$$

The interval evaluation of $|\mathbf{A}_I|$ may be calculated as [–2,7]. Hence the closed-form of the determinant allows one to show that $|\mathbf{A}|$ will always be positive for any value of x, y in [1,2], while the use of the interval matrix does not allow such conclusion. We have put an emphasis on interval matrices that will be justified by the influence of uncertainties.

2.3 The Influence of Uncertainties

Uncertainties are inherent part of a real system such as a robot. They occur at the modeling level: the geometry of the real robot differs from its theoretical model due to the manufacturing tolerances (for example for the Gough platform the locations of the A_i, B_i are known only up to a known accuracy). Uncertainties are also due to control: there will be a deviation of the robot motion from the theoretical motion variety.

An ideal singularity detection scheme should be able to determine if the robot may be in a singular pose in spite of these uncertainties. Although we may add the uncertainties as additional unknowns in the components of $\mathbf{J}^{-1}$, a drawback is that the calculation of the closed-form of the determinant may become difficult. For example for the Gough platform `Maple` is no more able to calculate the determinant as soon as we add the uncertainties on the A_i, B_i. In that case we have to resort to a numerical interval evaluation of the determinant based on the interval version of $\mathbf{J}^{-1}$, but we have seen that this leads to a large overestimation of the determinant, that will result in a large computation time for the singularity detection scheme. It is thus necessary to develop methods that check the regularity of the set of matrices defined by an interval matrix, without calculating its determinant. These methods should take into account that $\mathbf{J}^{-1}$ is a *parametric matrix*, i.e. that its components are not independent.

3. Various Methods for Regularity Check

3.1 A Classical Regularity Check

Checking the regularity of all matrices in a set defined by an interval matrix is a classical problem in interval analysis and is known to be NP-hard. Among possible approaches the one having shown the largest efficiency in our case has been a method proposed by Rohn [Kreinovich 00]. We define the set H as the set of all n-dimensional vector $\mathbf{h}$ whose components are either 1 or -1. For a given box we denote by $[\underline{a_{ij}}, \overline{a_{ij}}]$ the interval evaluation of the component J_{ij}^{-1} of $\mathbf{J^{-1}}$ at the i-th row and j-th column. Given two vectors $\mathbf{u}, \mathbf{v}$ of H, we then define the set of matrices $\mathbf{A^{uv}}$ whose elements $A_{ij}^{\mathbf{uv}}$ are

$$A_{ij}^{\mathbf{uv}} = \overline{a_{ij}} \text{ if } u_i.v_j = -1, \underline{a_{ij}} \text{ if } u_i.v_j = 1$$

These matrices have thus fixed numerical components corresponding to lower or upper bound of the interval J_{ij}^{-1}. There are 2^{2n-1} such matrices since $\mathbf{A^{uv}} = \mathbf{A^{-u,-v}}$. If the determinant of all these matrices have the same sign, then all the matrices $\mathbf{A'}$ whose components have a value within the interval evaluation of J_{ij}^{-1} are regular. Hence for the 6×6 $\mathbf{J^{-1}}$ of a Gough platform if the determinant of the 2048 matrices of $\mathbf{A^{uv}}$ have the same sign, then all matrices in the set are regular.

But $\mathbf{A^{uv}}$ includes matrices that are not inverse jacobian as the dependency of the components of the matrix are not taken into account. This may be seen, for example, for the interval matrix $\mathbf{A}_I$ (2) that includes the following matrices

$$\mathbf{A_1} = \begin{pmatrix} 1 & 1 \\ 1 & 4 \end{pmatrix} \quad \mathbf{A_2} = \begin{pmatrix} 1 & 2 \\ 2 & 2 \end{pmatrix} \quad \mathbf{A_3} = \begin{pmatrix} 1 & 2 \\ 1 & 2 \end{pmatrix} \tag{3}$$

The matrices $\mathbf{A_1}, \mathbf{A_2}$ belong to the set $\mathbf{A^{uv}}$ and have determinants with opposite signs. Consequently the test proposed by Rohn fails, which is quite normal as the matrix $\mathbf{A_3}$, that belongs to $\mathbf{A}_I$ is singular. For the Gough platform the first column of $\mathbf{J^{-1}}$ is written as $x + F_i$, x being a coordinate of the center of the platform; if the range for x is $[\underline{x}, \overline{x}]$ while the range for F_i is $[a_i, b_i]$, then $\mathbf{A^{uv}}$ includes matrices with elements $\underline{x} + a_i$ and $\overline{x} + b_k$ that does not belong to the set of inverse jacobian matrices.

3.2 Pre-conditioning

A classical approach in interval analysis for regularity check is to pre-condition the matrix by multiplying it by a real matrix $\mathbf{K}$, usually the inverse of the *mid-matrix*, i.e. the matrix whose components are the mid-point of each range of the components. The purpose of this strategy is

to get $\mathbf{S} = \mathbf{K}\mathbf{J}^{-1}$ close to the identity matrix so that its determinant $|\mathbf{S}| = |\mathbf{K}||\mathbf{J}^{-1}|$ may be interval evaluated with a lower overestimation. If we apply this strategy to the matrix (2) the inverse of the mid-matrix and the interval matrix $\mathbf{K}\mathbf{A}_I$ are:

$$\mathbf{K} = \begin{pmatrix} 4/3 & -2/3 \\ -2/3 & 2/3 \end{pmatrix} \mathbf{S} = \mathbf{K}\mathbf{A}_I = \begin{pmatrix} [0,2] & [-4/3,4/3] \\ [-2/3,2/3] & [0,2] \end{pmatrix} \quad (4)$$

The interval evaluation of $|\mathbf{S}|$ is $[-8/9, 44/9] \approx [-0.8889, 4.88889]$ while $|\mathbf{K}|$ is positive. In term of sign determination this interval evaluation is indeed sharper than the one obtained with a direct evaluation of $|\mathbf{A}|$, but is still not satisfactory. We propose another method which consists first to compute *symbolically* the matrix $\mathbf{S}$, using k_{ij} as components of $\mathbf{K}$ and then plugging in the numerical values. The symbolic matrix $\mathbf{S}_s = \mathbf{A}\mathbf{K}$ and its interval version $\mathbf{S}_K$ for the numerical $\mathbf{K}$ are

$$\mathbf{S}_s = \begin{pmatrix} x(k_{11}+k_{21}) & x(k_{12}+k_{22}) \\ y(k_{11}+2\,k_{21}) & y(k_{12}+2\,k_{22}) \end{pmatrix} \mathbf{S}_K = \begin{pmatrix} 2x/3 & 0 \\ 0 & 2y/3 \end{pmatrix} \quad (5)$$

If we use now the range [1,2] for x, y the interval evaluation of $|\mathbf{S}|$ is [4/3,8/3] that shows that all matrices have a positive determinant. Note that we have used $\mathbf{A}\mathbf{K}$ instead of $\mathbf{K}\mathbf{A}$, which is justified as it allows to reduce the multiple occurrences of the variables. However as $\mathbf{J}^{-1}$ exhibits the same variables in a column it is better to pre-multiply it by the conditioning matrix.

3.3 A Regularity Test for Parametric Matrices

Assume that some components of some rows (denoted the *linear rows*) of a parametric matrix $\mathbf{A} = a_{ij}$ can be written as linear combination with real or interval coefficients of a set of unknowns $\{x_1, x_2, \ldots, x_n\}$.

We denote by $\mathbf{A}'$ the set of real or interval matrices that can be derived from $\mathbf{A}$ by assigning independently to each linear rows either a lower or upper bound to each unknown x_i that appears in the linear combination. For example for matrix $\mathbf{A}$ the set $\mathbf{A}'$ is

$$\mathbf{A}' = \{\begin{pmatrix} 1 & 1 \\ 1 & 2 \end{pmatrix}, \begin{pmatrix} 1 & 1 \\ 2 & 4 \end{pmatrix}, \begin{pmatrix} 2 & 2 \\ 1 & 2 \end{pmatrix}, \begin{pmatrix} 2 & 2 \\ 2 & 4 \end{pmatrix}\} \quad (6)$$

The following theorem hold:

Theorem 1: If the determinant of all matrices in the set $\mathbf{A}'$ have all the same sign, then *all matrices in the set* $\mathbf{A}$ *are regular.*

Proof (derived from [Popova 04]): Assume that there is a singular matrix $\mathbf{A_0}$ in the set $\mathbf{A}$. Without lack of generality we will assume that

the first row of $\mathbf{A_0}$ is linear. We consider the unknown x_1, whose value for $\mathbf{A_0}$ is x_1^0 and lie in $[\underline{x_1}, \overline{x_1}]$. Each component of the first row of $\mathbf{A}$ may be written either as $\lambda_{1j}^1 x_1 + b_{1j}$ or a_{1j}^0 if the component is not linear. Using row expansion the determinant of the matrix may be written as

$$|\mathbf{A}| = \sum_{k=j_1,\ldots,j_m} (-1)^{k+1}(\lambda_{1k}^1 x_1 + b_{1k}) M_{1k} + \sum_{l \notin \{j_1,\ldots,j_m\}} (-1)^{l+1} a_{1l} M_{1l} \quad (7)$$

where $\{j_1, \ldots, j_m\}$ are the column indices of the linear components of $\mathbf{A}$ and M_{1j} denotes the minor associated to the first line and column j.

For $x_1 = x_1^0$ this expression will cancel. If we assume now that $x_1 = x_1^0 + dx_1$ we get

$$|\mathbf{A}| = dx_1 \Big(\sum_{k=j_1,\ldots,j_m} (-1)^{k+1} \lambda_{1k}^1 \Big) = dx_1 K_1 \quad (8)$$

K_1 being either a real number or an interval. We may always assign dx_1 to either $\overline{x_1} - x_1^0$ or $\underline{x_1} - x_1^0$ so that $|\mathbf{A}|$ is positive or has a positive upper bound. Thus by assigning $\underline{x_1}$ or $\overline{x_1}$ to x_1 we have constructed a matrix $\mathbf{A_1^+}$ whose determinant will be positive or has a positive upper bound. The process may be repeated for constructing a matrix $\mathbf{A_1^-}$ whose determinant will be negative or has a negative lower bound. Starting from these matrices we may now assign x_2 to $\underline{x_2}$ or $\overline{x_2}$ to get a matrix $\mathbf{A_{12}^+}$ whose determinant is $|\mathbf{A_1^+}|$ plus a positive quantity (i.e. still positive) and a matrix $\mathbf{A_{12}^-}$ whose determinant will be lower than the determinant of $|\mathbf{A_1^-}|$ (i.e. still negative). The process is repeated for each unknowns in the row. As soon as all unknowns in the row have a fixed value the process is repeated for the next linear row. When all linear rows have been processed the matrices $\mathbf{A}^+$, $\mathbf{A}^-$ belong to $\mathbf{A}'$. Note however that the assignment of the unknowns in a row to ensure that $|\mathbf{A}^+|$ is positive may differ between two linear rows. Hence if there is a singular matrix in $\mathbf{A}$, then we are able to determine matrices whose determinant have opposite signs (or whose lower bound is negative and upper bound is positive), which concludes the proof.

For example as all matrices in $\mathbf{A}'$ defined by (6) have the same determinant sign, then the set $\mathbf{A}$ contains only regular matrices. Another theorem may be derived for the full inverse jacobian matrices that have Plücker vectors as rows. Let us define $A_i(a_i^1, a_i^2, a_i^3)$ and $B_i(b_i^1, b_i^2, b_i^3)$ as two points that belong to the line associated to the Plücker vector i. A row of $\mathbf{J}^{-1}$ may be written as

$$((b_1 - a_1, b_2 - a_2, b_3 - a_3, a_2 b_1 - a_1 B_2, a_3 b_1 - a_1 b_3, a_1 b_2 - a_2 b_1)) \quad (9)$$

so that each row is linear in the b_i. Assume now that the locations of the A_i are fixed, while the locations of the B_i are functions of the end-effector motion. Using interval analysis (or an optimization method)

being given ranges for the motion parameter we may find a bounding box $\mathcal{B}_i$ for the location of each B_i. Let $\mathbf{J}_\star^{-\mathbf{1}}$ be the set of inverse jacobian that may be obtained for the motion parameters ranges. Theorem 1 allows one to state the following corollary:

Corollary: Let $\mathbf{A}^\star$ be the set of matrices obtained by choosing as location of B_i all possible combinations of the corners of $\mathcal{B}_i$ (there will be 8^6 such matrices). If the determinants of all matrices in $\mathbf{A}^\star$ have the same sign, then all matrices in $\mathbf{J}_\star^{-\mathbf{1}}$ are regular.

The number of matrices in $\mathbf{A}^\star$ may even be reduced in some cases, using the property that we may choose as B_i any point on the line. Assume that the bounding box $\mathcal{B}_i$ is defined by the set of ranges $[\underline{b_{ij}}, \overline{b_{ij}}]$, $j \in [1,3]$ for b_j. The following cases may occur:

• $a_k \in [\underline{b_{ik}}, \overline{b_{ik}}]$ for two indices in [1,2,3], while $a_k < \underline{b_{ik}}$ or $a_k > \overline{b_{ik}}$ for one index. The line always enters the bounding box $\mathcal{B}_i$ by the face defined by $b_k = .\underline{b_{ik}}$ or $b_k = \overline{b_{ik}}$. We may thus choose as B_i the intersection point of the line with this face i.e. fix the value of b_k. Hence only 4 corners will have to be checked

• $a_k \in [\underline{b_{ik}}, \overline{b_{ik}}]$ for only one index. The line may enter the bounding box by 2 faces and we have to check 6 corners

• $a_k \notin [\underline{b_{ik}}, \overline{b_{ik}}]$ for all index. The line may enter the bounding box by 3 faces and we have 7 corners to check

• $a_k \in [\underline{b_{ik}}, \overline{b_{ik}}]$ for all index. In that case the corresponding row of the jacobian may include a line of 0 and the ranges for the motion parameters must be bisected

In practice we will have between 4^6 and 7^6 matrices in $\mathbf{A}^\star$. Uncertainties in the locations of the A_i may also be dealt with by considering that the matrices in $\mathbf{A}^\star$ are interval matrices.

Theorem 2 shows that checking the extreme poses of the B_i may be sufficient to check the regularity of $\mathbf{J}^{-1}$ over the whole workspace.

4. Examples

The proposed regularity check has been implemented in the singularity detection scheme and has been extensively tested. It appears that among the three regularity checks the most efficient combination is to use first the pre-conditioning and then to apply Rohn test on the resulting matrix. A 6D workspace $\mathcal{W}$ is defined with the ranges x, y in [–15,15], z in [45,50] and the three Euler angles having the ranges [–15,15] degree. The computation time on a Dell D400 laptop (1.7 Ghz) is established as follows:

• 6D workspace without uncertainty: for $\mathcal{W}$ no singularity detected in 3.12s. If the orientation ranges of $\mathcal{W}$ is extended to [−40,40] degree a singularity is detected in 9.46s.

• 6D workspace with uncertainties: for a $\pm$ 0.05 uncertainty on each coordinates of the A_i, B_i points no singularity is detected in $\mathcal{W}$ in 43mn on a cluster of 15 PC's without the regularity checks and only in 263s on a laptop if they are incorporated in the detection scheme. For an uncertainty of $\pm$ 0.1 the computation time establishes respectively at 10h 22mn and 1176s.

5. Conclusion

We have proposed regularity checks for the inverse jacobian of parallel robots that may be used to determine if such matrix may be singular over a motion variety. They allow to deal with uncertainties in the robot modeling and control and have been proved to be very efficient. One of this regularity check, that is sufficient but not necessary, is related to the extremal poses that can be reached by the end-effector: if the determinant of a finite number of real matrices that are related to these extremal poses have all the same sign, then the inverse jacobian matrix is regular.

References

Bonev I.A. and Zlatanov D. The mystery of the singular SNU translational parallel robot. www.parallemic.org/Reviews/Review004.html, June, 12, 2001.

Jaulin L., Kieffer M., Didrit O., and Walter E. *Applied Interval Analysis*. Springer-Verlag, 2001.

Kreinovich V. Optimal finite characterization of linear problems with inexact data. Technical Report CS-00-37, University of Texas at El Paso, 2000.

Merlet J. -P. Singular configurations of parallel manipulators and Grassmann geometry. *Int. J. of Robotics Research*, 8(5):45–56, October 1989.

Merlet J. -P. and Daney D. A formal-numerical approach to determine the presence of singularity within the workspace of a parallel robot. In F.C. Park C.C. Iurascu, editor, *Computational Kinematics*, pages 167–176. EJCK, Seoul, May, 20-22, 2001.

Monsarrat B. and Gosselin C.M. Singularity analysis of a three-leg six-degree-of-freedom parallel platform mechanism based on Grassman line geometry. *Int. J. of Robotics Research*, 20(4):312–328, April 2001.

Moore R.E. *Methods and Applications of Interval Analysis*. SIAM Studies in Applied Mathematics, 1979.

Popova E. D. *Strong Regularity of Parametric Interval Matrices* 33th Spring Conference of the Union of Bulgarian Mathematicians, Borovets, April 1, 2004.

Wolf A. and others. Application of line geometry and linear complex approximation to singularity analysis of the 3-dof CaPaMan manipulator. *Mechanism and Machine Theory*, 39(1):75–95, January 2004.

PARALLEL ROBOTS THAT CHANGE THEIR GROUP OF MOTION

Pietro Fanghella
Dept. of Mechanics and Design of Machines
University of Genoa, Italy
pietro.fanghella@unige.it

Carlo Galletti
Dept. of Mechanics and Design of Machines
University of Genoa, Italy
carlo.galletti@unige.it

Elena Giannotti
Dept. of Computer, Control and Communication Engineering
University of Genoa, Italy
elena@dist.unige.it

Abstract In this work we present several parallel robots with reduced mobility whose platforms can change their subgroups of displacement when the robot is displaced continuously from one set of positions to another one. In some cases, also the number of degrees of freedom of the platform may change, in other cases, only the group of displacement or its invariant properties are modified. By using some results on mobility of single-loop kinematic chains based on the theory of the displacement groups, the way to synthesize these robots is discussed.

Keywords: Parallel robots, displacement groups, kinematotropy, mobility

1. Introduction

In recent years the literature on robot mechanisms shows a growing interest in parallel robots with reduced numbers of degree of freedom whose mobility can be carefully investigated, (e.g., Kong and Gosselin, 2004, Kong and Gosselin, 2005, Gogu, 2005). In general, a platform of a robot of this kind can move in a subgroup of the Euclidean displacement group, or in a subset of a subgroup.

In a different field of kinematics, various studies have been performed related to mechanisms in which variations in the position variables can

J. Lenarčič and B. Roth (eds.), Advances in Robot Kinematics, 49–56.

result in changes in the permanent finite mobility of the mechanisms. Wohlhart, 1996, called this very peculiar mobility property kinematotropy.

In this paper, some results concerning kinematotropic kinematic chains are used to synthesize parallel robots with reduced mobility, whose platforms change their subgroups of displacement when the robot is displaced from one set of positions to another one. Several robots are obtained in this way and their mobility properties are presented.

In Section 2, three single-loop kinematotropic chains are shown and their finite mobility discussed.

In Section 3, the single-loop kinematotropic chains are used to synthesize 3 parallel robots that change both their displacement groups and the numbers of their degrees of freedom.

In Section 4, the proposed approach leads to 2 parallel robots that change their displacement groups but not the numbers of their degrees of freedom, and 1 robot that only change the invariant properties of its displacement group.

In Section 5 alternative ways for selecting the robot joints and the driver locations are discussed.

In this paper it is assumed that the readers have a basic knowledge of the displacement groups in kinematics, as can be found, for instance, in Hervé, 1978 and in Section 5.3 of Angeles, 1988.

2. Single-loop Kinematotropic Chains

Figure 1 shows three single-loop kinematotropic chains presented by Galletti and Fanghella, 2001. They are shown in the singular position that separates the two branches of positions in which the displacements between bodies a_1 and b_2 belong to different displacement groups.

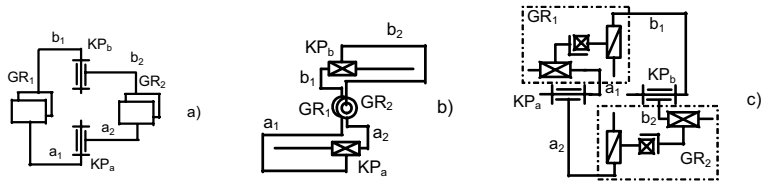

Figure 1. Single-loop kinematotropic chains.

All these chains can be represented by the scheme of Fig. 2. The subchain from body a_1 to b_1 generates a displacement group G_1, and the subchain from body a_2 to b_2 generates a group G_2. The kinematic pairs KP_a and KP_b provide displacements between bodies a_1 and a_2, and b_1 and b_2 respectively: the meaning of G_1, G_2, KP_a, and KP_b, are given in Table 1.

Let $G_{\cap}$ be the intersection group between G_1 and G_2. By moving KP_a and KP_b the group $G_{\cap}$ changes and, as a consequence, the group of displacement between bodies a_1 and b_2 varies.

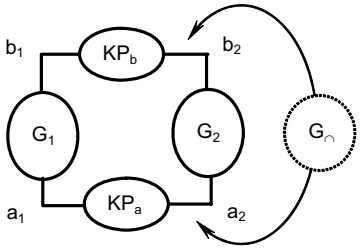

Figure 2. Scheme of a kinematotropic chain.

Table 1. Groups and pairs in Fig. 1.

Case	$G_1 = G_2$	$KP_a = KP_b$	Displacements between a_1 and b_2
a	E (planar)	R (revolute)	From planar E to cylindrical C
b	S (spherical)	P (prismatic)	From spherical S to cylindrical C
c	Y (translating screw)	R (revolute)	From translating screw Y to cylindrical C

The last column in Table 1 shows the resulting displacements between bodies a_1 and b_2 when a chain, passing through the singular position, is displaced from one branch of positions to the other one.

3. Robots that Change Displacement Group and Number of Degrees of Freedom

The scheme of Fig. 2 is now applied for synthesizing parallel robots whose platforms can change the number of degrees of freedom (d.o.f.) and the displacement group. Since a maximum of 3 d.o.f. can be achieved by all chains, 3 legs are introduced to connect the platform and the robot frame. The general scheme of the kinematic chain of the robots is shown in Fig. 3. The kinematic chains of the 3 robots obtained in this way are reported in Fig. 4. Each chain is shown in the singular position that separates the two branches of positions belonging to different groups (E, S, Y and C).

In order to exemplify the characteristics of these chains, let us consider the chain in Fig. 4-a, obtained from case a) of Table 1. Suppose there are drivers on pairs P_1, P_2, P_3 and P_4.

Starting from the singular position, by moving the drivers P_1, P_2 and P_3 the revolutes P_6 and P_4-P_5 become unaligned, so they cannot rotate

anymore. Therefore, the robot acts as a standard planar platform, with 3 d.o.f., with drivers P_1, P_2 and P_3.

Starting again from the singular position, by moving driver P_4 the plane formed by pairs P_1-P_{11}-P_{12}, and the planes formed by P_2-P_7-P_8 and P_3-P_9-P_{10} become not parallel, so their intersection group gives a prismatic constraint with axis parallel to the common axis of pairs P_4, P_5, and P_6. Therefore, the robot acts as "cylindrical" platform, with 2 d.o.f., with two drivers: one of P_4, P_5 or P_6, and one of P_1, P_2 or P_3.

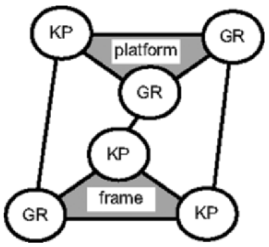

Figure 3. General scheme of a 3-legs robot.

An analogous discussion shows that the motion of the platform in Fig. 4-b switches from spherical (S) to cylindrical (C) and that, for the platform in Fig. 4-c, it changes from translating screw (Y) to cylindrical (C).

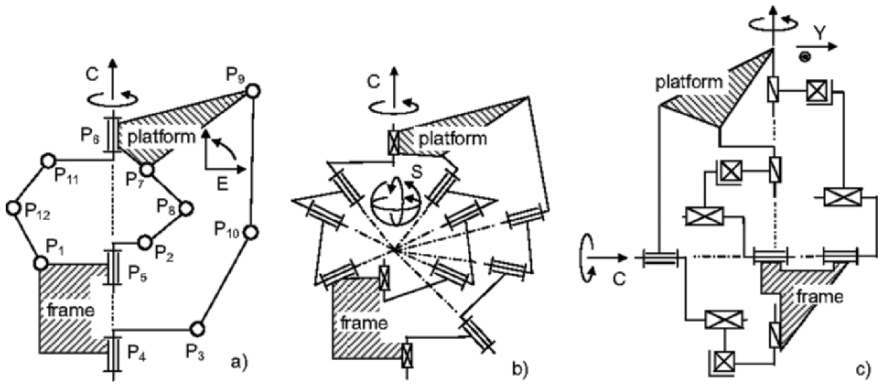

Figure 4. Robots that change No. of d.o.f. and displacement group.

4. Robots that Change Displacement Group or their Invariant Properties

As shown in Section 2, the change of displacement group between bodies a_1 and b_2 is a consequence of the change of the intersection group $G_\cap$. The chains of Fig. 1 ensure the change of $G_\cap$ and of the number of

d.o.f. of the chains. It is also possible to obtain chains that change $G_{\cap}$ but not the number of d.o.f. Using again the scheme of Fig. 2, the results reported in Table 2 can be achieved (see Fanghella and Galletti, 1994). From these results the schemes of Fig. 5 are obtained. Other similar configurations can be obtained through suitable permutations of kinematic pairs and groups.

Table 2. Modified groups and pairs in Fig. 1.

Case	$G_1 = G_2$	$KP_a = KP_b$	Displacements between a_1 and b_2
d	E (planar)	X (Schoenflies)	From E to a subset of X with 3 d.o.f.
e	Y (translating screw)	X (Schoenflies)	From Y to a subset of X with 3 d.o.f.

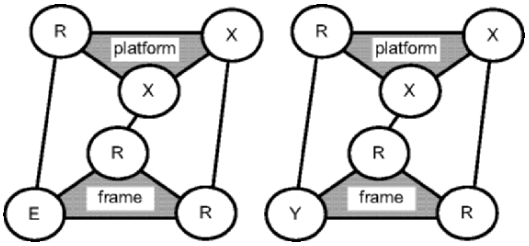

Figure 5. Robots with E, X, Y, and R groups.

Figure 6 shows the kinematic chains resulting from the two cases *d* and *e* of Table 2. The chains are drawn in their singular position that separates the two branches of positions belonging to different groups.

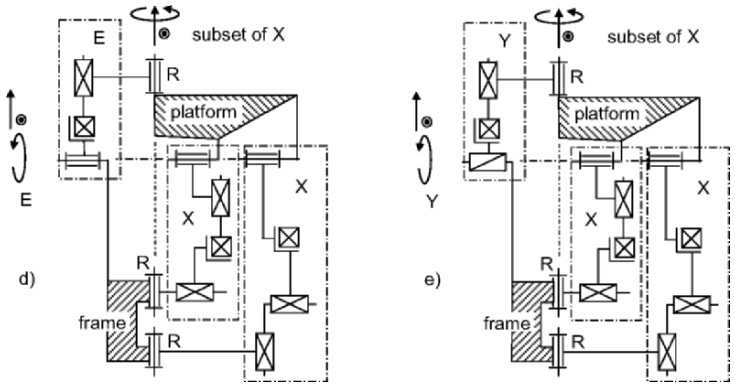

Figure 6. Robots that change displacement group but not No. of d.o.f.

For example, in the case *d*, starting from the position drawn and rotating the revolutes with horizontal axes, the robot acts as a standard planar platform, with 3 d.o.f. Starting again from the singular position, by moving the revolutes with vertical axes, the platform of the robot has a displacement that is a subset of the group X, with 3 d.o.f. (2 translations and 1 rotation). Then, the group of displacement is changed, but the number of d.o.f. is preserved.

An analogous situation applies to case *e*.

A slightly different case can be derived from a further interesting intersection group. Two Schoenflies groups X can give a group $G_{\cap} = X$ or a group $G_{\cap} = U$ (three-dimensional translation), depending on the relative positions of their rotation directions (see Fanghella and Galletti, 1994). Therefore, according to Fig. 2, the following chain can be derived.

Case	$G_1 = G_2$	$KP_a = KP_b$	Displacements between a_1 and b_2
f	X (Schoenflies)	R	From the original X (Schoenflies) to an X (Schoenflies) with the axis parallel to the axis of R

Since a group X with 4 d.o.f. is obtained in both branches, the platform must have 4 legs in order to apply one driver to each leg, according to the scheme of Fig. 7.

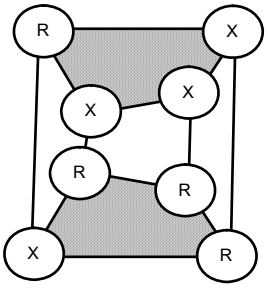

Figure 7. Scheme of a 4-legs robot.

Figure 8 shows the resulting kinematic chain of the robot in the singular position where the two branches merge.

Starting from this position and rotating the revolutes with horizontal axes, the platform moves in an X group with a horizontal rotation axis, the vertical revolutes being locked. The number of d.o.f. is 4. Starting again from the singular position, by moving the revolutes with vertical axes, the platform moves in an X group with a vertical rotation axis, the horizontal revolutes resulting locked. Again the number of d.o.f. is 4. The

group of displacement is not changed, but its invariant property (rotation axis) is changed.

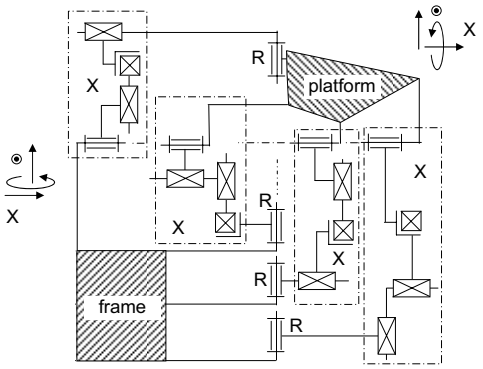

Figure 8. Robot that changes the invariant of its displacement group.

5. Joint Modifications, Actuators and Branches

The schemes of Figs. 3, 5, and 7, define kinematic structures in which specific displacement groups are generated by sequences of bodies and pairs. It is evident that in order to obtain the aforesaid mobility properties, the way in which the groups GR are realized is immaterial. For instance, it is well known that the group X can be generated by 3 non parallel prismatic pairs and one revolute, by 3 parallel revolutes and 1 prismatic pair not normal to them, and so on. Moreover, the revolutes KP in the chains can be substituted, in several circumstances by helical pairs. Therefore, many different robot structures can be obtained starting from the schemes of Figs. 3, 5, and 7.

From a practical point of view, in order to control the motion of a kinematotropic chain in a branch it is necessary to provide a number of drivers equal to the number of degrees of freedom of the chain in that branch. For a complete control of the chain in all branches, it is necessary to provide a set of drivers equal to the union of the drivers used to control each branch. In each branch, the chain is actuated only by the drivers associated with that branch, while other drivers become driven; when passing through a singular position (where the number of infinitesimal degrees of freedom grows), all drivers must act either to maintain their position or to drive the chain to a specific branch.

Finally, it is worth noting that, in some cases, starting from the singular positions in Figs. 4, 6 and 8, more than two branches may be reached. For example, for the mechanism in Fig. 6-d, a translation in the direction orthogonal to the drawing plane leads to a branch in which the

allowed relative motion between the frame and the platform is a pure planar translation. In the paper, for each case, the discussion is limited to the two branches with the highest number of degrees of freedom.

6. Conclusions

Special kinematic chains, in which displacements between two bodies can belong to different displacement groups when the chains are moved by one branch to another, are the basic components we have used for synthesizing a particular type of parallel robots. Three different situations arise for the displacement of the platform when the robot is displaced continuously from one set of positions to another one: i) in 3 cases the platform can change its group of displacement and the number degrees of freedom; ii) in 2 cases only the group of displacement is altered; iii) in 1 case only the invariant properties of the group of displacement are modified.

Acknowledgement

This work has been developed under a grant of Italian MIUR.

References

Angeles J. (1988), *Rational Kinematics*, Springer.

Fanghella P. and Galletti C. (1994), Mobility Analysis of Single-Loop Kinematic Chains: An Algorithmic Approach Based on Displacement Groups, *Mechanism and Machine Theory*, Vol. 29, pp. 1187-1204.

Galletti C. and Fanghella P. (2001), Single-Loop Kinematotropic Mechanisms, *Mechanism and Machine Theory*, Vol. 36, pp. 743-761.

Gogu G. (2005), Mobility Criterion and Overconstraints of Parallel Manipulators, *Proc. of CK2005 Int. Workshop on Computational Kinematics*, Cassino, Paper 22-CK2005, pp. 1-16.

Hervé J. (1978), Analyse Structurelle des Mécanismes par Groupe des Déplacements, *Mechanism and Machine Theory*, Vol. 13, pp. 437-450.

Kong X. and Gosselin C. (2004), Type Synthesis of 3T1R 4-DOF Parallel Manipulators Based on Screw Theory, *IEEE Transactions on Robotics and Automation*, Vol. 20, pp. 181-190.

Kong X. and Gosselin C. (2005), Type Synthesis of 3-DOF PPR-Equivalent Parallel Manipulators Based on Screw Theory and the Concept of Virtual Chain, *ASME J. of Mechanical Design*, Vol. 127, pp. 1113-1121.

Wohlhart K. (1996), Kinematotropic Mechanisms, *Recent Advances in Robot Kinematics*, (J. Lenarcic and V. Parenti Castelli, Eds.), Kluwer, pp. 359-368.

APPROXIMATING PLANAR, MORPHING CURVES WITH RIGID-BODY LINKAGES

Andrew P. Murray
University of Dayton, Department of Mechanical & Aerospace Engineering
Dayton, OH USA
murray@udayton.edu

Brian M. Korte and James P. Schmiedeler
The Ohio State University, Department of Mechanical Engineering
Columbus, OH USA
korte.16@osu.edu & schmiedeler.2@osu.edu

Abstract This paper presents a procedure to synthesize planar linkages, composed of rigid links and revolute joints, that approximate a shape change defined by a set of curves. These "morphing curves" differ from each other by a combination of rigid-body displacement and shape change. Rigid link geometry is determined through analysis of piecewise linear curves, and increasing the number of links improves the shape-change approximation. The framework is applied to an open-chain example.

Keywords: Shape change, morphing structures, planar synthesis

1. Introduction

For a mechanical system whose function depends on its geometric shape, the controlled ability to change that shape can enhance performance or expand applications. Examples of adaptive or morphing structures include antenna reflectors (Washington, 1996) and airfoils (Bart-Smith & Risseeuw, 2003) proposed to include many smart material actuators. Compliant mechanisms also provide a means of achieving shape changes. Saggere & Kota, 2001 developed a synthesis procedure for compliant four-bars that guide their flexible couplers through discrete prescribed "precision shapes" that involve both shape change and rigid-body displacement. Lu & Kota, 2003 introduced a more general approach using finite element analysis and a genetic algorithm to determine an optimized compliant mechanism's topology and dimensions.

The present work introduces synthesis techniques for planar, rigid-body mechanisms that approximate a desired shape change defined by an arbitrary number of curves, one morphing into another. Higher load-carrying capacity makes rigid-body mechanisms better suited than

J. Lenarčič and B. Roth (eds.), Advances in Robot Kinematics, 57−64.

compliant mechanisms for applications with large applied loads. Similarly, rigid-body mechanisms would likely require fewer actuators acting in parallel, such as along an airfoil with changing camber. Furthermore, actuation is not an additional development need because existing technology rather than, for example, smart material technology, is typically used to actuate rigid-body mechanisms. With rigid links, synthesis can be purely kinematic, so the system can be modeled precisely without *a priori* knowledge of exact external loads. Finally, rigid-body mechanisms can typically achieve larger displacements, enabling more dramatic shape changes. This paper details a methodology for designing rigid links that can be joined together in a chain by revolute joints to approximate the shapes of a set of morphing curves. The methodology is applicable to both open and closed chains, and an open-chain example is presented.

2. Rigid Link Geometry

The procedure for generating rigid links that compose a shape-changing linkage involves converting the desired curves, denoted as "design profiles", into "target profiles" that are readily manipulated and compared. The target profiles are divided into segments, and corresponding segments from all of the target profiles are used to generate the rigid links. The key is to divide the target profiles and then generate the rigid links so as to reduce the error in approximating the design profiles.

Design Profiles and Target Profiles. A design profile is a curve defined such that an ordered set of points on the curve and the arc length between any two such points can be determined. The piecewise linear curve (solid line) in Fig. 1 is a simple example of a design profile. A set of p design profiles defines a shape change problem. Because the change will be approximated with a rigid-body linkage, the error in the approximation is generally smaller if all p profiles have roughly equal arc length, though this is not an explicit requirement of the methodology.

A target profile is formed by distributing n points, separated by equal arc lengths, along a design profile. Thus, a target profile is a piecewise linear curve composed of the line segments connecting the ordered set of points, and any design profile can be represented by a target profile of two or more points. In Fig. 1, five (x, y) points generate a target profile from the design profile defined by three (a, b) points. The target profile includes the dashed line and does not pass through the design profile's second point. In this case, three points could be used to exactly represent the design profile, but the approach is more generally applicable to any design profile. The motivation is to convert a set of p design profiles into target profiles all defined by n points such that corresponding points can

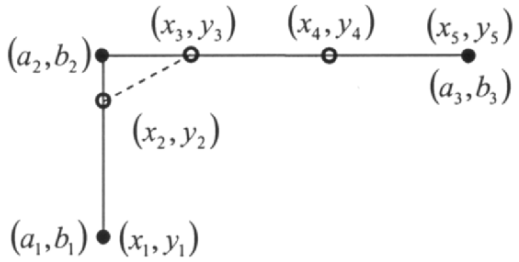

Figure 1. Three-point (a, b) design profile and five-point (x, y) target profile.

be found on each target profile. For a closed curve design profile, any point can be deemed the first/last point, yielding a closed target profile.

Important characteristics of a target profile include the fact that its arc length is always shorter than the design profile it represents. The most significant loss of shape information occurs where the curvature is largest for a continuous design profile or where the angle at a vertex is smallest in magnitude for a piecewise linear design profile. Since points on the target profile are separated by equal arc lengths along the design profile, they are not at equidistant intervals along the target profile. Large values of n produce smaller variations between the design profile and target profile and in the distances between consecutive points on the target profile. A useful heuristic is selection of n such that the target profile arc length is greater than 99% of the design profile arc length.

Shifted Profiles. The j^{th} target profile is defined by, $\vec{z}_{j_i} = \{x_{j_i}\ y_{j_i}\}^T$, i=1,...n. A rigid-body transformation in the plane,

$$\vec{Z}_{j_i} = A\vec{z}_{j_i} + \vec{d}, \text{ where } A = \begin{bmatrix} \cos\theta & -\sin\theta \\ \sin\theta & \cos\theta \end{bmatrix} \text{ and } \vec{d} = \begin{Bmatrix} d_1 \\ d_2 \end{Bmatrix},$$

will relocate the profile preserving the respective distances between points in it. Any profile relocated in this fashion is called a shifted profile. Target and mean profiles (described below) are both shifted to perform useful design operations without altering the original design problem.

The "distance" between target profiles j and k is defined to be,

$$D = \sum_{i=1}^{n} (x_{j_i} - x_{k_i})^2 + (y_{j_i} - y_{k_i})^2 = \sum_{i=1}^{n} |\vec{z}_{j_i} - \vec{z}_{k_i}|^2.$$

(Subsequent summations are $i = 1,...n$.) Viewing the target profile's n points as a single point in $2n$-dimensional space, this distance is the square of the Euclidean norm in that space, so D is an appropriately defined metric. To determine the rigid-body transformation that shifts

target profile j to the location that minimizes D with respect to target profile k, one must find θ and $\vec{d}$ such that $\frac{\partial D}{\partial \theta} = \frac{\partial D}{\partial d_1} = \frac{\partial D}{\partial d_2} = 0$, where,

$$D = \sum \vec{z}_{j_i}^T \vec{z}_{j_i} + \vec{d}^T \vec{d} + \vec{z}_{k_i}^T \vec{z}_{k_i} + 2\vec{d}^T A \vec{z}_{j_i} - 2\vec{z}_{k_i}^T A \vec{z}_{j_i} - 2\vec{d}^T \vec{z}_{k_i}.$$

Introducing the definition $\sum \vec{z}_{j_i} = \vec{z}_{j_T} = \{x_{j_T}\ y_{j_T}\}^T$ yields a solution,

$$\tan\theta = \frac{\frac{1}{n}(x_{k_T} y_{j_T} - x_{j_T} y_{k_T}) - \sum(x_{k_i} y_{j_i} - x_{j_i} y_{k_i})}{\sum(x_{j_i} x_{k_i} + y_{j_i} y_{k_i}) - \frac{1}{n}(x_{j_T} x_{k_T} + y_{j_T} y_{k_T})}, \quad \vec{d} = \frac{1}{n}(\vec{z}_{k_T} - A\vec{z}_{j_T}).$$

Mean Profiles and Segmentation. A mean profile is one profile that approximates the shapes of all target profiles in a set. A mean profile is formed by shifting target profiles 2 through p to minimize their respective distances relative to reference target profile 1. A new piecewise linear curve defined by n points, each the geometric center of the set of p corresponding points in the shifted target profiles, is generated. For example, two target profiles in Fig. 2a are shifted in Fig. 2b to their respective distance minimizing positions relative to the first profile. Fig. 2c shows the mean profile that approximates the target profiles when regarded as rigid bodies. In Fig. 2d, this mean profile is shifted to approximate the shape and location of the target profiles. The described procedure could convert a shape-changing problem to a rigid-body guidance problem, as the three locations of the mean profile in Fig. 2d define three finitely separated positions of a moving lamina.

A chain of two or more rigid links connected by revolute joints can better approximate a shape change than can a single rigid body with the shape of a mean profile. The procedure for generating a mean profile may be applied to any segment of the target profiles. To generate a linkage composed of s rigid links, an initial solution divides the target profiles into s segments of roughly equal numbers of points, the last point of a segment being the first of the next segment. A mean profile is generated for each set of segments. For example, given target profiles of $n = 102$ points, if $s = 4$, the segments are composed of points 1-26, 26-51, 51-76, and 76-102. The first three segments and their corresponding mean profiles each have 26 points, and the last has 27. Once generated, each mean profile can be shifted individually to the location relative to its corresponding segment in each target profile that minimizes D. The positions of the s mean profiles relative to each other will differ as they are superimposed on each target profile. The end points of the segments in general will not coincide in any of the positions at this stage.

Error Reducing Segmentation. Non-uniform target profile segmentation can reduce the error in approximating a shape change by shortening segments on the profile where shape change is most dramatic.

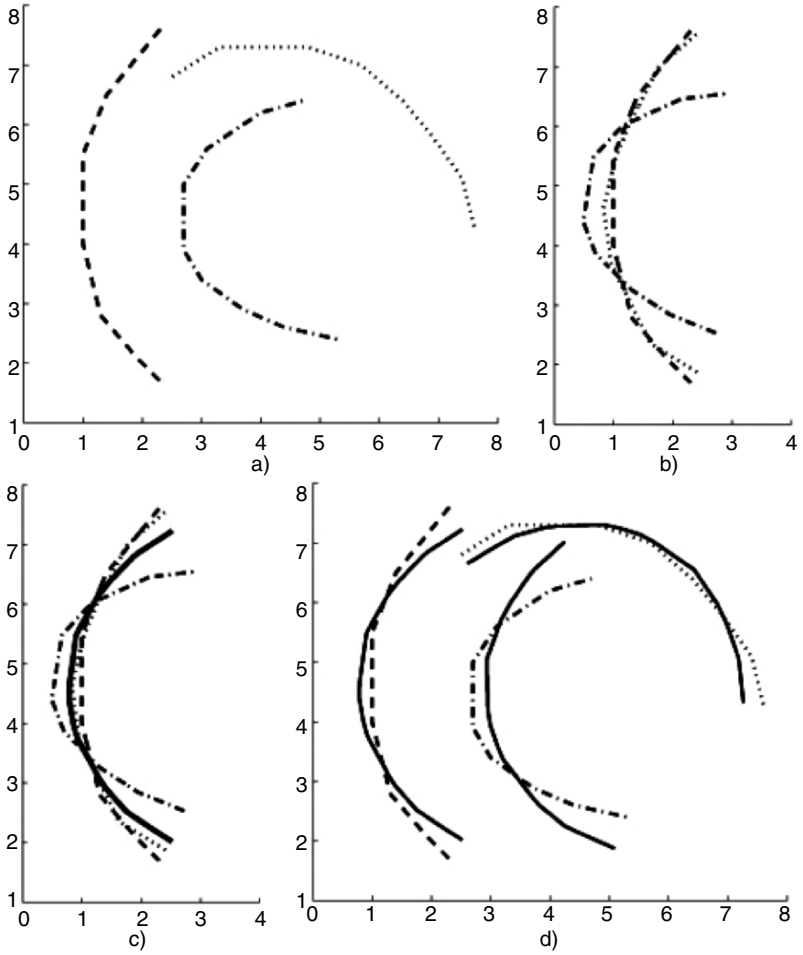

Figure 2. a) Three target profiles, b) Shifted target profiles to minimize D, c) Mean profile (solid line), d) Mean profile shifted to minimize D for each target profile.

The distance D is a poor segmentation metric because it depends on a segment's number of points. A better metric, the error E, is defined as follows. For mean profile l, the error E_{l_j} associated with matching the corresponding segment in target profile j is the maximum distance between any two corresponding points on the two profiles when the mean profile is shifted to the distance-minimizing location relative to the target profile segment. The error E_l associated with this mean profile is the maximum value of E_{l_j} for all target profiles $j = 1,...p$. The overall error E is the maximum value of E_l for all mean profiles $l = 1,...s$.

To reduce E, the segmentation locations on the target profiles are moved. Starting with segment 1, the number of points in each segment

l, except the last segment s, is increased by one if $E_l < \bar{E}$ and decreased by one if $E_l > \bar{E}$, where $\bar{E}$ is the average of the E_l's. Segments 1 and s change by one point, and the others by two. E_s does not explicitly determine whether segment s increases or decreases in length, but its effect on E and $\bar{E}$ does so indirectly. With the target profile segments redefined, a new mean profile for each set is generated, the error E recomputed, and the process repeated until E ceases to decrease. To avoid local minima, the process continues for several iterations after E increases, and each E is compared to several previous iterations instead of just the immediate predecessor. The segmentation providing the smallest E is the error reducing segmentation, and the corresponding mean profiles define the geometry of the rigid links that compose the linkage. Because the target profiles typically contain thousands of points, altering segments by two points is a modest change, and exhaustive approaches involving single-point alterations are unlikely to offer significant benefit.

An alternative approach for initial segmentation is to specify an acceptable error E_a instead of a number of segments, and "grow" segments, starting with 1, point by point until the error E_l of the corresponding mean profile exceeds E_a. This generates an unknown number of segements, the last of which generally has the smallest error.

3. Example

The three design profiles used to generate the target profiles in Fig. 2a are defined by the points listed in Tb. 1, and their arc lengths are 6.72, 6.78, and 6.76, respectively. The target profiles contain 1800 points, as does the mean profile in Fig. 2c. The subset of points from the mean profile listed in Tb. 1 are key points that mark the locations of significant change in slope along the mean profile. Figure 3 plots the error

Table 1. Defining points of design profiles and key points of mean profile in Fig. 2. Mean profile points are in two columns, each ordered top to bottom.

Design Profile 1	Design Profile 2	Design Profile 3	Mean Profile	
(2.3,7.6)	(7.6,4.3)	(4.7,6.4)	(2.52,7.23)	(0.78,4.39)
(1.4,6.5)	(7.4,5.1)	(4.0,6.2)	(1.94,6.85)	(0.85,4.01)
(1.0,5.5)	(6.9,5.8)	(3.1,5.6)	(1.87,6.80)	(0.90,3.83)
(1.0,4.0)	(6.4,6.4)	(2.7,5.0)	(1.46,6.38)	(0.94,3.73)
(1.3,2.8)	(5.7,7.0)	(2.7,3.9)	(1.32,6.19)	(1.29,3.08)
(1.9,2.1)	(4.8,7.3)	(3.0,3.4)	(1.24,6.10)	(1.38,2.93)
(2.3,1.7)	(4.0,7.3)	(3.7,2.9)	(0.93,5.54)	(1.74,2.53)
	(3.3,7.3)	(4.4,2.6)	(0.91,5.49)	(1.76,2.52)
	(2.5,6.8)	(5.3,2.4)	(0.90,5.48)	(2.04,2.32)
			(0.79,4.64)	(2.52,2.02)

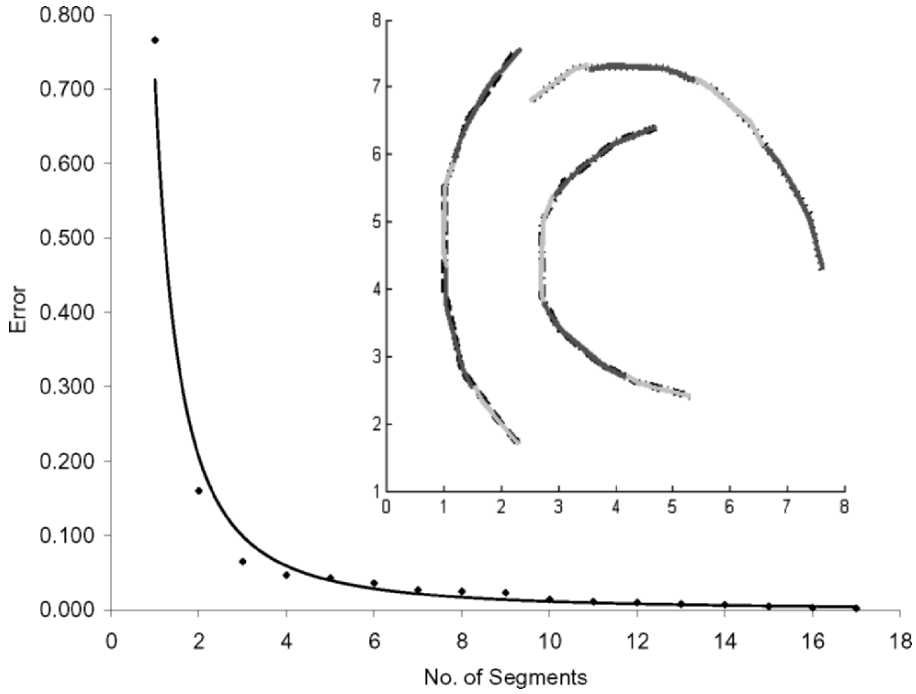

Figure 3. Error in matching target profiles shown in Fig. 2a as a function of number of segments. Inset shows 4-segment solution superimposed on target profiles. Solution segments correspond to unassembled rigid links of a shape-changing linkage.

E in matching the target profiles as a function of the number of segments, with a curve fit to the data to more clearly illustrate the trend. The data point for 1 segment represents the solution shown in Fig. 2d, for which the error clearly is defined by the top end point of the middle target profile. In Fig. 3, increasing the number of segments beyond 4 offers noticably diminishing returns in terms of reduced error. The plot inset in Fig. 3 contains the 4-segment solution superimposed on the target profiles with the segments shown in alternating shades of gray.

4. Mechanization

Once the geometry of the rigid links is determined, the links are joined together at their end points with revolute joints to form a linkage. This increases the error since it requires movement of the links from their distance-minimizing positions to bring together the generally non-coincident adjacent endpoints. Furthermore, the relative motion

required between adjacent links to achieve their distance-minimizing positions is more general than that allowed by revolute joints. Still, if the error prior to connecting the links is small, the linkage approximates well the desired shape change. With the links joined, it is often desirable to add additional links that constrain the linkage to have a reduced number of degrees of freedom. To constrain an s-link open chain to be a 1-DOF mechanism, $s + 1$ binary links must be added. If five or fewer design profiles are involved, circle and center points for additional binary links can be found exactly, but for six or more design profiles, least-square approximations such as those developed by Sarkisyan, et al., 1973 are required. The details of mechanization are beyond the scope of this paper, but each additional link further constrains the motion of the shape-change-approximating links, thereby increasing the error.

5. Conclusions

This work introduces a systematic procedure to determine the geometry of rigid links that can be assembled together with revolute joints to compose a linkage that approximates a desired shape change defined by an arbitrary number of morphing curves. The procedure involves comparing piecewise linear curves to reduce the error in the shape change approximation, and increasing the number of links generally reduces that error. Mechanizing the generated chains of rigid links presents a number of challenges, but rigid-body mechanisms have great potential as morphing structures, particularly in heavy load applications.

6. Acknowledgements

This material is based upon work supported in part by the National Science Foundation under Grant No. #0422731 to A. Murray.

References

Bart-Smith, H., & Risseeuw, P.E. (2003), High authority morphing structures, *Proc. ASME International Mechanical Engineering Congress*, Washington, D.C., USA.

Lu, K.J., & Kota, S. (2003), Design of compliant mechanisms for morphing structural shapes, *Journal of Intelligent Material Systems & Structures*, vol. 14, pp. 379–391.

Saggere, L., & Kota, S. (2001), Synthesis of planar, compliant four-bar mechanisms for compliant-segment motion generation, *ASME Journal of Mechanical Design*, vol. 123, no. 4, pp. 535–541.

Sarkisyan, Y.L., Gupta, K.C., & Roth, B. (1973), Kinematic geometry associated with the least-square approximation of a given motion, *ASME Journal of Engineering for Industry*, vol. 95, no. 2, pp. 503–510.

Washington, G.N. (1996), Smart aperture antennas, *Journal of Smart Materials & Structures*, vol. 5, no. 6, pp. 801–805.

ON THE VELOCITY ANALYSIS OF NON-PARALLEL CLOSED CHAIN MECHANISMS

Matteo Zoppi[a], Dimiter Zlatanov[b], Rezia Molfino[a]
[a] *Università di Genova, via Opera Pia 15A, 16145, Genova, Italia*
[b] *Département de Génie Mécanique, Université Laval, Québec, QC, Canada*
[zoppi,molfino]@dimec.unige.it, zlatanov@gmc.ulaval.ca

Abstract In parallel mechanisms (PMs), the passive joint velocities can be eliminated from the velocity equations by a standard screw-theory method, obtaining a system of linear input-output equations. A general method for the elimination of the passive joint velocities in non purely parallel mechanisms is not yet known. The paper addresses the problem by studying the instantaneous kinematics of two non-parallel closed-chain 4-dof mechanisms derived from a 5-dof PM. With some modifications and appropriate geometric reasoning the PM methodology can be successfully applied to the analysis of non-parallel mechanisms.

Keywords: Velocity analysis, parallel mechanisms, closed chain mechanisms

1. Introduction

Parallel mechanisms (PMs) are composed of an end-effector connected to the base by separate serial leg chains, Fig. 1. Most published closed spatial kinematic chains are PMs, but occasionally authors describe as "parallel" kinematic chains that do not strictly belong to this class.

A relatively simple generalization of a parallel (or serial) mechanism is when the kinematic chain is a two-terminal series-parallel graph connecting the base to the end-effector. Starting with a parallel (or serial) chain, substitute individual joints with parallel subchains; a *mostly parallel (or serial) series-parallel (S-P) chain (and mechanism, S-PM)* is the result (Fig. 2). More complex chains can be obtained from a mostly parallel S-P connection when subchains (with at least one joint) are added between links belonging to different leg chains. Such mechanisms can be referred to as *interconnected chains* (IC) mechanisms (ICMs) (Fig. 3).

In a PM, out of singularities, the input-output velocity equations (relating the output twist, $\boldsymbol{\xi} = (\boldsymbol{\omega}, \mathbf{v})$, or $(\boldsymbol{\omega}^T|\mathbf{v}^T)^T$ as a column vector, and the actuated joint velocities, $\dot{\mathbf{q}}$) are obtained in the form: $\mathbf{Z}\boldsymbol{\xi} = \boldsymbol{\Lambda}\dot{\mathbf{q}}$.

For PMs, $\mathbf{Z}$ and $\boldsymbol{\Lambda}$ are computed by a screw-theory based method that can be considered standard. It is relatively easy (ignoring unusual

J. Lenarčič and B. Roth (eds.), Advances in Robot Kinematics, 65–72.

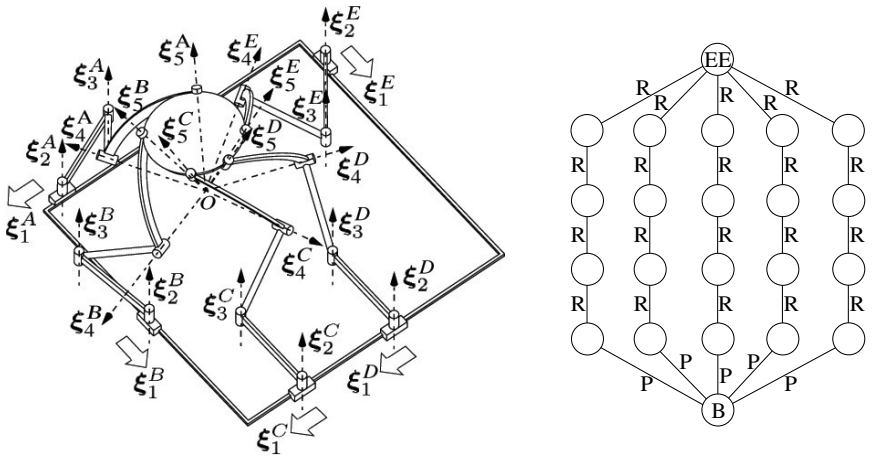

Figure 1. 5-dof PM: architecture with leg screws (left) and graph (right).

singularities such as RPM or IIM singularities, (Zlatanov et al., 1994)) to generalize the passive-velocity elimination for series-parallel chains. The method cannot be used, without changes, for ICMs. In the general case, one deals with the velocity loop equations (rather than linear expressions of $\boldsymbol{\xi}$ in terms of the leg's joint screws). Analogously, Ohm's laws suffice when an electrical network is series-parallel; otherwise the more general Kirchhoff laws are needed (Davies, 1981).

As we have shown (Zoppi et al., 2006), the ideas of PM velocity analysis can be applied successfully to ICMs. The present paper illustrates this further by studying two new non-PMs. We modify a 5-dof PM and its analysis to obtain and solve first a 4-dof S-PM and then a 4-dof ICM.

2. A 5-dof PM

In the 5-dof PM in Fig. 1 (Huang and Li, 2003), the PRRRR legs are identical and labeled $L = A, \ldots, E$. Numerical indices count the leg's joints, always from the base. The joint screws and their directions are $\boldsymbol{\xi}_i^L$ and $\mathbf{k}_i^L$, $i = 1, \ldots, 5$, while the links are denoted $\boldsymbol{b}_i^L$, with $\boldsymbol{b} = \boldsymbol{b}_0^L, \boldsymbol{e} = \boldsymbol{b}_5^L$ the base and platform. The P joints are horizontal while axes 2 and 3 are vertical in plane π_{23}^L with normal $\mathbf{n}_{23}^L$. Axes 4 and 5 intersect at the rotation center O fixed in the platform; their plane is π_{45}^L.

2.1 Constraint and Mobility Analysis

Assume nonsingular leg postures. The leg system of structural constraints (wrenches reciprocal to all leg joints) is $\mathcal{W}_L = \mathrm{Span}\,(\boldsymbol{\varphi}_z)$, with $\boldsymbol{\varphi}_z$ a vertical force at O. The actuated constraints (reciprocal to the leg passive joints) are $\mathcal{V}_L = \mathrm{Span}\,(\boldsymbol{\varphi}_z, \boldsymbol{\varphi}^L)$, with force $\boldsymbol{\varphi}^L$ along $\pi_{23}^L \cap \pi_{45}^L$.

The combined constraint systems are: $\mathcal{W} = \sum_L \mathcal{W}_L = \mathrm{Span}\,(\boldsymbol{\varphi}_z)$; $\mathcal{V} = \sum_L \mathcal{V}_L = \mathcal{W} + \mathrm{Span}\,(\boldsymbol{\varphi}^A, \ldots, \boldsymbol{\varphi}^E)$. So the platform has full rotational capability about its point O, which can translate horizontally. Out of singularity, $\dim \mathcal{V} = 6$ and the mechanism can be controlled by actuating the five P joints.

2.2 Jacobian Analysis

The screw-theoretical method for the velocity analysis of PMs was developed in works like (Hunt, 1978); (Mohamed and Duffy, 1985); (Kumar, 1992); (Agrawal, 1990); (Zlatanov et al., 1994); (Zlatanov et al., 2002); (Joshi and Tsai, 2002). We provide a detailed general formulation in (Zoppi et al., 2006).

For each leg, a non-unique actuation system, $\mathcal{U}_L$, is identified, $\mathcal{V}_L = \mathcal{W}_L \oplus \mathcal{U}_L$, for this PM we use $\mathcal{U}_L = \mathrm{Span}\,(\boldsymbol{\varphi}^L)$. The reciprocal product of the actuations (any basis of $\mathcal{U}_L$) eliminates the passive joint velocities from the leg twist equation, here $\boldsymbol{\xi} = \dot{q}_1^L \boldsymbol{\xi}_1^L + \sum_{i=2}^5 \omega_i^L \boldsymbol{\xi}_i^L$.

To obtain an equation $\mathbf{Z}\boldsymbol{\xi} = \boldsymbol{\Lambda}\dot{\mathbf{q}}$ with coefficients in terms of the PM's geometry, we need symbolic expressions for the actuation screws $\boldsymbol{\varphi}^L = (\mathbf{f}^L, \mathbf{m}^L)$. We use a moving frame $O\mathbf{ijk}$, Oz always vertical. Since $\boldsymbol{\varphi}^L$, a pure force, and the origin are in π_{45}^L, $\mathbf{m}^L = r^L \mathbf{n}_{45}^L$, where $\mathbf{n}_{45}^L$ is the unit normal to π_{45}^L and r^L is the distance of $\boldsymbol{\varphi}^L$ from O. Since the intensity is irrelevant, $\mathbf{f}^L = \mathbf{n}_{45}^L \times \mathbf{n}_{23}^L$ and, ignoring the singularity $\pi_{23} \parallel \pi_{45}$:

$$\boldsymbol{\varphi}^L = (\mathbf{n}_{45}^L \times \mathbf{n}_{23}^L \mid \left|\mathbf{n}_{45}^L \times \mathbf{n}_{23}^L\right| r^L {\mathbf{n}_{45}^L}^T)^T \tag{1}$$

We can now write the input-output equations. The structural constraints amount to the condition $v_z = 0$, in $\boldsymbol{\xi} = (\omega_x, \omega_y, \omega_z | v_x, v_y, v_z)^T$. The v_z output velocity can be ignored and the system becomes five-dimensional:

$$\left[\begin{array}{c|cc} f^A r^A {\mathbf{n}_{45}^A}^T & f^A{}_x & f^A{}_y \\ f^B r^B {\mathbf{n}_{45}^B}^T & f^B{}_x & f^B{}_y \\ f^C r^C {\mathbf{n}_{45}^C}^T & f^C{}_x & f^C{}_y \\ f^D r^D {\mathbf{n}_{45}^D}^T & f^D{}_x & f^D{}_y \\ f^E r^E {\mathbf{n}_{45}^E}^T & f^E{}_x & f^E{}_y \end{array}\right] \bar{\boldsymbol{\xi}} = \underset{L\,=\,A,\ldots,E}{\mathrm{diag}} \; (\mathbf{k}_1^L \cdot \mathbf{f}^L) \left[\begin{array}{c} \dot{q}_1^A \\ \dot{q}_1^B \\ \dot{q}_1^C \\ \dot{q}_1^D \\ \dot{q}_1^E \end{array}\right] \tag{2}$$

$\bar{\boldsymbol{\xi}}$ is $\boldsymbol{\xi}$ with the z coordinate of its moment suppressed.

3. A 2R2T 4-dof S-PM

The PM of Fig. 1 has instantaneous end-effector motions spanned by 2 translations and 3 rotations, all independent. Mobility types allowing

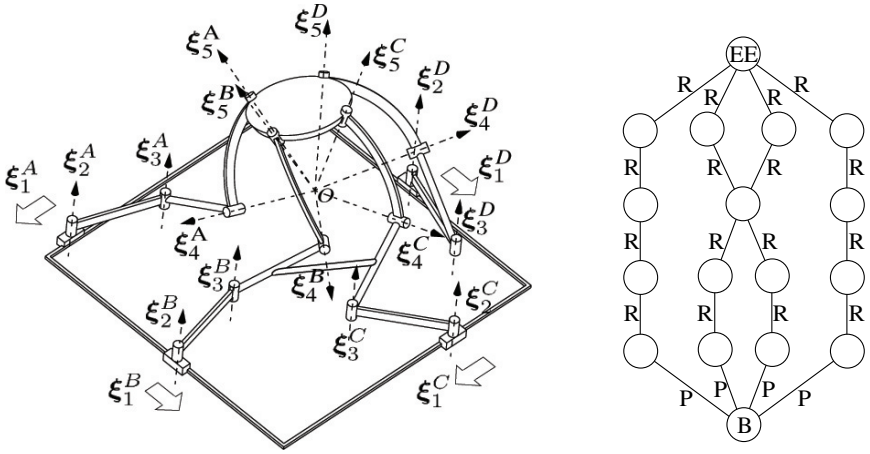

Figure 2. 4-dof 2R2T S-PM: architecture with leg screws (left) and graph (right).

instantaneous motions spanned by 2 translations and 2 rotations (2R2T) are potentially useful for possible practical application and because of the few mechanisms proposed in the technical literature having this mobility.

The 5 dof of the PM of Fig. 1 are reduced to 4 if two third links, say $\boldsymbol{b}_3^B$ and $\boldsymbol{b}_3^C$, are joined in one $\boldsymbol{b}_3^{BC}$. The result is an S-PM, Fig. 2. (The same result can be obtained from the PM by an extra link between $\boldsymbol{\xi}_3^B$ and $\boldsymbol{\xi}_3^C$ creating an immobile spatial 4-bar, see Fig. 3.)

3.1 Constraint and Mobility Analysis

Legs B and C are combined in a mostly serial leg BC, composed of a planar PM and a passive spherical 4-bar in series.

The spherical 4-bar's coupler, $\boldsymbol{e}$, has one dof with respect to $\boldsymbol{b}^{BC}$ and a constraint 5-system $\mathcal{W}_{BC}^b = \mathrm{Span}\,(\boldsymbol{\varphi}_x, \boldsymbol{\varphi}_y, \boldsymbol{\varphi}_z, \boldsymbol{\mu}_{45}^B, \boldsymbol{\mu}_{45}^C)$, where $\boldsymbol{\varphi}_x$, $\boldsymbol{\varphi}_y$, $\boldsymbol{\varphi}_z$ span all forces at O and $\boldsymbol{\mu}_{45}^L$ is a couple about $\mathbf{n}_{45}^L$. All four joints are passive, hence $\mathcal{V}_{BC}^b = \mathcal{W}_{BC}^b$.

The 2-PRR planar PM from $\boldsymbol{b}$ to $\boldsymbol{b}^{BC}$ imposes the (planar) structural constraints, $\mathcal{W}_{BC}^a = \mathrm{Span}\,(\boldsymbol{\varphi}_z, \boldsymbol{\mu}_x, \boldsymbol{\mu}_y)$, and the actuated constraints $\mathcal{V}_{BC}^a = \mathcal{W}_{BC}^a \oplus \mathrm{Span}\,(\boldsymbol{\varphi}^B, \boldsymbol{\varphi}^C)$. The actuation L can be any nonvertical force in π_{23}^L, in particular (out of singularity) $\boldsymbol{\varphi}^L$ as chosen in Section 2.1.

The whole leg BC imposes the constraint systems: $\mathcal{W}_{BC} = \mathcal{W}_{BC}^a \cap \mathcal{W}_{BC}^b = \mathrm{Span}\,(\boldsymbol{\varphi}_z, \boldsymbol{\mu}_0^{BC})$, where $\boldsymbol{\mu}_0^{BC}$ is a pure moment with direction $\mathbf{k} \times \mathbf{n}_{45}^B \times \mathbf{n}_{45}^C$; and $\mathcal{V}_{BC} = \mathcal{V}_{BC}^a \cap \mathcal{V}_{BC}^b = \mathcal{W}_{BC} \oplus \mathrm{Span}\,(\boldsymbol{\varphi}^B, \boldsymbol{\varphi}^C) = \mathrm{Span}\,(\boldsymbol{\varphi}^B, \boldsymbol{\varphi}^C, \boldsymbol{\varphi}_z, \boldsymbol{\mu}_0^{BC})$.

The combined platform constraints, for the 4-legged S-PM, are: $\mathcal{W} = \sum_L \mathcal{W}_L = \mathrm{Span}\,(\boldsymbol{\varphi}_z, \boldsymbol{\mu}_0^{BC})$; $\mathcal{V} = \sum_L \mathcal{V}_L = \mathrm{Span}\,(\boldsymbol{\varphi}^A, \boldsymbol{\varphi}^B, \boldsymbol{\varphi}^C, \boldsymbol{\varphi}^D) \oplus \mathcal{W}$

($\boldsymbol{\varphi}^A$, $\boldsymbol{\varphi}^D$ as in Section 2.1). $\dim \mathcal{V} = 6$ and the S-PM is commanded by the four actuated P_1^L. (Leg E is thus not needed and removed.)

3.2 Jacobian Analysis

The velocity analysis proceeds as in the original PM. Locking any P_1^L adds one independent basis screw in $\boldsymbol{\varphi}^L$, as in the original PM. Therefore, we can proceed writing the velocity equations along the four serial chains (two of which share $\boldsymbol{b}^{BC}$) and eliminating the passive joint velocities without considering the presence of the additional link.

The velocity equations are $\boldsymbol{\xi} = \dot{q}_1^L \boldsymbol{\xi}_1^L + \sum_{i=2}^{5} \omega_i^L \boldsymbol{\xi}_i^L$, $L = A, B, C, D$. We eliminate the passive joint velocities from the L-th equation by reciprocal product with $\boldsymbol{\varphi}^L$ from Eq. (1).

The couple $\boldsymbol{\mu}_0^{BC}$ is horizontal. In a reference frame $O\mathbf{ijk}$ with $\mathbf{i} \parallel \boldsymbol{\mu}_0^{BC}$, the ω_x and v_z components of $\boldsymbol{\xi}$ are zero, and the system of four velocity equations becomes four-dimensional. From Eq. (2), we obtain:

$$\left[\begin{array}{cc|cc} f^A r^A n^A_{45y} & f^A r^A n^A_{45z} & f^A{}_x & f^A{}_y \\ f^B r^B n^B_{45y} & f^B r^B n^B_{45z} & f^B{}_x & f^B{}_y \\ f^C r^C n^C_{45y} & f^C r^C n^C_{45z} & f^C{}_x & f^C{}_y \\ f^D r^D n^D_{45y} & f^D r^D n^D_{45z} & f^D{}_x & f^D{}_y \end{array}\right] \bar{\boldsymbol{\xi}} = \operatorname*{diag}_{L=A,\ldots,D} (\mathbf{k}_1^L \cdot \mathbf{f}^L) \left[\begin{array}{c} \dot{q}_1^A \\ \dot{q}_1^B \\ \dot{q}_1^C \\ \dot{q}_1^D \end{array}\right] \tag{3}$$

4. A 2R2T 4-dof ICM

Consider finally the ICM in Fig. 3, derived from the S-PM in Fig. 2 by moving the fifth joints of legs A and D from the end-effector to links $\boldsymbol{b}_4^B$ and $\boldsymbol{b}_4^C$, respectively.

We refer three subchains as "legs": the central S-P leg BC (same as in the S-PM); and the the two lateral $\mathsf{P4R}$ serial chains, from the base to $\boldsymbol{b}_4^B$ and $\boldsymbol{b}_4^C$.

4.1 Constraint and Mobility Analysis

From Section 3.1, the structural constraint applied to the end-effector by leg BC is $\mathcal{W}_{BC} = \text{Span}\,(\boldsymbol{\varphi}_z, \boldsymbol{\mu}_0^{BC})$. Lateral leg A applies on $\boldsymbol{b}_4^B$ the same structural constraint $\text{Span}\,(\boldsymbol{\varphi}_z)$, which is also reciprocal to $\boldsymbol{\xi}_5^B$, and similarly for leg D and $\boldsymbol{b}_4^C$. Thus, the combined structural constraint on the end-effector is still $\mathcal{W} = \text{Span}\,(\boldsymbol{\varphi}_z, \boldsymbol{\mu}_0^{BC})$ as for the S-PM; $\dim \mathcal{W} = 2$ and the ICM has the same 4-dof mobility.

For the actuated end-effector constraint, we consider joints $\boldsymbol{\xi}_1^B$, $\boldsymbol{\xi}_1^C$ and $\boldsymbol{\xi}_1^A$, $\boldsymbol{\xi}_1^D$ separately.

Consider first the constraint when actuators B and C are locked. Because $\boldsymbol{\xi}_1^A$ and $\boldsymbol{\xi}_1^D$ are free, it does not matter whether the lateral legs

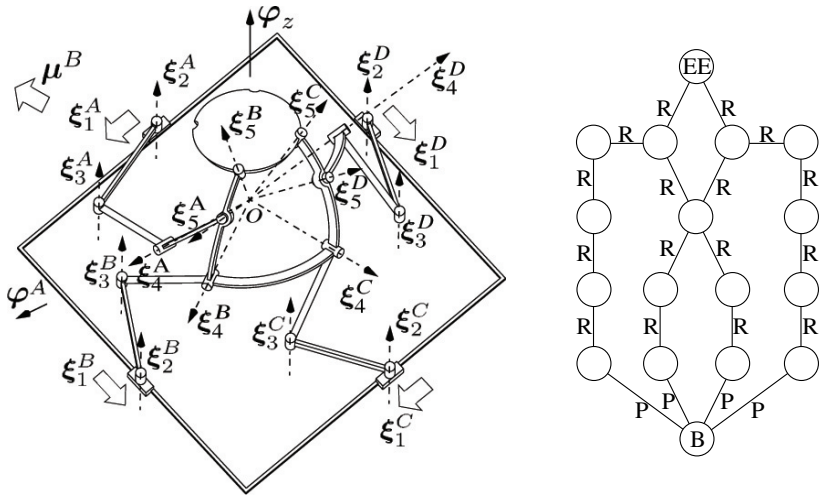

Figure 3. 4-dof 2R2T ICM: architecture with leg screws (left) and graph (right).

are connected to the end-effector or to $\boldsymbol{b}_4^L$ and, as in Section 3.1, the actuation wrenches are $\boldsymbol{\varphi}^L$, $L = B, C$, $\mathcal{V}_{BC} = \mathcal{W} + \text{Span}\,(\boldsymbol{\varphi}^B, \boldsymbol{\varphi}^C)$.

Consider now the contribution of leg A. We analyze, first, the constraint on $\boldsymbol{b}_4^B$. Joint $\boldsymbol{\xi}_1^A$ is locked: the constraint of leg A on $\boldsymbol{b}_4^B$ is $\text{Span}\,(\boldsymbol{\varphi}_z, \boldsymbol{\varphi}^A)$. The constraint on $\boldsymbol{b}_4^B$ coming from leg BC is $\text{Span}\,(\boldsymbol{\varphi}_z, \boldsymbol{\mu}^B)$, where $\boldsymbol{\mu}^B$ is a pure moment with direction $\mathbf{k} \times \mathbf{k}_4^B$. The total actuated constraint on $\boldsymbol{b}_4^B$ with $\boldsymbol{\xi}_1^A$ locked is $\mathcal{V}_4^A = \text{Span}\,(\boldsymbol{\varphi}_z, \boldsymbol{\varphi}^A, \boldsymbol{\mu}^B)$. This is an IB(h = 0,$\gamma$) 3-system containing pure forces with direction $\mathbf{k}$ in the plane π_0^A through O orthogonal to $\boldsymbol{\mu}^B$, and pure forces in the pencil centered at the point P^A where $\boldsymbol{\varphi}^A$ intersects π_0^A, in the plane through $\boldsymbol{\varphi}^A$ parallel to $\mathbf{k}$.

Only wrenches reciprocal to $\boldsymbol{\xi}_5^B$ are transmitted to the platform. The subsystem $\mathcal{V}_{4e}^A = \mathcal{V}_4^A \cap \text{Span}\,(\boldsymbol{\xi}_5^B)^\perp$ is a cylindroid, $\text{Span}\,(\boldsymbol{\varphi}_z, \boldsymbol{\varphi}_e^A)$, $\boldsymbol{\varphi}_e^A$ in the pencil at P^A and intersecting $\boldsymbol{\xi}_5^B$. Another wrench in $\mathcal{V}_{4e}^A$ is $\boldsymbol{\zeta}^{AB}$, obtained by linear combination of $\boldsymbol{\varphi}^A$ and $\boldsymbol{\mu}^B$:

$$\boldsymbol{\zeta}^{AB} = (\boldsymbol{\xi}_5^B \circ \boldsymbol{\mu}^B)\boldsymbol{\varphi}^A - (\boldsymbol{\xi}_5^B \circ \boldsymbol{\varphi}^A)\boldsymbol{\mu}^B = \lambda_1^{AB}\boldsymbol{\varphi}^A + \lambda_2^{AB}\boldsymbol{\mu}^B \qquad (4)$$

Thus, the platform constraint with $\boldsymbol{\xi}_1^A$ locked is $\mathcal{V}^A = \mathcal{W} \oplus \text{Span}\,(\boldsymbol{\zeta}^{AB})$. Similarly, $\mathcal{V}^D = \mathcal{W}_{BC} \oplus \text{Span}\,(\boldsymbol{\zeta}^{DC})$ and, out of singularities, $\mathcal{V} = \mathcal{V}_A + \mathcal{V}_{BC} + \mathcal{V}_D$ is the 6-system.

4.2 Jacobian Analysis

In this case, the analysis needs to be changed significantly. We cannot proceed as before, because the "legs" do not all reach the end-effector.

We analyze, first, leg A and the subchain B of leg BC. The velocity equations are:

$$\boldsymbol{\xi} = \dot{q}_1^A \boldsymbol{\xi}_1^A + \sum_{i=2}^{5} \omega_i^A \boldsymbol{\xi}_i^A + \omega_5^B \boldsymbol{\xi}_5^B \tag{5}$$

$$\boldsymbol{\xi} = \dot{q}_1^B \boldsymbol{\xi}_1^B + \sum_{i=2}^{5} \omega_i^B \boldsymbol{\xi}_i^B \tag{6}$$

We compute the reciprocal product of Eqs. (5) and (6) by $\lambda_1^{AB}\boldsymbol{\varphi}^A$ and $\lambda_2^{AB}\boldsymbol{\mu}^B$, respectively. Then we add them and simplify using Eq. (4) and $\boldsymbol{\xi}_5^B \circ \boldsymbol{\zeta}^{AB} = 0$. The same is done for leg D and subchain C of leg BC. We obtain:

$$\boldsymbol{\xi} \circ \boldsymbol{\zeta}^{LM} = \dot{q}_1^L \boldsymbol{\xi}_1^L \circ \lambda_1^{LM} \boldsymbol{\varphi}^L \qquad (L, M) = (A, B), (D, C) \tag{7}$$

Two more velocity equations come from the subchains B and C of leg BC: $\boldsymbol{\xi} = \dot{q}_1^L \boldsymbol{\xi}_1^L + \sum_{i=2}^{5} \omega_i^L \boldsymbol{\xi}_i^L$, $L = B, C$. The passive joint velocities are eliminated by computing the reciprocal products with $\boldsymbol{\varphi}^B$ and $\boldsymbol{\varphi}^C$, respectively, obtaining: $\boldsymbol{\xi} \circ \boldsymbol{\varphi}^L = \dot{q}_1^L \boldsymbol{\xi}_1^L \circ \boldsymbol{\varphi}^L$. These equations and (7) can be arranged in the matrix form:

$$\begin{bmatrix} \tilde{\boldsymbol{\zeta}}^{AB} \\ \tilde{\boldsymbol{\varphi}}^B \\ \tilde{\boldsymbol{\varphi}}^C \\ \tilde{\boldsymbol{\zeta}}^{DC} \end{bmatrix} \bar{\boldsymbol{\xi}} = \begin{bmatrix} \boldsymbol{\xi}_1^A \circ \lambda_1^{AB} \boldsymbol{\varphi}^A & 0 & 0 & 0 \\ 0 & \boldsymbol{\xi}_1^B \circ \boldsymbol{\varphi}^B & 0 & 0 \\ 0 & 0 & \boldsymbol{\xi}_1^C \circ \boldsymbol{\varphi}^C & 0 \\ 0 & 0 & 0 & \boldsymbol{\xi}_1^D \circ \lambda_1^{DC} \boldsymbol{\varphi}^D \end{bmatrix} \begin{bmatrix} \dot{q}_1^A \\ \dot{q}_1^B \\ \dot{q}_1^C \\ \dot{q}_1^D \end{bmatrix} \tag{8}$$

The matrices in Eq. (9) are written as in terms of the geometry parameters. We use $\boldsymbol{\xi}_1^L = \left(0 | \mathbf{k}_1^L\right)$; $\boldsymbol{\varphi}^L = \left(\mathbf{f}^L | f^L r^L \mathbf{n}_{45}^L\right)$, r^L as in Section 2.2. Also, $\lambda_1^{LM} = k_{45\,z}^M$; $\lambda_2^{LM} = f^L r^L \mathbf{k}_5^M \cdot \mathbf{n}_{45}^L$ $\boldsymbol{\zeta}^{LM} = k_{45\,z}^M \left(\mathbf{f}^L | (1 - f^L r^L) \mathbf{n}_{45}^L\right)$, $k_{45\,z}^M = \mathbf{k}_1^M \mathbf{k}_4^M \mathbf{k}_5^M$; $(L, M) = (A, B); (D, C)$. Thus:

$$\left[\begin{array}{cc|cc} k_{45z}^B (1 - f^A r^A) n_{45y}^A & k_{45z}^B (1 - f^A r^A) n_{45z}^A & k_{45z}^B f_x^A & k_{45z}^B f_y^A \\ f^B r^B n_{45y}^B & f^B r^B n_{45z}^B & f_x^B & f_y^B \\ f^C r^C n_{45y}^C & f^C r^C n_{45z}^C & f_x^C & f_y^C \\ k_{45z}^C (1 - f^D r^D) n_{45y}^D & k_{45z}^C (1 - f^D r^D) n_{45z}^D & k_{45z}^C f_x^D & k_{45z}^C f_y^D \end{array}\right] \bar{\boldsymbol{\xi}}$$

$$= \begin{bmatrix} k_{45z}^B \mathbf{k}_1^A \cdot \mathbf{f}^A & 0 & 0 & 0 \\ 0 & \mathbf{k}_1^B \cdot \mathbf{f}^B & 0 & 0 \\ 0 & 0 & \mathbf{k}_1^C \cdot \mathbf{f}^C & 0 \\ 0 & 0 & 0 & k_{45z}^C \mathbf{k}_1^D \cdot \mathbf{f}^D \end{bmatrix} \begin{bmatrix} \dot{q}_1^A \\ \dot{q}_1^B \\ \dot{q}_1^C \\ \dot{q}_1^D \end{bmatrix} \tag{9}$$

5. Conclusions

The paper shows by means of two examples how, with some modifications, the standard method for the constraint and velocity analysis of PMs can be applied for the derivation of the input-output velocity equations of non-parallel closed chain mechanisms.

In such mechanisms part of the constraint wrenches applied to the end-effector are not in the vector-space sum of the leg constraint systems. These additional constraints have to be taken into account in order to eliminate the passive joint velocities from the velocity equations.

References

Agrawal, S. (1990), Rate kinematics of in-parallel manipulator systems, *IEEE Int. Conf. on Robotics and Automation ICRA90*, pp. 104–109, vol. 1.

Davies, T. (1981), Kirchhoff's circulation law applied to multi-loop kinematic chains, *Mechanism and Machine Theory* **16**, 171–183.

Huang, Z. and Li, Q. (2003), Type synthesis of symmetrical lower mobility parallel mechanisms using the constraint synthesis method, *Int. J. of Robotics Research* **22**(1), 59–79.

Hunt, K. H. (1978), *Kinematic Geometry of Mechanisms*, Oxford University Press.

Joshi, S. and Tsai, L. (2002), Jacobian analysis of limited-dof parallel manipulators, *ASME Journal of Mechanical Design* **124**, 254–258.

Kumar, V. (1992), Instantaneous kinematics of parallel-chain robotic mechanisms, *ASME J. of Mechanical Design* **114**(3), 349–358.

Mohamed, M. and Duffy, J. (1985), A direct determination of the instantaneous kinematics of fully parallel robot manipulators, *ASME J. of Mechanisms, Transmissions and Automation in Design* **107**(2), 226–229.

Zlatanov, D., Benhabib, B. and Fenton, R. (1994), Velocity and singularity analysis of hybrid chain manipulators, *ASME 23rd Biennial Mechanism Conference in DETC94*, Vol. 70, Minneapolis, MN, USA, pp. 467–476.

Zlatanov, D., Bonev, I. and Gosselin, C. (2002), Constraint singularities of parallel mechanisms, *IEEE ICRA'02*, pp. 496–502 vol. 1, Washington DC.

Zoppi, M., Zlatanov, D. and Molfino, R. (2006), On the velocity analysis of interconnected chains mechanisms, to appear in *Mechanism and Machine Theory*.

Properties of Mechanisms

KINEMATICS OF MICRO PLANAR PARALLEL ROBOT COMPRISING LARGE JOINT CLEARANCES

Hagay Bamberger[1,2], Moshe Shoham[2], Alon Wolf[2]
[1]*RAFAEL – Armament Development Authority Ltd.*
[2]*Robotics Laboratory*
Department of Mechanical Engineering
Technion – Israel Institute of Technology
hagayb@rafael.co.il
shoham@technion.ac.il
alonw@technion.ac.il

Abstract Manufacturing of micro-robots by MEMS technology may cause large clearance at the joints – only one order smaller and even of the same order of magnitude as the links themselves. Due to the clearances, the direct kinematic solutions are not discrete, but form a volume that is defined here as the "Clearance-space". When clearances are large enough, two separate regions of the clearance-space may unite, causing a major failure as the forward kinematic may be shifted into a different unwanted solution. This paper suggests an algorithm that calculates the minimal value of the joint clearance in which this severe phenomenon occures.

Keywords: Clearance, direct kinematics, parallel robot, MEMS, micro joint

1. Introduction

Contemporary MEMS technology enables manufacturing of micro-robot using masks and lithograpy process. This technolgical process requires keeping relatively large gaps between links in order to maintain the mechanism's motion. These gaps result in clearances between moving parts, that can be as large as about the same order of magnitude as the typical dimensions of the mechanism itself. These were the circumstances in traditional machinery during the 18th century that caused inaccuracy of the mechanism, shocks, vibrations, noise and wear at the joints, as opposed to the high accuracy achievable in the macro-world nowadays.

Modeling of clearances is always implemented by adding degrees-of-freedom to enable parasitic motion between the joint parts. The motion in these degrees-of-freedom is limited by the joint geometry, where the most common ones are the revolute, prismatic, and spherical joints. Consequently, most of the models deal with these three joints. It is worth

J. Lenarčič and B. Roth (eds.), Advances in Robot Kinematics, 75–84.

noting that some of the models can be expanded to helical or cylindrical joints. Most models assume that the clearances are small, thus enable using linearization and similar simple mathematical tools.

Dubowsky and Freudenstein, 1971, have investigated the dynamics of revolute and spherical joints with clearances, and discovered some interesting dynamic phenomena, like limit cycles and natural frequencies changing vs. the motion amplitude. Stoenescu and Marghitu, 2003, have solved the dynamics of a slider-crank-mechanism, and applied impacts when the two parts contact.

Other researches focus on the static behavior of mechanisms with clearances, that are subjected to an external load. Wang and Roth, 1989, have shown all the relative situations between the journal and bearing of a spatial revolute joint. The mathematical conditions relate the joint geometry and reactions at the joint due to the external load, and the valid situation must satisfy the conditions ensuring that all normal forces are positive. Parenti-Castelli and Venanzi, 2002, have applied a gravitation force on moving robots, and assumed that the motion is quasi-static, thus one can find the contact points using static analysis. They have found that the accuracy of the parallel robot is quite good compared with the serial counterpart, except for near singular configuration.

One example for dealing with relatively large clearances, without assuming that they are much smaller than the links, is given in Voglewede and Ebert-Uphoff, 2004. In their work, the authors have calculated the possible poses of the end effectors of two planar parallel robots resulting from the clearances, and have shown that the effect of clearances becomes worse near or at singular configurations. This kinematic approach is based only on the robot geometry, without taking into account the loads applied on the robot.

Behi et al., 1990, and DeVoe et al., 2000, were the first to build, based on MEMS technology, 3RRR and 3PRR planar parallel robots, respectively. Kosuge et al., 1991, was aware of the clearances in the 3RRR version, and calculated their affect on the accuracy of the moving platform, while assuming that the clearances are very small compared to the robot links.

The present paper deals with large joint clearances that are typical of MEMS manufacturing, and determines the clearance conditions under which two forwards kinematic solutions merge, which results in an undetermined location of the output link.

2. The Clearance-Space as an Expansion of the Direct Kinematics Solutions

The 3RRR and 3PRR kinematic structures are discussed hereinafter. Fig. 1 shows the 3PRR robot[1].

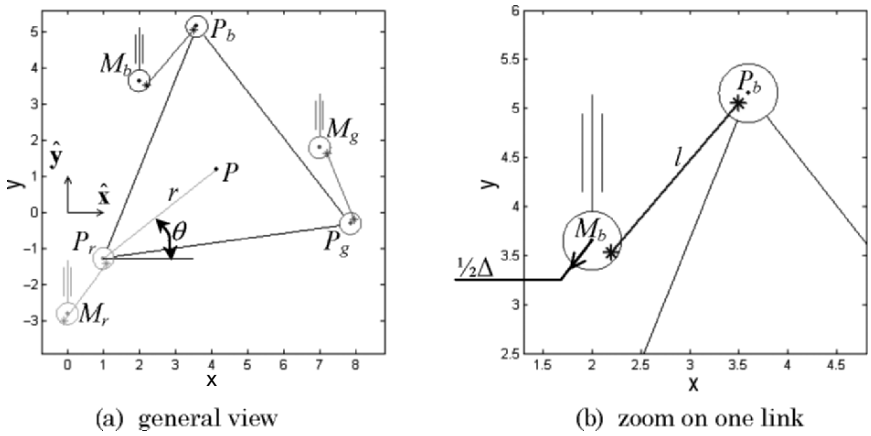

(a) general view (b) zoom on one link

Figure 1. The 3PRR robot.

The robot consists of an equilateral triangle platform, whose center is the point P. The platform pose is determined by point P x and y coordinates and by the platform orientation θ. Points P_r, P_g, and P_b are located on the platform in an equal distance r from the platform center P. The linear motors detemine the vectors $\mathbf{p}^{M_r}$, $\mathbf{p}^{M_g}$, and $\mathbf{p}^{M_b}$, where $\mathbf{p}$ stands for a position vector from the origin to the corresponding point. In case of 3RRR kineamtic structure the motors would be rotational, although this is not shown here. The physical length of the links which are marked by asterisks, and which connect the motors with the platform, is l, meaning that under zero clearance, this would be the distance between each motor and the corresponding point on the platform.

It is likely that the manufacturing process would introduce clearances into all six revolute joints. The clearance is expressed by an offset between the axes of the bearing and the journal. Therefore, those axes are not coincident, but may be distant from each other. The simplest model assumes that the difference in radius between the bearing and the journal of any joint is ½Δ (see Fig. 1b). Therefore, the distances between each motor and the corresponding point on the platform, which we refer

[1] '*r*', '*g*', and '*b*' stand for the red, green, and blue links, respectively. All colored figures can be found at the website *http://robotics.technion.ac.il/Projects/hagay/Robochip.html*

to as the "effective lengths" of the links M_rP_r, M_gP_g, and M_bP_b, is bounded by:

$$l-\Delta \le \left|{}^{M_r}\mathbf{p}^{P_r}\right|,\quad \left|{}^{M_g}\mathbf{p}^{P_g}\right|,\quad \left|{}^{M_b}\mathbf{p}^{P_b}\right| \le l+\Delta. \tag{1}$$

Defining the parameters s_r, s_g, and s_b such that

$$-1 \le s_r,\quad s_g,\quad s_b \le 1 \tag{2}$$

enables writing the effective lengths as

$$\begin{aligned}\left|{}^{M_r}\mathbf{p}^{P_r}\right| &= l+s_r\Delta\\ \left|{}^{M_g}\mathbf{p}^{P_g}\right| &= l+s_g\Delta.\\ \left|{}^{M_b}\mathbf{p}^{P_b}\right| &= l+s_b\Delta\end{aligned} \tag{3}$$

In order to find the possible locations of point P, three auxiliary annuli are drawn. They are described in the next figure, with the robot arranged in a specific orientation θ.

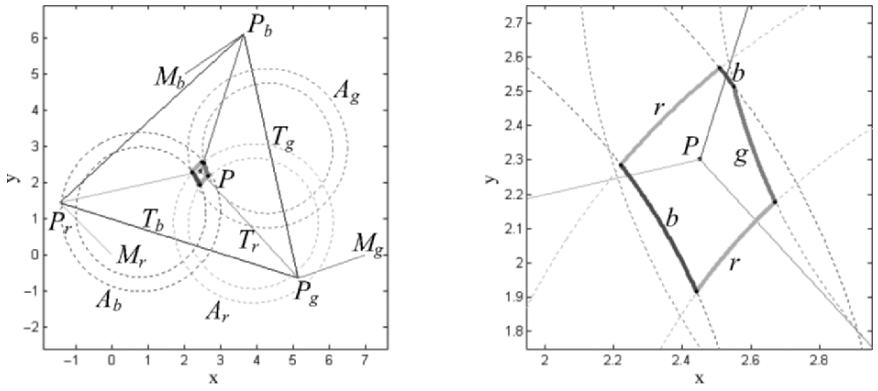

(a) the robot and the annuli (b) zoom near the point P

Figure 2. Possible positions for a given platform orientation due to clearances at the joints.

Note that the angle θ determines the vectors ${}^{P_r}\mathbf{p}^{P}$, ${}^{P_g}\mathbf{p}^{P}$, and ${}^{P_b}\mathbf{p}^{P}$, which are pointing from the platform corners to its center. Those vectors lead to the auxiliary points T_r, T_g, and T_b, which can be calculated by

$$\begin{aligned}{}^{M_r}\mathbf{p}^{T_r} &= {}^{P_r}\mathbf{p}^{P}\\ {}^{M_g}\mathbf{p}^{T_g} &= {}^{P_g}\mathbf{p}^{P}.\\ {}^{M_b}\mathbf{p}^{T_b} &= {}^{P_b}\mathbf{p}^{P}\end{aligned} \tag{4}$$

The annuli A_r, A_g, and A_b of the radii l–Δ and l+Δ are centered at points T_r, T_g, and T_b, respectively. The annulus A_r, for example, describes the possible positions of point P, if only the red link is connected to the platform. When all links are connected, point P is forced to be at the intersection of the three annuli. This area is bolded in Fig. 2, and can be calculated by $A_r \cap A_g \cap A_b$, as shown in Voglewede and Ebert-Uphoff, 2004. If the three annuli do not intersect, then there is no solution for the direct kinematic problem for this specific orientation angle θ.

Physically, when the robot tracks the bolded green curve in Fig. 2, the effective length of the green link is always l–Δ ($s_g = -1$), while the effective lengths of the other links are in the boundaries defined in Eqs. 1 and 2. Furthermore, moving along the long blue curve ($s_b = -1$) changes the length of the red link between its extreme values ($s_r = -1$ and $s_r = 1$), while the green link is always in the allowed range. The intersecting point between two curves means a configuration where the clearances of two links are closed.

Fig. 2 describes a specific orientation of the platform. Generalizing it to all possible orientations yields the "Clearance-Space", shortly named "Cl-space". This space is a sub-space of the configuration-space, and it consists of six boxes that describe all possible platform poses resulting from the clearances. Note that the term "box" is being used since it has eight vertices, although its shape is not cubic. Actually, the "Cl-space" for 3RRR or 3PRR robots is identical to the workspace of an equivalent 3RPR robot, whose link lengths are limited as described in Eq. 1 (Voglewede and Ebert-Uphoff, 2004).

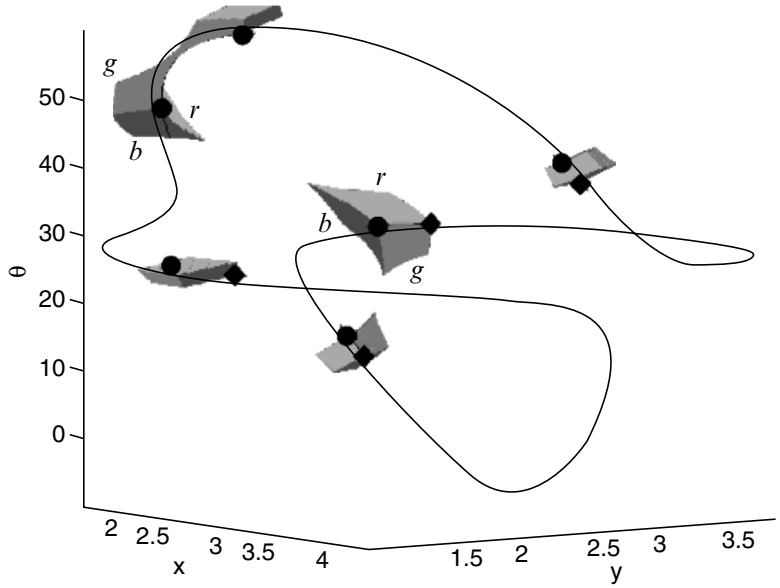

Figure 3. The clearance-space.

In the case of no clearance, the direct kinematics problem has six solutions, as shown in Gosselin and Merlet, 1994. These solutions are points in the 3D C-space, and each of them is located in one of the boxes in Fig. 3. Therefore, it can be concluded that each of the boxes in the Cl-space is an expansion of one of the direct kinematics solutions.

Each of the boxes has six side walls, which are two degree-of-freedom manifolds: two red, two green, and two blue. As described before, the red side wall, for example, includes poses in which the clearances in the joints of the red link are closed, i.e. the effective length is minimal or maximal (see Eq. 1). Therefore, while manipulating the robot along an intersecting curve of two side walls, which is a one degree-of-freedom manifold, the effective lengths of the two relevant links remain fixed. In fact, this motion is similar to the motion of a four bar mechanism that consists of a platform that serves as a coupler, and the two fixed length links. The black curve in Fig. 3 describes the motion of such a four bar mechanism, in which the lengths of the red and green links are minimal ($s_r = s_g = -1$). Indeed, this curve meets all the boxes along the intersecting curve of the two relevant side walls. The motion of the mechanism is limited by the third link, since its effective length is constrained by Eq. 1. However, when clearance Δ is large enough, the effective length of the third link does not limit the motion of the four bar mechanism.

Each of the boxes in Fig. 3 has eight vertices, which correspond to the poses where all the clearances are closed. These poses can be calculated analytically using the algorithm in Gosselin and Merlet, 1994, since each of the extreme situations can be treated as an equivalent 3RPR robot, whose link lengths are fixed and known. For example, the circles in Fig. 3 indicate the poses where all the effective lengths are minimal ($s_r = s_g = s_b = -1$), while the cases of maximal blue link ($s_r = s_g = -1$, $s_b = 1$) are marked by the diamonds. As expected, there are six circles and six diamonds, and all of them lay on the black curve.

When the clearance increases, the volumes of the boxes also increases and may cause two adjacent boxes to meet. Kinematically, such a case must be avoided, since the robot may pass from one direct kineamtic solution to another, thus resulting in an undesired platform pose. The interesting question is how to quantify a boundary for the clearance in order to prevent this phenomenon.

3. Merging Conditions of Clearance-Space Boxes

In order to find an analytical answer for the above question, note that two boxes meet when their vertices meet. As explained, the vertices are calculated by solving a direct kinematics problem, so it can be concluded that this problem has at least one multiple solution. Since the direct kinematics problem yields a six degree polynomial equation, conditions where such a polynomial has multiple roots should be found.

Lemma: Given the general polynomial equation:

$$gz^6 - fz^5 + ez^4 - dz^3 + cz^2 - bz + a = 0\,. \tag{5}$$

It can be shown that this equation has multiple roots if its coefficients satisfy the next equation:

$$b^2c^2d^2e^2f^2 - 4b^2c^2d^2e^3g - 27a^2d^4e^2f^2 + 38880a^4bfg^4 + \ldots = 0\,. \tag{6}$$

This equation has 246 terms, so only some of its terms are shown. The complete expression can be found online at the website *http://robotics.technion.ac.il/Projects/hagay/Robochip.html*

Proof: If the solutions of Eq. 5 are z_1, z_2, z_3, z_4, z_5, and z_6, it is evident that:

$$\begin{aligned} & g(z-z_1)(z-z_2)(z-z_3)(z-z_4)(z-z_5)(z-z_6) \\ &= gz^6 - fz^5 + ez^4 - dz^3 + cz^2 - bz + a = 0\,. \end{aligned} \tag{7}$$

Therefore,

$$\begin{aligned} \frac{a}{g} &= z_1z_2z_3z_4z_5z_6 \\ \frac{b}{g} &= z_1z_2z_3z_4z_5 + z_1z_2z_3z_4z_6 + z_1z_2z_3z_5z_6 \\ &\quad + z_1z_2z_4z_5z_6 + z_1z_3z_4z_5z_6 + z_2z_3z_4z_5z_6 \\ \frac{c}{g} &= z_1z_2z_3z_4 + z_1z_2z_3z_5 + z_1z_2z_3z_6 + z_1z_2z_4z_5 + z_1z_2z_4z_6 \\ &\quad + z_1z_2z_5z_6 + z_1z_3z_4z_5 + z_1z_3z_4z_6 + z_1z_3z_5z_6 + z_1z_4z_5z_6 \\ &\quad + z_2z_3z_4z_5 + z_2z_3z_4z_6 + z_2z_3z_5z_6 + z_3z_4z_5z_6 + z_2z_4z_5z_6 \\ \frac{d}{g} &= z_1z_2z_3 + z_1z_2z_4 + z_1z_2z_5 + z_1z_2z_6 + z_1z_3z_4 + z_1z_3z_5 + z_1z_3z_6 \\ &\quad + z_1z_4z_5 + z_1z_4z_6 + z_1z_5z_6 + z_2z_3z_4 + z_2z_3z_5 + z_2z_3z_6 + z_2z_4z_5 \\ &\quad + z_2z_4z_6 + z_2z_5z_6 + z_3z_4z_5 + z_3z_4z_6 + z_3z_5z_6 + z_4z_5z_6 \\ \frac{e}{g} &= z_1z_2 + z_1z_3 + z_1z_4 + z_1z_5 + z_1z_6 + z_2z_3 + z_2z_4 + z_2z_5 \\ &\quad + z_2z_6 + z_3z_4 + z_3z_5 + z_3z_6 + z_4z_5 + z_4z_6 + z_5z_6 \\ \frac{f}{g} &= z_1 + z_2 + z_3 + z_4 + z_5 + z_6 \end{aligned} \tag{8}$$

Substituting Eq. 8 into Eq. 6 yields

$$g^{10}\begin{bmatrix}(z_1-z_2)(z_1-z_3)(z_1-z_4)(z_1-z_5)(z_1-z_6)\\(z_2-z_3)(z_2-z_4)(z_2-z_5)(z_2-z_6)(z_3-z_4)\\(z_3-z_5)(z_3-z_6)(z_4-z_5)(z_4-z_6)(z_5-z_6)\end{bmatrix}^2=0, \tag{9}$$

meaning that there exists at least one pair of multiple roots.

The following equation is obtained while solving the direct kinematical problem:

$$\begin{aligned}&\left(g_2\Delta^2+g_1\Delta+g_0\right)t^6-\left(f_2\Delta^2+f_1\Delta+f_0\right)t^5+\left(e_2\Delta^2+e_1\Delta+e_0\right)t^4\\&-\left(d_2\Delta^2+d_1\Delta+d_0\right)t^3+\left(c_2\Delta^2+c_1\Delta+c_0\right)t^2-\left(b_2\Delta^2+b_1\Delta+b_0\right)t,\\&+\left(a_2\Delta^2+a_1\Delta+a_0\right)=0\end{aligned} \tag{10}$$

where:

$$t=\tan\left(\frac{\theta}{2}\right), \tag{11}$$

and all coefficients a_0, a_1, a_2, …, g_0, g_1, g_2 are known functions of the geometric parameters $\mathbf{p}^{M_r}$, $\mathbf{p}^{M_g}$, $\mathbf{p}^{M_b}$, l, r and s_r, s_g, and s_b.

Substituting the coefficients of Eq. 10 into Eq. 6 yields a polynomial equation in Δ only:

$$\sum_{i=0}^{20}\kappa_i\Delta^i=0. \tag{12}$$

For all the solutions of the above equation, Eq. 10 has multiple solutions. The smallest positive solution has a physical meaning, since it is the clearance Δ where the vertices of two different boxes meet. For a complete solution, it is required to repeat the calculation for all eight combinations ($s_r = \pm 1$, $s_g = \pm 1$, $s_b = \pm 1$), in order to find the first meeting of two boxes, whereas it cannot be known in advance in which of the eight vertices the meeting will occur.

4. Numerical Example

Given the motor positions at $\mathbf{p}^{M_r} = 0\hat{\mathbf{x}} + 0\hat{\mathbf{y}}$, $\mathbf{p}^{M_g} = 7\hat{\mathbf{x}} + 0\hat{\mathbf{y}}$, $\mathbf{p}^{M_b} = 2\hat{\mathbf{x}} + 5\hat{\mathbf{y}}$, and the geometric parameters $l = 2$, $r = 4$. Fig. 2 shows a possible area for the platform center P at a constant orientation angle θ=12.5° due to a clearance $\Delta = 0.2$, which is one order smaller than the link lengths. Fig. 3 shows all the Cl-space for $\Delta = 0.1$.

Implementation of the process described in Eqs. 10 and 6 for each of the combinations of s_r, s_g, and s_b yields eight equations in Δ. For example, for $s_r = s_g = -1$, $s_b = 1$, one gets:

$$\begin{aligned} &0.04096 + 1.7241\Delta + 6.4984\Delta^2 - 261.64\Delta^3 + 474.52\Delta^4 + 2071.7\Delta^5 \\ &- 3280.5\Delta^6 - 8679.5\Delta^7 + 10067\Delta^8 + 19083\Delta^9 - 17010\Delta^{10} - 20825\Delta^{11} \\ &+ 14420\Delta^{12} + 10771\Delta^{13} - 4820.9\Delta^{14} - 2523.8\Delta^{15} + 415.36\Delta^{16} \\ &+ 147.69\Delta^{17} - 17.53\Delta^{18} - 1.9558\Delta^{19} + 0.21726\Delta^{20} = 0 \end{aligned} \quad (13)$$

The real solutions of Eq. 13 are –7.2367, –3.5072, –2.3201, –1.5742, –0.8661, –0.7204, 0.1279, 0.8696, 1.1962, 4.8039, 7.7946, and 8.9655.

The lowest positive solutions of the eight combinations of s_r, s_g, and s_b are shown in the next table:

Table 1. The clearances causing meeting of vertices of the Cl-space.

s_r	s_g	s_b	$\Delta_{\min}$
1	1	1	5.7662
		–1	0.7204
	–1	1	0.2776
		–1	0.1528
–1	1	1	0.5665
		–1	0.1656
	–1	1	**0.1279**
		–1	0.4935

The smallest value in the table is bolded and, as expected, it results in meeting of the two vertices that are indicated by a diamond in the top of Fig. 3. The next figure shows the Cl-space for $\Delta = 0.14$, and it can be seen that the two boxes became one and there are only four solutions for $s_r = s_g = -1$, $s_b = 1$.

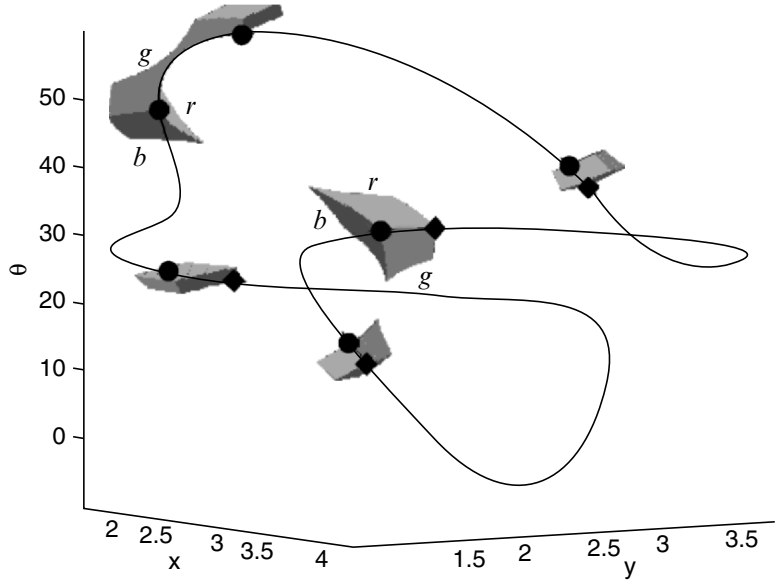

Figure 4. The clearance-space for large clearances.

5. Conclusions

The kinematic effects of large joint clearances in parallel robots was discussed. It was shown that the direct kinematics solutions expand due to the clearances, and the clearance-space was defined as the set of possible platform poses resulting from given clearances. Instability of direct kinematics solutions may occur, as the clearances get bigger when two distinct clearance-space boxes might merge. An analytical approach for finding the minimal clearance that causes this unwanted behavior was suggested, along with a numerical example showing that for a 3 DOF planar parallel robot, clearance of about 10% of the typical robot link length may be problematic. Future work will investigate the effects of clearances on the static and the dynamic behaviors of micro-robots.

References

Behi, F., Mehregany, M., and Gabriel, K.J. (1990), A Microfabricated Three-Degree-of-Freedom Parallel Mechanism, Proceedings of IEEE Micro Electro Mechanical Systems – An Investigation of Micro Structures, Sensors, Actuators, and Machines, pp. 159-165.

DeVoe, D., et al., 3 DOF Planar Micromechanism (2000), *http://www.isr.umd.edu/ISR/accomplishments/032_ParallelFabrication/*, The Institute for Systems Research, University of Maryland, MD, USA.

Dubowsky, S., and Freudenstein, F. (1971), Dynamic Analysis of Mechanical Systems with Clearances, Part 1: Formation of Dynamical Model; Part 2: Dynamic Response, Journal of Engineering for Industry, Transactions of the ASME, Series B., Vol. 93, No. 1, pp. 305-316.

Gosselin, C.M., and Merlet, J.P. (1994), The Direct Kinematics of Planar Parallel Manipulators: Special Architectures and Number of Solutions, Mechanism and Machine Theory, Vol. 29, No. 8, pp. 1083-1097.

Kosuge, K., Fukuda, T., and Mehregany, M. (1991), Kinematic Analysis of Precision Planar Manipulator on Silicon, International Conference on Solid-State Sensors and Actuators (Transducers'91), San Francisco, CA, USA, pp. 618-621.

Parenti-Castelli, V., and Venanzi, S. (2002), On the Joint Clearance Effects in Serial and Parallel Manipulators, Proceedings of the Workshop on Fundamental Issues and Future Research Directions for Parallel Mechanisms and Manipulators, Quebec, Canada, pp. 215-223.

Stoenescu, E.D., and Marghitu, D.B. (2003), Dynamic Analysis of a Planar Rigid-Link Mechanism with Rotating Slider Joint and Clearance, Journal of Sound and Vibration, Vol. 266, No. 2, pp. 394-404.

Voglewede, P., and Ebert-Uphoff, I. (2004), Application of Workspace Generation Techniques to Determine the Unconstrained Motion of Parallel Manipulators, Journal of Mechanical Design, Transactions of the ASME, Vol. 126, No. 2, pp. 283-290.

Wang, H.H.S., and Roth, B. (1989), Position Errors Due to Clearance in Journal Bearings, Journal of Mechanisms, Transmissions, and Automation in Design, Vol. 111, pp. 315-320.

STIFFNESS MAPPING OF PLANAR COMPLIANT PARALLEL MECHANISMS IN A SERIAL ARRANGEMENT

Hyun K. Jung, Carl D. Crane III
University of Florida
Department of Mechanical and Aerospace Engineering
hyunkwon.jung@gmail.com, ccrane@ufl.edu

Rodney G. Roberts
Florida State University, FAMU-FSU College of Engineering
Department of Electrical and Computer Engineering
rroberts@eng.fsu.edu

Abstract This paper presents a stiffness mapping of a mechanism having two planar compliant parallel mechanisms in a serial arrangement. The stiffness matrix of the mechanism is obtained by taking a derivative of the static equilibrium equations. A derivative of spring force connecting two moving bodies is derived and it is applied to obtain the stiffness matrix of the mechanism. A numerical example is presented.

Keywords: Stiffness matrix, compliant coupling, parallel mechanism

1. Introduction

There are many robotic tasks involving contacts of man and machine or the robot and its environment. A small amount of positional error of the robot system, which is almost inevitable, may cause serious damage to the robot or the object with which it is in contact. Compliant couplings which may be inserted between the end effecter and the last link of the robotic manipulator can be a solution to this problem (Whitney, 1982, Peshkin, 1990, and Griffis, 1991).

Dimentberg, 1965, studied properties of an elastically suspended body using Screw theory which was introduced by Ball, 1900. Screw theory is employed throughout this paper to describe the motion of rigid bodies (twist) and the forces applied to rigid bodies (wrench) (Crane et al., 2006). A small twist applied to the compliant coupling generates a small change of the wrench which the compliant coupling exerts on the environment. This relation is well described by the stiffness matrix of the compliant coupling.

J. Lenarčič and B. Roth (eds.), Advances in Robot Kinematics, 85–94.

Parallel mechanisms have several advantages over serial mechanisms such as high stiffness, compactness, and small positional errors at the cost of a smaller work space and increased complexity of analysis. Griffis, 1991, obtained a global stiffness model for parallel mechanism-based compliant couplings. Huang and Schimmels, 1998, Ciblak and Lipkin, 1999, and Roberts, 1999, studied synthesis of stiffness matrices.

2. Problem Statement

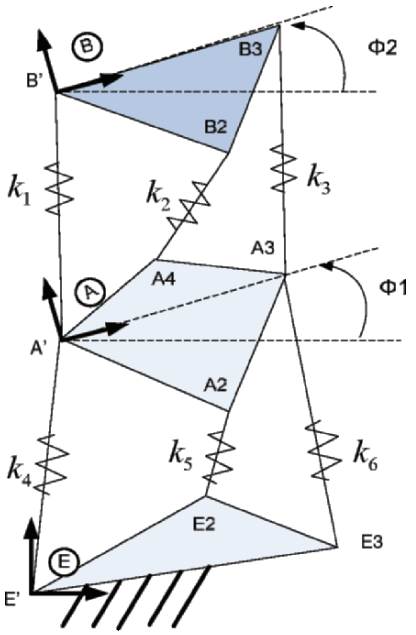

Figure 1. Mechanism having two planar parallel mechanisms in a serial arrangement.

Figure 1 depicts the compliant mechanism whose stiffness matrix will be obtained in this paper. Body A is connected to ground by three compliant couplings and body B is connected to body A in the same way. Each compliant coupling has a revolute joint at each end and a prismatic joint with a spring in the middle. It is assumed that an external wrench $\underline{\mathbf{w}}_{ext}$ is applied to body B and that both body B and body A are in static equilibrium. The poses of body A and body B and the spring constants and free lengths of all compliant couplings are known.

The stiffness matrix $[K]$ which maps a small twist of the moving body B in terms of the ground, ${}^{E}\delta\underline{\mathbf{D}}^{B}$, into the corresponding wrench variation, $\delta\underline{\mathbf{w}}_{ext}$, is desired to be derived. This relationship can be written as

$$\delta \underline{\mathbf{w}}_{ext} = \left[K\right]^{E} \delta \underline{\mathbf{D}}^{B} . \tag{1}$$

The static equilibrium equation of bodies B and A can be written by

$$\begin{aligned} \underline{\mathbf{w}}_{ext} &= \underline{\mathbf{f}}_1 + \underline{\mathbf{f}}_2 + \underline{\mathbf{f}}_3 \\ &= \underline{\mathbf{f}}_4 + \underline{\mathbf{f}}_5 + \underline{\mathbf{f}}_6 \end{aligned} \tag{2}$$

where $\underline{\mathbf{f}}_i$ are the forces from the compliant couplings.

The stiffness matrix will be derived by taking a derivative of the static equilibrium equation, Eq. 2, to yield

$$\begin{aligned} \delta \underline{\mathbf{w}}_{ext} &= \delta \underline{\mathbf{f}}_1 + \delta \underline{\mathbf{f}}_2 + \delta \underline{\mathbf{f}}_3 \\ &= \delta \underline{\mathbf{f}}_4 + \delta \underline{\mathbf{f}}_5 + \delta \underline{\mathbf{f}}_6 \end{aligned} . \tag{3}$$

Expressions for $\delta \underline{\mathbf{f}}_i$ for the compliant couplings joining body A and ground, i.e., for i = 4, 5, 6, were obtained by Griffis, 1991.

The contribution of this new effort is in the analysis of the derivative of the spring force joining bodies A and B which will lead to the derivation of the compliant matrix that will relate the change in the external wrench to the twist of body B with respect to ground.

3. Derivative of Spring Force Connecting Two Moving Bodies

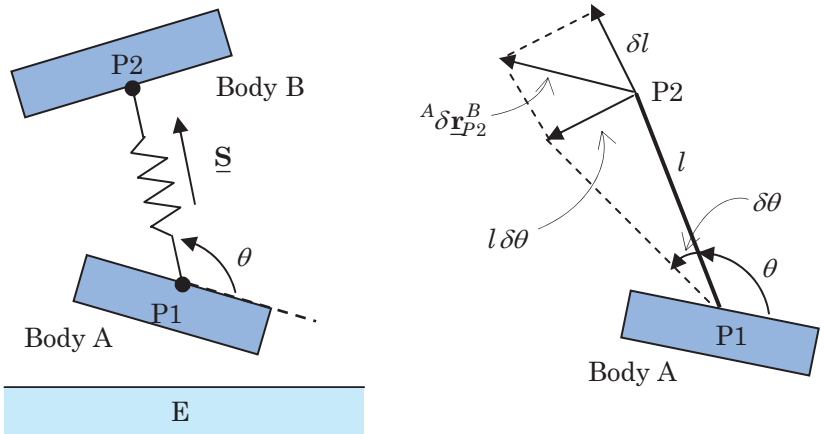

Figure 2. Compliant coupling conneting two moving bodies and variation of point P2 due to twist of body B with respect to body A.

Figure 2 depicts two rigid bodies connected to each other by a compliant coupling with a spring constant k, a free length l_o, and a current length l. The spring force may be written as

$$\underline{\mathbf{f}} = k(l - l_o)\underline{\$} \tag{4}$$

where

$$\underline{\$} = \begin{bmatrix} \underline{\mathbf{S}} \\ {}^{E}\underline{\mathbf{r}}^{A}_{P1} \times \underline{\mathbf{S}} \end{bmatrix} = \begin{bmatrix} \underline{\mathbf{S}} \\ {}^{E}\underline{\mathbf{r}}^{B}_{P2} \times \underline{\mathbf{S}} \end{bmatrix} \tag{5}$$

and where, $\underline{\mathbf{S}}$ is a unit vector along the compliant coupling. ${}^{E}\underline{\mathbf{r}}^{A}_{P1}$ and ${}^{E}\underline{\mathbf{r}}^{B}_{P2}$ are the position vector of the point P1 in body A and that of point P2 in body B, respectively, measured with respect to the reference system embedded in ground (body E).

The derivative of the spring force as in Eq. 4 can be written by

$${}^{E}\delta\underline{\mathbf{f}} = k\,\delta l\,\underline{\$} + k(l - l_o)\,{}^{E}\delta\underline{\$}\,. \tag{6}$$

From the twist equation, the variation of position of point P2 in body B with respect to body A can be expressed as

$${}^{A}\delta\underline{\mathbf{r}}^{B}_{P2} = {}^{A}\delta\underline{\mathbf{r}}^{B}_{o} + {}^{A}\delta\underline{\boldsymbol{\varphi}}^{B} \times {}^{A}\underline{\mathbf{r}}^{B}_{P2} \tag{7}$$

where ${}^{\mathrm{A}}\underline{\mathbf{r}}^{\mathrm{B}}_{\mathrm{P2}}$ is the position of P2, which is embedded in body B, measured with respect to a coordinate system embedded in body A which at this instant is coincident and aligned with the reference system attached to ground. In addition, ${}^{A}\delta\underline{\boldsymbol{\varphi}}^{B}$ is the differential of angle of body B in terms of body A. It can also be decomposed into two perpendicular vectors along $\underline{\mathbf{S}}$ and $\frac{{}^{A}\partial\underline{\mathbf{S}}}{\partial\theta}$ which is a known unit vector perpendicular to $\underline{\mathbf{S}}$. These two vectors correspond to the change of the spring length δl and the directional change of the spring $l\delta\theta$ in terms of body A as shown in Fig. 2. Thus Eq. 7 can be rewritten as

$$\begin{aligned} {}^{A}\delta\underline{\mathbf{r}}^{B}_{P2} &= \left({}^{A}\delta\underline{\mathbf{r}}^{B}_{P2} \cdot \underline{\mathbf{S}}\right)\underline{\mathbf{S}} + \left({}^{A}\delta\underline{\mathbf{r}}^{B}_{P2} \cdot \frac{{}^{A}\partial\underline{\mathbf{S}}}{\partial\theta}\right)\frac{{}^{A}\partial\underline{\mathbf{S}}}{\partial\theta} \\ &= \delta l\,\underline{\mathbf{S}} + l\delta\theta\frac{{}^{A}\partial\underline{\mathbf{S}}}{\partial\theta} \end{aligned} \tag{8}$$

where

$${}^{A}\frac{\partial\underline{\$}}{\partial\theta} = \begin{bmatrix} \frac{{}^{A}\partial\underline{\mathbf{S}}}{\partial\theta} \\ {}^{A}\underline{\mathbf{r}}^{A}_{P1} \times \frac{{}^{A}\partial\underline{\mathbf{S}}}{\partial\theta} \end{bmatrix}. \tag{9}$$

From Eqs. 7 and 8, δl and $l\delta\theta$ can be expressed as

$$\begin{aligned}\delta l &= {}^{A}\delta\underline{\mathbf{r}}_{P2}^{B}\cdot\underline{\mathbf{S}} = {}^{A}\delta\underline{\mathbf{r}}_{o}^{B}\cdot\underline{\mathbf{S}} + {}^{A}\delta\underline{\boldsymbol{\varphi}}^{B}\times{}^{A}\underline{\mathbf{r}}_{P2}^{B}\cdot\underline{\mathbf{S}}\\ &= {}^{A}\delta\underline{\mathbf{r}}_{o}^{B}\cdot\underline{\mathbf{S}} + {}^{A}\delta\underline{\boldsymbol{\varphi}}^{B}\cdot{}^{A}\underline{\mathbf{r}}_{P2}^{B}\times\underline{\mathbf{S}}\\ &= \underline{\$}^{T}\,{}^{A}\delta\underline{\mathbf{D}}^{B}\end{aligned} \tag{10}$$

$$\begin{aligned}l\delta\theta &= {}^{A}\delta\underline{\mathbf{r}}_{P2}^{B}\cdot\frac{{}^{A}\partial\underline{\mathbf{S}}}{\partial\theta} = {}^{A}\delta\underline{\mathbf{r}}_{o}^{B}\cdot\frac{{}^{A}\partial\underline{\mathbf{S}}}{\partial\theta} + {}^{A}\delta\underline{\boldsymbol{\varphi}}^{B}\times{}^{A}\underline{\mathbf{r}}_{P2}^{B}\cdot\frac{{}^{A}\partial\underline{\mathbf{S}}}{\partial\theta}\\ &= {}^{A}\delta\underline{\mathbf{r}}_{o}^{B}\cdot\frac{{}^{A}\partial\underline{\mathbf{S}}}{\partial\theta} + {}^{A}\delta\underline{\boldsymbol{\varphi}}^{B}\cdot{}^{A}\underline{\mathbf{r}}_{P2}^{B}\times\frac{{}^{A}\partial\underline{\mathbf{S}}}{\partial\theta}\\ &= \frac{{}^{A}\partial\underline{\$}'^{T}}{\partial\theta}\,{}^{A}\delta\underline{\mathbf{D}}^{B}\end{aligned} \tag{11}$$

where

$$\frac{{}^{A}\partial\underline{\$}'}{\partial\theta} = \begin{bmatrix} \dfrac{{}^{A}\partial\underline{\mathbf{S}}}{\partial\theta} \\ {}^{A}\underline{\mathbf{r}}_{P2}^{B}\times\dfrac{{}^{A}\partial\underline{\mathbf{S}}}{\partial\theta}\end{bmatrix}. \tag{12}$$

$\dfrac{{}^{A}\partial\underline{\$}'}{\partial\theta}$ has the same direction as $\dfrac{{}^{A}\partial\underline{\$}}{\partial\theta}$ but has a different moment term.

${}^{E}\delta\underline{\$}$ in Eq. 6 is a derivative of the unit screw along the spring in terms of the inertial frame and may be written as

$${}^{E}\delta\underline{\$} = \begin{bmatrix} {}^{E}\delta\underline{\mathbf{S}} \\ {}^{E}\delta\underline{\mathbf{r}}_{P1}^{A}\times\underline{\mathbf{S}} + {}^{E}\underline{\mathbf{r}}_{P1}^{A}\times{}^{E}\delta\underline{\mathbf{S}}\end{bmatrix}. \tag{13}$$

Using an intermediate frame attached to body A,

$${}^{E}\delta\underline{\mathbf{S}} = {}^{A}\delta\underline{\mathbf{S}} + {}^{E}\delta\underline{\boldsymbol{\varphi}}^{A}\times\underline{\mathbf{S}}\,. \tag{14}$$

Then, ${}^{E}\delta\underline{\$}$ may be decomposed into three screws as follows

$$\begin{aligned}{}^{E}\delta\underline{\$} &= \begin{bmatrix} {}^{E}\delta\underline{\mathbf{S}} \\ {}^{E}\delta\underline{\mathbf{r}}_{P1}^{A}\times\underline{\mathbf{S}} + {}^{E}\underline{\mathbf{r}}_{P1}^{A}\times{}^{E}\delta\underline{\mathbf{S}}\end{bmatrix}\\ &= \begin{bmatrix} {}^{A}\delta\underline{\mathbf{S}} + {}^{E}\delta\underline{\boldsymbol{\varphi}}^{A}\times\underline{\mathbf{S}} \\ {}^{E}\delta\underline{\mathbf{r}}_{P1}^{A}\times\underline{\mathbf{S}} + {}^{E}\underline{\mathbf{r}}_{P1}^{A}\times\left({}^{A}\delta\underline{\mathbf{S}} + {}^{E}\delta\underline{\boldsymbol{\varphi}}^{A}\times\underline{\mathbf{S}}\right)\end{bmatrix}.\\ &= \begin{bmatrix} {}^{A}\delta\underline{\mathbf{S}} \\ {}^{E}\underline{\mathbf{r}}_{P1}^{A}\times{}^{A}\delta\underline{\mathbf{S}}\end{bmatrix} + \begin{bmatrix} {}^{E}\delta\underline{\boldsymbol{\varphi}}^{A}\times\underline{\mathbf{S}} \\ {}^{E}\underline{\mathbf{r}}_{P1}^{A}\times\left({}^{E}\delta\underline{\boldsymbol{\varphi}}^{A}\times\underline{\mathbf{S}}\right)\end{bmatrix} + \begin{bmatrix} \underline{\mathbf{0}} \\ {}^{E}\delta\underline{\mathbf{r}}_{P1}^{A}\times\underline{\mathbf{S}}\end{bmatrix}\end{aligned} \tag{15}$$

Since $\underline{\mathbf{S}}$ is a function of θ alone from the vantage of body A and $l\delta\theta$ is already described in Eq. 11, the first screw in Eq. 15 can be written as

$$\begin{bmatrix} {}^{A}\delta\underline{\mathbf{S}} \\ {}^{E}\underline{\mathbf{r}}^{A}_{P1} \times {}^{A}\delta\underline{\mathbf{S}} \end{bmatrix} = \begin{bmatrix} \dfrac{{}^{A}\partial\underline{\mathbf{S}}}{\partial\theta}\delta\theta \\ {}^{E}\underline{\mathbf{r}}^{A}_{P1} \times \dfrac{{}^{A}\partial\underline{\mathbf{S}}}{\partial\theta}\delta\theta \end{bmatrix}. \tag{16}$$

$$= \frac{{}^{A}\partial\underline{\$}}{\partial\theta}\frac{1}{l}l\delta\theta = \frac{1}{l}\frac{{}^{A}\partial\underline{\$}}{\partial\theta}\frac{{}^{A}\partial\underline{\$}'^{T}}{\partial\theta}\,{}^{A}\delta\underline{\mathbf{D}}^{B}$$

As to the second screw in Eq. 15, ${}^{E}\delta\underline{\boldsymbol{\varphi}}^{A} \times \underline{\mathbf{S}}$ has the same direction as $\dfrac{{}^{A}\partial\underline{\mathbf{S}}}{\partial\theta}$ with magnitude of ${}_{E}\delta\phi_{A}$ and thus may be written as

$${}^{E}\delta\underline{\boldsymbol{\varphi}}^{A} \times \underline{\mathbf{S}} = {}_{E}\delta\phi_{A}\frac{{}^{A}\partial\underline{\mathbf{S}}}{\partial\theta}. \tag{17}$$

Then the second screw in Eq. 15 can be expressed as

$$\begin{bmatrix} {}^{E}\delta\underline{\boldsymbol{\varphi}}^{A} \times \underline{\mathbf{S}} \\ {}^{E}\underline{\mathbf{r}}^{A}_{P1} \times \left({}^{E}\delta\underline{\boldsymbol{\varphi}}^{A} \times \underline{\mathbf{S}} \right) \end{bmatrix} = \begin{bmatrix} \dfrac{{}^{A}\partial\underline{\mathbf{S}}}{\partial\theta}\,{}_{E}\delta\phi_{A} \\ {}^{E}\underline{\mathbf{r}}^{A}_{P1} \times \dfrac{{}^{A}\partial\underline{\mathbf{S}}}{\partial\theta}\,{}_{E}\delta\phi_{A} \end{bmatrix}. \tag{18}$$

$$= \frac{{}^{A}\partial\underline{\$}}{\partial\theta}\,{}_{E}\delta\phi_{A} = \frac{{}^{A}\partial\underline{\$}}{\partial\theta}\begin{bmatrix} 0 & 0 & 1 \end{bmatrix}{}^{E}\delta\underline{\mathbf{D}}^{A}$$

As to the third screw in Eq. 15, ${}^{E}\delta\underline{\mathbf{r}}^{A}_{P1}$ can be decomposed into two perpendicular vectors along $\underline{\mathbf{S}}$ and $\dfrac{{}^{A}\partial\underline{\mathbf{S}}}{\partial\theta}$, respectively as

$$\begin{aligned} {}^{E}\delta\underline{\mathbf{r}}^{A}_{P1} &= {}^{E}\delta\underline{\mathbf{r}}^{A}_{o} + {}^{E}\delta\underline{\boldsymbol{\varphi}}^{A} \times {}^{E}\underline{\mathbf{r}}^{A}_{P1} \\ &= \left({}^{E}\delta\underline{\mathbf{r}}^{A}_{P1} \cdot \underline{\mathbf{S}} \right)\underline{\mathbf{S}} + \left({}^{E}\delta\underline{\mathbf{r}}^{A}_{P1} \cdot \frac{{}^{A}\partial\underline{\mathbf{S}}}{\partial\theta} \right)\frac{{}^{A}\partial\underline{\mathbf{S}}}{\partial\theta} \end{aligned} \tag{19}$$

where

$$\begin{aligned} {}^{E}\delta\underline{\mathbf{r}}^{A}_{P1} \cdot \underline{\mathbf{S}} &= {}^{E}\delta\underline{\mathbf{r}}^{A}_{o} \cdot \underline{\mathbf{S}} + {}^{E}\delta\underline{\boldsymbol{\varphi}}^{A} \times \underline{\mathbf{r}}^{A}_{P1} \cdot \underline{\mathbf{S}} \\ &= {}^{E}\delta\underline{\mathbf{r}}^{A}_{o} \cdot \underline{\mathbf{S}} + {}^{E}\delta\underline{\boldsymbol{\varphi}}^{A} \cdot \underline{\mathbf{r}}^{A}_{P1} \times \underline{\mathbf{S}} \\ &= \underline{\$}^{T}\,{}^{E}\delta\underline{\mathbf{D}}^{A} \end{aligned} \tag{20}$$

$$\begin{aligned} {}^{E}\delta\underline{\mathbf{r}}^{A}_{P1} \cdot \frac{{}^{A}\partial\underline{\mathbf{S}}}{\partial\theta} &= {}^{E}\delta\underline{\mathbf{r}}^{A}_{o} \cdot \frac{{}^{A}\partial\underline{\mathbf{S}}}{\partial\theta} + {}^{E}\delta\underline{\boldsymbol{\varphi}}^{A} \times \underline{\mathbf{r}}^{A}_{P1} \cdot \frac{{}^{A}\partial\underline{\mathbf{S}}}{\partial\theta} \\ &= {}^{E}\delta\underline{\mathbf{r}}^{A}_{o} \cdot \frac{{}^{A}\partial\underline{\mathbf{S}}}{\partial\theta} + {}^{E}\delta\underline{\boldsymbol{\varphi}}^{A} \cdot \underline{\mathbf{r}}^{A}_{P1} \times \frac{{}^{A}\partial\underline{\mathbf{S}}}{\partial\theta} \\ &= \frac{{}^{A}\partial\underline{\$}^{T}}{\partial\theta}\,{}^{E}\delta\underline{\mathbf{D}}^{A} \end{aligned} \tag{21}$$

By combining Eqs. 19, 20, and 21, ${}^{E}\delta\underline{\mathbf{r}}_{P1}^{A}$ can be written as

$$ {}^{E}\delta\underline{\mathbf{r}}_{P1}^{A} = \left(\underline{\$}^{T}\,{}^{E}\delta\underline{\mathbf{D}}^{A}\right)\underline{\mathbf{S}} + \left(\frac{{}^{A}\partial\underline{\$}^{T}}{\partial\theta}\,{}^{E}\delta\underline{\mathbf{D}}^{A}\right)\frac{{}^{A}\partial\underline{\mathbf{S}}}{\partial\theta}. \tag{22} $$

Then the third screw in Eq. 15 can be written as

$$ \begin{aligned} \begin{bmatrix} \underline{\mathbf{0}} \\ {}^{E}\delta\underline{\mathbf{r}}_{P1}^{A}\times\underline{\mathbf{S}} \end{bmatrix} &= \begin{bmatrix} \underline{\mathbf{0}} \\ \left\{\left(\underline{\$}^{T}\,{}^{E}\delta\underline{\mathbf{D}}^{A}\right)\underline{\mathbf{S}} + \left(\frac{{}^{A}\partial\underline{\$}^{T}}{\partial\theta}\,{}^{E}\delta\underline{\mathbf{D}}^{A}\right)\frac{{}^{A}\partial\underline{\mathbf{S}}}{\partial\theta}\right\}\times\underline{\mathbf{S}} \end{bmatrix} \\ &= \begin{bmatrix} \underline{\mathbf{0}} \\ \left(\frac{{}^{A}\partial\underline{\$}^{T}}{\partial\theta}\,{}^{E}\delta\underline{\mathbf{D}}^{A}\right)\frac{{}^{A}\partial\underline{\mathbf{S}}}{\partial\theta}\times\underline{\mathbf{S}} \end{bmatrix} = \begin{bmatrix} \underline{\mathbf{0}} \\ -\frac{{}^{A}\partial\underline{\$}^{T}}{\partial\theta}\,{}^{E}\delta\underline{\mathbf{D}}^{A} \end{bmatrix} \\ &= -\begin{bmatrix} 0 \\ 0 \\ 1 \end{bmatrix}\frac{{}^{A}\partial\underline{\$}^{T}}{\partial\theta}\,{}^{E}\delta\underline{\mathbf{D}}^{A} = -\left(\frac{{}^{A}\partial\underline{\$}}{\partial\theta}\begin{bmatrix} 0 & 0 & 1 \end{bmatrix}\right)^{T}\,{}^{E}\delta\underline{\mathbf{D}}^{A} \end{aligned} \tag{23} $$

because $\frac{{}^{A}\partial\underline{\mathbf{S}}}{\partial\theta}\times\underline{\mathbf{S}} = -1\left(\underline{\mathbf{k}}\right)$.

By substituting δl and ${}^{E}\delta\underline{\$}$ in Eq. 6 with Eqs. 10, 16, 18, and 23 and arranging the terms by the twists, the derivative of the spring force can be written as

$$ \begin{aligned} {}^{E}\delta\underline{\mathbf{f}} &= k\delta l\underline{\$} + k(l-l_o)\,{}^{E}\delta\underline{\$} \\ &= \left[K_F\right]{}^{A}\delta\underline{\mathbf{D}}^{B} + \left[K_M\right]{}^{E}\delta\underline{\mathbf{D}}^{A} \end{aligned} \tag{24} $$

where

$$ \left[K_F\right] = k\underline{\$}\underline{\$}^{T} + k(1-\frac{l_o}{l})\frac{{}^{A}\partial\underline{\$}}{\partial\theta}\,\frac{{}^{A}\partial\underline{\$}'^{T}}{\partial\theta} \tag{25} $$

$$ \left[K_M\right] = k(l-l_o)\left(\frac{{}^{A}\partial\underline{\$}}{\partial\theta}\begin{bmatrix} 0 & 0 & 1 \end{bmatrix} - \left(\frac{{}^{A}\partial\underline{\$}}{\partial\theta}\begin{bmatrix} 0 & 0 & 1 \end{bmatrix}\right)^{T}\right). \tag{26} $$

As shown in Eq. 24, the derivative of the spring force joining two rigid bodies depends not only on a relative twist between two bodies but also on the twist of the intermediate body, in this case body A, in terms of the inertial frame. $\left[K_F\right]$ is identical to the stiffness matrix of the spring connecting a moving body to the ground which was derived by Griffis, 1991. $\left[K_M\right]$ is newly introduced from this research and results from the motion of the base frame, in this case body A. $\left[K_M\right]$ takes a skew symmetric form in general.

4. Stiffness Matrix of the Mechanism

The stiffness matrix $[K]$ which maps a small twist of body B in terms of the inertial frame into the corresponding change of the wrench on body B is derived from Eq. 3 (see Fig. 1). The derivatives of spring forces can be written by Eqs. 27 and 28 since Springs 4, 5, and 6 connect body A and ground and Springs 1, 2, and 3 join two moving bodies.

$$\begin{aligned}\delta \underline{\mathbf{f}}_4 + \delta \underline{\mathbf{f}}_5 + \delta \underline{\mathbf{f}}_6 &= [K_F]_4 \, {}^E\delta \underline{\mathbf{D}}^A + [K_F]_5 \, {}^E\delta \underline{\mathbf{D}}^A + [K_F]_6 \, {}^E\delta \underline{\mathbf{D}}^A \\ &= [K_F]_{R,L} \, {}^E\delta \underline{\mathbf{D}}^A\end{aligned} \tag{27}$$

$$\begin{aligned}\delta \underline{\mathbf{f}}_1 + \delta \underline{\mathbf{f}}_2 + \delta \underline{\mathbf{f}}_3 &= [K_F]_1 \, {}^A\delta \underline{\mathbf{D}}^B + [K_F]_2 \, {}^A\delta \underline{\mathbf{D}}^B + [K_F]_3 \, {}^A\delta \underline{\mathbf{D}}^B \\ &\quad + [K_M]_1 \, {}^E\delta \underline{\mathbf{D}}^A + [K_M]_2 \, {}^E\delta \underline{\mathbf{D}}^A + [K_M]_3 \, {}^E\delta \underline{\mathbf{D}}^A \\ &= [K_F]_{R,U} \, {}^A\delta \underline{\mathbf{D}}^B + [K_M]_{R,U} \, {}^E\delta \underline{\mathbf{D}}^A\end{aligned} \tag{28}$$

where

$$[K_F]_{R,L} = \sum_{i=4}^{6} [K_F]_i \,, \; [K_F]_{R,U} = \sum_{i=1}^{3} [K_F]_i \,, \; [K_M]_{R,U} = \sum_{i=1}^{3} [K_M]_i$$

and where $[K_F]_i$ and $[K_M]_i$ are defined as Eqs. 25 and 26.

Then from Eqs. 3, 27, and 28 the derivative of the external wrench can be written by

$$\begin{aligned}\delta \underline{\mathbf{w}}_{ext} &= [K] \, {}^E\delta \underline{\mathbf{D}}^B \\ &= [K_F]_{R,L} \, {}^E\delta \underline{\mathbf{D}}^A \\ &= [K_F]_{R,U} \, {}^A\delta \underline{\mathbf{D}}^B + [K_M]_{R,U} \, {}^E\delta \underline{\mathbf{D}}^A\end{aligned} \,. \tag{29}$$

Finally, from Eq. 29 and the twist equation, Eq. 30, the stiffness matrix can be obtained as Eq. 31.

$${}^E\delta \underline{\mathbf{D}}^B = {}^E\delta \underline{\mathbf{D}}^A + {}^A\delta \underline{\mathbf{D}}^B \tag{30}$$

$$[K] = [K_F]_{R,L} \left([K_F]_{R,L} + [K_F]_{R,U} - [K_M]_{R,U} \right)^{-1} [K_F]_{R,U} \tag{31}$$

5. Numerical Example

The geometry information and spring properties of the mechanism in Fig. 1 and the external wrench $\underline{\mathbf{w}}_{ext}$ are given below.

$$\underline{\mathbf{w}}_{ext} = \begin{bmatrix} 0.01 & N \\ -0.02 & N \\ 0.03 & Ncm \end{bmatrix}$$

Table 1. Spring properties (Unit: N/cm for k, cm for l_o).

Spring No.	1	2	3	4	5	6
Stiffness constant k	0.2	0.3	0.4	0.5	0.6	0.7
Free length l_o	5.0040	2.2860	4.9458	5.5145	3.1573	5.2568

Table 2. Positions of pivot points in terms of the inertial frame (Unit: cm).

Pivot points	E1	E2	E3	B1	B2	B3
X	0.0000	1.5000	3.0000	0.0903	1.7063	1.9185
Y	0.0000	1.2000	0.5000	9.8612	8.6833	10.6721

(continue)

A1	A2	A3	A4
0.9036	2.5318	2.7236	1.6063
4.5962	3.4347	5.4255	5.4659

The stiffness matrices $[K]$ is obtained by using Eq. 31.

$$[K] = \begin{bmatrix} 0.0108 & N/cm & -0.0172 & N/cm & -0.0797 & N \\ -0.0172 & N/cm & 0.3447 & N/cm & 0.8351 & N \\ -0.0997 & N & 0.8251 & N & 2.6567 & Ncm \end{bmatrix}$$

To evaluate the result, a small wrench $\delta \underline{\mathbf{w}}_G$ is applied to body B and the static equilibrium pose of the mechanism is obtained by a numerically iterative method. From the equilibrium pose of the mechanism, the twist of body B with respect to ground ${}^E\delta\underline{\mathbf{D}}^B$ is obtained as below.

$$\delta \underline{\mathbf{w}}_G = 10^{-4} \times \begin{bmatrix} 0.5 & N \\ 0.2 & N \\ 0.4 & Ncm \end{bmatrix}$$

$${}^E\delta\underline{\mathbf{D}}^B = \begin{bmatrix} 0.0077 & cm \\ -0.0012 & cm \\ 0.0007 & rad \end{bmatrix}$$

Then the twist ${}^E\delta\underline{\mathbf{D}}^B$ is multiplied by the stiffness matrices to see if the given small wrench $\delta \underline{\mathbf{w}}_G$ results.

$$\delta\underline{\mathbf{w}} = [K]\,{}^E\delta\underline{\mathbf{D}}^B = 10^{-4} \times \begin{bmatrix} 0.4991 & N \\ 0.1988 & N \\ 0.4016 & Ncm \end{bmatrix}$$

The numerical example indicates that $[K]$ produces the given wrench $\delta \underline{\mathbf{w}}_G$ with high accuracy.

6. Conclusion

In this paper, a derivative of spring force connecting two moving bodies was derived by using screw theory and an intermediate frame and applied to obtain a stiffness matrix of a mechanism having two compliant parallel mechanisms serially arranged. A derivative of spring force connecting two moving bodies depends not only on a relative twist between the two bodies but also on the twist of the intermediate body in terms of the inertial frame. This result also can be applied for mechanisms having any arbitrary number of parallel mechanisms in a serial arrangement.

7. Acknowledgements

The authors would like to gratefully acknowledge the support provided by the Department of Energy via the University Research Program in Robotics (URPR), grant number DE-FG04-86NE37967.

References

Ball, R.S. (1900), *A Treatise on the Theory of Screws,* London, Cambridge University Press.

Ciblak, N. and Lipkin, H. (1999), Synthesis of Cartesian Stiffness for Robotic Applications. *Proceedings of the IEEE International Conference on Robotics and Automation,* Detroit, MI, USA.

Crane, C.D., Rico, J.M, and Duffy, J. (2006), *Screw Theory and Its Application to Spatial Robot Manipulators*, London, Cambridge University Press.

Dimentberg, F.M. (1965), *The Screw Calculus and its Applications in Mechanics,* Foreign Technology Division, Wright-Patterson Air Force Base, Ohio. Document No. FTD-HT-23-1632-67.

Griffis, M.A. (1991), *Novel Theory for Simultaneously Regulating Force and Displacement,* PhD dissertation, University of Florida, Gainesville, USA.

Huang, S. and Schimmels, J.M. (1998), The Bounds and Realization of Spatial Stiffness Achieved with Simple Springs Connected in Parallel, *IEEE Transactions on Robotics and Automation,* no. 3, vol. 14, pp. 466-475.

Peshkin, M. (1990), Programmed Compliance for Error Corrective Assembly, *IEEE Transactions on Robotics and Automation,* no. 4, vol. 6.

Roberts, R.G. (1999), Minimal Realization of a Spatial Stiffness Matrix with Simple Springs Connected in Parallel, *IEEE Transactions on Robotics and Automation,* no. 5, vol. 15.

Whitney, D.E. (1982), Quasi-static assembly of compliantly supported rigid parts, *ASME Journal of Dynamic Systems, Measurement, and Control,* vol. 104, pp. 65-77.

LARGE KINEMATIC ERROR PROPAGATION IN REVOLUTE MANIPULATORS

Yunfeng Wang
Department of Mechanical Engineering
The College of New Jersey
Ewing, NJ 08628, USA
jwang@tcnj.edu

Gregory S. Chirikjian
Department of Mechanical Engineering
Johns Hopkins University
Baltimore, MD 21218, USA
gregc@jhu.edu

Abstract Understanding how errors propagate in serial revolute manipulators is important for developing better designs and planning algorithms, as well as understanding the practical limitations on accuracy of multi-link arms. In this paper we provide a systematic propagation methodology and numerical example that illustrates how large kinematic errors propagate by convolution on the Euclidean motion group.

Keywords: Kinematic error, error propagation, revolute manipulators

1. Introduction

Kinematic errors arising from spatial uncertainties put strong limitations on the performance of serial manipulators. The accumulation of these errors could lead to the failure of executing nominal tasks. Evaluating the propagation effects of kinematic errors is essential in manipulator design, failure prediction, and algorithms planninng. It is also important for understanding the practical limitations on accuracy of multi-link arms.

In this paper, we presents a systematic methodology of propagating large errors in revolute manipulators from the point view of Euclidean motion group. Our approach is to treat errors using probability densities on the Euclidean group. Whereas concepts such as integration and convolution of these densities follow in a natural way when considering the Lie group setting [Chirikjian and Kyatkin, 2001], standard concepts associated with the Gaussian distribution in $\mathbb{R}^N$ do not follow in a

J. Lenarčič and B. Roth (eds.), Advances in Robot Kinematics, 95–102.

natural way to Lie groups. Several of the most closely related works are reviewed below. These include the theory of Lie groups, robot kinematics, methods for describing spatial uncertainty, and state estimation.

Murray, Li and Sastry [Murray, Li and Sastry, 1994] and Selig [Selig, 1996] presented Lie-group-theoretic notation and terminology to the robotics community, which has now become standard vocabulary. Park and Brockett [Park and Brockett, 1994] showed how dexterity measures can be viewed in a Lie group setting, and how this coordinate-free approach can be used in robot design. Wang and Chirikjian [Wang and Chirikjian, 2004] showed that the workspace densities of manipulators with many degrees of freedom can be generated by solving a diffusion equation on the Euclidean group. Blackmore and Leu [Blackmore and Leu, 1992] showed that problems in manufacturing associated with swept volumes can be cast within a Lie group setting. Kyatkin and Chirikjian [Chirikjian and Kyatkin, 2001] showed that many problems in robot kinematics and motion planning can be formulated as the convolution of functions on the Euclidean group.

Starting with the pioneering work of Brockett [Brockett, 1972], the controls community has embraced group-theoretic problems for many years. This includes PD control on the Euclidean group [Bullo and Murray, 1999; Leonard and Krishnaprasad 1995], tracking problems [Han and Park, 2001; Han, 2004], and estimation [Lo and Eshleman, 1979]. The representation and estimation of spatial uncertainty has also received attention in the robotics and vision literature [Smith and Cheeseman, 1986; Su and Lee, 1992]. Recent work on error propagation described by the concatenation of random variables on groups has also found promising applications in mobile robot navigation [Smith, Drummond, and Roussopoulos, 2003]. We note that while all of these works focus on small errors, our emphasis is a formulation that applies to large errors as well.

2. Review of Rigid-Body Motions

2.1 Euclidean Motion Group

The Euclidean motion group, $SE(N)$, is the semi direct product of $\mathbb{R}^N$ with the special orthogonal group, $SO(N)$. We denote elements of $SE(N)$ as $g = (\mathbf{a}, A) \in SE(N)$ where $A \in SO(N)$ and $\mathbf{a} \in \mathbb{R}^N$. For any $g = (\mathbf{a}, A)$ and $h = (\mathbf{r}, R) \in SE(N)$, the group law is written as $g \circ h = (\mathbf{a} + A\mathbf{r}, AR)$, and $g^{-1} = (-A^T\mathbf{a}, A^T)$. It is often convenient to express an element of $SE(N)$ as an $(N+1) \times (N+1)$ homogeneous

transformation matrix of the form:

$$g = \begin{pmatrix} A & \mathbf{a} \\ \mathbf{0}^T & 1 \end{pmatrix}.$$

In this way, rotation and translation are combined into a single matrix. A homogeneous transformation matrix takes the place of the pair $(\mathbf{a}, A)$, and the group operation becomes the matrix multiplication

For example, each element of $SE(2)$ parameterized using polar coordinates can be written as:

$$g(r, \phi, \theta) = \begin{pmatrix} \cos\theta & -\sin\theta & r\cos\phi \\ \sin\theta & \cos\theta & r\sin\phi \\ 0 & 0 & 1 \end{pmatrix}, \tag{1}$$

where $0 \leq \phi, \theta \leq 2\pi$ and $0 \leq r \leq \infty$. $SE(2)$ is a 3-dimensional manifold much like $\mathbb{R}^3$. We can integrate over $SE(2)$ using the volume element $d(g(r, \theta, \phi)) = r dr d\theta d\phi$.

2.2 Motion-Group Fourier Transform

The Fourier transform of a function on $G = SE(N)$ is defined as:

$$\hat{f}(p) = \int_G f(g) U(g^{-1}, p)\, d(g) \tag{2}$$

where $d(g)$ is a volume element at g, and $U(g, p)$ is an infinite-dimensional unitary matrix called an irreducible unitary representation, or IUR [Chirikjian and Kyatkin, 2001]. It possess the important homomorphism property, $U(g_1 \circ g_2, p) = U(g_1, p)U(g_2, p)$. One can show that the generalization of the classical Fourier transform in (2) admits a convolution theorem due to the homomorphism property of $U(g, p)$, and that the following inverse transform can be used to reconstruct the original function:

$$f(g) = \int_0^\infty \text{trace}(\hat{f}(p)U(g, p))p^{N-1} dp. \tag{3}$$

This is because the matrix elements of the full set of IURs form an orthonormal basis with which to expand functions on $SE(N)$.

A number of works [Chirikjian and Kyatkin, 2001] have shown that the matrix elements of the IURs for $SE(2)$ can be expressed as

$$u_{mn}(g(r, \phi, \theta), p) = i^{n-m} e^{-i[n\theta + (m-n)\phi]} J_{n-m}(p\, r) \tag{4}$$

where $J_\nu(x)$ is the ν^{th} order Bessel function, and m and n take values in the integers.

The Fourier inverse transform can be written in terms of elements as

$$f(g) = \sum_{m,n \in \mathbf{Z}} \int_0^\infty \hat{f}_{mn} u_{nm}(g,p) p dp. \tag{5}$$

The motion-group Fourier transform has the property that when applied to convolutions of the form

$$(f_1 * f_2)(g) = \int_G f_1(h) f_2(h^{-1} \circ g) d(h),$$

the result is the product of Fourier transform matrices: $\hat{f}_2(p)\hat{f}_1(p)$.

3. Propagation of Error in Serial Linkages

Suppose we are given a manipulator consisting of two concatenated serial links connected with a revolute joint. One unit is stacked on top of the other one. The proximal unit will be able to reach each frame $h_1 \in SE(3)$ with some error when its proximal end is located at the identity $e \in SE(3)$. This error may be different for each different frame h_1. This is expressed mathematically as a real-valued function of $g_1 \in SE(3)$ which has a peak in the neighborhood of h_1 and decays rapidly away from h_1. If the unit could reach h_1 exactly, this function would be a delta function. Explicitly the error may be described by one of many possible density functions depending on what error model is used. However, it will always be the case that it is of the form $\rho_1(h_1, g_1)$ for $h_1, g_1 \in SE(3)$. That is, the error will be a function of $g_1 \in SE(3)$ for each frame h_1 that the top of the module tries to attain relative to its base. Likewise, the second module will have an error function $\rho_2(h_2, g_2)$ for $h_2, g_2 \in SE(3)$ that describes the distribution of frames around h_2 that might be reached when h_2 is the expected end frame for module 2 relative to its base, and the base of module 2 is located at the identity $e \in SE(3)$.

The error distribution that results from the concatenation of two mod-modules with errors $\rho_1(\cdot)$ and $\rho_2(\cdot)$ results from sweeping the error distribution of the second module by that of the first. This is written mathematically as:

$$\begin{array}{rl} & \rho(h_1 \circ h_2, g) \\ = & (\rho_1 \otimes \rho_2)(h_1 \circ h_2, g) \\ \stackrel{\triangle}{=} & \int_{SE(3)} \rho_1(h_1, g_1) \rho_2(h_2, g_1^{-1} \circ g) d(g_1). \end{array} \tag{6}$$

Here $d(g)$ is the unique bi-invariant integration measure for $SE(3)$ evaluated at g [Chirikjian and Kyatkin, 2001]. Sometimes this is simply

written as dg. In the case of no error, the multiplication of homogeneous transforms h_1 and h_2 as $h_1 \circ h_2$ represents the composite change in position and orientation from the base of the lower unit to the interface between units, and from the interface to the top of the upper unit. In the case of inexact kinematics, the error function for the upper unit is shifted by the lower unit ($\rho_2(h_2, g_1^{-1} \circ g)$), weighted by the error distribution of the lower unit ($\rho_1(h_1, g_1)$) and integrated over the support of the error distribution of the lower unit (which is the same as integrating over all of $SE(3)$ since outside of the support of the error distribution the integral is zero). The result of this integration is by definition the error density function around the frame $h_1 \circ h_2$, and this is denoted as $(\rho_1 \otimes \rho_2)(h_1 \circ h_2, g)$. It should be noted that (6) holds regardless of the size of the errors or the form of the error density.

It is often convenient to suppress the explicit dependence of $\rho_i(\text{cot})$ on h_i, which can be viewed as a constant set of parameters. When this is done, Eq. 6 reduces to a convolution on $SE(N)$.

4. Numerical Example

Consider the three-link planar revolute manipulator shown in Figure 1. Each rigid link has length L, and each joint has some backlash that is described by a probability distribution $f(\theta - \theta_0)$ centered around the value $\theta_0 = 30$ degrees. The error density for a single link is then of the form

$$\rho(g(r, \phi, \theta)) = f(\theta - \theta_0)\delta(\phi - \theta)\delta(r - L)/r \tag{7}$$

where $\delta(\cdot)$ is the usual Dirac delta function in one dimension and an arbitrary element of $g(r, \phi, \theta) \in SE(2)$ is parametrized as in Eq. 1. Integration over $G = SE(2)$ is then integration over all values of $r \in \mathbb{R}^+$ and $\phi, \theta \in [0, 2\pi]$.

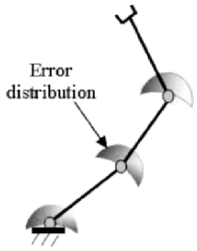

Figure 1. A three-link planar manipulator with joint backlash.

In Equation 7, the delta functions enforce the rigidity of the links, and division by r is due to the r in the volume element. The function

$f(\theta)$ has its mode at 0, but the backlashes can be potentially large (i.e., not highly concentrated). For this reason, we cannot take it to be a Gaussian, but rather, a folded Gaussian of the form:

$$\begin{aligned} f(\theta,\sigma) &= \tfrac{1}{2\pi}\textstyle\sum_{n=-\infty}^{\infty} e^{-n^2\sigma^2} e^{in\theta} \\ &= \tfrac{1}{\sqrt{2\pi}\sigma}\textstyle\sum_{n=-\infty}^{\infty} e^{-(\theta-2\pi n)^2/2\sigma^2} \end{aligned} \tag{8}$$

The error density that accumulates at the end effector due to backlashes in each of the joints is computed as the convolution

$$\rho_{ee}(g) = (\rho * \rho * \rho)(g).$$

Computing this numerically by the definition of convolution is not as convenient as using the $SE(2)$-convolution theorem and the corresponding concept of Fourier transform, which is what we shall do here.

Computing the $SE(2)$-Fourier transform of the one-link backlash-error density in Equation 7, one finds (after the delta functions kill the integrals over r and ϕ) that:

$$\begin{aligned} \hat{\rho}_{mn}(p) &= i^{n-m} J_{m-n}(pL) \textstyle\int_0^{2\pi} f(\theta-\theta_0) e^{in\theta} d\theta \\ &= i^{n-m} J_{m-n}(pL) e^{in\theta_0 - n^2\sigma^2}. \end{aligned} \tag{9}$$

Using the convolution theorem, we compute $\hat{\rho}_{ee}(p) = \hat{\rho}\,\hat{\rho}\,\hat{\rho}$, where the matrix elements of $\hat{\rho}$ are given by Equation 9. Then the original error density $\rho_{ee}(g(r,\phi,\theta))$ can be reconstructed by applying the Fourier inversion formula (3) to $\hat{\rho}_{ee}(p)$. Since it is difficult to view the error density $\rho(g)$ graphically, the marginal density function $\rho(r,\phi)$ is computed. The marginal density function $\rho(r,\phi)$ is found by just integrating the Fourier reconstruction formula (3) for $\rho(g)$ with respect to θ as

$$\begin{aligned} \rho(r,\phi) &= \frac{1}{2\pi}\int_0^{2\pi} \rho(g) d\theta \\ &= \sum_{n\in\mathbf{Z}} i^{-n} e^{-in\phi} \int_0^{\infty} \hat{f}_{0n}(p) J_{-n}(pr) p dp. \end{aligned}$$

To validate the results obtained from our convolution-based error propagation method, the error distribution (8) is sampled and applied to each joint of the manipulator directly. Then brute force enumeration is used to obtain the error distribution directly.

The marginal error densities $\rho(r,\phi)$ obtained from both methods are plotted in Figures 2 and 3 with the left one from the propagation method and the right one from brute force. The variance σ^2 of 0.1 is given in Figure 2 and σ^2 of 0.3 in Figure 3.

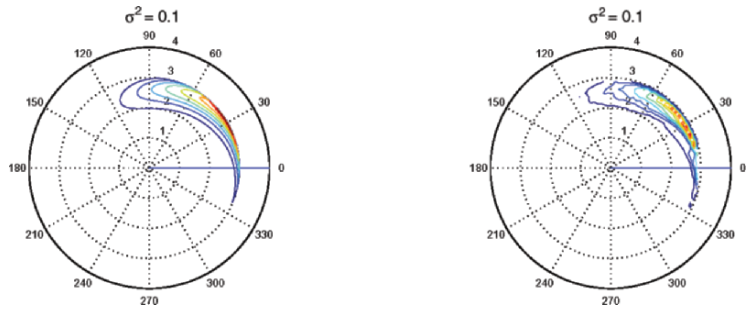

Figure 2. The marginal error density $\rho(r, \phi)$ for $\sigma^2 = 0.1$.

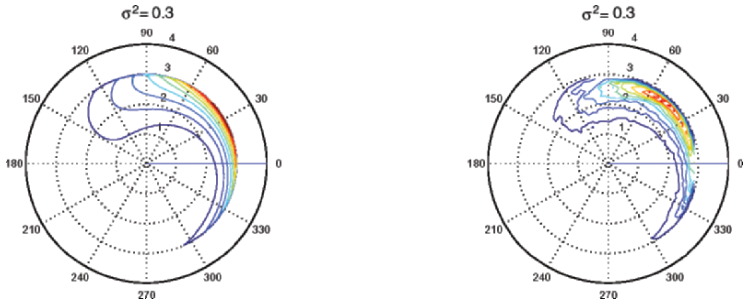

Figure 3. The marginal error density $\rho(r, \phi)$ for $\sigma^2 = 0.3$.

For the above computations, the link length L is taken as 1, and 60 samples points are generated for the distribution (8). The infinite-dimensional matrix function $U(g, p)$ in the $SE(2)$ Fourier transform is truncated at finite values of $|m|, |n| \leq 10$ (i.e., the dimension of $U(g, p)$ is $2 \times 10 + 1$). The band-limited approximation still gives very accurate results because the magnitude of the Fourier transform of a sufficiently smooth function can be ignored beyond a certain cutoff frequency. The frequency parameter p is sampled in the interval of 300 with an integration step of 0.2. All the calculations in this example (excluding the brute force method) took less then 3 minutes using Matlab with a 1.0 GHz, 516 MB RAM computer.

5. Conclusions

In this paper it is shown how the accumulation of large kinematic errors in serial manipulators can be computed by performing convolutions

on the Euclidean motion group. This theory is demonstrated with the example of a planar revolute manipulator with three links.

6. Acknowledgements

This work was performed under grant NSF-RHA 0098382 "Diffusion Processes in Motion Planning and Control."

References

Blackmore, D., Leu, M.C. (1992),"Analysis of Swept Volume via Lie Groups and Differential Equations," *The Int. J. of Robotics Research* Vol. 11, No. 6, pp. 516-537.

Brockett, R.W. (1972), "System Theory on Group Manifolds and Coset Spaces," *SIAM J. Control*, Vol. 10, No. 2, pp. 265-284.

Bullo, F., Murray R.M. (1999), "Tracking for fully actuated mechanical systems: a geometric framework," *Automatica*, 35 (1): 17-34.

Chirikjian, G.S., Kyatkin, A.B. (2001), *Engineering Applications of Noncommutative Harmonic Analysis*, CRC Press, Boca Raton, FL.

Han, Y.M. (2004), "Simultaneous translational and rotational tracking in dynamic, environments: Theoretical and practical viewpoints," *IEEE Transactions on Robotics and Automation*, 20 (2): 309-318.

Han, Y., Park, F.C. (2001), "Least squares tracking on the Euclidean group," IEEE Transactions on Automatic Control, 46 (7): 1127-1132.

Leonard, N.E., Krishnaprasad, P.S. (1995), "Motion Control on Drift-Free, Left-Invariant Systems on Lie Groups," *IEEE Transactions on Automatic Control*, Vol. 40, No. 9, pp. 1539-1554.

Lo, J. T.-H., Eshleman, L.R. (1979), "Exponential Fourier Densities on $SO(3)$ and Optimal Estimation and Detection for Rotational Processes," *SIAM J. Appl. Math.*, Vol. 36, No. 1, pp. 73-82.

Murray, R.M., Li, Z., Sastry, S.S. (1994), *A Mathematical Introduction to Robotic Manipulation*, CRC Press, Ann Arbor MI.

Park, F.C., Brockett, R.W. (1994), "Kinematic Dexterity of Robotic Mechanisms," *The International Journal of Robotics Research*, Vol. 13, No. 1, pp. 1-15.

Selig, J.M. (1996), *Geometrical Methods in Robotics*, Springer, New York.

Smith, P., Drummond, T., Roussopoulos, K. (2003), "Computing MAP trajectories by representing, propagating and combining PDFs over groups," *Proceedings of the 9th IEEE Int. Conf. on Computer Vision*, volume II, pages 1275-1282, Nice.

Smith, R.C., Cheeseman, P. (1986),"On the Representation and Estimation of Spatial Uncertainty," *The Int. J. of Robotics Research*, Vol. 5, No. 4, pp. 56-68.

Su, S., Lee, C.S.G. (1992), "Manipulation and Propagation of Uncertainty and Verification of Applicability of Actions in assembly Tasks," *IEEE Transactions on Systems, Man, and Cybernetics*, Vol. 22, No. 6, pp. 1376-1389.

Wang, Y.F., Chirikjian, G.S. (2004), "Workspace Generation of Hyper-Redundant Manipulators as a Diffusion Process on SE(N)," *IEEE Transactions on Robotics and Automation*, Vol. 20, No. 3, pp. 399-408.

A FRAMEWORK FOR THE ANALYSIS, SYNTHESIS AND OPTIMIZATION OF PARALLEL KINEMATIC MACHINES

Andreas Pott and Manfred Hiller
Chair of Mechatronics
University Duisburg-Essen, Germany
{pott, hiller}@imech.de

Abstract Analysis and design of parallel robots are often treated separately due to different methods. Thus, a framework is needed to combine important aspects of both tasks. In this paper, it is shown that workspace calculation/verification and synthesis/optimization can be summarized within the context of an interval analysis based constrained global optimization. Specializing this general formulation leads to a flexible technique which can be used to solve each of the aforementioned subtasks. In this setting, the constraints specify the machine's properties like size and quality of the workspace of the machine. Starting with workspace calculation for some criterions, one extends the requirements and seamlessly advance to parameter synthesis and optimization. These techniques present a framework for workspace calculation, parameter design, and optimization which allows for analysis and synthesis by means of the same model. The method is demonstrated for a 6 d.o.f. Gough-platform.

Keywords: Parallel Robot, Analysis, Optimization, Interval Analysis, Modular Framework

1. Introduction

For the design of parallel kinematic machines (PKM), it is important to make an appropriate choice for the geometrical parameters in order to fulfill the customers requirements. Unfortunately, one cannot start with the design of new machines unless one can cope with a number of issues that are related to the analysis of parallel machines. In particular, this includes the determination of the size, shape, and properties of the workspace. In the last two decades, many scientists have been working on different aspects of analysis. Especially for spatial parallel robots, most results can only be determined numerically due to the inherent complexity of PKMs. But mostly these results cannot be used to solve the design problem, i.e. how one has to choose the parameters so that the resulting machines have the desired properties. For example,

J. Lenarčič and B. Roth (eds.), Advances in Robot Kinematics, 103–112.

the widely used calculation of the workspace by discretization reveals nothing about how one has to change the geometry of the machine to enlarge the workspace. Thus, methods are needed that allow for both analysis and synthesis within one framework to assist during the whole development process: Firstly, a preliminary analysis is needed to prove the concept of a machine. Subsequently, one switches to parameter design with respect to given process requirements and optimization due to factors like costs. Finally, one has to verify that the developed machine has all desired properties.

In this paper, interval analysis based constraint satisfaction is used as common framework to perform workspace calculation and parameter synthesis. It is shown how the general form of a constrained global optimization problem can be specialized to perform workspace calculation, parameter synthesis, and optimization using an extendable scheme of constraints. The paper is organized as follows: In section 2 interval methods for constraint satisfaction and optimization are reviewed and applied to the design problem of PKMs. In section 3, the constraints for Gough-platforms are deduced from imperative process requirements and examples from the analysis, synthesis, and optimization are given in section 4. Conclusions are drawn in section 5.

2. Constraint Satisfaction and Global Optimization

At first, consider the constrained global optimization problem of the form

$$\begin{aligned} \text{minimize} \quad & f(\boldsymbol{g}) && (1)\\ \text{s.t.} \quad & \boldsymbol{\Phi}(\boldsymbol{g},\boldsymbol{x}) > \mathbf{0} && (2)\\ & \forall \ \boldsymbol{x} \in \mathcal{W}, && (3) \end{aligned}$$

where f is the objective function, $\boldsymbol{\Phi}$ is a system of nonlinear constraints, $\boldsymbol{g}$ is the vector of the design parameters (calculation domain), $\mathcal{W}$ is the compact set of configurations to be verified, and the configuration $\boldsymbol{x}$ is any vector from the set $\mathcal{W}$. In contrast to classical optimization problems, this formulation is extended by constraints, that must be fulfilled for *all* configurations $\boldsymbol{x}$ given by the set $\mathcal{W}$. In this paper, it is assumed that the set $\mathcal{W}$ can be approximated by hypercubes. Thus, this special type of optimization problem is denoted as *global constrained optimization over intervals*.

As pointed out above, the analysis, design, and optimization of PKMs can be regarded as such a constrained global optimization problem. For PKMs, one identifies $\boldsymbol{\Phi}$ with imperative process requirements, $\boldsymbol{g}$ with

the geometrical design parameters of the machine, $\boldsymbol{x}$ are the world coordinates (position and orientation) of the platform, and $\mathcal{W}$ is the desired workspace of the robot.

The basic algorithm to solve this problem is based on interval analysis and can be found in (Hansen, 1992). Interval analysis is a powerful tool to deal with both, the constraint satisfaction problem (CSP) given by Eqs. (2)-(3) and the constrained global optimization problem which is generated by Eqs. (1)-(3). Interval analysis have been applied to PKMs for analysis by e.g. (Chablat et al., 2002; Chablat et al., 2004; Merlet, 2004), and (Pott et al., 2004). Furthermore, interval analysis based algorithms were successfully used for the design of PKMs by (Merlet, 2001), (Hao and Merlet, 2005), (Pott et al., 2005), and (Pott and Hiller, 2006). Since the algorithm is already known, the key features are quickly reviewed. Interval methods are implemented such that numerical round-off errors are taken into account. Furthermore, interval analysis based constraint solvers and optimizers do not rely on a point-wise discretization of the parameter space. Therefore, it is guaranteed that constraints hold in any point of the considered set and optimizers are able to find guaranteed bounds for both, the optimum of the objective function and the environment of the parameter space containing the optimum.

2.1 Framework

The main advantage of the proposed framework is that one can save much development time, because the same solver algorithm and the same model equations are used to perform the different investigations. Furthermore, the system $\boldsymbol{\Phi}$ is composed from subsets of inequations that are related to different properties of the machine, e.g. taking into account geometric relations for the workspace, limits on the active and passive joints, link interference, and bounds on the dexterity. The presented framework allows among others

- to verify, if a given machine design $\boldsymbol{g}_0$ exhibits a given orientation workspace $\mathcal{W}_0$,
- to calculate the constant orientation workspace $\mathcal{W}_{\text{co}}$ and the total orientation workspace $\mathcal{W}_{\text{to}}$ for a given machine design $\boldsymbol{g}_0$ and
- to determine all machine designs $\boldsymbol{g}$ that provide a given (orientation) workspace $\mathcal{W}_0$.

Here, *workspace* includes all criterions that are introduced by the requirements $\boldsymbol{\Phi}$, e.g. the verified/calculated workspace is guaranteed to be consistent with active and passive joint limits and free of link interference. The different investigations can be deduces from the general form

as follows. Firstly, one can verify that a machine with given parameters $\boldsymbol{g}_0$ exhibits the given workspace $\mathcal{W}_0$ by analyzing

$$\boldsymbol{\Phi}(\boldsymbol{g}_0, \boldsymbol{x}) > \mathbf{0} \quad \forall \quad \boldsymbol{x} \in \mathcal{W}_0, \tag{4}$$

with the CSP solver. In contrary, determining all poses $\boldsymbol{x}$, where

$$\boldsymbol{\Phi}(\boldsymbol{g}_0, \boldsymbol{x}) > \mathbf{0}, \tag{5}$$

responds the problem to calculate the workspace of a given machine design. Finally, the determination of all $\boldsymbol{g}$ that fulfill

$$\boldsymbol{\Phi}(\boldsymbol{g}, \boldsymbol{x}) > \mathbf{0} \quad \forall \quad \boldsymbol{x} \in \mathcal{W}_0 \tag{6}$$

corresponds to the design problem for PKMs, i.e. finding all machine designs that fulfill given requirements throughout a given workspace $\mathcal{W}_0$. Such designs are then called *feasible*. Finally, the objective function f can be taken into account to find an optimal machine within the set of feasible designs generated by the CSP.

2.2 Modular Program Design

A flexible framework is intended to provide the following properties:

- Switch quickly between workspace verification (Eq. 4), workspace calculation (Eq. 5), parameter design (Eq. 6), and optimization.
- Add or remove constraints for reachable workspace, limits on active/passive joints, link interference, etc.
- Constraints should be independent from each other. New requirements may be added without reconsideration of other constraints.
- Workspace requirements can be used for parameter synthesis and optimization.

To achieve this, a modular program design of the framework is proposed (Fig. 1). This algorithm was proposed by (Pott and Hiller, 2006). A generic implementation of the interval based CSP solver (or the global optimizer) passes the interval boxes $\boldsymbol{g}$ to the constraint abstraction layer (CAL) that encapsulates the system of constraints for evaluation. The result of the evaluation is an abstract information like *valid*, *invalid*, or *undefined* that can be interpreted by the algorithm without further information on the system. To achieve the desired reconfigurability for the framework, the constraints must not be fixed to one special set of variables. This adaptability is realized by storing all variables that may be considered in a shared database. During the initialization, a mapping is set up between the constraints $\boldsymbol{\Phi}$ and the variables in the database

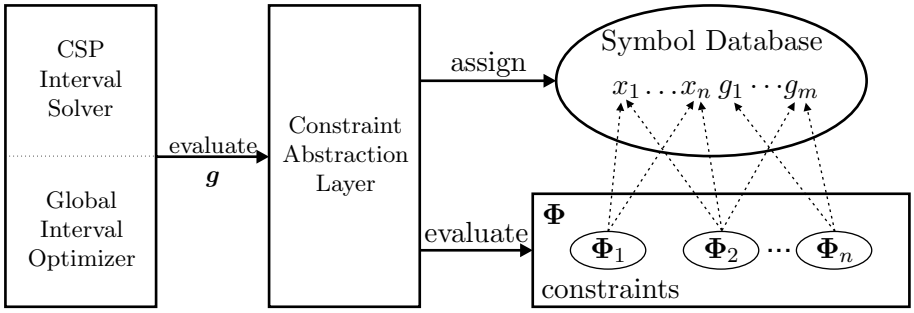

Figure 1. Structure of the modular interval CSP solver and optimizer.

that the user defines to be unknown. All other variables in the database are set to constant values. Before evaluating the constraints $\mathbf{\Phi}$, the CAL copies the actual values from $\boldsymbol{g}$ into the database. Note, that the implementation in C++ manages these apparent complicated relations very efficiently by means of pointers and virtual function.

The constraints $\mathbf{\Phi}$ are generated with computer algebra (Maple) and transformed into C++ code with Maple's automatic code generator. At this point, a little post-processing is needed to prepare the code to be used with interval analysis. For a calculation, one has only to select the variables/constraints to be taken into account from a library and assign initial values to the variables.

3. Process Related Constraints

The constraints $\mathbf{\Phi}$ for this framework are deduced from imperative process requirements, like the size of the workspace or limits for the passive joints. As shown by (Pott et al., 2005) for PKMs with constant length legs, one can also take into account auto-collision in terms of link interference, as well as, bounds on the kinematic dexterity. Due to space limitation of this paper, the following list is rather an example than an comprehensive list of requirements. To set up the equations, firstly a machine model has to be introduced.

3.1 Simplified Symmetric Manipulator (SSM)

To deduce constraints for the well-known simplified symmetric manipulator (SSM, Merlet, 2000, p. 62), the inverse kinematics is quickly reviewed. The SSM has a planar hexagonal base and platform where the platform is connected to the base by six legs which consist of prismatic joints with universal and spherical joints at their ends. The pivot points

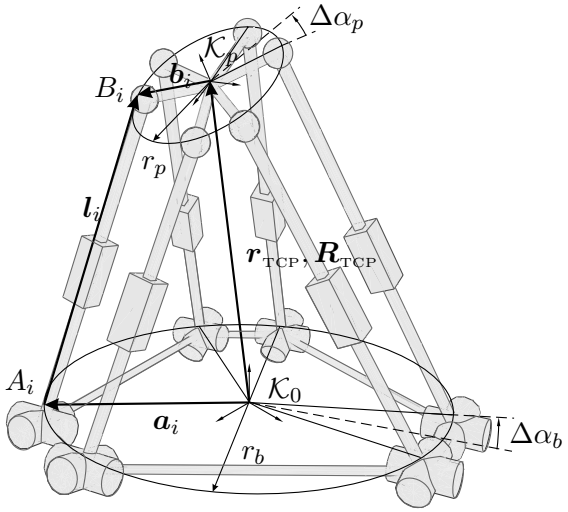

Figure 2. Parameter and kinematics of a SSM robot.

of the legs are arranged on circle with radii r_p and r_b for platform and base, respectively. The distribution of the pivot points on platform and base is shown in Fig. 2. The position of the platform is given in world coordinates $\boldsymbol{r}_{\mathrm{TCP}}$ and the orientation is defined by the matrix $\boldsymbol{R}_{\mathrm{TCP}}$ with respect to the base frame $\mathcal{K}_0$. Using a vector loop yields the closure condition

$$\boldsymbol{l}_i = \boldsymbol{r}_{\mathrm{TCP}} + \boldsymbol{R}_{\mathrm{TCP}}\boldsymbol{b}_i - \boldsymbol{a}_i \quad \text{for} \quad i = 1, \dots 6, \tag{7}$$

where $\boldsymbol{a}_i$ and $\boldsymbol{b}_i$ are the positions of the pivot points on the base and the platform, respectively. The length $l_i = |\boldsymbol{l}_i|$ of the leg can be easily determine from a given pose $\boldsymbol{r}_{\mathrm{TCP}}, \boldsymbol{R}_{\mathrm{TCP}}$ of the platform. It is a necessary condition for a pose to belong to the workspace, that l_i does not exceed the stroke of the actuator $[l_{\min}, l_{\max}]$. Thus, from $l_{\min} \le l_i \le l_{\max}$ one receives the 12 inequations

$$\left.\begin{array}{rcl} l_i^2 - l_{\min}^2 & > & 0 \\ l_{\max}^2 - l_i^2 & > & 0 \end{array}\right\} \quad \text{for} \quad i = 1, \dots 6 \tag{8}$$

that can be added to the constraint system $\boldsymbol{\Phi} > \boldsymbol{0}$.

3.2 Limits on the Passive Joints

The universal and spherical joints may limit the motion of the platform due to their technical realization. Therefore, one has to take into account the mechanical limits of these joints. For universal joints, Merlet, 2000, p. 205f suggested to use a pyramid described by its four face

normals $\boldsymbol{n}_1, \boldsymbol{n}_2, \boldsymbol{n}_3, \boldsymbol{n}_4$, to take into account these limits. For spherical joints, the motion of the joints is limited by a cone with a known apex angle $\beta_{\max}$. Thus, one received the following inequality

$$\boldsymbol{l}_i \cdot \boldsymbol{u}_i - l_i \cos \beta_{\max} > 0 \quad \text{for} \quad i = 1, \dots 6, \tag{9}$$

where $\boldsymbol{u}_i$ is a unit vector of the direction of the leg at the reference configuration. A similar considerations can be used for the platform. In that case, one must take into account that the reference vector $\boldsymbol{v}_i$ is fixed to the platform frame and must be transformed to world coordinates by

$$\boldsymbol{l}_i \cdot \boldsymbol{R}_{\mathrm{TCP}} \boldsymbol{v}_i - l_i \cos \beta_{\max} > 0 \quad \text{for} \quad i = 1, \dots 6. \tag{10}$$

3.3 Technological Requirements

As an example for a technological requirement, the distance $\overline{A_i A_j}$ between neighboring pivot points on the base and/or on the platform is considered. Since the joints need a minimal installation space, there is a lower bound $\Delta a_{\min}$ for this distance. This can be taken into account by considering the constraints

$$r_i \sqrt{2 - 2\cos(2\Delta\alpha_i)} - \Delta a_{\min} > 0 \quad \text{for} \quad i \in \{p, b\}. \tag{11}$$

Technological requirements have often a very simple structure and can be easily implemented into the framework. Nevertheless, they introduce restrictions that are important in practise and allow to neglect many designs without considering any details of the workspace.

3.4 Objective Function

Since the system of constraints $\boldsymbol{\Phi}$ collects all imperative process requirements, the objective function f focuses on minimizing a selected criterion. For example, one can minimize the total volume of the machine. In general, this criterion may be chosen more sophisticated for example by taking into account the total monetary costs of manufacturing. In the framework of the proposed algorithm for global optimization, this function is not even required to be continuous. Therefore, it is easy to incorporate for example tables with costs of components like actuators or other available components. It is clearly out of the scope of kinematics, to define and discuss, how one can set up such cost calculations. But at this point, an interface is defined, that explicitly separates economic requirements in terms of the cost function f and technological requirements in terms of imperative process requirements $\boldsymbol{\Phi}$. For simplicity, in section 4 a simple minimization of the volume of the machine is performed as an example of the algorithm.

Table 1. Nominal Geometrical Parameters of the SSM.

Parameter	*value*	*Description*
r_b	1 m	radius of the base frame
r_p	0.25 m	radius of the mobile platform
$\Delta\alpha_b$	45°	angular offset for the pivot points on the base
$\Delta\alpha_p$	15°	angular offset for the pivot points on the platform
$l_{\min}$	1 m	minimal length of the strut
$l_{\max}$	2 m	maximal length of the strut
$\Delta\beta_{\max}$	45°	maximal rotation of the spherical joints

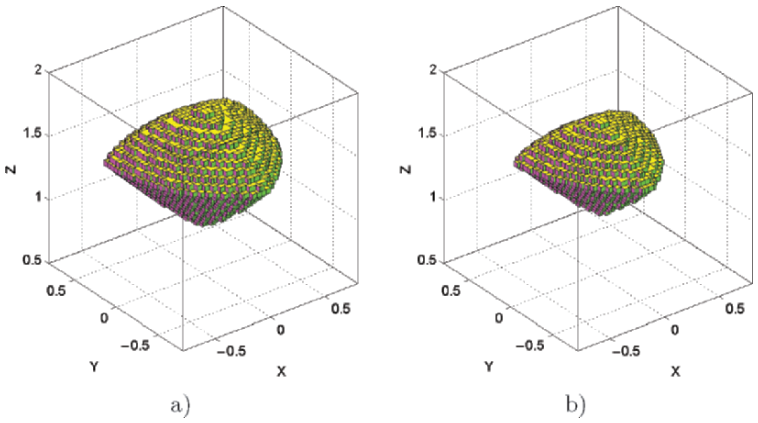

Figure 3. Workspace of the SSM a) constant orientation workspace b) total orientation workspace.

4. Computational Examples

In this section, the presented framework is applied step by step to a SSM. Parameters which are not part of the calculation, i.e. appear in $\boldsymbol{g}$ and $\boldsymbol{x}$ are assumed to have their nominal value (Table 1). All calculations are carried out for limits of the active joints, as well as limits of the passive joints at the base frame.

Workspace Calculation. At first, the workspace is determined using the CSP solver, i.e. both the constant orientation workspace ($\boldsymbol{R}_{\text{TCP}} = \boldsymbol{I}_3$) and the total orientation workspace is calculated. Fig. 3a shows the constant orientation workspace as it was determined by setting the vector of *design variables* to $\boldsymbol{g} = (x, y, z)$ and leaving the vector of configurations to be verified empty $\boldsymbol{x} = ()$. For the total orientation workspace

Table 2. Parameters for the *optimal* machine design of the SSM for a total orientation workspace of $200 \times 200 \times 200$mm.

Parameter:	r_p	r_b	$\Delta\alpha_b$	$\Delta\alpha_p$	Δz
	0.38125	0.278125	0.78125	0.625	0.753125

(Fig. 3b) all positions which can be reached with *all* orientations of Bryant-angles $\boldsymbol{x} = (\varphi \in [-0.1, 0.1], \theta \in [-0.1, 0.1], \psi \in [-0.1, 0.1])$ were determined. Accuracy was $\varepsilon = 0.025$ and the calculation time was $t = 1.7$s and $t = 41$s, respectively.

Parameter Synthesis. For the parameter synthesis example, the total orientation workspace of the robot is required to include a cubic workspace of size $200 \times 200 \times 200$mm. Thus, the desired workspace is described by $\boldsymbol{x} = (x \in [-0.1, 0.1], y \in [-0.1, 0.1], z \in [0.0, 0.2], \varphi \in [-0.1, 0.1], \theta \in [-0.1, 0.1], \psi \in [-0.1, 0.1])$ and all geometrical parameters $\boldsymbol{g} = (r_p, r_b, \Delta\alpha_p, \Delta\alpha_b)$ are sought, that fulfill this requirement. The solution set is described in the 4-dimensional parameter space and cannot be printed into a simple diagram. Therefore, only some key data are given. Totally, 214547 boxes with a volume of 7.2% out of a total search space volume were verified to be feasible designs by the CSP solver. The calculation time was ∼27h.

Optimization. The results from the parameter synthesis, i.e. the solution set from the constraint satisfaction problem can be used as input for the global optimization. As an example, the overall size of the machine and the distance between the pivot points is used as an objective function, which yields

$$f(r_p, r_b, \Delta\alpha_b, \Delta\alpha_p, \Delta z) = r_p^2 + \Delta z\ r_b^2 + (\Delta\alpha_p - 1)^2 + (\Delta\alpha_b - 1)^2 \quad (12)$$

Applying this optimization function to the CSP of the previous step, one obtains the values given in Table 2. The computational time of the program on a Pentium IV with 3.2GHz is 56min, and the optimizer performed approximately 57500 constraint evaluations per second, which demonstrates that the modular system can be implemented very efficiently. Note, that the combined use of the CSP solver and the optimizer can reduces significantly the calculation time.

5. Conclusions

In this paper, a framework for the analysis and design of parallel kinematic machines based on interval analysis and global optimization algorithms is proposed. It was shown how practically relevant calculations

for PKMs may be addressed in terms of a constrained global optimization problem. The proposed algorithm enforces the fulfillment of given process requirements throughout a workspace of desired size and guarantee the validity of the calculations. A global optimization is performed simultaneously, which assures to find the global minimum. Constraints were exemplarily deduced for the SSM and calculation results from the framework were presented.

Acknowledgement

This work is supported by the German Research Council (*Deutsche Forschungsgemeinschaft*) under HI370/19-3 as part of the priority program SPP1099 *Parallel Kinematic Machine Tools*.

References

Chablat, D., Wenger, P., Majou, F., and Merlet, J.-P. (2004). An Interval Analysis Based Study for the Design and the Comparison of 3-DOF Parallel Kinematic Machines. *International Journal of Robotics Research*.

Chablat, D., Wenger, P., and Merlet, J.-P. (2002). Workspace Analysis of the Orthoglide Using Interval Analysis. In *Advances in Robot Kinematics*, pages 397–406, Dordrecht, Netherlands. Kluwer Academic Publishers.

Hansen, E. (1992). *Global Optimization using Interval Analysis*. Marcal Dekker, Inc.

Hao, F. and Merlet, J.-P. (2005). Multi-criteria optimal design of parallel manipulators based on interval analysis. *Mechanism and Machine Theory*, 40(2):157–171.

Merlet, J.-P. (2000). *Parallel Robots*. Solid Mechanics and its Application. Kluwer Academic Publishers, Dordrecht.

Merlet, J.-P. (2001). An improved design algorithm based on interval analysis for spatial parallel manipulators with specified workspace. In *IEEE International Conference on Robotics and Automation*, Seoul, Korea.

Merlet, J.-P. (2004). Guaranteed in-the-workspace improved trajectory/surface/volume verification for parallel robots. In *IEEE International Conference on Robotics and Automation*, New Orleans, USA.

Pott, A., Boye, T., and Hiller, M. (2005). Parameter synthesis for parallel kinematic machines from given process requirements. In *Proceedings of the International Conference on Advanced Intelligent Mechatronics*, Monterey, California, USA, IEEE/ASME.

Pott, A., Franitza, D., and Hiller, M. (2004). Orientation workspace verification for parallel kinematic machines with constant leg length. In *Proceedings of Mechatronics and Robotics 2004*, pages 984–989, Aachen, Germany.

Pott, A. and Hiller, M. (2006). A parallel implementation for the optimization of parallel kinematic machines under process requirements. In *1st European Conference on Mechanism Science*, Obergurgl, Austria.

SEARCHING FOR UNDISCOVERED PLANAR STRAIGHT-LINE LINKAGES

Zhenjun Luo
Department of Mechanical Engineering
King's College London
zhenjun.luo@kcl.ac.uk

Jian S Dai
Department of Mechanical Engineering
King's College London
jian.dai@kcl.ac.uk

Abstract In this paper we investigate if there are undiscovered 6-bar linkages for generating a straight-line. First we successfully deduce the relationships in Hart's second straight-line mechanisms using symbolic methods. For more complicate cases, we formulate the problem as precision position synthesis problems, and solve the derived equations using classic iterative methods and verify solutions using interval methods. Although no new mechanisms have been found at the current stage, this research initiates an e ort towards an automatic approach for obtaining overconstrained linkages (Dai and Rees Jones, 1999).

Keywords: Path generation, algebraic curves, overconstrained, numerical methods

1. Introduction

Synthesis of planar linkages for curves generation is a classic topic in the field of kinematics. It had attracted many noted mathematicians and kinematicians since the time of industrial revolution. However before the Peaucellier-Lipkin linkage (Peaucellier, 1864) was discovered, most mathematicians doubted that there are linkages capable of drawing exact straight lines. Kempe (1873) enunciated a striking theorem that a portion of any algebraic curve on a plane can be generated by a planar linkage. Koenigs (1897) stated a spatial equivalence of Kempe's theorem. Those e orts predates a large body of modern work on theorems of "algebraic universality" starting from the 1970's (see Smith, 1998; Kapovich, 2002). Smith (1998) and Gao et al. (2000) presented new constructive approaches to prove Kempe's theorem. Nevertheless the constructive approaches are of less interests in practice since they

J. Lenarčič and B. Roth (eds.), Advances in Robot Kinematics, 113–122.

can only find feasible linkages with a large number of links. As Hunt stated in Chapter 4 of his book (Hunt, 1978):

> Yet neither Kempe nor anyone else since has established a method for isolating the best, or the simplest, linkage for tracing a particular curve.

In the history all feasible linkages with a small number of links for algebraic curves generation were invented by some great masters using their geometrical intuitions (Please see the Appendix for details). Nevertheless geometrical intuitions are difficult to be duplicated, and they may not guarantee all solutions for a synthesis problem be found. The above investigation raises a question: Are there any undiscovered 6-bar linkages for straight-line generation? This paper proposes a numerical approach to attack the problem. Note that it is possible to extend the approach for finding spatial 6R single loop overconstrained mechanisms (see remarks at the end of Section 2.2).

2. Searching for 6-bar Straight-line Linkages

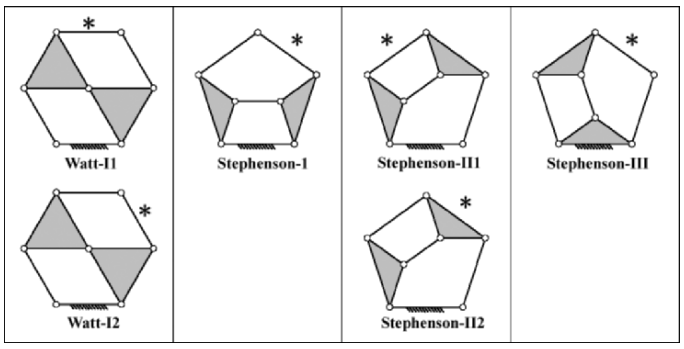

Figure 1. Six arrangements of 6-bar linkages for a path generation, with the asterisk denoting the position of coupler-point.

Figure 1 illustrates 6 possible arrangements of 6-bar linkages for straight-line generation. As can be seen from Fig. 4 that the existing straight-line 6-bar linkages are either Watt-I1 linkages or Stephenson-I linkages. Indeed based on the principle of inversion and Robert's cognate theorem, we can conclude that Stephenson-II2 linkages and Stephenson-III linkages cannot generate a straight-line. Other arrangements should be

[1]This is still an open problem. Smith, 1998 tried to prove it but failed.
[2]According to (Artobolevskii, 1964), Alekseyev, 1939 discovered the dimensional relationships of the generalized linkage on 1939, but the authors are not able to find Alekseyev's proof, while the short proof given in Artobolevskii's book is indeed invalid.

examined individually. Synthesizing straight-line linkages is closely related to the derivation of coupler-curve equations of general planar linkages (see Primrose et al., 1967, Almadi, 1996, and Wampler, 1999). However it is important to develop problem-specific methods based on symbolic analysis (Dukkipati, 2001, Karger, 1998) or numerical analysis (Luo and Dai, 2005).

2.1 Synthesize Stephenson-I Linkages for a Straight-line Motion

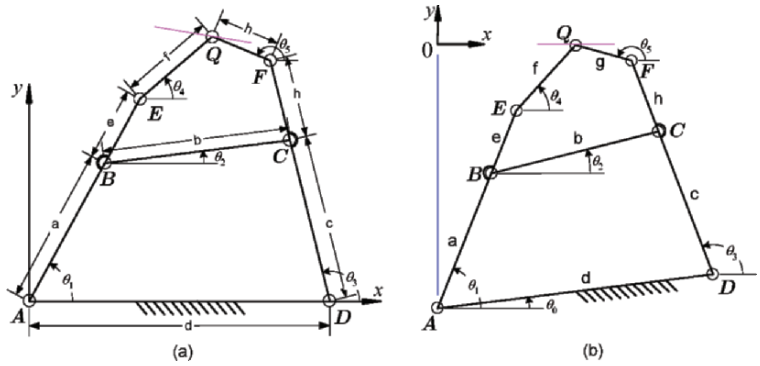

Figure 2. Two representations for synthesizing Stephenson-I linkages. (a) is Alekseyev's representation (see Artobolevskii, 1964), and (b) is a new representation.

In Alekseyev's representation, suppose a coupler-curve equation in (x_Q, y_Q) is obtained, the coupler curve is a straight line *if and only if* there exist (x_0, θ) which satisfy $y_Q \equiv \tan\theta\,(x_Q - x_0)$. However since $\tan\theta$ can vary from zero to in nity, (x_Q, y_Q) should be parameterized. In our representation, we assume the straight-line is along the x-axis, thus $y_Q \equiv 0$. We further specify $x_A = 0$. As can be seen, there are 10 structural parameters $(a, b, c, e, f, g, h, y_A, x_D, y_D)$. Alternatively we can use $(a, b, c, d, e, f, g, h, y_A, \theta_0)$. Refer to Fig. 2(b), we obtain the following three loop-closure equations:

$$\begin{aligned} a\cos\theta_1 + b\cos\theta_2 - c\cos\theta_3 &= x_D - x_A \\ a\sin\theta_1 + b\sin\theta_2 - c\sin\theta_3 &= y_D - y_A \end{aligned} \tag{1}$$

$$\begin{aligned} (a+e)\cos\theta_1 + f\cos\theta_4 &= x_Q - x_A \\ (a+e)\sin\theta_1 + f\sin\theta_4 &= y_Q - y_A \end{aligned} \tag{2}$$

$$\begin{aligned} (c+h)\cos\theta_3 + g\cos\theta_5 &= x_Q - x_D \\ (c+h)\sin\theta_3 + g\sin\theta_5 &= y_Q - y_D \end{aligned} \tag{3}$$

Using classic resultant methods, it is not difficult to eliminate $\theta_i (i = 1, \ldots, 5)$ and a 16^{th} degree bivariate polynomial in (x_Q, y_Q) is obtained.

Since $y_Q \equiv 0$, we obtain a univariate polynomial in x_Q. Denote it as:

$$P_{s1} = \sum_{i=0}^{16} a_i x_Q^i = 0 \tag{4}$$

Since the linkage can pass infinity many points along the x axis, all the coefficients of P_{s1} should be incidentally zero. Using a symbolic computing software such as Mathematica, we obtain that:

$$a_{16} = 0;\ a_{15} = 0;\ a_{14} = 65536\, a^2c^2(ce - ah)^2d^2 \tag{5}$$

Since link lengths can not be zero, we obtain $ce = ah$. It follows that $a_{13} = 0$. Substitute $c = ah/e$ into a_{12} we obtain

$$-a^2b^2 + a(-2b^2 + d^2)e + (-b^2 + d^2)e^2 = 0 \tag{6}$$

Solve the above equation yields $e_1 = ab^2/(d^2 - b^2)$ or $e_2 = -a$. Only e_1 is feasible. It follows that $h = cb^2/(d^2 - b^2)$ and $a_{11} = 0$. Substitute the above into coefficients a_{10} to a_7 yields

$$\begin{aligned} a_{10} &= f_1(a, b, c, d, f, g, \theta_0) \\ a_9 &= f_2(a, b, c, d, f, g, \theta_0) \\ a_8 &= f_3(a, b, c, d, f, g, y_A, \theta_0) \\ a_7 &= f_4(a, b, c, d, f, g, y_A, \theta_0) \end{aligned} \tag{7}$$

Note that we use $x_D = x_A + d\cos\theta_0$, $y_D = y_A + d\sin\theta_0$ to simplify symbolic expressions. One may want to eliminate (y_A, θ_0) from the above equations and then solve for $(f,\ g)$. Unfortunately those equations are quite complicate to solve due to the "pyramidal effect" (Karger, 1998).

We then adapt Karger's technique to the problem and try to obtain more information (see Karger, 1998 for more details).

Karger's Proposition: Let $P(x) = \sum_{j=0}^{n} (a_j + b_j \cos x) \sin^j x = 0$ for all x. Then $a_j = b_j = 0 (j = 0, \ldots, n)$.

Now we eliminate $\theta_i (i = 2, \ldots, 5)$ and x_Q using Resultant methods, this leads to

$$P(\theta_1) = \sum\nolimits_{j=0}^{7} (a_j + b_j \cos\theta_1) \sin^j \theta_1 = 0 \tag{8}$$

Following the procedures in (Karger, 1998), we obtain the coefficients of the two terms with the highest order in variables $(\cos\theta_1, \sin\theta_1)$.

$$\begin{aligned} a_7 &= g_1(a, c, f, h, y_A, x_D, y_D) \\ b_6 &= g_2(a, c, h, y_A, x_D, y_D) \end{aligned} \tag{9}$$

Incidentally $b_7 = 0$, and e is substituted by ah/c. From the above equations, we obtain

$$x_D = 0 \quad \text{or} \quad y_D = 0 \tag{10}$$

When $x_D = 0$, we have $\theta_0 = \pi/2$, Substitute $\theta_0 = \pi/2$ into Eq. (7), from f_1 we can obtain

$$f^2 - g^2 = \frac{b^2c^2d^2 - a^2b^2d^2}{(d^2 - b^2)^2} \tag{11}$$

Substitute the above equation into f_2 in Eq. (7), we obtain

$$f = \frac{bcd}{d^2 - b^2} \quad \text{and} \quad g = \frac{adb}{d^2 - b^2} \tag{12}$$

When $= 0$, Eq. (7) still can't be simpli ed. Currently we are not able to get enough information using symbolic computation.

It seems that even for the simplest case of 6-bar linkages, symbolic deductions are not quite straightforward. Indeed we have tried the above procedure to synthesize other generic 6-bar linkages but currently no analogous results have been obtained. However a supercomputer may help the symbolic computations. In contrast, we can use numerical algorithms to solve the above problem conveniently. For example, given 10 points along the x-axis, we obtain a system of 10 polynomials (i.e. Eq. (4)) in 10 unknown variables $(a, b, c, e, f, g, h, y_A, x_D, y_D)$. Together with tunnelling techqniques, random restarts of Levenberg-Marquart method can nd multiple solutions (see Luo and Dai, 2005 for more information).

2.2 Synthesize Watt-I2 Linkages for a Straight-line Motion

Symbolic Synthesis Equations. Consider a generic Watt-I2 mechanism shown in Fig. 3, let's call the illustrated pose the initial pose of the

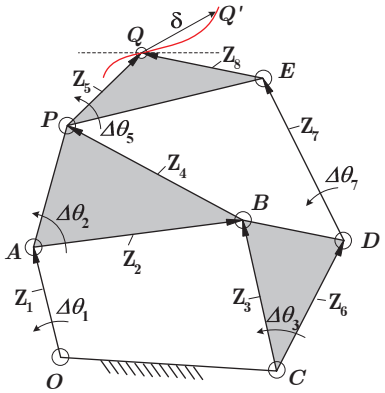

Figure 3. Design parameters in the Watt-I2 mechanism.

mechanism. For simplicity, we set the the origin of the xed frame coincident with the coupler-point Q at the initial pose. There are 14 design variables $(x_O,\ y_O,\ x_A, y_A, x_B, y_B, x_C, y_C, x_D, y_D, x_E, y_E, x_P, y_P)$. Alternatively, we can use complex vectors $\mathbf{Z}_i$ $(i = 1, \ldots, 7)$ as design variables. For this problem, we prefer to derive the synthesis equations using complex numbers for compactness. Referring to Fig. 3, when Q is moved to a new position Q' after a displacement of $\boldsymbol{\delta} = x + iy$, the following three loop-closure vector equations can be obtained

$$\mathbf{Z}_1(e^{i\Delta\theta_1} - 1) + \mathbf{Z}_2(e^{i\Delta\theta_2} - 1) - \mathbf{Z}_3(e^{i\Delta\theta_3} - 1) = 0 \tag{13a}$$

$$\mathbf{Z}_3(e^{i\Delta\theta_3} - 1) + \mathbf{Z}_4(e^{i\Delta\theta_2} - 1) + \mathbf{Z}_5(e^{i\Delta\theta_5} - 1) = \boldsymbol{\delta} \tag{13b}$$

$$\mathbf{Z}_6(e^{i\Delta\theta_3} - 1) + \mathbf{Z}_7(e^{i\Delta\theta_7} - 1) + \mathbf{Z}_8(e^{i\Delta\theta_5} - 1) = \boldsymbol{\delta} \tag{13c}$$

Rearrange Eqs. (13a) and (13b), one obtains:

$$\mathbf{Z}_1 e^{i\Delta\theta_1} = \mathbf{Z}_3(e^{i\Delta\theta_3} - 1) - \mathbf{Z}_2(e^{i\Delta\theta_2} - 1) + \mathbf{Z}_1 \tag{14a}$$

$$\mathbf{Z}_5 e^{i\Delta\theta_5} = \boldsymbol{\delta} - \mathbf{Z}_3(e^{i\Delta\theta_3} - 1) - \mathbf{Z}_4(e^{i\Delta\theta_2} - 1) + \mathbf{Z}_5 \tag{14b}$$

The angles $\Delta\theta_1$ and $\Delta\theta_5$ can be eliminated by multiplying each side of Eqs. (14a) and (14b) with its complex conjugate. Expanding and rearranging the results yields

$$p_1 e^{i\Delta\theta_2} + p_2 e^{-i\Delta\theta_2} + p_3 = 0 \tag{15a}$$

$$p_4 e^{i\Delta\theta_2} + p_5 e^{-i\Delta\theta_2} + p_6 = 0 \tag{15b}$$

where $p_i (i = 1, \ldots, 6)$ are expressions in θ_3 and the 14 design variables. Note that Eqs. (15a) and (15b) are indeed two real number equations. Solve Eqs. (15a) and (15b) for $e^{i\Delta\theta_2}$ and $e^{-i\Delta\theta_2}$ by Cramer's rule, and then apply the identity $e^{i\Delta\theta_2} e^{-i\Delta\theta_2} = 1$ leads to

$$(p_1 p_6 - p_3 p_4)(p_2 p_6 - p_3 p_5) + (p_1 p_5 - p_2 p_4)^2 = 0 \tag{16}$$

It is easy to verify that Eq. (16) is also a real number equation. Denote $e^{i\Delta\theta_3}$ as $\boldsymbol{\theta}_3$, and multiply the above equation by $\boldsymbol{\theta}_3^3$, a sixth-order polynomial in $\boldsymbol{\theta}_3$ can be obtained as:

$$m_6\boldsymbol{\theta}_3^6 + m_5\boldsymbol{\theta}_3^5 + m_4\boldsymbol{\theta}_3^4 + m_3\boldsymbol{\theta}_3^3 + m_2\boldsymbol{\theta}_3^2 + m_1\boldsymbol{\theta}_3 + m_0 = 0 \tag{17}$$

where the coe cients $_i($ $= 0$ 6) are expressions in design variables.

Similarly, by manipulating Eqs. (13b) and (13c), one obtains another two equations

$$(q_1 q_6 - q_3 q_4)(q_2 q_6 - q_3 q_5) + (q_1 q_5 - q_2 q_4)^2 = 0 \tag{18}$$

$$n_6\boldsymbol{\theta}_3^6 + n_5\boldsymbol{\theta}_3^5 + n_4\boldsymbol{\theta}_3^4 + n_3\boldsymbol{\theta}_3^3 + n_2\boldsymbol{\theta}_3^2 + n_1\boldsymbol{\theta}_3 + n_0 = 0 \tag{19}$$

The necessary condition for Eqs. (17) and (19) to have a common solution of $\boldsymbol{\theta}_3$ is that the determinant of their resultant matrix becomes zero. Here the Bezout resultant matrix will be used, which can be obtained using the Bezout-Cayley formulation (Almadi, 1996).

$$B = [b_{ij}]_{6\times 6} \tag{20}$$

Expand the determinant of the Bezout matrix, one obtains

$$\det(B) = \sum_{m=0}^{r}\sum_{n=0}^{r} a_{mn}x^m y^n = 0, \quad m+n \le r \tag{21}$$

where a_{mn} are expressions in the aforementioned 14 design variables, while r is case dependent. In a generic case where $\mathbf{Z}_8 \neq 0, \mathbf{Z}_5 \neq 0$, $r = 54$; in case $\mathbf{Z}_8 = 0$, $r = 16$; while in case $\mathbf{Z}_5 = 0$, $r = 8$. It can be veri ed that the imaginary component of the determinant is identically zero. Eq. (21) can be further factored since it always has a trivial factor:

$$\gcd(m_6m_0, n_6n_0) = (x - x_C)^2 + (y - y_C)^2 \tag{22}$$

where gcd means the greatest common factor. Thus for a generic Watt-I2 linkage, its coupler curve equation is a bivariate polynomial of order 52, which in general has 1431 monomials. It is impractical to expand $\det(B)$ and collect coe cients of x as did in subsection 3.1.

Numerical Approach and Analysis. In path generation synthesis, for each given precision point $\boldsymbol{\delta} = x + iy$, Eq. (21) is a polynomial in 14 design variables. Therefore if 14 precision points besides the origin are speci ed, a determined system of 14 polynomials in 14 design variables will be obtained. In other words, a Watt-I2 linkage generally can pass at maximum 15 precision points including the origin. Therefore if it can pass 16 precision points on a line, then theoretically it must contain a segment of that line.

Note that in precision position synthesis problems there are generally positive dimensional manifolds of extraneous solutions. Extraneous solutions arise when m_6m_0 or n_6n_0 is identically zero. It can be shown that the conditions for m_6m_0 or n_6n_0 to be identically zero are,

$$\mathbf{Z}_3 = 0 \ \text{ or } \ \mathbf{Z}_2 + \mathbf{Z}_4 = 0 \ \text{ or } \ \mathbf{Z}_1 + \mathbf{Z}_2 - \mathbf{Z}_3 = 0 \tag{23}$$

$$\mathbf{Z}_3 = 0 \ \text{ or } \ \mathbf{Z}_6 = 0 \ \text{ or } \ \mathbf{Z}_5 = \mathbf{Z}_8 = 0 \ \text{ or } \ \mathbf{Z}_5\mathbf{Z}_6 - \mathbf{Z}_3\mathbf{Z}_8 = 0 \tag{24}$$

Some of the conditions correspond to degenerated linkages while other are mathematical gments. An e ective approach to exclude such extraneous solutions is the tunnelling (deflation) method (Luo and Dai, 2005).

Although the above formulation is compact, numerical tests show that classic iterative methods normally can not converge within 1000 iterations when double-precision oat-point arithmetic is used. Therefore we should choose equations with less nonlinearity. Besides multi-precision arithmetic may be preferable for better accuracy and reliability. Currently we use the following approach for better reliability.

1 Two real equations Eq. (16) and Eq. (18) are used rstGiven 15 points (besides the origin) to be passed along the x-axis, there are the 14 structural variables $(x_O, y_O, x_A, y_A, x_B, y_B, x_C, y_C, x_D, y_D, x_E, y_E, x_P, y_P)$ and 15 incremental angular variables $\triangle\theta_{3_k}(k = 1, \ldots, 15)$. There are 30 equations in 29 variables. Multi-start of Levenberg-Marquart method is used to solve the system.

2 Once a converged point is obtained, we then assign small intervals to the 14 structural parameters of the converged point, and use interval arithmetic to evaluate the corresponding interval box.

After a coupler of days of program running, we have got a large number of converged approximate solutions. It is observed that most runs can converge to stationary points with a function residual smaller than 1.0e-10. However all the converged solutions are not exact solutions. Most converged approximate solutions pass 14 precision points in di erent con gurations and pass near a $15^{\mathtt{th}}$ point. Later we have also added more points to increase the reliability. However there is no obvious positive e ect. Currently we are programming to include another constraint that the instantaneous center of velocity at the initial pose should be on the y-axis. Meanwhile we are planning to run interval method use parallelized computers to identify potential interval boxes. The obtained interval boxes will then be used as the search domains of multi-start classic iterative methods to accelerate the process.

The numerical approach can be extended to the synthesis of overconstrained spatial single-loop mechanisms. It is well known that a spatial 6R manipulator has up to 16 con gurations, while a spatial 5R open chain can reach 21 precision positions (Perez, 2003). Therefore give more than 16 rotation angles about a xed axis, spatial 6R single-loop overconstrained mechanisms can be found by precision position synthesis. Nevertheless similar numerical di culties arise, e.g. planar 6R mechanisms should be avoided using tunnelling techniques.

3. Conclusions

In this paper, we have investigated the problem of searching for undiscovered straight-line linkages. The dimensional relationships in Hart's

second straight-line linkage have been deduced using symbolic calculations. A numerical approach is then proposed for solving more complicate cases. Although no new mechanisms have been found at the current stage, this research is a first step towards an automatic approach for discovering new overconstrained mechanisms.

References

Alekseyev, N.I., (1939), Hart's straight line mechanism. Scientific Reports of the Moscow Hydro-improvement Institute, VI.

Almadi, A.N., (1996), On new foundations of kinematics using classical and modern algebraic theory and homotopy. PhD thesis, University of Wisconsin-Milwaukee.

Artobolevskii, I.I., (1964), *Mechanisms for the Generation of Plane Curves*. Translated by Wills, R.D. & Johnson, W., Macmillan NY.

Bricard, R., (1927), *Lecons de Cinématique* (2 volumes), Gauthier-Villar, Paris.

Dai, J.S. and Rees Jones, J., (1999), Mobility in metamorphic mechanisms of foldable/erectable kinds, *ASME J. of Mechanical Design*, vol. 121, no. 3, pp. 375–382.

Dijksman, E., (1975), Kempe's (focal) linkage generalized, particularly in connection with hart's second straight-line mechanism, *Mechanism and Machine Theory*, vol. 10, no. 6, pp. 445–460.

Dukkipati, R.V., (2001), *Spatial Mechanisms, Analysis and Synthesis*, Chapter 4.1 Existence Criteria of Mechanisms, Alpha Science Press.

Gao, X.S., Zhu, C.C., Chou, S.C., and Ge, J.X., (2001), Automated generation of Kempe linkages for algebraic curves and surfaces. *Mechanism and Machine Theory*, vol. 36, pp. 1019–1033.

Harry Hart, (1877), On some cases of parallel motion. *Proc. London Math Soc.* vol. 8, pp. 286–289.

Hunt, K.H., (1978), *Kinematic Geometry of Mechanisms*, Oxford University Press.

Kapovich, M., Millson, J., (2002), Universality theorem for configuration spaces of planar linkages, *Topology*, vol. 41, no. 6, pp. 1051–1107.

Karger, A., (1998), Classification of 5R closed kinematic chains with self mobility. *Mechanism and Machine Theory*, vol. 33, pp. 213-222.

Kempe, A.B., (1873), On the solution of equations by mechanical means, *Cambridge Messenger of Mathematics*, vol. 2, pp. 51–52.

Kempe, A.B., (1877), How to Draw a Straight Line, London: Macmillan and Co.

Koenigs, G., (1897), Leçons de cinématique, Hermann, Paris. [4.4, 9.3, 14.4, 14.6 15.3]

Luo, Z.J. and Dai, J.S., (2005), Pattern bootstrap: a new method which gives efficiency for some precision position synthesis problems, *ASME J. Mechanical Design* (Accepted).

Peaucellier, C., (1873), Note sur une question de geometrie de compass, *Nouvelles Annales der Mathematiques*, vol. 12, pp. 71–81.

Primrose, E.J.F., Freudenstein, F., Roth, B., (1967), Six-Bar Motion. *Archive for Rational Mechanics and Analysis*, vol. 24, pp. 22–41.

Smith, W.D., 1998, Plane mechanisms and the "downhill principle", in the series of "*Computational power of machines made of rigid parts*", lectures given at Princeton University, pp. 1–26.

Sylvester, J.J., (1875), History of the plagiograph, *Nature*, vol. 12, pp. 214–216.

Wampler, C.W., (1999), Solving the kinematics of planar mechanisms, *ASME J. Mechanical Design*. vol. 121, pp. 387–391.

Perez, A., (2003), Dual Quaternion Synthesis of Constrained Robotic Systems, PhD thesis, University of California, Irvine.

Appendix: Existing 6-bar Straight-Line Linkages

Figures 4 illustrates four known 6-bar straight-line linkages. Cases (a) is based on the principle of inversor (Hart, 1877). Case (b) is a generalized case of Case (a) discovered by Sylvester, 1875 and Kempe, 1877. Cases (c) and (d) were first invented by Hart, 1877 and Bricard, 1927 respectively. Later Dijksman, 1975 unified the two cases into a generalized Case (e). For all four cases, the coupler points drawing a straight-line are labelled as Q. Especially in case (c), Q_1 and Q_2 trace two perpendicular straight-lines, while any other point G on the same coupler traces an ellipse. In case (a), $BD = CE$, $BE = CD$, $OC = BC$, $BO/BE = CP/CE = BP/BD, O_PO = O_PP$. In case (b), $BD = CE$, $BE = CD, \Delta OBE \backsim \Delta QBD \backsim \Delta PCE$, and $\theta = \angle POQ$ In the generalized case of Cases (c) and (d), $AB = a, BC = b, CD = c, AD = d, BE = e, CF = h, EQ = f, GQ = g, e = ab^2/(d^2 - b^2), f = cdb/(d^2 - b^2), g = adb/(d^2 - b^2), h = cb^2/(d^2 - b^2)$. Especially in case (c), $AB = BC, OC = CB$; and in case (d), $AE = CF, EQ = FQ$.

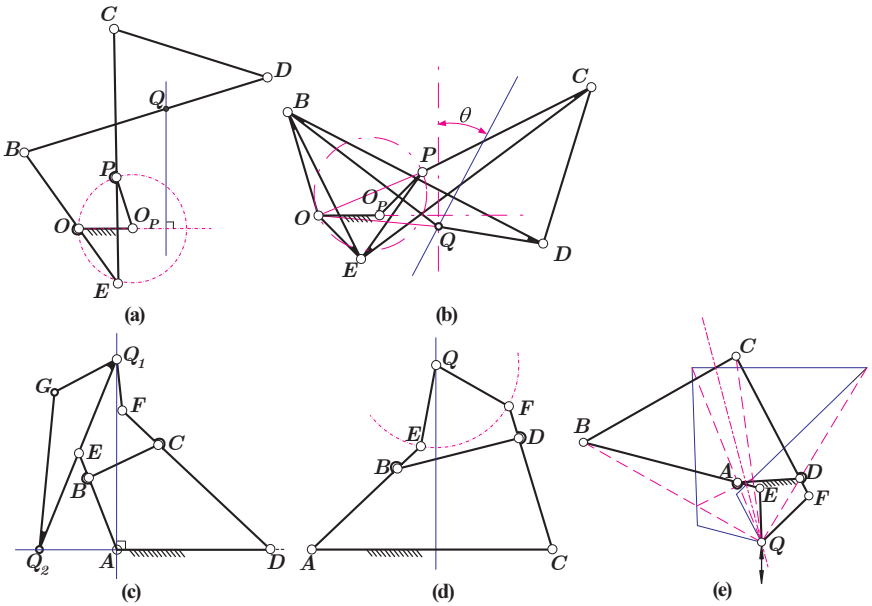

Figure 4. Four known 6-bar linkages for a straight-line motion.

TYPE SYNTHESIS OF THREE-DOF UP-EQUIVALENT PARALLEL MANIPULATORS USING A VIRTUAL-CHAIN APPROACH

Xianwen Kong
Département de Génie Mécanique, Université Laval,
Québec, Québec, Canada, G1K 7P4
xwkong@gmc.ulaval.ca

Clément M. Gosselin
Département de Génie Mécanique, Université Laval,
Québec, Québec, Canada, G1K 7P4
gosselin@gmc.ulaval.ca

Abstract Three-DOF UP-equivalent parallel manipulators are the parallel counterparts of the 3-DOF UP serial manipulators, which are composed of one U (universal) and one P (prismatic) joint. Such parallel manipulators can be used either independently or as modules of hybrid manipulators. Using the virtual-chain approach that we proposed elsewhere for the type synthesis of parallel manipulators, this paper deals with the type synthesis of this class of 3-DOF parallel manipulators. In addition to all the 3-DOF UP-equivalent parallel manipulators proposed in the literature, a number of new 3-DOF overconstrained or non-overconstrained UP-equivalent parallel manipulators are identified.

Keywords: Three-DOF parallel manipulator, Type synthesis, Virtual chain, Screw Theory, Overconstrained mechanism

1. Introduction

Three-DOF UP-equivalent parallel manipulators have a wide range of applications including assembly and machining. Such parallel manipulators can be used either independently or as modules of hybrid manipulators. Two UP-equivalent parallel manipulators, which are used as modules in hybrid manipulators, have been proposed in [Neumann, 1988; Huang et al., 2005]. However, the systematic type synthesis of the UP-equivalent parallel manipulator is very difficult and has not been investigated yet. In order to provide alternatives to the current

J. Lenarčič and B. Roth (eds.), Advances in Robot Kinematics, 123–132.

UP-equivalent parallel manipulators, the type synthesis of UP-equivalent parallel manipulators needs further investigation.

Using the virtual-chain approach proposed in [Kong and Gosselin, 2005a][1], the type synthesis of UP-equivalent parallel manipulators is dealt with in this paper. In Section 2, the virtual-chain approach for the type synthesis of parallel manipulators is recalled. The type synthesis of 3-DOF single-loop kinematic chains is performed in Section 3. In Section 4, we discuss how to construct UP-equivalent parallel kinematic chains and UP-equivalent parallel manipulators using 3-DOF single-loop kinematic chains. Two new UP-equivalent parallel manipulators are also presented. Finally, conclusions are drawn.

In this paper, we limit ourselves to non-redundant parallel manipulators.

2. The Virtual-chain Approach

2.1 The Virtual Chain

As proposed in [Kong and Gosselin, 2005a], the motion pattern of an f-DOF parallel manipulator can be represented by a virtual chain which is the simplest serial or parallel kinematic chain that can express the motion pattern well.

The virtual chain for the motion pattern of the 3-DOF PMs to be synthesized in this paper is the UP virtual chain shown in Fig. 1(a). In the UP virtual chain, the direction of the P (prismatic) joint is perpendicular to the axis of its adjacent R (revolute) joint within the U (universal) joint.

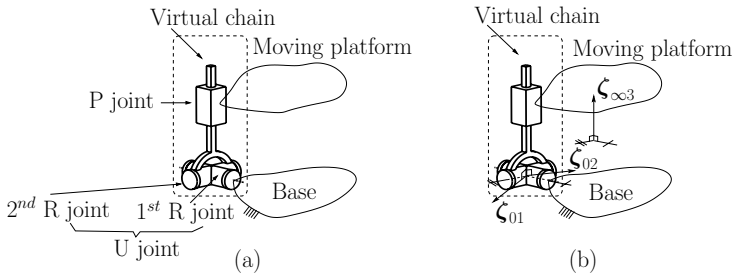

Figure 1. UP virtual chain: (a) schematic representation and (b) wrench system.

2.2 Representation of Instantaneous Constraints

In the type synthesis of parallel manipulators, one needs to deal with the instantaneous constraints. Screw theory, see [Kumar et al.,

2000; Davidson and Hunt, 2004] for example, provides an efficient tool to address this issue.

The instantaneous constraints exerted on the moving platform by the base through the kinematic chain (virtual chain, leg of a parallel kinematic chain or a parallel kinematic chain) is represented by a screw system which is called the wrench system of the kinematic chain (virtual chain, leg of a parallel kinematic chain or a parallel kinematic chain). For brevity, the wrench system of a leg is also called a leg-wrench system.

Wrench system of UP-equivalent parallel kinematic chains. In any general configuration, a UP-equivalent parallel kinematic chain and its corresponding UP virtual chain have the same wrench system. Finding the wrench system of the UP-equivalent parallel kinematic chain is thus equivalent to finding the wrench system of the UP virtual chain [Fig. 1(b)].

It can be found without difficulty that the wrench system of the UP-equivalent parallel kinematic chain is a 2-$\boldsymbol{\zeta}_0$-1-$\boldsymbol{\zeta}_\infty$-system [see Fig. 1(b)]. Here, $\boldsymbol{\zeta}_0$ and $\boldsymbol{\zeta}_\infty$ denote, respectively, a wrench of zero pitch and a wrench of infinite-pitch. One base of the 2-$\boldsymbol{\zeta}_0$-1-$\boldsymbol{\zeta}_\infty$-system is composed of (a) two non-collinear $\boldsymbol{\zeta}_0$ whose axes pass through the center of the U joint and are perpendicular to the direction of the P joint and (b) a $\boldsymbol{\zeta}_\infty$ whose direction is perpendicular to the axes of the R joints within the U joint.

Leg-wrench system of UP-equivalent parallel kinematic chains. As the wrench system of a parallel kinematic chain is the linear combination of all of its leg-wrench systems in any configuration [Kumar et al., 2000], it is then concluded that the wrench system of any leg in a UP-equivalent parallel kinematic chain is a $c^i(0 \leq c^i \leq 3)$-$\boldsymbol{\zeta}$-system, including 2-$\boldsymbol{\zeta}_0$-1-$\boldsymbol{\zeta}_\infty$-system, 2-$\boldsymbol{\zeta}_0$-system, 1-$\boldsymbol{\zeta}_0$-1-$\boldsymbol{\zeta}_\infty$-system, 1-$\boldsymbol{\zeta}_0$-system, 1-$\boldsymbol{\zeta}_\infty$-system and 0-system, in any general configuration.

2.3 Conditions for a UP-equivalent Parallel Manipulator

When we connect the base and the moving platform of a parallel kinematic chain by an appropriate UP virtual chain, the function of the parallel kinematic chain is not affected (Fig. 2). Any of its legs and the UP virtual chain will constitute a 3-DOF single-loop kinematic chain.

Thus, a parallel kinematic chain is a UP-equivalent parallel kinematic chain if it satisfies the following two conditions:

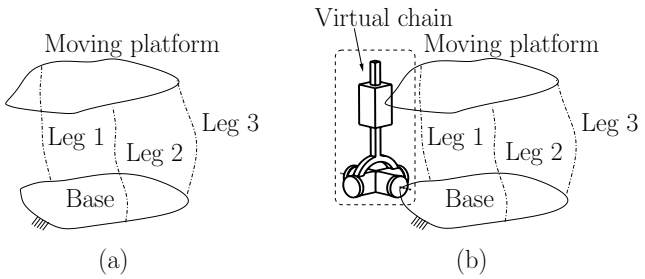

Figure 2. (a) Three-legged UP-equivalent parallel kinematic chain; (b) Three-legged UP-equivalent parallel kinematic chain with a UP virtual chain added.

(1) Each leg of the parallel kinematic chain and the same UP virtual chain constitute a 3-DOF single-loop kinematic chain.

(2) The wrench system of the parallel kinematic chain is the same as that of the UP virtual chain in any one general configuration.

The first condition guarantees that the moving platform can undergo at least the UP-motion. The second condition further guarantees that the degree of freedom of the moving platform is three.

Based on the above conditions, the type synthesis of parallel manipulators can be performed by first performing the type synthesis of 3-DOF single-loop kinematic chains and then constructing UP-equivalent parallel manipulators using the types of 3-DOF single-loop kinematic chains.

3. Type Synthesis of 3-DOF Single-loop Kinematic Chains Involving a UP Virtual Chain

In Section 2.2, the wrench systems of legs for UP-equivalent parallel manipulators have been determined. Then, the number of 1-DOF joints of a leg with a $c^i (0 \leq c^i \leq 2)$-$\boldsymbol{\zeta}$-system is equal to $(6 - c^i)$. In the case of $c^i = 0$, the associated single-loop kinematic chains are not overconstrained. Such a single-loop kinematic chain is composed of the UP virtual chain and six R and P joints. Many types of single-loop kinematic chains can be obtained. Among these types, the types with simple structure, such as UPSV, PUSV and RUSV, are of practical interest.

In the following, we will focus on the type synthesis of overconstrained single-loop kinematic chains involving a UP virtual chain.

As pointed out in [Kong and Gosselin, 2005b], the types of over constrained single-loop kinematic chains can be constructed using seven compositional units. A compositional unit is a serial kinematic chain with specific characteristics, namely: *In any general configuration, the*

Table 1. Composition of 3-DOF overconstrained single-loop kinematic chains with a UP virtual chain.

c^i	*Leg-wrench system*	*Composition*				
		Planar unit	*Spherical unit*	*Coaxial unit*	*Codirectional unit*	*Parallelaxis unit*
3	2-ζ_0-1-ζ_∞			2	1	
2	1-ζ_0-1-ζ_∞		1	1		
	2-ζ_0		1		1	
1	1-ζ_∞			1		1
		1				1
						2
	1-ζ_0	1	1			

wrench system of each of these kinematic chains always includes a specified number of independent wrenches of zero-pitch or infinite-pitch.

By analyzing the wrench system of the compositional units, it can be found that a single-loop kinematic chain that has a UP virtual chain and a specified leg-wrench system is composed of two or three of the following five compositional units as shown in Table 1.

(a) *Parallelaxis compositional units.* Serial kinematic chains composed of at least one R joint and at least one P joint in which the axes of all the R joints are parallel and not all the directions of the P joints are perpendicular to the axes of the R joints.

(b) *Planar compositional units.* Serial kinematic chains in which all the links are moving along parallel planes. A planar serial kinematic chain is denoted by $()_E$.

(c) *Spherical compositional units.* Serial kinematic chains composed of two or more concurrent R joints. Each R joint of a spherical serial kinematic chain is denoted by $\dot{\mathrm{R}}$.

(d) *Coaxial compositional units.* Serial kinematic chains composed of two coaxial R joints.

(e) *Codirectional compositional units.* Serial kinematic chains composed of two P joints whose directions are parallel. Each P joint of a codirectional serial kinematic chain is denoted by $\mathrm{P}^{\parallel}$.

For each class of single-loop kinematic chains that has a UP virtual chain and a specified leg-wrench system, the specific types can be readily

obtained and shown in Table 2. It is noted that in the existing works on the type synthesis of single-loop mechanisms, a mechanism with a coaxial or codirectional compositional unit is regarded to be degenerated and is therefore discarded. In the type synthesis of parallel mechanisms, however, a single-loop kinematic chain that contains a coaxial or codirectional compositional unit should be used since one joint of the coaxial or codirectional compositional unit belongs to one leg of a parallel mechanism while the other joint belongs to the virtual chain.

In the representation of types of 3-DOF single-loop kinematic chains involving a UP virtual chain, the following notations are used. The joints within a $()^{|}_{E}$ constitute a planar kinematic chain, whose associated plane of relative motion is parallel to the direction of the P joint of the UP virtual chain. The joints within a $()^{\parallel}_{E}$ constitute a planar kinematic chain, whose associated plane of relative motion is parallel to the direction of the P joint of the UP virtual chain and perpendicular to the axis of the second R joint within the U joint of the UP virtual chain. The P joint whose direction is parallel to the direction of the P joint within the UP virtual chain is denoted by $\mathrm{P}^{\parallel}$. The R joints are represented by $\dot{\mathrm{R}}$, $\check{\mathrm{R}}$, $\ddot{\mathrm{R}}$, $\bar{\mathrm{R}}$, $\acute{\mathrm{R}}$ and $\acute{\mathrm{R}}$ due to the different geometric conditions that the R joints satisfy. The axes of all the $\dot{\mathrm{R}}$ joints within a leg intersect at a common point on the axis of the first R joint within the U joint of the UP virtual chain. The axes of all the $\check{\mathrm{R}}$ joints within a leg intersect at the center of the U joint of the UP virtual chain. $\ddot{\mathrm{R}}$ ($\bar{\mathrm{R}}$) denotes an R joint that is coaxial with the first (second) R joint within the U joint of the UP virtual chain. $\acute{\mathrm{R}}$ ($\acute{\mathrm{R}}$) denotes an R joint whose axis is parallel to the axes of the the first (second) R joint within the U joint of the virtual chain.

Considering that each leg of the UP-equivalent parallel kinematic chain and the same UP virtual chain constitute a 3-DOF single-loop kinematic chain, the above notations can also be used to represent the types of UP-equivalent parallel kinematic chains, UP-equivalent parallel manipulators and their legs. The geometric conditions for the UP-equivalent parallel kinematic chains, UP-equivalent parallel manipulators and their legs can be obtained as follows.

All the $\mathrm{P}^{\parallel}$ joints are along the same direction. All the planes of relative motion of the planar chains associated with $()^{\parallel}_{E}$ are parallel. The above planes, the planes of relative motion of the planar chains associated with $()^{|}_{E}$ as well as the direction of the $\mathrm{P}^{\parallel}$ joints all parallel to a common direction. The axes of the $\acute{\mathrm{R}}$ joints are parallel to a line that is perpendicular to (a) the planes of relative motion of the planar chains associated with $()^{\parallel}_{E}$, (b) the intersection of the planes of relative motion of the planar chains associated with $()^{|}_{E}$, and (c) the direction

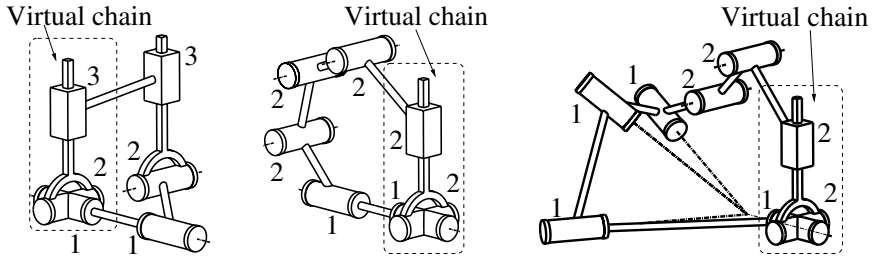

(a) $\ddot{\mathrm{R}}\bar{\mathrm{R}}\mathrm{P}^{\parallel}\mathrm{V}$. (b) $\ddot{\mathrm{R}}(\mathrm{RRR})^{\parallel}_{E}\mathrm{V}$. (c) $\dot{\mathrm{R}}\dot{\mathrm{R}}\dot{\mathrm{R}}(\mathrm{RR})^{\parallel}_{E}\mathrm{V}$.

Figure 3. Three-DOF single-loop kinematic chains involving a UP virtual chain or some legs for UP-equivalent parallel kinematic chains.

of the $\mathrm{P}^{\parallel}$ joints. The axes of $\ddot{\mathrm{R}}$ joints, the intersections of the $\dot{\mathrm{R}}$ joints within the same leg, the intersections of the $\check{\mathrm{R}}$ joints within the same leg, and the intersection of the axes of the $\ddot{\mathrm{R}}$ joint and the $\bar{\mathrm{R}}$ joint within the same leg determine a common line. The axes of the $\check{\mathrm{R}}$ joints are parallel to the above common line.

For a better understanding of the notation used, a few single-loop kinematic chains involving a UP virtual chain are shown in Fig. 3. In Fig. 3, the UP virtual chain is enclosed using dashed lines. The joints of a single-loop kinematic chain indicated by the same number form a compositional unit.

As mentioned above, single-loop kinematic chains [Figs. 3(a)–3(b)] involving a coaxial or codirectional compositional unit are usually regarded to be degenerated in the literature. However, these kinematic chains are useful in the type synthesis of parallel manipulators.

4. Construction of UP-equivalent Parallel Manipulators

Now let us see how to construct UP-equivalent parallel manipulators from the 3-DOF single-loop kinematic chain involving a virtual chain.

By removing the virtual chain in a 3-DOF single-loop kinematic chain involving a virtual chain, one leg for UP-equivalent parallel manipulators can be obtained. For example, by removing the virtual chain in a $\dot{\mathrm{R}}\dot{\mathrm{R}}\dot{\mathrm{R}}(\mathrm{RR})^{\parallel}_{E}\mathrm{V}$ kinematic chain [Fig. 3(c)], an $\dot{\mathrm{R}}\dot{\mathrm{R}}\dot{\mathrm{R}}(\mathrm{RR})^{\parallel}_{E}$ leg can be obtained . Such a leg has a 1-$\boldsymbol{\zeta}_0$-system. The $\boldsymbol{\zeta}_0$ passes through the common point of the axes of three $\dot{\mathrm{R}}$ joints and is parallel to the axes of the R joints within $(\mathrm{RR})^{\parallel}_{E}$. Using this approach, a large number of

Table 2. Three-DOF single-loop kinematic chains with a UP virtual chain or Legs for UP-equivalent parallel kinematic chains.

c^i	*Leg-wrench system*	N^o	*Type (Remove V if representing legs)*
3	2-$\boldsymbol{\zeta}_0$-1-$\boldsymbol{\zeta}_\infty$	1	$\ddot{\mathrm{R}}\bar{\mathrm{R}}\mathrm{P}^{\parallel}\mathrm{V}$
2	1-$\boldsymbol{\zeta}_0$-1-$\boldsymbol{\zeta}_\infty$	2–8	$\ddot{\mathrm{R}}(\mathrm{RRR})^{\parallel}_{E}\mathrm{V}$ $\ddot{\mathrm{R}}(\mathrm{RRP})^{\parallel}_{E}\mathrm{V}$ $\ddot{\mathrm{R}}(\mathrm{RPR})^{\parallel}_{E}\mathrm{V}$ $\ddot{\mathrm{R}}(\mathrm{PRR})^{\parallel}_{E}\mathrm{V}$ $\ddot{\mathrm{R}}(\mathrm{RPP})^{\parallel}_{E}\mathrm{V}$ $\ddot{\mathrm{R}}(\mathrm{PRP})^{\parallel}_{E}\mathrm{V}$ $\ddot{\mathrm{R}}(\mathrm{PPR})^{\parallel}_{E}\mathrm{V}$
	2-$\boldsymbol{\zeta}_0$	9	$\dot{\mathrm{R}}\dot{\mathrm{R}}\dot{\mathrm{R}}\mathrm{P}^{\parallel}\mathrm{V}$
1	1-$\boldsymbol{\zeta}_\infty$	10–58	R̈ŔPPPV R̈PŔPPV R̈PPŔPV R̈PPPŔV R̈ŔŔPPV R̈ŔPŔPV R̈PŔŔPV R̈PPŔŔV R̈PŔPŔV R̈ŔŔŔPV R̈ŔŔPŔV R̈ŔPŔŔV R̈PŔŔŔV R̋R̋ŔŔŔV R̋R̋R̋ŔV PR̋ŔŔŔV R̋PŔŔŔV R̋R̋PŔŔ R̋R̋ŔPŔV R̋R̋ŔŔPV PR̋R̋ŔŔ R̋PR̋ŔŔV R̋R̋PŔŔV R̋R̋R̋PŔ R̋R̋R̋ŔPV PR̋PŔŔV PR̋ŔPŔV PR̋ŔŔPV R̋PPŔŔV R̋PŔPŔV R̋PŔŔPV R̋R̋PPŔV R̋R̋PŔPV R̋R̋ŔPPV PPR̋ŔŔV PR̋PŔŔV R̋PPŔŔV PR̋PPŔV PR̋PŔPV PR̋ŔPPV R̋PPPŔV R̋PPŔPV R̋PŔPPV PPR̋PŔV PR̋PPŔV R̋PPPŔV PPR̋ŔPV PR̋PŔPV R̋PPŔPV
	1-$\boldsymbol{\zeta}_0$	59–80	$\dot{\mathrm{R}}\dot{\mathrm{R}}\dot{\mathrm{R}}(\mathrm{RR})^{\parallel}_{E}\mathrm{V}$ $\dot{\mathrm{R}}\dot{\mathrm{R}}(\mathrm{RRR})^{\parallel}_{E}\mathrm{V}$ $\dot{\mathrm{R}}\dot{\mathrm{R}}\dot{\mathrm{R}}(RP)^{\parallel}_{E}\mathrm{V}$ $\dot{\mathrm{R}}\dot{\mathrm{R}}\dot{\mathrm{R}}(PR)^{\parallel}_{E}\mathrm{V}$ $\dot{\mathrm{R}}\dot{\mathrm{R}}(RRP)^{\parallel}_{E}\mathrm{V}$ $\dot{\mathrm{R}}\dot{\mathrm{R}}(RPR)^{\parallel}_{E}\mathrm{V}$ $\dot{\mathrm{R}}\dot{\mathrm{R}}(PRR)^{\parallel}_{E}\mathrm{V}$ $\dot{\mathrm{R}}\dot{\mathrm{R}}\dot{\mathrm{R}}(PP)^{\parallel}_{E}\mathrm{V}$ $\dot{\mathrm{R}}\dot{\mathrm{R}}(RPP)^{\parallel}_{E}\mathrm{V}$ $\dot{\mathrm{R}}\dot{\mathrm{R}}(PRP)^{\parallel}_{E}\mathrm{V}$ $\dot{\mathrm{R}}\dot{\mathrm{R}}(PPR)^{\parallel}_{E}\mathrm{V}$ $\check{\mathrm{R}}\check{\mathrm{R}}\check{\mathrm{R}}(\mathrm{RR})^{\vert}_{E}\mathrm{V}$ $\check{\mathrm{R}}\check{\mathrm{R}}(\mathrm{RRR})^{\vert}_{E}\mathrm{V}$ $\check{\mathrm{R}}\check{\mathrm{R}}\check{\mathrm{R}}(RP)^{\vert}_{E}\mathrm{V}$ $\check{\mathrm{R}}\check{\mathrm{R}}\check{\mathrm{R}}(PR)^{\vert}_{E}\mathrm{V}$ $\check{\mathrm{R}}\check{\mathrm{R}}(RRP)^{\vert}_{E}\mathrm{V}$ $\check{\mathrm{R}}\check{\mathrm{R}}(RPR)^{\vert}_{E}\mathrm{V}$ $\check{\mathrm{R}}\check{\mathrm{R}}(PRR)^{\vert}_{E}\mathrm{V}$ $\check{\mathrm{R}}\check{\mathrm{R}}\check{\mathrm{R}}(PP)^{\vert}_{E}\mathrm{V}$ $\check{\mathrm{R}}\check{\mathrm{R}}(RPP)^{\vert}_{E}\mathrm{V}$ $\check{\mathrm{R}}\check{\mathrm{R}}(PRP)^{\vert}_{E}\mathrm{V}$ $\check{\mathrm{R}}\check{\mathrm{R}}(PPR)^{\vert}_{E}\mathrm{V}$
0	0-system	81–	omitted

legs for UP-equivalent parallel manipulators have been obtained and are listed in Table 2. In Table 2, only the basic types of legs are listed. The variations of UP-equivalent parallel manipulators involving U, C (cylindrical) and S (spherical) joints and parallelograms can be obtained using the techniques summarized in [Kong and Gosselin, 2005c].

Using the types of legs obtained in Section 3 and Condition (2) for UP-equivalent parallel kinematic chains, we can obtain a large number of UP-equivalent parallel kinematic chains. By further applying the validity condition of actuated joints [Kong and Gosselin, 2005a], we

Table 3. Families of 3-DOF m-legged UP-equivalent parallel manipulators.

m	*Family*						
	Overconstrained					*Non-overconstrained*	
2	3-3	3-2	3-1	2-2		3-0	2-1
3	3-3-3	3-3-2	3-3-1	3-2-2	3-3-0	3-0-0	2-1-0
	3-2-1	2-2-2	3-2-0	3-1-1	2-2-1	1-1-1	
	3-1-0	2-2-0	2-1-1				
4	3-3-3-3	3-3-3-2	3-3-3-1	3-3-2-2	3-3-3-0	3-0-0-0	2-1-0-0
	3-3-2-1	3-2-2-2	3-3-2-0	3-3-1-1	3-2-2-1	1-1-1-0	
	2-2-2-2	3-3-1-0	3-2-2-0	3-2-1-1	2-2-2-1		
	3-3-0-0	3-2-1-0	3-1-1-1	2-2-2-0	2-2-1-1		
	3-2-0-0	3-1-1-0	2-2-1-0	2-1-1-1	3-1-0-0		
	2-2-0-0	2-1-1-0	1-1-1-1				

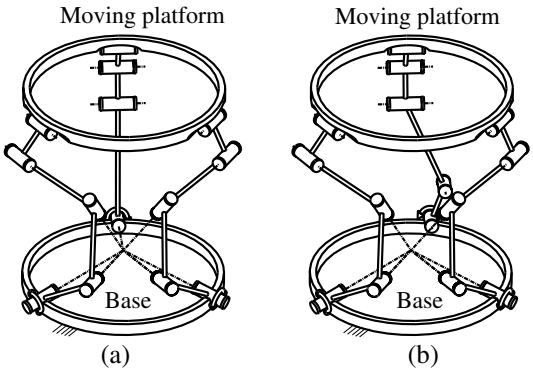

Figure 4. Two UP-equivalent parallel manipulators: (a) $\ddot{\mathrm{R}}(\mathrm{RRR})^{\parallel}_{E}$-2-$\check{\mathrm{R}}\check{\mathrm{R}}\check{\mathrm{R}}(\mathrm{RR})^{|}_{E}$, and (b) $\acute{\mathrm{R}}\acute{\mathrm{R}}(\mathrm{RRR})^{\parallel}_{E}$-2-$\check{\mathrm{R}}\check{\mathrm{R}}\check{\mathrm{R}}(\mathrm{RR})^{|}_{E}$.

can obtain a large number of $m(m \geq 2)$-legged UP-equivalent parallel manipulators. Due to the large number of UP-equivalent parallel manipulators, we only list the families of UP-equivalent parallel manipulators in Table 3 and show two new 3-legged UP-equivalent parallel manipulators in Fig. 4. The $\ddot{\mathrm{R}}(\mathrm{RRR})^{\parallel}_{E}$-2-$\check{\mathrm{R}}\check{\mathrm{R}}\check{\mathrm{R}}(\mathrm{RR})^{|}_{E}$ parallel manipulator shown in Fig. 4(a) belongs to Family 2-1-1 and is overconstrained. The $\acute{\mathrm{R}}\acute{\mathrm{R}}(\mathrm{RRR})^{\parallel}_{E}$-2-$\check{\mathrm{R}}\check{\mathrm{R}}\check{\mathrm{R}}(\mathrm{RR})^{|}_{E}$ shown in Fig. 4(b) belongs to Family 1-1-1 and is not overconstrained.

It is noted that the UP-equivalent parallel manipulators proposed in [Neumann, 1988; Huang et al., 2005] belong respectively to Families 3-0-0-0 and 3-0-0 listed in Table 3.

5. Conclusions

The type synthesis of UP-equivalent parallel manipulators has been systematically solved using the virtual-chain approach proposed in [Kong and Gosselin, 2005a]. Both overconstrained and non-overconstrained UP-equivalent parallel manipulators can be obtained. The UP-equivalent parallel manipulators obtained include some new UP-equivalent parallel manipulators as well as all the known UP-equivalent parallel manipulators.

The optimal selection of types of UP-equivalent parallel manipulators based on kinematic and dynamic indices is still an open issue.

6. Acknowledgements

The authors would like to acknowledge the financial support of the Natural Sciences and Engineering Research Council of Canada (NSERC) and of the Canada Research Chairs Program.

Notes

1. In addition to our approach to the type synthesis of parallel manipulators, there are also several others, such as those proposed by Profs. J. M. Hervé, J. Angeles, Z. Huang, L.-W. Tsai, T.-L. Yang, G. Gogu and their colleagues. For a comprehensive list of references on this issue, see [Kong and Gosselin, 2005a; Kong and Gosselin, 2005c] and visit the webpage of Dr. Jean-Pierre Merlet at http://www-sop.inria.fr/coprin/equipe/merlet/merlet_eng.html.

References

Neumann, K.E. (1988), "Robot," United States Patent 4732525.

Huang, T., Li, M., Zhao, X.M., Mei, J.P., Chetwynd, D.G., and Hu, S.J. (2005), "Conceptual design and dimensional synthesis for a 3-DOF module of the TriVariant–a novel 5-DOF reconfigurable hybrid robot," *IEEE Transactions on Robotics*, **21**(3), pp. 449–456.

Kong, X., and Gosselin, C.M. (2005a), "Type synthesis of 3-DOF PPR parallel manipulators based on screw theory and the concept of virtual chain," *ASME Journal of Mechanical Design*, **127**(6), pp. 1113–1121.

Kong, X., and Gosselin, C.M. (2005b), "Mobility analysis of parallel mechanisms based on screw theory and the concept of equivalent serial kinematic chain," *Proceedings of the ASME 2005 International Design Engineering Technical Conferences and the Computers and Information in Engineering Conference*, Long Beach, California, USA, Paper DETC2005-85337.

Kumar, V., Waldron, K.J., Chrikjian, G., and Lipkin, H. (2000), *Applications of screw system theory and Lie theory to spatial kinematics: A Tutorial*, 2000 ASME Design Engineering Technical Conferences, Baltimore, USA.

Davidson, J.K., and Hunt, K.H. (2004), *Robots and Screw Theory: Applications of Kinematics and Statics to Robotics*, Oxford University Press.

Kong, X., and Gosselin, C.M. (2005c), "Type synthesis of 5-DOF parallel manipulators based on screw theory," *Journal of Robotic Systems*, **22**(10), pp. 535–547.

THE MULTIPLE VIRTUAL END-EFFECTORS APPROACH FOR HUMAN-ROBOT INTERACTION

Agostino De Santis
PRISMA Lab, Dipartimento di Informatica e Sistemistica
Università degli Studi di Napoli Federico II
Via Claudio 21, 80125 Napoli, Italy
agodesa@unina.it

Paolo Pierro
PRISMA Lab, Dipartimento di Informatica e Sistemistica
Università degli Studi di Napoli Federico II
Via Claudio 21, 80125 Napoli, Italy
paolopierro@tin.it

Bruno Siciliano
PRISMA Lab, Dipartimento di Informatica e Sistemistica
Università degli Studi di Napoli Federico II
Via Claudio 21, 80125 Napoli, Italy
siciliano@unina.it

Abstract In this paper, a method for managing redundancy for a mobile robot manipulator is proposed, which is aimed at kinematic control of the system in interaction tasks with humans. The method considers those parts of the manipulator structure —virtual end-effectors (VEEs)— which could potentially hit objects or persons during human-robot interaction. The positioning of each of these various VEEs is considered as a lower-priority task in the inverse kinematics resolution of the robot manipulator, while the order of priorities is dynamically changed during task execution. In addition, it is shown that suitable trajectories are to be planned for VEEs using sensory data, e.g., with potential field methods. A simulation case study for anthropic domains is proposed.

Keywords: Redundancy resolution, physical human-robot interaction, safety, potential fields, obstacle avoidance

J. Lenarčič and B. Roth (eds.), Advances in Robot Kinematics, 133–144.

1. Introduction

Human-robot interaction addresses important issues to avoid that the physical body of a robot could result in damages to humans. In the latest years the attention was focused on cognitive aspects of the growing interaction from robots and humans, like mental models and interfaces. It is important to notice that the presence of physical "bodies" is a crucial aspect in the interaction between humans and robots. In particular, physical human-robot interaction (pHRI) addresses the two crucial issues of safety and dependability, especially when environments are unstructured. The physical interaction with a robot in anthropic domains becomes every day more interesting for assistance and service robotics in the houses and for the elderly-dominated society. The EURON project PHRIDOM (Albu-Schaffer et al., 2005), e.g., is addressing these issues. The crucial goals of safety and dependability are related to technical issues such as collision avoidance, redundancy resolution, compliance control and sensory-based safety systems for close interaction.

Safe and dependable interaction can be accomplished both in a passive and in an active fashion. Passive safety is introduced, e.g., using springs, elastic joints (De Luca, 2000); other interesting techniques were also proposed, like the variable-stiffness actuators (Bicchi et al., 2001) and the distributed macro-mini actuation (Zinn et al., 2002). To improve safety, and also to add dependability for the users, active control of the physical interaction is to be considered. Force control (Siciliano and Villani, 1999) and safe postures of robot manipulators should be focused as fundamental issues. In addition, the whole kinematic structure of a manipulator must be controlled, because the robot can hit a person with different parts of the structure.

This paper considers the problem of controlling the positioning of crucial parts of the kinematic structure of a robot in interaction tasks, which are termed "virtual end-effectors" (VEEs). Proper Closed-Loop Inverse Kinematics (CLIK) schemes (Siciliano, 1990) are adopted to achieve resolution in the presence of redundancy, so as to take into account the issues discussed above in the positioning of such VEEs. Each VEE is controlled with a different level of priority with respect to the task, programming the positioning of each dangerous part of the articulated structure in a safe configuration; then, the priorities between the tasks are handled in a hierarchical inverse kinematics scheme (Siciliano and Slotine, 1991). The trajectory planning phase is designed to make the multiple VEEs approach suitable to control of the interaction. In detail, an obstacle avoidance technique based on the well-known potential field

method (Khatib, 1986) is adopted to dynamically change the priority order according to the position of goals and objects in the environment.

2. Modelling

The application domain hereby considered is domestic assistance. For dependable pHRI a redundant mobile robot is needed: movements in a room, objects picking and other tasks may be accomplished, for instance, with a manipulator mounted on a mobile base.

2.1 Kinematics

The mobile robot manipulator considered for the purpose of the present study has the kinematic structure of Fig. 1, which is equivalent to the assembly of a commercial mobile robot (Pioneer PowerBot) and an industrial robot manipulator (Comau Smart-3S), although the method is at all applicable for any kinematic structure with a known Jacobian. In the figure, several critical points are evidenced (A, B, C, D, E), which describe those extremities of the robot that can collide with a human being. Also, they are crucial in order to locate the positions of the manipulator links, since the robot can run into an obstacle not only by a VEE, but also with an intermediate point between two VEEs located on a link.

It should be pointed out, however, that safety issues suggest using accurate sensor information to localize goals and obstacles, lightweight structures and other additional facilities to make the robot intrinsically safe in event of collisions. Here, however, only kinematic aspects are focused. By the way, the manipulator should be lightweight, while industrial manipulators are heavy and cart robots able to carry them are not yet available for potential use in houses.

2.2 Redundancy Resolution

Redundancy resolution is related to the problem of finding movements of available joints that respect the desired motion of the end-effector, while satisfying some additional task. The solution of the problem can be found on the basis of the well-known differential mapping

$$\dot{\boldsymbol{p}} = \boldsymbol{J}(\boldsymbol{q})\dot{\boldsymbol{q}} \tag{1}$$

where

$$\boldsymbol{p} = [\, x \quad y \quad z \,]^{\mathrm{T}}$$
$$\boldsymbol{q} = [\, q_1 \quad q_2 \quad \ldots \quad q_n \,]^{\mathrm{T}}$$

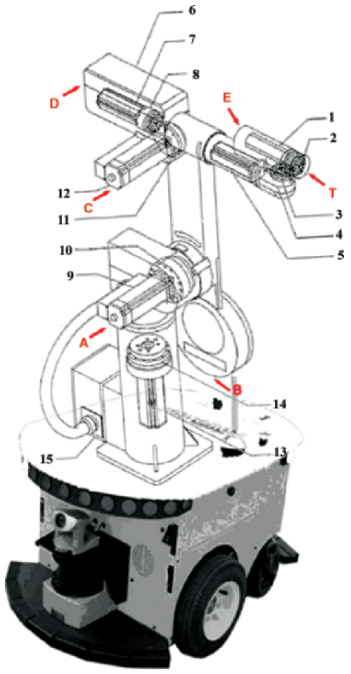

Figure 1. Mobile robot manipulator with VEEs A, B, C, D, E.

are respectively the end-effector position vector and the joint position vector of an n-DOF mobile robot manipulator, and $\boldsymbol{J}$ denotes the usual Jacobian. For the purpose of the present work, the end-effector orientation is not considered, while $n = 8$, i.e. 2 DOF's for the mobile base and 6 DOF's for the manipulator. Since the robot is redundant ($n > 3$), the simplest way to invert the mapping (1) is to use the pseudo-inverse of the Jacobian matrix, which corresponds to the minimization of the joint velocities in a least-square sense (Sciavicco and Siciliano, 2000). Because of the different characteristics of the available DOFs, it could be required to modify the velocity distribution. This might be achieved by adopting a weighted pseudo-inverse $\boldsymbol{J}_W^{\dagger}$

$$\boldsymbol{J}_W^{\dagger} = \boldsymbol{W}^{-1}\boldsymbol{J}^{\mathrm{T}}(\boldsymbol{J}\boldsymbol{W}^{-1}\boldsymbol{J}^{\mathrm{T}})^{-1} \tag{2}$$

with the $(n \times n)$ matrix $\boldsymbol{W}^{-1} = \mathrm{diag}\{\beta_1, \beta_2, ..., \beta_n\}$, where β_i is a weight factor belonging to the interval $[0, 1]$ such that $\beta_i = 1$ corresponds to full motion for the i-th degree of mobility and $\beta_i = 0$ corresponds to freeze the corresponding joint (De Santis et al., 2005a).

Redundancy of the system can be further exploited by using a task-priority strategy (Nakamura, 1991) corresponding to a solution to (1) of the form

$$\dot{\boldsymbol{q}} = \boldsymbol{J}_W^{\dagger}(\boldsymbol{q})\boldsymbol{v} + \left(\boldsymbol{I}_n - \boldsymbol{J}_W^{\dagger}(\boldsymbol{q})\boldsymbol{J}(\boldsymbol{q})\right)\dot{\boldsymbol{q}}_a \tag{3}$$

where $\boldsymbol{I}_n$ is the $(n \times n)$ identity matrix, $\dot{\boldsymbol{q}}_a$ is an arbitrary joint velocity vector and the operator $\left(\boldsymbol{I}_n - \boldsymbol{J}_W^{\dagger}\boldsymbol{J}\right)$ projects the joint velocity vector in the null space of the Jacobian matrix. Also in (3), $\boldsymbol{v} = \dot{\boldsymbol{p}}_d + k(\boldsymbol{p}_d - \boldsymbol{p})$ which provides a feedback correction term of $\boldsymbol{p}$ to the desired position $\boldsymbol{p}_d$, according to the well-known CLIK algorithm, being $k > 0$ a suitable gain (Siciliano, 1990). This solution generates an internal motion of the robotic system (secondary task) which does not affect the motion of the end-effector while fulfilling the primary task.

The kind of secondary tasks employed for the algorithm discussed in this work are based on the inverse kinematics of a reduced part of the structure. As an example of positioning of different parts of manipulator (rather than only the actual end-effector), consider the human arm: the structure is redundant for the positioning of the hand, and thus it is possible to position the elbow (which can be considered a first VEE); the so-computed joint values can then be used as references for the positioning of the wrist (second VEE), and so far for the hand (real end-effector) (De Santis et al., 2005b). Therefore, a hierarchical solution of redundancy is achieved, where the various lower-priority tasks are to be selected according to some suitable criteria (Featherstone, 1988).

3. The multiple VEEs approach

Virtual end-effectors (VEEs) are parts of the manipulator structure, whose positions are to be controlled in addition to the control of the end-effector of the mobile robot manipulator. In detail, let $\boldsymbol{q}_i$ denote the vector of the n_i joint variables which determine the position $\boldsymbol{p}_i$ of the i-th VEE. Therefore, the differential mapping for the VEE is

$$\dot{\boldsymbol{p}}_i = \boldsymbol{J}_i(\boldsymbol{q}_i)\dot{\boldsymbol{q}}_i \tag{4}$$

where $\boldsymbol{J}_i$ denotes the associated Jacobian.

The multiple VEEs approach is hereby introduced in a general fashion, by adopting a multiple task priority strategy for specifying secondary tasks, along with a proper trajectory planning technique for the desired motion of each VEE. The result is a nested N-layer CLIK scheme, where N is the number of considered VEEs. To this regard, please notice that the end-effector is included in the counting of the VEEs; in fact, it may well be the case the highest priority be assigned to an intermediate VEE

other than to the end-effector, say when an obstacle is obstructing the end-effector motion.

With this approach, the control of different points is not considered in a global matrix, but with multiple mappings. The VEEs approach can be used for maneuvering a kinematic structure in a volume, e.g., for tube inspections and endoscopy with snake robots, by considering the most critical prominences of the structure as VEEs.

3.1 Nested Closed-loop Inverse Kinematics

Inverse kinematics with the VEEs approach orders the VEE positioning tasks according to a priority management strategy. Since the trajectories of lower priority VEEs are assigned as secondary task, they will be followed only if they do not interfere with the higher priority task to be fulfilled. Hence, a list of VEEs is considered, starting from the one with highest priority. When a VEE gets close to an obstacle, its desired path following (necessary to avoid the obstacle) becomes of higher priority for the CLIK scheme and the priority order is switched with respect to the distance of each VEE from the obstacle. This can be achieved by considering the N-layer priority algorithm described in the following. The idea is summarized in Fig. 2, being N the lowest priority.

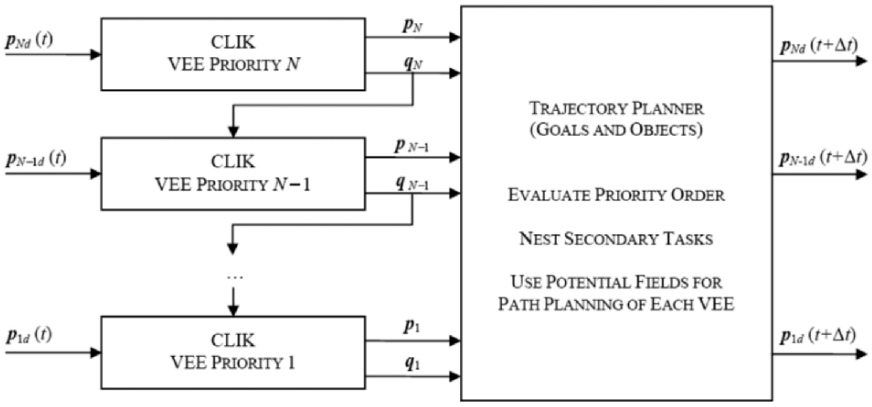

Figure 2. Scheme of nested CLIK with VEEs.

At the lowest layer, the differential mapping corresponding to the velocity of the VEE with lowest priority is considered, i.e. (4) with $i = N$. Hence, a CLIK algorithm with weighted pseudo-inverse is adopted to compute the inverse kinematics:

$$\dot{\boldsymbol{q}}_N = \boldsymbol{J}_N^{\dagger}(\boldsymbol{q}_N)\boldsymbol{v}_N, \tag{5}$$

with $\boldsymbol{v}_N = \dot{\boldsymbol{p}}_{Nd} + k_N(\boldsymbol{p}_{Nd} - \boldsymbol{p}_N)$, being $\boldsymbol{p}_{Nd}$ the desired position for the VEE with lowest priority and $k_N > 0$. The pseudo-inverse matrix is substantially weighted as in (2).

At the generic i-th layer of the nested scheme, with $i = N-1, \ldots, 1$, the inverse kinematics is computed as in (3), i.e.

$$\dot{\boldsymbol{q}}_i = \boldsymbol{J}_{iW}^{\dagger}(\boldsymbol{q}_i)\boldsymbol{v}_i + \left(\boldsymbol{I}_{n_i} - \boldsymbol{J}_{iW}^{\dagger}(\boldsymbol{q}_i)\boldsymbol{J}_i(\boldsymbol{q})\right)\dot{\boldsymbol{q}}_{ia} \tag{6}$$

where

$$\boldsymbol{J}_{iW}^{\dagger} = \boldsymbol{W}_i^{-1}\boldsymbol{J}_i^{\mathrm{T}}(\boldsymbol{J}_i\boldsymbol{W}_i^{-1}\boldsymbol{J}_i^{\mathrm{T}})^{-1} \tag{7}$$

with $\boldsymbol{W}_i^{-1} = \mathrm{diag}\{\beta_{i1}, \beta_{i2}, ..., \beta_{in_i}\}$ and $\boldsymbol{v}_i = \dot{\boldsymbol{p}}_{id} + k_i(\boldsymbol{p}_{id} - \boldsymbol{p}_i)$, being $\boldsymbol{p}_{id}$ the desired position for the VEE with priority i, and $k_i > 0$. Further, $\dot{\boldsymbol{q}}_{ia}$ is the gradient of the objective function:

$$G_i = -\frac{1}{n_i}\sum_{j=1}^{n_i}\frac{q_{i,j} - q_{i+1,j}}{q_{i,jM} - q_{i,jm}}$$

where $q_{i,jM}$ ($q_{i,jm}$) is the maximum (minimum) value of the joint variable $q_{i,j}$, i.e. the j-th component of the joint vector $\boldsymbol{q}_i$. The above choice corresponds to achieving a joint motion for the joint variables as close as possible to that computed in the previous layer $\boldsymbol{q}_{i+1}$, which are feeded as secondary reference values to the next layer, providing a way to fulfill inverse kinematics of different parts of the structure, with different priorities.

Going on, the nested CLIK algorithm computes the inverse kinematics for the structures ending with each of the considered VEEs. It is worth emphasizing that the order of priorities is dynamically changed during task execution. As illustrated in Fig. 2, the scheme takes the desired positions for the ordered VEEs at time t; then, the output of the CLIK algorithms at the N levels are input to a trajectory planning block which re-evaluates the priority order among the various VEEs according to the positions of the goals and the obstacles in the environment, and thus generates the new ordered sequence of desired positions for the VEEs at time $t + \Delta t$, where Δt is the sampling time at which the CLIK algorithm is discretized for practical implementation; the planning aspects are discussed in the following section.

The weights β_{ij} of the matrices $\boldsymbol{W}_i$ are chosen according to the criterion described above (De Santis et al., 2005a). In particular, the joints of the mobile base have a higher weight with the respect to the joints of the manipulator. In Fig. 3 it is possible to see how trajectories are followed for various VEEs with different priorities. It is easy to recognize that planned trajectories for VEEs with lower priorities are abandoned

when they interfere with the higher priority planned trajectories. With the priority strategy, which ranks the VEEs, it is possible to fulfill the most critical positioning problems on line.

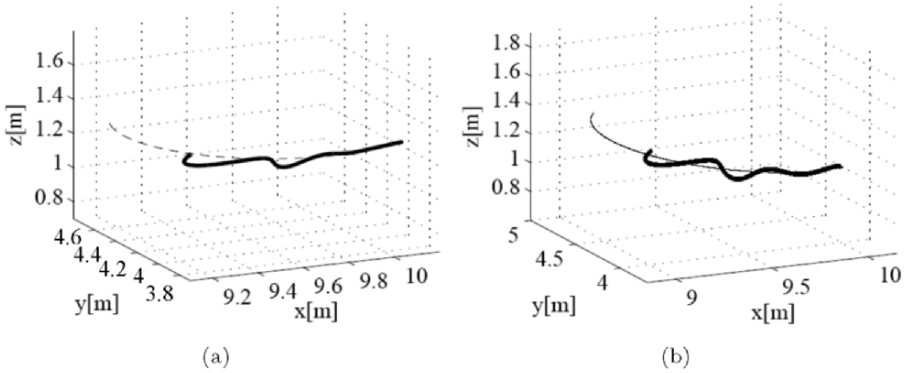

Figure 3. Planned (gray) and actual (black) trajectory for the VEE labelled with A and B in Fig. 1.

The time history of a joint variable is also reported in Fig. 4; movements planned in the task space are abandoned if they interfere with higher-priority tasks.

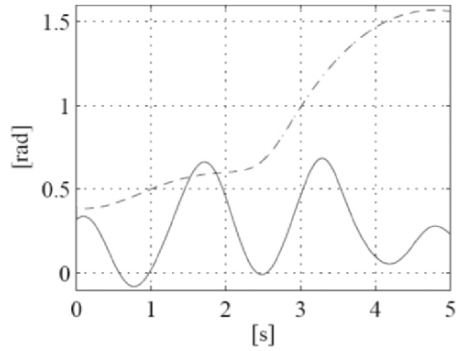

Figure 4. Planned (dashed) and actual (solid) trajectory for the joint value q_4.

The priority management strategy is crucial: if a mobile robot manipulator is considered, which avoids the head of a person in a room with the end-effector, it is difficult to predict the possibility of hitting him/her with other parts of the structure, because a possible avoidance movement can be incompatible with the path of the real end-effector or of a VEE with higher priority.

3.2 Trajectory Planning

For each VEE it should be possible to plan a complete trajectory off-line, but this approach is not satisfying, since the trajectories imposed to the VEEs, if planned a priori, do not have realistic application (most obstacles are moving and their trajectories are not known a priori). Furthermore, the positioning of VEEs in task space is only a secondary task for the positioning of other VEEs with higher priority. On-line trajectory planning is needed: potential fields methods (Khatib, 1986) can be used for such a planning: the manipulator moves in a field of forces; the position to be reached is an attractive pole for the end-effector, and obstacles are repulsive surfaces for the manipulator parts. The field of artificial forces F is produced by a differentiable potential function, with $F(\boldsymbol{p}_i) = -\nabla(U(\boldsymbol{p}_i))$, where $\nabla(U(\boldsymbol{p}_i))$ is the gradient vector of U at $\boldsymbol{p}_i$, that is the position of the VEE under the field effect.

The potential U is constructed as the sum of two elementary potential functions: $U(\boldsymbol{p}_i) = U_{att}(\boldsymbol{p}_i) + U_{rep}(\boldsymbol{p}_i)$ In this relation U_{att} is the attractive potential and depends only on the final position, whereas U_{rep} is the repulsive function and depends only on the obstacles position. During the simulation, the attractive potential field is chosen to be a parabolic well, centered in the goal positions, whereas a repulsive field is related to a distance of influence from obstacles. So, the goal is a source of an attractive potential field; obstacles are sources of repulsive potential fields.

Simulations of robot movements with this approach are shown in the next section. Notice again the importance of the priority management in the CLIK schemes, as discussed above: even with on-line path planning, a desired path could be not executable, so it is necessary to switch the priority order, as emphasized by the trajectory planning block in Fig. 2.

4. A Case Study

In this section, operations of the considered mobile manipulator are examined in an anthropic domain, while the robot is performing an assistance task. The model has been simulated under the Virtual Reality Toolbox (VRT) in Matlab. The VRT is a solution for interacting with virtual reality models of dynamic systems over time. The complete CLIK algorithm with multiple priority handling and potential fields method for trajectory planning is considered. The robot has to take a soda can which is placed in a fitted cupboard, where an impaired person cannot arrive. In the first phase, the person on the wheelchair is a moving obstacle to be avoided. When the robot takes the can, the person becomes a goal point to be reached by the end-effector bringing

the can. The first desired position for the robot is the location of the can on the cupboard; after the end of the goal reaching, the second desired position is the location of the person, who is moving in an independent way. The anthropic environment where the task is executed is shown in Fig. 5.

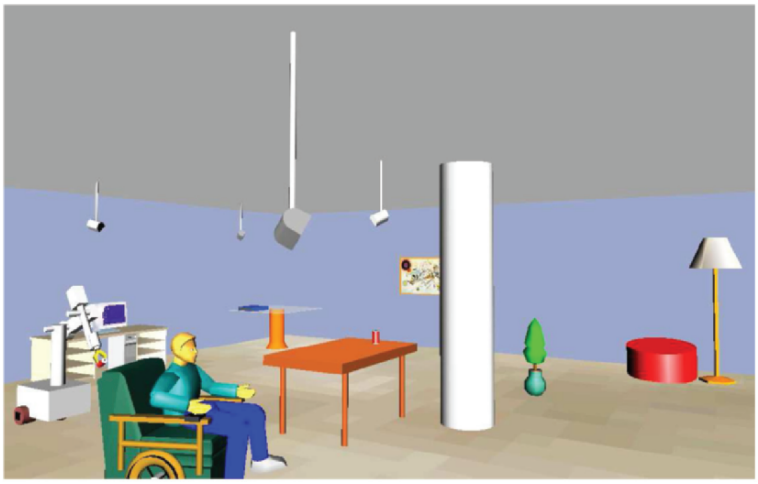

Figure 5. Interaction with the service robot in an anthropic environment.

In the shown environment, the robot has to avoid the lamps (it has to slow down in order to keep away from objects attached to the ceiling), as well as the person (turning around him/her) and finally the desktop and the table. The obstacles are modelled as spheres: a lamp is a sphere having a small radius, whereas a person is a set of spheres with different radiuses. Notice that these radiuses may take into account cognitive evaluations. As an example, consider the potentially unpredictable behaviours of children in the scene: in such a case, safety issues suggest to magnify the radiuses for repulsive potential fields. It is possible, in intelligent environments, to provide radio-frequency identification tags to assign different set of parameters, depending on the skills of interacting people, for robot kinematic and force control. The table has been modelled differently: it is characterized by a succession of points (each point represents a corner or the lower point of a foot of the table). The robot is equipped with seven leds, each one placed next to one critical points: when a particular VEE assumes the highest priority, its led lights up. The priority assignment for the nested CLIK of the different VEEs is reported in Fig. 6, where EE stands for the end-effector and WMR for the wheeled-mobile robot.

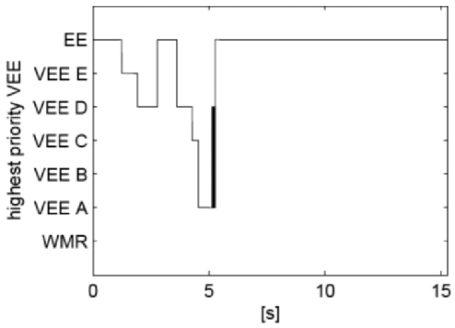

Figure 6. Time history of priority assignments.

In Fig. 7 it is possible to see the paths for one VEE and the EE avoiding the obstacles as well as the motion of the impaired person. Strong hypothesis about sensory system are assumed: positions of robot, people and objects are exactly known and tracked.

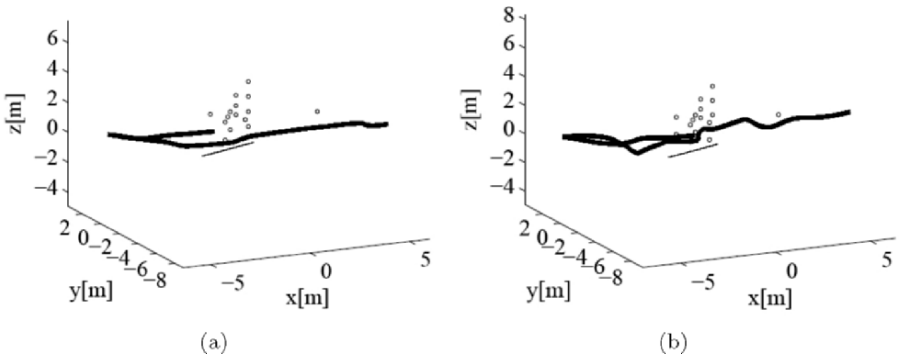

Figure 7. Trajectories for the VEE labelled with A and the EE of the robot (solid) in the task of Fig. 5, where the spheres are edges of obstacles and the thin line is the trajectory of the impaired person during the task.

5. Conclusion

The virtual end-effectors (VEEs) approach has been proposed for simultaneous inverse kinematics, with proper trajectory planning, of mobile robot manipulators operating in unstructured environments. For pHRI, the VEEs approach can actually complement interaction schemes, where intrinsical and active safety issues are to be considered. The proposed approach may be also used to keep a robot in proper postures in narrow spaces (e.g., snake robots) and for self-collision avoidance too.

For comparison, a global optimization of different forces acting on the manipulator without null-space techniques should also be considered, with a weighted extended Jacobian approach. In addition, automatic techniques for the location of the VEEs should be of interest as well. Future work will also be devoted to add soft-computing techniques for both trajectory planning and inverse kinematics, and to consider integration with force control on real mobile robot manipulators.

References

Albu-Schaffer, A., Bicchi, A., Boccadamo, G., Chatila, R., De Luca, A., De Santis, A., Giralt, G., Hirzinger, G., Lippiello, V., Mattone, R., Schiavi, R., Siciliano, B., Tonietti, G., Villani, L., "Physical Human-Robot Interaction in Anthropic Domains: Safety and Dependability", *4th IARP/IEEE-EURON Workshop on Technical Challenges for Dependable Robots in Human Environments*, Nagoya, J, July 2005.

De Luca, A., "Feedforward/feedback laws for the control of flexible robots" *2000 IEEE International Conference of Robotics and Automation*, San Francisco, CA, USA, April 2000.

Bicchi, A., Tonietti, G., Bavaro, M., Piccigallo, M., "Variable stiffness actuators for fast and safe motion control", *11th International Symposium of Robotics Research*, Siena, I, October 2003.

Zinn, M., Khatib, O., Roth, B., Salisbury, J.K., "A new actuation approach for human friendly robot design", *International Symposium on Experimental Robotics*, S. Angelo d'Ischia, I, July 2002.

Siciliano, B., Villani, L., *Robot Force Control*, Kluwer Academic Publishers, Boston, MA, 1999.

Siciliano, B., "A closed-loop inverse kinematic scheme for on-line joint-based robot control", *Robotica*, 8, 231–243, 1990.

Sciavicco, L., Siciliano, B., *Modelling and Control of Robot Manipulators*, (2nd Ed.), Springer-Verlag, London, UK, 2000.

Siciliano, B., Slotine, J.J.E., "A general framework for managing multiple tasks in highly redundant robotic systems, *5th International Conference on Advanced Robotics*, Pisa, I, June 1991.

Khatib, O., "Real-time obstacle avoidance for robot manipulators and mobile robots", *International Journal of Robotics Research*, 5(1), 90–98, 1986.

De Santis, A., Siciliano, B., Villani, L., "Fuzzy trajectory planning and redundancy resolution for a fire fighting robot operating in tunnels", *2005 IEEE International Conference on Robotics and Automation*, Barcelona, E, April 2005.

Nakamura, Y., *Advanced Robotics: Redundancy and Optimization*, Addison-Wesley, Reading, Mass., 1991.

De Santis, A., Caggiano, V., Siciliano, B., Villani, L., Boccignone, G., "Anthropic inverse kinematics of robot manipulators in handwriting tasks", *12th Conference of the International Graphonomics Society*, Fisciano, Italy, June 2005.

Featherstone, R., "Resolving manipulator redundancy by combining task constraints", *Int. Meeting Advances in Robot Kinematics*, Ljubljana, Yugoslavia, Sep. 1988.

Humanoids and Biomedicine

BALANCE AND CONTROL OF HUMAN INSPIRED JUMPING ROBOT

Jan Babič, Damir Omrčen and Jadran Lenarčič
"Jožef Stefan" Institute, Department of Automatics, Biocybernetics and Robotics Ljubljana, Slovenia
jan.babic@ijs.si, damir.omrcen@ijs.si, jadran.lenarcic@ijs.si

Abstract The purpose of this study is to describe the necessary conditions for the motion controller of a humanoid robot to perform the vertical jump. We performed vertical jump simulations using three different control algorithms and showed the effects of each algorithm on the vertical jump performance. We showed that motion controllers which consider one of two conditions separately are not appropriate to control the vertical jump. We demonstrated that the motion controller has to satisfy both conditions simultaneously in order to achieve a desired vertical jump.

Keywords: Humanoid robot, Vertical jump, dynamic stability

1. Introduction

The vertical jump is an example of a fast explosive movement that requires quick and completely harmonized coordination of all segments of the robot, for the push-off, for the flight and, finally, for the landing. The most important part of the vertical jump which influences the efficiency and therefore the height of the jump is the push-off phase. The push-off phase can be defined as a time interval when the feet are touching the ground before the flight. The primary task of the actuators during the push-off phase is to keep the robot balanced during the entire jump. The secondary task of the actuators is to accelerate the robot's center of mass upwards in the vertical direction to the extended body position.

In the past, several research groups developed and studied jumping robots but most of these were simple mechanisms not similar to humans. They were controlled by empirically derived control strategies. Probably the best-known hopping robots were designed by Raibert, 1986 and his team. They developed different hopping robots, all with telescopic legs and with a steady-state control algorithm. Later, De Man et al., 1996 developed a trajectory generation strategy based on the angular momentum theorem which was implemented on a model with articulated legs. Recently Hyon et al., 2003 developed a one-legged hopping robot with a structure based on the hind-limb model of a dog. They used an empirically derived controller based on the characteristic dynamics.

J. Lenarčič and B. Roth (eds.), Advances in Robot Kinematics, 147–156.

The purpose of this study is to mathematically formulate the necessary conditions that the motion controller of a humanoid robot has to consider in order to perform the vertical jump.

2. Dynamical Model of Jumping Robot

The model of the jumping robot is planar and is composed of four segments which represent the foot, shank, thigh and trunk (Fig. 1). The segments are connected by frictionless rotational hinges whose axes are perpendicular to the sagittal plane. The model consists of two parts, the model of the robot in the air and the model of the robot in contact with the ground. While the tip of the foot is on the ground, the contact between the foot tip and the ground is modelled as a rotational hinge joint between the foot tip and the ground at point F. Therefore, the robot has six degrees of freedom during flight and four degrees of freedom during stance (with the assumption that the foot tip of the robot does not slip and does not bounce back). The generalized coordinates used to describe the motion of the robot are coordinates x_F and y_F of the foot tip measured in the reference frame and joint angles α, β, γ, δ.

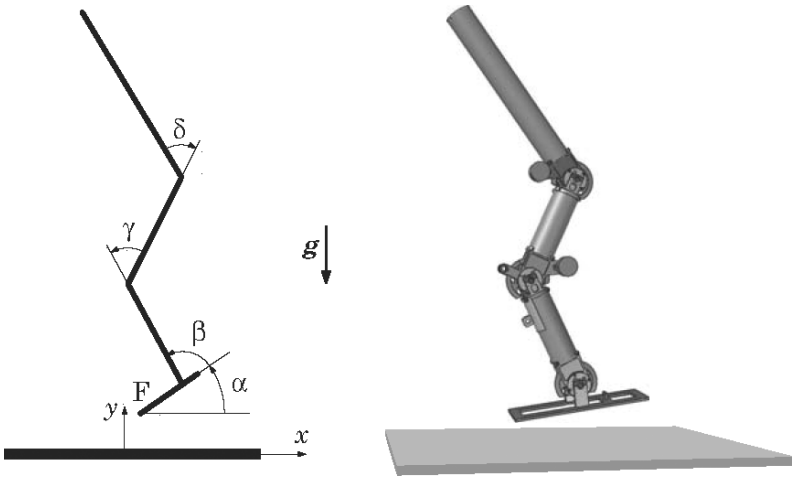

Figure 1. Jumping robot during flight.

3. Vertical Jump Conditions and Control Algorithm

To assure the verticality of the jump, the robot's center of mass (COM) has to move in the upward direction above the support polygon during the push-off phase of the jump. The second condition, which

refers to the balance of the robot during the push-off phase, is the position of the zero moment point (ZMP). ZMP is the point on the ground at which the net moment of the inertial forces and the gravity forces has no component along the horizontal axes (Vukobratović et al., 2004). In the following sections we will analyse how these two conditions influence the vertical jump. First we will design two control algorithms based on the COM condition and ZMP condition separately and then we will design a control algorithm that considers both conditions together.

Equations that define the position of COM are

$$x_{com} = \frac{\sum_{i=1}^{n} m_i x_i}{\sum_{i=1}^{n} m_i}, \qquad y_{com} = \frac{\sum_{i=1}^{n} m_i y_i}{\sum_{i=1}^{n} m_i}, \tag{1}$$

where x_{com} and y_{com} are horizontal and vertical positions of COM of the whole system, respectively. x_i and y_i are the coordinates of COM of the i-th segment, m_i is the mass of the i-th segment and n is the number of segments.

The position of ZMP is

$$x_{zmp} = \frac{\sum_{i=1}^{n} m_i x_i(\ddot{y}_i + g) - \sum_{i=1}^{n} m_i y_i \ddot{x}_i + \tau_z}{\sum_{i=1}^{n} m_i(\ddot{y}_i + g)}, \tag{2}$$

where

$$\tau_z = \sum_{i=1}^{n} (\mathbf{I}_i \dot{\omega}_i + \omega_i \times \mathbf{I}_i \omega_i). \tag{3}$$

g is the quadratic norm of the gravity vector, $\mathbf{I}_i$ is the inertial tensor of the $i-th$ segment around its COM and ω_i is the angular velocity of the $i-th$ segment. When the robot is at rest, the position of ZMP coincides with the horizontal position of COM.

For the control purposes we have to find the second derivatives of x_{com} and y_{com} (Eq. 1). We get the following equations

$$\ddot{x}_{com} = k_{11}\ddot{\alpha} + k_{12}\ddot{\beta} + k_{13}\ddot{\gamma} + k_{14}\ddot{\delta} + d_1 \tag{4}$$

and

$$\ddot{y}_{com} = k_{21}\ddot{\alpha} + k_{22}\ddot{\beta} + k_{23}\ddot{\gamma} + k_{24}\ddot{\delta} + d_2, \tag{5}$$

where the parameters k_{ij} and d_i are functions of joint angles ($k_{ij} = f(\alpha, \beta, \gamma, \delta)$, $d_i = f(\alpha, \beta, \gamma, \delta)$).

The position of ZMP on the ground can not be described in this form because the denominator of Eq. 2 is also a function of joint angles.

However, in many cases we can freely move the coordinate system to coincide with the position of the desired ZMP and the balancing condition becomes $x_{zmp} = 0$. In this case we can express x_{zmp} as

$$x_{zmp} = 0 = k_{31}\ddot{\alpha} + k_{32}\ddot{\beta} + k_{33}\ddot{\gamma} + k_{34}\ddot{\delta} + d_3. \tag{6}$$

Eqs. 4, 5 and 6 can be combined and written in the matrix form

$$\begin{bmatrix} \ddot{x}_{com} \\ \ddot{y}_{com} \\ 0 \end{bmatrix} = \begin{bmatrix} k_{11} & k_{12} & k_{13} & k_{14} \\ k_{21} & k_{22} & k_{23} & k_{24} \\ k_{31} & k_{32} & k_{33} & k_{34} \end{bmatrix} \begin{bmatrix} \ddot{\alpha} \\ \ddot{\beta} \\ \ddot{\gamma} \\ \ddot{\delta} \end{bmatrix} + \begin{bmatrix} d_1 \\ d_2 \\ d_3 \end{bmatrix}, \tag{7}$$

where $\ddot{x}_{com}$ and x_{zmp} are the conditions that relate with the balance. On the other hand, $\ddot{y}_{com}$ is the prescribed vertical acceleration of the robot's COM during the push-off phase of the jump which enables the robot to jump.

3.1 Control of x_{com}

In the first case we analyse the vertical jump when the motion controller keeps the horizontal position of the robot's COM over the virtual joint connecting the foot with the ground at point F during the entire push-off phase of the vertical jump. Motion controller does not control the position of ZMP x_{zmp}.

By rewriting Eq. 7 for x_{com} and y_{com} we get

$$\begin{bmatrix} \ddot{x}_{com} \\ \ddot{y}_{com} \end{bmatrix} = \begin{bmatrix} k_{11} & k_{12} & k_{13} & k_{14} \\ k_{21} & k_{22} & k_{23} & k_{24} \end{bmatrix} \begin{bmatrix} \ddot{\alpha} \\ \ddot{\beta} \\ \ddot{\gamma} \\ \ddot{\delta} \end{bmatrix} + \begin{bmatrix} d_1 \\ d_2 \end{bmatrix}. \tag{8}$$

Since the system is under-determinate (the degree of redundancy is two), we have to set up two additional constraints. To achieve a human like motion of the vertical jump we chose the following simple constraints

$$\ddot{\gamma} = c_1\ddot{\beta}, \qquad \ddot{\delta} = c_2\ddot{\beta}, \tag{9}$$

where c_1 and c_2 are constants. By substitution of Eq. 9 into Eq. 8 we get

$$\begin{bmatrix} \ddot{x}_{com} \\ \ddot{y}_{com} \end{bmatrix} = \begin{bmatrix} k_{11} & k_{12} + c_1k_{13} + c_2k_{14} \\ k_{21} & k_{22} + c_1k_{23} + c_2k_{24} \end{bmatrix} \begin{bmatrix} \ddot{\alpha} \\ \ddot{\beta} \end{bmatrix} + \begin{bmatrix} d_1 \\ d_2 \end{bmatrix}. \tag{10}$$

The system of equations is determinate and the joint accelerations can be written as

$$\begin{bmatrix} \ddot{\alpha} \\ \ddot{\beta} \end{bmatrix} = \begin{bmatrix} k_{11} & k_{12} + c_1 k_{13} + c_2 k_{14} \\ k_{21} & k_{22} + c_1 k_{23} + c_2 k_{24} \end{bmatrix}^{-1} \left(\begin{bmatrix} \ddot{x}_{com} \\ \ddot{y}_{com} \end{bmatrix} - \begin{bmatrix} d_1 \\ d_2 \end{bmatrix} \right). \quad (11)$$

3.2 Control of x_{zmp}

In the second case we analyse the vertical jump when the motion controller keeps the position of ZMP aligned with the virtual joint at point F. The motion controller does not control the horizontal position of COM (x_{com}).

By rewriting Eq. 7 for x_{zmp} and y_{com} we get

$$\begin{bmatrix} \ddot{y}_{com} \\ 0 \end{bmatrix} = \begin{bmatrix} k_{21} & k_{22} & k_{23} & k_{24} \\ k_{31} & k_{32} & k_{33} & k_{34} \end{bmatrix} \begin{bmatrix} \ddot{\alpha} \\ \ddot{\beta} \\ \ddot{\gamma} \\ \ddot{\delta} \end{bmatrix} + \begin{bmatrix} d_2 \\ d_3 \end{bmatrix}. \quad (12)$$

Similarly as in the previous case we have to find the joint accelerations. If we again use the same constraints (9) we get the following determinate system of equations

$$\begin{bmatrix} \ddot{y}_{com} \\ 0 \end{bmatrix} = \begin{bmatrix} k_{21} & k_{22} + c_1 k_{23} + c_2 k_{24} \\ k_{31} & k_{32} + c_1 k_{33} + c_2 k_{34} \end{bmatrix} \begin{bmatrix} \ddot{\alpha} \\ \ddot{\beta} \end{bmatrix} + \begin{bmatrix} d_2 \\ d_3 \end{bmatrix}, \quad (13)$$

and the joint accelerations are

$$\begin{bmatrix} \ddot{\alpha} \\ \ddot{\beta} \end{bmatrix} = \begin{bmatrix} k_{21} & k_{22} + c_1 k_{23} + c_2 k_{24} \\ k_{31} & k_{32} + c_1 k_{33} + c_2 k_{34} \end{bmatrix}^{-1} \left(\begin{bmatrix} \ddot{y}_{com} \\ 0 \end{bmatrix} - \begin{bmatrix} d_2 \\ d_3 \end{bmatrix} \right). \quad (14)$$

3.3 Control of x_{com} and x_{zmp}

In the third case we will analyse the vertical jump when the motion controller considers both conditions from the precedent two sections. It keeps the position of ZMP and the horizontal position of the robot's COM aligned with the virtual joint at point F.

In this case the degree of redundancy is one. The following constraint that abolishes the redundancy of Eq. 7 is the relationship of the ankle and knee joint accelerations

$$\ddot{\gamma} = C_1 \ddot{\beta}, \quad (15)$$

where C_1 is a constant. By substitution of Eq. 15 into Eq. 7 we get

$$\begin{bmatrix} \ddot{x}_{com} \\ \ddot{y}_{com} \\ 0 \end{bmatrix} = \begin{bmatrix} k_{11} & k_{12} + C_1 k_{13} & k_{14} \\ k_{21} & k_{22} + C_1 k_{23} & k_{24} \\ k_{31} & k_{32} + C_1 k_{33} & k_{34} \end{bmatrix} \begin{bmatrix} \ddot{\alpha} \\ \ddot{\beta} \\ \ddot{\delta} \end{bmatrix} + \begin{bmatrix} d_1 \\ d_2 \\ d_3 \end{bmatrix}, \tag{16}$$

and the joint accelerations are

$$\begin{bmatrix} \ddot{\alpha} \\ \ddot{\beta} \\ \ddot{\delta} \end{bmatrix} = \begin{bmatrix} k_{11} & k_{12} + C_1 k_{13} & k_{14} \\ k_{21} & k_{22} + C_1 k_{23} & k_{24} \\ k_{31} & k_{32} + C_1 k_{33} & k_{34} \end{bmatrix}^{-1} \left(\begin{bmatrix} \ddot{x}_{com} \\ \ddot{y}_{com} \\ 0 \end{bmatrix} - \begin{bmatrix} d_1 \\ d_2 \\ d_3 \end{bmatrix} \right). \tag{17}$$

3.4 Motion Controller

For the control of the robot we used a simple feed forward joint acceleration controller

$$\boldsymbol{\tau}_c = \mathbf{H}(\boldsymbol{q})\ddot{\boldsymbol{q}}_c + \mathbf{C}(\dot{\boldsymbol{q}}, \boldsymbol{q}) + \boldsymbol{g}(\boldsymbol{q}), \tag{18}$$

where $\boldsymbol{\tau}_c$ and $\boldsymbol{q}$ denote the control torque and the vector of joint positions, respectively. $\mathbf{H}$, $\mathbf{C}$ and $\boldsymbol{g}$ denote the inertia matrix, the vector of Coriolis and centrifugal forces and the vector of gravity forces, respectively. $\ddot{\boldsymbol{q}}_c$ is the vector of control accelerations ($\ddot{\boldsymbol{q}}_c = \left[\ddot{\alpha}, \ddot{\beta}, \ddot{\gamma}, \ddot{\delta}\right]^T$). During the push-off phase of the jump $\ddot{\boldsymbol{q}}_c$ is defined by Eqs. (11),(14) or (17). During the flight phase, when the robot is in the air, the angular momentum and the linear momentum are conserved and the $\ddot{\boldsymbol{q}}_c$ is set in such a way that the joint motions stops and the robot is prepared for landing.

4. Simulation Study

We performed vertical jump simulations using three different control algorithms described in the previous section. First we simulated the vertical jump using the control algorithm based on the COM condition, then we simulated the vertical jump using the control algorithm based on the ZMP condition and, finally, we simulated the jump where the controller considered both conditions together.

Control of x_{com}. In this case we controlled $\ddot{y}_{com}$ and $\ddot{x}_{com}$ as defined by Eq. 11. From the requirement that $\ddot{x}_{com}$ has to be above the support polygon (point F) follows that $x_{com} = 0$ and $\ddot{x}_{com} = 0$. Figure 2 shows the position of COM during the jump. The solid line represents the horizontal position while the dashed line represents the vertical position of COM. Dotted line shows the moment of take-off. It is evident that the horizontal position of COM remains zero, i.e. COM is above point F.

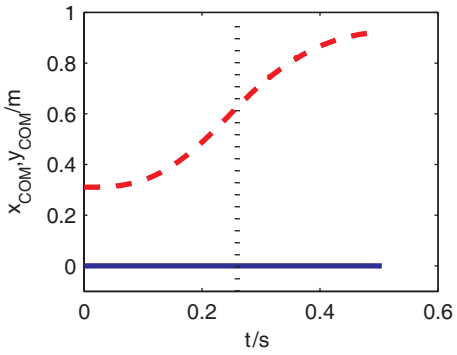

Figure 2. Position of center of mass during vertical jump considering only the COM condition.

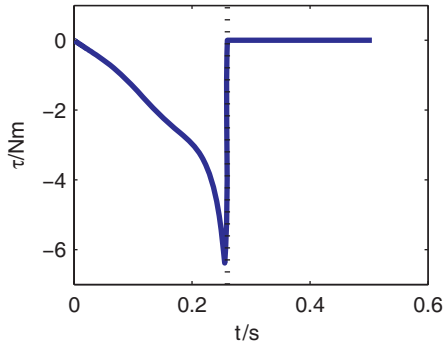

Figure 3. Required torque in virtual joint considering only COM condition.

Due to the fact that we did not control the position of ZMP, the required torque in the virtual joint between the foot and the ground during the push-off phase of the jump is not zero (see Fig. 3). As this torque can not be applied to the real robotic system, this controller is not appropriate for performing the vertical jump. Without applying this torque at the virtual joint the robot becomes unbalanced. Figure 4 shows the configurations of the robot during the jump.

Control of x_{zmp}. In this case we controlled $\ddot{y}_{com}$ and x_{zmp}, as defined by Eq. 14. To satisfy the balance criteria x_{zmp} has to be over the support polygon ($x_{zmp} = 0$). As evident from Fig. 5, the horizontal position of COM during the push-off phase of the jump is not zero and, therefore, the robot does not perform the vertical jump as it should.

On the other hand, the torque in the virtual joint is zero (Fig. 6) and the system is balanced without the torque in the virtual joint between the foot and the ground. Therefore, the robot performs a jump, but this is not a vertical jump, since COM is not above point F at the take-off moment. Figure 7 shows the configurations of the robot during the jump.

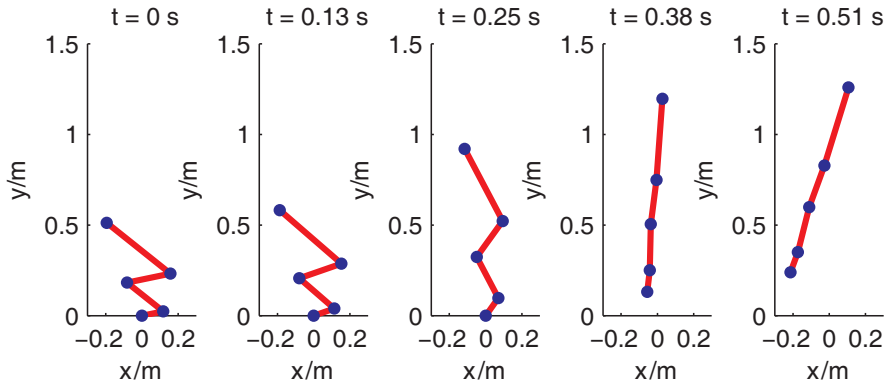

Figure 4. Configurations of robot during vertical jump considering only COM condition.

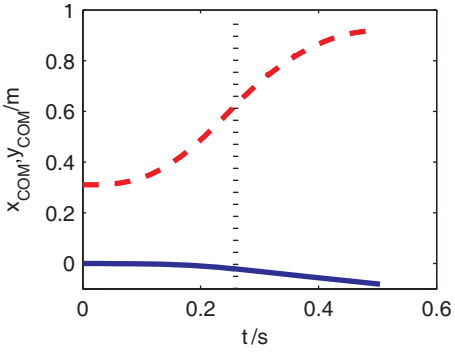

Figure 5. Position of center of mass during vertical jump considering only ZMP condition.

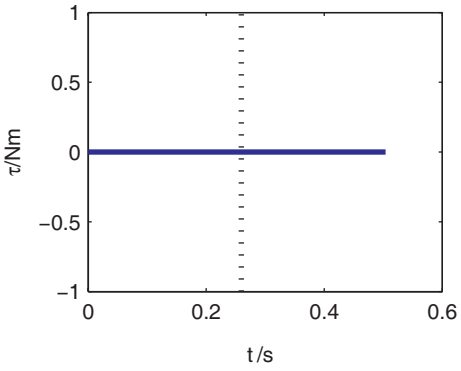

Figure 6. Torque in virtual joint considering only ZMP condition.

Control of x_{com} and x_{zmp}. In this case we controlled $\ddot{y}_{com}$ together with both $\ddot{x}_{com}$ and x_{zmp}, as defined by Eq. 17. Figure 8 shows the position of COM during the jump and Fig. 9 shows the torque in the virtual joint. As the position of COM is always above point F and the torque in the virtual joint is zero, the robot performs the desired vertical jump. Therefore, both conditions have to be fulfilled to assure the verticality of the jump. Both, the horizontal position of COM and the position of ZMP have to coincide with point F. Figure 10 shows the configurations of the robot during the jump when the motion controller considers both necessary conditions.

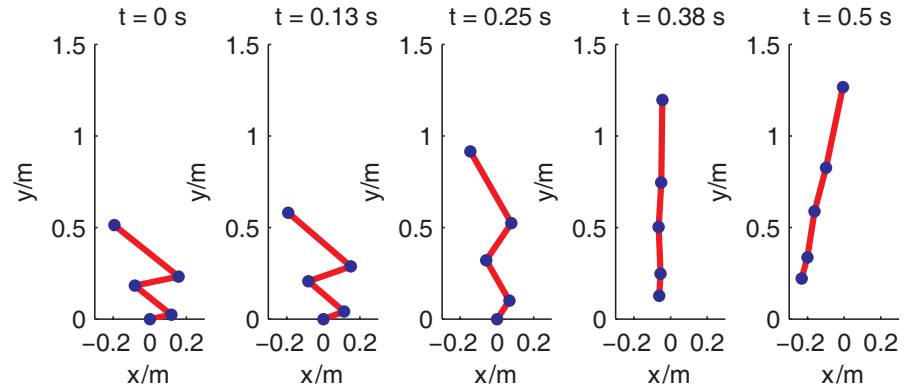

Figure 7. Configurations of robot during vertical jump considering only ZMP condition.

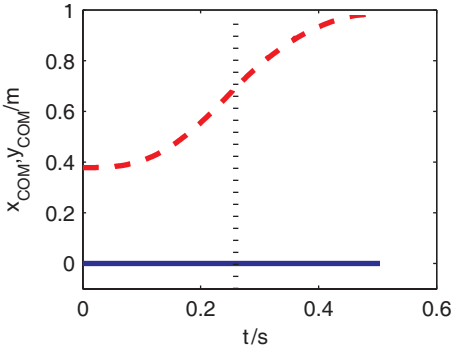

Figure 8. Position of center of mass during vertical jump considering both COM and ZMP conditions.

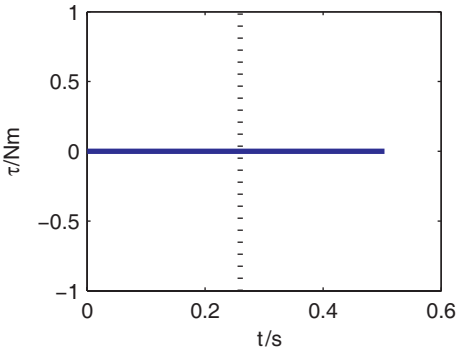

Figure 9. Torque in virtual joint considering both COM and ZMP conditions.

5. Conclusions

In this study, we mathematically formulated the necessary conditions which have to be considered by the motion controller to perform the vertical jump. The first condition refers to the robot's center of gravity which has to move in the upward direction above the support polygon during the push-off phase of the jump. The second condition refers to the position of the zero moment point that has to lie inside the support polygon to assure the balance of the robot. We analysed how these two conditions influence the vertical jump performance. Based on these conditions we designed three different control algorithms and used them in vertical jump simulations. We showed that motion controllers that

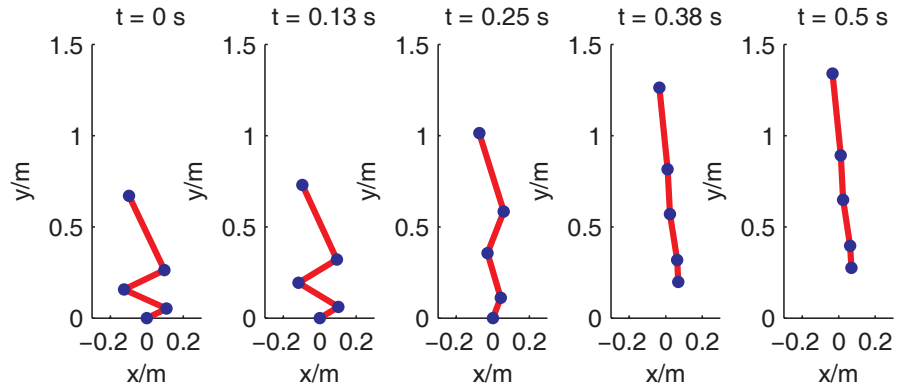

Figure 10. Configurations of robot during vertical jump considering both COM and ZMP conditions.

consider one of two conditions separately are not appropriate for the control of the vertical jump. We demonstrated that the motion controller has to satisfy both conditions simultaneously in order to achieve a desired vertical jump.

6. Acknowledgement

This study was supported by the Slovenian Ministry of Higher Education, Science and Technology.

References

De Man H., Lefeber D., Daerden F., and Faignet E. Simulation of a new control algorithm for a one-legged hopping robot (using the multibody code mechanica motion). In *Proceedings International Workshop on Advanced Robotics and Intelligent Machines*, pages 1–13, Manchester, UK, 1996.

Raibert M. *Legged Robots That Balance*. MIT Press, 1986.

Vukobratović M. and Borovac B. Zero-moment point – thirty five years of its life. *International Journal of Humanoid Robotics*, 1(1):157–173, 2004.

Hyon S., Emura T., and Mita T. Dynamics-based control of a one-legged hopping robot. *Journal of Systems and Control Engineering*, 217(2):83–98, 2003.

A CONVEX OPTIMIZATION ALGORITHM FOR STABILIZING WHOLE-BODY MOTIONS OF HUMANOID ROBOTS

Juyong Park and Frank C. Park
School of Mechanical & Aerospace Engineering
Seoul National University
juyong.park@gmail.com, fcp@snu.ac.kr

Abstract This paper presents a convex optimization algorithm for the stabilization of whole-body motions for humanoid robots. Given a possibly unstable input reference trajectory in the form of joint and base frame acceleration time profiles, the algorithm determines, at each time step, the optimal acceleration profile subject to stability constraints on the zero-moment point (ZMP), and under the assumption that joint position and velocity measurements are available. We show that the above optimization can be formulated as a second-order cone programming (SOCP) problem, a well-known class of convex optimization problem that admits efficient interior-point algorithms. Simulations suggest that efficient whole-body stabilization is possible for typical humanoid structures, even in dynamic environments.

Keywords: Whole-body motion, humanoid robot, motion stabilization, convex optimization, second-order cone programming

1. Introduction

This paper addresses the problem of refining a reference whole-body motion for a humanoid robot such that it is stable, and closely approximates the reference motion. As a possible application scenario, one can envision a reference motion obtained from human motion capture data; directly transferring this data to a humanoid robot can easily result in an unstable motion, causing the robot to lose balance. We seek an online algorithm that optimally tracks the reference motion, in an appropriate least-squares sense, while ensuring stability as prescribed by the zero-moment point (ZMP) condition.

Since the early work of [Vukobratovic and Borovac, 2004] on dynamic stability and stabilization of legged robots using the zero moment point, many methods have been proposed for generation of stable motions for humanoid robots based on the ZMP notion. One of the first optimization-based approaches to whole-body motion stabilization is the work of Kagami et al. [Kagami et al., 2000], who develop an

J. Lenarčič and B. Roth (eds.), Advances in Robot Kinematics, 157–166.

algorithm to achieve dynamic balance for humanoid robots based on the least square method while satisfying desired ZMP and center-of-gravity (COG) constraints. The main disadvantage with this approach is that COG is constrained from moving along x and y axes in order to simplify the problem. Sugihara and Nakamura [Sugihara et al., 2002] propose an alternative COG optimization-based method for balancing a humanoid with two different loops; this algorithm assumes a stable reference trajectory that is subject to short-term disturbances, whereas our objective is to stably adjust an unstable trajectory. Park et al. [Park et al., 2005] propose a control algorithm for tracking a ZMP trajectory and the motions of some links which want to be controlled. This method is useful for real-time control, but the resulting ZMP tracking errors can lead to unstable motions. Related work preceding the above is [Nishiwaki et al., 2002], [Morisawa et al., 2005], which investigate pattern generation algorithms for stable motions.

In this paper we present a convex optimization algorithm for the stabilization of whole-body motions for humanoid robots. Given a (possibly unstable) input reference trajectory in the form of joint and base frame acceleration time profiles, the algorithm determines, at each time step, the optimal acceleration profile subject to stability constraints on the zero-moment point (ZMP), and under the assumption that state measurements (*i.e.*, the joint position and velocity) are available.

We show that the above optimization can be formulated as a second-order cone programming (SOCP) problem, which is a well-known class of convex optimization problems that admit efficient interior-point algorithms. Simulation results suggest that online whole-body stabilization is possible for typical humanoid structures, even in dynamic environments.

2. Problem Formulation

We assume an n degree-of-freedom humanoid robot with a tree topology structure, and define the optimization vector to be

$$x = \begin{bmatrix} \dot{V}_0 \\ \ddot{q} \end{bmatrix} \tag{1}$$

where $\dot{V}_0 \in se(3)$ denotes the generalized acceleration of the root link, and $\ddot{q} \in \Re^n$ denotes the joint acceleration vector. The ensuing constrained optimization problem is formulated as

$$\begin{aligned} \min \quad & \|x - x_{ref}\|^2 && (2) \\ \text{subject to} \quad & A_{eq}x = b_{eq} && (3) \end{aligned}$$

$$A_{ineq}x \leq b_{ineq} \tag{4}$$
$$f(x) \leq 0, \tag{5}$$

The kinematics and dynamics equations can be formulated as

$$\dot{V}_i = A_{\dot{V}_i}x + b_{\dot{V}_i} \tag{6}$$
$$\mathcal{F}_{ZMP} = M_{ZMP}x + C_{ZMP} \tag{7}$$

where $\dot{V}_i \in se(3)$ is the generalized acceleration of link i, and $\mathcal{F}_{ZMP}$ is the generalized force between the robot and environment, described in the coordinates whose origin is at the desired ZMP. $A_{\dot{V}_i}$, $b_{\dot{V}_i}$, M_{ZMP} and C_{ZMP} are functions of position and velocity. From these equations the linear equality constraint (3) follows:

$$A_{eq} \equiv \begin{bmatrix} A_{\dot{V}} \\ M_{ZMP,Mxy} \end{bmatrix} \quad b_{eq} \equiv \begin{bmatrix} \dot{V}_{const} - b_{\dot{V}} \\ -C_{ZMP,Mxy} \end{bmatrix} \tag{8}$$

where $A_{\dot{V}}$ and $b_{\dot{V}}$ are made by stacking $A_{\dot{V}_i}$ and $b_{\dot{V}_i}$ of some links whose motions need to be constrained (*e.g.,* foot link), and $M_{ZMP,Mxy}$ and $C_{ZMP,Mxy}$ denote the components of the moments about the x and y axes in M_{ZMP} and C_{ZMP}.

The linear inequality constraint (4) comes from the static constraint and joint bounds. The static constraint causes the motion to stay within a statically stable region, and can be approximated as a linear inequality. The nonlinear constraint comes from the friction constraint, which can be expressed as

$$f(x) \equiv -\mathcal{F}_{ZMP,fz} + \|\mathcal{F}_{ZMP,fxy}\|/\mu + |\mathcal{F}_{ZMP,Mz}|/\mu_n \tag{9}$$

where μ is the friction coefficient about the force in the xy plane, μ_n is the rotational friction coefficient about the z axis, $\mathcal{F}_{ZMP,fz}$ is the force along the z axis, $\mathcal{F}_{ZMP,fxy}$ is the force in the xy plane, and $\mathcal{F}_{ZMP,Mz}$ is the moment about the z axis of $\mathcal{F}_{ZMP}$. This problem can be recast as a second-order cone programming (SOCP) problem by introducing some additional variables as follows:

$$\begin{aligned} \min \quad & t_1 \\ \text{subject to} \quad & \|x - x_{ref}\| \leq t_1 \\ & \|M_{ZMP,fxy}x + C_{ZMP,fxy}\| \leq \mu t_2 \\ & |M_{ZMP,Mz}x + C_{ZMP,Mz}| \leq \mu_n t_3 \\ & 0 \leq -A_{eq}x + b_{eq} \\ & 0 \leq A_{eq}x - b_{eq} \\ & 0 \leq -A_{ineq}x + b_{ineq} \\ & 0 \leq M_{ZMP,fz}x + C_{ZMP,fz} - t_2 - t_3 \end{aligned} \tag{10}$$

Efficient interior point algorithms for SOCP problems have been developed in, *e.g.*, [Boyd and Vandenverghe, 2004], [Lobo et al., 1998], [MOSEK]. These algorithms are shown to have complexity $O(n^3)$, where n denotes the dimension of the optimization vector, and typically converge in around 50 iterations for very wide range of problem size. For typical humanoid robots where n is around 30, online solutions to the optimization are feasible.

3. Case Study

In this section, we evaluate the algorithm through simulations with a humanoid robot model with 25 degrees of freedom: six at each limb and one at the waist along the z axis as shown in Figure 1. To obtain natural reference motions we capture some human motions and transform them to those compatible with our humanoid robot model. Each optimization is performed using Matlab version 6.5, running on a Pentium 4 (1.8 GHz) personal computer.

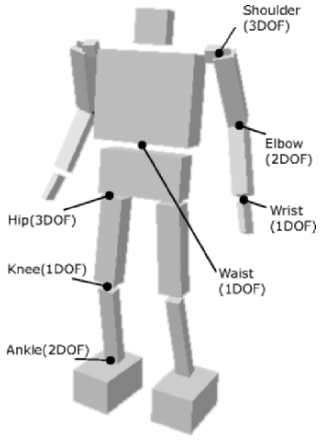

Figure 1. Humanoid robot model.

3.1 Whole-Body Motion Stabilization

Using the algorithm, we stabilize some motions obtained from motion capture data as shown in Table 1. Here beta refers the ratio between the support polygon and the region of the original motion's projected center of mass (CoM) distribution. In the case of beta = 0, the original motion's projected CoM is located at the center of the support polygon.

From the values of Beta and time per step, we can observe that the results are dependent on the complexity of the motion. If the motion is too complex or too fast for the robot, it cannot be stabilized at every

Table 1. Stabilization of given motions.

Motions	*Beta*	*Time/step (sec)*
Right leg raise forward	0.4	0.891918
Right kick forward	0.4	0.862366
Right leg raise aside	0	0.961157
Right kick aside($\times$0.95)	0	0.635591
Bartender Motion	0.1	0.629111
Easy dance($\times$0.9)	0	0.502345

moment. In this case from the values of Beta we can conclude that the motion along the x axis, which is the forward direction of the robot, is easier to stabilize; the characteristics of the robot model can be regarded as a cause of these results. The computational time per step for the optimization, coded in Matlab, is less than 1 second in all cases, clearly suggesting that online solutions are feasible.

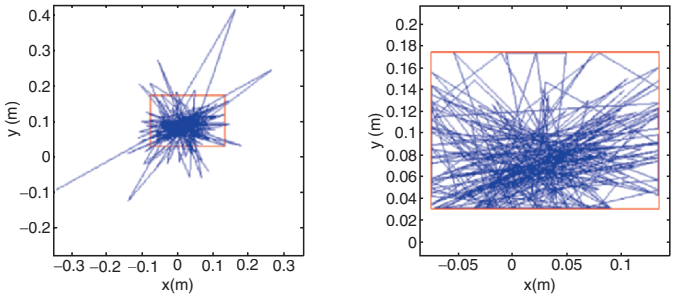

(a) ZMP trajectory before stabilization

(b) ZMP trajectory after stabilization

Figure 2. ZMP trajectories before and after stabilization.

The dynamic stability of the "right kick forward" motion before and after stabilization can be ascertained in Figure 2. The red square in the figure denotes the support polygon. The $+x$ and $+y$ directions are the forward and left directions of the robot. From the figures we can verify that the resulting motion has been stabilized.

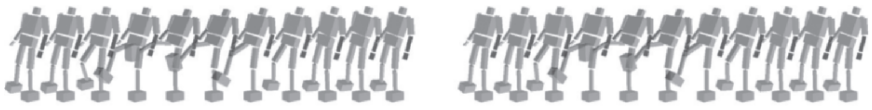

(a) Reference motion

(b) Stabilized motion

Figure 3. Motions before and after stabilization.

From Figure 3 we can see the motion after stabilization is similar to the reference motion. In the stabilized motion, the robot appears to stabilize itself much as a human would, by repeatedly overcompensating and reacting. While the reference motion looks reasonable in the figure, this motion is unstable and will cause the robot to fall over.

3.2 Posture Stabilization in Dynamic Environments

One of the important features of our proposed algorithm is that it can be applied online. The algorithm depends only on the states at each time, in this case the joint position and velocity measurements. One can thus achieve posture stabilization in a dynamically changing environment; in what follows we consider a simple standing posture, *i.e.*, $\theta = 0$.

Table 2. Posture stabilization in a dynamic environment.

Acceleration profile ($\lambda = 2\pi/t_f$)	α (m/s^2 or deg $/s^2$)	*Time/step (sec)*
$\alpha \sin \lambda t$	1	0.400948
(translation along x axis)	−0.7	0.460664
$-\alpha\lambda^2 \sin \lambda t$	6	0.336903
(rotation along y axis)	−5	0.334582

For the test cases of a dynamically varying environment, the standing posture is stabilized as shown in Table 2. α, a coefficient for the acceleration profile, is described in m/s^2 in the case of translational motions of the environment and deg $/s^2$ in the case of rotational motions. From the Table we see that the algorithm works satisfactorily in our sample dynamic environments.

From the ZMP and projected CoM trajectories in Figure 4 and 5, both dynamic and static stability of the motions can be examined. In both cases the reference motion, which is not dynamically stable, is stabilized. In Figure 5(b) and 5(d) we can see how the trajectory has been stabilized intuitively.

We can observe from Figures 6(a) and 6(b) that the reaction of the robot resembles that of a human. The motions shown Figure 6(a) resemble the reaction of human standing in a moving vehicle.

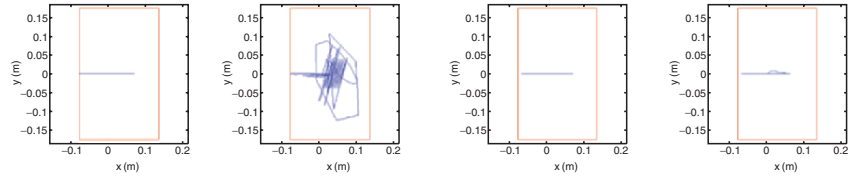

Figure 4. ZMP and projected CoM trajectories before and after stabilization of a standing posture in a translating moving environment when $\alpha = 1$.

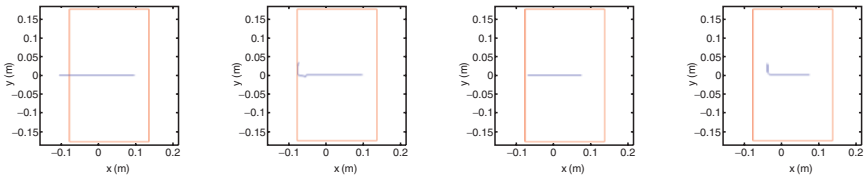

(a) ZMP trajectory before stabilization

(b) ZMP trajectory after stabilization

(c) Projected CoM trajectory before stabilization

(d) Projected CoM trajectory after stabilization

Figure 5. ZMP and projected CoM trajectories before and after stabilization of a standing posture in a rotating environment when $\alpha = 6$.

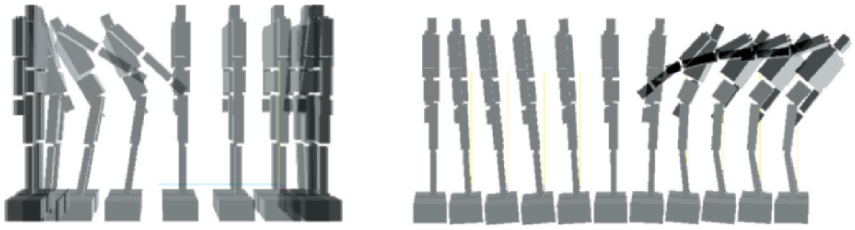

(a) Translating environment when $\alpha = 1$

(b) Rotating environment when $\alpha = 6$

Figure 6. Stabilized motions in a dynamic environment.

3.3 Motion Stabilization in a Dynamic Environment

From the former section, we can see the algorithm is applicable to the case of dynamic environments, and that the results resemble the natural reactions of a human. Based on these results we evaluate the performance

mance of the algorithm by attempting to stabilize a reference motion in a dynamic environment. The reference motion in this simulation is the "right kick forward" motion.

Table 3. Motion stabilization in a dynamic environment.

Acceleration profile ($\lambda = 2\pi/t_f$)	α (m/s^2 or deg $/s^2$)	*Time/step (sec)*
$\alpha \sin \lambda t$	0.6	0.752351
(translation along x axis)	−0.55	0.769769
$\alpha \sin \lambda t$	0.45	0.658306
(translation along y axis)	−0.45	0.805410
$-\alpha\lambda^2 \sin \lambda t$	4	0.862881
(rotation along y axis)	−2.5	0.676269
$-\alpha\lambda^2 \sin \lambda t$	2.5	0.730828
(rotation along x axis)	−2.5	0.882090

From the results of Table 3, we can see that motions can be successfully stabilized in various cases of dynamic environments. The obtained results are similar to the reference motion, and stable as shown in Figures 7 and 8.

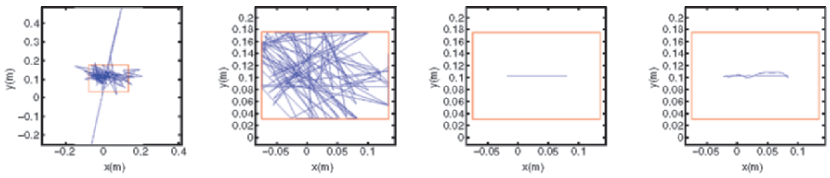

(a) ZMP trajectory before stabilization (b) ZMP trajectory after stabilization (c) Projected CoM trajectory before stabilization (d) Projected CoM trajectory after stabilization

Figure 7. ZMP and projected CoM trajectories before and after stabilization of "right kick forward" motion in a rotating environment when $\alpha = 4$.

(a) Reference motion (b) Stabilized motion

Figure 8. Motions before and after stabilization in a rotating environment about the y axis.

4. Conclusion

This paper has proposed an algorithm that stabilizes whole-body motions for humanoid robots, even in dynamically changing environments, via the solution of a convex optimization problem at each timestep. By expressing the stabilization constraints as linear equalities and inequalities in the acceleration vector, we show that the whole-body stabilization problem can be formulated as a second-order conic programming problem. The optimization depends only the current states (*i.e.,* position and velocity), and can be solved in nearly real-time for moderately complex humanoid models with up to thirty kinematic degrees of freedom.

References

Boyd, S. and Vandenverghe, L. (2004), *Convex Optimization*, Cambridge University Press.

Kagami, S., Kanehiro, F., Tamiya, Y., Inaba, M., and Inoue, H. (2000), AutoBalancer: An Online Dynamic Balance Compensation Scheme for Humanoid Robots, *Proceedings of International Workshop Algorithmic Foundations Robotics (WAFR)*, Hanover, Germany.

Kuffner Jr., J.J., Kagami, S., Nishiwaki, K., Inaba, M., and Inoue, H. (2002), Dynamically Stable Motion Planning for Humanoid Robots, *Autonomous Robots*, vol. 12, no. 1, pp. 105–118.

Lobo, M.S., Vandenverghe, L., Boyd, S., and Lebret, H. (1998), Applications of second-order cone programming, *Linear Algebra and its Applications*, vol. 284, pp. 193-228.

Morisawa, M., Kajita, S., Kaneko, K., Harada, K., Kanehiro, F., Fujiwara, K., and Hirukawa, H. (2005), Pattern Generation of Biped Walking Constrained on Parametric Surface, *Proceedings of IEEE International Conference on Robotics and Automation*, Barcelona, Spain.

MOSEK, http://www.mosek.com

Nishiwaki, K., Kagami, S., Kuniyoshi, Y., Inaba, M., and Inoue, H. (2002), Online Generation of Humanoid Walking Motion based on a Fast Generation Method of Motion Pattern that Follows Desired ZMP, *Proceedings of IEEE/RSJ International Conference on Intelligent Robots and Systems*, Lausanne, Switzerland.

Park, F.C., Bobrow, J.E., and Ploen, S.R. (1995), A Lie group formulation of robot dynamics, *International Journal of Robotics Research*, vol. 14, no. 6, pp. 609–618.

Park, F.C., Choi, J., and Ploen, S.R. (1999), Symbolic formulation of closed chain dynamics in independent coordinates, *Mechanism and Machine Theory*, vol. 34, no. 5, pp. 731–751.

Park, F.C., and Jo, G. (2004), Movement primitives and principal component analysis, *Advances in Robot Kinematics*, Dordrecht, Kluwer.

Park, J., Youm, Y., and Chung, Wan-K. (2005), Control of Ground Interaction at the Zero-Moment Point for Dynamic Control of Humanoid Robots, *Proceedings of IEEE International Conference on Robotics and Automation*, Barcelona, Spain.

Sugihara, T., and Nakamura, Y. (2002), Whole-body Cooperative Balancing of Humanoid Robot using COG Jacobian, *Proceedings of IEEE/RSJ International Conference on Intelligent Robots and Systems*, Lausanne, Switzerland.

Vukobratovic, M., and Borovac, B. (2004), Zero-Moment Point – Thirty Five Years of Its Life, *International Journal of Humanoid Robotics*, vol. 1, no. 1, pp. 157–173.

PARALLEL MECHANISMS FOR KNEE ORTHOSES WITH SELECTIVE RECOVERY ACTION

Raffaele Di Gregorio
Department of Engineering – University of Ferrara
Via Saragat, 1 – 44100 FERRARA, ITALY
rdigregorio@ing.unife.iti

Vincenzo Parenti-Castelli
DIEM – University of Bologna
Viale Risorgimento, 2 – 40136 BOLOGNA, ITALY
vincenzo.parenticastelli@mail.ing.unibo.it

Abstract A procedure to design new orthoses for the human knee articulation is presented. The design is based on knee equivalent parallel mechanisms whose links closely replicate the main knee anatomical structures; this makes it possible to design orthoses which can either re-establish the complete functionality of the knee articulation or, selectively, only the function of an injured knee structure.

Keywords: Articulation, knee, equivalent mechanisms, orthoses

1. Introduction

Recent studies showed that the human knee passive motion, i.e. the relative motion of femur and tibia under virtually unloaded conditions, can be replicated quite well by mechanisms (equivalent mechanisms) with one degree of freedom (dof). Early studies (Goodfellows and O'Connor, 1978; O'Connor et al., 1989; Fuss, 1989) proposed planar equivalent mechanisms, which replicate the knee motion in the sagittal plane. Later in (Wilson and O'Connor, 1997; Wilson et al., 1998; Parenti-Castelli and Di Gregorio, 2000; Di Gregorio and Parenti-Castelli, 2003, Ottoboni et al., 2005) spatial mechanisms were proposed that replicate the femur-tibia spatial motion.

The equivalent spatial mechanisms (ESMs) rely upon the clinical evidence that some fibers of the three main ligaments (the anterior cruciate (ACL), the posterior cruciate (PCL) and the medial collateral (MCL) ligament) are almost isometric during the knee flexion and guide

J. Lenarčič and B. Roth (eds.), Advances in Robot Kinematics, 167–176.

the knee motion while the femur and tibial condyles remain in mutual contact.

The proposed ESMs (Fig. 1) model the ACL, PCL and MCL by means of three binary links each joined to the tibia and to the femur by a universal joint (U) and a spherical pair (S) respectively, and consider two contact points between the condyle surfaces. Different approximations of the surfaces lead to different mechanisms. In (Wilson and O'Connor, 1997; Wilson et al., 1998), the femur condyles σ_1 and σ_2 are spherical and the tibia condyles π_1 and π_2 are planar (Fig. 1(a) mechanism ESM-1). In (Parenti-Castelli and Di Gregorio, 2000) both the femur (σ_1, σ_2) and tibia (δ_1, δ_2) condyles are spherical surfaces (Fig. 1(b) mechanism ESM-2), whereas in (Di Gregorio and Parenti-Castelli, 2003) all condyles are general smooth surfaces. In Fig. 1 points C_i, i = 1,2, and D_i, i = 1,2 are the centers of the spherical surfaces. The geometry of the ESMs was determined by slightly adjusting the measurements on the knee specimen taken from cadavers.

This paper focuses on the knee orthoses, i.e. on orthopedic devices which support or fully replace the functionality of the human knee (Thoumie et al., 2001).

The knee orthoses available on the market mainly try to replicate the femur-tibia motion by means of a revolute pair whose axis must be cleverly located (Schache et al., 2005). This is an empirical approach based on a rough approximation of the actual motion which is indeed a complex spatial motion. Up to now the ESMs have not been exploited to build orthoses. Orthoses based on ESMs could be devised either to re-establish the complete functionality of the knee articulation or selectively support (replace) specific structures of the knee which are injured or do not

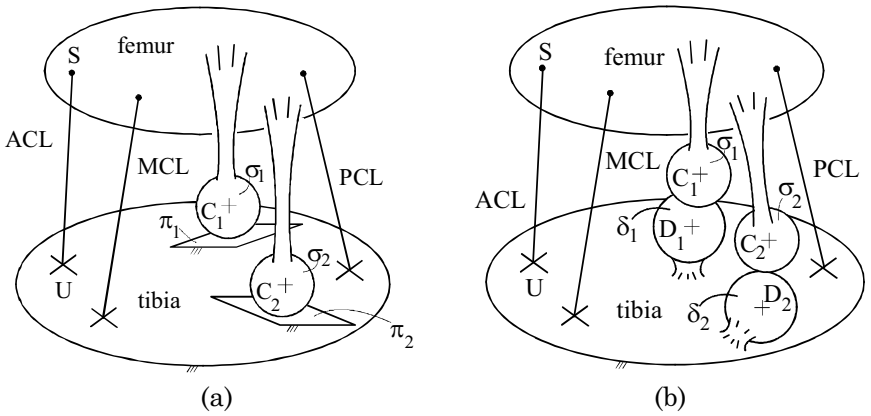

Figure 1. Equivalent spatial mechanisms of the knee: (a) ESM-1, (b) ESM-2.

work properly. The use of the ESMs for such applications requires efficient techniques both for the measurement of the knee motion and for the determination of the ESMs' geometry.

Taking as a reference for the orthosis design an equivalent mechanism of the knee passive motion could be considered as a limitation. However, this approximation is believed to be of the same order of other uncertainty factors such as, for instance, measurement errors, and therefore acceptable.

In this paper, the potentiality of using ESM-1 and/or ESM-2 as a basic reference for building orthoses for either a single patient or a class of them, is investigated. Issues on both the measurement of the tibia-femur spatial motion in the healthy knee and the determination of the corresponding ESM geometry are addressed. Finally, guidelines for the design of new orthosis architectures capable either for global or selective re-habilitation actions are presented.

2. Determination of the ESMs' Geometry

The synthesis of an ESM requires: (i) the data to compute the passive motion of the healthy knee and (ii) the topology of the ESM to synthesize. Then, synthesis algorithms can be applied to determine the ESM geometry that replicates the assigned knee motion.

2.1 Motion Data of the Healthy Knee

Measurement of the relative passive motion between the femur and tibia can be performed by several techniques (DellaCroce et al., 2005; Freeman and Pinskerova, 2005), provided external loads are somehow compensated. Compliant-adaptive and haptic devices can be also used to this purpose.

Data collection consistent with the anatomical parameters of the patients is another important issue. Indeed, direct measurements on the patient under treatment might not be possible for various reasons. The problem, however, can be solved in different ways. For instance, by measurements performed on the other healthy knee of the patient (if possible) or by adjusting data taken from a database of a class of people the patient belongs to (same age, sex, height, etc.).

In the first case it seems reasonable to reconstruct the motion of the damaged knee from the motion of the other knee under the hypothesis that the two motions are symmetric with respect to the sagittal plane. In other words a one-to-one correspondence between shin-thigh relative

poses of one leg is established with the shin-thigh relative poses of the other leg. The relationships that provide the motion data of one knee from those of the other can be explicitly written by using the notations of Fig. 2. In Fig. 2, O is a point of the sagittal plane. $\mathbf{n}$ is a unit vector perpendicular to the sagittal plane. B_i, are points embedded in the left thigh. B'_i, are points that are symmetric to B_i, with respect to the sagittal plane, and are fixed to the right thigh. A_i, are points embedded in the left shin. A'_i, are points that are symmetric to A_i, with respect to the sagittal plane, and are fixed to the right shin.

With these notations, the following vector relationships hold:

$$(\mathbf{A'}_i - \mathbf{O}) = [\mathbf{1}_3 - 2\,\mathbf{n}\,\mathbf{n}^T]\,(\mathbf{A}_i - \mathbf{O}) \quad (1)$$

$$(\mathbf{B'}_i - \mathbf{O}) = [\mathbf{1}_3 - 2\,\mathbf{n}\,\mathbf{n}^T]\,(\mathbf{B}_i - \mathbf{O}) \quad (2)$$

where $\mathbf{1}_3$ is the 3×3 identity matrix, and T is for transpose.

If the coordinates, in a Cartesian reference system, of the points A_i and B_i (A'_i and B'_i) are available from measurements on the healthy leg, the coordinates of the points A'_i and B'_i (A_i and B_i), in the same reference system, can be computed through relationships (1) and (2). Once the coordinates of shin points and of thigh points are known for each leg posture the shin-thigh relative pose parameters can be calculated and referred to a set of standard reference systems (Grood and Suntay (1983).

2.2 Synthesis of the ESM

The determination of the ESM's geometry may resort to the solution of a rigid body guidance problem. The shin (thigh) is the guided body, the thigh (shin) is the frame, the healthy knee motion data provides the path to generate, and the topology of the one-dof mechanism to synthesize is that of ESM-1 or ESM-2.

The solution of the body guidance problem can be addressed either (I) through techniques based on precision points, or (II) through optimization techniques. The first technique consists in imposing that the guided body assumes a finite number of assigned poses (precision points). The second one consists in the minimization of an objective function which somehow measures the "distance" between the path of the guided body and the path to generate.

2.2.1 Precision point techniques: The techniques based on precision points usually start writing, in all the assigned poses, the equations that express the constraint, on the guided body motion, due to each serial kinematic chain (leg) which connects the guided body to the frame. The resulting system has the geometric parameters of each leg as unknowns

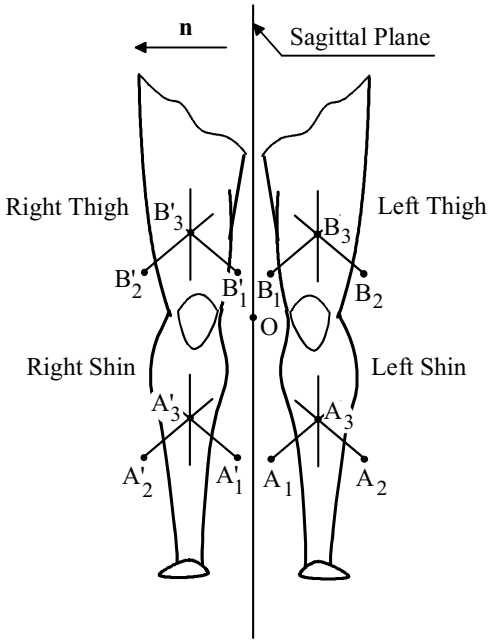

Figure 2. Notations.

and can be arranged into a number of decoupled subsystems equal to the number of the different leg topologies that appear in the one-dof mechanism to synthesize. Then, all the subsystems are separately solved.

Finally, the solutions of each subsystem are combined with the solutions of the other subsystems, according to the combinatorial calculus' rules, for generating the geometry of all mechanisms that make the guided body move through the assigned poses. If the number of assigned poses is sufficient to write a number of equations equal to the number of the unknown geometric parameters for each subsystem, a finite number of mechanism geometries will be obtained.

General methodologies for writing and solving the constraint equations of a wide number of leg topologies have been presented in (Chen and Roth, 1969a, 1969b; Nielsen and Roth, 1995; Wampler et al., 1990). Moreover, some papers (Innocenti, 1995; Liao and McCarthy, 2001; Di Gregorio, 2005) have found the analytic solution of leg topologies that are particularly interesting for the applications.

The ESM-1, has two different leg topologies (Fig. 1(a)): three legs of US topology and two sphere-plane contact pairs, each kinematically equivalent to a leg of RRS topology (R is for revolute pair, the spherical pair S is centered in C_1 (C_2) and the two revolute pairs have axes orthogonal to the plane π_1 (π_2). This, in fact, constrains the point C_1 (C_2) to move in a plane parallel to π_1 (π_2) at a distance equal to the radius of

the spherical condyle σ_1 (σ_2)). Analogously, the contact sphere-sphere in the ESM-2 (Fig. 1(b)) can be modeled by a leg of US topology with U and S pairs centered at points D_1 (D_2) and C_1 (C_2) respectively. Therefore, from a kinematic viewpoint, the ESM-1 and ESM-2 are one-dof fully parallel mechanisms with three legs of type US plus two legs of type RRS, and with five legs of type US respectively.

A US leg makes the distance between a point of the guided body and a point of the frame constant. Such a geometric constraint is analytically expressed by one scalar equation with seven geometric parameters: the three coordinates of the guided-body's point, the three coordinates of the frame's point and the constant distance between the two points. Thus, if seven poses are assigned, a system of seven equations in seven unknowns will result. This system was analytically solved (Innocenti, 1995) and reduced to the solution of a 20^{th} degree univariate polynomial equation. Therefore, the system admits 20 solutions in the complex field and at most 20 real solutions.

An RRS leg makes a point of one body move on a plane belonging to the other body. The analytic expression of this constraint is a scalar equation with six geometric parameters: the three coordinates of the point and the three parameters which identify the location of the plane (e.g. two components of the unit vector normal to the plane, and the signed distance of the plane from the origin of the Cartesian reference system). Thus, if six poses are assigned, a system of six equations in six unknowns will result. Such a system was analytically solved (Nielsen and Roth (1995) and reduced to the solution of a 10^{th} degree univariate polynomial equation. Therefore, it admits 10 solutions in the complex field and at most 10 real solutions.

Thus, by using the rules of the combinatorial calculus, the ESM-1 geometries that solve the body guidance problem are at most the combinations in triplets of the 20 solutions of the US leg by the combinations in couples of the 10 solutions of the RRS leg, that is:

$$\binom{20}{3}\binom{10}{2} = 51300 \tag{3}$$

The ESM-2 geometries that solve the same problem are at most the combinations in quintets of the 20 solutions of the US leg, that is:

$$\binom{20}{5} = 15504 \tag{4}$$

Despite the high number of complex solutions, the real solutions are in general much less than 20 for the US leg and less than 10 for the RRS leg. Therefore, the number of real mechanisms' geometries dramatically reduces, and, sometimes, there is no real geometry for one or the other mechanism topology. Moreover, the order that the assigned poses must follow to reproduce the knee motion and the smoothness of the path performed by the guided body between two successive assigned poses are not guaranteed.

2.2.2 Optimization techniques: In order to overcome these drawbacks, optimization techniques can be used. One technique to introduce an optimization criterion is to arbitrarily change one (or more than one) assigned pose until the path performed by the guided body is satisfactory. This approach reduces the number of precision points, but still maintains some of them.

In general, optimization techniques use the constraint equations in a great number (much more than 7) of poses, and calculate the geometric parameters (which now are much less than the equations) by minimizing an objective function related to the sum of the absolute values of the errors in each equation. For instance, one objective function might be the mean square root of the errors. These techniques allow the introduction of equations that take into account some limitations on the values of the searched geometric parameters. The main drawback of this approach is that the equations are nonlinear which makes the resulting optimization process cumbersome. Moreover, the computed mechanism geometry does not make the guided body pass through any assigned pose even though its path is near to the desired path.

3. Design of the Orthosis

Once a satisfactory geometry of ESM-1 or ESM-2 has been identified, the design stage of the orthosis starts. The design problem is now to manufacture the identified ESM by satisfying the following conditions: (a) all the kinematic chains, i.e. the legs of type US and RRS must be external to the patient's knee; (b) the joints of the legs must be simple and free of problems like jamming; (c) the workspace of each leg must contain the path to generate; (d) when the orthosis is applied to the patient's leg, the patient should still be able to wear trousers.

All legs in the ESM-1 and ESM-2 are of type US or RRS, that is of type 5R if considering that a U joint and an S spherical pair are in practice kinematically equivalent, respectively, to an RR chain with the two R axes intersecting each other and to an RRR chain with the three R axes intersecting at one common point. Figures 3(a) and 3(b) show a schematic

of a 5R leg kinematically equivalent to a US leg (Fig. 3(a)) and to an RRS leg (Fig. 3(b)) respectively.

A 5R leg can satisfy all the above said conditons. Indeed, condition (a) is easily satisfied since the hardware of the revolute pairs can be arbitrarily located along their axes. Condition (b) is satisfied because the revolute pairs do not undergo jamming. Condition (c) can be satisfied by suitably sizing the geometric parameters of the 5R chain. Finally, when a US leg is manufactured, the leg hardware can be confined into a thin shell located near the patient's knee. Moreover, when an RRS leg is manufactured, the planar RR chain – that reproduces the motion of the condylar contact point in the 5R leg – in the worst conditions (considering that experimental data reported in (Wilson et al., 1998) show that the condylar contact point moves inside a rectangle whose sides are shorter than 40 mm) does not occupy regions farther than 25 mm from the patient's knee. Therefore, condition (d) can be satisfied too.

The endings of each 5R leg are connected to rigid rings fixed to the thigh (guided body in Figures 3(a) and 3(b)) and to the shin (frame in Figures 3(a) and 3(b)) respectively by means of braces (Fig. 3 (c)).

It is worth noting that for both ESM-1 and ESM-2, each 5R leg has an anatomical structure as a direct counterpart: namely a ligament or a condylar surface contact pair. Therefore, when only one or a few specific anatomical structures of the knee must be replicated by the orthosis, the ESM synthesis can be focused on the corresponding 5R legs of the mechanism, so that the synthesized ESM fairly reproduces the motion constraints due to those structures. The correspondence between the legs' geometry and the articular structures to be replaced can be checked through radiographs before the orthosis is sized. After such a

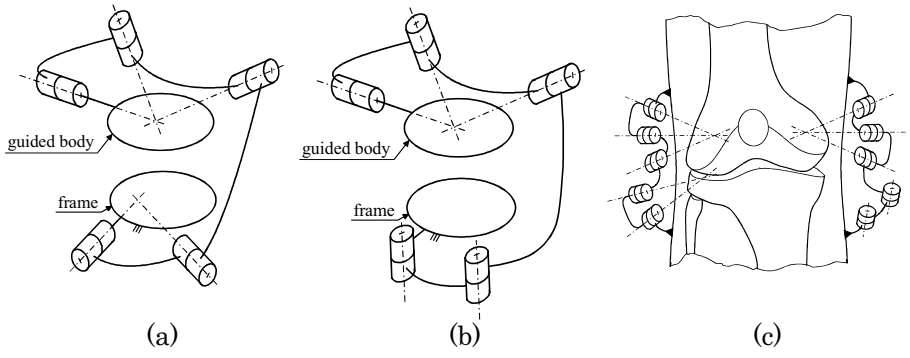

Figure 3. 5R kinematic chains: (a) US leg (sphere-sphere contact), (b) RRS leg (sphere-plane contact), (c) 5R legs applied to the knee.

correspondence is verified, an orthosis, which contains only the legs corresponding to the damaged structures of the knee, can be manufactured. This opportunity is particularly appealing for the post-reconstruction therapy of many knee traumas. For instance, the reconstruction of a knee ligament is frequent among players of many popular sports, and ligament breakdowns occur both to professional players and to amateurs.

4. Conclusions

A procedure has been presented that leads to design novel knee orthoses inspired by equivalent spatial mechanisms (ESM) proposed recently in the literature for replicating the human knee passive motion.

In particular, in-vivo measurement issues of knee motion as well as techniques for the synthesis of ESM have been addressed. Finally, guidelines for the design of new orthoses that can reestablish either the complete functionality of the knee articulation or selectively only the functionality of the injured knee structures have been presented.

Acknowledgments

Fruitful discussions with Federico Corazza and Alberto Leardini at IOR (Orthopedic Rizzoli Institute) are gratefully acknowledged.

This paper has been supported by funds of the Italian MIUR.

References

Chen, P. and Roth, B., 1969a, "A unified theory for the finitely and infinitesimally separated position problems of kinematic synthesis," *ASME J. of Engineering for Industry*, Vol. 91B, pp. 203-208.

Chen, P. and Roth, B., 1969b, "Design equations for the finitely and infinitesimally separated position synthesis of binary links and combined link chains," *ASME J. of Engineering for Industry*, Vol. 91B, pp. 209-219.

DellaCroce, U., Leardini A., Chiari L., and Cappozzo, A., 2005, "Human movement analysis using strereophotogrammetry. Part 4: assessment of anatomical landmark dislocation and its effects on joint kinematics," *Gait & Posture*, 21, pp. 226-237.

Di Gregorio, R., 2005, "On the polynomial solution of the synthesis of five plane-sphere contacts or PPS chains that guide a rigid body through six assigned poses," *Proc. of the 2005 ASME Design Engineering Technical Conferences*, Long Beach, California (USA), Paper No: DETC2005-84788.

Di Gregorio, R. and Parenti-Castelli, V., 2003, "A Spatial Mechanism with Higher Pairs for Modelling the Human Knee Joint," *ASME Journal of Biomechanical Engineering*, Vol. 125, Issue 2 (April 2003), pp. 232-237.

Freeman, M.A.R., and Pinskerova, V., 2005 "The movement of the normal tibio-femoral joint," *Journal of Biomechanics*, 38, pp. 197-208.

Fuss, S.K., 1989, "Anatomy of the cruciate ligaments and their function in extension and flexion of the human knee joint," *American Journal of Anatomy*, 184, pp. 165-176.

Goodfellows, J.D., and O'Connor, J.J., 1978, "The mechanics of the knee and prosthesis design," *Journal of Bone Joint Surgery* [Br] 60-B, pp. 358-369.

Grood, E.S., and Suntay, W. J., 1983, "A joint coordinate system for the clinical description of three-dimensional motion: application to the knee," *ASME Journal of Biomechanical Engineering*, Vol. 105, pp. 136-144.

Innocenti, C., 1995, "Polynomial solution of the spatial Burmester problem," *ASME J. of Mechanical Design*, Vol. 117, No. 1, pp. 64-68.

Liao, Q. and McCarthy, J.M., 2001, "On the seven position synthesis of a 5-SS platform linkage," *ASME J. of Mechanical Design*, Vol. 123, No. 1, pp. 74-79.

Nielsen, J. and Roth, B., 1995, "Elimination methods for spatial synthesis," Computational Kinematics, J.P. Merlet and B. Ravani eds., Vol. 40 of *Solid Mechanics and its Applications*, pp. 51-62, Kluwer Academic Publishers.

O'Connor, J.J., Shercliff, T.L., Biden, E., and Goodfellow, J.W., 1989, "The geometry of the knee in the sagittal plane," *Proceedings, institute of Mechanical Engineering* Part H. *Journal of Engineering in Medicine*, 203, pp. 223-233.

Ottoboni, A., Parenti-Castelli, V., and Leardini, A., 2005, "On the limits of the articular surface approximation of the human knee passive motion models," *Proc. of the XVII AIMETA Congress*, Florence, Italy, Paper No: 228.

Parenti-Castelli, V., and Di Gregorio, R., 2000,"Parallel mechanisms apply to the human knee passive motion simulation,"*Advances in Robot Kinematics*, eds., Lenarčič J. and Stanisic M. M., Kluwer Academic Publishers, Netherlands, ISBN 0-7923-6426-0, pp. 333-344.

Parenti-Castelli, V., Leardini, A., Di Gregorio, R., and O'Connor, J.J., 2004, "On the modeling of passive motion of the human knee joint by means of equivalent planar and spatial parallel mechanisms," *Autonomous Robots*, Vol. 16, issue 2 (March 2004), pp. 219-232.

Schache, A. G., Baker, R., and Lamoreux L.W., 2005, "Defining the knee join flexion-extension axis for purposes of quantitative gait analysis: An evaluation of methods," *Gait & Posture*, in press.

Thoumie, P., Sautreuil, P., and Mevellec, E., 2001, "Orthèses de genou. Évaluation de l'efficacité clinique à partir d'une revue de la littérature," *Ann Readaptation Med Phys*, 44, pp. 567-580.

Wampler, C.W., Morgan, A.P., and Sommese, A.J., 1990, "Numerical continuation methods for solving polynomial systems arising in kinematics," *ASME J. of Mechanical Design*, Vol. 112, No. 1, pp. 59-68.

Wilson, D.R., and O'Connor, J.J., 1997, "A three-dimensional geometric model of the knee for the study of joint forces in gait," *Gait and Posture*, 5, pp. 108-115.

Wilson, D.R., Feikes, J.D., and O'Connor, J.J., 1998. "Ligament and articular contact guide passive knee flexion," *Journal of Biomechanics*, 31, pp. 1127-1136.

MODELING TIME INVARIANCE IN HUMAN ARM MOTION COORDINATION

Satyajit Ambike
The Ohio State University, Department of Mechanical Engineering
Columbus, OH USA
ambike.1@osu.edu

James P. Schmiedeler
The Ohio State University, Department of Mechanical Engineering
Columbus, OH USA
schmiedeler.2@osu.edu

Abstract This paper proposes that two-degree-of-freedom Curvature Theory provides a mathematical representation of the kinematics of planar human arm motion coordination. Arguing that an internal inverse, time-invariant kinematic model is fundamental to human motor coordination, Curvature Theory provides a concise, efficient mapping of a desired output trajectory geometry to the joint angles' instantaneous speed ratios. If the speed ratios for a motion are learned through experience, one can subsequently execute the motion at different speeds. This formulation is consistent with a structure for the internal model that the central nervous system may use as a feed-forward element for planning motions. A simple example is presented to illustrate how the model works.

Keywords: Human motor coordination, arm kinematics, Curvature Theory

1. Introduction

A well-recognized theory in modern motor control research suggests that through experience, the central nervous system (CNS) builds and maintains internal models of the motor apparatus and external world (Atkeson, 1989). Experimental work (Flanagan et al., 1999 and Lacquaniti *et al.*, 1982) shows that separate internal kinematic and dynamic models are consistent with typical behavior. Further evidence indicates that the internal kinematic model separates time-invariant and time-dependent aspects of motion. Hand path shape in reaching, often a straight line, is independent of trajectory speed, and tangential hand velocity has a single, bell-shaped curve regardless of magnitude (Atkeson & Hollerbach, 1985, Morasso, 1981, Soechting & Lacquaniti, 1981). Fixed relations between instantaneous elbow and shoulder angular positions

J. Lenarčič and B. Roth (eds.), Advances in Robot Kinematics, 177–184.

are observed across a range of tasks and speeds (Lacquaniti & Soechting, 1982, Soechting & Lacquaniti, 1981). Based on these observed time invariances in human movement, this paper theorizes that the fundamental internal model employed for motor coordination is based on a geometric mapping of position and higher order motion properties. While significant research has focused on explaining observed hand trajectories with dynamics-based theories (Hollerbach & Flash, 1982), this work proposes that an internal inverse dynamic model is an additional layer of a unified, coherent model for motion planning whose foundation is kinematic. The separation offers computational benefits compared to an exclusively dynamic model in which the mappings for geometrically equivalent motions would be stored completely separate from one another.

Consider that a pianist sight-reading a piece of new music plays the notes more slowly than prescribed by the piece, but in proper relation to one another. At this stage, he is learning the kinematic geometry of the finger motion – represented in a mathematical model by the instantaneous speed ratios. Experimental studies show that the ratios between interstroke intervals in piano playing are in fact independent of duration (Soechting *et al.*, 1996). After gaining experience with the piece, he "plays back" the same kinematic finger geometry at increasing speed until mastering it at the proper tempo. When teaching the piece to someone else, though, the pianist can still demonstrate it at slower speeds because his CNS has learned the piece by separating the time-invariant and time-dependent aspects of the motion.

Roth, 2004 showed how to derive geometric properties from time-based planar 1-DOF motions and to determine all time-dependent motions that generate trajectories with identical geometric properties. His work inspired the idea introduced in this paper that Curvature Theory offers a compact mathematical representation of the internal inverse kinematic model humans use for motor coordination. The focus here, though, is 2-DOF motion, so the formulation follows closely Lorenc *et al.*, 1995, who presented a general form of planar 2-DOF Curvature Theory and applied it to trajectory generation in planar path tracking systems. While they suggested use of a processed video image to calculate the instantaneous speed ratios required for coordination of robotic systems, humans are more likely to "learn" the speed ratios required to execute a desired motion over the course of several motions. Furthermore, the CNS likely applies the internal kinematic model for motion planning in a feed-forward control loop augmented by a feedback loop that allows adaptation to novelty in the current situation (Atkeson, 1989).

This paper applies 2-DOF Curvature Theory to be a mathematical description of how a human's internal kinematic model could be built

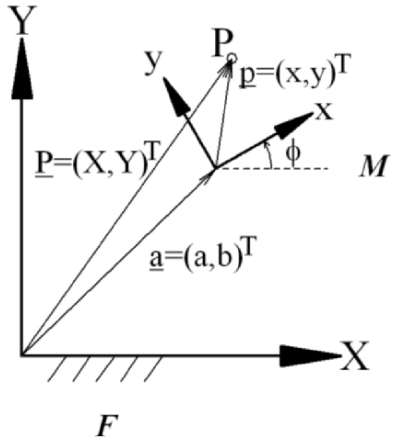

Figure 1. General planar motion of a point P in moving frame M.

over the course of several hand motions. This building of the internal model may be how the CNS learns to coordinate arm movement. The motivation for the work is ultimately to achieve a better understanding of human motor coordination, with potential applications such as enhancing rehabilitation for stroke patients.

2. Internal Kinematic Model

The internal kinematic model for planning multi-joint arm movements is an inverse model that maps desired hand motion to required shoulder and elbow motions. Time invariance provides for model compactness, which should reduce the CNS's computational load. The proposed mathematical representation of this model assumes that wrist motion is decoupled from elbow and shoulder motions to separate the problems of positioning and orienting the hand, which has been observed in human reaching (Lacquaniti & Soechting, 1982). The formulation also assumes that motion planning takes place in the visual coordinate system defining the output space and sensing takes place in a kinesthetic coordinate system defining the control space (Soechting & Lacquaniti, 1981, Morasso, 1981). The model focuses on planar reaching motions, which involve only the 2 DOF's associated with positioning the wrist in the plane.

Mathematical Formulation. Frame M moving in a plane with respect to fixed frame F is shown in Fig. 1. The coordinates of the

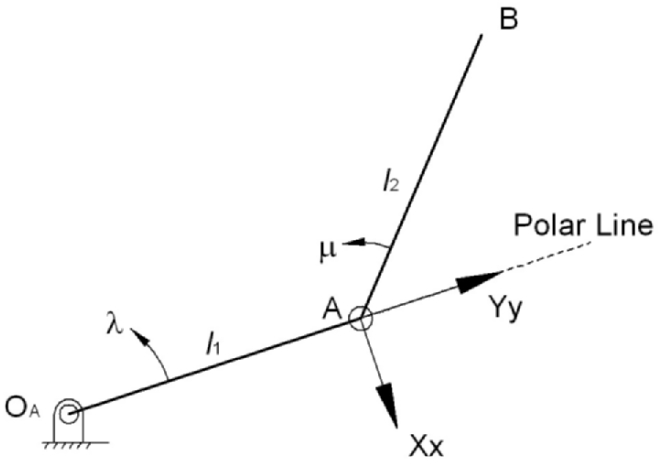

Figure 2. Planar RR representation of the human arm with the canonical coordinate system located at the elbow.

origin of M in F are (a, b), and ϕ is the orientation of M with respect to F. Point P has coordinates (x, y) in M and (X, Y) in F, related as,

$$\begin{Bmatrix} X \\ Y \end{Bmatrix} = \begin{bmatrix} \cos\phi & -\sin\phi \\ \sin\phi & \cos\phi \end{bmatrix} \begin{Bmatrix} x \\ y \end{Bmatrix} + \begin{Bmatrix} a \\ b \end{Bmatrix}. \tag{1}$$

If point P is the wrist center, M is fixed in the forearm and F is fixed in the trunk for purposes of positioning the hand relative to the body. An additional transformation would be required to relate these frames to the environment since the trunk-fixed and visual coordinate systems do not coincide (Schmiedeler *et al.*, 2004). In Fig. 2, the arm is represented by the two-link RR open chain in which O_A and A indicate the shoulder and elbow joints, respectively. The angular displacements of the upper arm and forearm are λ and μ, and the motion variables are functions of these: $a = a(\lambda, \mu), b = b(\lambda, \mu), \phi = \phi(\lambda, \mu)$. Without loss of generality, the depicted position is taken to be the zero position. Using a trailing subscript to indicate a derivative evaluated in the zero position $\Big($i.e. $X_\lambda = \frac{\partial X}{\partial \lambda}|_{\lambda,\mu=0}$, $Y_{\lambda\mu} = \frac{\partial^2 Y}{\partial \lambda \partial \mu}|_{\lambda,\mu=0}\Big)$, the second-order Taylor series expansion of Eq. 1 about the zero position is,

$$\begin{Bmatrix} X \\ Y \end{Bmatrix} = \begin{Bmatrix} x + X_\lambda\lambda + X_\mu\mu + \frac{1}{2}(X_{\lambda\lambda}\lambda^2 + 2X_{\lambda\mu}\lambda\mu + X_{\mu\mu}\mu^2) \\ y + Y_\lambda\lambda + Y_\mu\mu + \frac{1}{2}(Y_{\lambda\lambda}\lambda^2 + 2Y_{\lambda\mu}\lambda\mu + Y_{\mu\mu}\mu^2) \end{Bmatrix}, \tag{2}$$

where $X_\lambda = a_\lambda - y\phi_\lambda$, $Y_{\lambda\mu} = b_{\lambda\mu} + x\phi_{\lambda\mu} - y\phi_\lambda\phi_\mu$, etc. The time dependent

motion of point P with respect to F is obtained by differentiating Eq. 2 with respect to time.

$$\left\{ \begin{array}{c} \dot{X} \\ \dot{Y} \end{array} \right\} = \left\{ \begin{array}{c} (-y\phi_\lambda + a_\lambda)\dot{\lambda} + (-y\phi_\mu + a_\mu)\dot{\mu} \\ (x\phi_\lambda + b_\lambda)\dot{\lambda} + (x\phi_\mu + b_\mu)\dot{\mu} \end{array} \right\}, \tag{3}$$

$$\left\{ \begin{array}{c} \ddot{X} \\ \ddot{Y} \end{array} \right\} = \left\{ \begin{array}{c} [-y\phi_\lambda + a_\lambda]\ddot{\lambda} + [-y\phi_\mu + a_\mu]\ddot{\mu} \\ +[-x(\phi_\lambda\dot{\lambda} + \phi_\mu\dot{\mu})\phi_\lambda - y(\phi_{\lambda\lambda}\dot{\lambda} + \phi_{\lambda\mu}\dot{\mu}) + a_{\lambda\lambda}\dot{\lambda} + a_{\lambda\mu}\dot{\mu}]\dot{\lambda} \\ +[-x(\phi_\lambda\dot{\lambda} + \phi_\mu\dot{\mu})\phi_\mu - y(\phi_{\mu\mu}\dot{\mu} + \phi_{\lambda\mu}\dot{\lambda}) + a_{\mu\mu}\dot{\mu} + a_{\lambda\mu}\dot{\lambda}]\dot{\mu} \\ \\ [x\phi_\lambda + b_\lambda]\ddot{\lambda} + [x\phi_\mu + b_\mu]\ddot{\mu} \\ +[x(\phi_{\lambda\lambda}\dot{\lambda} + \phi_{\lambda\mu}\dot{\mu}) - y(\phi_\lambda\dot{\lambda} + \phi_\mu\dot{\mu})\phi_\lambda + b_{\lambda\lambda}\dot{\lambda} + b_{\lambda\mu}\dot{\mu}]\dot{\lambda} \\ +[x(\phi_{\mu\mu}\dot{\mu} + \phi_{\lambda\mu}\dot{\lambda}) - y(\phi_\lambda\dot{\lambda} + \phi_\mu\dot{\mu})\phi_\mu + b_{\lambda\mu}\dot{\lambda} + b_{\mu\mu}\dot{\mu}]\dot{\mu} \end{array} \right\}. \tag{4}$$

The simplest description of the motion is obtained in the canonical coordinate system (Bottema & Roth, 1979), which is desirable to provide for model compactness. The canonical system satisfies three conditions: 1) frames M and F are instantaneously coincident in the zero position, 2) the Yy axes are aligned with the polar line, which in this case passes through the shoulder and elbow joints, and 3) the instantaneously coincident origins of M and F are placed on the polar line such that at least one of the three second order Taylor coefficients $b_{\lambda\lambda}$, $b_{\lambda\mu}$, and $b_{\mu\mu}$ has zero magnitude. The remaining non-zero Taylor coefficients are the instantaneous invariants. With the canonical coordinate system located at the elbow, as shown in Fig. 2, the instantaneous invariants for the planar RR mechanism are $a_\lambda = -l_1$, $\phi_\lambda = 1$, $\phi_\mu = 1$, and $b_{\lambda\lambda} = -l_1$.

3. Discussion

According to the proposed model, the instantaneous invariants obtained here mathematically would be "learned" by the CNS. The CNS would likely use information gathered over a substantial period of time and resulting from many hand motions to determine the invariants. This can be represented mathematically as the generation of Eqs. 3 and 4 multiple times over several hand motions and then solved simultaneously for the invariants. This activity would be a continuous process when an individual is growing since the length of the upper arm l_1 changes. Even later, refinement in the values of the invariants would be anticipated, given that data obtained by the CNS is likely to contain noise.

The CNS's planning and control of a desired new hand motion can be explained in terms of the present model as follows. A target toward which the hand will reach is typically defined in the visual coordinate

system, and the corresponding hand path, typically a straight line, is planned in the same coordinate system. The instantaneous geometry of the path is thus defined, and the CNS maps the path geometry to instantaneous first and second order speed ratios of the arm n and n', where $n = \frac{\dot{\lambda}}{\dot{\mu}}$ and $n' = \frac{\ddot{\lambda}}{\ddot{\mu}}$. Lorenc *et al.*, 1995 show that the speed ratios can be expressed in terms of the geometry of the path,

$$n = -\frac{a_\lambda - \theta_\lambda y_p}{a_\mu - \theta_\mu y_p} \tag{5}$$

$$n' = n' \left(a_\lambda, a_\mu, \theta_\lambda, \theta_\mu, a_{\lambda\lambda}, a_{\mu\mu}, a_{\lambda\mu}, \theta_{\lambda\lambda}, \theta_{\mu\mu}, \theta_{\lambda\mu}, n, (PJ)_x\right), \tag{6}$$

where y_p is the distance from the origin to the instant center and $(PJ)_x$ is the projection of the inflection circle's diameter through the instant center onto the Xx axes. For the planar RR mechanism in Fig. 2, the speed ratios are $n = -\frac{y_p + l_1}{y_p}$ and $n' = \frac{(1+n)^3 (PJ)_x}{l_1}$.

The CNS does not measure y_p and $(PJ)_x$. Rather, these geometric quantities represent in the present formulation the mapping that the CNS learns through experience and updates with each new movement. Once the speed ratios are obtained, the joint angles λ and μ can be controlled using the second order Taylor series,

$$\mu = n\lambda + \frac{1}{2} n' \lambda^2, \tag{7}$$

or its inverse that expresses λ as a function of μ. Regardless, the two parameters are coordinated to instantaneously achieve the desired hand motion. Further, the desired path can be traversed at any speed, as $\dot{\lambda}$ and $\ddot{\lambda}$ can be chosen arbitrarily and $\dot{\mu}$ and $\ddot{\mu}$ can be computed (or vice versa) for the same speed ratios n and n'.

Since only second order coordination of λ and μ is presented here, the model would require regular recalculation of speed ratios to accurately track a desired hand path. As the hand moves away from the position in which the speed ratios were calculated, the error in path-tracking increases. Higher order coordination would reduce the error and require less frequent updates for accurate tracking, suggesting a computational trade-off between this approach and the regular updating of lower order coordination. To detect these errors, visual and/or kinesthetic feedback is required and would generally be expected throughout the course of the motion. When an unanticipated disturbance is encountered, the desired instantaneous path may be entirely redefined. The speed ratios can be obtained again, with the motion shifting toward the new target.

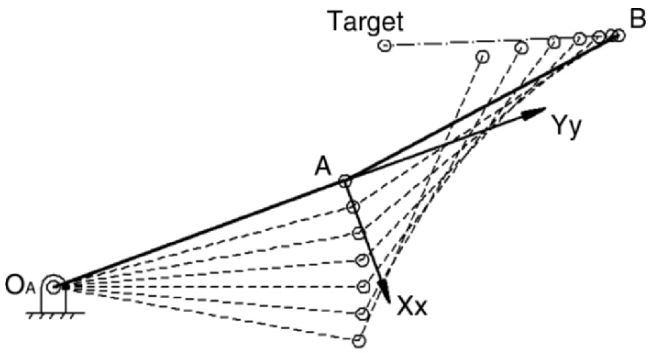

Figure 3. Example of motion planning showing desired and actual hand paths.

4. Numerical Example

As an example, the arm segment lengths are taken to be $l_1 = l_2 = 500$ mm. An arbitrary zero position of the arm-segments in which the forearm is at an angle of 98 degrees relative to the Xx axis is shown in Fig. 3. The target location expressed in the canonical coordinate system is (–183.4 mm, 134.8 mm), so the desired straight-line hand path toward the target is 378 mm long. The instant center and inflection circle are constructed, but not shown in the figure, to obtain $y_p = 473.2$ mm and $(PJ)_x = -367.4$ mm, along the Yy and Xx axes, respectively. Eqs. 5 and 6 yield speed ratios of $n = -2.06$ and $n' = 0.87$, and Eq. 7 is then used to compute angles λ and μ. In Fig. 3, λ is plotted in 5-degree increments to illustrate the motion. Near the zero position, the hand motion closely tracks the desired path, but after λ has been incremented by 30 degrees, the hand position deviates from the path by 24.5 mm. This highlights the need for regular feedback to update the motion planning accomplished with the internal kinematic model.

5. Conclusion

This work applies an established formulation of 2-DOF Curvature Theory to the coordination of planar human arm motion. The result is a concise and computationally efficient model explaining the kinematics of planar arm motion. The model requires knowledge of the instantaneous invariants and the geometry of the desired path. The invariants are the same for any planar motion, and the path tangent and curvature represent the novelty in each situation. Mathematically, the invariants are formulated, and the path properties measured. By analogy, the CNS must learn through experience the mapping between the trajectory

tangent and curvature in the output space (hand path and curvature) and the control space (first and second order joint angle speed ratios) that is mathematically defined by these geometric quantities. Since the mapping is time invariant, a motion can be repeated at any speed. The model also offers an explanation as to how a feed-forward and a feedback system may be employed by the CNS to coordinate the arm motion with limited computational effort.

6. Acknowledgements

This material is based upon work supported in part by the National Science Foundation under Grant No. #0546456 to J. Schmiedeler.

References

Atkeson, C.G. (1989), Learning arm kinematics and dynamics, *Annual Review of Neuroscience*, vol. 12, pp. 157–183.

Atkeson, C.G., & Hollerbach, J.M. (1985), Kinematic features of unrestrained arm movements, *Journal of Neuroscience*, vol. 5, no. 9, pp. 2318–2330.

Bottema, O., & Roth, B. (1979), *Theoretical Kinematics*, Amsterdam, North Holland.

Flanagan, J.R., Nakano, E., Imamizu, H., Osu, R., Yoshiyoka T., & Kawato, M. (1999), Composition and decomposition of internal models in motor learning under altered kinematic and dynamic environments, *Journal of Neuroscience*, vol. 19, no. 20, RC34.

Hollerbach, J.M., & Flash, T. (1982), Dynamic interactions between limb segments during planar arm movement, *Biological Cybernetics*, vol. 44, pp. 67–77.

Lacquaniti, F., & Soechting, J.F. (1982), Coordination of arm and wrist motion during a reaching task, *Journal of Neuroscience*, vol. 2, no. 4, pp. 399–408.

Lacquaniti, F., Soechting, J.F., & Terzuolo C. (1982), Some factors pertinent to the organization and control of arm movements, *Brain Research*, vol. 252, pp. 394–397.

Lorenc, S.J., Stanišić, M.M., & Hall, A.S. (1995), Application of instantaneous invariants to the path tracking control problem of planar two degree-of-freedom systems: A singularity free mapping of trajectory geometry, *Mechanisms and Machine Theory*, vol. 30, no. 6, pp. 883–896.

Morasso, P. (1981), Spatial control of arm movements, *Experimental Brain Research*, vol. 42, pp. 223–237.

Roth, B. (2004), Time-invariant properties of planar motion, *On Advances in Robot Kinematics*, Dordrecht: Kluwer Academic Publishers, pp. 79–88.

Schmiedeler, J.P., Stephens, J.J., Peterson, C.R., & Darling, W.G. (2004), Human hand movement kinematics and kinesthesia, *On Advances in Robot Kinematics*, Dordrecht: Kluwer Academic Publishers, pp. 163–170.

Soechting, J.F., Gordon, A.M., & Engel, K.C. (1996), Sequential hand and finger movements: Typing and piano playing, In: Bloedel, J.R., Ebner, T.J. and Wise, S.P., eds. *Acquisition of motion behavior in vertibrates*, Cambridge, MA: MIT Press, pp. 343–359.

Soechting, J.F., & Lacquaniti, F. (1981), Invariant characteristics of a pointing movement in man, *Journal of Neuroscience*, vol. 1, no. 7, pp. 710–720.

ASSESSMENT OF FINGER JOINT ANGLES AND CALIBRATION OF INSTRUMENTAL GLOVE

Mitja Veber
University of Ljubljana, Faculty of Electrical Engineering
Laboratory of Robotics and Biomedical Engineering
mitja.veber@robo.fe.uni-lj.si

Tadej Bajd
University of Ljubljana, Faculty of Electrical Engineering
Laboratory of Robotics and Biomedical Engineering
tadej.bajd@robo.fe.uni-lj.si

Marko Munih
University of Ljubljana, Faculty of Electrical Engineering
Laboratory of Robotics and Biomedical Engineering
marko.munih@robo.fe.uni-lj.si

Abstract The aim of the paper is to present a method for assessment of joint angles in human fingers. The method is based on an optical tracking device and a kinematical model of human hand. The method was validated against already proposed optimization methods for assessment of joint centers of rotation. The segment lengths acquired from statistical anthropometry and those from the calculated centers of rotation do not differ notably. The joint angles estimated by our method and those from centers of rotation, are also comparable. The proposed method requires small number of markers which makes it suitable for the calibration of an instrumental glove. The results of the glove calibration show that its accuracy is limited to ±5º.

Keywords: Hand modeling, assessment of joint angles, instrumental glove calibration

1. Introduction

Understanding of kinematics of grasping is a demanding task. Although first anthropomorphic hands were designed more than two decades ago, control of many degrees of freedom to carry out specific task remains to be a challenging problem.

At the moment a generally accepted system for accurate noninvasive assessment of hand kinematics is not available. A well established

J. Lenarčič and B. Roth (eds.), Advances in Robot Kinematics, 185–192.

technique, which does not hinder the movement as exoskeletons do, includes reflective markers, which are placed over bony landmarks. Due to its accuracy, the method can be taken as a reference. Modeling of upper extremity or finger kinematics is performed by using rigid bodies, which are linked together with the ball or hinge joints. In the optimization methods (Halvorsen et al., 1999, Zhang et al., 2003), it is assumed that a marker attached to the rigid body traces out a sphere or circle. The difficulty in capturing hand kinematics originates from relatively large number of degrees of freedom concentrated in a very small place. Large skin artifacts compared to the distances between markers, make the reconstruction of a frame attached to the rigid body even more difficult. Besides, the range of motion of some joints is very small. As a consequence, characteristic patterns of the finger motion are to be used in finding the centers of rotation (Miyata et al., 2004). In this case the number of markers can be reduced.

The main drawback of optical tracking system is occlusion of markers. This deficiency becomes obvious when the number of markers is increased and it is the main reason why an optical tracking system is not suitable for assessment of hand kinematics during dexterous manipulation of an object. The object of this work is to develop a method using the minimal possible set of markers, which would still enable the reconstruction of hand kinematics and would be suitable for the calibration of an instrumental glove.

The instrumental glove has been used in many experiments. In most cases the raw data from the glove was used. Significant effort in experiment design was made to compensate the offset in the response, which occurs when the bend sensors are fully extended, and to estimate the sensitivity of individual bend sensor. The claim that the calibration of the glove can be carried out by a set of specific hand movements is misleading. By the movements across the whole range of motion in finger joints, only the active range of analog to digital converters can be established. For a hand with known range of joint motions, rough estimates of joint angles can be given. However, due to the nonlinear response of the bend sensors, the accuracy can not be estimated. We are not aware of any article which would describe the results of measurements in actual units and compare those results with a reference method. The described deficiency of the instrumental glove is most often hidden behind the statistical analysis of the data measured. The second aim of this work was instrumental glove calibration and its validation against the reference method.

2. Methods

2.1 Kinematic Model of a Human Hand

Hand kinematics can be described by Denavit-Hartenberg (D-H) notation. Four degrees of freedom (DOF) were used to describe each finger, two for metacarpophalangeal joint (MCP) flexion/extension (f/e) and abduction/adduction (ab/ad) and two for the proximal interphalangeal (PIP) and distal interphalangeal (DIP) joint f/e. The model of a thumb is not covered in this paper.

The center of wrist rotation was selected for the origin of the model. The base frame of the i-th finger (i = 2, 3, 4, 5; j = 0) was attached to the center of i-th MCP joint. Transformation from the wrist frame to the i-th finger base can be described by Eq. 1, where PJ_{i1x} and PJ_{i1z} denote position of the i-th MCP joint relative to the wrist frame. Transformation from the frame j-1 to j (j = 1, 2, …) can be described by Eq. 2, where parameters a_j, d_j, α_j, and Θ_j denote translations along x and z axis and rotations around x and z axis respectively.

$$\mathbf{T}_{w0i} = trans(PJ_{i1x}, 0, PJ_{i1z})roty(-\pi/2)rotx(\pi) \tag{1}$$

$$\mathbf{T}_{j-1,j} = rotz(\Theta_j)trans(0,0,d_j)trans(a_j,0,0)rotx(\alpha_j) \tag{2}$$

Position and orientation of the i-th fingertip can be obtained by post-multiplication of transformation matrix in Eq. 1 by matrices from Eq. 2. D-H parameters are collected within Table 1, where parameter PJ_{i2} denotes the distance from i-th MCP joint to PIP joint, PJ_{i3} from PIP to DIP joint, and PL_{i4} the length of i-th proximal phalanx.

Table 1. Denavit-Hartenberg parameters for fingers

Θ	d	a	α
Θ_{i1}	0	0	–π/2
Θ_{i2}	0	PJ_{i2}	0

Θ	d	a	α
Θ_{i3}	0	PJ_{i3}	0
Θ_{i4}	0	PL_{i4}	0

The model was parameterized by hand length and by palm width, as proposed by Buchholz et al., 1992.

2.2 Inverse Kinematics

The joint angles were obtained by solving the inverse kinematics problem. Each finger is a serial manipulator with four internal variables q_0, q_1, q_2, and q_3 which are related to MCP ab/ad and MCP, PIP, and DIP f/e respectively. A direct solution of finger inverse kinematics can be

obtained when the fingertip position and its orientation are given. When only fingertip position $M[X_M, Y_M, Z_M]$ is known, the simplification from Eq. 3 can be applied. It is justified as f/e angles of PIP and DIP joints are, due to the anatomical structure of ligaments, not independent. Coefficients c which describe the correlations of PIP and DIP joint angles, were reported by Kamper et al., 2003.

$$q_3 = cq_2 \tag{3}$$

The triangle relationships in Fig. 1 A leads to a system of Eq. 4 to Eq. 7:

$$L_0^2 = X_M^2 + Y_M^2, \tag{4}$$

$$\begin{aligned} L_1^2 &= L_{prox}^2 + L_{mid}^2 + 2L_{prox}L_{mid}\cos q_2 \\ &= L_0^2 + L_{dist}^2 - 2L_0L_{dist}\cos\left(q_2 + q_3 - \beta\right), \end{aligned} \tag{5}$$

$$L_2^2 = L_{mid}^2 + L_{dist}^2 + 2L_{mid}L_{dist}\cos q_3 \;= L_0^2 + L_{prox}^2 - 2L_0L_{prox}\cos\beta, \tag{6}$$

$$q_1 = \arctan\left(Y_M / X_M\right) - \beta. \tag{7}$$

Its solution is obtained by numerical computation which yields the angles β, q_2, and q_3. Internal coordinate q_0 can be according to Fig. 1 B calculated from Eq. 8. However, if position of DIP joint is known, an explicit solution of the inverse kinematics for q_0, q_1, and q_2 can be written, while a good approximation of q_3 is obtained with Eq. 3.

$$q_0 = \arctan\left(Z_M / X_M\right). \tag{8}$$

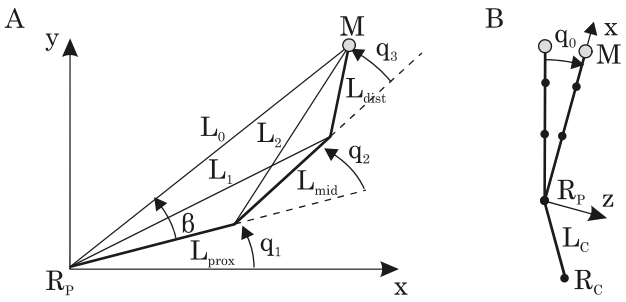

Figure 1. Inverse kinematics of a finger, A flexion/extension, B abduction/adduction.

A motion tracking system (Optotrak, Northern Digital Inc.) was used for validation of the model and DataGlove (DataGlove Ultra Series, 5DT Inc., 14 DOF) kinematic calibration. The index and middle finger

kinematics of one subject, free from any musculoskeletal disorders, was considered. A set of two cameras was used in the investigation. Infrared markers were attached to the anatomical landmarks of the hand, above MCP, PIP, and DIP joints and on the fingertips. An additional three markers were attached to the hand dorsum.

The initial data acquisition was performed for f/e of MCP joints with immobilized PIP and DIP joints, and f/e of PIP and DIP joints at fixed angle in MCP joints. The method validation and kinematic calibration of the glove comprised simultaneous f/e of MCP, PIP and DIP joints. The data from the motion tracking system and instrumental glove were recorded simultaneously.

2.3 Finger Joints Centers of Rotation

A general method for lower or upper extremity joint axis and center of rotation (AoR, CoR) estimation is not appropriate for fingers. Satisfactory results can be obtained when markers are separated apart from each other as far as possible. This can be achieved by a small set of markers. 3D parameter estimation problem for PIP and DIP joints was simplified to a 2D one, as proposed by Zhang et al., 2003. Parameters for estimation of PIP and DIP joint locations were obtained by minimizing a cost function defined by Eq. 9, where D_{PIP} and D_{DIP} denote the depths of PIP and DIP joints below surface marker and D_{PIPk} and D_{DIPk} the depths calculated for the k-th frame. N stands for the number of all frames. The average of the cost function is due to a non-uniform distribution of the acquired samples, weighted by wk.

$$C = \sum_{k=1}^{N} w_k \left(\left(D_{PIPk} - D_{PIP} \right)^2 + \left(D_{DIPk} - D_{DIP} \right)^2 \right) \tag{9}$$

The calculation of the cost function is explained in Fig. 2. L_{mid} and L_{dist} denote lengths of middle and distal phalange and m are the positions of markers. The lengths L_{dist}, L_{mid}, D_{DIP}, and D_{PIP} are changed during optimization subjected to linear constraints to obtain the minimum of Eq. 9.

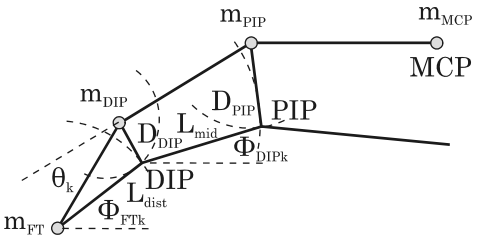

Figure 2. Calculation of PIP and DIP joint centers of rotation.

In the case of MCP joint improved results can be obtained by using the marker which is distant from the joint, as proposed by Miyata et al., 2004. The coordinate frame C_{ref}, defined by markers m_{MCP}, m_{PIP}, and m_{DIP}, was positioned to the PIP joint marker. Its z-axis formed a normal vector to the common plane defined by m_{MCP}, m_{PIP}, and m_{DIP}, while x-axis pointed in the direction of the proximal phalange. The CoR for MCP joint was found by minimization of the cost function (Eq. 10), where T_k denotes a transformation matrix which moves the coordinate frame C_{ref} from the initial ($k=1$) to the k-th ($k = 2, \ldots, N$) pose. c_{MCP} represents a point, which is invariant to transformations T_k and can be taken for CoR of the MCP joint. The average is for similar reasons as in PIP and DIP joint CoR estimation weighted with wk.

Parameters c_{MCP}, L_{dist}, L_{mid}, D_{DIP}, and D_{PIP} were obtained during the initial data acquisition. The relative position of PIP and DIP joints was calculated from the calibration movements (simultaneous f/e of MCP, PIP, and DIP joints) as an intersection of circles, as shown in Fig. 2, while c_{MCP} represented a standstill point within the coordinate frame attached to the hand dorsum.

$$C = \sum_{i=1}^{N} w_k \left\| \mathbf{T}_k \mathbf{c}_{\mathrm{MCP}} - \mathbf{c}_{\mathrm{MCP}} \right\|^2 \tag{10}$$

The reference joint angles were calculated from the known positions of CoR. The lengths of finger segments were obtained as a by-product of CoR estimation.

3. Results

The hand width of a subject who took part in the study was 90 mm and hand length 204 mm. The mean lengths of proximal (*Lprox*), middle (*Lmid*) and distal phalanx (*Ldist*), which were obtained from CoR estimation, are presented in Table 2 for index and middle finger. They are compared to the lengths estimated from hand external dimensions via scaling factors reported by Buchholz et al., 1992.

The f/e angles in MCP, PIP, and DIP joints of index finger are presented in Fig. 3. They were calculated for the simultaneous flexion in MCP, PIP, and DIP joints. The angles acquired through inverse kinematics are presented with dash-doted line and compared to the reference angles, plotted with full lines. The reference angles were estimated from CoR. The mean differences and accompanying standard deviations are shown in Table 3.

Table 2. Length of proximal, middle, and distal phalanx of index and middle finger

	From CoR		
Finger	Lprox (mm)	Lmid (mm)	Ldist (mm)
Index	47.35±0.65	25.37±0.60	23.81±0.08
Middle	44.63±0.50	30.82±0.85	24.63±0.03
	Statistically-based		
Index	45.48±0.45	25.96±0.21	22.99±0.06
Middle	41.95±0.13	30.87±0.22	25.85±0.08

Table 3. Mean difference and standard deviation between reference joint angles and angles acquired through inverse kinematics

Finger	MCP (°)	PIP (°)	DIP (°)
Index	2.7±1.7	–7.9±2.9	6.3±2.1
Middle	1.3±3.0	–6.6±2.9	–1.5±3.5

One record of simultaneous f/e in MCP, PIP, and DIP joints, obtained from the optical tracking device and instrumental glove, was used for the glove calibration. Four records were used to validate the calibration. Joint angles for calibration were estimated through inverse kinematics. Analytic functions, which transform analog to digital converter raw values from the glove into the bend angles of individual sensors were obtained as a result of calibration. Angles reported by the calibrated glove were compared with the reference angles estimated from CoR.

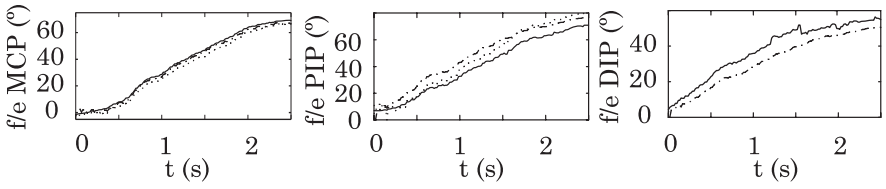

Figure 3. Validation of the method.

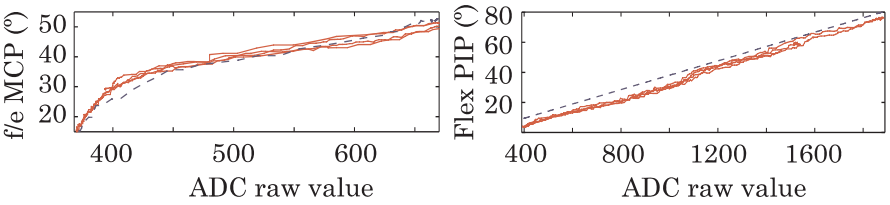

Figure 4. Data Glove calibration results.

The responses of bend sensors attached above the MCP and PIP joints of index finger are shown in Fig. 4 with dashed line. They are compared to the reference angles, which were acquired via estimated CoR, and are presented with full lines. The mean difference and standard deviation between joint angles recorded with the calibrated glove and the reference angles reached $(-1.7 \pm 1.8)^\circ$ and $(-5.1 \pm 0.6)^\circ$ for PIP and DIP joints, respectively.

5. Conclusions

A method for assessment of finger joint angles and calibration of instrumental glove based on optical tracking system and a kinematic model of a hand has been proposed. The model and the method were validated against the methods for estimation of joint CoR. The results show that lengths of finger segments, which were obtained from external dimensions of the hand and from the CoR of joints, are comparable. The angles obtained by the proposed method slightly differ from reference angles, however, the number of markers which is to be used for the reconstruction of finger motion is considerably smaller. Only markers on fingertips and additional 3 markers on hand dorsum are required. The proposed method was used for the instrumental glove calibration and proved to be appropriate for this application.

References

Buchholz, B., Armstrong, T.J., and Goldstein, S.A. (1992), Anthropometric data for describing the kinematics of the human hand, Ergonomics, no. 3, vol. 35, pp. 261-273.

Halvorsen, K., Lesser, M., and Lundberg, A. (1999), A new method for estimating the axis of rotation and the center of rotation, Journal of Biomechanics, no. 11, vol. 32, pp. 1221-1227.

Kamper, D.G., Cruz, E.G., and Siegel, M.P. (2003), Stereotypical fingertip trajectories during grasp, Journal of Neurophysiology, no. 6, vol. 90, pp. 3702-3710.

Miyata, N., Kouchi, M., Kurihara, T., and Mochimaru, M. (2004), Modeling of human hand link structure from optical motion tracking data, Proceedings of 2004 IEEE/RSJ International Conference on Intelligent Robotics and Systems, Sendai, Japan.

Zhang X., Lee, S.W., and Braido, P. (2003), Determining finger segmental centers of rotation in flexion-extension based on surface marker measurement, Journal of Biomechanics, no. 8, vol. 36, pp. 1097-1102.

ALL SINGULARITIES OF THE 9-DOF DLR MEDICAL ROBOT SETUP FOR MINIMALLY INVASIVE APPLICATIONS

Rainer Konietschke[1], Gerd Hirzinger
German Aerospace Center, Institute of Robotics and Mechatronics
P.O. Box 1116, D-82230 Weßling, Germany
[1] Rainer.Konietschke@dlr.de

Yuling Yan
University of Hawaii at Manoa, Mechanical Engineering
2540 Dole Street – Holmes Hall 302, Honolulu HI 96822, USA

Abstract This paper shows that it is possible to determine analytically all singular configurations of the 9-DoF DLR medical robot setup for minimally invasive applications. It is shown that the problem can be devided into the determination of the singularities of the general 7-DoF DLR medical arm and of the 2-DoF surgical instrument, used in a minimally invasive application. The formula of Cauchy-Binet is used to calculate the singularities of the redundant medical arm, and an interpretation of this formula for any serial redundant robot design is given.

Keywords: Medical robotics, singularities, manipulability, robotic assistance, minimally invasive surgery, optimization, robot design

1. Introduction

In robotically assisted minimally invasive applications, a surgical robot is used to access the operating field inside the human body through small incisions with thin cylindrical instruments. The design of such robotic devices for medical applications is liable to exceptionally high requirements in terms of safety and reliability. A thorough analysis of the robot's kinematic structure is important to ensure complete reachability as well as the absence of any singular configuration inside the desired workspace. The desired workspace is usually defined by the operator during a planning step, and serves to determine the optimal robot setup (Adhami, 2002; Konietschke et al., 2004). The robot setup comprises the position and orientation of the robot base and the position of the entry point into the human body as well as any adjustable DH parameter (as for example adjustable instrument lengths).

J. Lenarčič and B. Roth (eds.), Advances in Robot Kinematics, 193–200.

The determination of the singular configurations of a robot is especially important in the case of teleoperation, where the exact path is not known in advance. Though singular configurations can be detected by monitoring certain manipulability measures as e.g. in Yoshikawa, 1990; Konietschke et al., 2004, these measures are to the author's knowledge insufficient to signal vicinity to singular configurations. Since the behaviour of robots near singularities is in most cases not very intuitive for the operator, it is highly desirable to restrict the workspace admissible to the operator to a space that does not contain any singularities or to control the robot in a way that singular configurations are avoided. This is facilitated if an analytic description of all singularities of the robot design is known, since the use of computationally cheap strategies for singularity avoidance in analogy with well known strategies for joint limit avoidance becomes possible.

In the next section, the kinematic structure of the considered robotic system is presented. The singularities of the DLR medical arm and the attached surgical instrument are given in the sections 3 and 4. Section 5 gives a short conclusion.

2. Kinematic Structure

The kinematic structure of the considered robot with the attached actuated instrument and the used coordinate frames are shown in Fig. 1. The medical robot itself has 7 DoF ($\phi_{1...7}$) and the attached instrument disposes of two additional DoF ($\phi_{8,9}$). The kinematic chain of the robot itself is denoted thereafter as K_1, that of the actuated instrument as K_2.

In the following, the problem of determining the singular configurations of the robot kinematics is divided into two subproblems. This is possible due to the restrictions at the entry point (see section 4).

3. The Singular Configurations of the DLR Medical Arm

Written in the wrist frame $\{\mathbf{W}\}$, the geometric Jacobian $\mathbf{J}$ of the forward kinematics has the following form (Yoshikawa, 1990):

$$\begin{pmatrix} \mathbf{v}_W \\ \omega_W \end{pmatrix} = \mathbf{J}\dot{\phi} = \begin{pmatrix} \mathbf{J}_{11} & \mathbf{0} \\ \mathbf{J}_{21} & \mathbf{J}_{22} \end{pmatrix} \dot{\phi}, \quad \text{with} \quad \begin{pmatrix} \mathbf{v}_W \\ \omega_W \end{pmatrix} \tag{1}$$

the translational and rotational velocity of the wrist frame $\{\mathbf{W}\}$ and

$$\mathbf{J}_{11},\ \mathbf{J}_{21} \in \mathbb{R}^{3\times 4},\ \mathbf{J}_{22} \in \mathbb{R}^{3\times 3}\ . \tag{2}$$

A singular configuration occurs if the following determinant equals zero:

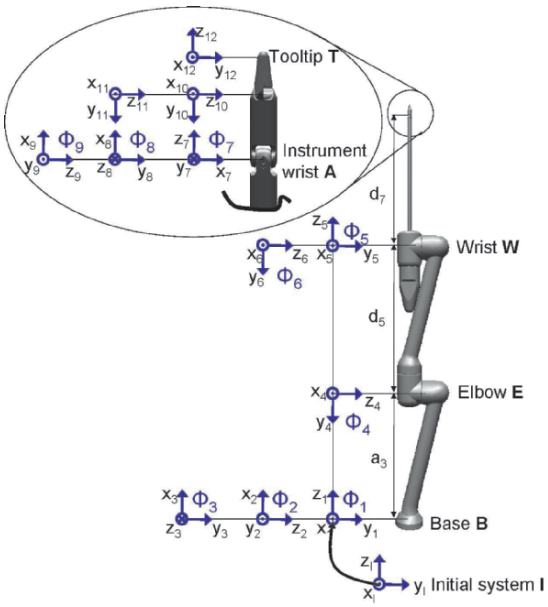

Figure 1. Kinematic description of the considered kinematic chains (K_1 and K_2).

$$\left|\mathbf{J}\mathbf{J}^{\mathbf{T}}\right| = 0. \tag{3}$$

With the formula of Cauchy-Binet (see e.g. Gantmacher, 1959), Eq. 3 can be transformed into a sum of squares of determinants:

$$\left|\mathbf{J}\mathbf{J}^{\mathbf{T}}\right| = \sum_{i=1}^{4} \left| \begin{pmatrix} \mathbf{J}_{11}^{i} & \mathbf{0} \\ \mathbf{J}_{21}^{i} & \mathbf{J}_{22} \end{pmatrix} \right|^2 + \sum_{i=1}^{3} \left| \begin{pmatrix} \mathbf{J}_{11} & \mathbf{0} \\ \mathbf{J}_{21} & \mathbf{J}_{22}^{i} \end{pmatrix} \right|^2 , \tag{4}$$

with $\mathbf{J}_{mn}^{i}$ the i-th submatrix (minor) obtained by suppressing column i of the matrix $\mathbf{J}_{mn}$. The terms of the first sum have a lower block triangular form and can be combined to:

$$\sum_{i} \left| \begin{pmatrix} \mathbf{J}_{11}^{i} & \mathbf{0} \\ \mathbf{J}_{21}^{i} & \mathbf{J}_{22} \end{pmatrix} \right|^2 = |\mathbf{J}_{22}|^2 \sum_{i} \left|\mathbf{J}_{11}^{i}\right|^2 = |\mathbf{J}_{22}|^2 \left|\mathbf{J}_{11}\mathbf{J}_{11}^{\mathbf{T}}\right|. \tag{5}$$

In the last step, the formula of Cauchy-Binet is applied inversely. Since the sum in Eq. 4 consists of squared summands, all of them have to equal zero in a singular configuration. Simplifications are possible with consideration of the rank of the Jacobian. Due to the special structure of $\mathbf{J}$, a sufficient condition for a singular configuration is:

$$\operatorname{rank}\left(\mathbf{J}_{11}\right) < 3\,. \tag{6}$$

For the remaining singular configurations, a necessary condition is:

$$\operatorname{rank}(\mathbf{J}_{22}) < 3\,. \tag{7}$$

Thus, the second sum of Eq. 4 has to be evaluated only for joint angles that cause $|\mathbf{J}_{22}|$ to be zero. The following singularities e_i can thus be determined, with $k \in \mathbb{N}$:

$$e_1: \quad \phi_4 = \pi k\,, \tag{8}$$

$$e_2: \quad \phi_2 = \frac{\pi}{2} + \pi k \,\wedge\, \phi_3 = \frac{\pi}{2} + \pi k\,, \tag{9}$$

$$e_3: \quad \phi_2 = \frac{\pi}{2} + \pi k \,\wedge\, \phi_4 = \pm \arccos\left(-\frac{a_3}{d_5}\right) + 2\pi k\,, \tag{10}$$

$$e_4: \quad \phi_2 = \frac{\pi}{2} + \pi k \,\wedge\, \phi_6 = \pi k\,, \text{ and} \tag{11}$$

$$e_5: \quad \phi_5 = \frac{\pi}{2} + \pi k \,\wedge\, \phi_6 = \pi k\,. \tag{12}$$

The singular configuration e_3 only appears if $\|a_3\| \leq \|d_5\|$. Details about the zero points of the relevant determinants are given in the appendix. The classical "wrist singularity" ($\phi_6 = \pi k$) that occurs in many 6-DoF kinematic chains (consider for example a kinematic chain K_1' obtained with joint ϕ_3 held constant) does only appear in conjunction with additional conditions (Singularities $e_{4,5}$). To illustrate this, the pseudo inverse $\mathbf{J}_a^+$ of the Jacobian $\mathbf{J}_a$ in the non singular configuration $\phi_a = (0,\, 0,\, 0,\, \pi/2,\, 0,\, 0,\, 0)^{\mathbf{T}}$ as shown left in figure 2 is considered, written in frame $\{\mathbf{I}\}$:

$$\mathbf{J}_a^+ = \mathbf{J}_a^{\mathbf{T}} \left(\mathbf{J}_a \mathbf{J}_a^{\mathbf{T}}\right)^{-1},\; \mathbf{J}_a^+ = \begin{pmatrix} 0 & 0 & 0 & 0 & 0 & 1 \\ \frac{1}{a_3} & 0 & 0 & 0 & 0 & 0 \\ 0 & \frac{1}{a_3} & 0 & 0 & 0 & -\frac{d_5}{a_3} \\ -\frac{1}{a_3} & 0 & -\frac{1}{d_5} & 0 & 0 & 0 \\ 0 & \frac{1}{2\,a_3} & 0 & \frac{1}{2} & 0 & -\frac{d_5}{2\,a_3} \\ 0 & 0 & \frac{1}{d_5} & 0 & 1 & 0 \\ 0 & \frac{1}{2\,a_3} & 0 & \frac{1}{2} & 0 & -\frac{d_5}{2\,a_3} \end{pmatrix}. \tag{13}$$

With $d_5/a_3 \approx 1$, all joint velocities remain small for arbitrary rotations of the tool tip. Particularly, pure rotation around an axis b as shown left in Fig. 2 (perpendicular to the rotation axes of ϕ_6 and ϕ_7 and intersecting them), constituting the singular direction in case of a

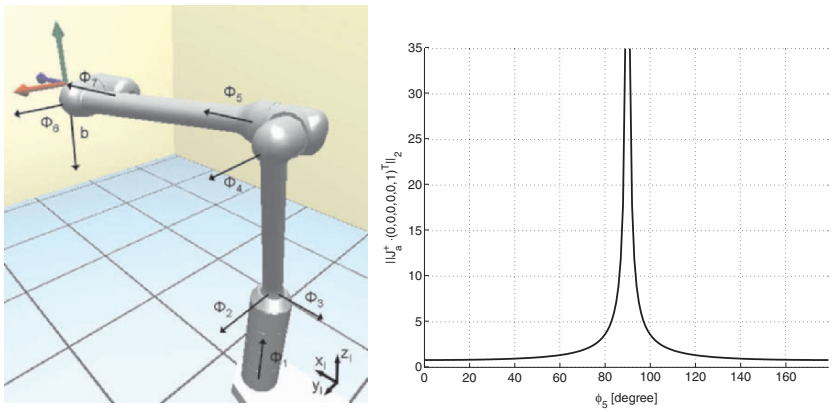

Figure 2. In case of the considered robot, pure rotations around the axis b can still be performed even if $\phi_6 = 0$ (left). Only if also $\phi_5 = \pi/2 + \pi k$, a singular configuration occurs, as can be seen on the right where the norm $||\mathbf{J}_a^+ \cdot (0,\, 0,\, 0,\, 0,\, 0,\, 1)^{\mathbf{T}}||_2$ is shown as a function of the joint angle ϕ_5.

kinematic chain as K_1' in this configuration, leads to the following (reasonably small) joint velocities:

$$\dot{\phi} = \mathbf{J}_a^+ \cdot (0,\, 0,\, 0,\, 0,\, 0,\, 1)^{\mathbf{T}} = (1,\, 0,\, -\frac{d_5}{a_3},\, 0,\, -\frac{d_5}{2\,a_3},\, 0,\, -\frac{d_5}{2\,a_3})^{\mathbf{T}}. \quad (14)$$

On the right of Fig. 2 the norm $||\mathbf{J}_a^+ \cdot (0,\, 0,\, 0,\, 0,\, 0,\, 1)^{\mathbf{T}}||_2$ is shown as a function of the joint angle ϕ_5 with all other angles remaining in configuration ϕ_a.

3.1 Generalisation to the Case of a Serial Robot with n-fold Redundancy

The singular configurations of a general, n-fold redundant robot can be calculated by considering the roots of the following determinant:

$$\left|\mathbf{J}\mathbf{J}^{\mathbf{T}}\right| = \sum_{i=1}^{\frac{(m+n)!}{2(m!)}} |\mathbf{J}_i|^2\,, \quad \mathbf{J} \in \mathbb{R}^{m\times(m+n)}, \quad (15)$$

with $\mathbf{J}_i$ representing all $\frac{(m+n)!}{2(m!)}$ (different) matrices obtainable by suppressing n columns of the Jacobian $\mathbf{J}$. It can be seen from Eq. 15 that the singularities of a serial redundant structure with $m + n$ joints of which n are redundant are identical with the intersection of the singularities of all those robotic structures obtained by fixing any possible set of n joints

of the redundant structure. It has to be noted however, that already for the case of a 2-fold redundant robot with 8 DoF, $\frac{8!}{2\cdot 6!} = 28$ minors have to be considered, each of which being usually a rather complex function of the joint angles ϕ.

4. Singularities of the Instrument in a Minimally Invasive Application

The kinematics in minimally invasive applications have the peculiarity of a fulcrum point where the surgical instrument enters into the human body. At that point, a constraint is imposed upon the system, resulting in a loss of two DoF. In order to regain full dexterity inside of the patient, an articulated instrument can be used, adding two DoF (ϕ_8 and ϕ_9, see Fig. 3) to obtain full 6 DoF at the distal end of the instrument. To analyze the singular configurations introduced by the fulcrum point and the two extra DoF of the instrument, the following Jacobian matrix is considered:

$$\begin{pmatrix} \mathbf{v}_9 \\ \omega_9 \end{pmatrix} = {}^6_9\mathbf{J}_v \begin{pmatrix} \dot{x}_6 \\ \dot{y}_6 \\ \dot{z}_6 \\ \dot{\phi}_7 \\ \dot{\phi}_8 \\ \dot{\phi}_9 \end{pmatrix}, \quad {}^6_9\mathbf{J}_v = \begin{pmatrix} \frac{d'_7-d_7}{d'_7} & 0 & 0 & 0 & 0 & 0 \\ 0 & 1 & 0 & 0 & 0 & 0 \\ 0 & 0 & \frac{d'_7-d_7}{d'_7} & 0 & 0 & 0 \\ 0 & 0 & \frac{1}{d'_7} & 0 & -c_7 & -s_7c_8 \\ 0 & 0 & 0 & -1 & 0 & s_8 \\ -\frac{1}{d'_7} & 0 & 0 & 0 & -s_7 & c_7c_8 \end{pmatrix}, \tag{16}$$

with $\mathbf{v}_9$ resp. ω_9 the translational and rotational velocity of frame $\{\mathbf{9}\}$ and $(\dot{x}_6, \dot{y}_6, \dot{z}_6)$ the translational velocities of frame $\{\mathbf{W}\}$. The determinant of ${}^6_9\mathbf{J}_v$ yields:

$$\left|{}^6_9\mathbf{J}_v\right| = -\frac{(d_{7,a} - d_7)^2 \, c_8}{d_{7,a}^2}\,, \tag{17}$$

and a singular configuration can be stated when

$$c_8 = 0\,, \tag{18}$$

with the axes z_7 and z_9 aligned. The singular configuration that occurs if

$$d_{7,a} = d_7 \tag{19}$$

corresponds to a configuration where the fulcrum point is coincident with the origin of $\{\mathbf{W}\}$. In this case, translations of the frame $\{\mathbf{W}\}$ are partly restricted by the constraint of the fulcrum point, and an altered Jacobian matrix (a matrix that takes into consideration the rotation of

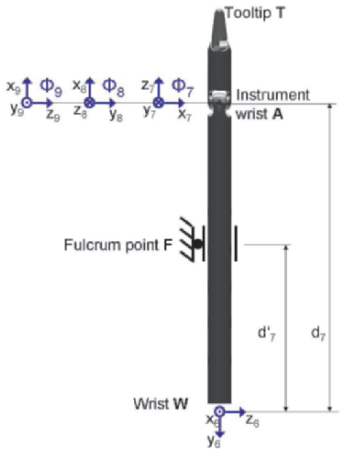

Figure 3. Kinematic description of the articulated instrument in MIS. The length d_7' signifies the distance between the wrist frame $\{\mathbf{W}\}$ and the fulcrum point.

frame $\{\mathbf{W}\}$ rather than its translation) would have to be considered. Since, due to the design of the considered robot, the wrist joint cannot be coincident with the fulcrum point this case is not further analyzed.

5. Conclusion

In this paper the analytical solution for the determination of all singularities of the DLR medical robot with attached articulated instrument is given. The use of the formula of Cauchy-Binet simplifies the equations considerably and is suggested for the calculation of the singularities of similar redundant kinematic structures. Particularly, the singular configurations of both the DLR light weight robots II and III (7-DoF robots) can be easily determined. As for the DLR medical robot, all singularities except for e_1 $(\phi_4 = \pi k)$ and e_5 $\left(\phi_5 = \frac{\pi}{2} + \pi k \wedge \phi_6 = \pi k\right)$ are outside of the joint limits.

Appendix

The relevant determinants yield:

$$|\mathbf{J}_{22}| = -s_6, \quad \left|\mathbf{J}_{11}^1\right| = -a_3 d_5 c_3 s_4 \left(d_5 c_4 + a_3\right),$$

$$\left|\mathbf{J}_{11}^2\right| = a_3 d_5 c_2 s_3 s_4 \left(d_5 c_4 + a_3\right), \quad \left|\mathbf{J}_{11}^3\right| = a_3 d_5 s_4 \left(s_2 c_3 \left(a_3 + d_5 c_4\right) + d_5 c_2 s_4\right),$$

$$\left|\mathbf{J}_{11}^{4}\right| = 0, \quad \left|\begin{pmatrix} \mathbf{J}_{11} & \mathbf{0} \\ \mathbf{J}_{21} & \mathbf{J}_{22}^{1} \end{pmatrix}\right| = -a_3 d_5 c_2 s_4 \left(d_5 s_6 + a_3 s_4 c_5 c_6 + a_3 c_4 s_6\right),$$

$$\left|\begin{pmatrix} \mathbf{J}_{11} & \mathbf{0} \\ \mathbf{J}_{21} & \mathbf{J}_{22}^{2} \end{pmatrix}\right| = a_3^2 d_5 c_2 s_4^2 s_5 s_6, \quad \left|\begin{pmatrix} \mathbf{J}_{11} & \mathbf{0} \\ \mathbf{J}_{21} & \mathbf{J}_{22}^{3} \end{pmatrix}\right| = a_3^2 d_5 c_2 s_4 c_5;$$

The determinants equal zero for the following joint angles:

$$\left|\mathbf{J}_{11}^{1}\right| = 0: \quad \phi_3 = \frac{\pi}{2} + \pi k \quad \vee \quad \phi_4 = \pi k \quad \vee \quad \phi_4 = \pm \arccos\left(-\frac{a_3}{d_5}\right) + 2\pi k;$$

$$\left|\mathbf{J}_{11}^{2}\right| = 0: \quad \phi_2 = \frac{\pi}{2} + \pi k \vee \phi_3 = \pi k \vee \phi_4 = \pi k \vee \phi_4 = \pm \arccos\left(-\frac{a_3}{d}\right) + 2\pi k;$$
$$_5$$

$$\left|\mathbf{J}_{11}^{3}\right| = 0: \quad \phi_4 = \pi k \quad \vee \quad \phi_2 = \pm \arctan\left(\frac{s_4 d_5}{c_3\left(d_5 c_4 + a_3\right)}\right) + \pi k,$$

$$\left|\mathbf{J}_{11}^{4}\right| = 0 \,\forall\, \phi_i;$$

$$\left|\begin{pmatrix} \mathbf{J}_{11} & \mathbf{0} \\ \mathbf{J}_{21} & \mathbf{J}_{22}^{1} \end{pmatrix}\right|_{s_6=0} = 0: \phi_2 = \frac{\pi}{2} + \pi k \quad \vee \quad \phi_4 = \pi k;$$

$$\left|\begin{pmatrix} \mathbf{J}_{11} & \mathbf{0} \\ \mathbf{J}_{21} & \mathbf{J}_{22}^{2} \end{pmatrix}\right|_{s_6=0} = 0, \forall\, \phi_i;$$

$$\left|\begin{pmatrix} \mathbf{J}_{11} & \mathbf{0} \\ \mathbf{J}_{21} & \mathbf{J}_{22}^{3} \end{pmatrix}\right|_{s_6=0} = 0: \phi_2 = \frac{\pi}{2} + \pi k \quad \vee \quad \phi_4 = \pi k \quad \vee \quad \frac{\pi}{2} + \pi k;$$

References

Louaï Adhami. *An Architecture for Computer Integrated Mini-Invasive Robotic Surgery: Focus on Optimal Planning.* Ph.D. Thesis, Ecole des Mines de Paris, Paris, 2002.

Felix R. Gantmacher. *The Theory of Matrices.* American Mathematical Society, 1959.

Rainer Konietschke, Tobias Ortmaier, Holger Weiss, Gerd Hirzinger, and Robert Engelke. Manipulability and Accuracy Measures for a Medical Robot in Minimally Invasive Surgery. In *Advances in Robot Kinematics*, Genua, Italy, 2004.

Rainer Konietschke, Holger Weiss, Tobias Ortmaier, and Gerd Hirzinger. A Preoperative Planning Prœdure for Robotically Assisted Minimally Invasive Interventions. *In 3. Jahrestagung der Deutschen Gesellschaft für Computer- und Roboterassistierte Chirurgie (CURAC)*, München, Germany, 8.-9. Dezember 2004.

Tsuneo Yoshikawa. *Foundations of Robotics: Analysis and Control.* The MIT Press, 1990.

ON THE INVERSE KINEMATICS OF A FRAGMENT OF PROTEIN BACKBONE

Guanfeng Liu[†], R.J. Milgram[‡], A. Dhanik[†], and J.C. Latombe[†]
[†] *Department of Computer Science, Stanford University*
[‡] *Department of Mathematics, Stanford University*
{liugf,ankur,latombe}@cs.stanford.edu and milgram@math.stanford.edu

Abstract This paper studies the structure of the inverse kinematics (IK) map of a fragment of protein backbone with 6 torsional degrees of freedom. The images (critical sets) of the singularities of the orientation and position maps are computed for a slightly idealized kinematic model. They yield a decomposition of $SO(3)$ and $\mathcal{R}^3$ into open regions where the number of IK solutions is constant. A proof of the existence of at least one 16-solution cell in $\mathcal{R}^3 \times SO(3)$ is given and one such case is shown.

Keywords: Protein backbone, inverse kinematics, critical sets

1. Introduction

A protein (Creighton, 1993) is a sequence of amino-acids connected by peptide bonds. It is often modeled as a serial linkage, the *backbone*, with short side-chains. Each amino-acid contributes three atoms – N, C_α, and C – and two torsional degrees of freedom (dofs) to the backbone (Fig. 1). These dofs correspond to the dihedral angles ϕ and ψ around the N – C_α and the C_α – C bonds. The inverse kinematics of the backbone is of considerable interest in biology (Coutsias et al., 2004).

Let F be a backbone fragment with 6 dihedral angles ϕ and ψ, and f be its forward kinematics. It is well-known that the number of solutions of the inverse kinematics (IK) map f^{-1} has 16 as an upper bound, but it has often been questioned whether this bound is tight (Coutsias et al., 2004). Available algorithms only compute these solutions for *given* poses of the moving frame T of F. Here, we study the *global* structure of f^{-1} over the entire 6-D manifold of poses of T in $\mathcal{R}^3 \times SO(3)$. The images of the singularities of f are the *critical* poses, which, according to the Morse-Sard theorem, decompose the noncritical part of the image into open regions, such that in each region E, $f^{-1}(x)$ for each $x \in E$ contains the same number of points. These decompositions of the 6-D manifold can be very complex, so we study the position map p and an orientation map ρ separately. It turns out ρ is quite easy to understand and the original question reduces to studying the projection to $\mathcal{R}^3$ from

J. Lenarčič and B. Roth (eds.), Advances in Robot Kinematics, 201–208.

the inverse images of ρ. Given the frame associated to T, the set of configurations that give the frame is either a copy of $(S^1)^3$ or a copy of the disjoint union $(S^1)^3 \sqcup (S^1)^3$. Focusing on these $(S^1)^3$, we can compute p^{-1} more efficiently and we find regions with 16 inverse image points. This result is reasonable since a 6-dof protein fragment does not satisfy any of the conditions under which the IK of a 6-dof serial linkage has less than 16 solutions (Mavroidis and Roth, 1994).

2. Kinematic Model of a Protein Fragment

Let F be a 6-dof fragment of a protein backbone as illustrated in Fig. 1. The coordinates of F are the 3 dihedral angles ϕ_i around the bonds N^i–C^i_α, and the 3 dihedral angles ψ_i around the bonds C^i_α–C^i. For convenience, we rename ϕ_i by θ_{2i-2} and ψ_i by θ_{2i-1}, so each conformation of F is specified by a 6-tuple $\theta = (\theta_1, \ldots, \theta_6) \in (S^1)^6$.

We represent F by a kinematically equivalent sequence of 3 identical units, each made of two perpendicular links, a "long" one of length ℓ_2 and a "short" one of length ℓ_1, as shown in Fig. 2. We number the links $1, 2, \ldots, 6$, so that each link $2i-1$ is a long link and each link $2i$ is a short link. Angle θ_{2i-1} rotates short link $2i$ about long link $2i-1$. So, each short link moves in a plane perpendicular to the preceding long link. Angle θ_{2i} rotates the long link $2i+1$ about an axis parallel to long link $2i-1$ and passing through the extremity of short link $2i$. Link $2i+1$ makes the constant angle $\alpha = 19$ degrees with the plane perpendicular to link $2i-1$. Finally, we add a long link 7 to F. This is the link associated with the moving frame T.

We summarize these remarks and put them into a mathematical setting as follows. Set

$$R_i = \begin{bmatrix} \cos(\theta_i) & -\sin(\theta_i) & 0 \\ \sin(\theta_i) & \cos(\theta_i) & 0 \\ 0 & 0 & 1 \end{bmatrix}, \qquad L = \begin{bmatrix} -\sin(\alpha) & 0 & \cos(\alpha) \\ 0 & -1 & 0 \\ \cos(\alpha) & 0 & \sin(\alpha) \end{bmatrix},$$

where $\alpha \sim .105556\pi$ is fixed and $L^T = L^{-1} = L$. Then, the orientations of the frames are given by

$$O_1 = I_{3\times 3}, \quad O_{2i} = O_{2i-1}R_{2i-1}, \quad O_{2i+1} = O_{2i}R_{2i}L,$$

and f is the composition of p and ρ with

$$p : (S^1)^6 \to \mathcal{R}^3, \quad \theta \to (R_{1;2}L + R_{1;2}LR_{3;4}L)v_1 + (R_1 + R_{1;2}LR_3 + R_{1;2}LR_{3;4}LR_5)v_2, \tag{1}$$

$$\rho : (S^1)^6 \to SO(3), \quad \theta \to R_{1;2}LR_{3;4}LR_{5;6}L, \tag{2}$$

where $R_{i;j} = R_iR_j$, $v_1 = [0,\ 0,\ \ell_2]^T$, and $v_2 = [\ell_1,\ 0,\ 0]^T$.

This paper studies the structure of the inverse kinematics $f^{-1} = (p, \rho)^{-1}$. Noticing that for any $(X, R) \in \mathcal{R}^3 \times SO(3)$,

$$(p, \rho)^{-1}(X, R) = p^{-1}(X) \cap \rho^{-1}(R),$$

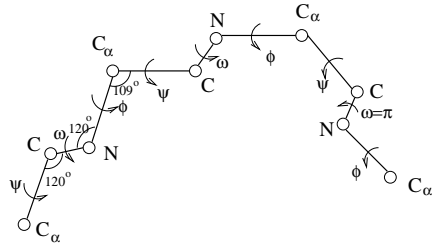

Figure 1. 6-dof fragment.

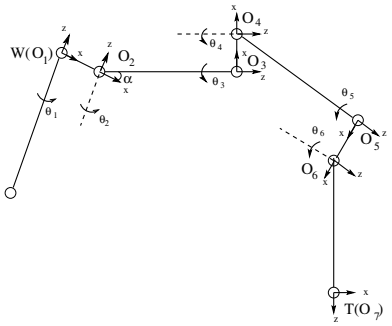

Figure 2. Equivalent model.

we proceed in two steps. First, we derive the inverse orientation map $\rho^{-1} : SO(3) \to (S^1)^6$ and show that in general $\rho^{-1}(R)$ is the disjoint union of two 3-D tori $\mathcal{M}_1$ and $\mathcal{M}_2$. Next, we compute $p_k^{-1}(X)$, where p_k, $k \in 1, 2$, is the map p with its domain restricted to $\mathcal{M}_k$.

3. Inverse Orientation Map

Reduction. In Eq. (2) only the sums $\theta_{2i-1}+\theta_{2i}$ appear. So, we write $\tau_i = \theta_{2i-1} + \theta_{2i}$, $i = 1,\ 2,\ 3$, and $\tau = (\tau_1, \tau_2, \tau_3)$. As θ runs over $(S^1)^6$, τ runs over the 3-D torus $(S^1)^3$, and ρ factors as composition

$$\rho \ = \ \hat{\rho} \circ (+) : (S^1)^6 \to (S^1)^3 \to SO(3)$$

where $\hat{\rho} : (S^1)^3 \to SO(3),\ \tau \to R_{\tau_1} L R_{\tau_2} L R_{\tau_3} L$. R_{τ_i} is the rotation of angle τ_i around the z axis. Given $R \in SO(3)$, the values of $\hat{\rho}^{-1}(R)$ are the solutions of $\hat{\rho}(\tau) := R_{\tau_1} L R_{\tau_2} L R_{\tau_3} L \ = \ R$, which is equivalent to:

$$\hat{\rho}(\tau) L := R_{\tau_1} L R_{\tau_2} L R_{\tau_3} \ = \ RL. \tag{3}$$

Since $\hat{\rho}(\tau)L$ defines the frame on the z-axis, (which is fixed by R_{τ_3}, we further reduce Eq. (3) by eliminating the variable τ_3. To do this, we define $A_z : SO(3) \to S^2,\ \ R \to Rz$, where $z = [0,\ 0,\ 1]^T$ and S^2 denotes the unit 2-D sphere. Since $A_z(R_{\tau_3}) = z$, applying A_z to both sides of Eq. (3) yields:

$$A_z(\hat{\rho}(\tau) L) := R_{\tau_1} L R_{\tau_2} L z \ = \ RLz \tag{4}$$

where $R_{\tau_1} L R_{\tau_2} L$ defines the orientation of the z-axis of frame 6 in W. We can solve this equation for (τ_1, τ_2). The value of τ_3 is then uniquely determined by:

$$R_{\tau_3} = (R_{\tau_1} L R_{\tau_2} L)^T RL. \tag{5}$$

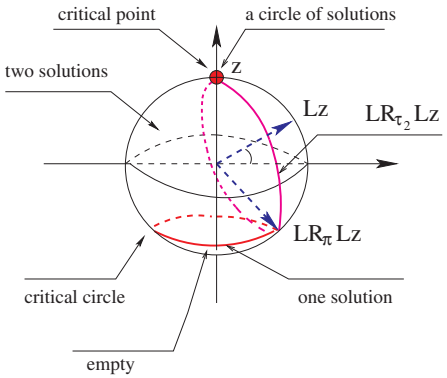

Figure 3. Critical set of η.

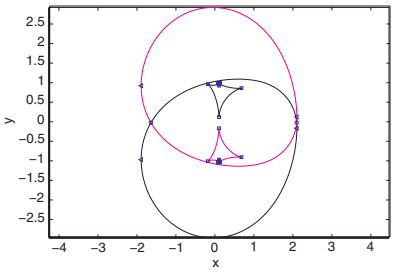

Figure 4. The discriminant curve $\mathcal{X}_d$ computed with $\gamma = \pi$ and $d = -0.32$.

To each solution $\tau = (\tau_1, \tau_2, \tau_3)$ of Eqs. (4) and (5) corresponds a set of values of $\theta = (\theta_1, ..., \theta_6)$ such that $\theta_{2i-1} + \theta_{2i} = \tau_i$ for $i = 1,\ 2,\ 3$. This set is a 3-D torus $(S^1)^3$.

Singular set. The singularities of $\hat{\rho}$ are the points in $(S^1)^3$ where the 3×3 Jacobian matrix $J\hat{\rho}$ has rank less than 3. When working with Lie groups, the Jacobian is $(d\hat{\rho})\hat{\rho}^{-1}$. This gives a map to the Lie algebra. The Lie algebra of $SO(3)$ is 3-dimensional and a change of basis gives $J\hat{\rho} = [z,\ R_{\tau_1}Lz,\ R_{\tau_1}LR_{\tau_2}Lz]$, z as above. $J\hat{\rho}$ has at least rank 2. It has has rank exactly 2 if and only if: $det(J\hat{\rho}) = \sin(\tau_2)\cos(\alpha) = 0$. As $\cos(\alpha) \neq 0$, the singular set of $\hat{\rho}$ is $\{\tau \mid \tau_2 = 0\} \cup \{\tau \mid \tau_2 = \pi\}$.

Critical set and number of solutions. The quotient map $\eta : (S^1)^3 \to SO(3) \to S^2$ that appears in the left-hand side of Eq. (4), has the same singular set as $\hat{\rho}$. The critical set of η – i.e., the image of $\{\tau \mid \tau_2 = 0\} \cup \{\tau \mid \tau_2 = \pi\}$ – is the union of $C_1 = R_{\tau_1}R_{\tau_3}z = z$ and $C_2 = R_{\tau_1}LR_\pi LR_{\tau_3}z = R_{\tau_1}LR_\pi Lz$ for all $\tau_1 \in S^1$. C_1 is the point that corresponds to the situation where the z-axes of W and frame 6 are parallel. Indeed, when $\tau_2 = 0$, the z-axis of frame 6 is parallel to the z-axis of W for any value of τ_1. On the other hand, $R_{\tau_1}LR_\pi Lz = [(\sin(2\alpha)\cos(\tau_1),\ \sin(2\alpha)\sin(\tau_1),\ -\cos(2\alpha)]^T$, so C_2 is the circle perpendicular to the z-axis and passing through the point $LR_\pi Lz$. See Fig. 3.

The inverse map η^{-1}, hence $\hat{\rho}^{-1}$, has a constant structure in C_1, C_2, and in each of the two open subsets of S^2 bounded by C_1 and C_2. We notice that: $L(LR_{\tau_2}Lz) = [\cos(\alpha)\cos(\tau_2),\ \cos(\alpha)\sin(\tau_2),\ \sin(\alpha)]^T$. So, $LR_{\tau_2}Lz$ is a circle perpendicular to Lz contained in the subset of S^2

between C_1 and C_2, except at $\tau_2 = 0$ and $\tau_2 = \pi$ where it coincides with C_1 and C_2, respectively (Fig. 3). For any fixed $\tau_1 \in S^1$, the set $R_{\tau_1} L R_{\tau_2} L z$ is the circle obtained by rotating $L R_{\tau_2} L z$ by τ_1 around the z axis. Thus, for every point s in the region between C_1 and C_2, $R_{\tau_1} L R_{\tau_2} L z$ contains s for two distinct values of τ_1. We conclude that η^{-1} has two values (τ_1^k, τ_2^k), $k = 1,\ 2$. In C_1, $s = z$ and $\eta^{-1}(s) = \{(\tau_1, 0) \mid \tau_1 \in S^1\}$. For any $s \in C_2$, $\eta^{-1}(s)$ has a single value of the form (τ_1, π). Elsewhere $\eta^{-1}(s)$ is empty.

Corresponding to each value (τ_1, τ_2) of $\eta^{-1}(s)$ there is a unique value of τ_3 given by Eq. (5), hence a single value of $\hat{\rho}^{-1}(R)$. Thus, as we initialize an orientation $R \in SO(3)$ not in the critical sets C_1 and C_2, $\rho^{-1}(R)$ is the disjoint union of two 3-D tori, written $\mathcal{M}_k$, $k = 1, 2$.

4. Inverse Position Map

Restriction to $\mathcal{M}_k$. We now study $p_k^{-1}(X)$, where $X \in \mathcal{R}^3$ and p_k, $k \in 1, 2$, is the position map p with its domain restricted to $\mathcal{M}_k$. Since $\theta_{2j-1} + \theta_{2j}$, $j = 1,\ 2,\ 3$, are constant on $\mathcal{M}_k$ and equal to τ_j^k, each point on $\mathcal{M}_k$ is uniquely defined by the values of θ_1, θ_3, and θ_5. Eq.(1) yields:

$$p_k : (S^1)^3 \to \mathcal{R}^3, \quad (\theta_1, \theta_3, \theta_5) \to v_{0,k} + (R_1 + R_{\tau_1^k} L R_3 + R_{\tau_1^k} L R_{\tau_2^k} L R_5) v_2$$

where $v_{0,k} = (R_{\tau_1^k} L + R_{\tau_1^k} L R_{\tau_2^k} L) v_1$ is a constant vector and $\{R_1 v_2\}$, $\{R_{\tau_1^k} L R_3 v_2\}$, and $\{R_{\tau_1^k} L R_{\tau_2^k} L R_5 v_2\}$ are constant circles of radius ℓ_1 contained in three different planes.

Computing $p_k^{-1}(X)$ amounts to solving the equation:

$$X' = \hat{p}_k(-\theta_2, \theta_3, \theta_5) := R_{-2} v_2 + L R_3 v_2 + L R_{\tau_2^k} L R_5 v_2, \tag{6}$$

where $X' = R_{\tau_1^k}^T (X - v_{0,k})$ and R_{-2} is the rotation of $-\theta_2$ around z.

Critical set. Here we directly determine the critical positions X' where the number of solutions of $\hat{p}_k$ changes. We rewrite Eq. (6) as:

$$X' - r(w) = q(t, u), \tag{7}$$

where we rename the variables as $t = -\theta_2$, $u = \theta_3$, $w = \theta_5$, and $\gamma = \tau_2^k$. $X' - r(w)$ is a unit circle centered at X' and $q(t, u)$ spans a quartic surface Q in $\mathcal{R}^3$. Q is the Minkowski sum of two circles, so it is bounded and connected. Eq. 7 can be solved by computing the intersections between $X' - r(w)$ and the coss-section curve of Q by the plane containing $X' - r(w)$. We compute $r(w) = \hat{x} c_w + \hat{y} s_w$. $\hat{x} = [s_\alpha^2 c_\gamma + c_\alpha^2,\ s_\gamma s_\alpha,\ s_\alpha c_\alpha (1 - c_\gamma)]^T$ and $\hat{y} = [-s_\alpha s_\gamma,\quad c_\gamma,\ c_\alpha s_\gamma]^T$ form an orthonormal basis for the plane

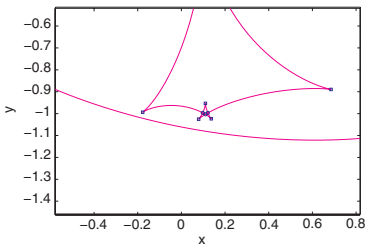

Figure 5. Zoom on a portion of $\mathcal{X}_d$ in Fig. 4. The centers of the small squares and the small circles are cusp points and self-intersection points, respectively.

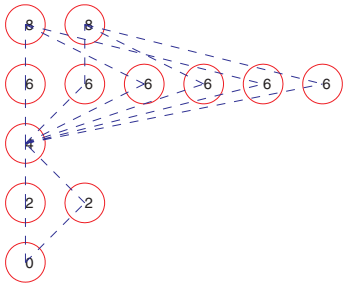

Figure 6. The planar graph determined by the discriminant curve of Fig. 4. The number of solutions is shown in each node.

containing the circle $r(w)$. Setting $\hat{z} = \hat{x} \times \hat{y}$, the equation of the plane containing $X' - r(w)$ is:

$$\hat{z}^T q \quad = \quad d \tag{8}$$

where $d = \hat{z}^T X'$. We let P_d denote the plane defined by this equation. When X' spans $\mathcal{R}^3$, P_d translates, but its orientation remains constant.

On the other hand, we can easily compute:

$$q(t,u) \quad = \quad [c_t - s_\alpha c_u, \quad s_t - s_u, \quad c_\alpha c_u]^T . \tag{9}$$

By replacing q by this expression in Eq. (8), we get the equation of the cross-section Q_d of Q by P_d in terms of (t,u):

$$c_{(u-\gamma)} + K(\gamma) s_{(t+\beta)} \quad = \quad \frac{d}{c_\alpha} \tag{10}$$

where $c_\beta = -\frac{s_\gamma}{K(\gamma)}$, $s_\beta = \frac{s_\alpha(1-c_\gamma)}{K(\gamma)}$, and $K(\gamma) = \sqrt{s_\gamma^2 + s_\alpha^2(1-c_\gamma)^2}$.

The number of intersection points in $Q_d \cap (X' - r(w))$ varies as X' runs over $\mathcal{R}^3$. The X' such that the circle is tangent to Q_d form the critical set $\mathcal{X} \subset \mathcal{R}^3$ of $\hat{p}_k$. Let $d_{\min}$ and $d_{\max}$ be the extreme values of d between which the plane $\hat{z}^T q = d$ and Q intersect. For any $d \in [d_{min}, d_{max}]$, the values of X' such that $X' - r(w)$ lies in the plane P_d and is tangent to Q_d form a curve $\mathcal{X}_d$ called the *discriminant curve* at d. The union of the discriminant curves for d in $[d_{\min}, d_{\max}]$ is the critical surface $\mathcal{X}$ of $\hat{p}_k$. Fig. 4 shows a discriminant curve, with several cusp and self-intersection points. An animation of both the cross-section of Q and the corresponding discriminant curve when d varies is available at `www.stanford.edu/~phwu1/curve` when $\gamma = \pi$.

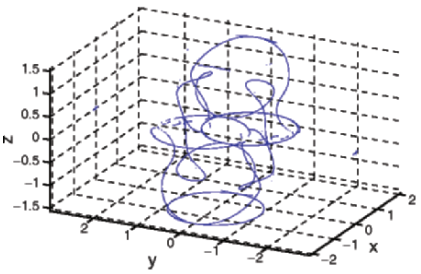

Figure 7. The cusp curves when $\gamma = \pi$.

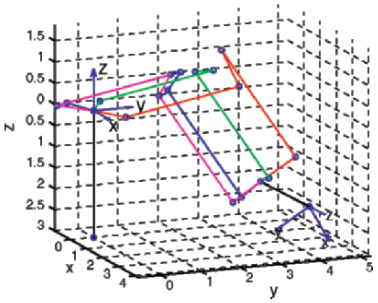

Figure 8. Four of the 16 solutions.

Decomposition of $\mathcal{R}^3$ into regions. The surface $\mathcal{X}$ decomposes $\mathcal{R}^3$ into open 3-D regions such that the number of solutions of the inverse position map is constant over each one. We first compute the decomposition of a plane P_d by $\mathcal{X}_d$. Next, we partition $[d_{min}, d_{max}]$ into smaller open intervals, such that over each such interval the discriminant curves $\mathcal{X}_d$ are equivalent. We get the decomposition of $\mathcal{R}^3$ by "stacking" the decompositions in the successive intervals.

Decomposition of P_d: We sweep a line L parallel to the y-axis across the plane P_d from left to right to construct a set S of sub-regions and their adjacency relations. S is initialized to the empty set. During the sweep, whenever L crosses a cusp point, a self-intersection point, or a vertical tangency point, sub-regions are added to S and the adjacency relation is updated. When the sweep is completed, adjacent sub-regions in S not separated by $\mathcal{X}_d$ are merged to form the decomposition of P_d. The outcome is a planar *graph* in which the nodes are the computed regions and the edges represent the adjacency relation. The number of solutions of the inverse position map varies by 2 at each crossing of a region boundary. We compute cusp and self-intersection points numerically by approximating the discriminant curve by line segments. Fig. 6 shows the graph computed from the discriminant curve shown in Fig. 4. An animation of the discriminant curve and the corresponding graph when d varies is available at `www.stanford.edu/~phwu1/curve` when $\gamma = \pi$.

Decomposition of $\mathcal{R}^3$: As d varies from d_{min} to d_{max}, the planar graph in P_d changes only at a finite number of *critical* values of d, which we denote d_i, $i = 1, ..., m$. Over each open interval (d_i, d_{i+1}), $i = 0, ..., m$, with $d_0 = d_{min}$ and $d_{m+1} = d_{max}$, the discriminant curves are equivalent and the planar graph remains constant. Let G_i be the planar graph in

interval (d_i, d_{i+1}). The decomposition of $\mathcal{R}^3$ is obtained by merging every pair of regions from G_i and G_{i+1}, for all $i = 0, ..., m$, that are adjacent, but not separated by $\mathcal{X}$. The corresponding nodes of the planar graphs are also merged to obtain the graph of the decomposition of $\mathcal{R}^3$.

The 2-D surface $\mathcal{X}$ is made of smooth patches separated by cusp and self-intersection curves. The cusp (resp. self-intersection) curves are the locus $\mathcal{X}^{\text{cusp}}$ (resp. $\mathcal{X}^{\text{self}}$) of all the cusp (self-intersection) points of the discriminant curves $\mathcal{X}_d$ when d varies. The critical values of d are contributed by $\mathcal{X}\backslash(\mathcal{X}^{\text{cusp}} \cup \mathcal{X}^{\text{self}})$, $\mathcal{X}^{\text{cusp}}$, and $\mathcal{X}^{\text{self}}$. For lack of space, we do not describe their computation here. Fig. 7 shows $\mathcal{X}^{\text{cusp}}$ for $\gamma = \pi$.

5. Existence of a 16-Solution Cell

Theorem 1. *There exists a nonempty open region in* $\mathcal{R}^3 \times SO(3)$ *such that for all* (X, R) *in this region,* $(p, \rho)^{-1}(X, R)$ *contains* 16 *points.*

Proof: Consider first an orientation $R_0 \in SO(3)$ that lies in the critical circle C_2. $\rho^{-1}(R_0)$ is a copy of $(S^1)^3$. There is a nonempty open region $E_0 \subset C_2$ such that for all R in E_0, $p(\rho^{-1}(R))$ has an open region U so that $p^{-1}(X)$ contains 8 points for $X \in U$ (see Fig. 6). Let R' be a noncritical orientation that is close to R_0. Then $\rho^{-1}(R')$ is a disjoint union of two 3-D tori $\mathcal{M}_k$, $k = 1, 2$. For each p_k, there exists a nonempty open region E_k with 8 inverse image points. Moreover, for R' sufficiently close to R_0, $E = E_1 \cap E_2$ is nonempty. Then $(p, \rho)^{-1}(X, R')$ has 16 solutions for all $X \in E$. ■

Using the idea in the proof, we constructed the following pose (X, R) of T:

$$X = \begin{bmatrix} 1.9760 \\ 4.5809 \\ -2.2402 \end{bmatrix} \quad \text{and} \quad R = \begin{bmatrix} 0.6742 & -0.3715 & -0.6383 \\ 0.2378 & -0.7091 & 0.6638 \\ -0.6992 & -0.5993 & -0.3897 \end{bmatrix},$$

such that $(p, \rho)^{-1}(X, R)$ contains 16 solutions (for a fragment in which $\ell_1 = 1$ and $\ell_2 = 3$). Four of them are shown in Fig. 8. (It is easily seen that the existence of 16-solution cell is independent of the link lengths as long as the short links all have the same length.)

Acknowledgements: This research was funded by NSF grant DMS-0443939.

References

Coutsias, E.A., Seok, C., Jacobson, M.P., and Dill, K.A. (2004), A kinematic view of loop closure. *J. Comp. Chem.*, 25:510–528.

Creighton, T.E. (1993), *Proteins: Structures and molecular properties*, W. H. Freeman and Company, New York, 2nd edition.

Mavroidis, C., and Roth, B. (1994), Structural Parameters which reduce the number of manipulator configurations. *J. Mech. Design, Trans. ASME*, vol. 116, pp. 3–10.

PREDICTING REACHING POSTURES USING A KINEMATICALLY CONSTRAINED SHOULDER MODEL

Vincent De Sapio, James Warren, and Oussama Khatib
Artificial Intelligence Laboratory
Stanford University
{vdesap, warren, khatib}@stanford.edu

Abstract We present a new muscle effort criteria for predicting physiologically accurate upper limb motion in human subjects based on skeletal kinematics, muscle routing kinematics, and muscle strength characteristics. The new criteria properly accounts for the cross-joint coupling associated with the routing kinematics of multi-articular muscles. We also employ a new kinematically constrained model of the human shoulder complex, which is critical for the proper evaluation of our muscle effort criteria. Through a set of subject trials we have shown good correlation between natural reaching postures and our proposed criteria.

Keywords: Muscle effort, shoulder complex, constraints, muscle routing kinematics

1. Introduction

The prediction and synthesis of human movement has presented a daunting challenge to the biomechanics, neuroscience, and robotics communities. In the presence of this challenge there is a significant motivation to understand and emulate human movement. Given a specific task the prediction of kinematically redundant upper limb motion is a problem of choosing one of a multitude of control solutions which all yield kinematically feasible solutions. It has long been observed that humans resolve this redundancy problem in a relatively consistent manner (Lacquaniti and Soechting, 1982; Kang et al., 2005). For this reason general mathematical models have proven to be valuable tools for motor control prediction across human subjects.

Many of the models for predicting human arm movement, including the minimum work model (Soechting et al., 1995) and the minimum torque-change model (Uno et al., 1989), do not involve any direct inclusion of muscular properties such as routing kinematics and strength properties. Even models described as employing biomechanical variables (Kang et al., 2005) typically employ only variables derivable purely from skeletal kinematics and not musculoskeletal behavior. We feel that the

J. Lenarčič and B. Roth (eds.), Advances in Robot Kinematics, 209–218.

utilization of a model-based characterization of muscle systems (Zajac, 1993; Delp and Loan, 2000), which accounts for muscle kinematic and strength properties, is critical to authentically simulating human motion since all human motion is rooted in, and bounded by, physiological capabilities.

We will present a new methodology for predicting arm configuration in reaching movements by examining the muscular effort required to perform positioning tasks. This is built upon the work of Khatib et al., 2004, but involves a number of improvements in methodology. An important element of this approach is the implementation of a sufficiently sophisticated musculoskeletal model of the upper limb that accounts for kinematic coupling between the constituents of the human shoulder complex (Holzbaur et al., 2005). This provides fidelity in predicting muscle forces, joint moment arms, and resulting muscle induced joint moments, particularly in the shoulder complex. With our methodology and physiological models we show that natural task-driven human arm postures can be predicted accurately using a criteria based on a skeletal kinematics, muscle routing kinematics, and muscle strength characteristics. This is validated through a set of targeted subject trials.

2. Human Upper Extremity Model

The upper extremity model of Holzbaur et al., 2005, has been employed, with some modification, in this work. The model, consisting of a shoulder complex and a lower arm, has been implemented in the SIMM (**S**oftware for **I**ntegrated **M**usculoskeletal **M**odeling) environment (Delp and Loan, 2000). A minimal set of 7 generalized coordinates were chosen to describe the configuration of the shoulder complex, elbow, and wrist (3 for the shoulder complex, 2 for elbow flexion and pronation, and 2 for wrist flexion and deviation). This is depicted in Fig. 1.

Fidelity in predicting muscle action was an important requirement for the model employed in this work. In particular, proper kinematics of the shoulder complex is critical in generating realistic muscle paths and associated joint moments. While the purpose of the shoulder complex is to produce spherical articulation of the humerus, the resultant motion does not exclusively involve motion of the glenohumeral joint (see Fig. 1). The shoulder girdle, which is comprised of the clavicle and scapula, connects the glenohumeral joint to the torso and produces some of the motion associated with the overall articulation of the humerus. While this motion is small compared to the glenohumeral motion its impact on overall arm function is significant (Klopčar and Lenarčič, 2001; Lenarčič

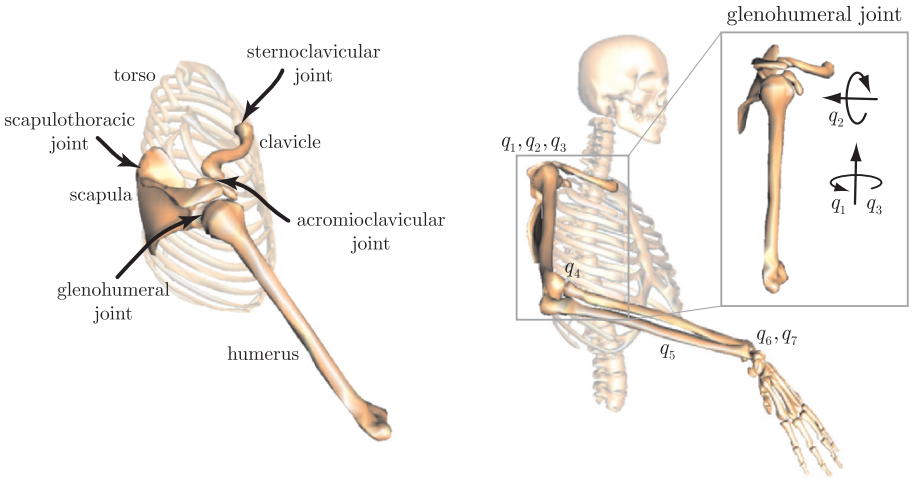

Figure 1. (Left) Constituents of the shoulder complex including the scapula, clavicle, and humerus. The glenohumeral joint produces spherical motion of the humerus. The shoulder girdle attaches the glenohumeral joint to the torso and influences the resultant motion of the humerus. (Right) Kinematic parameterization of the model of Holzbaur et al.

et al., 2000). Part of this impact is related to the shoulder girdle's influence on the muscle routing kinematics.

The constrained movement of the shoulder girdle was determined from the shoulder rhythm regression analysis of de Groot and Brand, 2001. The model obtained from this regression analysis was shown to fit well for an independent set of shoulder motions and on a different set of subjects than was used for the regression analysis. For these reasons the model of de Groot and Brand is considered to be superior in predicting shoulder motion than a simple unconstrained model which only reflects glenohumeral rotation. Using the results of de Groot and Brand the constraints that model the shoulder girdle are implicitly handled, with all motions of the shoulder girdle being dependent on the three glenohumeral rotation coordinates. These are elevation plane, q_1, elevation angle, q_2, and shoulder rotation, q_3.

Due that fact that SIMM restricts any joint motion to a function of a single independent generalized coordinate, the regression equations were simplified by Holzbaur et al. to be a function of only thoracohumeral (humerus elevation) angle, q_2. The shoulder kinematics for this parameterization are shown in Table 1.

The terms $\boldsymbol{d}_1$, $\boldsymbol{d}_2$, and $\boldsymbol{d}_3$ are fixed translation vectors and $\boldsymbol{Q}_1, \cdots, \boldsymbol{Q}_7$ are rotation matrices associated with spins about successive local

Table 1. Shoulder kinematics using a minimal set of generalized coordinates.

Translation	**Rotation**
clavicle	
${}^t\boldsymbol{d}_c = \boldsymbol{d}_1$	${}^t_c\boldsymbol{Q} = \boldsymbol{Q}_1(c_1 q_2)\boldsymbol{Q}_2(c_2 q_2)$
scapula	
${}^t\boldsymbol{d}_s = {}^t\boldsymbol{d}_c + {}^t_c\boldsymbol{Q}\boldsymbol{d}_2$	${}^t_s\boldsymbol{Q} = \boldsymbol{Q}_3(c_3 q_2)\boldsymbol{Q}_4(c_4 q_2)\boldsymbol{Q}_5(c_5 q_2)$
humerus	
${}^t\boldsymbol{d}_h = {}^t\boldsymbol{d}_s + {}^t_s\boldsymbol{Q}\boldsymbol{d}_3$	${}^t_h\boldsymbol{Q} = \boldsymbol{Q}_6(q_1)\boldsymbol{Q}_7(q_2)\boldsymbol{Q}_6(-q_1)\boldsymbol{Q}_6(q_3)$

coordinate axes, where the arguments identify the spin angles. The superscript t refers to the torso as the frame of reference. The constraint constants, $\boldsymbol{c}$, associated with the dependency on humerus elevation angle, q_2, were obtained from the regression analysis of de Groot and Brand, 2001.

De Sapio et al., 2006, provide an extensive analysis of the impact of shoulder girdle motion, associated with glenohumeral coupling constraints, on the muscle routing kinematics and moment arms about the glenohumeral joint. The constrained model employed here typically generates moment arms of substantially larger magnitude than those of a simple model with no kinematic coupling between glenohumeral and shoulder girdle motion. The resulting moment generating capacities associated with the constrained model are also typically larger in magnitude than those associated with the simple model. This is of paramount importance for the implementation addressed in the following section.

3. Muscle Effort Minimization

A scalar measure of instantaneous (path independent) muscle effort at a specific configuration can be defined based on the necessary gravity torque to maintain the configuration and the muscle strength capacity at the configuration. Activation, which represents the normalized exertion of muscles, provides a natural measure for this. Specifically, the magnitude of the muscle activation vector, $\boldsymbol{a}$, has been used as a scalar optimization criteria in both static and dynamic optimizations. That is, we can choose our instantaneous muscle effort measure, U, to be $U(\boldsymbol{q}, \dot{\boldsymbol{q}}) = \|\boldsymbol{a}\|^2$. To express this measure we first represent the joint torques, $\boldsymbol{\Gamma}$ in terms of muscle action,

$$\boldsymbol{\Gamma}(\boldsymbol{q}, \dot{\boldsymbol{q}}, \boldsymbol{a}) = \boldsymbol{K}_\Gamma(\boldsymbol{q}, \dot{\boldsymbol{q}})\boldsymbol{a} \tag{1}$$

where $\boldsymbol{K}_\Gamma(\boldsymbol{q}, \dot{\boldsymbol{q}})$ is the muscle torque-activation gain matrix. That is, it maps muscle activation, $\boldsymbol{a}$, to joint torque (De Sapio et al., 2005). Due to the fact that there are typically more muscles spanning a set of joints than the number of generalized coordinates used to describe those joints this equation will have an infinite set of solutions for $\boldsymbol{a}$. Choosing the solution, $\boldsymbol{a}_o$, which has the smallest magnitude yields,

$$\boldsymbol{a}_o = \boldsymbol{K}_\Gamma^+ \boldsymbol{\Gamma} = \boldsymbol{K}_\Gamma^T (\boldsymbol{K}_\Gamma \boldsymbol{K}_\Gamma^T)^{-1} \boldsymbol{\Gamma} \tag{2}$$

where $\boldsymbol{K}_\Gamma^+$ is the pseudoinverse of $\boldsymbol{K}_\Gamma$. Our muscle effort measure can then be expressed as,

$$U(\boldsymbol{q}) = \|\boldsymbol{a}_o\|^2 = \boldsymbol{g}^T (\boldsymbol{K}_\Gamma \boldsymbol{K}_\Gamma^T)^{-1} \boldsymbol{g} \tag{3}$$

Note that we have eliminated the dependency on $\dot{\boldsymbol{q}}$, as we will concern ourselves only with static configurations for the remainder of our analysis. Similarly, $\boldsymbol{\Gamma}$ has been replaced with the configuration space gravity vector, $\boldsymbol{g}$, since in the static case $\boldsymbol{\Gamma} \rightarrow \boldsymbol{g}$. Expressing this in terms of constituent terms we have,

$$U(\boldsymbol{q}, \dot{\boldsymbol{q}}) = \boldsymbol{g}^T [\boldsymbol{L}^T (\boldsymbol{K}_f \boldsymbol{K}_f^T) \boldsymbol{L}]^{-1} \boldsymbol{g} \tag{4}$$

where we have made use of the relationship, $\boldsymbol{K}_\Gamma = \boldsymbol{L}^T \boldsymbol{K}_f$. The muscle force-activation gain matrix, $\boldsymbol{K}_f$, maps muscle activation to muscle force (De Sapio et al., 2005). The transpose, $\boldsymbol{L}^T$, of the muscle Jacobian is a kinematic quantity, based on muscle routing kinematics, that maps muscle force to joint torque (Khatib et al., 2004). If we dissect the structure of this effort criteria as follows,

$$U = \boldsymbol{g}^T \overbrace{[\ \underbrace{\boldsymbol{L}^T}_{\text{kinematics}}\ \underbrace{(\boldsymbol{K}_f \boldsymbol{K}_f^T)}_{\text{kinetics}}\ \underbrace{\boldsymbol{L}}_{\text{kinematics}}\ ]}^{\text{muscular capacity}}{}^{-1} \boldsymbol{g} \tag{5}$$

we gain some physical insight into what is being measured. The terms inside the brackets represent a measure of the net capacity of the muscles. This is a combination of the force generating kinetics of the muscles as well as the mechanical advantage of the muscles, as determined by the muscle routing kinematics. The terms outside of the brackets represent the kinetic requirements of the task/posture; in this case the gravity torques at the joints.

Eq. 5 represents a generalization of the joint decoupled measure used by Khatib et al., 2004. That measure projected muscle strength capacities to the joint level in a decoupled manner. Consequently, the cross-joint coupling associated with multi-articular muscles (muscles that span

more than one joint) was ignored. The measure of Eq. 5 properly accounts for multi-articular muscle coupling in the musculoskeletal system.

It is noted that the solution of Eq. 1 expressed in Eq. 2 corresponds to a constrained minimization of $\|\boldsymbol{a}\|^2$, however, this solution does not enforce the constraint that muscle activation must be positive (muscles can only produce tensile forces). Imposing the inequality constraint, $a \geqslant 0$, on the activations requires a quadratic programming approach to performing the constrained minimization. In this case the solution to Eq. 1 which minimizes $\|\boldsymbol{a}\|^2$ and satisfies $a \geqslant 0$ can be represented in shorthand as,

$$\boldsymbol{a}_o = \mathrm{qp}(\boldsymbol{K}_\Gamma, \boldsymbol{\Gamma}, \|\boldsymbol{a}\|^2,\ a_i \geqslant 0) \tag{6}$$

where $\mathrm{qp}(\cdot)$ represents the output of a quadratic programming function (eg. `quadprog()` in the Matlab optimization toolbox). Our muscle effort criteria is then $U(\boldsymbol{q}) = \|\boldsymbol{a}_o\|^2$, where $\boldsymbol{a}_o$ is given by Eq. 6. Despite the preferred use of quadratic programming for computational purposes, Eq. 5 provides valuable insights at a conceptual level.

To find a task consistent static configuration which minimizes $U(\boldsymbol{q})$, we first define the self-motion manifold associated with a fixed task point, $\boldsymbol{x}_o$. This is given by $M(\boldsymbol{x}_o) = \{\boldsymbol{q} \,|\, \boldsymbol{x}(\boldsymbol{q}) = \boldsymbol{x}_o\}$ where $\boldsymbol{x}(\boldsymbol{q})$ is the operational point of the kinematic chain (e.g. the position of the hand). The problem of finding a minimal effort task consistent configuration can then be stated as minimizing $U(\boldsymbol{q})$ on $M(\boldsymbol{x}_o)$.

4. Experiments

A set of experiments was conducted to provide validation for the muscle effort minimization approach of Section 3. The subjects chosen were six right-handed adult males with normal or corrected-to-normal vision. The subjects were seated with a test fixture directly in front of them. The test fixture contained five visual targets represented as physical markers positioned at different locations. A set of weights (5, 8, and 15 lbs) were placed to the side of the subjects. An eight-camera Qualisys retroreflective motion capture system was used to record subject motion during the trials at a capture rate of 250 Hz.

The subjects performed a set of tasks designed to isolate upper limb reaching motion. While seated each subject was instructed to pick up a weight and move it to each target and hold a static configuration at the target for 4 seconds (see Fig. 2). The subjects were instructed to perform the movement in any manner which felt natural and comfortable to them. Five consecutive trials were performed for each weight (8, 12, and 15lb) as well as a trial with no weight in hand, for a total of 20

trials. The total number of 20 trials took each subject roughly an hour to perform; including time for hardware set up and marker placement.

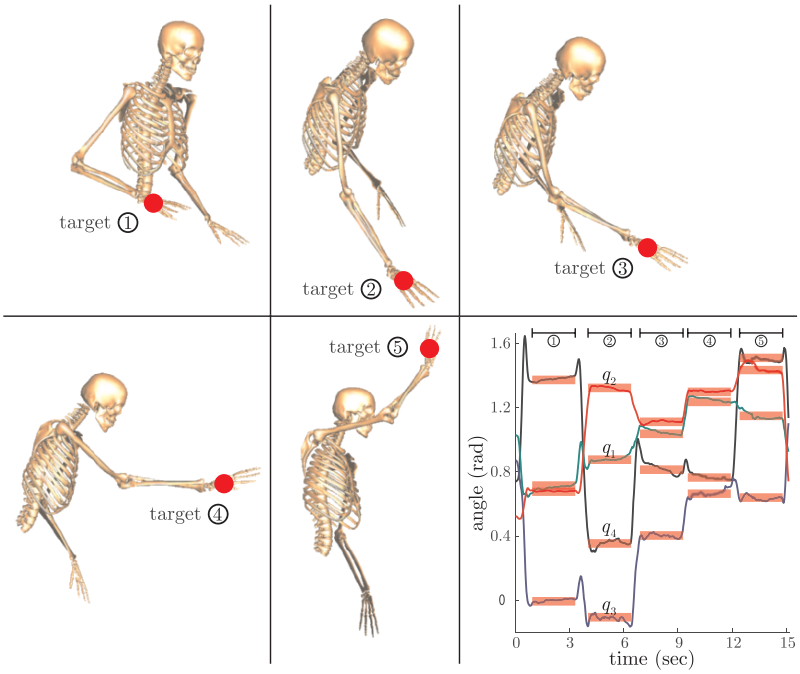

Figure 2. Subject reaching to a set of 5 target locations from a seated configuration. The subject performs these targeted reaching movements freehand and with a total of three different weights in hand. Time histories of shoulder joint angles, q_1, q_2, and q_3, and elbow joint angle, q_4, show steady state configurations at each of the targets.

Following motion capture the marker data was segmented using the Qualisys Track Manager software. To obtain joint space trajectories, custom Matlab scripts were written based on the inverse kinematics of the constrained shoulder complex presented in Section 2. The steady state configurations associated with the five targets were obtained from the joint space trajectories for each trial (see Fig. 2). For each configuration a 1-dimensional self motion manifold, $M(\boldsymbol{x}_o)$, was computed numerically given the fixed target location, $\boldsymbol{x}_o$. The manifold was associated with the variation of the 3 shoulder complex joint angles, q_1, q_2, and q_3, and the elbow joint angle, q_4.

The muscle effort criteria of Section 3 was then computed. SIMM was used to generate the maximum muscle induced moments over the self motion manifold for each trial. Matlab scripts were then written to construct the muscle torque-activation gain matrix, $\boldsymbol{K}_\Gamma$, from the computed muscle moments as well as the gravity vector, $\boldsymbol{g}$. A quadratic

programming routine (`quadprog()` from Matlab's optimization toolbox) was used to enforce positive values for muscle activation.

Figure 3 depicts the results of the muscle effort computations for one of the subject trials with no weight in hand. The subject's chosen configuration was typically within several degrees (norm based metric along the self motion manifold) of the predicted configuration associated with minimizing the computed muscle effort. This was consistent across the set of subjects, with the largest deviation between experimental and predicted configurations being on the order of 25° and more commonly under 10°.

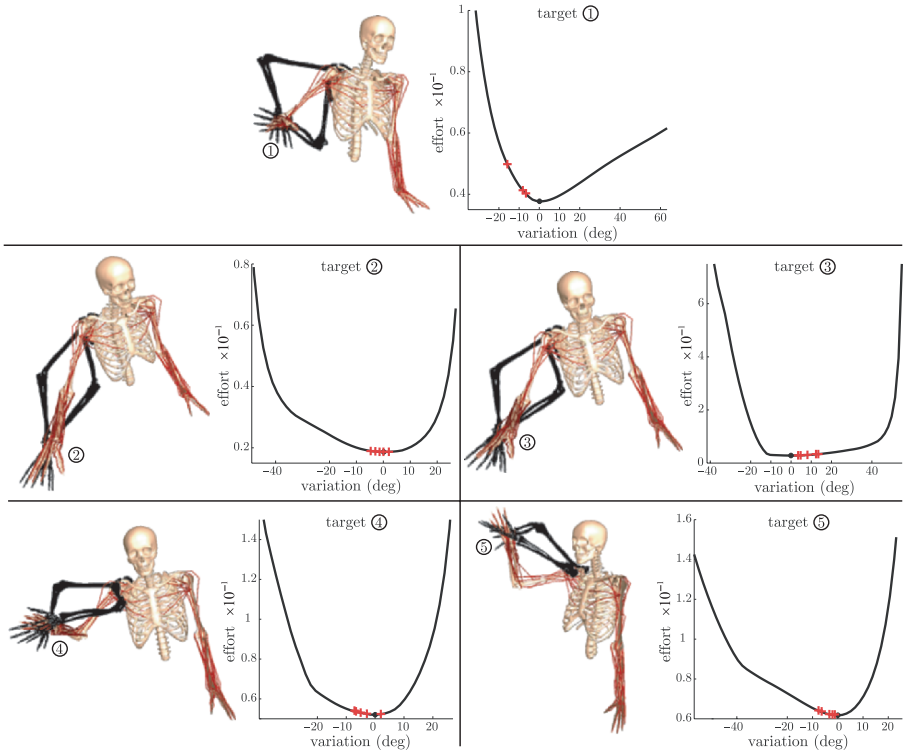

Figure 3. Muscle effort variation for one of the subject trials with no weight in hand. Each plot depicts the muscle effort for one of the five target configurations. The locations of the subject's chosen configurations are depicted with a red +. The full range of motion is depicted by the black silhouettes (±90° from nominal).

Figure 4 depicts the results of the muscle effort computations for a set of trials with different weights. In each case the weight at the hand was projected into joint space and added to the gravity vector associated with the limb segments. The arm configurations at the targets did not

dramatically change with increased weight at the hand. This implies that the subjects tended to generate stereotyped reaching postures that were not highly sensitive to the weight being carried. As a consequence we included a weighting between the component of the gravity vector associated with limb masses and the component associated with the external weight carried at the hand. With this weighting we were able to maintain good predictions with increases in the weight at the hand.

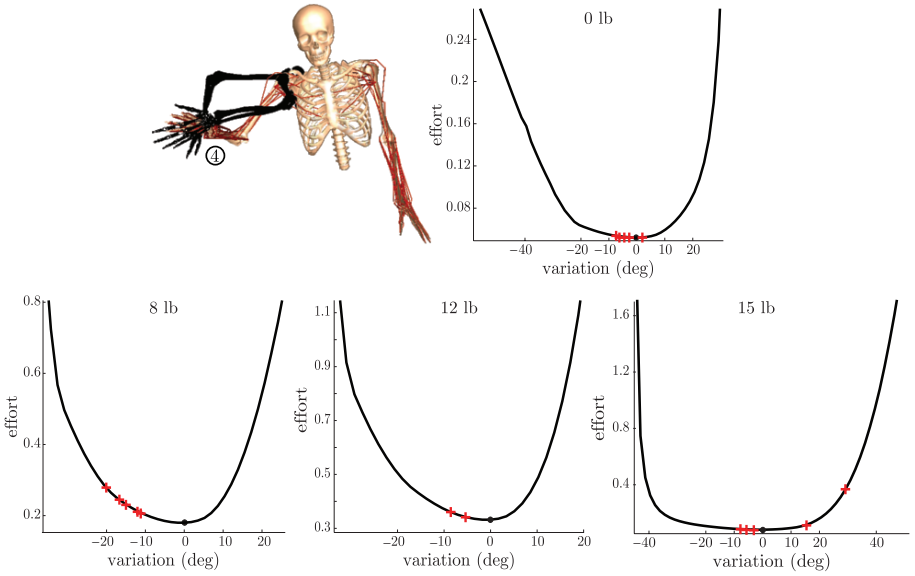

Figure 4. Muscle effort variation for a set of trials to the fourth target location with different weights in hand. The weight at the hand was projected into joint space and added to the gravity vector associated with the limb segments The locations of the subject's chosen configurations are depicted with a red +.

5. Conclusions

Building upon the work of Khatib et al., 2004, we have implemented a new muscle effort criteria for predicting physiologically accurate upper limb motion. This criteria is a generalization of the joint decoupled measure used previously. The new criteria properly accounts for the cross-joint coupling associated with multi-articular muscle routing kinematics. We also employ a new kinematically constrained model of the human shoulder complex (Holzbaur et al., 2005). The modeling of the shoulder rhythm using constraints between the scapula, clavicle, and humerus provides more physiologically accurate muscle routing kinematics and, consequently, better estimates of muscle induced moment arms

about the glenohumeral joint (De Sapio et al., 2006). Through a set of subject trials we have shown good correlation between natural reaching postures and those predicted by our proposed criteria.

6. Acknowledgements

The authors would like to thank Scott Delp and Katherine Holzbaur for their helpful comments on this work. Additionally, the motion capture support of Chris Dyrby is gratefully acknowledged.

References

de Groot, J. H., and Brand, R. (2001), A three-dimensional regression model of the shoulder rhythm, *Clinical Biomechanics*, vol. 16, pp. 735-743.

De Sapio, V., Warren, J., Khatib, O., and Delp S. (2005), Simulating the Task-level Control of Human Motion: A Methodology and Framework for Implementation, *The Visual Computer*, vol. 21, no. 5, pp. 289-302.

De Sapio, V., Holzbaur, K.R., and Khatib, O. (2006), The Control of Kinematically Constrained Shoulder Complexes: Physiological and Humanoid Examples, *Proceedings of the 2005 IEEE International Conference on Robotics and Automation*, vol. 1, pp. 470-475, Barcelona, April 2005.

Delp, S.L., and Loan, J.P. (2000), A Computational Framework for Simulating and Analyzing Human and Animal Movement, *IEEE Computing in Science and Engineering*, vol. 2, no. 5, pp. 46-55.

Holzbaur, K.R., Murray, W.M., and Delp, S.L. (2005), A Model of the Upper Extremity for Simulating Musculoskeletal Surgery and Analyzing Neuromuscular Control, *Annals of Biomedical Engineering*, vol. 33, no. 6, pp. 829-840.

Kang, T., He, J., Helms Tillery, S.I. (2005), Determining natural arm configuration along a reaching trajectory, *Experimental Brain Research*, vol. 167, pp. 352-361.

Khatib, O., Warren, J., De Sapio, V., and Sentis, L. (2004), Human-like motion from physiologically-based potential energies, Lenarčič, J., Galletti, C.(eds.),*On advances in robot kinematics*, pp. 149-163, Boston: Kluwer, 2004.

Klopčar, N., and Lenarčič, J. (2001), Biomechanical Considerations on the Design of a Humanoid Shoulder Girdle, *Proceedings of the 2001 IEEE/ASME International Conference on Advanced Intelligent Mechatronics*, vol. 1, pp. 255-259, Como, Italy.

Holzbaur, K.R., Murray, W.M., and Delp, S.L. (1982), Coordination of Arm and Wrist Motion During a Reaching Task, *Journal of Neuroscience*, vol. 2, no. 4, pp. 399-408.

Lenarčič, J., Stanišić, M.M., and Parenti-Castelli, V. (2000), Kinematic design of a humanoid robotic shoulder complex, *Proceedings of the 2000 IEEE International Conference on Robotics and Automation*, vol. 1, pp. 27-32, San Francisco, CA.

Soechting, J.F., Buneo, C.A., Herrmann, U., Flanders, M. (1995), Moving Effortlessly in Three Dimensions: Does Donders Law Apply to Arm Movement? *Journal of Neuroscience*, vol. 15, pp. 6271-6280.

Uno, Y., Kawato, M., Suzuki, R. (1989),Formation and control of optimal trajectory in human multijoint arm movement, *Biological Cybernetics*, vol. 61, pp. 89-101.

Zajac, F.E. (1993) Muscle coordination of movement: a perspective, *Journal of Biomechanics*, vol. 26, pp. 109-124.

Analysis of Mechanisms

SELF MOTIONS OF A SPECIAL 3-$\underline{R}PR$ PLANAR PARALLEL ROBOT

Damien Chablat, Phlippe Wenger
Institut de Recherche en Communications et Cybernétique de Nantes
1, rue de la Noë, 44321 Nantes, FRANCE
[damien.chablat, philippe.wenger]@irccyn.ec-nantes.fr

Ilian A. Bonev
École de technologie supérieure
1100, rue Notre-Dame Ouest, Montréal (Québec) H3C 1K3, CANADA
ilian.bonev@etsmtl.ca

Abstract This paper studies the kinematic geometry of a 3-$\underline{R}PR$ planar parallel robot with actuated base joints and congruent equilateral base and mobile platform. The singularity loci are first determined. Then the global behavior at all singularities is geometrically described by studying the degeneracies of the direct kinematic model. This study is made easier by the fact that one of the two direct kinematic solutions is trivial and singular. It is shown that this parallel robot has Cardanic self motions.

Keywords: Kinematic geometry, planar parallel mechanism, singularity, self motion

1. Introduction

Often, the main drawback of choosing design conditions for which the direct kinematic problem of a parallel robot becomes simplified is the appearance of self motions (Husty and Zsombor-Murray, 1994; Karger, 2002; Wohlhart, 2002). While self motions are certainly the worst type of singularity a parallel robot could cross, they should simply be avoided like any other type of singularity. Then, why not use parallel robots with self motions if these robots have simpler direct kinematics?

For example, in a recent paper (Bonev et al., 2006), the authors have shown that all singularities of the popular spherical parallel robot design, known as the *Agile Eye*, correspond to self motions, yet this design is arguably the "best" spherical wrist. (In the *Agile Eye*, any two axes that are fixed to one another are orthogonal.) Indeed, the singularity loci of the *Agile Eye* are not surfaces but curves, which means that the robot's theoretical workspace is undivided and unlimited. Furthermore,

J. Lenarčič and B. Roth (eds.), Advances in Robot Kinematics, 221–228.

while the *Agile Eye* still has eight assembly modes, like any other 3-$\underline{R}RR$ parallel wrist (R stands for revolute and P for prismatic joint, and an underline indicates which joint is actuated), half of them correspond to four singular orientations and the other half are easily found in cascade.

Self motions have been investigated mainly for Stewart-Gough platforms. Few planar parallel robots with self motions have been studied, and the kinematics of the general 3-$\underline{R}PR$ planar parallel robot was only briefly considered in two papers (Merlet, 1996; Bonev et al., 2003). We came up with a special design for this peculiar planar parallel robot on a fruitless search for a planar equivalent to the *Agile Eye*. While our special 3-$\underline{R}PR$ planar parallel robot is certainly not the most useful one, the study of its self motions brings insight into the complex relationship between direct kinematics and singularities of parallel robots.

In the next section, we will briefly present the analytic expression for the singularity loci of our special 3-$\underline{R}PR$ planar parallel robot. We will identify a range of orientations for which the robot has a sufficiently large singularity-free workspace. Then, in Section 3, we will describe the several types of singular configurations by studying the degeneracies of the direct kinematics and show that they belong to self motions. Conclusions are given in the last section.

2. Singularity Loci

The special 3-$\underline{R}PR$ planar parallel robot is shown in Fig. 1. Its mobile platform and base form congruent equilateral triangles. We denote with O_i and B_i (in this paper, $i = 1, 2, 3$) the intersections of the base and platform revolute joint axes, respectively, with a plane normal to these axes. Then, let Oxy and $Cx'y'$ be the base and mobile reference frames, respectively. The generalized coordinates locating the mobile platform, i.e., the mobile frame $Cx'y'$, in the base frame Oxy will be denoted by x, y, and ϕ. We define each active-joint variable θ_i as the angle between the x-axis and a unit vector $\mathbf{v}_i$ that defines the direction of the prismatic joint of leg i, measured in counter-clockwise sense. Finally, the directed distance from point O_i to point B_i along vector $\mathbf{v}_i$ is denoted by ρ_i.

Skipping the derivation and referring the reader to (Bonev et al., 2003), the velocity equation for the 3-$\underline{R}PR$ planar parallel robot is

$$\mathbf{A}\dot{\boldsymbol{q}} = \begin{bmatrix} m_1 & \mathbf{f}_1^T \\ m_2 & \mathbf{f}_2^T \\ m_3 & \mathbf{f}_3^T \end{bmatrix} \begin{bmatrix} \dot{\phi} \\ \dot{x} \\ \dot{y} \end{bmatrix} = \begin{bmatrix} \rho_1 & 0 & 0 \\ 0 & \rho_2 & 0 \\ 0 & 0 & \rho_3 \end{bmatrix} \begin{bmatrix} \dot{\theta}_1 \\ \dot{\theta}_2 \\ \dot{\theta}_3 \end{bmatrix} = \mathbf{B}\dot{\boldsymbol{\theta}}\,, \tag{1}$$

where

$$\mathbf{f}_i \;=\; \mathbf{E}\,\mathbf{v}_i = \begin{bmatrix} -\sin\theta_i \\ \cos\theta_i \end{bmatrix} = \mathbf{E}\,(\mathbf{r}_{OC} + \mathbf{r}_{CB_i} - \mathbf{r}_{OO_i})/\rho_i, \tag{2}$$

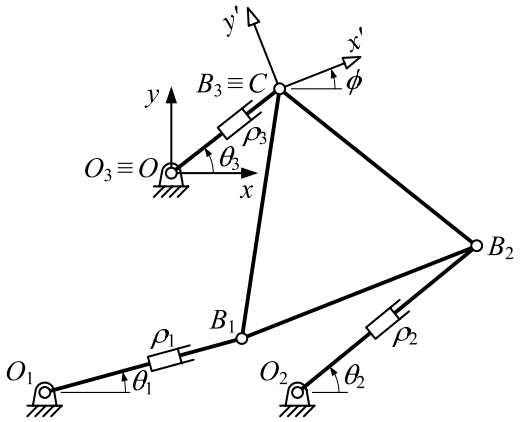

Figure 1. 3-$\underline{R}PR$ planar parallel robot with congruent equilateral base and platform.

$$m_i \;=\; \mathbf{f}_i^T\,\mathbf{E}\,\mathbf{r}_{CB_i} = \mathbf{f}_i^T\,\mathbf{E}\,\mathbf{R}\,\mathbf{r}'_{CB_i}, \tag{3}$$

and

$$\mathbf{E} = \begin{bmatrix} 0 & -1 \\ 1 & 0 \end{bmatrix},\; \mathbf{R} = \begin{bmatrix} \cos\phi & -\sin\phi \\ \sin\phi & \cos\phi \end{bmatrix}. \tag{4}$$

Furthermore, $\mathbf{r}_{OC} = [x, y]^T$, $\mathbf{r}_{OO_i}$ and $\mathbf{r}_{CB_i}$ are the vectors along OO_i and CB_i, respectively, expressed in the base frame, and $\mathbf{r}'_{CB_i}$ is the vector along CB_i expressed in the mobile frame. Without loss of generality, we define these vectors as

$$\mathbf{r}_{OO_1} = \mathbf{r}'_{CB_1} = \begin{bmatrix} -1/2 \\ -\sqrt{3}/2 \end{bmatrix},\; \mathbf{r}_{OO_2} = \mathbf{r}'_{CB_2} = \begin{bmatrix} 1/2 \\ -\sqrt{3}/2 \end{bmatrix},$$

$$\mathbf{r}_{OO_3} = \mathbf{r}'_{CB_3} = \begin{bmatrix} 0 \\ 0 \end{bmatrix},$$

or, in other words, we set the sides of the base and platform to unity, and fix the base and platform frames at points O_3 and B_3, respectively.

Type 2 singularities occur when $\mathbf{A}$ is singular. Geometrically, this means that the lines normal to the directions of the prismatic joints and passing through points B_i are concurrent or parallel. Simplifying the determinant of $\mathbf{A}$ and zeroing yields:

$$\det(\mathbf{A}) = \frac{\sqrt{3}(\cos\phi - 1)}{2\rho_1\rho_2\rho_3}\left((x - x_c)^2 + (y - y_c) - r^2\right) = 0, \tag{5}$$

where

$$x_c = -\frac{1}{\sqrt{3}}\sin\phi,\; y_c = -\frac{1}{\sqrt{3}}(1 - \cos\phi),\; r = \sqrt{\frac{2(1 - \cos\phi)}{3}}.$$

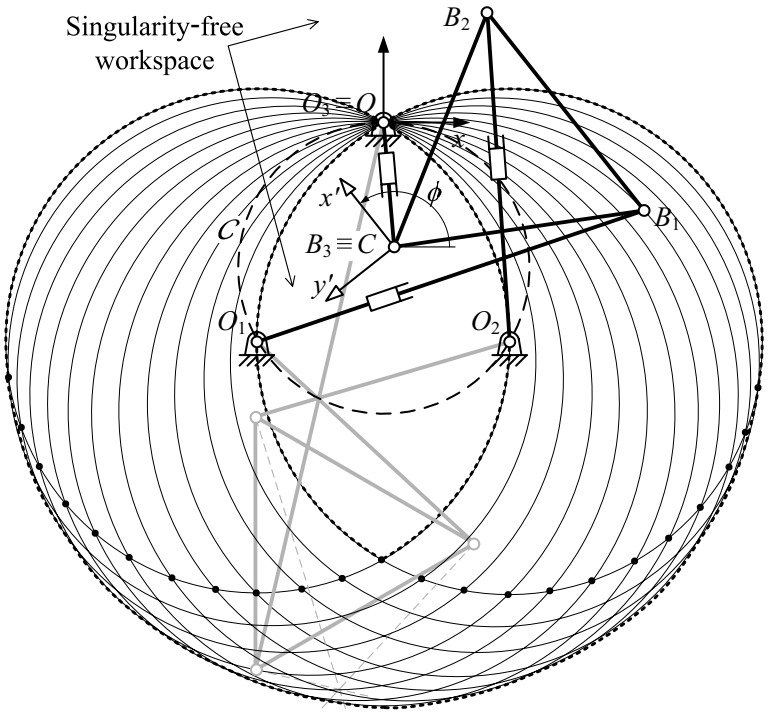

Figure 2. Singularity loci and singularity-free workspace for $\phi \in [120°, 240°]$.

Therefore, Type 2 singularity loci for this mechanism are (a) the whole xy-plane, when $\phi = 0$ (the directions of all prismatic joints are parallel), and (b) a circle of radius r, centered at (x_c, y_c), which passes through O_3, when $\phi \neq 0$. Note, however, that Eq. (1) is of indeterminate form (0/0) at a Type 1 singularity. Indeed, at a Type 1 singularity, a motor can freely rotate without affecting the pose of the platform. Such a pose would be Type 2 singular only for specific combinations of the active-joint variables that correspond to singular legs.

We will conclude this section by proposing a range of orientations for which the singularity-free workspace is sufficiently large. Apparently, this range needs to exclude $\phi = 0$, and if symmetry is to be observed, the best choice would be a range centered at $\phi = 180°$. Figure 2 shows our parallel robot with a series of Type 2 singularity circles corresponding to $\phi = 120° + k10°$ $(k = 0, 1, 2, ..., 12)$. The dots correspond to Type 1 singularities. The singularity-free workspace for the orientation range $\phi \in [120°, 240°]$ is the one that excludes the circle-swept region in Fig. 2.

Based on this purely algebraic analysis, it is certainly not obvious, but one can verify by using Eq. (5) that for any Type 2 singular configuration for which $\phi \neq 0$, lines O_iB_i intersect at a common point lying on the circumcircle of the base (see the gray-colored configuration in Fig. 2).

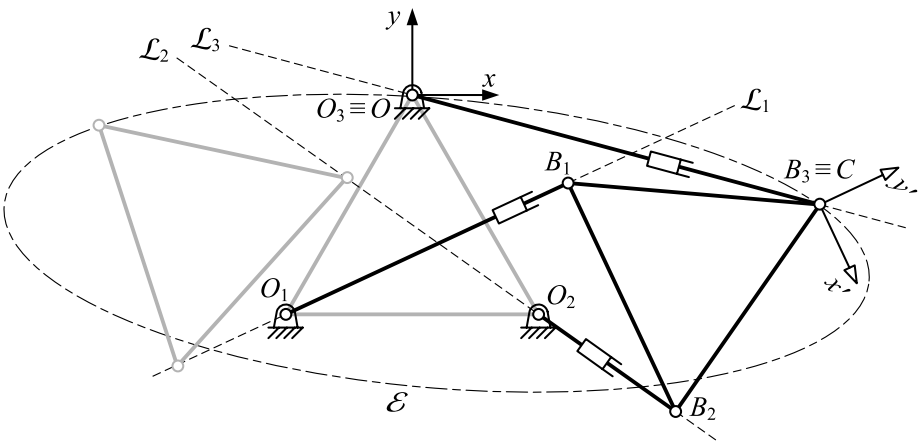

Figure 3. Geometric interpretation of the direct kinematic model.

3. Degeneracies of the Direct Kinematics

In order to study the global behavior of the parallel robot at all singularities, we will analyze its direct kinematic model. Indeed, this approach is the most intuitive one and gives a clear geometric interpretation of all singular configurations. It is usually very difficult or even impossible to follow this approach, but in our case the direct kinematic model is particularly simple. Indeed, whatever the active-joint variables, there is always the trivial solution when the base and platform coincide.

Merlet (1996) showed that the direct kinematic problem of 3-*RPR* planar parallel robots is equivalent to intersecting an ellipse with a line, but did not study any special cases. Let us dismount the revolute joint at B_3. For given active-joint variables, points B_1 and B_2 are constrained to move along two lines (Fig. 3), $\mathcal{L}_1$ and $\mathcal{L}_2$, respectively, and the mobile platform undergoes a Cardanic movement (see for example Tischler et al., 1998). As a result, B_3 describes a curve, $\mathcal{E}$, that is an ellipse, two parallel lines, a line, or a doubly traced line segment. Obviously, this curve contains point O_3 (i.e., O). Considering leg 3, B_3 should also lie on a line passing through O_3, denoted by $\mathcal{L}_3$. Thus, the direct kinematic problem is equivalent to finding the intersections between $\mathcal{L}_3$ and $\mathcal{E}$.

Let us now derive the elliptic curve $\mathcal{E}$. We can write the following closure equation for point $C \equiv B_3$:

$$\mathbf{r}_{OC} = \mathbf{r}_{OO_1} + \rho_1 \mathbf{v}_1 - \mathbf{r}_{CB_1} = \mathbf{r}_{OO_2} + \rho_2 \mathbf{v}_2 - \mathbf{r}_{CB_2}. \tag{6}$$

This yields the following system of two equations:

$$-1 + \rho_1 \cos\theta_1 + \cos\phi - \rho_2 \cos\theta_2 = 0, \tag{7}$$

$$\rho_1 \sin\theta_1 + \sin\phi - \rho_2 \sin\theta_2 = 0. \tag{8}$$

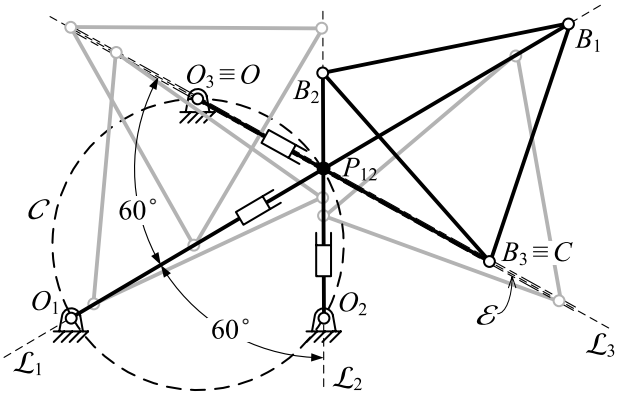

Figure 4. Cardanic self motion when the legs are concurrent and make equal angles.

Solving Eqs. (7) and (8) for ρ_1 and ρ_2, and substituting the results in Eq. (6), we obtain the following parametric equation in ϕ:

$$x = \left(\frac{\cos\theta_1 \sin\theta_2}{\sin(\theta_1 - \theta_2)} + \frac{1}{2}\right)(\cos\phi - 1) - \left(\frac{\cos\theta_1 \cos\theta_2}{\sin(\theta_1 - \theta_2)} + \frac{\sqrt{3}}{2}\right)\sin\phi, \quad (9)$$

$$y = \left(\frac{\sin\theta_1 \sin\theta_2}{\sin(\theta_1 - \theta_2)} + \frac{\sqrt{3}}{2}\right)(\cos\phi - 1) - \left(\frac{\sin\theta_1 \cos\theta_2}{\sin(\theta_1 - \theta_2)} - \frac{1}{2}\right)\sin\phi. \quad (10)$$

The above parametric equation is not defined when $\sin(\theta_1 - \theta_2) = 0$, a case that will be studied later. If $\sin(\theta_1 - \theta_2) \neq 0$, i.e., if $\mathcal{L}_1$ and $\mathcal{L}_2$ are not parallel, then the elliptic curve degenerates if, and only if, its curvature is zero for any ϕ. The curvature, κ, of $\mathcal{E}$ can be derived as

$$\kappa = \frac{\dot{x}\ddot{y} - \dot{y}\ddot{x}}{(\dot{x}^2 + \dot{y}^2)^{3/2}} = \frac{\sin(\theta_1 - \theta_2 + \pi/3)}{D^3}, \quad (11)$$

where D is a relatively large expression in θ_1, θ_2, and ϕ.

Therefore, when $\mathcal{L}_1$ and $\mathcal{L}_2$ make a 60° angle, $\kappa = 0$, and $\mathcal{E}$ degenerates to a line. In other words, if, and only if, the point of intersection between $\mathcal{L}_1$ and $\mathcal{L}_2$, denoted by P_{12}, lies on the curcumcircle of the base, denoted by $\mathcal{C}$, $\mathcal{E}$ degenerates to a line (Fig. 4). In fact, it degenerates to a doubly traced line segment of length $4/\sqrt{3}$ (Tischler et al., 1998). This line segment is centered at P_{12} and passes through O. When $P_{12} \equiv O$, the doubly traced line segment is parallel to O_1O_2.

As we said before, the direct kinematic problem is equivalent to finding the two intersection points between $\mathcal{L}_3$ and $\mathcal{E}$, of which one is always O. We will not present an actual algorithm for determining the other intersection point (x, y) and the corresponding platform orientation ϕ, but only investigate the singular configurations corresponding to all particular cases in which there is a single or infinitely many solutions.

Case 1a: $\sin(\theta_1 - \theta_2) = 0$ and $\cos\theta_1 \cos\theta_2 \neq 0$
In this case, $\mathcal{L}_1$ and $\mathcal{L}_2$ are parallel and $\mathcal{E}$ degenerates to two lines parallel to $\mathcal{L}_1$ and $\mathcal{L}_2$, one of which passes through O.

- ✗ If $\mathcal{L}_3$ is parallel to $\mathcal{L}_1$ and $\mathcal{L}_2$, the platform vertices can slide along $\mathcal{L}_1$, $\mathcal{L}_2$ and $\mathcal{L}_3$, with $\phi = 0$, even though all actuators are blocked.
- ✗ If $\mathcal{L}_3$ is not parallel to $\mathcal{L}_1$ and $\mathcal{L}_2$, the platform can assume a nonsingular configuration, as well as the trivial solution $\mathbf{q} = \mathbf{0}$, for which the corresponding configuration is only Type 1 singular (i.e., the platform is not shaky; in fact, it is jammed).

Case 1b: $\cos\theta_1 = 0$ and $\cos\theta_2 = 0$
In this case, $\mathcal{L}_1$ and $\mathcal{L}_2$ are parallel to the y-axis and $\mathcal{E}$ degenerates to a single line parallel to $\mathcal{L}_1$ and $\mathcal{L}_2$, and passing through O.

- ✗ If $\mathcal{L}_3$ is parallel to $\mathcal{L}_1$ and $\mathcal{L}_2$, the platform vertices can slide along $\mathcal{L}_1$, $\mathcal{L}_2$ and $\mathcal{L}_3$, with $\phi = 0$, even though all actuators are blocked.
- ✗ If $\mathcal{L}_3$ is not parallel to $\mathcal{L}_1$ and $\mathcal{L}_2$, the platform can assume only the trivial solution $\mathbf{q} = \mathbf{0}$, and the configuration is Type 1 and Type 2 singular (the platform can rotate infinitesimally).

Case 2: $\sin(\theta_1 - \theta_2 + \pi/3) = 0$
In this case, $\mathcal{L}_1$ and $\mathcal{L}_2$ make a 60° angle and their intersection point, P_{12}, lies on $\mathcal{C}$ (Fig. 4). The curve $\mathcal{E}$ degenerates to a doubly traced line segment passing through P_{12} and O (if $P_{12} \equiv O$, $\mathcal{E}$ is parallel to O_1O_2).

- ✗ If $\mathcal{L}_3$ is collinear with $\mathcal{E}$, then point B_3 can slide along $\mathcal{E}$ while the platform changes orientation simultaneously (Fig. 4), even though all actuators are blocked (as in Reuleaux straight-line mechanism).
- ✗ If $\mathcal{L}_3$ is not collinear with $\mathcal{E}$, then the platform can assume two possible poses. The first one is the trivial solution $\mathbf{q} = \mathbf{0}$, while the second one is $\mathbf{q} = [180^\circ, 0, 0]^T$. For both poses, the corresponding configurations are only Type 1 singular (the platform is jammed).

Case 3: $\sin(\theta_1 - \theta_2 + \pi/3)\sin(\theta_1 - \theta_2) \neq 0$
In this case, $\mathcal{L}_1$ and $\mathcal{L}_2$ intersect at a point that does not lie on $\mathcal{C}$, and $\mathcal{E}$ is an ellipse (Fig. 3).

- ✗ If $\mathcal{L}_3$ is tangent to $\mathcal{E}$ at O, then the platform can assume only the pose $\mathbf{q} = \mathbf{0}$, and the corresponding configuration is both Type 1 and Type 2 singular (there is no self motion). Indeed, it can be shown that at this configuration, the normals to $\mathcal{L}_1$, $\mathcal{L}_2$ and $\mathcal{L}_3$ passing through B_1, B_2 and B_3, respectively, are concurrent.
- ✗ If $\mathcal{L}_3$ is not tangent to the ellipse, then the mobile platform can assume the pose $\mathbf{q} = \mathbf{0}$, for which the corresponding configuration is only Type 1 singular, and another nonsingular pose (Fig. 3).

4. Conclusions

This paper described the kinematic geometry of a 3-$\underline{R}PR$ planar parallel robot with congruent equilateral base and mobile platform. It was shown that the only singular configurations, for which the base and mobile platform do not coincide, belong to self motions. They occur when the legs intersect at the circumcircle of the base or are parallel. Once again, It was demonstrated that careful analysis of the degeneracies of the direct kinematic model provides a convenient geometrical tool for better understanding the global behavior of singularities.

Parallel robots with identical base and mobile platform allow self motions but have interesting characteristics and simpler geometric models. The authors believe that these robots deserve further attention as they are likely to find use in practice or lead to better understanding some theoretical issues. This design simplification approach will next be applied to 3-$\underline{R}RR$ planar parallel robots. These robots are undoubtedly the cheapest alternative for planar motion, from the hardware point of view, but are still too complex to design optimally.

References

Bonev, I.A., Chablat, D., and Wenger, P. (2006), Working and assembly modes of the Agile Eye, *Proceedings of the 2006 IEEE International Conference on Robotics and Automation*, Orlando, Florida, May 15–19.

Bonev, I.A., Zlatanov, D., and Gosselin, C.M. (2003), Singularity analysis of 3-DOF planar parallel mechanisms via screw theory, *Journal of Mechanical Design*, vol. 125, no. 3, pp. 573–581.

Husty, M., and Zsombor-Murray, P. (1994), A special type of singular Stewart-Gough platform, *Advances in Robot Kinematics and Computational Geometry*, J. Lenarčič; and B. Ravani (eds.), Kluwer Academic Publishers, The Netherlands, pp. 449–458.

Karger, A. (2002), Singularities and self motions of a special type of platforms, *Advances in Robot Kinematics*, J. Lenarčič; and F. Thomas (eds.), Kluwer Academic Publishers, The Netherlands, pp. 449–458.

Merlet, J.-P. (1996), Direct kinematics of planar parallel manipulators, *Proceedings of the 1996 IEEE International Conference on Robotics and Automation*, Minneapolis, Minnesota, pp. 3744–3749.

Tischler, C.R., Hunt, K.H., and Samuel, A.E. (1998), A spatial extension of Cardanic movement: its geometry and some derived mechanisms, *Mechanism and Machine Theory*, vol. 33, no. 8, pp. 1249–1276.

Wohlhart, K. (2002). Synthesis of architecturally mobile double-planar platforms, *Advances in Robot Kinematics*, J. Lenarčič; and F. Thomas (eds.), Kluwer Academic Publishers, The Netherlands, pp. 473–482.

GRAPHICAL SINGULARITY ANALYSIS OF 3-DOF PLANAR PARALLEL MANIPULATORS

Amir Degani
Robotics Institute
Carnegie Mellon University
degani@cmu.edu

Alon Wolf
Dept. of Mechanical Engineering
Technion – Israel Institute of Technology
alonw@tx.technion.ac.il

Abstract This paper introduces a new approach to identify singularities of planar parallel manipulators (PPMs). This method is based on Maxwell's reciprocal figure theory which establishes a duality between self-stress frameworks and reciprocal figures. We use line geometry tools to introduce a new graphical construction called the Mechanism's Line of action Graph (MLG). The MLG is introduced in order to implement Maxwell's Reciprocal Figure theory to mechanisms. In this paper, we show that the configurations where the MLG has a connected reciprocal figure imply a singularity type-II in the mechanism. This singularity analysis tool is also used to trace the singularity loci of the PPM.

Keywords: Graphical Analysis, Maxwell's Reciprocal Figure Theory, Parallel Manipulators, Singularity

1. Introduction

This paper focuses on the singularity analysis of planar parallel manipulators (PPMs). Specifically we analyze the type-II singularity of fully parallel planar manipulators which are planar three-degree-of-freedom (3-DOF) parallel manipulators, consisting of three limbs, each consisting of one actuated joint and two unactuated (passive) joints. Most of the approaches to finding singularities of parallel manipulators address the singularity types that were introduced by Gosselin and Angeles (Gosselin and Angeles, 1990). These types of singularities are based on the singularity of the Jacobian matrix, which maps the Cartesian velocities of the end-effector onto the joint velocity vector.

We confront the problem of the singularity analysis somewhat differently than most approaches. We first represent the manipulator graphically using a known line geometry tool, the reciprocal screw. This

J. Lenarčič and B. Roth (eds.), Advances in Robot Kinematics, 229–238.

screw, which is reciprocal to all the unactuated joint twists of the limb, represents the line of action of a limb, which is the wrench that a limb applies to the end-effector. We represent the line of action of each limb of the manipulator as an edge in the Mechanism's Line of action Graph (MLG). Then, in order to find the "graphical singularities" we use a theory that goes back to the mid 19th century, Maxwell's Reciprocal Figure theory (Maxwell, 1864), to construct a dual graph (reciprocal figure) of the MLG. We will show that when a reciprocal figure of the MLG can be constructed, this specific configuration of the manipulator is a type-II singular configuration (Gosselin and Angeles, 1990). A different starting point of the analysis is with a connected reciprocal figure upon which the MLG is built. In this type of analysis, when the configuration of the reciprocal figure is changed (while still being connected), the corresponding manipulator will change configuration but will continuously be in a singular configuration, resulting in the PPM's singularity loci.

2. Preliminaries

We first present a brief explanation of the tools that led to the development of the presented graphical approach.

2.1 Reciprocal Screws and the Limb's Line of Action

Finding the line of action for each limb of the manipulator is the first step in constructing the Mechanism's Line of Action Graph (MLG). We use reciprocal screws to find these lines of action. Tsai developed a specific procedure for the derivation of reciprocal screw and its application for the Jacobian analysis of parallel manipulators (Tsai, 1998). Bonev used derivations of reciprocal screws in the specific case of PPMs (Bonev, 2002), which is relevant for the current analysis.

The reciprocal screw, which is reciprocal to the two unactuated joints of each limb, is a wrench which if applied to the platform, can be resisted solely by the actuated joint of the limb. This reciprocal screw is the line of action of the i^{th} limb, also known as the governing line of the limb (Hunt, 1978; Tsai, 1998). The two most common cases of unactuated joints in PPMs are either two revolute joints or one revolute joint and one prismatic joint. A third, less common case, is a limb consisting of two unactuated prismatic joints. In the case of two revolute joints, the reciprocal screw is a pure force (zero pitch screw) passing through the two unactuated revolute joints (Fig. 1a,b,c). In the case of one revolute and one prismatic unactuated joints, the screw is a pure force passing through the unactuated revolute joint and perpendicular to the axis of

the unactuated prismatic joint (Fig. 1d,e). In the case of a limb consisting of two unactuated prismatic joints, the line of action is a pure torque in the direction going out of the plane (Fig. 1f), which will only enable a pure torque and will constrain the platform to rotation only. For this reason, only one such limb can be included in the design of a PPM.

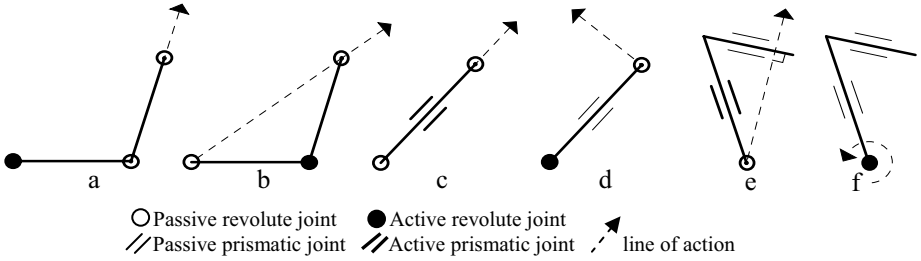

Figure 1. Examples of typical limbs of PPMs and their reciprocal screws corresponding to the lines of action.

2.2 Maxwell's Reciprocal Figure Theory

In the mid 19th century James Clerk Maxwell (Maxwell, 1864) described a three-way connection between self stresses in planar bar-joint framework (static rigidity), reciprocal figures, which are dual figures of the bar framework, and spatial polyhedra. In this paper, we only focus on the first two components of the theory, i.e. the connection between self stress framework and the existence of a reciprocal figure.

A *bar framework* in the plane is a graph which represents a structure constructed out of bars and joints. The bars are represented as edges and the joints as vertices. If the i^{th} vertex is marked $\mathbf{p}_i$ then the direction of the edge connected by the i^{th} and j^{th} joint is represented as $\mathbf{p}_i - \mathbf{p}_j$. The force inside the bar is in the direction of the edge multiplied by a scalar ω_{ij} which is the scale of the force in the bar ($\omega_{ij} \geq 0$ represents tension and $\omega_{ij} \leq 0$ represents compression.)

The forces reach equilibrium at the joint $\mathbf{p}_i$ if the sum of the forces in j bars connected to the joint $\mathbf{p}_i$ is equal to zero:

$$\sum_j \omega_{ij}(\mathbf{p}_j - \mathbf{p}_i) = 0 \tag{1}$$

A *self stress* of a bar framework is an assignment of scalars ω_{ij} to the edges such that, for each vertex $\mathbf{p}_i$, Eq. 1 will be realized.

A bar framework is *fully self stressed* if for all ω_{ij}, $\omega_{ij} \neq 0$.

Maxwell's *reciprocal figure theory* states that a plane framework or a planar graph supports a full self stress if and only if it has a reciprocal figure. Moreover, this graph should be vertex 2-connected and edge 3-connected which means that removing any one vertex and its edges

leaves the vertex set connected by the remaining edges, and removing any two edges leaves the vertex set connected by the remaining edges.

A graph is a *reciprocal figure* to another if the two graphs consist of an equal number of edges, corresponding edges in the two graphs are perpendicular, and corresponding edges which converge to a point in one graph form a closed polygon in the other. This definition of a reciprocal figure clarifies the connection between Eq. 1 (equilibrium at a vertex in a self stressed framework), and the duality between edges converging to a point in one graph and edges forming a closed polygon in the other.

This connection between reciprocal figure and self stress in a framework is the foundation of the connection we present between reciprocal figure and singularity type-II of a PPM. For additional insights and a complete proof of Maxwell's reciprocal figure theory we refer the reader to (Crapo and Whiteley, 1993).

3. Singularity Analysis Method and Examples

When using the singularity analysis method presented in this paper one should apply the following three main steps on a given PPM:

STEP 1: Construct an MLG for the specific PPM.

STEP 2: Construct a reciprocal graph based on the obtained MLG.

STEP 3: Find the configurations of the manipulator in which the reciprocal graph is connected. In these configurations the manipulator is in type-II singularity.

As mentioned earlier, we conduct our investigation on fully parallel planar manipulators which consist of three limbs, each containing one actuated joint and two unactuated (passive) joints. Even though the examples provided in this paper are of identical limb manipulators, the method can be applied to different types of PPMs. We use the conventional notation of PPMs by using R to describe revolute joints and P to describe prismatic (linear) joints. Actuated joints are marked with an underline. When the three limbs of the PPM are identical the manipulator is marked by a preceding '3' (for example: 3-$\underline{\text{R}}$RR).

3.1 Constructing the MLG of PPMs

Given a PPM we represent its kinematic structure in a graphical representation which mainly represents the line of action of each of the limbs of the PPM. This graphical representation is then used as a planar graph with Maxwell's reciprocal figure theory. In order to construct the Mechanism's Line of action Graph (MLG) we identify the reciprocal screw for each of the limbs of the PPM (as described in Section 2.1).

The three limbs of a PPM can be connected to the end-effector either by revolute joints or by prismatic joints. This difference will affect the construction of the MLG. To begin an MLG construction of a PPM connected with revolute joints (Fig. 2a), the three vertices of the end-effector should be marked (Fig. 2b). From each of the end-effector's vertices an edge corresponding to the line of action of the limb is constructed. Figure 2c illustrates the three reciprocal screws corresponding to the line of action of each limb (marked as dotted arrows). Even though the length of the edge corresponding to the line of action is not essential for this method, we draw the length of the edge equal to the length of the link closest to the end-effector (Fig. 2d). Finally, the three ground vertices of the line of actions' edges are to be connected (Fig. 2e). The ground vertices are located at the distal end of the line of action's edge with respect to the end-effector.

The MLG is changed depending on the configuration of the manipulator. In most PPMs, the ground vertices in the MLG are not static (as in the case of the 3-RRR in Fig. 2). This does not affect our results because we are only analyzing the instantaneous kinematics of the manipulator's end-effector. A similar step by step construction of an MLG of a 3-RPR is shown in Fig. 3.

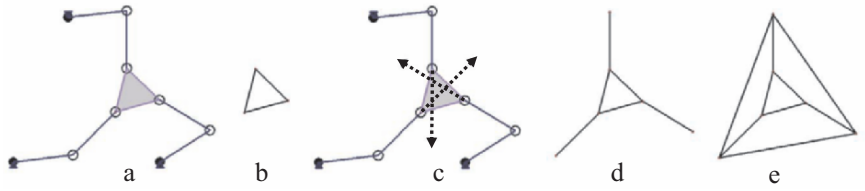

Figure 2. Example of the construction of the MLG for a 3-RRR manipulator.

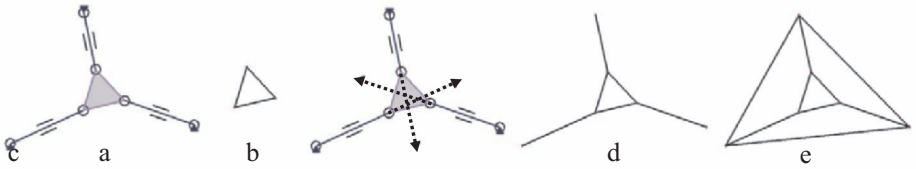

Figure 3. Constructing the MLG for a 3-RPR manipulator.

The main difference between the two MLGs in Fig. 2e and Fig. 3e is the line of action of each limb. In Fig. 3 the reciprocal screws that correspond to the lines of action of the limbs pass through the center of the passive revolute joints of the limb (first and third joints). In Fig. 2 the lines of action pass through the second and third joints which are the passive ones.

In the case of a limb connected to the end-effector by prismatic joints (Fig. 4a), the construction of the MLG should begin from the ground

vertices. First the three ground vertices are constructed. From each of the ground vertices an edge corresponding to the line of action of the limb is constructed (Fig. 4b). Three vertices are constructed on each of the edges corresponding to the line of action at a constant, arbitrary unit distance from the ground vertex (Fig. 4c). Connecting these three vertices and the three ground vertices finalizes the construction of the MLG (Fig. 4d).

An example of a degenerate case of a PPMs end-effector, in which the three distal joints create a line, is shown in Fig. 5a. To construct an MLG for this special case the end-effector should still be thought of as a triangle in a degenerate configuration (Fig. 5b).

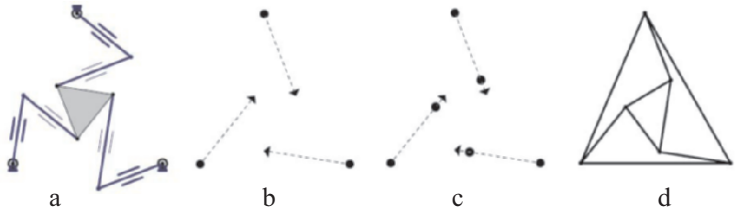

Figure 4. Example of the construction of the MLG for a 3-RPP manipulator.

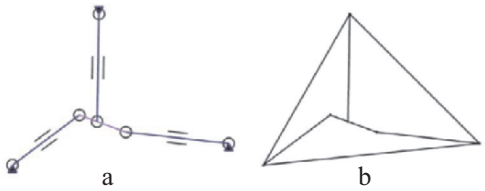

Figure 5. Construction the MLG for a 3-RPR manipulator with degenerate end-effector.

It is important to note that for now it is not feasible when using this method to represent the line of action of a limb consisting of two passive prismatic joint in an MLG (i.e. a pure torque out of the plane).

3.2 Constructing a Reciprocal Graph of the PPM's MLG

Figure 6 presents a step by step construction of the reciprocal figure of the 3-RPR. We use a dynamic geometry program that enables us to construct the reciprocal figure for a given configuration so that when the mechanism is moved, the reciprocal figure will change correspondingly. We note that these constructions can be drawn using a simple ruler and a compass (most likely the tools that the late Maxwell originally used), but for every different configuration, a new reciprocal graph should be

drawn. The MLG that was constructed for the 3-RPR PPM in Fig. 3, is given in Fig. 6a. To start the construction of the reciprocal figure an arbitrary inner polygon in the MLG is picked (polygon (1,2,3,4)). An initial vertex is drawn and the four perpendicular lines corresponding to the polygon's edges are constructed (Fig. 6b). Then another vertex is drawn on line (4) since its corresponding edge is shared by the top two inner polygons in the MLG. Next, the three perpendicular lines corresponding to the remaining edges of the top right polygon in the MLG (edges 5, 6, and 7) are constructed (Fig. 6c). The reciprocal graph should eventually consist of edges and not infinite lines. In order to correctly trim the lines we have constructed we need to determine the intersections that are actually vertices that correspond to closed polygons in the MLG. The intersections that join lines correspond to edges of the closed polygons that have not yet been addressed need to be marked, i.e. the bottom polygon, the center triangle and the outer triangle. In Fig. 6d the three vertices are marked (3/7, 1/5, 6/2). For example the 1/5 vertex corresponds to the 1,4,3,2 polygon, and so forth. To finalize the construction of the reciprocal figure, edges 8 and 9 (from the bottom polygon) should be added to the bottom vertex of the reciprocal figure, perpendicular to their corresponding edges (Fig. 6e). Note that these two edges (8, 9) are not connected to their correct vertices (vertices p and q). This means that the reciprocal figure cannot be constructed for this particular configuration. Therefore, the specific configuration of the PPM (Fig. 3a) for which this MLG was constructed (Fig. 3e), is not a type-II singularity. We note that the order in which we construct the reciprocal figure may change the resulting edges that are not connected; however, this does not change the overall existence of the reciprocal figure. The construction of the reciprocal figure for the 3-RRR manipulator is done in a similar way since the MLGs are similar.

The construction of the degenerate end-effector (Fig. 5) can also be constructed in a similar way, while keeping in mind that the three joints (in this case on a line) are actually a degenerate triangle. In this case three of the edges of the reciprocal figure will always be parallel to each other and will always coincide at infinity.

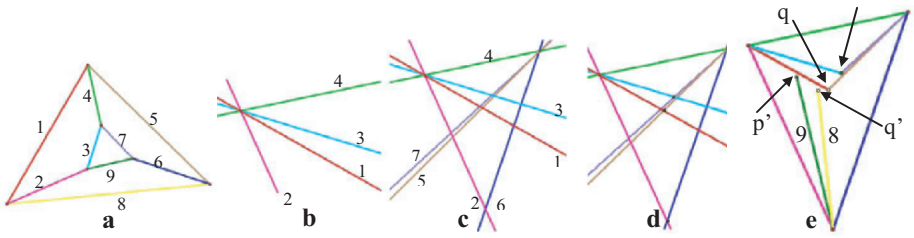

Figure 6. Construction of the reciprocal figure for a 3-RPR PPM.

3.3 The Singularity/Self Stress Connection

Once the MLG of a PPM and a reciprocal figure are constructed, one can use them for the singularity analysis of PPMs. Maxwell's theory (section 2.2) presents a connection between the existence of a reciprocal figure and self stress in a framework. We will now analyze a self-stressed MLG (Fig. 7) in order to demonstrate the connection between self-stress and singularity. Based on the definition of self stress framework, when a bar-joint framework is in self stress, the sum of the forces of the bars connected to a joint is equal to zero. Three equations corresponding to the sum of forces in the three vertices 1,2,3 can be written as:

Sum of forces in vertex 1: $\mathbf{a} + \mathbf{d} + \mathbf{f} = \mathbf{0}$, (2)

Sum of forces in vertex 2: $\mathbf{b} - \mathbf{d} + \mathbf{e} = \mathbf{0}$, (3)

Sum of forces in vertex 3: $\mathbf{c} - \mathbf{e} - \mathbf{f} = \mathbf{0}$. (4)

These three equations are vector summations. We arbitrarily assign the direction of the forces and consistently add the forces. Therefore, some of the forces in Eq. 2-4 are negated. Summing Eq. 2, 3, and 4:

$$\mathbf{a} + \mathbf{b} + \mathbf{c} = \mathbf{0} \quad (5)$$

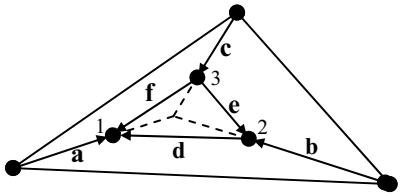

Figure 7. "Singular" (self stress) configuration of MLG.

Equation 5 confirms a linear dependency of the three forces **a**, **b**, and **c**. These three forces are the forces corresponding to the lines of action of the three limbs. The meaning of this dependency is that these three limbs cannot generate instantaneous work (virtual work (Hunt, 1978)) on the end-effector while it is moving in an instantaneous twist deformation resulting from an external wrench applied on it. Therefore, self stress in a framework is equivalent to a type-II singularity of a PPM. It is now evident that the existence of a reciprocal figure indicates a self stress framework, and in a similar way indicates a singular configuration in a mechanism.

3.4 Locating the Singular Configurations

To find the configurations where there exists a reciprocal figure to a particular PPM, and therefore it is in a singular configuration, one should move the manipulator by changing its joint parameters while tracking for configurations in which the reciprocal figure is visually

connected, e.g. in Fig. 6e, vertices p and q merge with p' and q' respectively. Figure 8 shows examples of PPM configurations in which the reciprocal figure is connected and the manipulator is in a singular configuration.

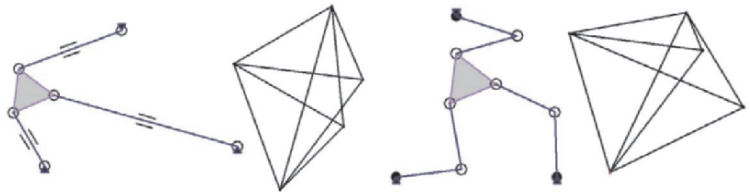

Figure 8. Two examples of singular configurations and the connected reciprocal figures (3-RPR left, 3-RRR right).

So far the search for a singular configuration was carried out by changing the joint parameters of the manipulator and checking for the existence of a connected reciprocal figure. If the analysis is constructed the other way around, so that a connected reciprocal figure is first constructed and only then an MLG is constructed to be reciprocal to it, we can trace the loci of the singular configurations of the manipulator by changing the reciprocal figure while keeping it connected (Fig. 9 left). Note that the construction of the reciprocal figure in this case is based on mechanical constraints of the PPM, e.g. the fixed shape of the end-effector. Moreover, the singular configuration's loci are traced relative to a constant orientation of the PPM in order to enable us to plot the loci as a 2-D graph. We refer the readers to (Sefrioui and Gosselin, 1995) to examine the consistency of the results.

More examples, including JAVA applets of this method, can be found at: www.cs.cmu.edu/~adegani/graphical/.

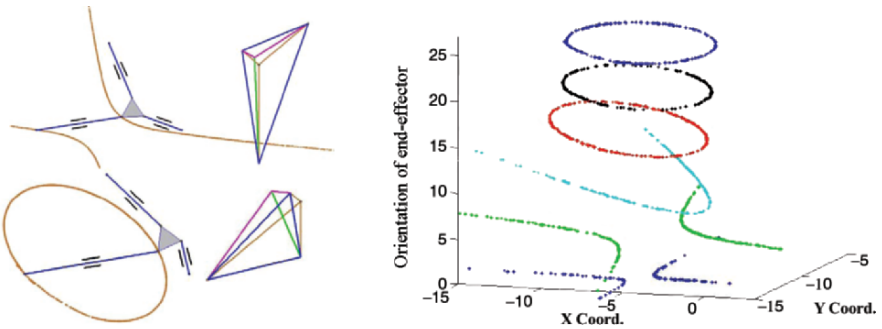

Figure 9. (Left) Singularity loci of 3-RPR in two different constant orientations of the end-effector. (Right) A loci plot from six different orientations of the end-effector (0,5, 10, 15, 20, and 25 degrees).

4. Conclusion and Future Work

The graphical method which is presented and implemented in this paper results in comparable outcomes to those obtained by other approaches (e.g. Sefrioui and Gosselin, 1995), yet avoids some of the complexities involved in analytic derivations. It is worth mentioning that the method we present can be potentially applied to non-identical limb manipulators and to other types of mechanisms as well. The method makes use of reciprocal screws to represent the lines of action of PPMs' limbs in a Mechanism's Line of action Graph (MLG), an insightful graphical representation of the mechanism. Maxwell's theory of reciprocal figure and self stress is then applied to create a dual figure of the MLG. Analyzing this dual (reciprocal) figure provides us with the singular configurations of the PPM and with the loci of singular configurations of the manipulator.

We are currently facing the challenge of expanding this graphical method to the analysis of three-dimensional manipulators. We hope to be able to use our relatively simple method to find the singular configurations of complex three-dimensional manipulators, such as a 6-DOF Gough-Stewart platform. One possible way to achieve this goal is to project the spatial lines of action of the limbs on one or more planes (Karger, 2004). We believe a self-stress analysis of these projected graphs, similar to the one done on PPM, will offer insight into the singular configuration of these non-planar manipulators.

References

Bonev, I.A. (2002), *Geometric analysis of parallel mechanisms*. Ph.D. Thesis, Laval University, Quebec, QC, Canada.

Crapo, H., and Whiteley, W. (1993), Plane self stresses and projected polyhedra I: The basic pattern. *Structural Topology* no. 1, vol. 20, pp. 55-78.

Gosselin, C., and Angeles, J. (1990), Singularity analysis of closed-loop kinematic chains. *IEEE Transactions on Robotics and Automation* no. 3, vol. 6, pp. 281-290.

Hunt, K.H. (1978), *Kinematic Geometry of Mechanisms*, Oxford, Clarendon Press.

Karger, A. (2004), Projective properties of parallel manipulators, J. Lenarčič and C. Galletti, *Advances in Robot Kinematics*, Kluwer Acad. Publ., pp. 89-96.

Maxwell, J.C. (1864), On reciprocal figures and diagrams of forces. *Phil. Mag* no. 27, vol. 4, pp. 250-261.

Sefrioui, J., and Gosselin, C.M. (1995), On the quadratic nature of the singularity curves of planar three-degree-of-freedom parallel manipulators. *Mechanism and Machine Theory* no. 4, vol. 30, pp. 533-551.

Tsai, L.W. (1998), The Jacobian analysis of a parallel manipulator using reciprocal screws, *Proceedings of the 6th International Symposium on Recent Advances in Robot Kinematics*, Salzburg, Austria.

DIRECT SINGULARITY CLOSENESS INDEXES FOR THE HEXA PARALLEL ROBOT

Carlos Bier*, Alexandre Campos, Jürgen Hesselbach
Institute of Machine Tools and Production Technology – TU Braunschweig
Langer Kamp 19b, 38106 Braunschweig, Germany
* c.bier@tu-bs.de

Abstract Direct kinematic singularities constrain the internal robot workspace and the proximity to them must be detected online as fast as possible for non deterministic trajectories. Direct singularity proximity for the Hexa parallel robot is measured by means of three measure indexes with two different physical bases. In this paper a new index based on Grassmann geometry to measure the singularity closeness is introduced. This method and methods based on constraint minimization are applied and validated in the Hexa robot. From the results we observe, for instance, that the new index requires less time than the constraint minimization methods but requires a better knowledge of the robot structure.

Keywords: Parallel Manipulator Singularities, Grassmann Geometry, Constrained Minimization

1. Introduction

A measure of the direct singularity closeness for parallel manipulators is required aiming at a safe operation space. For parallel robots as the Hexa robot (Fig. 3d), workspace is limited by direct kinematic singularities as well as by inverse kinematic singularities. Direct kinematic singularities allow the end effector to gain unconstrained movements. Its identification has been studied from different perspectives. The vanishing of the Jacobian determinant has been used for particular parallel robots. However it is a product of factors and thus it suffers from the fact that close to a singularity, where a factor shrinks to zero, other factors may be big enough and the determinant does not indicate the singularity closeness. Additionally, the physical meaning of the determinant is not clear.

Qualitative conditions, based on Grassmann geometry, are proposed to detect singularities of triangular simplified symmetric manipulators [Merlet, 2000]. Quantitative approaches use a numerical measure to determine how close a robot position is to a singularity. Different mea-

J. Lenarčič and B. Roth (eds.), Advances in Robot Kinematics, 239–246.

sures have been used for this task, *e.g.* the natural frequency measure [Voglewede and Ebert-Uphoff, 2004], the power and the stiffness inspired measure [Pottmann et al., 1998] based on a constraint minimization method as well as the condition number [Xu et al., 1994] based on matrix algebra.

In this paper a new method for quantitative measures of the direct singularity closeness based on Grassmann geometry is presented. This new method as well as the minimization based methods are applied to the Hexa robot and the results are analyzed.

The six DOF Hexa robot is composed by six limbs connecting the basis to the end effector, see Fig. 3d. Each limb contains an active rotative joint A_i (for $i = 1, \cdots, 6$). Its axes are fixed to the basis plane, a passive universal joint B_i and a passive spherical joint C_i connected to the end effector, so that all C_i joints define the end effector plane. The cranks and the passive links are connected at B_i. The six limbs of the Hexa robot are arranged in three pairs of two active joints with collinear rotational axes. The pairs of active joints are axisymmetrical, *i.e.* 120^o between each pair.

2. Parallel Manipulator Singularities

In spatial parallel manipulators the relationship between actuator coordinates q and end effector Cartesian coordinates x can be stated as a function $f(q, x) = 0$, where 0 is the 6-dimensional null vector. Therefore the differential kinematic relation may be determined as

$$J_q\dot{q} - J_x\$_t = 0; J_q\dot{q} = J_x\$_t \tag{1}$$

where $\$_t$ is the end effector velocity twist in ray order and, J_x, J_q and $J = J_q^{-1}J_x$ are the direct, inverse and standard Jacobian matrices, respectively.

The rows of the direct kinematic matrix J_x may correspond to the normalized screw of wrenches, in axis order acting upon the end effector through the passive link, *i.e.* the distal link of each limb [Davidson and Hunt, 2004]. Therefore, a static relation may be stated as $J_x^T\tau = \left[\hat{\$}_{r1}, \cdots, \hat{\$}_{r6}\right]\tau = \$_r$, where $\$_r$ is the result wrench acting upon the end effector in axis order, $\tau = [\tau_1, \cdots, \tau_6]$ are the input wrench magnitudes and the columns of J_x^T are the normalized screws (axial order) of wrenches acting on the end effector.

Singular configurations appear if either J_x or J_q drops rank. If J_x is singular, a direct singularity is encountered and the end effector gains one or more uncontrollable degrees of freedom (DOF), on other hand if

J_q drops rank it looses at least one DOF. The direct singularity occurs in the workspace and is the main aim of this paper.

The new method as well as the minimization based methods are introduced and applied to the Hexa robot.

3. Constraint Minimization

The constraint minimization method determines closeness to singularity through an optimization problem that results in a corresponding generalized eigenvalue problem. Using this methodology it is possible to describe the instantaneous behavior of the end effector near singularities for parallel manipulators in general [Voglewede and Ebert-Uphoff, 2004, Hesselbach et al., 2005]. In this approach, an objective function $F(\$_t)$ to be optimized is subject to move on a constraint h. This is formulated mathematically as:

$$M(X) = \begin{cases} \min/\max & F(\$_t) = \$_t^T J^T S J \$_t \\ \text{subject to} & h = \$_t^T T \$_t - c = 0 \end{cases} \tag{2}$$

where S (positive semidefinite) and T (positive definite) are $n \times n$ symmetric matrix and c is some positive constant, *e.g.* $c = 1$. The solution of Eq. (2) gives the closeness measure to a singularity $M(X)$ at a particular position and orientation X of the manipulator. The proposed constrained optimization problem is found with the application of a Lagrange multiplier λ. The local extrema of the Lagrangian $\zeta(\$, \lambda) = F(\$_t) - \lambda h(\$_t)$ are determined by its derivation. For a nontrivial solution to exist, the minimization (or maximization) of Lagrangian yields $det(J^T S J - \lambda T) = 0$, which is called the corresponding general eigenvalue problem. The smallest eigenvalue λ_{min} will be the minimum value of the objective function $F(\$_t)$, and so it can be utilized as a measure value.

In general, this minimization problem was formulated based on an arbitrary quantity for S and T [Voglewede and Ebert-Uphoff, 2004]. Taking $J = J_x$, $S = I_{6x6}$ and $T = diag[000111]$, then $\sqrt{\lambda_{min}}$ is associated to the minimum power $[\sim W]$ of the system, which indicates the manipulator singularity closeness.

Another possible way is to choose S as the stiffness matrix of the actuators K_{Act} and T as the mass matrix of the manipulator M_{EE} (or for simplicity the end effector mass matrix, *i.e.* neglecting the limb masses). Therefore, $\sqrt{\lambda_{min}}$ is associated to the ω natural frequency $[\sim Hz]$ of the system ($M_{EE}\ddot{X} - \omega^2 K_{EE} = 0$), indicating the singularity closeness.

Both methods are applied in the Hexa robot (Fig. 3d) for its singularity approximation measure. The measure behaviors of the minimum power of the system through a singularity (Fig. 1a) is showed in Fig. 1b,

here the end effector twists θ° around the $\$_{min}$ (the end effector twist which requires minimum power in this singularity). The singularity occurs when $\sqrt{\lambda_{min}} = 0$, but a singular range exists due to clearance and compliance of the system, where the end effector is still unconstrained. The singular range bound is experimentally identified as $0.029 \sim W$ and upon it the manipulator stiffness is warranted into the whole workspace.

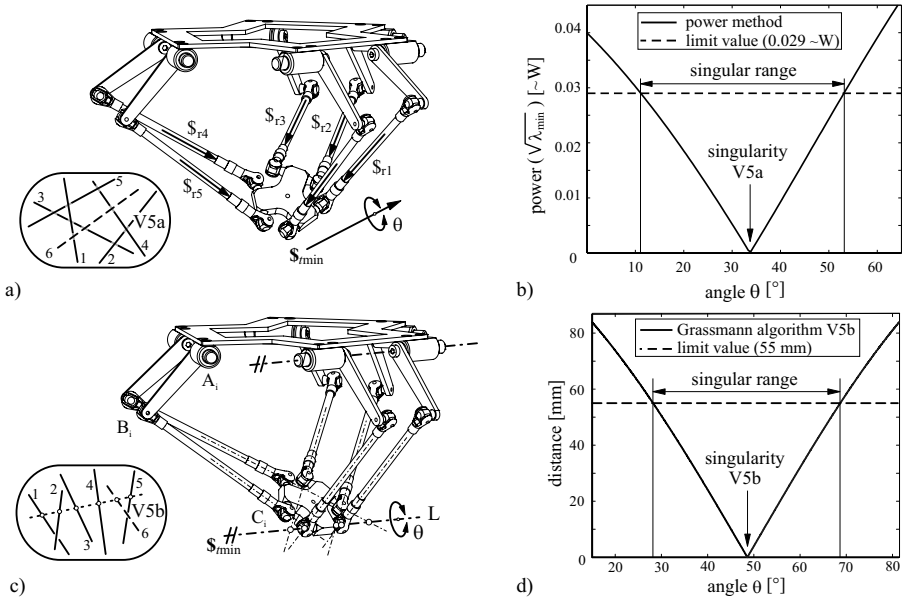

Figure 1. a) Grassmann variety V5a on the Hexa; b) Power based index; c) Grassman variety V5b; d) Grassman V5b based index.

The same behavior is obtained through the frequency method. It is important to notice that both methods detect all the singularities with a unique index.

4. Grassmann Geometry

A new index to determine closeness to singularities is obtained based on Grassmann geometry. Grassmann (1809–1877) studied the varieties of lines, *i.e.* the sets of linear dependent lines to n given independent lines, and characterized them geometrically according to their rank $(1, \cdots, 6)$ [Hesselbach et al., 2005]. A singular configuration of the manipulator may be associated with a linear dependent set of lines, also

called line based singularities. In general, the reciprocal wrenches $\$_r$ (Fig. 1a) to the passive twists of each manipulator leg are associated to lines in the direction of the forces acting upon the end effector, also called Plücker vectors. Linear dependence among these lines represents a direct singularity. These wrenches compose the J_x matrix (Sec. 2).

Using the Grassmann geometry we recognize that the Hexa robot may be associated to several varieties. Some singularities of the Hexa robot as well as correspondent varieties are shown in Figs. 1a, 1c and 2. In the Hexa configurations of Fig. 2a, two wrenches are collinear and so $\$_{r1}$ and $\$_{r2}$ represent a Grassmann variety 1 (for short V1). Figure 2b shows that four wrenches ($\$_{r1}$, $\$_{r2}$, $\$_{r3}$ and $\$_{r6}$) are on a flat pencil V2b. Given that the Hexa robot has six wrenches acting upon the end effector, the configuration in Fig. 2a may be associated to V5a and the configuration in Fig. 2b to V4d. In Fig. 2c all wrenches are parallel to each other and they form a bundle of lines V3b. In Fig. 2d all wrenches lie in a plane with different intersection points and represent a V3d. In Fig. 1a all wrenches belong to a linear complex V5a, and Fig. 1c shows an example where all wrenches are meeting one given line V5b. Each unconstrained DOF of the end effector is represented by one $\$_{min}$ in the Figs. 1a, 1c and 2.

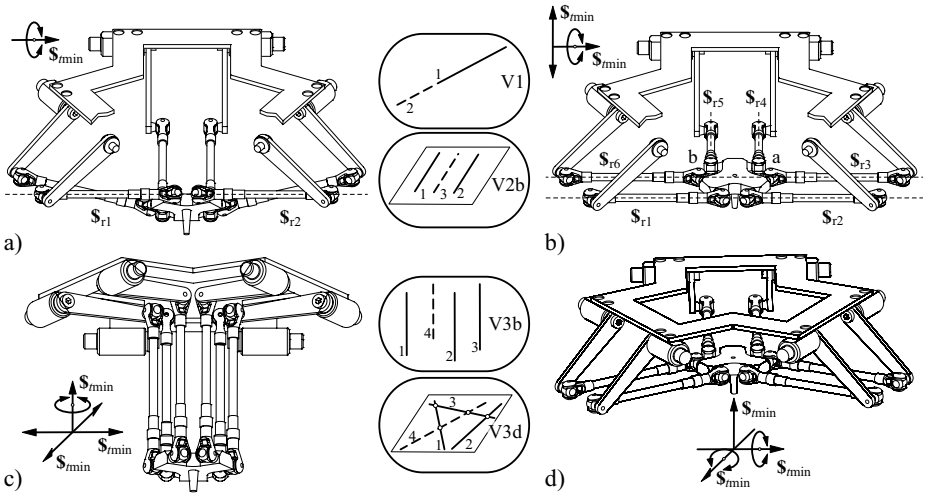

Figure 2. Grassmann variety on the Hexa robot: a) V1; b) V2b; c) V3b; d) V3d.

Considering the workspace of the Hexa robot which is limited by the actuated joint angles, the possible Grassmann varieties may be reduced to two: V5a and V5b. Thus only singularities of Fig. 1a and 1c may

occur. With the help of the Grassmann geometry all possible singular configurations on the Hexa robot are known. Aiming at quantify the closeness to the singularities of Fig. 1a and Fig. 1c, a measure algorithm is presented in the sequence.

A complex is generated by five skew symmetric lines (*e.g.* wrench axes). Let π be a plane tangent to the complex that contains a point of the line $\overline{B_6C_6}$ (correspondent to the sixth wrench). The distance between a certain point of this line and π gives a closeness measure to that singularity. It is possible to build a 4×4 skew symmetric matrix G so that $B_i^T G\, C_i = 0$ where B_i and C_i (Fig. 1c) are in projective coordinates. This linear system has six unknowns and five equations. For simplicity and without loss of validity one unknown is set to 1. A pencil of lines of the complex that contains B_6 defines π. Mathematically, if a projective point $X_p = [x\ y\ z\ 1]^T \neq B_6$ is an element of π, then $B_6^T G\ X_p = 0$. Considering the vector $U = [u_1, \cdots, u_4]^T = B_6^T G$, the affine component of plane is $u_1x + u_2y + u_3z + u_4 = 0$. The distance between C_6 and π may be interpreted as a measure for the line $\overline{B_6C_6}$ of the complex:

$$d(C_6, \pi) = v_1 C_{6,x} + v_2 C_{6,y} + v_3 C_{6,z} + v_4 = 0; v_i = \frac{ui}{\sqrt{u_1^2 + u_2^2 + u_3^2}} \quad (3)$$

If all the lengths $\overline{B_iC_i}$ are the same and no other variety occurs, $d(C_6, \pi)$ is a distance measure of the manipulator to a singularity V5a.

Singularity of V5b occurs if all six wrench axes $\overline{B_iC_i}$ intersect one line L. This line crosses two wrenches in the points C. These points must belong to legs whose drive axes are collinear and L must be parallel to these drive axes. The maximal distance between L and all the six wrenches is a measure to a singularity V5b of the Hexa robot.

This algorithm is applied in order to measure the closeness of the Hexa robot to a singularity V5b as shown in Fig. 1c. The resulting distance measure to the singularity is presented in Fig. 1d, where it linearly falls down to zero in the singularity. Similarly to the minimization method, a singular range is observed under the limit of 55 mm.

5. Conclusion

The Grassmann approach as well as the power and frequency methods are experimentally validated in the Hexa robot and investigated for online singularity detection. All three methods allow a safe monitoring of such positions and present some properties are described next.

The experiment presented in Figs. 3a and 3b shows the end effector movement (manually drived) from a rigid position, through a singularity V5b and twice singularity V5a, to a rigid position. Figure 3a compares

both Grassmann algorithms with the power method and shows that a Grassmann algorithm V5a does not detect a singularity of V5b and vice versa. A combined Grassmann index, the lower of the both algorithms, may be used due to that both present the same limit range of 55mm, which is a general property. Comparing the combined Grassmann index with the power and the frequency method in Fig. 3b, it can be observed that all three methods have an equivalent behavior. It is important to notice that a scale factor is required due to the different physical base of each method. Additionally, it allows the use of a unique singularity limit value.

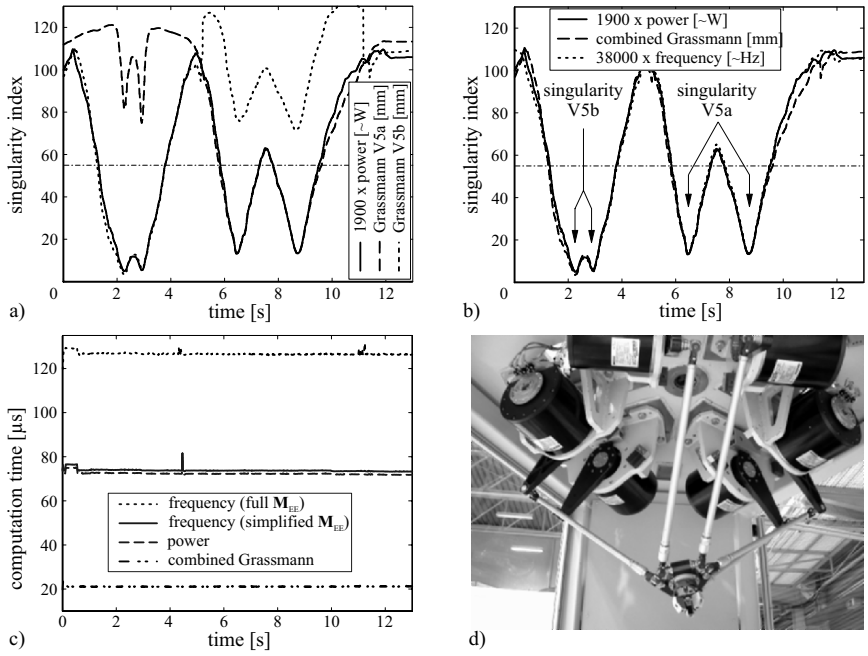

Figure 3. a) and b) Comparison of the singularity closeness indexes; c) Computational time; d) Hexa robot of Collaborative Research Center 562.

For the online application of an approach, the computing time is a decisive factor. For the same trajectory of example Fig. 3a, a computing time comparison is presented in Fig. 3c. The combined Grassmann algorithm is notably faster than the minimization methods. Additionally, in the frequency approach has been observed that using only the end effector instead of the whole manipulator mass matrix M_{EE}, the computation time decreases without any loss of measure accuracy. Therefore, it seems plausible to only use a simplified model of M_{EE}.

Properties as computational time, number of measured indexes, physical index meaning, method complexity and implementation costs must to be considered to choose a suitable approach for a particular application. The frequency method is general and can be applied to any type of parallel manipulator. The drawback of this approach is its complexity and that non-kinematic quantities (mass and stiffness) are introduced to the measure. On the other hand the power approach does not present this drawback and is not so complex. However, it can not detect finite and infinite (pure translation) unconstrained screw movements of the end effector with the same index. Both minimization approach indexes have a physical meaning in particular conditions (*e.g.* only unitary wrenches acting upon the end effector), and generally they are only associated to this physical meaning. The Grassmann approach offers a fast and simple method to detect the singularities closeness with a geometrical meaning index. The main weakness is that more than one index is required if the robot presents more than one singular variety. It cannot taken for granted that the measure index can be always combined aiming at automatic singularity avoidance strategies.

In this paper, three singularity closeness indexes based on different physical meanings, are evaluated in the Hexa robot. Each index is able to detect all the direct singularities into the robot workspace. The properties of the new Grassmann based index are compared to the odder two approaches and conclusions are presented.

References

Davidson, J. and Hunt, K. (2004). *Robots and Screw Theory*. Oxford University Press.

Hesselbach, J., Bier, C., Campos, A., and Löwe, H. (2005). Direct kinematic singularity detection of a hexa parallel robot. *Proceedings - ICRA*, pp. 3249-3254. Barcelona.

Merlet, J. (2000). *Parallel Robots*. Kluwer Academic Publisher.

Pottmann, H., Peternell, M., and Ravani, B. (1998). Approximation in line space–applications in robot kinematics and surface reconstruction. In *Andvances in Robot Kinematics*, pp. 403-412, Salzburg. Kluwer Acad. Publ.

Sciavicco, L. and Siciliano, B. (1996). *Modeling and Control of Robot Manipulators*. McGraw-Hill.

Tsai, L. (1999). *Robot Analysis: the Mechanics of Serial and Parallel Manipulators*. John Wiley & Sons, New York.

Voglewede, P. and Ebert-Uphoff, I. (2004). Measuring closeness to singularities for parallel manipulators. In *Proceedings - ICRA*, New Orleans.

Xu, Y. X., Kohli, D., and Weng, T. C. (1994). Direct differential kinematics of hybrid-chain manipulators including singularity and stability analyses. *Journal of Mechanical Design*, vol. 116, no. 2, pp. 614-621.

STEWART-GOUGH PLATFORMS WITH SIMPLE SINGULARITY SURFACE

Adolf Karger
Charles University Praha
Faculty of Mathematics and Physics
Adolf.Karger@mff.cuni.cz

Abstract The singularity surface of a parallel manipulator is a very complicated algebraic surface of high degree in six-dimensional space of all possible positions of the manipulator (in the six-dimensional group of all space congruences). In this paper we show that for some classes of manipulators we can visualize the singularity set for any fixed orientation of the manipulator by a quadric in the space of translations. Some properties and examples are given.

Keywords: Stewart-Gough platforms, parallel manipulators, Study representation, singular positions

1. Introduction

The geometry of a parallel manipulator of the type of S.-G. platform is very complicated, in general it is given by 24 structural parameters – 18 spatial coordinates of 6 points in the base and 18 in the platform, 12 of which can be specialized by using twice the congruence group, which yields 12 parameters. This means that the description of the motion leads to complicated equations and in general it is not possible to study it in closed form.

To describe the singular set is still more complicated – the general equation of the singular set has about 10^6 terms and so it gives almost no information about its properties. To obtain some closed form information about singular positions of a parallel manipulator we have to simplify the problem.

One possibility is to choose a fixed orientation of the platform and for this orientation describe all singular positions. This can be done, but it is easy to see that in this case we in general obtain a cubic surface in E_3, as the singularity surface is cubic in translations. Cubic surfaces in space are still relatively complicated objects to give a good idea about their shape. Using the general equation of the singular set we can show that in case of S.-G. platforms with affinely corresponding platform and base the equation of the singular set becomes only quadratical and

J. Lenarčič and B. Roth (eds.), Advances in Robot Kinematics, 247–254.

therefore in this case the singular set for fixed orientation is given by a quadric, which is much simpler to represent.

If the platform and base are affinely correspondent and planar, we get much more specialized situation – the singular set factorizes into three factors – either points of the platform lie on a conic section or the orientation belongs to an algebraic hypersurface in the space of orientations and the manipulator is singular for all translations or there is a plane of singular positions (depending on the orientation). This describes the situation relatively well in both cases. It seems that the described situation is not the only possibility for which the singular set is quadratical, but the general solution seems to be difficult for non-planar base or platform. This means to describe all parallel manipulators for which the singular set is quadratical in translations. In the planar case the problem is not difficult to solve, we show one example.

2. Description of the motion of a Stewart-Gough platform

Let g be a matrix of a space displacement,

$$g = \begin{pmatrix} 1 & 0 \\ t_i & a_{ij} \end{pmatrix} \tag{1}$$

parametrized by Euler parameters $a_{ij} = a_{ij}(x_\alpha)$ and Study parameters $t_i = t_i(x_\alpha, y_\beta), i, j = 1, 2, 3, \alpha, \beta = 0, ..., 3$ in the usual way, see Botema, Roth, 1990, Husty, 1991, Husty, Karger, 2000, Karger, 2002.

We shall define the Study representation of the displacement group D_6 of the Euclidean space. We consider the 7-dimensional projective space P_7 of the vector space R^8 with coordinates $x_0, ..., x_3, y_0, ..., y_3$. Points of P_7 are determined by non-trivial 8-tuples $(x_0, x_1, x_2, x_3, y_0, y_1, y_2, y_3)$ of real numbers, given up to a nonzero multiple. From P_7 we remove the subspace given by equations $x_0 = 0, x_1 = 0, x_2 = 0, x_3 = 0$, let P_7' be the remaining part. Let S be the set in P_7' which is determined by the equation

$$U = x_0y_0 + x_1y_1 + x_2y_2 + x_3y_3 = 0.$$

S will be called the Study quadric. We have a 1-1 correspondence between points of S and elements of the group D_6 of space displacements.

To simplify computations we can normalize coordinates in S by the requirement

$$K \equiv x_0^2 + x_1^2 + x_2^2 + x_3^2 = 1.$$

Now we shall describe the geometry of the motion of Stewart-Gough platform. From kinematical point of view we can say that the upper part of the platform lies in the moving space, the lower part lies in the fixed space and the motion of the Stewart-Gough platform is generated

by telescopic legs which connect six points of the moving space with six points of the fixed space by spherical joints.

Let us suppose that we have chosen a system $\{O_1, \vec{e}_1, \vec{e}_2, \vec{e}_3\}$ ($\{O_2, \vec{f}_1, \vec{f}_2, \vec{f}_3\}$) of Cartesian coordinates in the moving (fixed) spaces, respectively.

Let $M = (A, B, C)$ be a point in the fixed space (lower part of the platform), $m = (a, b, c)$ be a point in the moving space (upper part of the platform).

Any point m of the moving space can be also expressed by coordinates $(\tilde{a}, \tilde{b}, \tilde{c})$ with respect to the fixed space, where

$$\begin{aligned}\tilde{a} &= t_1 + a_{11}a + a_{12}b + a_{13}c,\\ \tilde{b} &= t_2 + a_{21}a + a_{22}b + a_{23}c,\\ \tilde{c} &= t_3 + a_{31}a + a_{32}b + a_{33}c.\end{aligned}$$

The condition for the point m to lie on sphere with center at M and radius r is

$$(\tilde{a} - A)^2 + (\tilde{b} - B)^2 + (\tilde{c} - C)^2 - r^2 = 0.$$

In this equation we substitute Study parameters and the result is an equation of degree four in x_i, y_i. This equation simplifies considerably if we add $4U^2$ to it. Then the factor K factorizes out and we obtain a quadratical equation

$$h = RK + 4(y_0^2 + y_1^2 + y_2^2 + y_3^2) - 2x_0^2(Aa + Bb + Cc) +$$

$$2x_1^2(-Aa + Bb + Cc) + 2x_2^2(Aa - Bb - Cc) + 2x_3^2(Aa + Bb - Cc) +$$

$$4[x_0x_1(Bc - Cb) + x_0x_2(Ca - Ac) + x_0x_3(Ab - Ba) - x_1x_2(Ab + Ba) -$$

$$x_1x_3(Ac + Ca) - x_2x_3(Bc + Cb) +$$

$$(x_0y_1 - y_0x_1)(A - a) + (x_0y_2 - y_0x_2)(B - b) + (x_0y_3 - y_0x_3)(C - c) +$$

$$(x_1y_2 - y_1x_2)(C + c) - (x_1y_3 - y_1x_3)(B + b) + (x_2y_3 - y_2x_3)(A + a)] = 0, \quad (2)$$

where $R = A^2 + B^2 + C^2 + a^2 + b^2 + c^2 - r^2$, Husty, 1991, Husty, Karger, 2000.

Let us suppose that the Stewart-Gough platform is given by six arbitrary points $M_i = (A_i, B_i, C_i)$ in the lower part and six points $m_i = (a_i, b_i, c_i)$ in the upper part of the platform, r_i be also given, $i = 1, ..., 6$.

We substitute coordinates of M_i, m_i in (2) and we obtain 6 equations

$$h_1 = 0, ..., h_6 = 0. \quad (3)$$

By this way the geometry and kinematics of the platform is fully described, Husty, 1991.

We would like to show how we can describe the singular positions using the Study representation, because the reasoning is natural and

very simple. Let us suppose that r_i are given as functions of time, $r_i = r_i(t)$. This generates a motion in the moving space described by a curve $x_i = x_i(t), y_i = y_i(t), i = 0, ..., 3$ in P^7. We express the velocity operator for this motion. We can suppose that at instant $t = t_0$ the motion passes through identity (the frame in the moving space is identical with the frame in the fixed one),

$x_1(t_0) = 1, y_0(t_0) = 0, x_j(t_0) = y_j(t_0) = 0, j = 1, 2, 3.$

The matrix of the motion is a function of the time, $g = g(t)$ and for its derivative at $t = t_0$ we obtain

$$g'(t_0) = 2 \begin{pmatrix} 0 & 0 & 0 & 0 \\ v_1 & 0 & -u_3 & u_2 \\ v_2 & u_3 & 0 & -u_1 \\ v_3 & -u_2 & u_1 & 0 \end{pmatrix}, \tag{4}$$

where $u_j = x_j'(t_0), v_j = y_j'(t_0), j = 1, 2, 3$ and $x_0'(t_0) = y_0'(t_0) = 0$ as a consequence of $K = 1, U = 0$. The vector (u_1, u_2, u_3) yields the rotational part of the velocity operator, (v_1, v_2, v_3) yields its translational part.

The derivative of (2) at $t = t_0$ yields

$$\begin{aligned} r(t_0)r'(t_0)/2 = {} & u_1(Bc-Cb)+u_2(Ca-Ac) \\ & +u_3(Ab-Ba)+v_1(A-a)+v_2(B-b)+v_3(C-c). \end{aligned} \tag{5}$$

Application of this procedure to (3) yields a linear mapping ϕ which transforms velocities $(u_1, u_2, u_3, v_1, v_2, v_3)$ of the motion of the upper part of the platform (end effector) into the linear velocities $(r_1', ..., r_6')$ of telescopic motions of legs of the manipulator. In practical problems we more often need the inverse ϕ^{-1} of this mapping, to express velocities of the motion from velocities of legs. As we have 6 linear equations for 6 unknowns, it exists iff the matrix of coefficients of ϕ is regular. Coefficients are

$$(Bc - Cb, Ca - Ac, Ab - Ba, A - a, B - b, C - c), \tag{6}$$

which are the Plücker coordinates of the line connecting points m and M. Positions where ϕ is not invertible are called singular positions of the parallel manipulator, see Botema, Roth, 1990, Karger, 2001, Karger, 2002, Ma, Angeles, 1992, Merlet, 1992.

3. Singular Set for Special Parallel Manipulators

The singular surface is a very complicated hypersurface in the 6-dimensional space of all possible configurations of the parallel manipulator. It is of degree 10 in Study parameters and it has about 2000

terms in general for a given manipulator (with fully given geometry). To give at least a partial idea how it looks like we shall concentrate at special cases. We shall preserve translations as free parameters and use Euler parameters for the orientation. We observe that the singular set is of degree 3 in translations. This means that for given orientation of the platform we obtain an algebraic surface of degree 3 in E_3. Algebraic surfaces of degree three were intensively studied but they have a rather complicated structure. This is not very suitable for visualization or description. Therefore we shall concentrate at the case where the platform and the base are affinely equivalent. In this case we observe that there is a basic difference between the planar and nonplanar cases.

Let af first the platform (and base) be non-planar. We choose the system of Cartesian coordinates in such a way that $m_1 = [0, 0, 0], m_2 = [a_2, 0, 0], m_3 = [a_3, b_3, 0]$, and similarly for the base. We can suppose that $a_2 b_3 c_4 \neq 0$. Now let us suppose that there is an affine correspondence ψ between the platform and base such that $\psi(m_i) = M_i, i = 1, ..., 6$. ψ is

$$X = f_{11}x + f_{12}y + f_{13}z + f_1,$$

$$Y = f_{21}x + f_{22}y + f_{23}z + f_2,$$

$$Z = f_{31}x + f_{32}y + f_{33}z + f_3,$$

where x, y, z are coordinates in the moving (platform) space, X, Y, Z are coordinates in the fixed (base) space. Substitution of m_1 and M_1 yields $f_1 = f_2 = f_3 = 0$. Substitution of m_2 and M_2 yields $f_{11} = A_2/a_2, f_{21} = f_{31} = 0$. From m_3 and M_3 we obtain

$$f_{12} = \frac{A_3 a_2 - A_2 a_3}{a_2 b_3}, f_{22} = B_3/b_3, f_{32} = 0.$$

The fourth pair of points m_4 and M_4 yields $A_4 = f_{11}a_4, +f_{12}b_4 + f_{13}c_4$, $B_4 = f_{22}b_4 + f_{23}c_4, C_4 = f_{33}c_4$ and therefore $f_{33} = C_4/c_4$,

$$f_{23} = \frac{B_4 b_3 - B_3 b_4}{b_3 c_4}, f_{13} = \frac{b_3(A_4 a_2 - A_2 a_4) + b_4(A_2 a_3 - A_3 a_2)}{a_2 b_3 c_4}.$$

This finishes the computation of the affine correspondence and its equations are

$$X = \frac{A_2}{a_2}x + \frac{A_3 a_2 - A_2 a_3}{a_2 b_3}y + \frac{b_3(A_4 a_2 - A_2 a_4) + b_4(A_2 a_3 - A_3 a_2)}{a_2 b_3 c_4}z$$

$$Y = \frac{B_3}{b_3}y + \frac{B_4 b_3 - B_3 b_4}{b_3 c_4}z, Z = \frac{C_4}{c_4}z, \tag{7}$$

Points M_5, M_6 are determined by the correspondence ψ, because a spatial affine correspondence is determined by four pairs of corresponding points (in general position, which is our case). Let us write

$$Q = \Sigma_{i,j,k} s_{ijk} t_1^i t_2^j t_3^k$$

where the sum is over i, j, k, where $i \geq 0, j \geq, k \geq 0, i + j + k \leq 3$. We suppose at first that $s_{ijk} = s_{ijk}(a_{\alpha,\beta})$, which means that we do not substitute Euler parameters into coefficients of the orthogonal matrix of the orientation, to keep the expression into reasonable limits. The expansion of the equation of the singular set has then 164016 terms. We obtain coefficients of degree three in Q of the following length given in square brackets,
$[s_{300}] = 264, [s_{030}] = 708, [s_{003}] = 1224, [s_{210}] = 1200, [s_{201}] = 1590,$
$[s_{102}] = 708, [s_{021}] = 2484, [s_{021}] = 2418, [s_{012}] = 2928, [s_{111}] = 3930.$

Substitution from equations of the affine correspondence shows that all these coefficients are equal to zero. This shows that for given orientation the singular set is only a quadric in E_3.

Example 1. We choose points

$$m_1 = [0,0,0], m_2 = [1,0,0], m_3 = [2,1,0],$$
$$m_4 = [3,1,1], m_5 = [5,3,6], m_6 = [5,3,4]$$
$$M_1 = [0,0,0], M_2 = [2,0,0], M_3 = [3,2,0],$$
$$M_4 = [1,2,2], M_5 = [-17,6,12], M_6 = [-9,6,8]$$

and orientation given by

$$x_0 = 1/5, x_1 = 2/5, x_2 = -2/5, x_3 = 4/5.$$

The singular set can be seen at Fig. 1.

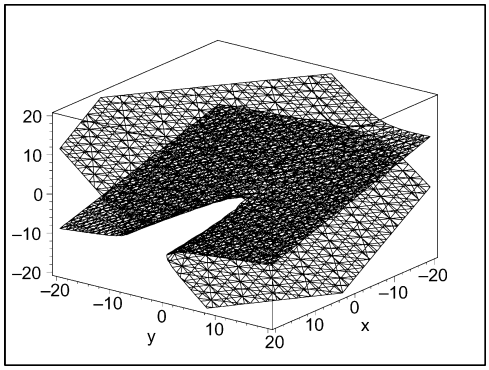

Figure 1. The singular set for non-planar platform from Example 1.

4. Planar Platform and Base

In the planar case we substitute $C_i = c_i = 0$ and the equation of the singular set becomes shorter, it has 14640 terms (without Euler

parameters). The equation of the singular set is still of third degree in translations, but the cubic part factorizes into three factors,

$$t_3[2t_1(x_0x_2 + x_1x_3) + 2t_2(x_0x_1 - x_2x_3) + t_3(-x_0^2 + x_1^2 + x_2^2 - x_3^2)]q_1,$$

where q_1 is linear in t_1, t_2, t_3 with rather complicated coefficients, it is not possible do display it here. This means that in general the singular surface in the planar case remains cubic, but it has three asymtotic planes. Let us have a look if the second factor can be equal to zero for all directions. This yields equations

$$x_0x_2 + x_1x_3 = 0, x_0x_1 - x_2x_3 = 0, x_0^2 + x_3^2 = x_1^2 + x_2^2 \,.$$

We obtain $x_0 = r\cos\alpha, x_3 = r\sin\alpha, x_1 = r\cos\beta, x_2 = r\sin\beta$, which yields $\cos(\alpha+\beta) = \sin(\alpha+\beta) = 0$, which is impossible. The equation $q_1 = 0$ can be explicitly solved as a linear sytem, but the solution is too large to be given here. Instead of this we present an example of a planar platform and base which are not affinely equivalent but they have a singular set quadratical in translations.

Example 2. We write only first two coordinates of points.

$$m_1 = [0,0], m_2 = [1,0], m_3 = [2,3], m_4 = [5,7]$$
$$m_5 = [5,8], m_6 = [12,10], M_1 = [0,0], M_2 = [2,0],$$
$$M_3 = [3,4], M_4 = [6,8], M_5 = [3,36/5], M_6 = [-2160/71, -2416/71].$$

The orientation is as in the first example. The singular set is at Fig. 2.

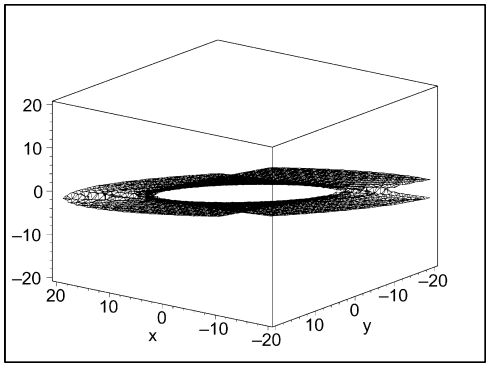

Figure 2. Singular set for the planar case from Example 2.

In the planar case the existence of an affine correspondence between platform and base is more restrictive. Points M_4, M_5, M_6 are given by the correspondence, as affine correspondence in the plane is determined by three pairs of points. The equation for the singular set factorizes into three factors, $\det(\phi) = Q_1.Q_2.Q_3$.

$Q_1 = 0$ iff points m_i lie on a conic section (is known for a long time), $Q_2 = 0$ depends only on the orientation of the platform and it

is independent of translations. This means that if $Q_2 = 0$, then the platform is singular for all translations. $Q_3 = 0$ is linear in translations. We have

$$Q_2 = (A_3a_2 - A_2a_3)(x_0^2x_2^2 - x_1^2x_3^2) + (b_3A_2 - B_3a_2)x_1x_2(x_0^2 + x_3^2) + (b_3A_2 + B_3a_2)x_0x_3(x_1^2 + x_2^2)$$

$$Q_3 = 2t_1a_2[x_1x_3(b_3 + B_3) + x_0x_2(b_3 - B_3)] + 2t_2[x_0x_1b_3(A_2 - a_2) + x_2x_3b_3(A_2 + a_2) + (A_3a_2 - A_2a_3)(x_0x_2 - x_1x_3)] + t_3[2(A_3a_2 - A_2a_3)(x_0x_3 + x_1x_2) + (b_3 - B_3)(a_2 - A_2)x_0^2 - (b_3 + B_3)(a_2 - A_2)x_1^2 - (b_3 - B_3)(a_2 + A_2)x_2^2 + (b_3 + B_3)(a_2 + A_2)x_3^2].$$

We see that in this case the singular set for given orientation is always a plane. A special case was studied in Karger, 2001.

Acknowledgements

The research of this contribution was supported by research project MSM0021620839 of the Ministery of Education of the Czech Republic.

5. Conclusions

In this paper we have found a large class of parallel robot-manipulators with the property that their singular set is at most quadratical in translations. In the non-planar case we have shown that this is true for affinely equivalent base and platform. For planar platform and base the situation is much simpler. For affine equivalent platform and base the singular set factorizes into three factors two are independent of translations and the third one is only linear in translations. In the planar case it is also possible to find all manipulators which are quadratical in translations, for the non-planar case the problem remains open.

References

Bottema, O., Roth, B.: Theoretical Kinematics, Dover Publishing, 1990.

Husty, M.L.: An algorithm for solving the direct kinematics of general Stewart-Gough platforms. Mech. Mach. Theory 31, 365-380, 1991.

Husty, M.L., Karger A.: Self-motions of Griffis-Duffy type parallel manipulators. Proceedings of the 2000 IEEE international Conference on Robotics & Automation, San Francisco, CA, April 2000, pp. 7-12.

Karger, A.: Singularities and self-motions of equiform platforms. MMT 36, 801-815, 2001.

Karger, A.: Singularities ans Self-Motions of a special type of platforms. In J. Lernarčič and F. Thomas, Advances in Robot Kinematics, Kluwer Acad. Publ. 2002, ISBN 0-7923-6426-0, pp. 355-364.

Ma, O., Angeles J.: Architecture Singularities of Parallel Manipulators. Int. Journal of Robotics and Automation 7, 23-29, 1992.

Merlet, J.P.: Singular Configurations of Parallel Manipulators and Grasssmann Geometry. Int. Journal of Robotics Research, 8, 45-56, 1992.

A ROBUST MODEL FOR 3D TRACKING IN OBJECT-ORIENTED MULTIBODY SYSTEMS BASED ON SINGULARITY-FREE FRENET FRAMING

Andrés Kecskeméthy
Chair of Mechanics
University Duisburg-Essen
andres.kecskemethy@uni-due.de

Martin Tändl
Chair of Mechanics
University Duisburg-Essen
martin.taendl@uni-due.de

Abstract The article presents an object-oriented representation of Frenet frame motion along spatial curves in multibody systems. In this setting, the spatial track is regarded as a kinetostatic transmission element transmitting motion and forces as in a generic joint. It is shown that for the Frenet frame parameterization it is possible to avoid singularities at the points of inflection by a special exponential blending technique. The combination of the simple Frenet frame formulas with singularity treatment leads to robust and efficient code for dynamic multibody simulation. All concepts have been tested within an industrial application of roller coaster design.

Keywords: Spatial motion, Frenet frame, singularity treatment, kinematics

1. Introduction

Guided motions along spatial curves have many applications in engineering such as, for example, in the simulation of railways and roller coaster tracks, in CNC machining (Šír and Jüttler, 2005), for guiding robot end effectors or for describing the motion of bodies measured with tracking systems (Kecskeméthy et al., 2003).

While in unconstrained motion the path geometries for translation and orientation are generated independently by dynamical equations, in guided motion, one has to produce smooth trajectories that ensure good dynamic behavior, and also create smooth rotation interpolations that follow the track accurately — termed *framings*. The framing of curves has been intensively studied in previous works (Bishop, 1975, Hanson and Ma, 1995). A simple

J. Lenarčič and B. Roth (eds.), Advances in Robot Kinematics, 255–264.

and computationally efficient frame parameterization uses the Frenet frame with the axes oriented in tangential, normal and binormal direction, respectively. Frenet curves have been used extensively in motion interpolation, ranging from physics, e.g., to describe the motion of macromolecules (Balakrishnan and Blumenfeld, 1997) and to mechanical engineering, where they have been used in constrained multibody systems using Lagrange equations of first kind (Pombo and Ambrosio, 2003, Hansen and Elliott, 2002). One still unsolved problem is that Frenet frames display a singularity when reaching points of inflection, which limits their broad application. The framing suggested by Bishop helps to circumvent this problem by minimizing angular velocity, but on the other hand it requires the solution of a system of differential equations in order to generate the trajectory, which is computationally expensive. The current paper describes an approach for avoiding singularities of the Frenet frame parameterizations and by this to provide a robust description that is suitable for encapsulated code, such as required in object-oriented modelling. The avoidance of singularities is achieved by a de l'Hospital limit analysis, allowing for a continuous Frenet frame distribution even in the presence of points of zero curvature.

The rest of the paper is organized as follows. Section 2 describes the idea of object-oriented representation of multibody dynamics. This idea is applied to spline joints in section 3. In the fourth section, the Frenet frame parameterization and the singularity treatment approach are described. Finally, the application of the developed implementations to industrial roller-coaster design is presented.

2. Kinetostatic transmission elements

For an object-oriented design, one requires a responsibility-driven approach (Wirfs-Brock and Wilkerson, 1989) that allows for invoking complex software by "clicking" at the elements. In mechanics, the most abstract "responsibility" of mechanical components can be regarded to be the transmission of motion and forces. In this view, a mechanical component acts as a kinetostatic transmission element mapping motion and forces from one set of state objects — the 'input' — to another set of state objects — the 'output' (Kecskeméthy and Hiller, 1994). Input and output state objects can be spatial reference frames and/or scalar variables, including associated velocities, accelerations and generalized forces. Let the dimension of the input vector $\underline{q}$ be n, and that of the output vector $\underline{q}'$ be m. Then, the overall transmission behavior has the form depicted in Fig. 1.

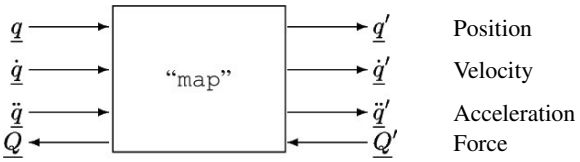

Figure 1. A simple transmission element.

The operation of *motion transmission* consists of the three sub-operations

$$\left.\begin{array}{lrcl} \underline{\text{position:}} & \underline{q}' & = & \underline{\phi}(\underline{q}) \\ \underline{\text{velocity:}} & \dot{\underline{q}}' & = & \mathbf{J}_\phi\, \dot{\underline{q}} \\ \underline{\text{acceleration:}} & \ddot{\underline{q}}' & = & \mathbf{J}_\phi\, \ddot{\underline{q}} + \dot{\mathbf{J}}_\phi\, \dot{\underline{q}} \end{array}\right\}, \tag{1}$$

where $\mathbf{J}_\phi = \partial\underline{\varphi}/\partial\underline{q}$ represents the $m \times n$ *Jacobian* of the transmission element. Furthermore, a force-transmission mapping can be defined by assuming that the transmission element neither generates nor consumes power, i.e., that it is *ideal*. Then, equating virtual work at the input and output yields

$$\delta\underline{q}^{\mathrm{T}}\, \underline{Q} = \delta\underline{q}'^{\mathrm{T}}\, \underline{Q}' \ ,$$

and, after substituting $\delta\underline{q}' = \mathbf{J}_\phi\, \delta\underline{q}$ and noting that this condition must hold for all $\delta\underline{q} \in \mathbf{R}^n$, one obtains the *force transmission* function

$$\underline{\text{force:}} \qquad \underline{Q} \ = \ \mathbf{J}_\phi^{\mathrm{T}}\, \underline{Q}'. \tag{2}$$

Thus, in general, force transmission takes place in opposite direction to velocity transmission with the transposed velocity Jacobian. This relationship holds independently of the complexity of the transmission element.

By the use of kinetostatic transmission elements, users can access the generic properties of mechanical objects without having to refer to their internal implementation details. As shown in Kecskeméthy and Hiller, 1994, it is possible to generate all closure conditions of closed loops as well as the equations of motion of minimal order using only the basic kinetostatic transmission functions. This allows one to combine models of mechanical elements without respect to their internal complexity, making open-architecture, object-oriented libraries possible (Kecskeméthy, 2003).

3. Splines as kinetostatic joints

In order to represent a guided motion as a kinetostatic transmission element, one needs to identify inputs and outputs and describe the corresponding transmission functions for motion and forces. Let a general curve be given as a vector function $\Delta\underline{r}(s)$ with respect to a basis frame $\mathcal{K}_1$ in dependency of the

path coordinate s (Fig. 2). The coordinate frame $\mathcal{K}_1$ may be located at some spatial pose with respect to the inertially fixed coordinate system $\mathcal{K}_0$. The motion along the curve is described by a moving frame $\mathcal{K}_2$, which represents the output of the kinetostatic transmission element. The inputs are embodied by the reference frame $\mathcal{K}_1$ as well as the path coordinate s.

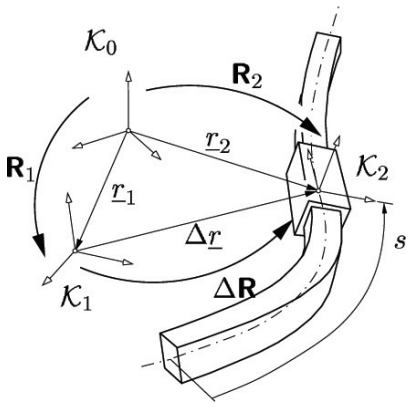

Figure 2. Model of a spline joint.

In the following, we assume in general vectors to be decomposed in the target frame, i.e., in the present case, in coordinates of $\mathcal{K}_2$. For other decompositions, we introduce the notation ${}_i^k\underline{b}_j$, where k denotes the frame of decomposition, i denotes the frame with respect to which the motion is measured, and j denotes the target frame. For motions measured with respect to frame $\mathcal{K}_0$, the index $i = 0$ is omitted. Likely, for decompositions in the target frame $k = j$, the index k is omitted. Hence $\underline{b}_1$ denotes the object ${}_0^1\underline{b}_1$. Furthermore, let $(\cdot)'$ denote the derivative of a quantity with respect to the path coordinate s, and let $\mathbf{R}_i$ denote the rotation matrix transforming coordinates with respect to frame $\mathcal{K}_i$ to coordinates with respect to frame $\mathcal{K}_0$. Then, the transmission behavior of the spline joint can be defined by the following equations.

For the orientation and position of the output frame $\mathcal{K}_2$, one obtains

$$\begin{aligned} \mathbf{R}_2 &= \mathbf{R}_1\Delta\mathbf{R} \\ \underline{r}_2 &= \Delta\mathbf{R}^{\mathrm{T}}(\Delta\underline{r} + \underline{r}_1) \end{aligned} \tag{3}$$

$\Delta\mathbf{R}$ depends on the framing of the curve as described in the next section. Translational ($\underline{v}_i$) and angular ($\underline{\omega}_i$) velocities of frame $\mathcal{K}_2$ are obtained as

$$\begin{bmatrix} \underline{\omega}_2 \\ \underline{v}_2 \end{bmatrix} = \underbrace{\begin{bmatrix} \Delta\mathbf{R}^{\mathrm{T}} & \underline{0} \\ -\Delta\mathbf{R}^{\mathrm{T}}\widetilde{\Delta\underline{r}} & \Delta\mathbf{R}^{\mathrm{T}} \end{bmatrix}}_{\mathbf{J}_g} \begin{bmatrix} \underline{\omega}_1 \\ \underline{v}_1 \end{bmatrix} + \mathbf{J}\,\dot{s} \tag{4}$$

where $\mathbf{J}_g$ is the rigid-body Jacobian, and $\mathbf{J}$ is the Jacobian mapping path velocity $\dot{s}$ to the velocity quantities of the output frame, as specified below for the particular parameterization. Moreover, we employ the notation $\widetilde{\underline{a}}$ for the skew-symmetric matrix generated by a vector $\underline{a} = [a_x\ a_y\ a_z]^{\mathrm{T}}$ as :

$$\widetilde{\underline{a}} = \begin{bmatrix} 0 & -a_z & a_y \\ a_z & 0 & -a_x \\ -a_y & a_x & 0 \end{bmatrix} \tag{5}$$

For the translational and angular acceleration, one obtains

$$\begin{bmatrix} \dot{\underline{\omega}}_2 \\ \underline{a}_2 \end{bmatrix} = \mathbf{J}_g \begin{bmatrix} \dot{\underline{\omega}}_1 \\ \underline{a}_1 \end{bmatrix} + \begin{bmatrix} \underline{0} \\ {}^2\widetilde{\underline{\omega}}_1^2 \Delta\mathbf{R}^{\mathrm{T}} \Delta\underline{r} \end{bmatrix} + \mathbf{J}\,\ddot{s} + \mathbf{J}'\,\dot{s}^2 + \begin{bmatrix} {}^2\widetilde{\underline{\omega}}_1 & \mathbf{0} \\ \mathbf{0} & 2\,{}^2\widetilde{\underline{\omega}}_1 \end{bmatrix} \mathbf{J}\,\dot{s}. \tag{6}$$

According to the force transmission behavior for ideal transmission elements, forces ($\underline{f}_i$) and moments ($\underline{\tau}_i$) at the output frame are mapped to the corresponding forces at the input frame. These are the force and moment at the frame $\mathcal{K}_1$ as well as the generalized force Q_s along the path coordinate. Hereby, the force-moment wrench is assumed to be given with respect to the origin, and all vectors are assumed to be decomposed in coordinates of the frame of reference. As shown in Kecskeméthy and Hiller, 1994, this transmission is realized by the transposed Jacobian:

$$\begin{bmatrix} \underline{\tau}_1 \\ \underline{f}_1 \\ Q_s \end{bmatrix} = \begin{bmatrix} \mathbf{J}_g^{\mathrm{T}} \\ \mathbf{J}^{\mathrm{T}} \end{bmatrix} \begin{bmatrix} \underline{\tau}_2 \\ \underline{f}_2 \end{bmatrix} \tag{7}$$

For the generation of spatial curves, one can employ existing spline algorithms from the literature. In the present context, the B-Spline routine of fifth order from the spline library DIERCKX (Dierckx, 1993) was used.

4. Frenet frame parameterization

The axes of the Frenet frame at path coordinate s are the tangent vector $\underline{t}(s)$, the normal vector $\underline{n}(s) = \Delta\underline{r}''(s)/\kappa(s)$ with curvature $\kappa = \| \Delta\underline{r}'' \|$ and the binormal vector $\underline{b}(s) = \underline{t}(s) \times \underline{n}(s)$. With ${}^1\underline{t}(s)$, ${}^1\underline{n}(s)$ and ${}^1\underline{b}(s)$ being the coordinate representations of $\underline{t}$, $\underline{n}$ and $\underline{b}$ in frame $\mathcal{K}_1$, the rotation matrix becomes

$$\Delta\mathbf{R} = \left[{}^1\underline{t}(s)\ {}^1\underline{n}(s)\ {}^1\underline{b}(s)\right]. \tag{8}$$

For the Jacobian matrix $\mathbf{J}$, one obtains

$$\mathbf{J} = \begin{bmatrix} \underline{u} \\ \underline{t} \end{bmatrix}; \quad \underline{u} = \begin{bmatrix} t_z''/\kappa \\ 0 \\ \kappa \end{bmatrix}; \quad \underline{t} = \begin{bmatrix} 1 \\ 0 \\ 0 \end{bmatrix} \tag{9}$$

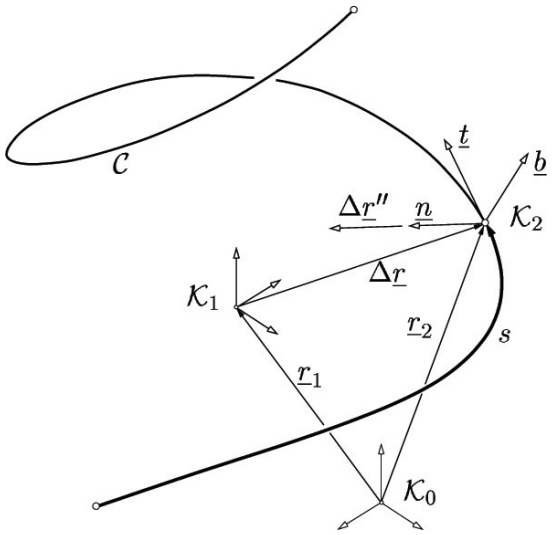

Figure 3. Frenet spline joint.

where $\underline{u}$ is the direction of the angular velocity of frame $\mathcal{K}_2$ for $\dot{s} = 1$ and $\underline{t}$ is the tangent vector, $\underline{t}'' = [t_x'' \; t_y'' \; t_z'']$ and $\underline{t}''' = [t_x''' \; t_y''' \; t_z''']$ are the second and third derivatives of $\underline{t}$ with respect to s, all decomposed in $\mathcal{K}_2$. The acceleration of $\mathcal{K}_2$ relative to $\mathcal{K}_1$ is

$$\begin{bmatrix} {}_1\dot{\underline{\omega}}_2 \\ {}_1\underline{a}_2 \end{bmatrix} = \mathbf{J}\,\ddot{s} + \mathbf{J}'\,\dot{s}^2 \quad \text{with} \quad \mathbf{J}' = \begin{bmatrix} \underline{u}' \\ \underline{t}' \end{bmatrix};$$
$$\underline{u}' = \begin{bmatrix} t_z'''/\kappa - 2\,t_y''\,t_z''/\kappa^2 \\ 0 \\ t_y'' \end{bmatrix}; \quad \underline{t}' = \begin{bmatrix} 0 \\ t_y' \\ t_z' \end{bmatrix} \tag{10}$$

5. Treatment of Frenet frame singularities

At points of inflection, the standard formula for determining the normal vector $\underline{n}$ fails, as both the nominator and the denominator vanish. However, by a limit analysis, this difficulty can be overcome. Let the curvature $\kappa = \| \Delta\underline{r}'' \|$ be described in the vicinity of the singularity by a linear approximation $k|s - s^\star|$ with a still-to-be-determined positive constant k. By substituting $k|s - s^\star|$ for κ and using de l'Hospital's rule, the right- and left-hand side limits of $\underline{n}$ become, for $\Delta\underline{r}'''(s^\star) \neq 0$,

$$\underline{n}^- = \lim_{s \to s^\star -} \frac{\Delta\underline{r}''(s)}{k|s - s^\star|} = -\frac{\Delta\underline{r}'''(s^\star)}{k} = -\lim_{s \to s^\star +} \frac{\Delta\underline{r}''(s)}{k|s - s^\star|} = -\underline{n}^+. \tag{11}$$

From the condition $\| \underline{n} \| \equiv 1$ one obtains $k = \| \Delta \underline{r}'''(s^\star) \|$ and the right-hand and left-hand limits become

$$\lim_{s \to s^\star -} \underline{n} = -\frac{\Delta \underline{r}'''(s^\star)}{\| \Delta \underline{r}'''(s^\star) \|} = -\lim_{s \to s^\star +} \underline{n}. \tag{12}$$

This creates a finite value, but induces a switch of direction of the normal vector at the singularity. In order to avoid this switch of direction, one defines a vector field $\underline{h}(s)$ along one side of the curve by introducing at equidistant support points $s_i = s_{i-1} + \Delta s,\ s_0 = 0,\ i = 0, \ldots, N_h$ unit vectors aligned with the normal vector $\underline{n}_i$ at that point and oriented such that $\underline{h}_{i-1}^{\mathrm{T}} \underline{h}_i > 0$ (Fig. 4 a)). The intermediate vector field $\underline{h}(s)$ is then obtained by linear interpolation. Using these vectors, one can define a smooth vector field

$$\overline{\underline{n}} = \underline{n}\ \mathrm{sgn}(\underline{h}(s)^{\mathrm{T}} \underline{n}(s)) \tag{13}$$

whose direction at each point coincides with that of the normal vector.

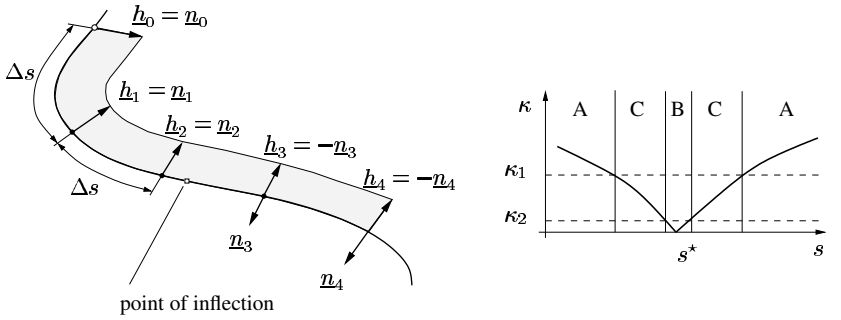

a) Vector field $\underline{h}(s)$ for orienting normal vectors. b) Domains for normal vector formulas.

Figure 4.

For practical applications, one needs to treat not only points in which the curvature is exactly zero, but also points for which the curvature almost vanishes. As the spline joints developed here must be suited for dynamic simulations, the transitions from one set of computations (regular Frenet frame formulas) to another (limit analysis Frenet frame formulas) must be smooth and differentiable. For this purpose, one defines two thresholds for the curvature, one for entering zero curvature domain (κ_2), and one for entering the regular region (κ_1). In-between, a blending procedure is applied which interpolates the result of the normal vector computation using the regular formulas and that using limit-analysis formulas. When the limit-analysis formula is applied to points near the singularity, the resulting limit vector $\underline{n}$ is no longer exactly normal to the tangent. This can be circumvented by taking the normal component of $\Delta \underline{r}'''$ through the projection

$$\overline{\underline{n}}(s) = \frac{\Delta \underline{r}''' - \underline{t}\,\underline{t}^{\mathrm{T}} \Delta \underline{r}'''}{\| \Delta \underline{r}''' - \underline{t}\,\underline{t}^{\mathrm{T}} \Delta \underline{r}''' \|}\ \mathrm{sgn}(\underline{h}^{\mathrm{T}} \Delta \underline{r}''') \quad \text{for} \quad \| s - s^\star \| \ll 1 \tag{14}$$

Let $\overline{\underline{n}}_A$ denote the normal vector as computed with the regular formula, and let $\overline{\underline{n}}_B$ denote the normal vector as computed with the singularity formula after orthogonalization with respect to the tangent. Then, for a typical trajectory passing through an inflection point, one obtains three domains: A (regular), C (transition) and B (singular) as depicted in Fig. 4 b). Then one can define for region A ($\kappa > \kappa_1$)

$$\overline{\underline{n}}(s) = \overline{\underline{n}}_A = \frac{\Delta\underline{r}''}{\kappa} \operatorname{sgn}(\underline{h}^{\mathrm{T}} \Delta\underline{r}''), \tag{15}$$

for region B ($\kappa \leq \kappa_2$)

$$\overline{\underline{n}}(s) = \frac{\Delta\underline{r}''' - \underline{t}\,\underline{t}^{\mathrm{T}} \Delta\underline{r}'''}{\| \Delta\underline{r}''' - \underline{t}\,\underline{t}^{\mathrm{T}} \Delta\underline{r}''' \|} \operatorname{sgn}(\underline{h}^{\mathrm{T}} \Delta\underline{r}''') \tag{16}$$

and for region C ($\kappa_2 \leq \kappa < \kappa_1$)

$$\overline{\underline{n}} = \frac{\underline{m}}{\| m \|} \quad \text{with} \tag{17}$$

$$\underline{m} = p_A \Delta\underline{r}'' \operatorname{sgn}(\underline{h}^{\mathrm{T}} \Delta\underline{r}'') + p_B \left(\Delta\underline{r}''' - \underline{t}\,\underline{t}^{\mathrm{T}} \Delta\underline{r}''' \right) \operatorname{sgn}(\underline{h}^{\mathrm{T}} \Delta\underline{r}'''). \tag{18}$$

Here, the exponential weighting functions

$$\begin{aligned} p_A = p_A(\alpha) &= e^{-c_A(1-\alpha)^2} \\ p_B = p_B(\alpha) &= e^{-c_B \alpha^2} \end{aligned}$$

with

$$\alpha = (\kappa - \kappa_2)/(\kappa_1 - \kappa_2)$$

are employed, in which the coefficients c_A and c_B can still be determined by the user in order to achieve optimal results. Although also other blending functions are conceivable, exponential blending functions have the advantage that (1) they offer C^∞ transitions for the two limit cases $\alpha \to 1$, $\alpha \to 0$, (2) the boundary conditions can be achieved easily, and (3) all derivatives are easy to compute. Moreover, the blending functions are related to the error function in statistics, so that they mimic an averaging procedure. Hence, no other types of blending functions have been considered in this context, although they could be incorporated easily. For computing $\underline{u}$ and $\underline{u}'$ one needs the first and second derivatives of $\underline{n}$, which are not reproduced here due to lack of space. Using $\underline{n}'$ and $\underline{n}''$, the coordinates of $\underline{u}$ can be computed using Poisson's formula and $\overline{\underline{b}} = \underline{t} \times \overline{\underline{n}}$ as:

$$\begin{aligned} u_x &= \overline{\underline{b}}^{\mathrm{T}}\, \overline{\underline{n}}' \\ u_y &= -\overline{\underline{b}}^{\mathrm{T}}\, \underline{t}' \\ u_z &= \overline{\underline{n}}^{\mathrm{T}}\, \underline{t}'. \end{aligned} \tag{19}$$

As well, the coordinates of $\underline{u}'$ become, with $\overline{\underline{b}}' = \underline{t}' \times \overline{\underline{n}} + \underline{t} \times \overline{\underline{n}}'$,

$$\begin{aligned} u_x' &= \overline{\underline{b}}'^{\mathrm{T}} \overline{\underline{n}}' + \overline{\underline{b}}^{\mathrm{T}} \overline{\underline{n}}'' - (\underline{t}^{\mathrm{T}} \overline{\underline{n}}')(\overline{\underline{b}}^{\mathrm{T}} \underline{t}') + (\underline{t}^{\mathrm{T}} \overline{\underline{b}}')(\overline{\underline{n}}^{\mathrm{T}} \underline{t}') \\ u_y' &= -\overline{\underline{b}}'^{\mathrm{T}} \underline{t}' - \overline{\underline{b}}^{\mathrm{T}} \underline{t}'' + (\overline{\underline{n}}^{\mathrm{T}} \overline{\underline{b}}'^{\mathrm{T}})(\overline{\underline{n}} \underline{t}'') + (\overline{\underline{n}}^{\mathrm{T}} \underline{t}')(\overline{\underline{b}}^{\mathrm{T}} \overline{\underline{n}}')r \\ u_z' &= \overline{\underline{n}}'^{\mathrm{T}} \underline{t}' + \overline{\underline{n}}^{\mathrm{T}} \underline{t}''. \end{aligned} \tag{20}$$

From these formulas, one obtains smooth Frenet frame rotations through points with low curvature. In the following, a nearly singular point at $s^\star \approx 7.7m$ with curvature $\kappa^\star = 10^{-4}\, m^{-1}$ was regarded. Figure 5 shows the magnitude of the vectors $\underline{u}$ and $\underline{u}'$ when using the proposed method for $\kappa_1 = 0.096$, $\kappa_2 = 0.012$ and $c_A = c_B = 5.0$ and the magnitudes obtained with the regular formula as reference. The peak in the angular velocity that might lead to problems during numerical integration is completely avoided using the blending procedure.

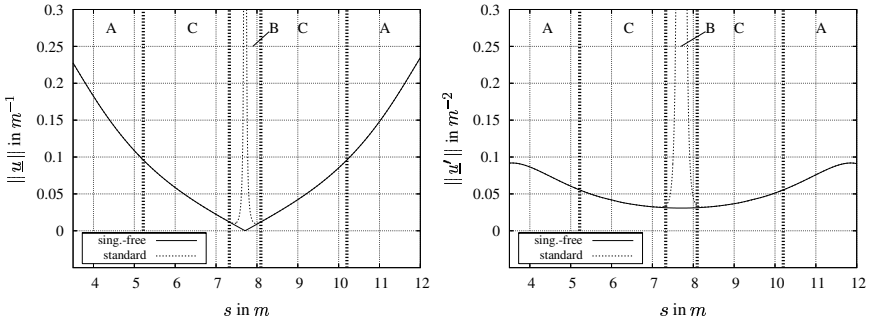

Figure 5. Comparison of $||\underline{u}||$ and $||\underline{u}'||$ for standard and singularity-free Frenet frame formulas.

6. Conclusions

The presented approach for generating guided spatial motion using Frenet frames prove to be useful for parameter-independent, object-oriented simulation of multibody systems. With the introduced limit analysis, it is possible to generate smooth Frenet frame motions through inflection points, which are required for robust numeric integration of the equations of motion. Using this description, it is possible to encapsulate the framing algorithm in easily applicable objects which can be used for online editing of spatial trajectories such as shown in Fig. 6 for the application in roller coaster design.

References

Balakrishnan, R. and Blumenfeld, R. (1997), Transformation of general curve evolution to a modified Belavin-Polyakov equation. *Journal of Mathematical Physics*, vol. 38, no. 11, pp. 5878–5888.

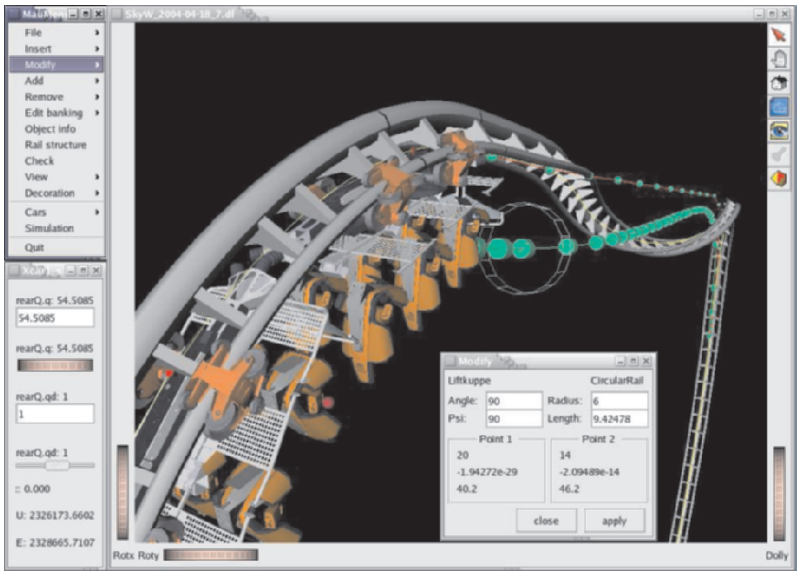

Figure 6. Roller coaster design environment.

Bishop, R. L. (1975), There is More than One Way to Frame a Curve. *American Mathematical Monthly*, vol. 82, no. 3, pp. 246–251.

Dierckx, P. (1993), *Curve and Surface Fitting with Splines*. Clarendon Press, Oxford.

Hansen, N. and A. Elliott, A. (2002), Improving Roller Coaster Design with Virtual Prototyping. In *ADAMS Users Conference*.

Hanson, A. J. and Ma, H. (1995), Quaternion frame approach to streamline visualization. *IEEE Transactions on Visualization and Computer Graphics*, vol. 1, no. 2, pp. 164–174.

Kecskeméthy, A. (2003), *MOBILE 1.3 User's Guide and Reference Manual*. University of Duisburg-Essen.

Kecskeméthy, A. and Hiller, M. (1994), An object-oriented approach for an effective formulation of multibody dynamics. *Computer Methods in Applied Mechanics and Engineering*, vol. 115, pp. 287–314.

Kecskeméthy, A., Stolz, M., Strobach, D., Saraph, V., Steinwender, G. and Zwick, B. (2003), Improvements in measure-based simulation of the human lower extremity. In *Proceedings of the IASTED Conference on Biomechanics*, pp. 155–160, Rhodes, Greece.

Pombo, J. and Ambrosio, J. (2003), General Spatial Curve Joint for Rail Guided Vehicles: Kinematics and Dynamics. *Multibody System Dynamics*, vol. 9, pp. 237–264.

Šír, Z. and Jüttler, B. (2005), Constructing acceleration continuous tool paths using Pythagorean Hodograph curves. *Mechanism and Machine Theory*, vol. 40, pp. 1258–1272.

Wirfs-Brock, R. and Wilkerson, B. (1989), Object-oriented design: A responsibility-driven approach. In *OOPSLA '89 Proceedings*, pp. 71–75.

SINGULARITY OF A CLASS OF GOUGH-STEWART PLATFORMS WITH THREE CONCURRENT JOINTS

Patricia Ben-Horin
Department of Mechanical Engineering
Technion – Israel Institute of Technology
patbh@tx.technion.ac.il

Moshe Shoham
Department of Mechanical Engineering
Technion – Israel Institute of Technology
shoham@tx.technion.ac.il

Abstract In this paper the singularity of all Gough-Stewart platforms (GSP) that have three concurrent joints is analyzed. The singularity analysis is based on Grassmann-Cayley algebra, and the general expression of the rigidity matrix of six lines connecting two bodies (Superbracket). For the class under consideration, this coordinate-free expression is easily reduced leading to a geometrically meaningful singularity condition.

Keywords: Singularity, decoupled parallel robot, Grassmann-Cayley algebra

1. Introduction

The growing interest in parallel robots during the last twenty years is accompanied with theoretical effort to cope with the singularity problems of these robots due to their instability characteristic at these points. The Gough-Stewart platform (GSP) is a paradigm for parallel robots and the singularities of some of its special forms were thoroughly studied. In this investigation we focus on a certain class of GSPs consisting of all the structures having three concurrent joints on the moving platform (or alternatively the stationary platform). These robots advantage is having the orientation of the platform and the position of one point on the platform decoupled. Several researchers addressed specific decoupled GSP structures, most of them dealt with the forward kinematics (Husain and Waldron, 1994, Wohlhart, 1994, Bruyninckx, 1997 and 1998). In addition to the forward kinematics analysis, Wohlhart (1994) obtained also the singularity condition of the general decoupled robot (also called 3-1-1-1). Following some algebraic manipulations of the Jacobian

J. Lenarčič and B. Roth (eds.), Advances in Robot Kinematics, 265–274.

determinant, he found two conditions, one constituting a linear complex and the second constituting a linear congruence of the lines along the manipulator extensible links. The same result was also obtained by Di Gregorio (2002) who used mixed products of vectors identified in the robot to obtain the singularity condition as a ninth-degree polynomial equation. Another decoupled robot whose singularity was found is the 3-2-1 structure. Using an ellipsoidal uncertainty model for a 3-2-1 wire-based system, Thomas et al. (2002), found that the singularity of this robot occurs when one of three tetrahedrons constituted by the joints is singular. The same result was obtained by Downing et al. (2002), who approached the problem by using the "pure condition" proposed by White (1983) (also used in the present paper). The results of Thomas et al. and Downing et al. go along with the comments of Hunt and Primrose (1993) regarding the singularity of the 3-2-1 structure.

The approach used in this paper is based on Grassmann-Cayley algebra. The origin of this algebra date back to Grassmann treatise "Theory of extension" in 1844. The basic elements of this algebra are geometric entities such as points, lines and planes and the basic operators are able to express algebraically the intersection (*meet*) or the union (*join*) of two or more elements. A complete definition of the meet operation came out after more than a century in the paper of Doubilet et al. (1974).

In the present investigation we provide a comprehensive study of the singularity conditions of a class of 18 robots that have three concurrent links on the moving, not generally planar, platform. This is a continuation of previous studies on the singularity of a class of seven GSPs having only pairs of concurrent joints (Ben-Horin and Shoham, 2005a) and a broad class of three-legged robots (Ben-Horin and Shoham, 2005b). The main aim of this paper is to demonstrate the simplicity of the use of Grassmann-Cayley algebra for decoupled robots as a class, while general and special cases are easily identified. The analysis is performed using the singularity condition of the general GSP in a coordinate-free decomposed form so that the spherical joint locations appear explicitly. Once the specific structure is substituted into the general expression, the geometric meaning of the condition is deduced using Grassmann-Cayley operators and properties.

The outline of this paper is as follows: Section 2 presents the full list of GSPs that belong to this class having three concurrent legs on a platform. Section 3 briefly presents the basic operations of the Grassmann-Cayley algebra. Section 4 contains the singularity condition of the general GSP, leading to the solutions of the decoupled structures of this paper in section 5.

2. A Class of Gough-Stewart Platforms

Innocenti and Parenti-Castelli (1994) enumerated a long list of GSPs, dividing them into two groups: 17 types that have only single or double spherical pairs and 4 types that have triplet spherical pairs. Subsequently, Faugere and Lazard (1995) presented a complete list of all combinations of GSPs containing a total of 35 types. The additional types presented are identified to be those having triplet spherical pairs. Table 1 lists all the structures that belong to the class under consideration, all of them (Fig. 1) appear in Faugere and Lazard's paper (1995). To have a unique identification of the robots we use the letters **a**,**b**,..,**j** defining the spherical joints connecting the legs, so as the robots in Fig. 1 are denoted as follows:

Table 1: Notation of the structures.

1. (**ae**,**af**,**ag**),**bh**,**ci**,**dj**	2. (**ae**,**af**,**ag**),**bh**,**ch**,**dj**	3. (**ae**,**af**,**ag**),**bh**,**ci**,**cj**
4. (**ae**,**af**,**ag**),**bh**,**bi**,**ci**	5. (**ae**,**af**,**ag**),**be**,**cf**,**dg**	6. (**ae**,**af**,**ag**),**bf**,**cg**,**dg**
7. (**ae**,**af**,**ag**),**be**,**bf**,**cg**	8. (**ae**,**af**,**ag**),**bg**,**ch**,**di**	9. (**ae**,**af**,**ag**),**be**,**cf**,**dh**
10.(**ae**,**af**,**ag**),**bg**,**cg**,**dh**	11.(**ae**,**af**,**ag**),**bg**,**ch**,**dh**	12.(**ae**,**af**,**ag**),**bg**,**ch**,**ci**
13.(**ae**,**af**,**ag**),**bf**,**bg**,**ch**	14.(**ae**,**af**,**ag**),**bg**,**bh**,**ci**	15.(**ae**,**af**,**ag**),**bg**,**bh**,**ch**
16.(**ae**,**af**,**ag**),**bf**,**cg**,**ch**	17.(**ae**,**af**,**ag**),**bg**,**cg**,**ch**	18.(**ae**,**af**,**ag**),**bf**,**bg**,**cg**
19.(**ae**,**af**,**ag**),**bh**,**ch**,**dh**		

Every pair of letters indicates a leg, the first three pairs being within parentheses since they are identical in all the structures. Structure No. 19 is always singular since, by definition, all the lines of the robot intersect the line passing through **a** and **h**, thus resulting in a general complex singularity.

Some of the structures were presented in the literature. As mentioned in the introduction, Wohlhart (1994), Husain and Waldron (1994) and Di Gregorio (2002) analyzed structure No. 1 (also called 3-1-1-1). Bernier et al. (1995) proposed a specific design of structure No. 1, where the actuation is through linear guides of the lower spherical joints instead of extension of the legs. Patarinski and Uchiyama (1993) studied structure No. 5 from the instantaneous kinematics point of view. Bruyninckx derived the forward kinematics of structure No. 2 with non-planar platforms (1997) and of No. 10, with both platforms being planar (1998). Structure No. 3 (also called 3-2-1) was addressed by Thomas et al. (2002) and Downing et al. (2002). Besides solving the forward kinematics of structure No. 1, Nanua and Waldron (1990) also addressed structure No. 18.

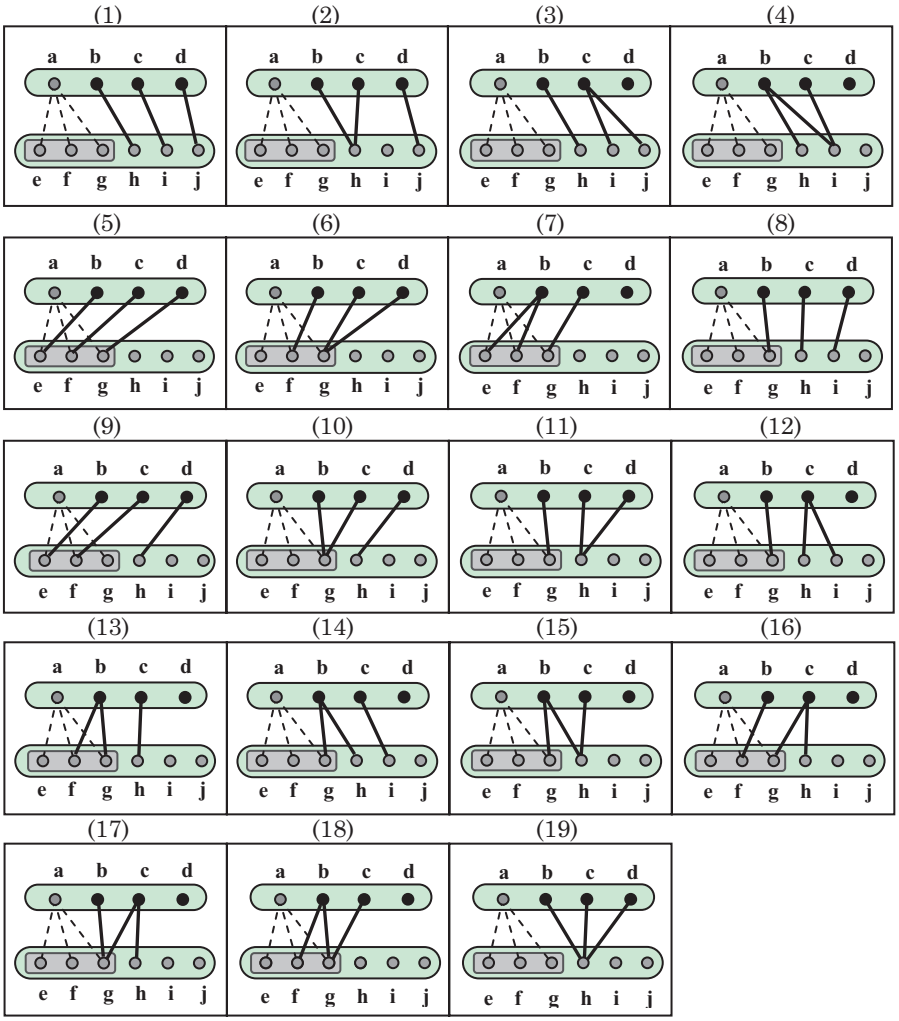

Figure 1. All versions of GSPs that have three concurrent legs.

3. Grassmann-Cayley Algebra

In this section a short introduction to the main notions of this algebra is given, including relevant examples to this paper. More details on Grassmann-Cayley algebra can be found in Ben-Horin and Shoham (2005a) and many references therein.

Consider a finite set of vectors $\{a_1,a_2,..,a_d\}$ defined in the d-dimensional vector space over the field P, V, where $a_i=x_{1,i},x_{2,i},..,x_{d,i}$ $(1\leq i\leq d)$. If M is a matrix having a_i $(1\leq i\leq d)$ as its columns, then the bracket of these vectors is defined to be the determinant of M:

$$\left[a_1, a_2, ..., a_d\right] = \det M = \begin{vmatrix} x_{1,1} & x_{1,2} & \cdots & x_{1,d} \\ \vdots & \vdots & \cdots & \vdots \\ x_{d,1} & x_{d,2} & \cdots & x_{d,d} \end{vmatrix}. \quad (1)$$

The brackets satisfy the following relations:

$$\left[a_1, a_2, ..., a_d\right] = 0\,, \quad (2)$$

If $a_i = a_j$ for some i, j with $i \neq j$, or $a_1, a_2, \ldots, a_d$ are dependent.

$$\left[a_1, a_2, ..., a_d\right] = sign(\sigma)\left[a_{\sigma 1}, a_{\sigma 2}, ..., a_{\sigma d}\right] \quad (3)$$

for any permutation σ of $1,2,\ldots,d$

$$\left[a_1, a_2, ..., a_d\right]\left[b_1, b_2, ..., b_d\right] = \sum_{i=1}^{d}\left[b_i, a_2, ..., a_d\right]\left[b_1, b_2, ..., b_{i-1}, a_1, b_{i+1}, ..., b_d\right] \quad (4)$$

Equations (2) and (3) stem from well-known determinant properties. The relations of the third type (4) are called *Grassmann-Plücker* relations or *syzygies* (White, 1975), and they correspond to generalized Laplace expansions by minors.

Let W be a k-dimensional subspace of V, let $\{w_1, w_2, .., w_k\}$ be a basis of W, and let **A** be a Plücker coordinate vector in the $\binom{d}{k}$-dimensional vector space V^k. Then this vector can be denoted symbolically as follows (White, 1994):

$$\mathbf{A} = w_1 \vee w_2 \vee \cdots \vee w_k \quad (5)$$

A is called an *extensor of step k*. Additionally, $\overline{A} = W$, where $\overline{A}$ is called the *support* of **A**. Two k-extensors **A** and **B** are equal up to a scalar multiplication if and only if their supports are equal, $\overline{A} = \overline{B}$.

Let $\mathbf{A}=a_1 \vee a_2 \vee .. \vee a_k$ and $\mathbf{B}=b_1 \vee .. \vee b_h$ (or simply $\mathbf{A}=a_1 a_2 .. a_k$ and $\mathbf{B}=b_1 .. b_h$) be extensors in V having steps k and h respectively, with $k+h<d$. Then the *join* of **A** and **B** is defined by

$$\boxed{\mathbf{A} \vee \mathbf{B} = a_1 \vee a_2 \vee \cdots \vee a_k \vee b_1 \vee \cdots \vee b_h = a_1 a_2 \cdots a_k b_1 \cdots b_h} \quad (6)$$

which is an extensor of step $k+h$. The join is non-zero if and only if $\{a_1, a_2, .., a_k, b_1, b_2, .., b_h\}$ is a linearly independent set.

Let $\mathbf{A}=a_1 a_2 \ldots a_k$ and $\mathbf{B}=b_1 b_2 \ldots b_h$, with $k+h \geq d$. Then the *meet* of these extensors is defined by the expression:

$$\mathbf{A} \wedge \mathbf{B} = \sum_{\sigma} \mathrm{sgn}(\sigma)[a_{\sigma(1)} a_{\sigma(2)} \ldots a_{\sigma(d-h)} b_1 \ldots b_h] a_{\sigma(d-h+1)} \ldots a_{\sigma(k)} \quad (7)$$

where the sum is taken over all permutations σ of $\{1,2,..,k\}$ such that $\sigma(1)<\sigma(2)<\ldots<\sigma(d-h)$ and $\sigma(d-h+1)<\sigma(d-h+2)<\ldots<\sigma(k)$. Alternatively, the permutations in Eq. (7) may be written using dots above the permuted elements instead of σ as follows:

$$\mathbf{A} \wedge \mathbf{B} = \sum_{\sigma} \mathrm{sgn}(\sigma)[\dot{a}_1 \dot{a}_2 \ldots \dot{a}_{d-h} b_1 \ldots b_h] \dot{a}_{d-h+1} \ldots \dot{a}_k \tag{8}$$

3.1. Examples of the Meet Operation

1. Let **K=ab** and **L=cd** be two extensors of step 2 ($k=h=2$) representing the lines K and L in the projective space Π^3 ($d=4$). In this case $k+h=d$. If K and L are skew lines, then $\mathbf{K} \cup \mathbf{L} = \Pi^3$ and $\mathbf{K} \cap \mathbf{L} = 0$, then $\mathbf{K} \wedge \mathbf{L}$ is a scalar. The calculation of this scalar gives six times the volume of a tetrahedron constructed from points **a**, **b**, **c** and **d** (see Fig. 2(a)). If the lines are coplanar, $\mathbf{K} \cup \mathbf{L} = \Pi^2 \neq \Pi^3$, then the meet is $\mathbf{K} \wedge \mathbf{L} = 0$, since this is a degenerate case of that of Fig. 2(b).

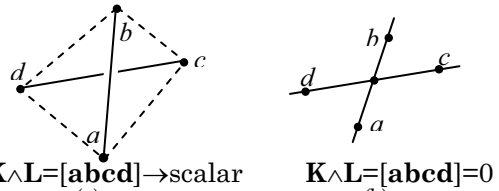

$\mathbf{K} \wedge \mathbf{L} = [\mathbf{abcd}] \rightarrow$ scalar (a) $\mathbf{K} \wedge \mathbf{L} = [\mathbf{abcd}] = 0$ (b)

Figure 2. Meet of lines in space.

2. Let **X=abc** and **Y=def** be two extensors of step 3 ($k=h=3$), representing two planes in the projective space Π^3 ($d=4$). Given the planes are not coplanar, then $\mathbf{X} \cup \mathbf{Y} = \Pi^3$, $\mathbf{X} \cap \mathbf{Y} \neq 0$, therefore in this case the meet of **X** and **Y** yields an extensor of step $k+h-d=2$, which indicates the line of intersection of X and Y:

$$\mathbf{X} \wedge \mathbf{Y} = \mathbf{abc} \wedge \mathbf{def} = [\mathbf{adef}]\mathbf{bc} - [\mathbf{bdef}]\mathbf{ac} - [\mathbf{cdef}]\mathbf{ba} = [\dot{\mathbf{a}}\,\mathbf{def}]\dot{\mathbf{b}}\,\dot{\mathbf{c}}$$

3. A line **gh** intersecting this line of intersection gives the same result as in the degenerate case in example 1, then the meet is equal to 0:

$$\mathbf{gh} \wedge \mathbf{abc} \wedge \mathbf{def} = \big([\mathbf{gabc}]\mathbf{h} - [\mathbf{habc}]\mathbf{g}\big) \wedge \mathbf{def} = [\dot{\mathbf{g}}\,\mathbf{abc}][\dot{\mathbf{h}}\,\mathbf{def}] = 0\,.$$

4. Singularity Condition of the General GSP

From the rigidity of frameworks point of view researchers have developed methods to find the condition for which the framework is infinitesimally non-rigid. This resulted in rigidity matrices of bar-and-joint frameworks (White and Whiteley, 1983) and bar-and-body frameworks (White and Whiteley, 1987). A special case of the latter frameworks is the case of two bodies interconnected by six bars, namely, the GSP. As known, the rigidity matrix (or the Jacobian) of this case has the Plücker coordinates of the bar-lines as its columns. A decomposition

of the determinant of this matrix was proposed by White (1983), calling it *Superbracket*. This expression includes bracket monomials containing symbolically only the connecting points. A significant simplification of this expression was provided by McMillan (1990), reducing to 24 bracket monomials. Below, McMillan's version is introduced.

Let [**ab**,**cd**,**ef**,**gh**,**ij**,**kl**] be the bracket of six 2-extensors representing lines *ab*, *cd*, *ef*, *gh*, *ij*, *kl* in space. Then the superbracket of these lines is:

$$[\mathbf{ab},\mathbf{cd},\mathbf{ef},\mathbf{gh},\mathbf{ij},\mathbf{kl}] = \left[\mathbf{abcd}\right]\left[\mathbf{ef}\overset{1}{\mathbf{g}}\overset{2}{\mathbf{i}}\right]\left[\overset{1}{\mathbf{h}}\overset{2}{\mathbf{j}}\mathbf{kl}\right] - \left[\mathbf{abc}\overset{3}{\mathbf{e}}\right]\left[\overset{3}{\mathbf{d}}\overset{4}{\mathbf{f}}\mathbf{gh}\right]\left[\mathbf{ijkl}\right] - \left[\mathbf{abc}\overset{5}{\mathbf{e}}\right]\left[\overset{5}{\mathbf{d}}\mathbf{gh}\overset{7}{\mathbf{i}}\right]\left[\overset{6}{\mathbf{f}}\overset{7}{\mathbf{j}}\mathbf{kl}\right] + \left[\mathbf{abc}\overset{8}{\mathbf{g}}\right]\left[\overset{8}{\mathbf{d}}\mathbf{ef}\overset{10}{\mathbf{i}}\right]\left[\overset{9}{\mathbf{h}}\overset{10}{\mathbf{j}}\mathbf{kl}\right] \tag{9}$$

where $\left[\mathbf{abcd}\right]\left[\mathbf{ef}\overset{1}{\mathbf{g}}\overset{2}{\mathbf{i}}\right]\left[\overset{1}{\mathbf{h}}\overset{2}{\mathbf{j}}\mathbf{kl}\right]$ denotes $\sum_{1,2}\text{sign}(1,2)\left[\mathbf{abcd}\right]\left[\mathbf{ef}\overset{1}{\mathbf{g}}\overset{2}{\mathbf{i}}\right]\left[\overset{1}{\mathbf{h}}\overset{2}{\mathbf{j}}\mathbf{kl}\right]$ and 1,2 are permutations of the 2-element sets {**g**, **h**}, {**i**, **j**}, respectively.

5. Singularity Solution of Three-concurrent-joint Robots

The singularity condition for the robots of the decoupled class is obtained by substituting the points of each robot in the general superbracket expression of Eq. (9). According to Eq. (2) and due to repetition of points in double or triple spherical pairs, this expression is reduced to two or one non-zero monomial terms for all the robots in the class.

The resulting non-zero terms for structure No.1 are (out of 24 terms):

$$[\mathbf{ae},\mathbf{af},\mathbf{ag},\mathbf{bh},\mathbf{dj},\mathbf{ci}] = -[\mathbf{aefg}][\mathbf{abhd}][\mathbf{ajci}] + [\mathbf{aefg}][\mathbf{abhj}][\mathbf{adci}] \tag{10}$$

After collecting equal terms the right hand side is written as

$$= [\mathbf{aefg}]([\mathbf{abhj}][\mathbf{adci}] - [\mathbf{abhd}][\mathbf{ajci}]) \tag{11}$$

The expressions in parentheses are identified to be the result of the meet operation, interchanging **j** and **d**:

$$= [\mathbf{aefg}]\left(\left[\mathbf{abh}\dot{\mathbf{j}}\right]\left[\mathbf{a}\dot{\mathbf{d}}\mathbf{ci}\right]\right) \tag{12}$$

These terms being equated to zero comprise the singularity conditions:

$$\boxed{[\mathbf{aefg}] = 0 \qquad \text{or} \qquad \mathbf{abh} \wedge \mathbf{aci} \wedge \mathbf{dj} = 0} \tag{13}$$

The first singularity condition occurs whenever the points **a**, **e**, **f** and **g** are coplanar. Since we refer to generic robots having this joint distribution, this condition does not necessarily mean that point **a** is on plane **efg**. For instance, the robot proposed by Bernier et al. (1995) which is actuated by linear actuators that change the spherical joints locations

can have point **g** lying on line **ef** thus leading to this singularity. The second singularity condition arises whenever line **dj** intersects the line of intersection of planes **abh** and **aci** (as may be identified from example No. 3 in Section 3.1).

Singularity of particular cases

Structure No. 2 in Table. 1 is one of the particular cases of No. 1, where point **i** coincides with point **h**. Therefore, the terms of Eq. (10) take the form

$$[\mathbf{ae},\mathbf{af},\mathbf{ag},\mathbf{bh},\mathbf{dj},\mathbf{ch}] = -[\mathbf{aefg}][\mathbf{abhd}][\mathbf{ajch}] + [\mathbf{aefg}][\mathbf{abhj}][\mathbf{adch}]. \quad (14)$$

Similarly to the solution of structure No. 1:

$$= [\mathbf{aefg}]([\mathbf{abhj}][\mathbf{adch}] - [\mathbf{abhd}][\mathbf{ajch}]) \quad (15)$$

$$= [\mathbf{aefg}]\left(\left[\mathbf{abh}\dot{\mathbf{j}}\right]\left[\mathbf{a}\dot{\mathbf{d}}\mathbf{ch}\right]\right) \quad (16)$$

These terms being equated to zero comprise the singularity conditions:

$$[\mathbf{aefg}] = 0 \qquad \text{or} \qquad \mathbf{abh} \wedge \mathbf{ach} \wedge \mathbf{dj} = 0 \quad (17)$$

These conditons have the same form as for structure No. 2. However, the second condition is calculated as follows:

$$(\mathbf{abh} \wedge \mathbf{ach}) \wedge \mathbf{dj} = 0 = \left(\cancel{[\mathbf{aach}]}\,\mathbf{bh} - [\mathbf{bach}]\mathbf{ah} - \cancel{[\mathbf{hach}]}\,\mathbf{ba}\right) \wedge \mathbf{dj} \quad (18)$$

$$= -[\mathbf{bach}]\mathbf{ah} \wedge \mathbf{dj} = -[\mathbf{bach}][\mathbf{ahdj}] \quad (19)$$

In conclusion, the singularity condition is:

$$\boxed{[\mathbf{aefg}] = 0 \qquad \text{or} \qquad [\mathbf{bach}] = 0 \qquad \text{or} \qquad [\mathbf{ahdj}] = 0} \quad (20)$$

The robot is singular whenever points **a**,**e**,**f** and **g**, or points **a**,**b**,**h** and **c** or **a**,**h**,**d** and **j** are coplanar. The condition of the first four points being coplanar was obtained for structure No. 1. This is related to the inability to resist forces applied on point **a**. The second two conditions are related to the inability to resist torques, thus gaining one or two angular degrees of freedom. This condition in structure No. 1 consists of the intersection of line **dj** with the intersection of planes **abh** and **aci**. In structure No. 2, the line of intersection of the respective planes **abh** and **ach** is line **ah** itself, as it is obtained in Eq.(19), so the second condition becomes Eq.(20).

Table 2: Singularity conditions of all GSP having three concurrent joints.

1.[**aefg**]=0, **abh**∧**ach**∧**dj**=0	2. [**aefg**][**abhj**][**adch**]=0	3.[**aefg**][**abhc**][**aicj**]=0
4. [**aefg**][**abhi**][**abci**]=0	5.[**aefg**]=0, **abe**∧**adg**∧**fc**=0	6. [**aefg**][**abfg**][**acdg**]=0
7. [**aefg**][**abef**][**abcg**]=0	8.[**aefg**]=0, **abg**∧**adi**∧**hc**=0	9.[**aefg**]=0,**abe**∧**adh**∧**fc**=0
10.[**aefg**][**abgc**][**agdh**]=0	11.[**aefg**][**abgh**][**acdh**]=0	12.[**aefg**][**abgc**][**ahci**]=0
13.[**aefg**][**abfg**][**abch**]=0	14.[**aefg**][**abgh**][**abci**]=0	15.[**aefg**][**abgh**][**abch**]=0
16.[**aefg**][**abfc**][**agch**]=0	17.[**aefg**][**abgc**][**agch**]=0	18.[**aefg**][**abfg**][**abcg**]=0

The condition obtained for structure No. 1 matches the result obtained by Wohlhart (1994) and the condition obtained for structure No. 2 is compatible with results obtained by Thomas et al. (2002) and Downing et al. (2002) for similar structures. While structure No. 2 was taken as an example, the same type of solution is obtained for structures No. 2, 3, 4, 6, 7, 10, 11, 12, 13, 14, 15, 16, 17 and 18, see Table 2. In the same way, structures No. 5, 8 and 9 have the same singularity condition as No. 1, all having three mutually separated legs. a Fig. 1 shows structure No. 17 in its regular and singular poses. In this case the singular pose is caused by the condition [abgc]=0.

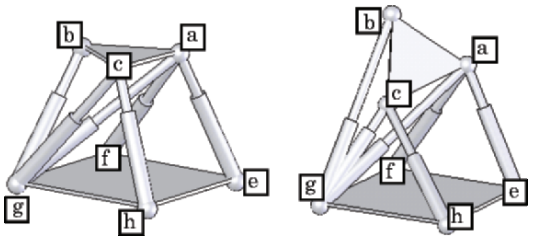

Figure 1. Structure No. 17 in a regular (left) and singular (right) poses.

6. Conclusions

In this paper the singularity of a GSP class having three concurrent joints was addressed using a decomposed form of the rigidity matrix determinant of the general GSP. This form contains combinations of bracket monomials, which are tools from Grassmann-Cayley algebra. Since the class of robots under consideration has at least one concurrent triplet of joints, the substitution of the joints of the robots into the general solution causes most of the bracket monomials to vanish. Consequently, the retrieval of the geometrical nature of the singularity condition of each robot using Grassmann-Cayley properties becomes a simple task. Starting with the most general structure and showing particular cases, the singularity conditions of all the 18 robots of the class were obtained. For the general cases it consists of the coplanarity of one tetrahedron associated with the three concurrent joints or the meet of one leg with the intersection line of two other planes. The singularity of the particular cases includes three possible coplanar tetrahedrons.

References

Ben-Horin P. and Shoham M. (2005a), Singularity Analysis of Parallel Robots Based on Grassmann-Cayley Algebra, *International Workshop on Computational Kinematics*, Cassino, May 4-6. Accepted for publication in Mechanism Mechanism and Machine Theory.

Ben-Horin P. and Shoham M. (2005b), Singularity condition of six degree-of-freedom three-legged parallel robots based on Grassmann-Cayley algebra, accepted for publication in *IEEE Transactions on Robotics*.

Bernier D., Castelain J.M., and Li X. (1995), A new parallel structure with six degrees of freedom, *9th World Congress on the Theory of Machines and Mechanisms*, pp. 8-12.

Bruyninckx H. (1997), The Analytical Forward Displacement Kinematics of the "31-12" Parallel Manipulator, *IEEE International Conference on Robotics and Automation*, pp. 2956-2960.

Bruyninckx H. (1998), Closed-form forward position kinematics for a $(3\text{-}1\text{-}1\text{-}1)^2$ fully parallel manipulator, *IEEE Transactions on Robotics and Automation*, No. 14, vol. 2, pp. 326-328.

Di Gregorio R. (2002), Singularity-locus expression of a class of parallel mechanisms*, Robotica*, vol. 20, pp. 323-328.

Doubilet P., Rota G.C., and Stein J. (1974), On the Foundations of Combinatorial Theory: IX, Combinatorial Methods in Invariant Theory, *Studies in Applied Mathematics*, vol. 53, no.3, pp. 185-216.

Downing D.M., Samuel A.E., and Hunt K.H. (2002), Identification of the Special Configurations of the Octahedral Manipulator using the Pure Condition, *The International Journal of Robotics Research*, vol. 21, No. 2, pp. 147-159.

Faugere J.C. and Lazard D. (1995), Combinatorial Classes of Parallel Manipulators, *Mechanism and Machine Theory*, No. 30, vol. 6, pp. 765-776.

Hunt K.H. and Primrose E.J.F. (1993), Assembly configurations of some in-parallel-actuated manipulators, *Mechanism and Machine Theory*, No. 28, vol. 1, pp. 31-42.

Husain M. and Waldron K.J. (1994), Direct position kinematics of the 3-1-1-1 Stewart platforms, *Journal of Mechanical Design*, vol. 116, pp. 1102-1107.

Innocenti C. and Parenti-Castelli V. (1994), Exhaustive Enumeration of Fully Parallel Kinematic Chains, *ASME Dynamics Systems and Control*, DSC-Vol 55-2, vol. 2, pp. 1135-1141.

McMillan T. (1990), Invariants of Antisymmetric Tensors, PhD Dissertation, University of Florida.

Nanua P. and Waldron K.J. (1990), Direct kinematic solution of a special parallel robot structure*, RoManSy*, vol. 8, pp. 134-142.

Patarinski S.P. and Uchiyama M. (1993), Position/Orientation decoupled parallel manipulators, *ICAR*, pp. 153-158.

Thomas F., Ottaviano E., Ros L., and Ceccarelli M. (2002), Uncertainty model and singularities of 3-2-1 wire-based tracking systems, *Advances in Robot Kinematics*, pp. 107-116.

White N. (1975), The Bracket Ring of a Combinatorial Geometry I, *Transactions of the American Mathematical Society*, vol. 202 pp. 79-95.

White N. (1983), The Bracket of 2-Extensors, *Congressus Numerantium*, vol. 40, pp. 419-428.

White N. (1994), Grassmann-Cayley Algebra and Robotics, *Journal of Intelligent and Robotics Systems*, vol. 11, pp. 91-107.

White N. and Whiteley W. (1983), The Algebraic Geometry of Stresses in Frameworks, *SIAM Journal on Algebraic and Discrete Methods*, Vol. 4, No. 4, pp. 481-511.

White N. and Whiteley W. (1987), The algebraic Geometry of Motions of Bar-and-Body Frameworks, *SIAM Journal on Algebraic and Discrete Methods*, vol. 8, no. 1, pp. 1-32.

Wohlhart K. (1994), Displacement analysis of the general spherical Stewart platform, *Mechanism and Machine Theory*, no. 29, vol. 4, pp. 581-589.

SINGULARITY ANALYSIS OF A 4-DOF PARALLEL MANIPULATOR USING GEOMETRIC ALGEBRA

Tanio K. Tanev
Central Laboratory of Mechatronics and Instrumentation
Bulgarian Academy of Sciences
Acad. G. Bonchev Str., Bl.1, Sofia-1113, Bulgaria
tanev_tk@hotmail.com

Abstract The paper presents a geometric algebra (Clifford algebra) approach to singularity analysis of a spatial parallel manipulator with four degrees of freedom. The geometric algebra provides a good geometrical insight in identifying the singularities of parallel manipulators with fewer than six degrees of freedom.

Keywords: Singularity, parallel manipulator, geometric algebra, kinematics

1. Introduction

Most of the investigations of the parallel manipulators are concerned with the six-degrees-of-freedom (6-dof) parallel manipulators such as Steward-Gough parallel manipulators. In recent years there is an increased interest in parallel manipulators with less than six degrees of freedom. The performance of such types of manipulators is satisfactory for some applications. Moreover, they have some advantages in comparison with the 6-dof parallel manipulators such as greater workspace and simpler mechanical designs. Comparatively a small number of papers have been dedicated to 4-dof and 5-dof parallel manipulators (e.g. Fang and Tsai, 2002; Lenarcic, et al., 2000; Pierrot and Company, 1999; Tanev, 1998).

The singularity of spatial parallel manipulators with fewer than six degrees of freedom (mainly 3-dof) has been studied by several researchers (Di Gregorio, 2001; Wolf et al., 2002; Zlatanov et al., 2002).

This paper presents a singularity analysis of a four-degrees-of-freedom three-legged parallel manipulator using geometric algebra (Clifford algebra) approach. Only a few papers are dedicated to application of Clifford algebra to robot kinematics (e.g. Collins and McCarthy, 1998; Rooney and Tanev, 2003). The geometric algebra provides a good geometrical insight and computer efficiency in designing and manipulating geometric objects.

J. Lenarčič and B. Roth (eds.), Advances in Robot Kinematics, 275–284.

2. Geometric Algebra

In this paper the author adopts the geometric algebra (Clifford algebra) approach developed by Hestens (Hestenes, 1999; Hestenes and Sobczyk, 1984). In an n-dimensional vector space $\mathcal{V}_n$ over real numbers, the geometric algebra $\mathcal{G}_n = \mathcal{G}(\mathcal{V}_n)$ is generated from $\mathcal{V}_n$ by defining a single basic kind of multiplication called *geometric product* between two vectors. The geometric product for all vectors in $\mathcal{V}_n$ obeys associative and distributive rules, multiplication by a scalar (λ) is defined and the square of any vector is a scalar. These properties, which hold for all vectors, are summarized as follows: $a(bc) = (ab)c$; $a(b+c) = ab + ac$; $(b+c)a = ba + ca$; $a\lambda = \lambda a$; $a^2 = \pm|a|^2$ where $|a|$ is a positive scalar called magnitude of a. The geometric algebra $\mathcal{G}_n = \mathcal{G}(\mathcal{V}_n)$ is a 2^n-dimensional algebra, i.e., $\mathcal{G}_n$ generates exactly 2^n linearly independent elements. The vector space $\mathcal{V}_n$ is closed under vector addition, but is not closed under multiplication. By multiplication and addition the vectors of $\mathcal{V}_n$ generate a larger linear space $\mathcal{G}_n = \mathcal{G}(\mathcal{V}_n)$ called the *geometric algebra* of $\mathcal{V}_n$. This linear space is closed under multiplication as well as addition.

The geometric product of two vectors a and b can be decomposed into symmetric and antisymmetric parts. i.e.,

$$ab = a \cdot b + a \wedge b, \tag{1}$$

where the *inner product* $a \cdot b$ and the *outer product* $a \wedge b$, respectevely, are defined by

$$a \cdot b = \frac{1}{2}(ab + ba) \quad \text{and} \quad a \wedge b = \frac{1}{2}(ab - ba). \tag{2}$$

The inner product $a \cdot b$ is a scalar-valued (drade 0). The result of the other product is neither a scalar nor a vector. For any two vectors a and b, the outer product $a \wedge b$ is an entity called *bivector* (grade 2). Geometrically, it represents a directed plane segment produced by sweeping a along b. Higher-grade elements can be constructed by introducing more vectors. Thus, *trivectors* $a \wedge b \wedge c$ (grade 3) represent volumes and so on, up to the dimension of the space under consideration. The outer product of k vectors $a_1, a_2, ..., a_k$ generates a new entity $a_1 \wedge a_2 \wedge \cdots \wedge a_k$ called a k-blade. The integer k is named a grade. A linear combination of blades with the same grade is called a k-vector. The geometric algebra $\mathcal{G}_n$ contains nonzero blades of maximum grade n which are called pseudoscalars of $\mathcal{G}_n$ or $\mathcal{V}_n$. Although geometric algebra can be constructed in an entirely basis-free form, in this particular application (Euclidean geometric algebra with signature (n,0)) it is useful to introduce a set of basis vectors which obey the following $e_i \cdot e_j = \delta_{ij}$; $\delta_{ij} = 1 (i = j)$ and $\delta_{ij} = 0$ $(i \neq j)$; $e_i \wedge e_i = 0$.

A generic element of the geometric algebra is called a *multivector* which can be written as

$$M = \sum_{k=0}^{n} \langle M \rangle_k, \tag{3}$$

where $\langle M \rangle_k$ denotes the k-vector part of M.

An extensive treatment of a geometric algebra is given in Hestenes, 1999.

3. Velocity of Parallel Manipulators

In this section, the velocity equations for parallel manipulators in terms of the geometric algebra are obtained.

3.1. Screws in terms of Geometric Algebra

Any oriented line l is uniquely determined by given its direction u and its moment m and in the geometric algebra $\mathcal{G}_3$ of 3-D vector space $\mathcal{V}_3$ with the basis $\{e_1, e_2, e_3\}$ it can be written as (Hestenes, 1999):

$$l = u + m \equiv u + r \wedge u, \tag{4}$$

where r is the position vector of a point on the line.

Thus, in the geometric algebra $\mathcal{G}_3$ of the 3-D vector space $\mathcal{V}_3$, a line is expressed as a multivector composed from a vector part plus a bivector. An extension of the equation of the line (Eq. 4), i.e. adding the moment corresponding to the pitch, leads to the equation of a screw:

$$s = u + r \wedge u + h\,iu \equiv v_1 e_1 + v_2 e_2 + v_3 e_3 + b_1 e_2 \wedge e_3 + b_2 e_3 \wedge e_1 + b_3 e_1 \wedge e_2, \tag{5}$$

where $v_i\,(i = 1,2,3)$ and $b_i\,(i = 1,2,3)$ are scalar coefficients; $i = e_1 e_2 e_3$ is the unit pseudoscalar of $\mathcal{G}_3$; h is the pitch of the screw.

In Eq. 5 the screw is expressed as a multivector in $\mathcal{G}_3$. It could also be expressed as a vector in the geometric algebra $\mathcal{G}_6$. In the geometric algebra $\mathcal{G}_6$ of 6-D vector space $\mathcal{V}_6$ with the basis $\{e_1, e_2, e_3, e_4, e_5, e_6\}$, a screw can be written as a vector (grade 1), i.e.,

$$S = v_1 e_1 + v_2 e_2 + v_3 e_3 + b_1 e_4 + b_2 e_5 + b_3 e_6, \tag{6}$$

where the coefficients are the same as in Eq. 5.

The operation of transformation of a screw into an elliptic polar screw (see Lipkin and Duffy, 1985) can be written as

$$\tilde{s} = i\langle s \rangle_1 + i^{-1} \langle s \rangle_2 \equiv b_1 e_1 + b_2 e_2 + b_3 e_3 + v_1 e_2 \wedge e_3 + v_2 e_3 \wedge e_1 + v_3 e_1 \wedge e_2, \tag{7}$$

where $\langle s \rangle_k$ denotes *k-vector part* of s; i^{-1} is the inverse of the unit pseudoscalar i for the $\mathcal{G}_3$.

From this section on the following notations for a screw are adopted: a lower case letter (s, l) denotes a screw written as a multivector in $\mathcal{G}_3$ of 3-D space; an upper case letter (S, L) denotes a screw written as a vector in $\mathcal{G}_6$ of 6-D space; letters with a tilde mark ($\tilde{s},\tilde{S}$) denote the elliptic polars of the screws (s and S), given in $\mathcal{G}_3$ and $\mathcal{G}_6$, respectively.

It has been pointed out by Lipkin and Duffy (1985) that the twists of non-freedom (wrenches of non-constraint) and wrenches of constraint (twists of freedom) are elliptic polars; twists of freedom (wrenches of constraint) and twists of non-freedom (wrenches of non-constraint) are orthogonal complements which together span a six space. These properties and relationships are used in the present paper in order to obtain the singularities of the considered parallel manipulator. Although orthogonality of screws is invariant with respect to rotations of the coordinate system but not with respect to the translations (Lipkin and Duffy, 1985), it is still useful for the purpose of the identification of singularities in this paper.

3.2. Velocity Equations

The moving platform and the base of a parallel manipulator are connected with n-legs, which can be considered as serial chains. The velocity of the moving platform can be expressed as a linear combination of the joint instantaneous twists

$$V_p = \sum_{i=1}^{f} {}^{j}\omega_i \, {}^{j}S_i, \qquad (j = 1,2...n), \tag{8}$$

where ${}^{j}\omega_i$ denotes the joint rate and ${}^{j}S_i$ represents the normalized screw associated with the ith joint axis of the jth leg; f is the dof of the jth leg . The left leading superscript denotes the leg number.

In case of a parallel manipulator with fewer than six degrees of freedom, some legs may not possess full mobility. In that case, we suppose that the remaining degrees of freedom are represented by dummy joints (or driven but locked joints) and associated with them dummy screws. Taking the outer product of five screws of the jth leg gives the following 5-blade:

$${}^{j}A_k = {}^{j}S_1 \wedge {}^{j}S_2 \wedge ... \wedge {}^{j}S_{k-1} \wedge {}^{j}S_{k+1} \wedge ... \wedge {}^{j}S_6 . \tag{9}$$

The 5-blade ${}^{j}A_k$ from Eq. 9 involves five screws (out of six with the exception of the ${}^{j}S_k$ screw). The kth joint is active. In a non-degenerate space, the dual of a blade represents the orthogonal complement of the subspace represented by the blade. The dual of the above 5-blade ${}^{j}A_k$ is given by the following geometric product:

$$ {}^{j}D_k = {}^{j}A_k I_6^{-1} = (-1)^{n(6-n)} I_6^{-1}\, {}^{j}A_k \,, \tag{10} $$

where $I_6 = e_1e_2e_3e_4e_5e_6$ is a unit pseudoscalar of the $\mathcal{G}_6$ and I_6^{-1} is its inverse; $n = 5$ (in case of 6-dof limb).

Pre-multiplying (inner product) both sides of Eq. 8 by ${}^{j}D_k$ one obtains:

$$ {}^{j}D_k \bullet V_p = {}^{j}\omega_k \, {}^{j}D_k \bullet {}^{j}S_k \,. \tag{11} $$

The result in Eq. 11 is obtained having in mind that ${}^{j}S_i \bullet {}^{j}D_k = 0 \; (i \neq k)$ and ${}^{j}S_k \bullet {}^{j}D_k = {}^{j}c_k$ (providing the joint screws of the *j*th leg are linearly independent); ${}^{j}c_k$ is a scalar.

Therefore, it follows from Eq. 11 that the rate of *k*th joint of the *j*th leg is

$$ {}^{j}\omega_k = \frac{1}{{}^{j}\tilde{R}_k \bullet {}^{j}S_k} \, {}^{j}R_k \bullet \tilde{V}_p \,, \tag{12} $$

where ${}^{j}R_k \equiv {}^{j}\tilde{D}_k$ is a screw reciprocal to the joint screws $S_1, {}^{j}S_2, \ldots, {}^{j}S_{k-1}, {}^{j}S_{k+1}, \ldots, {}^{j}S_6$ of the *j*th leg; and $\tilde{V}_p$ is the velocity of the moving platform with interchanged primary and secondary parts (the interchanging operation is algebraically the same as operation of transformation of a screw into an elliptic polar screw).

The screws ${}^{j}R_k$ form the rows of the inverse Jacobian.

4. Singularity of a 3-legged 4-DOF Parallel Manipulator

The considered three-legged parallel manipulator is shown in Fig.1. Two of the legs have SPS structure. The third leg has $R_1 \perp R_2 \perp P_3 \perp R_3$ structure (the R_1 revolute joint is attached to the base and R_3 revolute joint – to the moving platform, respectively).

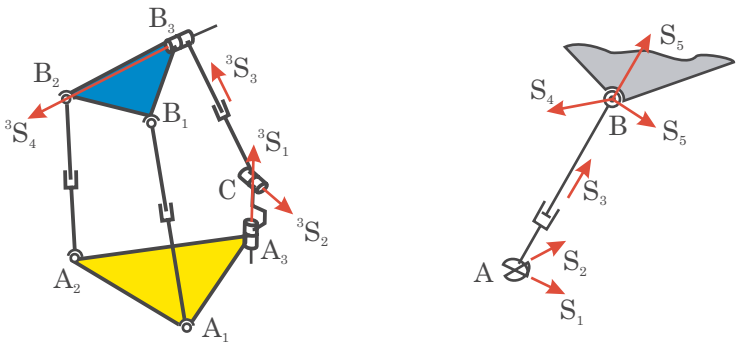

a) The 3-legged 4-dof parallel manipulator

b) The SPS (UPS) leg of the manipulator and the screw axes

Figure 1. The 3-legged 4-dof parallel manipulator and the joint screw axes.

The active (actuated) joints are as follows: i) the three prismatic joints of the legs; and ii) the revolute joint R_1 of the third leg which is connected to the base platform (for details see Tanev, 1998).

In a non-singular configuration the driven joints and the structure (or the dummy joints) of the manipulator sustain a general wrench applied to the moving platform. Referring to Eqs. 11 and 12, the condition for singular configuration can be written as

$$D_1 \wedge D_2 \wedge ... \wedge D_6 = 0, \tag{13}$$

where $D_i = {}^jA\ I_6^{-1}$ is a vector (grade 1), because the 5-blade ${}^jA$ also includes the screws associated with the dummy joints of the *j*th leg.

The 6-blade from Eq. 13 is zero, if and only if its six constituent vectors are linearly dependent. The first and the second legs (SPS legs) of the considered parallel manipulator have full mobility and each one has one driven joint (the P joint). The third leg (RRPR leg) has four degrees of freedom, two driven joints (R_1 and P_3) and in order to have full mobility two extra dummy joints (denoted by a superscript *d* in the equations) are added, which can be considered as active but locked. In this case, Eq. 13 can be rewritten as

$${}^1D_3 \wedge {}^2D_3 \wedge {}^3D_1 \wedge {}^3D_3 \wedge {}^3D_{d1} \wedge {}^3D_{d2} = 0. \tag{14}$$

The duals, which are needed for the velocity equations for the active and dummy joints of the third leg (RRPR leg), are as follows

$$\begin{aligned} {}^3D_1 &= ({}^3S_2 \wedge {}^3S_3 \wedge {}^3S_4 \wedge {}^3S_{d1} \wedge {}^3S_{d2})\, I_6^{-1}; \\ {}^3D_3 &= ({}^3S_1 \wedge {}^3S_2 \wedge {}^3S_4 \wedge {}^3S_{d1} \wedge {}^3S_{d2})\, I_6^{-1} \\ {}^3D_{d1} &= ({}^3S_1 \wedge {}^3S_2 \wedge {}^3S_3 \wedge {}^3S_4 \wedge {}^3S_{d2})\, I_6^{-1} \\ {}^3D_{d2} &= ({}^3S_1 \wedge {}^3S_2 \wedge {}^3S_3 \wedge {}^3S_4 \wedge {}^3S_{d1})\, I_6^{-1} \end{aligned} \tag{15}$$

Taking the outer product of the four vectors from Eq. 15 and after some manipulations one obtains

$${}^3D_1 \wedge {}^3D_3 \wedge {}^3D_{d1} \wedge {}^3D_{d2} = \lambda({}^3S_2 \wedge {}^3S_4) I_6^{-1}, \tag{16}$$

where $\lambda = -({}^3D_1 \bullet {}^3S_1)({}^3D_{d1} \bullet {}^3S_{d1})({}^3D_{d2} \bullet {}^3S_{d2})$ is a scalar; the above result is obtained keeping in mind that ${}^3D_i \bullet {}^3S_k = 0 (i \neq k)$ and ${}^3D_i \bullet {}^3S_k \neq 0 (i = k)$.

Since λ is a scalar, both 4-blades $\lambda({}^3S_2 \wedge {}^3S_4) I_6^{-1}$ and $({}^3S_2 \wedge {}^3S_4) I_6^{-1}$ represent one and the same subspace.

Therefore, the condition for singularity can be written as

$${}^1D_3 \wedge {}^2D_3 \wedge {}^3D = 0, \tag{17}$$

where ${}^1D_3 = ({}^1S_1 \wedge {}^1S_2 \wedge {}^1S_4 \wedge {}^1S_5 \wedge {}^1S_6)\, I_6^{-1}$;
${}^2D_3 = ({}^2S_1 \wedge {}^2S_2 \wedge {}^2S_4 \wedge {}^2S_5 \wedge {}^2S_6)\, I_6^{-1}$ and ${}^3D = ({}^3S_2 \wedge {}^3S_4) I_6^{-1}$.

It is clear that the condition for the singularity (Eq. 17) involves screws which represent all and only passive joints of the parallel manipulator. This condition can be easily generalized to any kind of parallel manipulator with less than six degrees of freedom.

The singular configurations of the manipulator can be algebraically obtained from Eq. 17. Further, in order to utilize the geometrical insight of the approach, the 6-blade from the left-hand side of Eq. 17 is factorized into six vectors (screws). The linear dependence of these six screws gives the condition for singularity. Since ${}^{1}D_3$ and ${}^{2}D_3$ are vectors, only the 4-blade ${}^{3}D$ is factorized into four vectors. These six dual screws yield their elliptic polars. It could be proved that if n screws are linearly dependent, so are their elliptic polars. The elliptic polars of ${}^{1}D_3$ and ${}^{2}D_3$ are two lines (L_1 and L_2) along the first and the second legs, respectively. The elliptic polars of the four factor vectors of the 4-blade ${}^{3}D$ are as follows: i)the line L_3 is along the third leg (CB_3); ii)the line L_4 is parallel to the joint screw axis ${}^{3}S_2$ and passes through B_3; iii)the line L_5 is parallel to the joint screw axis ${}^{3}S_4$ and passes through C; iv)the line L_6 intersects the two joint screw axes ${}^{3}S_2$ and ${}^{3}S_4$, and does not pass through C. These four lines are reciprocal to the two joint screws ${}^{3}S_2$ and ${}^{3}S_4$. Thus, the outer product of the elliptic polars of the latter four lines is

$$\tilde{L}_3 \wedge \tilde{L}_4 \wedge \tilde{L}_5 \wedge \tilde{L}_6 = \mu\, {}^{3}D, \tag{18}$$

where μ is a scalar.

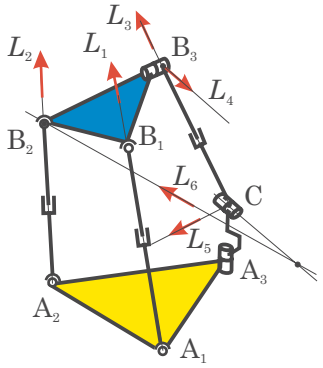

Figure 2. The arrangement of the six lines.

The six lines are shown in Fig. 2. They, actually, represent the wrenches of constraints, including those from the active (driven) joints, imposed to the moving platform. Therefore, the manipulator is in singular configuration if these six lines are linearly dependent, i.e.,

$$L_1 \wedge L_2 \wedge L_3 \wedge L_4 \wedge L_5 \wedge L_6 = 0. \tag{19}$$

Obviously, Eqs. 17 and 19 are equivalent and both represent the condition for singularity of the considered parallel manipulator.

4.1 Singular Configurations

The singular configurations of the manipulator can be identified using Eq. 17 (or Eq. 19). The following main types of singular configurations for the considered parallel manipulator can be distinguished: i) The first type of singular configuration occurs when one line is linearly dependent on three other lines (Fig. 3).

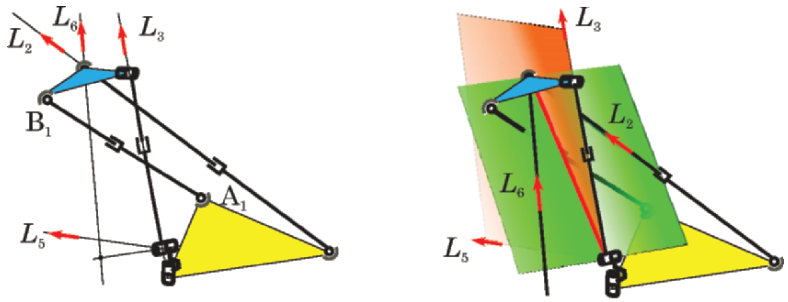

a) The singular configuration b) The two intersecting planes

Figure 3. Type 3b singular configuration.

This singularity is of type 3b according to the classification introduced by Merlet (Merlet, 1989; McCarthy, 2000). In this case the intersection line of two planes, defined by two pairs of intersecting lines (L_3, L_5 and L_2, L_6), passes through the two points of intersection of the two pairs of lines (Fig. 3-b). Interesting in this case is the fact that the manipulator is in singular configurations regardless of the leg length of the first leg (A_1B_1). In this singular configuration the uncontrollable motion is a general screw motion. ii) The second type of singular configuration is of type 4d – degenerate congruence. Fig. 4-a shows this singular configuration and the plane generated by two intersecting lines. The lines L_1, L_3 and L_5 lie in this plane, while the intersection point of the lines L_2 and L_6 is the same as the point of intersection of the two lines generating the plane. Here, the uncontrollable motion (twist of freedom) is a pure rotation about an axis $\$$ along the line B_2B_3. iii) The next type of singular configuration occurs when one of the lines is a linear combination of the remaining five lines (Fig. 4-b). In this particular case five of the lines (L_1, L_2, L_3, L_4 and L_6) intersect a single line B_2B_3 and the sixth line L_5 is parallel to the same line B_2B_3. In this singular configuration, the uncontrollable motion is a pure rotation about an axis $\$$ along the line B_2B_3. Although this type of singularity is not explicitly

listed in the Merlet's (Merlet, 1989; McCarthy, 2000) classification, it could be classified as 5b singularity. Let a screw S be a linear combination of five screws. Thus, the six screws are linearly dependent if and only if their outer product is zero, i.e.,

$$S \wedge S_1 \wedge S_2 \wedge S_3 \wedge S_4 \wedge S_5 = 0. \tag{20}$$

Postmultiplying both sides of Eq. 20 by I_6^{-1} leads to

$$(S \wedge S_1 \wedge S_2 \wedge S_3 \wedge S_4 \wedge S_5)I_6^{-1} = S \bullet [(S_1 \wedge S_2 \wedge S_3 \wedge S_4 \wedge S_5)I_6^{-1}] = 0. \tag{21}$$

Since $F = (S_1 \wedge S_2 \wedge S_3 \wedge S_4 \wedge S_5)I_6^{-1}$ is a unique screw, therefore it follows from Eq. 21 that any screw S, which is reciprocal to the elliptic polar screw ($\tilde{F}$) of F, is a linear combination of the five screws $S_i\,(i = 1...5)$. If $\tilde{F}$ is a real line (a screw with zero pitch), then S could be any line in space which intersects $\tilde{F}$, is coaxial with or parallel to $\tilde{F}$.

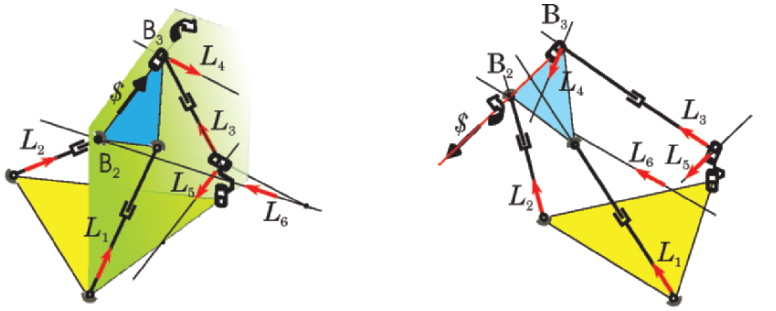

a) Type 4d singular configuration b) Type 5 singular configuration

Figure 4. Types 4 and 5 singular configurations.

In the considered particular singular case (Fig. 4-b) the dual of any 5-blade (the outer product of any five screws L_i) is a line and its elliptic polar is the line along B_2B_3 (Fig. 4-b). Five of the lines intersect the line B_2B_3 and the remaining sixth line is parallel to the same line B_2B_3.

5. Conclusions

The condition for singularity is expressed as a linear dependency of six lines using the language of geometric algebra. Several main types of singularity for the considered parallel manipulator have been identified. It has been proved that the equation for the singularity (the condition for singularity) involves the screws which represent all and only passive joints of the manipulator. Although the presented geometric algebra approach is applied to a particular parallel manipulator, it could be generalized for identifying the singularities of a general type of parallel manipulator and as well as of one with fewer than six degrees of freedom.

Acknowledgements

This paper is partly supported by the Bulgarian National Science Fund – TH-1510/05 project.

References

Collins, C.L., and McCarthy, J.M. (1998), The quartic singularity surfaces of planar platforms in the Clifford algebra of the projective plane, *Mechanism and Machine Theory*, vol. 33, No. 7, pp. 931-944.

Di Gregorio, R. (2001), Statics and singularity loci of the 3-UPU wrist**,** *Proc. IEEE/ASME International Conference on Advanced Intelligent Mechatronics,* Como, Italy, vol. 1, pp. 470-475.

Fang, Y., and Tsai, L-W. (2002), Structure Synthesis of a Class of 4-DOF and 5-DOF Parallel Manipulators with Identical Limb Structures**,** *The International Journal of Robotics Research*, vol. 21, No. 9, September 2002, pp. 799-810.

Hestenes, D. (1999), N*ew foundations for classical mechanics* (Second edition), Kluwer Academic Publishers, Dordrecht, The Netherlands.

Hestenes, D., and Sobczyk, G. (1984), *Clifford algebra to geometric calculus*, D. Reidel Publishing Company, Dordrecht, Holland.

Lenarcic, J., Stanisic, M.M., and Parenti-Castelli V. (2000), A 4-DoF parallel mechanism simulating the movement of the human sternum-clavicle-scapula complex. *In Advances in Robot Kinematics*, J. Lenarčič and M.M. Stanisic, (eds.), Kluwer Academic, pp. 325-332.

Lipkin, H., and Duffy, J. (1985), The elliptic polarity of screws, *ASME Journal of Mechanisms, Transmissions, and Automation in Design*, vol. 107, pp. 377-387.

McCarthy, J.M. (2000), *Geometric design of linkages,* Springer-Verlag.

Merlet, J-P. (1989), Singular configurations of parallel manipulators and Grassmann geometry, *International Journal of Robotics Research*, vol. 8, Issue 5, pp. 45-56.

Pierrot F., and Company O. (1999), H4: a new family of 4-dof parallel robots. *IEEE/ASME International Conference on Advanced Intelligent Mechatronics*, Atlanta, Georgia, USA, pp. 508-513.

Rooney, J., and Tanev, T. K. (2003), Contortion and Formation Structures in the Mappings between Robotic Jointspaces and Workspaces, *Journal of Robotic Systems*, vol. 20, No. 7, pp. 341-353.

Tanev, T.K. (1998), Forward Displacement Analysis of a Three-Legged Four-Degree-of-Freedom Parallel Manipulator, *In: Advances in Robot Kinematics: Analysis and Control*, Lenarcic J. and Husty M.L. (Eds.), Kluwer Academic Publishers, Dordrecht, pp. 147-154.

Wolf, A., Shohan, M., and Park, F.C. (2002), Investigation of singularities and self-motion of the the 3-UPU robot, *Advances in Robot Kinematics: Theory and Applications*, Lenarčič J., and Thomas, F. (eds), Kluwer Academic, Dordrecht, pp. 165-174.

Zlatanov, D., Bonev, I.A., Cosselin, C.M. (2002), Constraint singularities of parallel mechanisms, *Proc. IEEE Int. Con. Robotics and Automation,* Washington, DC, vol. 1, pp. 496-502.

A GEOMETRICAL INTERPRETATION OF 3-3 MECHANISM SINGULARITIES

Ronald Daniel
Oxford University
United Kingdom
ronald.daniel@engineering-science.oxford.ac.uk

Reg Dunlop
University of Canterbury
New Zealand
reg.dunlopr@canterbury.ac.nz

Abstract The singularities of a 6 degree of freedom Gough-Stewart 3-3 mechanism are examined by means of the Jacobian developed from applying constraints to the 9 dimensional parameter space. These parameters are based on the mechanism geometry so as to avoid the usual coordinate system based approach. The conditions that cause the determinate of the Jacobian to become zero are interpreted geometrically and clearly show the singularities of the Gough-Stewart 3-3 mechanism

Keywords: Parallel mechanism, kinematics, singularity, geometry

1. Introduction

The geometry of the structural singularities of a GS (Gough 1956, 1962; Stewart 1965) 6 DOF parallel mechanism is investigated. Consideration is restricted to the basic 3-3 structure as the 6-3 and scissor jack (Inoue et al. 1985) structures can be shown to reduce to an equivalent 3-3 structure. The intrinsic geometry of the mechanism is used to investigate the singularities that occur when mapping from SE(3) to control space which is equivalent to the 6 leg lengths (C6). This approach avoids all references to specific coordinate systems (c.f. Merlet 1988, 1990; Husty and Karger 2002) in order to avoid the algebraic difficulties that such approaches generate. It focuses only on the structural singularities arising from the platform geometry rather than from the coordinate system chosen. The objective is to derive simple geometric tests for all the singularities of the GS platform without use of rotations etc.

J. Lenarčič and B. Roth (eds.), Advances in Robot Kinematics, 285–294.

2. Singularities

Consider the 3-3 GS mechanism shown in Fig. 1. The figure shows an unshaded base triangle *a'b'c'* with adjacent prismatic legs *b'*a and *c'*a being the leg-pair that forms the shaded triangle *b'c'*a that defines a leg-plane. The plane of this leg-pair makes an angle θ_a with the base. The perpendicular from the base side *A'* to this leg-pair's apex *a* is shown as $\mathbf{r}_a$. The shaded moving platform *abc* is labelled so that opposite edges correspond to the labelling of the apexes, but are capitalised. Thus edge *A* is opposite vertex *a*. Each of the other two leg-pairs are similarly labelled but for clarity are not shown on the diagram. The choice of base triangle is arbitrary, but once chosen, the angles and lengths needed to completely define the platform are unique. Given the leg-pair triangles and the angles made with the base the platform pose is unique. There are 9 parameters defining the platform given the base, and if the moving platform size is also given, then three constraints are imposed on the 9 platform parameters.

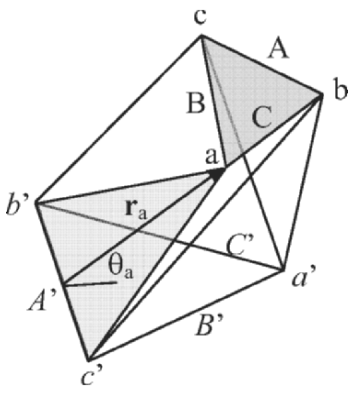

Figure 1. Intrinsic geometry of the 3-3 mechanism with platform *abc* and base *a'b'c'*.

The platform is articulated by changing the 6 leg lengths, and the three leg-pair angles with the base are defined once the leg-lengths are given. If the platform is not fully controllable at a given configuration then it is singular. If the actuators are considered to be prismatic, this singularity is equivalent to the collapse of the structure, i.e. the structure has become a mechanism in the sense used by Civil Engineers. Collapse corresponds to an instantaneous freedom in the motion of the leg-pair angles and this is possible if and only if a 3x3 Jacobian defined below is singular. This singularity corresponds to the projection from the 9 dimensional parameter space $\{l_1,l_2,l_3,l_4,l_5,l_6,\theta_a,\theta_b,\theta_c\}$ defining the platform onto the leg space $\{l_1,l_2,l_3,l_4,l_5,l_6\}$ being singular. If the platform is

articulated in some other way, such as having the angles with the base being controllable plus three other leg lengths, then the singularities of the platform are not those of structural collapse. There is thus a family of singularity surfaces (or varieties) corresponding to the methods of articulation, the member usually associated with prismatic actuated platform collapse only being a special case corresponding to pin-jointed structural collapse.

All the vectors such as $\mathbf{r}_a$ are assumed to be non-zero so that the angles made with the base are well defined. [If any leg-pair perpendicular is zero, the platform is singular i.e. the legs in the pair are collinear]. For consistency with the development below it is convenient to define the angle θ in this situation as the angle made by the platform with the collinear legs in a direction orthogonal to the legs.

The sides of the moving platform A B and C are fixed, and these define three constraint equations in the 9-dimensional parameter space defining a platform given a choice of base. The squares of these side lengths are also constrained, hence

$$\forall n : \delta^n\left(\|\mathbf{A}\|^2\right) = \delta^n\left(\|\mathbf{B}\|^2\right) = \delta^n\left(\|\mathbf{C}\|^2\right) = 0,$$

Expanding the constraints to first order yields

$$\begin{bmatrix} \dfrac{\partial\|\mathbf{A}\|^2}{\partial\boldsymbol{\theta}} & \dfrac{\partial\|\mathbf{A}\|^2}{\partial\mathbf{L}} \\ \dfrac{\partial\|\mathbf{B}\|^2}{\partial\boldsymbol{\theta}} & \dfrac{\partial\|\mathbf{B}\|^2}{\partial\mathbf{L}} \\ \dfrac{\partial\|\mathbf{C}\|^2}{\partial\boldsymbol{\theta}} & \dfrac{\partial\|\mathbf{C}\|^2}{\partial\mathbf{L}} \end{bmatrix} \begin{bmatrix} d\boldsymbol{\theta} \\ d\mathbf{L} \end{bmatrix} = \begin{bmatrix} 0 \\ 0 \\ 0 \end{bmatrix}$$

where $\mathbf{L}$ is a 6-vector of leg lengths and $\boldsymbol{\theta}$ is a 3-vector of angles. The actuation is chosen to be prismatic along the leg-pairs so that the variables $\mathbf{L}$ become control parameters which are arbitrary. The equation above can be re-written as

$$\begin{bmatrix} \dfrac{\partial\|\mathbf{A}\|^2}{\partial\boldsymbol{\theta}} \\ \dfrac{\partial\|\mathbf{B}\|^2}{\partial\boldsymbol{\theta}} \\ \dfrac{\partial\|\mathbf{C}\|^2}{\partial\boldsymbol{\theta}} \end{bmatrix} d\boldsymbol{\theta} = -\begin{bmatrix} \dfrac{\partial\|\mathbf{A}\|^2}{\partial\mathbf{L}} \\ \dfrac{\partial\|\mathbf{B}\|^2}{\partial\mathbf{L}} \\ \dfrac{\partial\|\mathbf{C}\|^2}{\partial\mathbf{L}} \end{bmatrix} d\mathbf{L}$$

The matrix expressions above are the derivatives of the projection mapping from the constraint surface in the 9-dimensional parameter

space onto the leg-plane angles and the leg-lengths respectively. Collapse of the structure corresponds to there being non-trivial solutions to the equation above for $d\mathbf{L} = 0$, i.e. if and only if the 3x3 Jacobian on the left is singular. This condition for singularity is based on the intrinsic geometry of the platform independent of choice of co-ordinates for describing the motion of the platform in SE(3), where the instantaneous freedoms of the platform are fully described by the null space of the 3x3 Jacobian between platform lengths and leg-plane angles.

3. Singularities of a Pin-jointed GS Platform

For the case of the 3-3 platform with prismatic joints, note that

$$\frac{\partial \|\mathbf{A}\|^2}{\partial \theta_a} = 0$$

$$\frac{\partial \|\mathbf{A}\|^2}{\partial \theta_b} = -2\frac{\partial \mathbf{r}_b}{\partial \theta_b} \cdot \mathbf{A}$$

$$\frac{\partial \|\mathbf{A}\|^2}{\partial \theta_c} = 2\frac{\partial \mathbf{r}_c}{\partial \theta_c} \cdot \mathbf{A}$$

This Jacobian relates changes in moving platform sides to changes in leg-plane angles and is given by

$$\mathbf{J}_{\boldsymbol{\theta}} = 2\begin{bmatrix} 0 & -\frac{\partial \mathbf{r}_b}{\partial \theta_b} \cdot \mathbf{A} & \frac{\partial \mathbf{r}_c}{\partial \theta_c} \cdot \mathbf{A} \\ \frac{\partial \mathbf{r}_a}{\partial \theta_a} \cdot \mathbf{B} & 0 & -\frac{\partial \mathbf{r}_c}{\partial \theta_c} \cdot \mathbf{B} \\ -\frac{\partial \mathbf{r}_a}{\partial \theta_a} \cdot \mathbf{C} & \frac{\partial \mathbf{r}_b}{\partial \theta_b} \cdot \mathbf{C} & 0 \end{bmatrix}$$

The condition for singularity is

$$\left(\frac{\partial \mathbf{r}_c}{\partial \theta_c} \cdot \mathbf{A}\right)\left(\frac{\partial \mathbf{r}_a}{\partial \theta_a} \cdot \mathbf{B}\right)\left(\frac{\partial \mathbf{r}_b}{\partial \theta_b} \cdot \mathbf{C}\right) - \left(\frac{\partial \mathbf{r}_b}{\partial \theta_b} \cdot \mathbf{A}\right)\left(\frac{\partial \mathbf{r}_c}{\partial \theta_c} \cdot \mathbf{B}\right)\left(\frac{\partial \mathbf{r}_a}{\partial \theta_a} \cdot \mathbf{C}\right) = 0$$

This can be rewritten as the singularity equation:

$$\left(\frac{\partial \mathbf{r}_c}{\partial \theta_c} \cdot \mathbf{A}\right)\left(\frac{\partial \mathbf{r}_a}{\partial \theta_a} \cdot \mathbf{B}\right)\left(\frac{\partial \mathbf{r}_b}{\partial \theta_b} \cdot \mathbf{C}\right) = \left(\frac{\partial \mathbf{r}_b}{\partial \theta_b} \cdot \mathbf{A}\right)\left(\frac{\partial \mathbf{r}_c}{\partial \theta_c} \cdot \mathbf{B}\right)\left(\frac{\partial \mathbf{r}_a}{\partial \theta_a} \cdot \mathbf{C}\right)$$

Singularity can be achieved by two distinct mechanisms. Either both sides of the equation are zero or they are non zero and equal. These two cases are examined separately, but in order to facilitate discussion of the various types of singularity, some geometry is first defined.

4. Tetrahedron Geometry

Consider the tetrahedron defined by the three leg-pair planes and the base. Call each surface of the tetrahedron S_a, S_b, S_c respectively, defined by the platform apex that the leg-pair is attached to i.e. S_a is defined by a and A' as shown in Fig. 1. The fourth side of the tetrahedron is the base of the GS mechanism. A line L_a parallel to the base side A' lies in the plane of the tetrahedron side S_a at a distance r_a from A' i.e. platform corner a lies somewhere along the line L_a. Similarly for lines that L_b and L_c that lie in S_b and S_c and contain the platform corners b and c respectively.

The three leg-planes S_a, S_b and S_c define a reference frame for the current configuration of the platform. Let the intersection of the three leg-planes define an 'origin' and then define three unit vectors lying along the intersections of the planes

$$\mathbf{L}_{ab} \subset S_a \cap S_b$$
$$\mathbf{L}_{bc} \subset S_b \cap S_c$$
$$\mathbf{L}_{ca} \subset S_c \cap S_a$$

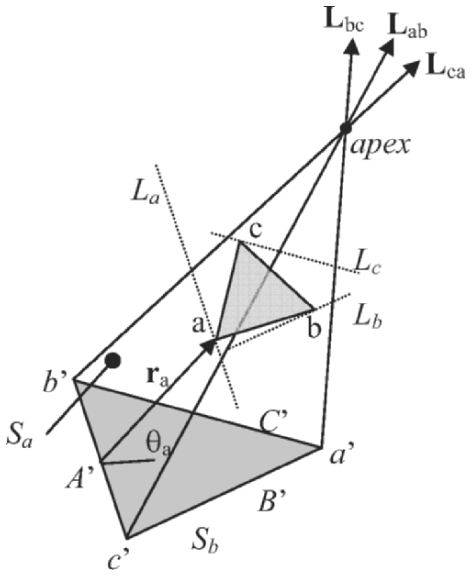

Figure 2. The tetrahedron *a'b'c'apex* is defined by the leg-planes and base. The platform corners *abc* lie in the planes S_a S_b S_c respectively that contain the sloping faces of the tetrahedron.

5. Each Side is Zero

If each side of the singularity equation is zero, then any of the three distinct terms on each side can be zero. This is expressed in tabular form on the following page. The singularities in each row arise from the same

types of platform poses and a simple re-labelling of the vertices and sides of the octahedron duplicates the results. Singularities 1, 5, and 9 are of the same type, while the others are of another type. Thus only singularities 1, 2, and 3 in the first row are discussed in detail. (Note that the possibility of **A, B,** or **C** being zero is not considered as the platform triangle would collapse to two lines.) Thus for a zero term in the singularity equation, the moving platform side must be orthogonal to the leg-plane normal, i.e. it must lie in the corresponding leg-pair plane.

Zero term	$\left(\frac{\partial \mathbf{r}_b}{\partial \theta_b} \cdot \mathbf{A}\right) = 0$	$\left(\frac{\partial \mathbf{r}_c}{\partial \theta_c} \cdot \mathbf{B}\right) = 0$	$\left(\frac{\partial \mathbf{r}_a}{\partial \theta_a} \cdot \mathbf{C}\right) = 0$
$\left(\frac{\partial \mathbf{r}_c}{\partial \theta_c} \cdot \mathbf{A}\right) = 0$	Singularity 1	Singularity 2	Singularity 3
$\left(\frac{\partial \mathbf{r}_a}{\partial \theta_a} \cdot \mathbf{B}\right) = 0$	Singularity 4	Singularity 5	Singularity 6
$\left(\frac{\partial \mathbf{r}_b}{\partial \theta_b} \cdot \mathbf{C}\right) = 0$	Singularity 7	Singularity 8	Singularity 9

5.1 Singularity 1

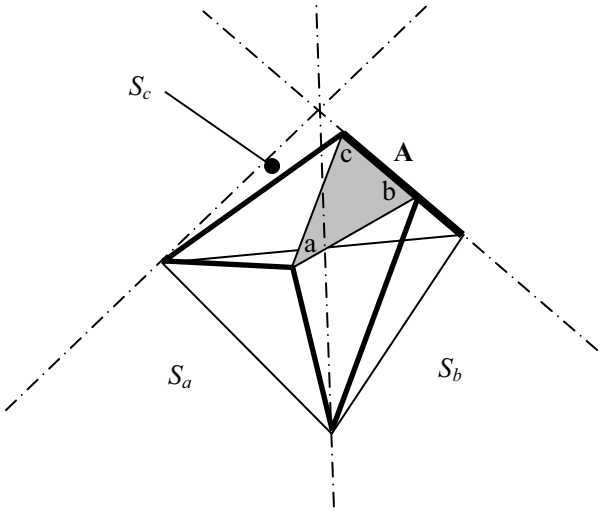

Figure 3. The tetrahedron defined by the leg-planes and the base with the prismatic legs to the moving platform shown as bold lines. The pose for a singularity of type 1 is shown with an edge of the platform aligned with an edge of the tetrahedron.

The conditions for singularity 1 are

$$\frac{\partial \mathbf{r}_c}{\partial \theta_c} \cdot \mathbf{A} = 0 \Rightarrow \mathbf{A} \subset S_c$$

$$\frac{\partial \mathbf{r}_b}{\partial \theta_b} \cdot \mathbf{A} = 0 \Rightarrow \mathbf{A} \subset S_b$$

As shown in Fig. 3 ***A*** must lie in the intersection of S_c and S_b, i.e. on the line where these planes intersect; it is shown above as an edge of the tetrahedron. NB since the edge of the tetrahedron passes along the plane that contains the moving platform, the vertex of the tetrahedron must lie in the plane of the moving platform.

5.2 Singularity 2

The conditions for singularity 2 are

$$\frac{\partial \mathbf{r}_c}{\partial \theta_c} \cdot \mathbf{A} = 0 \Rightarrow b \in S_c$$

$$\frac{\partial \mathbf{r}_c}{\partial \theta_c} \cdot \mathbf{B} = 0 \Rightarrow a \in S_c$$

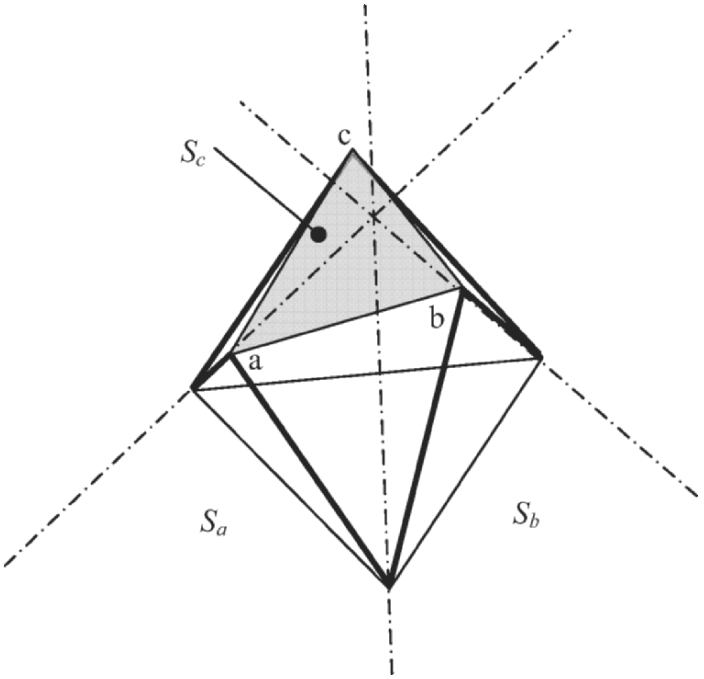

Figure 4. Platform lying in the plane of leg-pair 'c'. The pose for a singularity of type 2 is shown with the platform coplanar with a face of the tetrahedron.

By definition $c \in S_c$ so all three points in the moving platform lie in S_c as shown below. This is the 'classic' platform in the plane of a leg-pair singularity. NB since $c \in S_c$ all 3 corners of the moving platform are in S_c which also contains the vertex. Thus the vertex of the tetrahedron must lie in the plane of the moving platform.

5.3 Singularity 3

The conditions for singularity 3 are

$$\frac{\partial \mathbf{r}_c}{\partial \theta_c} \cdot \mathbf{A} = 0 \Rightarrow b \in S_c$$

$$\frac{\partial \mathbf{r}_a}{\partial \theta_a} \cdot \mathbf{C} = 0 \Rightarrow b \in S_a$$

Since $b \in S_b$ all 3 sides of the tetrahedron contain b, thus b must be at the vertex of the tetrahedron i.e. the vertex must lie in the plane of the platform.

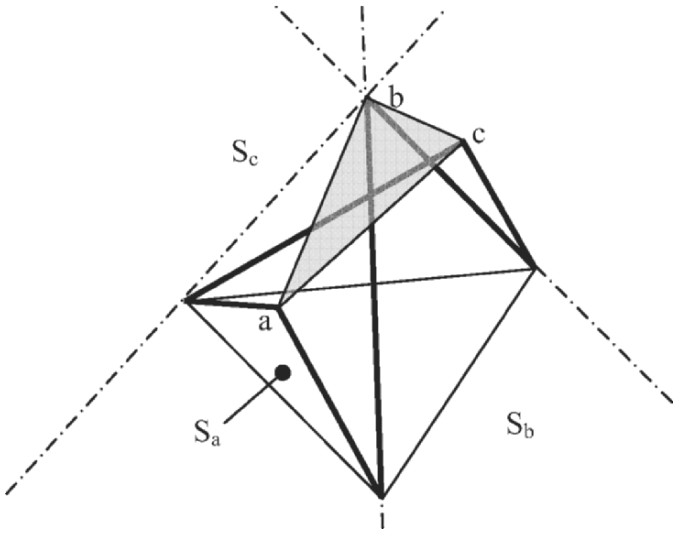

Figure 5. Platform corner b at the v ertex of the tetrahedron defined by the leg-planes. The pose for a singularity of type 3 is shown with a platform corner at the apex of the tetrahedron.

6. Each Side is Non Zero

The tabulated singularities of type 4 to 9 are of the same type as 1 to 3 with a labelling shift. However for the 10th singularity, both terms in the expansion of the determinant of the Jacobian are non-zero. The positions of the vertices of the moving platform and the sides are now

defined as using the unit vectors defined in section 4 and taking the vertex as the 'origin'. This is shown in Fig. 2.

$\mathbf{a} = \lambda_a\mathbf{L}_{ca} + \mu_a\mathbf{L}_{ab}$
$\mathbf{b} = \lambda_b\mathbf{L}_{ab} + \mu_b\mathbf{L}_{bc}$ so that the sides
$\mathbf{c} = \lambda_c\mathbf{L}_{bc} + \mu_c\mathbf{L}_{ca}$

$\mathbf{A} = \mathbf{c} - \mathbf{b} = (\lambda_c - \mu_b)\mathbf{L}_{bc} + \mu_c\mathbf{L}_{ca} - \lambda_b\mathbf{L}_{ab}$
$\mathbf{B} = \mathbf{a} - \mathbf{c} = (\lambda_a - \mu_c)\mathbf{L}_{ca} + \mu_a\mathbf{L}_{ab} - \lambda_c\mathbf{L}_{bc}$
$\mathbf{C} = \mathbf{b} - \mathbf{a} = (\lambda_b - \mu_a)\mathbf{L}_{ab} + \mu_b\mathbf{L}_{bc} - \lambda_a\mathbf{L}_{ca}$

Substituting these into the singularity equation yields $\lambda_a\lambda_b\lambda_c = -\mu_a\mu_b\mu_c$ and also $\mathbf{a}.\mathbf{b}\times\mathbf{c} = (\lambda_a\mathbf{L}_{ca} + \mu_a\mathbf{L}_{ab}).(\lambda_b\mathbf{L}_{ab} + \mu_b\mathbf{L}_{bc})\times(\lambda_c\mathbf{L}_{bc} + \mu_c\mathbf{L}_{ca}) = \mathbf{0}$, i.e. the singularity $\Rightarrow$ the position vectors **a**, **b** and **c** are coplanar hence the vertex of the tetrahedron lies in the plane of the moving platform.

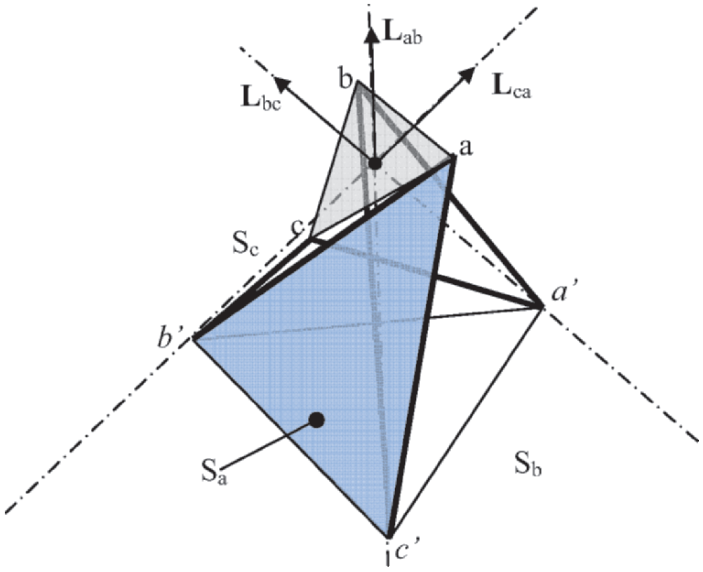

Figure 6. Platform in singular configuration 10. The vertex of the tetrahedron defined by the leg-pair planes is lying in the plane of the moving platform. The support triangle formed by leg-pair *b'a c'* is shown shaded for clarity.

Now suppose that the vertex of the tetrahedron lies in the plane of the moving platform. This implies that the position vectors **a**, **b** and **c** are coplanar. The sides of the moving platform may be expressed as the position vectors of the vertices resulting in

$$\det \mathbf{J}_\theta = \frac{\partial \mathbf{r}_c}{\partial \theta_c}\cdot(\mathbf{c}-\mathbf{b})\frac{\partial \mathbf{r}_a}{\partial \theta_a}\cdot(\mathbf{a}-\mathbf{c})\frac{\partial \mathbf{r}_b}{\partial \theta_b}\cdot(\mathbf{b}-\mathbf{a}) - \frac{\partial \mathbf{r}_b}{\partial \theta_b}\cdot(\mathbf{c}-\mathbf{b})\frac{\partial \mathbf{r}_c}{\partial \theta_c}\cdot(\mathbf{a}-\mathbf{c})\frac{\partial \mathbf{r}_a}{\partial \theta_a}\cdot(\mathbf{b}-\mathbf{a})$$

Invoking the orthogonality properties of the partial derivatives and the co-ordinate system being used yields

$$\det \mathbf{J}_\theta = -\frac{\partial \mathbf{r}_c}{\partial \theta_c} \cdot \mathbf{b} \frac{\partial \mathbf{r}_a}{\partial \theta_a} \cdot \mathbf{c} \frac{\partial \mathbf{r}_b}{\partial \theta_b} \cdot \mathbf{a} - \frac{\partial \mathbf{r}_b}{\partial \theta_b} \cdot \mathbf{c} \frac{\partial \mathbf{r}_c}{\partial \theta_c} \cdot \mathbf{a} \frac{\partial \mathbf{r}_a}{\partial \theta_a} \cdot \mathbf{b}$$

If **a**, **b** and **c** are coplanar then let $\mathbf{a} = \lambda\mathbf{b} + \mu\mathbf{c}$ and rewrite the Jacobian as

$$\boldsymbol{det}\, \boldsymbol{J}_\theta = -\frac{\partial \boldsymbol{r}_c}{\partial \theta_c} \cdot \boldsymbol{b} \frac{\partial \boldsymbol{r}_a}{\partial \theta_a} \cdot \boldsymbol{c} \frac{\partial \boldsymbol{r}_b}{\partial \theta_b} \cdot (\lambda \boldsymbol{b} + \mu \boldsymbol{c}) - \frac{\partial \boldsymbol{r}_b}{\partial \theta_b} \cdot \boldsymbol{c} \frac{\partial \boldsymbol{r}_c}{\partial \theta_c} \cdot (\lambda \boldsymbol{b} + \mu \boldsymbol{c}) \frac{\partial \boldsymbol{r}_a}{\partial \theta_a} \cdot \boldsymbol{b} = 0$$

Substituting in the original singular Jacobian for **ABC** in terms of **abc** yields $\mathbf{J_\theta = 0}$ i.e. a singular configuration.

7. Discussion and Conclusion

The three mechanisms described in section 5 that cause both terms of the determinant of the Jacobian to be zero, all have the vertex (of the tetrahedron defined by the leg pair-planes) within the plane of the moving platform. The general non-zero case discussed in section 6 also contains the 9 singularities discussed previously as special cases of the general case. Thus all 10 singularities have the platform plane containing the vertex. The conclusion is presented as a theorem:

> *The 3-3 GS platform is singular if and only if the vertex of the tetrahedron defined by the base and the three leg-planes lies in the plane of the moving platform.*

References

Gough, V. E. (1956), *Proc. Auto Div. Inst. mech. Engrs.*, pp. 392-395.

Gough, V. E. and Whitehall, S.G. (1962), Universal Tire Test Machine, *Proc. 9th Int. Technical Congress F.I.S.I.T.A*, vol. 117, pp. 117-135.

Husty, M.L. and Karger, A. (2002), Self motions of Stewart-Gough-Platforms, *Proc. Fundamental Issues and Future Research for Parallel Mechanisms and Manipulators,* (Eds), Gosselin and Ebert-Uphoff.

Inoue, H., Tsusaka, Y. and Fukuizumi, T. (1985), Parallel manipulator, *Proc. 3rd ISRR,* pp. 321-327.

Merlet, J.P. (1988), Parallel manipulators, Part 2: Theory, singular configurations and Grassmann geometry. *Research Report No. 791, Institut National de Recherche en Informatique et en Automatique, France.*

Merlet, J.P. (1990), Assembly modes and direct kinematics of parallel manipulator, *13th ISRAM.*

Stewart, D. (1965), A Platform with Six Degree of Freedom, *Proc. of the Institution of Mechanical Engineers*, vol. 180 (Part 1, 15), pp. 371-386.

Workspace and Performance

QUANTITATIVE DEXTEROUS WORKSPACE COMPARISONS

Juan A. Carretero and Geoff T. Pond
Department of Mechanical Engineering, University of New Brunswick
15 Dineen Dr., Fredericton, NB, E3B 5A3, Canada
{Juan.Carretero, Geoff.Pond}@unb.ca

Abstract Using a novel method for the formulation of Jacobian matrices, this paper will compare the dexterity of two parallel manipulators: the 3-PRS and 3-RPS. The newly obtained Jacobian matrix is square and dimensionless and its singular values have an evident physical meaning. These singular values are used to identify and compare regions of the manipulators' workspaces where either high end e ector velocities or a fine resolution over the manipulator pose may be obtained. Workspace plots for the two manipulators, corresponding to these attributes are presented and compared for arbitrarily chosen architectural parameters. The objective of the comparison is to illustrate the capability of the described method to quantitatively compare the dexterity of various complex degree of freedom manipulators.

Keywords: Parallel manipulators, Jacobian matrices, singular value decomposition, workspace, dexterity, complex degrees of freedom

1. Introduction

Studying the workspace characteristics of manipulators having either translational degrees of freedom (DOF) or rotational DOF is simplified due to the dimensional consistency within the manipulator's Jacobian matrix (*e.g.*, Tsai and Joshi, 2000). However, for manipulators having DOF in both translational and rotational directions, the conventional method of studying the workspace characteristics using the Jacobian matrix condition number is no longer possible. This is due to dimensional inconsistencies within the manipulator's Jacobian matrix.

Recently, a method has been introduced by Pond and Carretero, 2006, which produces a dimensionally homogeneous Jacobian matrix regardless of the manipulator's degrees of freedom, provided that only one type of actuator (either revolute or prismatic) is used in the manipulator architecture. This paper will further this work by quantitatively comparing the dexterity of different manipulators.

The manipulators included in this study are the 3-PRS mechanism (Carretero et al., 2000) and the 3-RPS mechanism (Lee and Shah, 1988).

J. Lenarčič and B. Roth (eds.), Advances in Robot Kinematics, 297–306.

The two mechanisms may be considered to have the same independent DOF. The resulting Jacobian matrix for both manipulators, when formulated by the method used in this paper, are the same size and are dimensionless. This will be explained further in the following section.

1.1 Jacobian Formulation

A detailed description of the method developed to obtain dimensionally homogeneous Jacobian matrices for use in dexterity analyses is described in Pond and Carretero, 2006 and therefore, only a brief introduction is provided here for completeness. The method presented therein, is a continuation of a method introduced by Gosselin, 1992, and later generalised by Kim and Ryu, 2003. This original method relates a vector containing the Cartesian velocities of three points on the end effector platform ($\dot{G}_1$, $\dot{G}_2$, and $\dot{G}_3$) to the vector $\dot{\mathbf{q}}$ of actuator velocities using $\dot{\mathbf{q}} = \mathbf{J}\dot{\mathbf{x}}$ where $\dot{\mathbf{x}} = [\dot{G}_{1_x}\ \dot{G}_{1_y}\ \dot{G}_{1_z}\ \dot{G}_{2_x}\ \dot{G}_{2_y}\ \dot{G}_{2_z}\ \dot{G}_{3_x}\ \dot{G}_{3_y}\ \dot{G}_{3_z}]^T$, $\dot{\mathbf{q}} = [\dot{b}_1\ \dot{b}_2\ \dot{b}_3]^T$ and the Jacobian matrix $\mathbf{J}$ relating the two is:

$$\mathbf{J} = \left[\frac{d\mathbf{q}}{d\mathbf{x}}\right] \tag{1}$$

This method relates actuator and end effector velocities for up to 6-DOF motion. However, use of this Jacobian's condition number or singular values in dexterity analyses may not be appropriate as at least 3 of the variables of $\dot{\mathbf{x}}$ are dependent on the remaining terms of $\dot{\mathbf{x}}$ (6 are dependent in the case of 3-DOF manipulators). Therefore the meaning of the Jacobian's singular values is unknown (Kim and Ryu, 2003).

Now consider the case of a 3-DOF manipulator such as one of those included in this study, having a translational degree of freedom perpendicular to the base platform and two rotational degrees of freedom around axes parallel to the base platform. Knowing the elevation of three points on the end effector platform relative to the base platform is sufficient to solve the inverse displacement problem (Pond and Carretero, 2006). Therefore, vector $\dot{\mathbf{x}}$ may be reduced to: $\dot{\mathbf{x}}' = [\dot{G}_{1_z}\ \dot{G}_{2_z}\ \dot{G}_{3_z}]^T$ and the general equation relating these end effector velocities to the actuator velocities is rewritten in the form $\dot{\mathbf{q}} = \mathbf{JP}\dot{\mathbf{x}}'$ where $\mathbf{P}$, which is used to map $\dot{\mathbf{x}}'$ to $\dot{\mathbf{x}}$, is expressed as:

$$\mathbf{P} = \left[\frac{d\mathbf{x}}{d\mathbf{x}'}\right] \tag{2}$$

In order to obtain the partial derivative elements of $\mathbf{P}$, constraint equations relating G_{i_z} to G_{i_x} and G_{i_y} must first be formulated. The first derivative with respect to time of these equations leads to the partial

derivative elements of **P**. In the case of the manipulators included in this comparison, where the actuated joints are all prismatic, the multiplication of **JP** yields a square, dimensionless Jacobian relating independent end effector velocities to the actuator velocities. That is,

$$\mathbf{JP} = \left[\frac{d\mathbf{q}}{d\mathbf{x}'}\right] \tag{3}$$

Therefore, the singular values of such a Jacobian matrix as **JP** in Eq. 3 have an evident physical meaning. The meaning of which is important in understanding the dexterous characteristics of the manipulator.

1.2 Dexterity Analysis

The dimensionally homogeneous matrix **JP** maps the system output $\dot{\mathbf{x}}'$ to the system input $\dot{\mathbf{q}}$. As such, useful system characteristics may be extracted from the information contained within this matrix. As explained by Pond and Carretero, 2006, the maximum and minimum singular values of **JP** correspond to the magnitude of the minimum and maximum system outputs corresponding to any unit system input. Therefore, for the case where relatively small singular values are obtained from **JP**, this corresponds to a manipulator pose where high end effector velocities may be obtained for a given set of actuator velocities. Conversely, where relatively large singular values are obtained, a finer resolution over the manipulator pose results as the system output is smaller for the same unit input.

Conventionally, the Jacobian matrix condition number is used to measure the dexterity of a particular manipulator pose. Mathematically, this is the ratio of maximum and minimum singular values. Physically, this compares the ease by which the manipulator may move in the fastest and slowest directions or whether the manipulator has similar resolution in each of the DOF. Poses where the condition number is exactly 1 are termed isotropic configurations (Angeles, 2003) and are considered ideal. Only by examination of both, the Jacobian's condition number and its singular values, can a true understanding of the workspace characteristics of a given manipulator be achieved.

2. The 3-PRS Mechanism

The 3-PRS, shown schematically in Fig. 1a consists of three identical kinematic chains. The kinematics for this manipulator have been previously presented in a variety of publications (*e.g.*, Carretero et al., 2000) and therefore only a brief review is provided here.

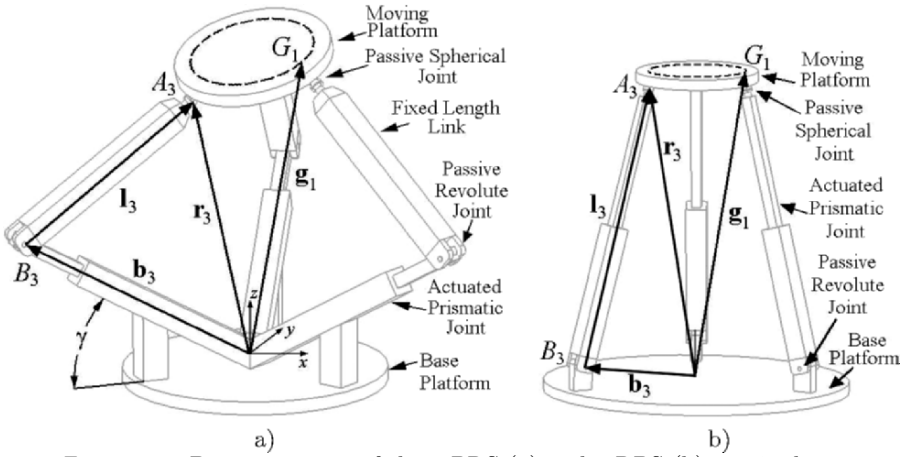

Figure 1. Basic structure of the 3-PRS (a) and 3-RPS (b) manipulators

Inverse Displacement Solution. Conventionally, the two mechanisms discussed in this paper have one translational DOF along the base frame's z-axis and two rotational DOF around the x and y axes depicted in Fig. 1a. However, as mentioned earlier, these degrees of freedom may also be modelled using the elevation of three points lying on the plane representing the moving platform (G_{1_z}, G_{2_z}, and G_{3_z}). Each of these three points is chosen as one of the two intersections of the circle concentric and coplanar with the end effector platform, with the plane defined by limb i, for $i = 1, 2, 3$. The plane defined by limb i is constrained to be perpendicular to the fixed xy plane. In order to compare between different architectures, the magnitude of the circle's radius where points G_i lie must be kept constant, and is preferably a unit circle. Constraint equations were developed in Pond and Carretero, 2006, relating G_{i_z} to G_{i_x} and G_{i_y} (for $i = 1, 2, 3$). As the derivation of these constraint equations is very involved, they will not be presented here.

As presented in Carretero et al., 2000, the displacement of the actuated prismatic joint $|\mathbf{b}_i|$ is solved by means of the vector loop representing limb i, depicted in Fig. 1a for $i = 3$. Given a platform elevation z and two angles ψ and θ around the fixed x and y axes, respectively, two solutions for this displacement are obtained by solving for the squared length of limb i as $|\mathbf{l}_i|^2 = |\mathbf{r}_i - \mathbf{b}_i|^2$.

Jacobian Formulation. As described by Pond and Carretero, 2006, any point on the plane defined by the moving platform, with respect to the base frame may be equated to a weighted sum of the three vectors $\mathbf{g}_i$ ($i = 1, 2, 3$), depicted in Fig. 1a. A point must now be identified which lies on this plane and may also be represented by a vector loop which includes the actuated prismatic joint. The logical choice is the

position of the spherical joint as this point obviously lies on the end effector plane and a vector loop including the actuated prismatic joint has already been used when solving for the actuator displacement. The vector $\mathbf{r}_i$, representing the position of the spherical joint with respect to the base frame, is equivalent to the vector sum $\mathbf{b}_i + \mathbf{l}_i$. Equating this to the weighted summation of vectors $\mathbf{g}_i$ yields:

$$\mathbf{b}_i + \mathbf{l}_i = k_{i,1}\mathbf{g}_1 + k_{i,2}\mathbf{g}_2 + k_{i,3}\mathbf{g}_3 \tag{4}$$

where the variables $k_{i,j}$ (j=1, 2, 3) are dimensionless constants and $k_{i,1} + k_{i,2} + k_{i,3} = 1$. Finally, taking the first time derivative and simplifying:

$$\mathbf{s}_{b_i}^T \mathbf{s}_{l_i} \dot{b}_i = k_{i,1}\mathbf{s}_{l_i}^T \dot{\mathbf{g}}_1 + k_{i,2}\mathbf{s}_{l_i}^T \dot{\mathbf{g}}_2 + k_{i,3}\mathbf{s}_{l_i}^T \dot{\mathbf{g}}_3 \tag{5}$$

where $\mathbf{s}_{b_i}$ and $\mathbf{s}_{l_i}$ are unit vectors in the directions of $\mathbf{b}_i$ and $\mathbf{l}_i$, respectively. The dimensionless constants $k_{i,j}$ are solved using Eq. 4. Equation 5 may be written three times corresponding to each of the three limbs to formulate the manipulator Jacobians:

$$\mathbf{J}_q \dot{\mathbf{q}} = \mathbf{J}_x \dot{\mathbf{x}} \tag{6}$$

where $\dot{\mathbf{x}}_{9\times1} = \begin{bmatrix} \dot{\mathbf{g}}_1^T & \dot{\mathbf{g}}_2^T & \dot{\mathbf{g}}_3^T \end{bmatrix}^T$, $\dot{\mathbf{q}}_{3\times1} = \begin{bmatrix} \dot{b}_1 & \dot{b}_2 & \dot{b}_3 \end{bmatrix}^T$ and

$$\mathbf{J}_q = \begin{bmatrix} \mathbf{s}_{b_1}^T \mathbf{s}_{l_1} & 0 & 0 \\ 0 & \mathbf{s}_{b_2}^T \mathbf{s}_{l_2} & 0 \\ 0 & 0 & \mathbf{s}_{b_3}^T \mathbf{s}_{l_3} \end{bmatrix}_{3\times3} \qquad \mathbf{J}_x = \begin{bmatrix} k_{1,1}\mathbf{s}_{l_1}^T & \mathbf{0} & \mathbf{0} \\ \mathbf{0} & k_{2,2}\mathbf{s}_{l_2}^T & \mathbf{0} \\ \mathbf{0} & \mathbf{0} & k_{3,3}\mathbf{s}_{l_3}^T \end{bmatrix}_{3\times9}$$

The Jacobian matrix, $\mathbf{J}$ in Eq. 1 is produced by multiplying $\mathbf{J}_x$ and $\mathbf{J}_q$, *i.e.,* $\mathbf{J} = \mathbf{J}_q^{-1}\mathbf{J}_x$. By taking the first time derivative of equations constituting the inverse displacement solution discussed in Section 2, the constraining matrix $\mathbf{P}$ in Eq. 2 is formulated. Finally, multiplication of the Jacobian $\mathbf{J}$ with the constraining matrix $\mathbf{P}$ produces the constrained, dimensionally homogeneous, square Jacobian $\mathbf{JP}$ in Eq. 3.

3. The 3-R<u>P</u>S Mechanism

The 3-R<u>P</u>S mechanism depicted in Fig. 1b has been previously studied in a variety of publications (*e.g.*, Lee and Shah, 1988).

Inverse Displacement Solution. Similarly to the 3-<u>P</u>RS Mechanism, the limbs of the 3-R<u>P</u>S Mechanism are also confined to move on a single plane. As such, the constraint equations relating the designated independent degrees of freedom (G_{1_z}, G_{2_z}, and G_{3_z}) to the dependent degrees of freedom (G_{i_x} and G_{i_y} for $i = 1, 2, 3$) are the same. The only

difference from the inverse displacement solution of the 3-PRS mechanism is in the final step where $\mathbf{l}_i = \mathbf{r}_i - \mathbf{b}_i$ is used to solve for the displacement of the actuated prismatic joint i, that is $|\mathbf{l}_i|$.

Jacobian Formulation. Due to similarity in the constraint equations for the 3-PRS and 3-RPS mechanisms, the development of the dimensionally homogeneous Jacobian $\mathbf{J}$ is also very similar. Consider Eq. 4 again. The vector $\mathbf{b}_i$ is a known constant in the architecture of the 3-RPS mechanism whereas the magnitude of vector $\mathbf{l}_i$ is now a variable. Taking the first time derivative of Eq. 4 yields:

$$\dot{l}_i = k_{i,1}\mathbf{s}_{l_i}^T\dot{\mathbf{g}}_1 + k_{i,2}\mathbf{s}_{l_i}^T\dot{\mathbf{g}}_2 + k_{i,3}\mathbf{s}_{l_i}^T\dot{\mathbf{g}}_3 \tag{7}$$

Writing Eq. 7 three times (once for each limb) to formulate the inverse and direct Jacobian matrices, as in Eq. 6, yields $\mathbf{J}_q = \mathbf{I}_{3\times3}$ and

$$\mathbf{J}_x = \begin{bmatrix} k_{1,1}\mathbf{s}_{l_1}^T & \mathbf{0} & \mathbf{0} \\ \mathbf{0} & k_{2,2}\mathbf{s}_{l_2}^T & \mathbf{0} \\ \mathbf{0} & \mathbf{0} & k_{3,3}\mathbf{s}_{l_3}^T \end{bmatrix}_{3\times9} \tag{8}$$

The Jacobian matrix $\mathbf{J}$ is obtained by the multiplication $\mathbf{J}_q^{-1}\mathbf{J}_x$. As previously mentioned, the constraint equations relating G_{1_z}, G_{2_z}, and G_{3_z} to G_{i_x} and G_{i_y} $(i = 1, 2, 3)$ are the same as those developed for the 3-PRS manipulator and therefore matrix $\mathbf{P}$ is identical. The resulting matrix $\mathbf{JP}$ is, again, square and dimensionally homogeneous.

4. Dexterous Workspace Comparison

The reachable workspace is defined here as all poses attainable by a manipulator without forcing it to transit a singular configuration when travelling from its datum position (explained later in this section). Before determining the reachable or dexterous workspaces, an understanding of the manipulator singular configurations must first be obtained.

Inverse singular configurations typically correspond to the absolute boundary of the reachable workspace, beyond which, poses are unattainable by the manipulator. Therefore, these singular configurations do not further limit the reachable workspace volume as defined in this paper. Direct singular configurations on the other hand, may exist inside the reachable workspace. In this work, only poses attainable without forcing the manipulator to transit a direct singular configuration, or toggle point, are included as part of the reachable workspace.

The 3-RPS and 3-PRS mechanisms share the same direct singular configuration where the vector $\mathbf{l}_i$ is parallel to the plane defined by points A_i.

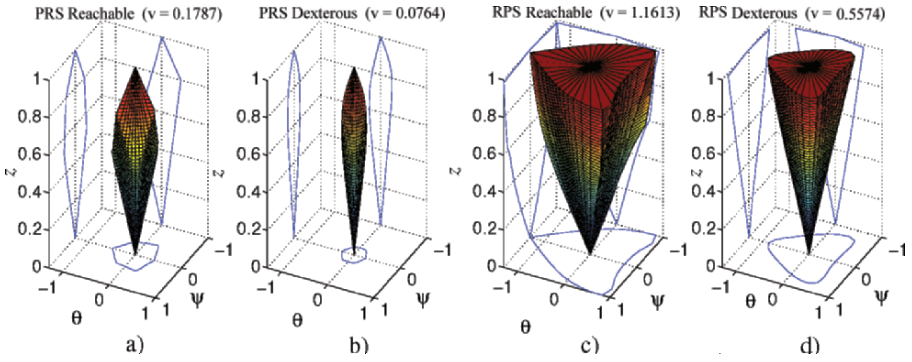

Figure 2. Reachable and Dexterous workspace for the 3-PRS (a and b) and the 3-RPS (c and d). Note θ and ψ are in radians, $r_p = 0.6$, for the 3-PRS: $\gamma = 0^{\circ}$ and $|\mathbf{l}_i| = 1$ and for the 3-RPS: $|\mathbf{b}_i| = 1$. Dexterous workspace boundary at $cond_{\max} = 6$.

At this pose, the manipulator gains the ability to toggle about the spherical joint A_i. For the 3-PRS and 3-RPS manipulators, when all three of the limbs are parallel with this plane, the end effector is at the minimum permissible elevation along the z-axis here referred to as the datum position. The 3-PRS has a second family of singular configurations which occur when one or more of the fixed-length links become perpendicular to the direction of their respective actuated prismatic joint.

4.1 Dexterity Measured by the Jacobian Condition Number

As the condition number of the Jacobian matrix is infinity at a singular pose, it is expected that dexterity decreases as the manipulator approaches a singular configuration. Both the reachable and dexterous workspaces for the 3-PRS mechanism are depicted in Figs. 2 a and b. The bottom apex of Fig. 2a corresponds to the direct singular configuration discussed earlier at $z = 0$. The dexterous workspace depicted in Fig. 2b is a subset of the reachable workspace. As the maximum permissible limit on the Jacobian condition number is reduced (not shown), the cross sectional area of the dexterous workspace continues to be reduced. The workspace will however, continue to exist throughout the entire range $0 \leq z \leq 1$. This tendency confirms that the manipulator is at isotropic conditions whenever the moving platform is perfectly parallel to the base platform where the **JP** is a scaled identity matrix.

Theoretically, the reachable workspace of the 3-RPS mechanism extends to a z-elevation of infinity. However, in order to provide a meaningful comparison to the 3-PRS mechanism, the range of z-elevations will be restricted to $0 \leq z \leq 1$. This limited workspace is depicted in Fig. 2. As the 3-RPS mechanism also experiences the toggle point at $z = 0$, the restricted range does not further limit the workspace on the lower

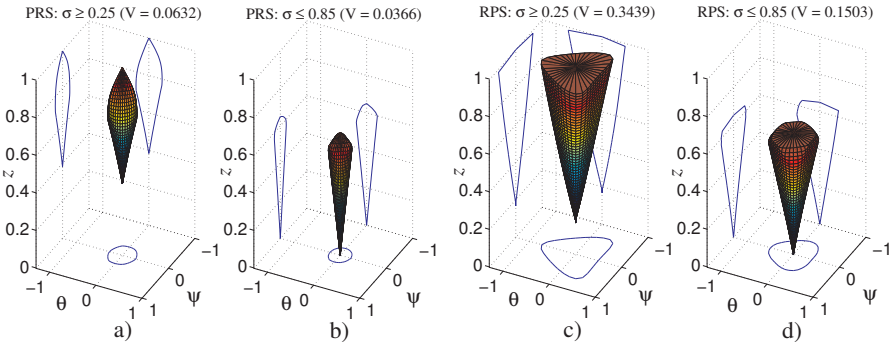

Figure 3. Regions of the workspace corresponding to high end effector velocities and fine resolution over the manipulator pose for the 3-PRS (a and b, respectively) and the 3-RPS (c and d, respectively). Angles θ and ψ are in radians.

boundary. Only the highest z-elevation is being imposed, which artificially limits the range of both the reachable and dexterous workspaces. Otherwise, the cross sectional area of the workspace would monotonically expand until, at $z = \infty$, the manipulator would be capable of 90° rotations around both the x and y axes (angles ψ and θ, respectively).

It should be noted that neither of these two architectures has been optimised. That is, the values chosen for architectural parameters such as the base and end effector platform radii, and the magnitude of the fixed length link have not been optimised to provide the largest possible workspace volume. The objective here is only to illustrate the ability of this method to compare the dexterity of various architectures, not to suggest any single architecture is in any way superior to others.

4.2 Dexterity Measured by both the Jacobian Condition Number and Singular Values

One of the greatest advantages of the comparison method presented in this paper is the ability to identify regions of the manipulator's workspace where either high end effector velocities may be achieved, or where a fine resolution over the manipulator pose exists. Depending on the application, either or both of these attributes may be highly desired. In the previous section, the condition that $cond(\mathbf{J}) \leq 6$ was arbitrarily chosen to determine the dexterous workspace. In this section, the dexterous workspace plots are further reduced by constraining the singular values of the Jacobian matrix to be within a defined range. In this way, regions of the workspace corresponding to either high end effector velocities, or fine resolution over the manipulator pose, are determined.

For the dexterous workspace of the 3-PRS manipulator, depicted in Fig. 2b, Jacobian matrix singular values vary within the range $0.003 \leq$

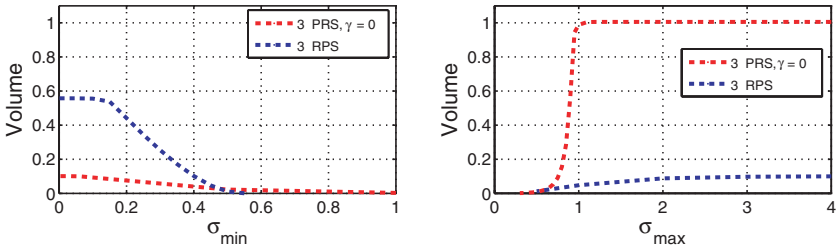

Figure 4. Workspace volume as a function of a minimum (left) and maximum (right) permissible singular values.

$\sigma \leq 15.565$. Figure 3a is produced by restricting the Jacobian condition number to be less than or equal to 6, and restricting all Jacobian matrix singular values to be greater than or equal to 0.25. That is, for a system output where $|\dot{\mathbf{x}}| = 1$, only poses where the magnitude of the vector $\dot{\mathbf{q}}$ is greater than 0.25, are allowed. Therefore, the workspace is restricted to poses where a minimum resolution over the end effector pose is allowed.

Similarly, Fig. 3b is produced by restricting the Jacobian matrix condition number to be less than or equal to 6, but in this case, only singular values less than or equal to 0.85 are allowed. In this manner, the workspace is restricted to poses where the of the vector $\dot{\mathbf{q}}$ is restricted to be less than 0.85, for any unit system output or, $|\dot{\mathbf{x}}| = 1$. Intuitively, this is not in the same region of the reachable workspace as poses were a fine resolution is obtained. Figures 3a and 3b confirm this as these two regions are at opposite ends of the workspace.

Similar limits on the 3-RPS manipulator were used to obtain Figs. 3c and 3d. Figure 3c shows that the 3-RPS has lost a relatively small volume by restricting the Jacobian matrix singular values to be less than or equal to 0.25. This should not be surprising as the permissible range $0 \leq \sigma \leq 0.85$ is a large portion of the overall range $0.0007 \leq \sigma \leq 1.0526$ observed when obtaining Fig. 2d.

The left portion of Fig. 4 compares the two manipulators' workspace volume as a function of the minimum permissible singular value. As this value is increased, an increasingly heavier emphasis is placed on high end effector velocities. Naturally then, as the $\sigma_{\min}$ is increased, a greater restriction is placed on the workspace and the workspace volume continues to decrease in magnitude. The 3-PRS mechanism experiences a much more gradual reduction in workspace volume as the minimum permissible singular value is decreased. This demonstrates its ability to achieve a high degree of accuracy throughout a relatively large portion of its workspace as compared to the 3-RPS.

Similarly, a gradual increase in the workspace volume is experienced by the 3-PRS mechanism as the maximum permissible singular value is increased, when compared to the 3-RPS (see the right portion of

Fig. 4). It is observed that, as $\sigma_{\max}$ is decreased, the workspace size is further restricted by a continuously heavier emphasis on the accuracy of the manipulator. It should be noted that the significantly smaller dexterous workspace volume of the 3-PRS manipulator is due in part, to the considerably wider range of singular values within the manipulator's reachable workspace when compared to the 3-RPS manipulator.

5. Conclusions

The method for developing dimensionally homogeneous square Jacobians **JP** has proven successful in comparing the dexterity of multiple parallel architectures. This method is suitable for comparing manipulators having the same number and type of actuators and also having the same independent degrees of freedom.

For illustration purposes, the 3-PRS and 3-RPS manipulators were compared using an arbitrary set of architectural parameters for each manipulator. Of the two, the 3-PRS manipulator was found to have the largest workspace if a high level of accuracy is required and the 3-RPS manipulator was found to have the largest workspace if high end effector velocities are required. Following optimisation, any of the manipulators may be the best candidate depending on the designer's desired compromise between the two characteristics.

Having identified a desired compromise between accuracy and velocity characteristics, the robot designer may use this method to optimise and compare a variety of manipulators in order to select the optimal architecture and architectural variables, for a specific application.

References

Angeles, J. (2003), *Fundamentals of Robotic Mechanical Systems*, Springer-Verlag.

Carretero, J.A., Podhorodeski, R.P., Nahon, M.A., and Gosselin, C.M. (2000), Kinematic analysis and optimization of a new three degree-of-freedom spatial parallel manipulator, *Journal of Mechanical Design*, vol. 122, No. 1, pp. 17-24.

Gosselin, C.M. (1992), The optimum design of robotic manipulators using dexterity indices, *Journal of Robotics and Autonomous Systems*, vol. 9, No. 4, pp. 213-226.

Kim, S.G., and Ryu, J. (2003), New dimensionally homogeneous Jacobian matrix formulation by three end-effector points for optimal design of parallel manipulators, *IEEE Transactions on Robotics and Automation*, vol. 19, No. 4, pp. 731-737.

Lee, K., and Shah, D. (1988), Kinematic analysis of a three-degrees-of-freedom in-parallel actuated manipulator, *IEEE Journal of Robotics and Automation*, vol. 4, No. 3, pp. 354-360.

Pond, G., and Carretero, J.A. (2006), Formulating Jacobian matrices for the dexterity analysis of parallel manipulators, To appear in *Mechanism and Machine Theory*.

Tsai, L.W., and Joshi, S. (2000), Kinematics and optimization of a spatial 3-UPU parallel manipulator, *Journal of Mechanical Design*, vol. 122, No. 4, pp. 439-446.

LEVEL-SET METHOD FOR WORKSPACE ANALYSIS OF SERIAL MANIPULATORS

Erika Ottaviano*, Manfred Husty** and Marco Ceccarelli*

* *LARM: Laboratory of Robotics and Mechatronics – DiMSAT – University of Cassino*
Via Di Biasio 43 - 03043 Cassino (Fr), Italy
{ ottaviano,ceccarelli }@unicas.it

** *Institute for Engineering Mathematics Geometry and Computer Science*
University of Innsbruck, Technikerstr. 13 A-6020 Innsbruck, Austria
manfred.husty@uibk.ac.at

Abstract This paper presents an application of the level-set method for workspace analysis of 3R manipulators. A formulation is presented and it allows to determine different topologies of manipulators as function of workspace manifolds. Numerical examples are presented to show the effects of kinematic parameters on workspace.

Keywords: Kinematics, Serial Manipulators, Level-Set Method, Workspace Analysis

1. Introduction

Serial manipulators are still the most used robots for industrial applications. This is due to their kinematic properties and construction features that aim to obtain suitable systems for industrial applications.

Since most of the industrial manipulators are wrist-partitioned, the workspace analysis of such manipulators can be performed by considering the positioning and orienting singularities separately. Early studies on serial manipulators were performed by (Roth 1975; Freudenstein and Primrose 1984; Parenti-Castelli and Innocenti 1988; Ceccarelli 1989; Smith and Lipkin 1993). Several authors have grouped manipulators into classes (Burdick 1985; Zein et al., 2005; Wenger 2000), but they have just considered special architectures, such as cuspidal or orthogonal structures, which have simplification in the architecture. In this paper we present a classification of a general 3R manipulator as based on kinematic properties, but not only on parameter simplification. As a completely new method we discuss the level-set belonging to the two-parameter set of curves, which constitutes the cross section of the workspace of the manipulator. The level-set surface directly linked to the level-set provides new and surprising insight in the internal structure of the workspace.

J. Lenarčič and B. Roth (eds.), Advances in Robot Kinematics, 307–314.

2. Level-Set Analysis for the Workspace of a General 3R Manipulator

The kinematic parameters of a general 3R manipulator are denoted according to the Hartenberg and Denavit (H-D) notation. Without loss of generality the base frame is assumed to be coincident with $X_1Y_1Z_1$ frame, which is fixed on first link when $\theta_1 = 0$, $a_0 = 0$ and $d_1 = 0$. A general 3R manipulator is described by the H-D parameters a_1, a_2, d_2, d_3, α_1 and α_2, and θ_i, for (i = 1,…,3). The end-effector point H is placed on the X_3 axis at a distance a_3 from O_3. The position $\mathbf{H}_0$ with respect to reference frame $X_0Y_0Z_0$ can be expressed as function of $\mathbf{H}_3$ vector in the classical form

$$\mathbf{H}_0 = T_0^1 \; T_1^2 \; T_2^3 \; \mathbf{H}_3 . \tag{1}$$

The workspace of a general 3R manipulator can be expressed in the form of radial and axial reaches r and z respectively. In particular, r is the radial distance of the operating point from Z_1-axis and z is the axial reach; both can be expressed as function of H-D parameters (Ceccarelli 1996). In fact, r and z can be evaluated as

$$r^2 = \left(H_0^x\right)^2 + \left(H_0^y\right)^2 = \left(H_1^x c\theta_1 - H_1^y s\theta_1\right)^2 + \left(H_1^x s\theta_1 + H_1^y c\theta_1\right)^2 \qquad z = H_0^z . \tag{2}$$

Equation (2) represents a 2-parameter family of curves, which gives the cross-section workspace in a cross-section plane (Freudenstein and Primrose 1984; Ceccarelli 1989). In the following this two-parameter set is interpreted as a level-set (Sethian 1996). The level-set of a differentiable function $f : \Re^n \to \Re$ corresponding to a real value "c" is the set of points

$$\left\{ (x_1, \ldots, x_n) \in \Re^n : f(x_1, \ldots, x_n) = c \right\}. \tag{3}$$

The potentiality of the level-set method is now applied to the workspace analysis of 3R manipulators. In particular, the level-set reconstruction for a serial manipulator can be obtained by using the 2-parameter-family of curves in Eq. (2). The level-sets belonging to constant values of θ_3 are curves in the rz-plane. Therefore this one parameter set of curves can be viewed as the contour map of a surface S, which conveniently can be used to analyze the workspace of the manipulator. The surface S is defined via the functions

$$X^2 = r^2 ; \quad Y = z \; ; \; Z = \tan\left(\frac{\theta_3}{2}\right). \tag{4}$$

By performing the half-tangent substitution $v = \tan(\theta_2/2)$ in Eq. (4) and eliminating the v parameter one can obtain an implicit equation of the surface S.

$$S: \; F(X, Y, Z) = 0 . \tag{5}$$

Equation (5) describes an algebraic surface which is of degree 20. It splits into two parts

$$F(X,Y,Z) = S_1(X,Y,Z)\ S_2(X,Y,Z) = 0\,. \tag{6}$$

S_1 represents four double planes parallel to XY plane, in which the height depends on the H-D parameters.

S_2 is the graph of the level-set function. The parameter lines on this surface belong to θ_2 = const or θ_3 = const. Geometrically S is generated by taking a cross-section of the workspace that is parameterized by θ_2 and θ_3 and explode the overlapping level-set curves in the direction of the Z-axis. The major advantage of this procedure is that on S one can see clearly the number of solutions of the Inverse Kinematics (IK).

In Fig. 1 this is shown for a general design. In Fig. 1a) the level-set curves are shown. It should be noted that in the displayed cross-section of the workspace in fact two different one-parameter sets of level-curves are displayed. The blue one belongs to θ_3 = const and the grey one belongs to θ_2 = const. In the following we only discuss the blue set of curves. A discussion of the other set would lead to similar results. On Fig. 1b) the corresponding surface S is displayed. Geometrically the level-set curves of Fig. 1a) are the orthogonal projections of the intersection curves with planes Z = const and the surface S onto the XY-plane. The blue level-set curves in Fig. 1a) are therefore a contour map of the surface S. Additionally we have displayed in Fig. 1b) a line parallel to the Z-axis. This line shows clearly four intersection points with the surface S. Therefore, the corresponding point in the level-set plane in Fig. 1a) corresponds to a four fold solution of the IK.

On the surface S_2 the θ_3 curves keep their closed curve nature and θ_2 ones are taken apart. In order to determine the algebraic degree of S_2 one has to homogenize and intersect with the plane at infinity. The resulting intersection is completely independent by the H-D parameters. It consists of a eight fold line Z = 0 and two complex double lines. Thus, the surface is of algebraic degree 12.

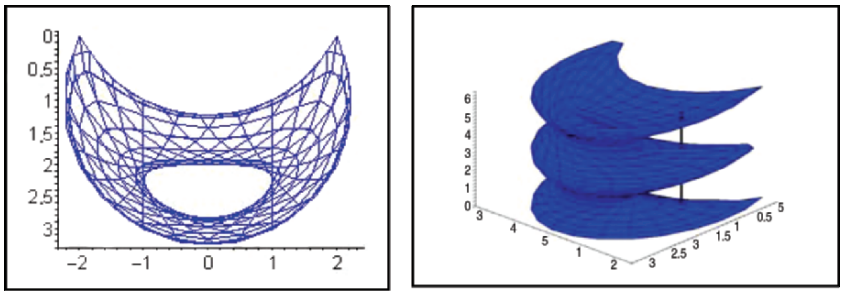

a) b)

Figure 1. A numerical example for a general 3R manipulator: a) workspace cross-section; b) corresponding S surface.

Manipulators having singularities on the surface S can be considered as an algebraically closed set. Indeed, a small perturbation on H-D parameters will change the behaviour of the manipulator. Singularities of the surface S can be found by considering the implicit equation of S, together with its partial derivatives with respect to X, Y, and Z, respectively (Gibson 1998). All these four functions have to vanish for a point on the surface being singular. Singular conditions can be expressed as functions of H-D dimensional parameters. There is an important observation that can be made. Considering just the one parameter set of level-set curves in the plane of parameters rz, one can observe singular points on the envelop curve of the set. These singular points have been discussed in the literature quite a lot. By considering a formulation for the cross-section workspace boundary of 3R manipulators as proposed in (Ottaviano et al., 2004) it is possible to determine the singularities on the inner boundary curve, which is a part of the enveloping curve. These singularities can be either double points or acnodes or cusps of the cross-section boundary curve (Ottaviano et al., 1999). The graph S of the level-set function reveals a very different nature of these highly interesting singular points. Some of them arise just from the projection of S into the level-set plane and some of them come from singularities of the surface S.

In this paper we have focused our analysis on 3R manipulators, and a classification can be obtained by looking at the singular configurations of S as function of H-D parameters. In order to determine the singularities of the surface S the two parts S_1 and S_2 are analyzed separately.
In particular, S_1 can be expressed in the form

$$S_1 = k_4 Z^4 + k_3 Z^3 + k_2 Z^2 + k_1 Z + k_0 . \tag{7}$$

where the coefficients k_i depend on H-D dimensional parameters. They can be expressed in the form

$$\begin{aligned} &k_4 = d_3^2 \sin^2(\alpha_2) + (a_3 - a_2)^2 ; \quad k_3 = 4 a_3 d_3 \sin(\alpha_2)\cos(\alpha_2) \\ &k_2 = 2\left[d_3^2 \sin^2(\alpha_2) + a_2^2 + a_3^2\left(2\cos^2(\alpha_2) - 1\right)\right] \\ &k_1 = k_3 ; \quad k_0 = d_3^2 \sin^2(\alpha_2) + (a_3 + a_2)^2 . \end{aligned} \tag{8}$$

In general $S_1 = 0$ can have real solutions. According to Decartes rule of signs a necessary and sufficient condition for having real solutions is iff there are changes in the signs of coefficients k_i. In particular, the number of real roots is equal to the number of changes of sign in the k_i coefficients. Other singularities can be found by analyzing surface S_2. Zeros of the set of equations $S_2 = 0$; $S_{2X} = 0$; $S_{2Y} = 0$; and $S_{2Z} = 0$, yield the geometric singularities of the surface S_2. Singularities of S_2 surface can be can expressed by the product of three polynomials in the form

$$\begin{aligned} &P_1 = d_3^2 \sin^2(\alpha_2) + (a_3 - a_2)^2 ; \quad P_2 = c_4 \cos^4(\alpha_2) + c_2 \cos^2(\alpha_2) + c_0 \\ &P_3 = d_3^2 \sin^2(\alpha_2) + \left(a_3^2 - a_2\right)^2 \cos^2(\alpha_2) . \end{aligned} \tag{9}$$

in which c_i coefficients are given by

$$c_4 = \left(d_3^2 + a_3^2\right)^2 \; ; \qquad c_2 = -2\left[\left(a_3^2 + d_3^2\right)^2 + a_2^2\left(d_3^2 - a_3^2\right)\right]$$
$$c_0 = \left(\left(a_2 + a_3\right)^2 + d_3^2\right)\left(\left(a_2 - a_3\right)^2 + d_3^2\right). \tag{10}$$

3. A Classification of the 3R Manipulators

A classification of 3R manipulator designs can be obtained by considering groups of manipulators having similar kinematic properties of surface S and workspace boundary. According to the proposed formulation, a classification into three groups is proposed as based on kinematic properties of 3R manipulators with general architecture.

3.1 Class A: General Manipulator

A manipulator that belongs to the Class A has no (real) singularities on the surface S. It may have either a changing posture behaviour or it can present a void within the workspace. A characteristic shape with corresponding cross-section figures are reported in the examples of Figs. 2 and 3. Such general manipulator is characterized to have no singularities on the level-set surface. In addition, it has been observed that cuspidality behaviour is not strictly related to special designs.

3.2 Class B: Manipulator with a Singularity on the Surface S

A manipulator that belongs to the Class B has only one singularity on the surface S. It is characterized by having $a_2 = a_3$; $d_3 = 0$ and $\alpha_2 = \pi/2$. Class B manipulators are characterized by the presence of 4-solution regions for the IK. By considering Eq. (9) P_1 and P_2 polynomials vanish. S_1 degenerates into an expression, which is independent by Z. They present a void iff the projections of the singularity of the surface S belongs to the workspace boundary too. If $a_2 \leq a_3$, the operation point can meet the second joint axis whenever $\theta_3 = \pm \arccos(-a_2/a_3)$. A characteristic shape with corresponding cross-sections are reported in the examples of Figs. 4 and 5.

3.3 Class C: Manipulator with Two Singularities on the Surface S

This class of manipulators is characterized by having two singularities on the surface S, which can be analyzed by considering Eqs.(9). Class C manipulators have $P_3 = 0$ and $a_3 > a_2$; $d_3 = 0$ and $\alpha_2 = \pi/2$. S_1 degenerates into an expression that contains only even powers of Z. Class C

manipulators have in general a 4-solution region for the IK and they have a void iff the projections of the singularities of the surface belong to the workspace boundary too. In the two singularities point H meets the second joint axis and the manipulator has infinite IK solutions. A characteristic shape with corresponding cross-sections are reported in the examples of Figs. 6 and 7.

4. Numerical Examples

Numerical examples show different topologies of the 3R manipulators. Figures 2 to 7 show manipulators belonging to the three classes.

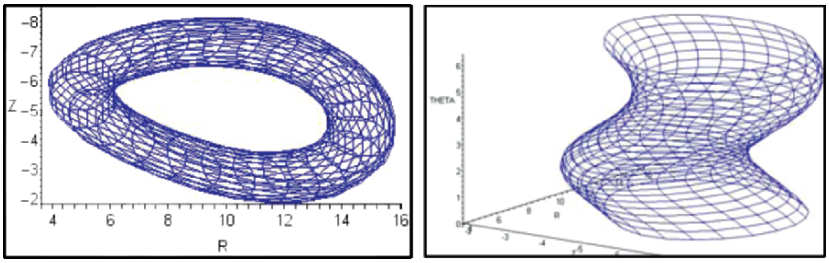

Figure 2. A numerical example for Case A with void, a_1=4.68; α_1=2.90; a_2=9.78, a_3 =1.15; d_2=4.48; α_2= 0.938, d_3=1.38: a) workspace cross-section; b) surface S. (u is unit lenght and angles are in radians).

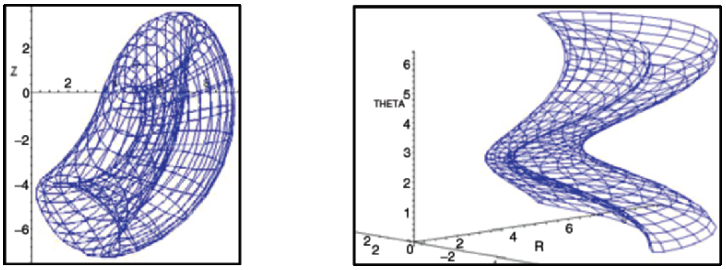

Figure 3. A numerical example for Case A without void, a_1=1.24; α_1=2.41; a_2 =5.58, a_3 =2.12; d_2=2.22; α_2=0.588, d_3=0.307: a) workspace cross-section; b) surface S (u is unit lenght and angles are in radians).

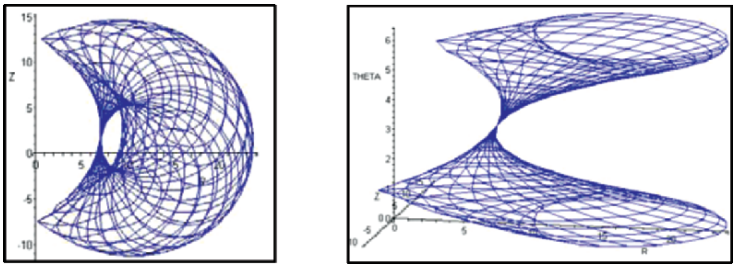

Figure 4. A numerical example for Case B with void, a_1=6.98; α_1=0.596; a_2 = a_3 =8.33; d_2=2.07; α_2=π/2, d_3 =0: a) workspace cross-section; b) surface S.

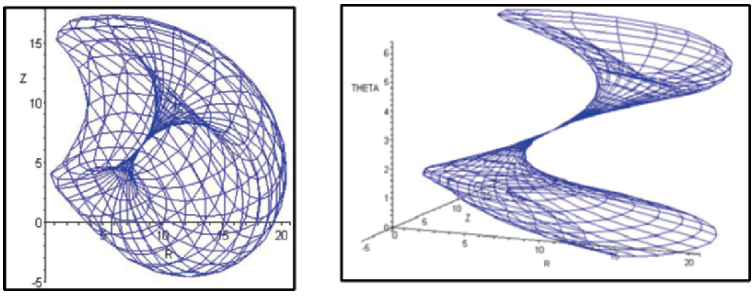

Figure 5. A numerical example for Case B without void, a_1=5.32; α_1=0.777; a_2= a_3=6.46; d_2=8.99; α_2=π/2,d_3=0: a) workspace cross-section; b) surface S (u is unit lenght and angles are in radians).

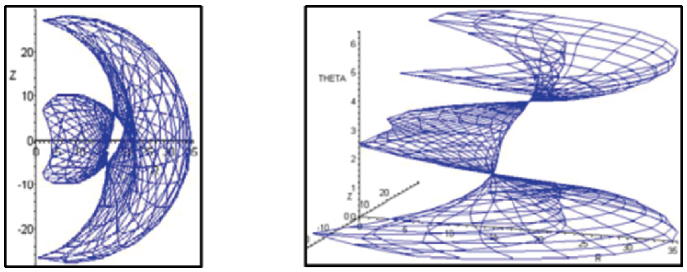

Figure 6. A numerical example for Case C with void, a_1=6.23; α_1=1.23; a_2=9.47, a_3=19.13; d_2=0.973; α=$_2\pi$/2,d_3=0: a) workspace cross-section; b) surface S. (u is unit lenght and angles are in radians).

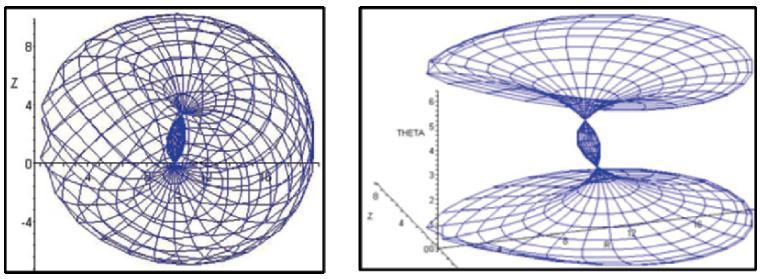

Figure 7. A numerical example for Case C without void, a_1=9.87; α_1 =0.852; a_2 =4.36, a_3 =4.99; d_2=1.84; α_2=π/2,d_3 =0: a) workspace cross-section; b) surface S. (u is unit lenght and angles are in radians).

4. Conclusions

This paper presents a novel analysis of the workspace of serial manipulators as based on the level-set reconstruction of the workspace. The method produces useful information for characterization of the workspace in Cartesian Space in terms of void existence. It has been found that the analysis of the cusps and double points on the cross-section boundary curve is not sufficient to determine the kinematic

characteristics of a manipulator. Singularities on the graph S of the level-set are singular configurations in which there is a value of θ_3 angle for which the manipulator encounters a singularity. In order to obtain complete information on the singularities of the workspace, one has to detect the presence of a void by considering the surface S, together with the analysis of the singularities of the cross-section boundary curve. A necessary condition to avoid a void is that the surface contains S singular points. They can be either double points and acnodes (hermit points) for the cross-section boundary curve. The presence of a void can be detected by considering the surface S and the cross-section boundary curve. If the surface S has no singularities and the cross-section boundary curve has double points then the manipulator has a void.

References

Burdick, J.W. (1995), A Classification of 3R Regional Manipulator Singularities and Geometries, *Mech. and Machine Theory*, vol. 30, no.1, pp. 71-89.

Ceccarelli M. (1989), On the Workspace of 3R Robot Arms, *Proc. 5th IFToMM Int. Symp. on Theory and Practice of Mechanism*, Bucharest, vol. II-1, pp. 37-46.

Ceccarelli M. (1996), A Formulation for the Workspace Boundary of General N-Revolute Manipulators, *Mech. and Machine Theory*, vol. 31, no. 5, pp. 637-646.

Freudenstein F., Primrose E.J.F. (1984), On the Analysis and Synthesis of the Workspace of a Three-Link, Turning-Pair Connected Robot Arm, *ASME Jnl of Mech., Transm. and Autom. in Design*, vol. 106, pp. 365-370.

Gibson C.G. (1998), Elementary Geometry of Algebraic Curves, Cambridge University Press.

Hunt, K.H. (1978), Kinematic Geometry, Clarendon Press, Oxford.

Ottaviano E., Ceccarelli M., Lanni C. (1999), A Characterization of Ring Void in Workspace of Three-Revolute Manipulators, *Proc. 10th World Congress on the Theory of Machines and Mechanisms*, Oulu, vol. 3, pp. 1039-1044.

Ottaviano E., Husty M., Ceccarelli M. (2004), A Cartesian Representation for the Boundary Workspace of 3R Manipulators, *on Advances in Robot Kinematics*, Sestri Levante, pp. 247-254, 2004.

Parenti-Castelli V., Innocenti C. (1988), Position Analysis of Robot Manipulators: Regions and Sub-Regions, *on Advances in Robot Kinematics*, Ljubljana, pp. 150-158.

Roth B., (1975), Performance Evaluation of Manipulators From a Kinematic Viewpoint, *National Bureau of Standards Special Publication*, no. 459, pp. 39-61.

Sethian J.A. (1996), Level-set Methods and Fast Marching Methods, Cambridge University Press.

Smith D.R., Lipkin H. (1993), Higher Order Singularities of Regional Manipulators, *Proc. IEEE Int. Conf. on Rob. and Autom.*, vol. 1, pp. 194-199.

Wenger P. (2000), Some Guidelines for the Kinematic Design of New Manipulators, *Mech. and Machine Theory*, vol. 35, no. 3, pp. 437-449.

Zein M., Wenger P., Chablat D., (2005), An Exhaustive Study of the Workspaces Topologies of All 3R Orthogonal Manipulators with Geometrical Simplifications, *Proc. Of CK2005, 12th International Workshop on Computational Kinematics*, paper 34-CK2005.

DETERMINATION OF THE WRENCH-CLOSURE WORKSPACE OF 6-DOF PARALLEL CABLE-DRIVEN MECHANISMS

M. Gouttefarde, J-P. Merlet and D. Daney
INRIA Sophia-Antipolis, France
Marc.Gouttefarde@sophia.inria.fr
Jean-Pierre.Merlet@sophia.inria.fr
David.Daney@sophia.inria.fr

Abstract The wrench-closure workspace of parallel cable-driven mechanisms is the set of poses of their mobile platform for which the cables can balance any external wrench. The determination of this workspace is an important issue since the cables can only pull and not push on the mobile platform. This paper deals with the wrench-closure workspace of six-degrees-of-freedom (DOF) parallel mechanisms driven by m cables, $m \geq 7$. The boundary of the constant-orientation cross sections of the wrench-closure workspace is shown to consist of parts of cubic surfaces and an efficient method that determine this workspace by delineating its boundary is proposed.

Keywords: Cable-driven mechanism, parallel mechanism, wrench-closure, workspace, Gough-Stewart platform

1. Introduction

A parallel cable-driven mechanism consists essentially of a mobile platform connected in parallel to a base by light weight links such as cables. The control of the length of the cables allows the control of the pose of the platform. For instance, a mechanism driven by eight cables is shown in Fig. 1. Parallel cable-driven mechanisms have several advantages over conventional rigid-link mechanisms (Barrette and Gosselin, 2005, Merlet, 2004, Roberts et al., 1998). The mass and inertia of the moving part is reduced and they are less expensive. Moreover, parallel cable-driven mechanisms are easier to build, transport and reconfigure and they have the possibility of working in a very large space. Consequently, parallel cable-driven mechanisms have been used in several applications such as, for instance, robotic cranes (Dagalakis et al., 1989), high speed manip-

J. Lenarčič and B. Roth (eds.), Advances in Robot Kinematics, 315–322.

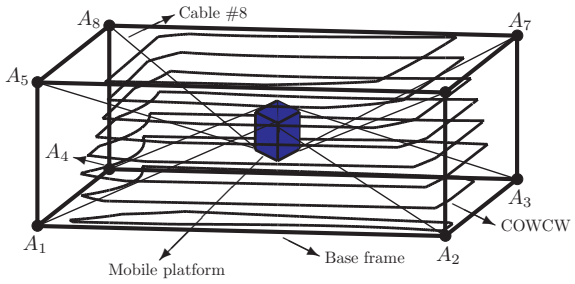

Figure 1. A 6-DOF Parallel Mechanism Driven by Eight Cables and its Constant-Orientation Wrench-Closure Workspace.

ulation (Kawamura et al., 2000), active suspension devices (Lafourcade, 2004) and virtual reality (Merlet, 2004).

This paper deals with the determination of the workspace of six-DOF parallel cable-driven mechanisms. This workspace may be limited by the total length of each cable, by the interferences between the cables and between the cables and the mobile platform and by the unidirectional nature of the forces applied by the cables on the mobile platform. The limitations due to the total lengths of the cables can be determined by means of algorithms presented in (Gosselin, 1990) and in (Merlet, 1999). However, the workspace will usually not be limited by the total lengths of the cables since large total lengths can generally be used. For a constant orientation of the mobile platform, the problem of the influence on the workspace of the cables interferences is addressed in (Merlet, 2004). The third limitation which is due to the unidirectional nature of the forces applied by the cables on the platform has been studied mainly in the case of planar parallel cable-driven mechanisms in (Barrette and Gosselin, 2005, Fattah and Agrawal, 2005, Gallina and Rosati, 2002, Gouttefarde and Gosselin, 2006, Roberts et al., 1998, Stump and Kumar, 2004, Verhoeven and Hiller, 2000, Verhoeven, 2004, Williams et al., 2003).

All these references do not share the same definition of the workspace and two different types of workspace can be distinguished. Indeed, we can study the set of poses of the mobile platform for which the cables can balance, by pulling on the mobile platform,

- a particular wrench or a particular set of wrenches, or
- any wrench.

When the first type of workspace is to be determined, the particular wrench or the particular set of wrenches must be chosen. Hence, the de-

termination of this workspace is useful when a particular task, for which the wrenches that must be generated at the mobile platform are known, is assigned to the cable-driven mechanism. The determination of the second type of workspace, called the wrench-closure workspace (WCW) in the present paper, does not need such a choice since it depends on the geometry of the mechanism only (Gouttefarde and Gosselin, 2006), i.e., on the number of cables, on the positions of the attachment points of the cables at the mobile platform and on the positions of the points of the base from which the cables are taut (points A_i in Fig. 1). Hence, the WCW is a property of the mechanism only and is consequently related to the general design problem of selecting geometry of mechanisms which have the ability to perform various types of tasks. More details on the different types of workspace of parallel cable-driven mechanisms can be found in (Bosscher and Ebert-Uphoff, 2004, Ebert-UpHoff and Voglewede, 2004, Gouttefarde and Gosselin, 2006, Gouttefarde, 2005).

In this paper, an efficient method that allows to determine the constant-orientation cross sections of the WCW, called the constant-orientation WCW (COWCW), is proposed. This method applies to any six-DOF parallel cable-driven mechanism and it determines the boundary of the COWCW which is shown to consist of parts of cubic surfaces. To the best of our knowledge, such a tool has never been introduced in previous papers dealing with six-DOF cable-driven mechanisms such as the works presented in (Hiller et al., 2005, Kawamura et al., 2000, Lafourcade, 2004, Pham et al., 2006, Tadokoro et al., 1996, Takeda and Funabashi, 2000, Verhoeven, 2004).

2. Nature of the Boundary of the COWCW

The relationship between the tensions in the cables and the wrench $\mathbf{w}_p$ applied by the cables on a reference point P of the platform is given by

$$\mathbf{W}\mathbf{t} = \mathbf{w}_p, \tag{1}$$

where $\mathbf{t}$ is the vector of cable tensions and $\mathbf{W}$ the $6 \times m$ pose dependent wrench matrix where m denotes the number of cables. Since the WCW of a six-DOF parallel cable-driven mechanism exists only if its mobile platform is driven by at least seven cables (Ming and Higuchi, 1994), in this paper, $m \geq 7$.

The WCW is defined as the set of poses of the mobile platform in which, for any wrench $\mathbf{w}_p$ in $\mathbb{R}^6$, there exists at least one vector $\mathbf{t}$ in $\mathbb{R}^m$, whose components are all nonnegative, such that Eq. 1 is verified. For

a constant orientation of the mobile platform, the COWCW is the set of positions of the reference point P of the platform which belongs to the WCW. The poses that belongs to the WCW can be characterized by several means (Gouttefarde, 2005) including the following theorem (Murray et al., 1994, Stump and Kumar, 2004).

Theorem 1 *Let* $\mathbf{w}_i$, $1 \leq i \leq m$, $m > 6$, *be the column vectors of the wrench matrix* $\mathbf{W}$ *and let us assume that* $\mathrm{rank}(\mathbf{W}) = 6$. *Then, a pose of the mobile platform belongs to the WCW if and only if all the hyperplanes* $\mathcal{H}$ *of* $\mathbb{R}^6$ *spanned by five wrenches* $\mathbf{w}_i$ *(linearly independent) are separating, i.e.,*

$$\exists\,(j,k),\ j \neq k,\ \textit{such that}\ \ \mathbf{w}_j^T\mathbf{q} > 0\ \ \textit{and}\ \ \mathbf{w}_k^T\mathbf{q} < 0, \tag{2}$$

where $\mathbf{q} \neq \overrightarrow{\mathbf{0}}$ *is a vector of* $\mathbb{R}^6$ *orthogonal to* $\mathcal{H}$.

Eq. 2 means that there exists at least one column of $\mathbf{W}$ lying on each side of the hyperplane $\mathcal{H}$.

Now, let us assume that the orientation of the mobile platform of a six-DOF parallel cable-driven mechanism is constant. Let us consider a position P_1 of the mobile platform which belongs to the COWCW and a continuous trajectory going from P_1 to a position P_2 which lies outside the COWCW. According to Theorem 1, on the part of the trajectory that belongs to the COWCW, all the hyperplanes $\mathcal{H}$ spanned by five columns of the wrench matrix $\mathbf{W}$ are separating. Moreover, at the point at which the trajectory leaves the COWCW, at least one of the hyperplane $\mathcal{H}$ ceases to be a separating hyperplane. But, a hyperplane $\mathcal{H}$ ceases to be a separating hyperplane if and only if the five columns of $\mathbf{W}$ which span $\mathcal{H}$ become linearly dependent or these five columns and an other column of $\mathbf{W}$ become linearly dependent. Hence, in the two cases, the trajectory leaves the COWCW since at least one combination of six columns of $\mathbf{W}$ becomes linearly dependent and *a position of the mobile platform belongs to the boundary of the COWCW only if six columns of the wrench matrix* $\mathbf{W}$ *are linearly dependent.*

This observation on the nature of the boundary of the COWCW is important. Indeed, the columns of the wrench matrix $\mathbf{W}$ are of the same nature as the columns of the transpose of the so-called jacobian matrix of a Gough-Stewart platform (Ebert-UpHoff and Voglewede, 2004, Gouttefarde and Gosselin, 2005) and, consequently, for a constant orientation of the mobile platform, *six columns of* $\mathbf{W}$ *are linearly dependent on a surface of the same nature as the constant-orientation singularity locus of a Gough-Stewart platform which is known to be a cubic surface*

(Mayer St-Onge and Gosselin, 2000), i.e., a surface whose equation can be written as a multivariate polynomial of degree three in the Cartesian coordinates of the mobile platform. Finally, we can state that *the boundary of the COWCW consists of parts of cubic surfaces of the same nature as the constant-orientation singularity locus of the Gough-Stewart platform*. This fundamental result is a generalization to the most general case of the similar result presented in (Gouttefarde and Gosselin, 2005) in the case of six-DOF parallel mechanisms driven by seven cables.

3. Efficient Determination of the COWCW

In this section, the main steps of an efficient method that determines the COWCW by finding its boundary are presented. This method takes advantage of the geometric nature of the boundary introduced in the previous section.

First, an orientation of the mobile platform is chosen and, for each combination of six columns of the wrench matrix $\mathbf{W}$, the equation of the cubic surface $\mathcal{S}_i$ on which these columns are linearly dependent is determined. A method that allows to obtain these equations is presented in (Mayer St-Onge and Gosselin, 2000). Then, in order to deal with curves instead of surfaces, a set of parallel planes is selected, e.g., planes orthogonal to the z-axis, and the part of the boundary of the COWCW which belongs to these planes is sought. Let us denote by $\mathcal{P}$ one of these planes. Without loss of generality, we can assume that the equation of $\mathcal{P}$ is $z = z_0$, i.e., that $\mathcal{P}$ is orthogonal to the z-axis. The part of the boundary of the COWCW which lies in $\mathcal{P}$ can be obtained by following the steps presented below.

Step 1: obtain the equations of the cubic curves $\mathcal{C}_i$ that lie in $\mathcal{P}$ and on which six columns of $\mathbf{W}$ are linearly dependent by substituting z_0 for z in the equations of the cubic surfaces $\mathcal{S}_i$.

According to section 2, if it exists, the part of the boundary of the COWCW which lies in $\mathcal{P}$ is composed of parts of the cubic curves $\mathcal{C}_i$. Moreover, the extremities of these parts are the points of intersection between the cubic curves $\mathcal{C}_i$.

Step 2: for each of the cubic curve $\mathcal{C}_i$, determine the points of intersection between $\mathcal{C}_i$ and the other cubic curves.

The points of intersection between the cubic curves $\mathcal{C}_i$ can be determined by means of an elimination method (Roth, 1993).

Step 3: for each of the cubic curve $\mathcal{C}_i$, find all its parts defined by the points of intersection computed at step 2 and eliminate all unbounded parts.

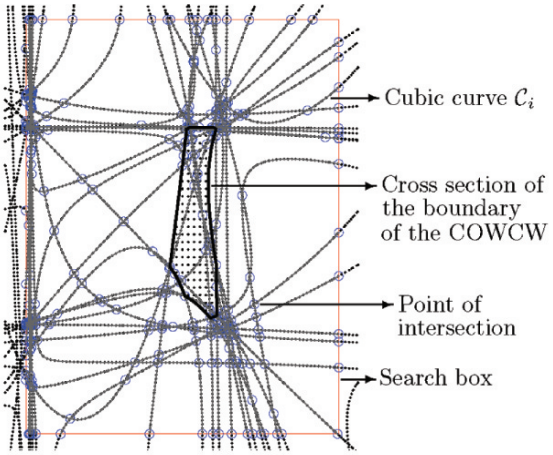

Figure 2. In a plane $\mathcal{P}$, the cubic curves $\mathcal{C}_i$ and the boundary of the COWCW.

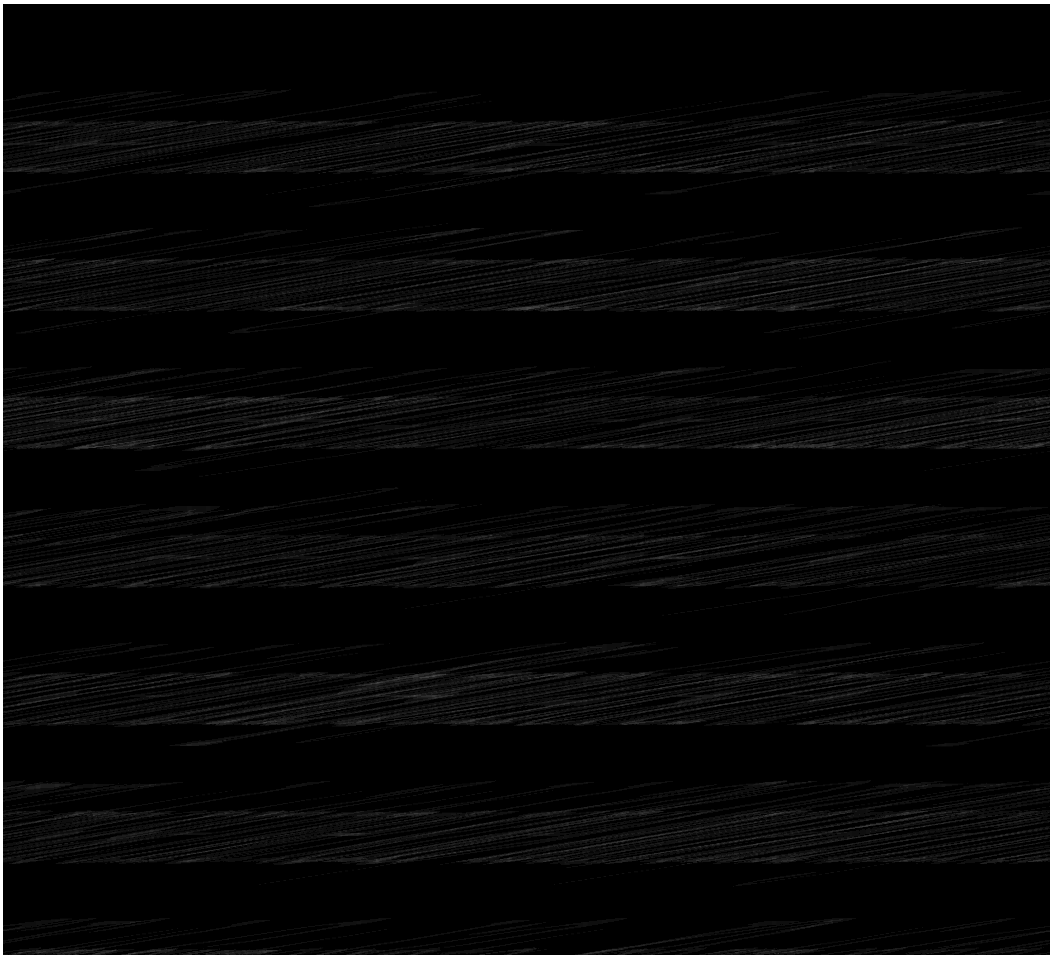

curves C_i, their points of intersection and the cross section of the boundary of the COWCW obtained by the method are shown in Fig. 2.

5. Conclusions

The determination of the WCW is an important issue for 6-DOF parallel cable-driven mechanisms since the cables cannot push on the mobile platform. Moreover, the COWCW turns out to be highly dependent on the geometry of the mechanism and on the orientation of its mobile platform. Hence, the method presented in this paper which allows to determine the COWCW is useful in order to analyze and design 6-DOF parallel cable-driven mechanisms. This method applies to 6-DOF mechanisms driven by an arbitrary number of cables and is based on the nature of the boundary of the COWCW which has been shown to consist of parts of cubic surfaces of the same nature as the constant-orientation singularity locus of Gough-Stewart platforms.

References

Barrette, G., and Gosselin, C. M. (2005), Determination of the dynamic workspace of cable-driven planar parallel mechanisms, *Journal of Mechanical Design*, vol. 127, no. 2, pp. 242–248.

Bosscher, P., and Ebert-Uphoff, I. (2004), Wrench-based analysis of cable-driven robots, *IEEE International Conference on Robotics and Automation*, New Orleans, LA, USA.

Dagalakis, N. G., Albus, J. S., Wang, B.-L., Unger, J., and Lee, J. D. (1989), Stiffness study of a parallel link robot crane for shipbuilding applications, *Journal of Offshore Mechanics and Arctic Engineering*, vol. 111, pp. 183–193.

Ebert-UpHoff, I., and Voglewede, P. A. (2004), On the connections between cable-driven robots, parallel manipulators and grasping, *IEEE International Conference on Robotics and Automation*, New Orleans, LA, USA.

Fattah, A., and Agrawal, S. K. (2005), On the design of cable-suspended planar parallel robots, *Journal of Mechanical Design*, vol. 127, pp. 1021–1028.

Gallina, P., and Rosati, G. (2002), Manipulability of a planar wire driven haptic device, *Mechanism and Machine Theory*, vol. 37, no. 2, pp. 215–228.

Gosselin, C. M. (1990), Determination of the workspace of 6-DOF parallel manipulators, *Journal of Mechanical Design*, vol. 112, no. 3, pp. 331–336.

Gouttefarde, M. (2005), *Analyse de l'espace des poses polyvalentes des mécanismes parallèles entraînés par câbles*, Ph.D. Dissertation, Laval University, Québec, Canada.

Gouttefarde, M., and Gosselin, C. M. (2006), Analysis of the wrench-closure workspace of planar parallel cable-driven mechanisms, *IEEE Transactions on Robotics*, to appear.

Gouttefarde, M., and Gosselin, C. M. (2005), Wrench-closure workspace of six-dof parallel mechanisms driven by 7 cables, *CCToMM Symposium on Mechanisms, Machines, and Mechatronics*, Montréal, Québec, Canada.

Hiller, M., Fang, S., Mielczarek, S., Verhoeven, R., and Franitza, D. (2005), Design, analysis and realization of tendon-based parallel manipulators, *Mechanism and Machine Theory*, vol. 40, pp. 429–445.

Kawamura, S., Kino, H., and Won, C. (2000), High-speed manipulation by using parallel wire-driven robots, *Robotica*, vol. 18, no. 1, pp. 13–21.

Lafourcade, P. (2004), *Contribution à l'étude des manipulateurs parallèles à câbles, application à la conception d'une suspension active pour soufflerie*, Ph.D. Dissertation, ONERA-DCSD, Toulouse, France.

Mayer St-Onge, B., and Gosselin, C. M. (2000), Singularity analysis and representation of the general Gough-Stewart platform, *The International Journal of Robotics Research*, vol. 19, no. 3, pp. 271–288.

Merlet, J-P. (2004), Analysis of the influence of wires interference on the workspace of wire robots, in *Advances in Robot Kinematics*, Sestri-Levante, Italy.

Merlet, J-P. (1999), Determination of 6D workspaces of Gough-type parallel manipulator and comparison between different geometries, *The International Journal of Robotics Research*, vol. 18, no. 9, pp. 902–916.

Merlet, J-P. (2004b), ALIAS, [Online]. Available: http://www-sop.inria.fr/coprin/logiciels/ALIAS/

Ming, A., and Higuchi, T. (1994), Study on multiple degree-of-freedom positioning mechanism using wires (Part 1) - concept, design and control, *International Journal of the Japan Society for Precision Engineering*, vol. 28, no. 2, pp. 131–138.

Murray, R., Li, Z., and Sastry, S. (1994), *A mathematical introduction to robotic manipulation*, CRC Press, Boca Raton, FL, USA.

Pham, C. B., Yeo, S. H., Yang, G., Kurbanhusen, M. S., and Chen, I-M. (2006), Force-closure workspace analysis of cable-driven parallel mechanisms, *Mechanism and Machine Theory*, vol. 41, no. 1, pp. 53–69.

Roberts, R. G., Graham, T., and Lippitt, T. (1998), On the inverse kinematics, statics, and fault Tolerance of cable-suspended robots, *Journal of Robotic Systems*, vol. 15, no. 10, pp. 581–597.

Roth, B. (1993), Computations in Kinematics, in *Computational Kinematics*, Dagstuhl Castle, Germany.

Stump, E., and Kumar, V. (2004), Workspace delineation of cable-actuated parallel manipulators, *ASME Design Engineering Technical Conferences*, Salt Lake City, UT, USA.

Tadokoro, S., Nishioka, S., Kimura, T., Hattori, M., Takamori, T., and Maeda, K. (1996), On fundamental design of wire configurations of wire-driven parallel manipulators with redundancy, *Proceedings of the 1996 Japan/USA Symposium on Flexible Automation*, Boston, MA, USA, pp. 151–158.

Takeda, Y., and Funabashi, H. (2000), Kinematic synthesis of spatial in-parallel wire-driven mechanism with six degrees of freedom with high force transmissibility, *ASME Design Engineering Technical Conferences*, Baltimore, MD, USA.

Verhoeven, R., and Hiller, M. (2000), Estimating the controllable workspace of tendon-based stewart platforms, in *Advances in Robot Kinematics*, Piran-Portoroz, Slovenia.

Verhoeven, R. (2004), *Analysis of the workspace of tendon-based Stewart platforms*, Ph.D. dissertation, Duisburg Essen University, Duisburg, Germany.

Williams II, R. L., Gallina, P., and Vadia, J. (2003), Planar translational cable-direct-driven robots, *Journal of Robotic Systems*, vol. 20, no. 3, pp. 107–120.

FULLY-ISOTROPIC HEXAPODS

Grigore Gogu
Mechanical Engineering Research Group, French Institute of Advanced Mechanics and University Blaise Pascal, Clermont-Ferrand, France
Grigore.Gogu@ifma.fr

Abstract The paper presents a special family of fully-isotropic parallel manipulators with six degrees of mobility called Isoglide6-E. The six motions of the moving platform are controlled independently by six actuators situated on the fixed base. A one-to-one correspondence exists between the actuated joint space and the operational space of the moving platform. The Jacobian matrix of the fully-isotropic hexapods presented in this paper is the 6×6 identity matrix throughout the entire workspace. A method is proposed for structural synthesis based on the theory of linear transformations. The special family of fully-isotropic hexapods includes 2197 solutions. As far as we are aware, this paper presents for the first time fully-isotropic parallel manipulators with six degrees of mobility.

Keywords: Parallel manipulators, hexapods, fully-isotropic, six degrees of mobility, structural synthesis

1. Introduction

The three translations (T) and the three rotations (R) of the moving platform in the fully-isotropic hexapods, called Isoglide6-E, presented in this paper can be controlled independently by three linear actuators and three rotary actuators situated on the fixed platform (base). A one-to-one correspondence exists between the actuated joint space and the operational space of the moving platform

$$ {}^{p}\begin{bmatrix} v \\ \omega \end{bmatrix}_{H} = [J][\dot{q}] \qquad (1) $$

where : $[v]=[v_x\ v_y\ v_z]^T$ is the velocity of a point H belonging to the moving platform, $[\omega]=[\omega_a\ \omega_\beta\ \omega_\delta]^T$ is the angular velocity of the moving platform, $[\dot{q}]=[\dot{q}_1\ \dot{q}_2\ \dot{q}_3\ \dot{q}_4\ \dot{q}_5\ \dot{q}_6]^T$ are the velocities of the actuated joints, $[J]$ is the Jacobian matrix and p is the coordinate system in which the velocities of the moving platform with respect to the fixed base are expressed.

We know that a parallel manipulator (PM) is fully-isotropic if the Jacobian J is a diagonal matrix with identical diagonal elements throughout the entire workspace. The Jacobian matrix of fully-isotropic hexapods presented in this paper is the identity matrix throughout the

J. Lenarčič and B. Roth (eds.), Advances in Robot Kinematics, 323–330.

entire workspace ($J = I_{6\times 6}$). The condition number and the determinant of the Jacobian matrix being equal to one, the manipulator performs very well with regard to force and motion transmission (Angeles, 1987). The isotropic design aims at ideal kinematic and dynamic performance of the manipulator (Fattah and Hasan Ghasemi, 2002).

Some important studies are now available to support the design of hexapods, such as the pioneering works of Hunt (1973, 1978, 1983), the comprehensive enumerations presented by Merlet (1997, 2000) and Tsai (2000). Although hexapods are known for more than half a century, no one fully-isotropic PM with six degrees of freedom has been proposed until now (Fassi et al., 2005). As far as we are aware, this paper proposes for the first time fully-isotropic parallel manipulators with six degrees of freedom. Only PMs with Schönflies motions T3R1-type (Gogu, 2004a, 2005a, Caricato, 2005), translational T3-type (Caricato and Parenti-Castelli, 2002, Kim and Tsai, 2002, Kong and Gosselin, 2002, Gogu, 2004b), planar T2R1-type (Gogu, 2004c), T2R2-type (Gogu, 2005b), T1R2-type (Gogu, 2005c) and spherical R2-type (Gogu, 2005d) fully-isotropic parallel manipulators have been previously proposed in the literature.

The general methods used for structural synthesis of parallel robotic manipulators can be divided into three approaches: the methods based on displacement group theory (Hervé, 1995, Hervé and Sparacino, 1993, Hervé, 2004, Angeles, 2004, Li et al., 2004), the methods based on screw algebra (Frisoli et al., 2000, Kong and Gosselin, 2001, 2004a, 2004b, 2004c, Fang and Tsai, 2002, Huang and Li, 2002, 2003, Caricato, 2005) and the methods based on the theory of linear transformations (Gogu, 2004a, 2004b, 2004c, 2005a, 2005b, 2005c, 2005d, 2005e). The method used in this paper is also founded on the theory of linear transformations.

2. Kinematic Structure

The general kinematic structure of the fully-isotropic PMs proposed in this paper is presented in Fig. 1. The legs A, B and C contribute to the the three independent translations of the intermediary platform $n_1 \equiv n_A \equiv n_B \equiv n_C$ and implicitly of the final mobile platform 5_F. They make a fully-isotropic translational parallel kinematic chain. The legs D, E and F contribute to the three independent rotations of the mobile platform 5_F and each integrates two homokinetic joints connected by telescopic shafts. Just the input and the output shafts are indicated in Fig. 1 for each homokinetic joint. The intermediary members of the homokinetic

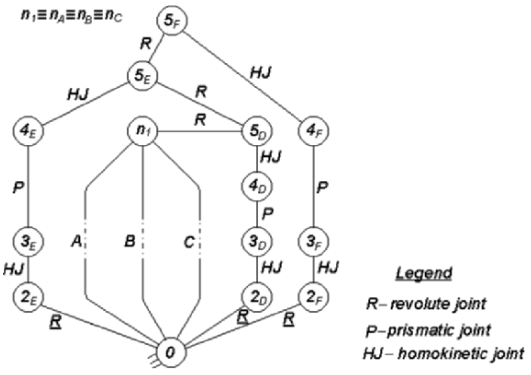

Figure 1. General kinematic structure of the fully-isotropic hexapods of Isoglide6-E family.

joints are not indicated. Various types of homokinetic joints could be used: Tracta, Weiss, Bendix, Dunlop, Rzeppa, Birfield, Glaenzer, Thompson, Triplan, Tripode, UF (undercut-free) ball joint, AC (angular contact) ball joint, VL plunge ball joint, DO (double offset) plunge ball joint, AAR (angular adjusted roller), helical flexure U-joints, etc. (Dudiță et al., 2001a, 2001b).

The first joint of each leg is actuated (underlined joint). The legs A, B and C are actuated by linear motors and the legs D, E and F by rotary motors. The six actuators are mounted on the fixed base.

The mechanism associated to a fully-isotropic PM with six degrees of mobility is denoted by *Q*. The existence of this mechanism involves the following conditions for the connectivity (spatiality) $S^Q_{n/1}$ between the moving (*n*) and the fixed (*1≡0*) platforms and for the base ($R^Q_{n/1}$) of the vector space of relative velocities of the moving platform:

a) general conditions for any position of the mechanism when $\dot{q}_1 \neq 0$, $\dot{q}_2 \neq 0$, $\dot{q}_3 \neq 0$, $\dot{q}_4 \neq 0$, $\dot{q}_5 \neq 0$ and $\dot{q}_6 \neq 0$

$$S^Q_{n/1} = 6, \tag{2}$$

$$\left(R^Q_{n/1}\right) = \left(\vec{v}_x, \vec{v}_y, \vec{v}_z, \vec{\omega}_\alpha, \vec{\omega}_\beta, \vec{\omega}_\delta\right), \tag{3}$$

b) particular conditions when one actuator is locked $\dot{q}_i = 0$ *(i = 1,…,6)*

$$S^Q_{n/1} = 5, \tag{4}$$

$$\left(R^Q_{n/1}\right) = \left(\vec{v}_y, \vec{v}_z, \vec{\omega}_\alpha, \vec{\omega}_\beta, \vec{\omega}_\delta\right), \text{ if } \dot{q}_1 = 0, \tag{5}$$

$$\left(R^Q_{n/1}\right) = \left(\vec{v}_x, \vec{v}_z, \vec{\omega}_\alpha, \vec{\omega}_\beta, \vec{\omega}_\delta\right), \text{ if } \dot{q}_2 = 0, \tag{6}$$

$$\left(R^Q_{n/1}\right) = \left(\vec{v}_x, \vec{v}_y, \vec{\omega}_\alpha, \vec{\omega}_\beta, \vec{\omega}_\delta\right), \text{ if } \dot{q}_3 = 0, \tag{7}$$

$$\left(R^Q_{n/1}\right) = \left(\vec{v}_x, \vec{v}_y, \vec{v}_z, \vec{\omega}_\beta, \vec{\omega}_\delta\right), \text{ if } \dot{q}_4 = 0, \tag{8}$$

$$\left(R_{n/1}^{Q}\right)=\left(\vec{v}_x,\vec{v}_y,\vec{v}_z,\vec{\omega}_\alpha,\vec{\omega}_\delta\right),\ \text{if}\ \ \dot{q}_5=0, \tag{9}$$

$$\left(R_{n/1}^{Q}\right)=\left(\vec{v}_x,\vec{v}_y,\vec{v}_z,\vec{\omega}_\alpha,\vec{\omega}_\beta\right),\ \text{if}\ \ \dot{q}_6=0, \tag{10}$$

The point H on the moving platform n is chosen such that the bases $(R_{n/1}^{Q})$ defined by Eqs. (3) and (5-10) represent the unique bases of the vector space of the relative velocities between the mobile and fixed platforms.

We recall that the connectivity (spatiality) $S_{n/1}^{Q}$ between the moving and the fixed platforms in the mechanism Q represents the number of relative independent infinitesimal displacements or velocities allowed by the mechanism between the two platforms. It is given by the dimension of the vector space $R_{n/1}^{Q}$ of the relative velocities between the two platforms (Gogu, 2005e)

$$S_{n/1}^{Q}=\dim(R_{n/1}^{Q})\,. \tag{11}$$

The moving platform is $n\equiv 5_F$ for the general kinematic structure of the fully-isotropic PM presented in Fig. 1.

Various solutions of legs A, B and C could be used in the general kinematic structure presented in Fig. 1:

- elementary legs $\underline{P}\perp P\perp P$, $\underline{P}\perp P\perp\|R\|R$, $\underline{P}\|R\perp P\perp\|R$, $\underline{P}\|R\|R\perp P$, $\underline{P}\|R\|R\|R$,
- complex legs with parallelogram loops $\underline{P}\perp P\perp\|Pa$, $\underline{P}\|Pa\perp P$, $\underline{P}\|Pa\|Pa$, $\underline{P}\|Pa\|R\|R$, $\underline{P}\|R\|R\|Pa$,
- complex legs with m ($m=1,2,\ldots$) rhombus loops $\underline{P}\|R\|Rb_1\|\ldots\|Rb_m\|R$,
- complex legs with bimobile planar loops $\underline{P}\|Pn2\|R$,
- complex legs with trimobile planar loops $\underline{P}\|Pn3\|R$.

In these notations P stands for prismatic pair, R for revolute pair, Pa for planar parallelogram loop, Rb for planar rhombus loop, $Pn2$ for bimobile planar loop and $Pn3$ for trimobile planar loop. The notations $\perp$ and $\|$ indicate the perpendicular or parallel positions of the joint axes. For example, the notation $\underline{P}\perp P\perp\|R\|R$ indicates that: the first three pairs have perpendicular axes/directions, the last two pairs have parallel axes and the axis of the third pair is in the same time parallel to the direction of the first pair. More details on the structural synthesis of the legs A, B, and C via theory of linear transformations could be get in Gogu, 2004b.

By various combinations of the five solutions of elementary legs and the eight solutions of complex legs A, B and C we obtain $13^3=2197$ distinct solutions of fully-isotropic PMs with six degrees of freedom. All these solutions obey conditions (2)-(10) and integrate only revolute and prismatic joints in the legs A, B and C. The family of these solutions could be more diversified by introducing helical, cylindrical and planar joints to replace some equivalent combinations of revolute and prismatic

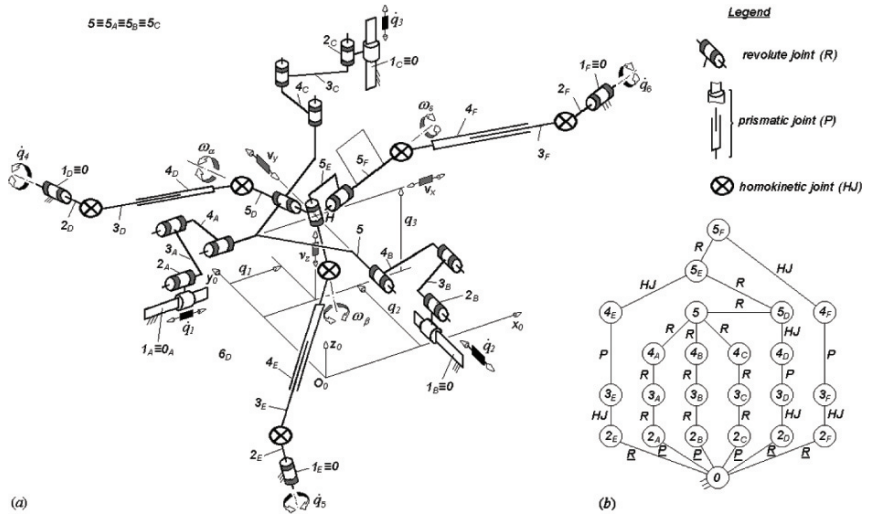

Figure 2. Example of fully-isotropic hexapod: Isoglide6-E1(a) and its associated graph (b).

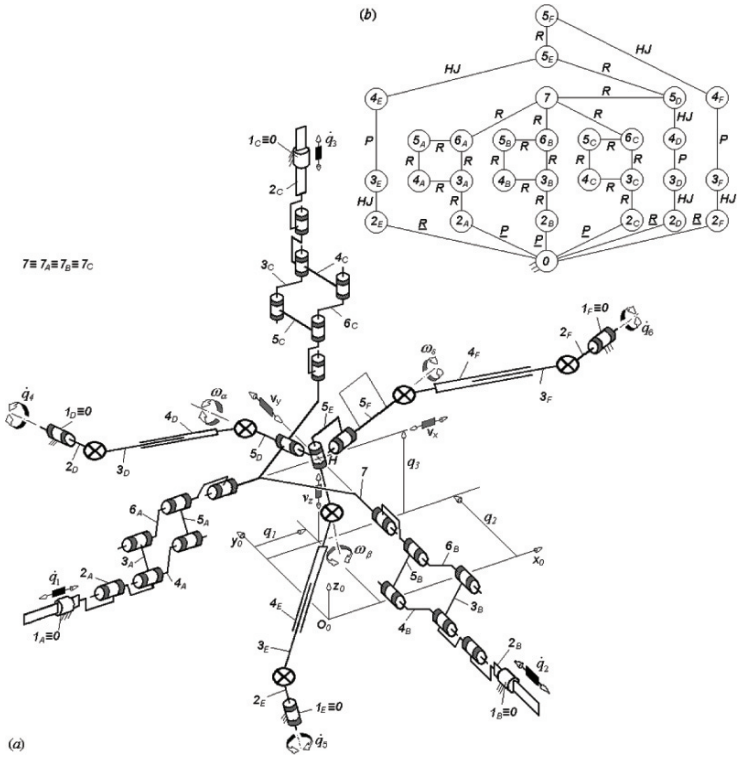

Figure 3. Example of fully-isotropic hexapod: Isoglide6-E2 (a) and its associated graph (b).

joints or by introducing some new joints with idle mobilities to obtain non overconstrained (isostatic) solutions. Due to space limitations, we have reduced our presentation in this paper to fully-isotropic overconstrained solutions without idle mobilities integrating just revolute and prismatic pairs in the legs A, B and C.

The two examples presented in Figs. 2 and 3 have elementary legs A, B and C of type $\underline{P}\|R\|R\|R$ (Fig. 2) and complex legs A, B and C of type $\underline{P}\|R\|Rb_1\|R$ (Fig. 3). The workspace of these solutions must be correlated with the angular capability of the homokinetic joints and translational capability of the telescopic shafts.

3. Conclusions

An approach has been proposed for structural synthesis of a family of 2197 fully-isotropic hexapods with six degrees of mobility called Isoglide6-E. Special legs were conceived to achieve fully-isotropic conditions. The Jacobian matrix mapping the joint and the operational vector spaces of the fully-isotropic hexapods presented in this paper is the 6×6 identity matrix throughout the entire workspace. These solutions realize a one-to-one mapping between the actuated joint velocity space and the operational velocity space. The condition number and the determinant of the Jacobian matrix being equal to one, the manipulator performs very well with regard to force and motion transmission. Moreover, the solutions of fully-isotropic hexapods presented in this paper have all actuators mounted directly on the fixed base. As far as we are aware, this paper presents for the first time fully-isotropic parallel manipulators with six degrees of freedom and a method for their structural synthesis.

4. Acknowledgement

This work was sustained by CNRS (The French National Council of Scientific Research) in the frame of the projects ROBEA-MAX (2002-2003) and ROBEA-MP2 (2004-2006).

References

Angeles, J. (1987), *Fundamentals of Robotic Mechanical Systems : Theory, Methods, and Algorithms*, New York, Springer.

Angeles, J. (2004), The qualitative synthesis of parallel manipulators, *Trans. ASME Journal Mech. Design*, vol. 126, pp. 617-624.

Carricato, M. and Parenti-Castelli, V. (2002), Singularity-free fully-isotropic translational parallel mechanisms, *Int. Journal of Robotics Research*, no. 2, vol. 22, pp. 161-174.

Caricato, M. (2005), Fully-isotropic four degrees-of-freedom parallel mechanisms for Schoenflies motion, *Int. Journal of Robotics Research*, no. 5, vol. 24, pp. 397-414.

Dudiță, F., Diaconescu, D., Jaliu, C., Bârsan, A. and Neagoe, M. (2001a), *Cuplaje mobile articulate*, Braşov, Ed. Orientul Latin.

Dudiță, F., Diaconescu, D., Lateş, M. and Neagoe, M. (2001b), *Cuplaje mobile podomorfe*, Braşov, Ed. Trisedes Press.

Fang, Y., and Tsai, L.-W. (2002), Structural synthesis of a class of 4-dof and 5-dof parallel manipulators with identical limb structures. *Int. Journal of Robotics Research*, no. 9, vol. 21, pp. 799-810.

Fassi, I., Legnani, G. and Tosi, D. (2005), Geometrical conditions for the design of partial or full isotropic hexapods, *Journal of Robotic Systems*, no. 10, vol. 22, pp. 505-518.

Fattah, A. and Hasan Ghasemi A.M. (2002), Isotropic design of spatial parallel manipulators. *Int. Journal of Robotics Research*, no. 9, vol. 21, pp. 811-824.

Frisoli, A., Checcacci, D., Salsedo F. and Bergamasco, M. (2000), Synthesis by screw algebra of translating in-parallel actuated mechanisms, in: Lenarčič, J. and Stanišić, M.M. (Eds), *Advances in robot kinematics*, Dordrecht, Kluwer Academic Publishers, pp. 433-440.

Gogu, G. (2004a), Fully-isotropic T3R1-type parallel manipulators, in: Lenarčič, J., Galletti, C. (Eds.), *On Advances in Robot Kinematics*, Dordrecht, Kluwer Academic Publishers, pp. 265-274.

Gogu, G. (2004b), Structural synthesis of fully-isotropic translational parallel robots via theory of linear transformations, *European Journal of Mechanics–A/Solids*, no. 6, vol. 23, pp. 1021-1039.

Gogu, G. (2004c), Fully-isotropic over-constrained planar parallel manipulators, *Proceedings of IEEE/RSJ Int. Conf. on Intelligent Robots and Systems (IROS 2004)*, Sendai, pp. 3519-3520.

Gogu, G. (2005a), Singularity-free fully-isotropic parallel manipulators with Schönflies motions, *Proceedings of 12th International Conference on Advanced Robotics (ICAR 2005)*, Seattle, pp. 194-201.

Gogu, G. (2005b), Fully-isotropic parallel robots with four degrees of freedom T2R2-type, *Proceedings of IEEE/RSJ International Conference on Intelligent Robots and Systems (IROS 2005)*, Edmonton, pp. 1190-1195.

Gogu, G. (2005c), Fully-isotropic T1R2-type parallel manipulators with three degrees of freedom, *Proceedings of International Design Engineering Technical Conferences & Computers and Information in Engineering Conference (IDETC/CIE 2005)*, Long Beach, Paper DETC2005-84313.

Gogu, G. (2005d), Fully-isotropic over-constrained parallel wrists with two degrees of freedom, *Proceedings of IEEE International Conference on Robotics and Automation (ICRA 2005)*, Barcelona, pp. 4025-4030.

Gogu, G. (2005e), Mobility and spatiality of parallel robots revisited via theory of linear transformations, *European Journal of Mechanics/A –Solids*, vol. 24, pp. 690-711.

Hervé, J.M. (1995), Design of parallel manipulators via the displacement group, *Proceedings of the 9th World Congress on the Theory of Machines and Mechanisms*, Milan, pp. 2079-2082.

Hervé, J.M. and Sparacino, F. (1993), Synthesis of parallel manipulators using Lie-groups: Y-STAR and H-ROBOT, *Proceedings of IEEE Intl. Workshop on Advanced Robotics*, Tsukuba, pp. 75-80.

Hervé, J.M. (2004), New translational parallel manipulators with extensible parallelogram, *Proceedings of the 11th World Congress in Mechanism and Machine Science*, vol. 4, China Machine Press, pp. 1599-1603.

Huang, Z. and Li, Q.C. (2002), General methodology for type synthesis of symmetrical lower-mobility parallel manipulators and several novel manipulators, *Int. Journal of Robotics Research*, no. 2, vol. 21, pp. 131-145.

Huang, Z. and Li, Q.C. (2003), Type synthesis of symmetrical lower-mobility parallel mechanisms using the constraint-synthesis method, *Int. Journal of Robotics Research*, no. 1, vol. 22, pp. 59-79.

Hunt, K.H. (1973), Constant-velocity shaft couplings: a general theory, *Trans. ASME Journal of Eng. Industry*, vol. 95B, pp. 455-464.

Hunt, K.H. (1978), *Kinematic Geometry of Mechanisms*, Oxford University Press.

Hunt, K.H. (1983), Structural kinematics of in-parallel-actuated robot arms, *Trans. ASME Journal Mech. Design*, vol. 105, pp. 705-712.

Kim, H.S. and Tsai, L.-W. (2002), Evaluation of a Cartesian parallel manipulator, in: J. Lenarčič and F. Thomas, eds., *Advances in Robot Kinematics*, Dordrecht, Kluwer Academic Publishers, pp. 21-28.

Kong, X., Gosselin, C.M. (2001), Generation of parallel manipulators with three translational degrees of freedom based on screw theory, *Proceedings of CCToMM Symposium on Mechanisms, Machines and Mechatronics*, Montreal.

Kong, X. and Gosselin, C.M. (2002), Type synthesis of linear translational parallel manipulators, in: J. Lenarčič and F. Thomas, eds., *Advances in Robot Kinematics*, Dordrecht, Kluwer Academic Publishers, pp. 453-462.

Kong, X. and Gosselin, C.M. (2004a). Type sysnthesis of 3T1R parallel manipulators based on screw theory, *IEEE Trans. Robotics and Automation*, no. 2, vol. 20, pp. 181-190.

Kong, X. and Gosselin, C.M. (2004b), Type synthesis of analytic translational parallel manipulators, *Proceedings of the 11th World Congress in Mechanism and Machine Science*, vol. 4, China Machine Press, pp. 1642-1646.

Kong, X. and Gosselin, C.M. (2004c), Type synthesis of 3-dof translational parallel manipulators based on screw theory, Trans. *ASME Journal of Mechanical Design*, vol. 126, pp. 83-92.

Li, Q., Huang, Z. and Hervé, J.M. (2004), Type synthesis of 3R2T 5-DOF parallel mechanisms using the Lie group of displacements. *IEEE Trans. Robotics and Automation*, no. 2, vol. 20, pp. 173-180.

Merlet, J.P. (1997), *Les robots parallèls*, 2e édition, Paris, Hermès.

Merlet, J.P. (2000), *Parallel Robots*, Dordrecht, Kluwer Academic Publishers.

Tsai, L.-W. (2000), *Mechanism Design: Enumeration of kinematic structures according to function*. CRC Press.

A NEW CALIBRATION STATEGY FOR A CLASS OF PARALLEL MECHANISMS

Philipp Last
Institute of Machine Tools and Production Technology
Langer Kamp 19b, 38106 Braunschweig, Germany
p.last@tu-bs.de

Jürgen Hesselbach
Institute of Machine Tools and Production Technology
Langer Kamp 19b, 38106 Braunschweig, Germany
j.hesselbach@tu-bs.de

Abstract Geometric calibration has been proven to be an efficient way to enhance absolute accuracy of robotic systems. The idea is to identify the geometric parameters of the kinematic model matching the real robots' geometry. Basically calibration is performed by analyzing the difference between conflicting information gained by the kinematic model and corresponding redundant information. In all existing robot calibration approaches required redundancy is achieved either by extra sensors or by special constraint devices. This paper for the first time proposes a calibration method that does not rely on any extra device, thus being very economical. The presented technique which only holds for parallel robots is based on a method that allows passing singularities of type two. By means of simulation studies using a FiveBar-structure as an example the approach is verified.

Keywords: Parallel Kinematics, Calibration, Singularities

1. Introduction

Although automated robot programming is a well engineered technology, most robotic systems are still programmed by using the teach-in approach. This is due to an insufficient absolute accuracy offered by most industrial robots. Positioning errors are mainly caused by a deviation between the controller model and the real robots' geometry effected by thermal influences, manufacturing and assembly tolerances [Mooring et al., 2005]. Geometric calibration has been shown to be a suitable method to overcome that drawback. It is a process by which the parameters of the kinematic model are estimated in a way that best fits the real robot. Parametric calibration requires redundant measurement information that is usually obtained by additional internal or external

J. Lenarčič and B. Roth (eds.), Advances in Robot Kinematics, 331–338.

measurement systems such as lasertracker-devices, theodolites, camera systems or passive joint sensors. Alternatively the robots' degree of freedom (dof) may be restrained by passive devices. In that case the actuator encoders of the system deliver enough information allowing for parameter identification. Various calibration technique of both categories are compared in [Hollerbach and Wampler, 1996].

This contribution for the first time presents a calibration strategy which does not require any calibration equipment. Due to the abandonment of external measurement systems or constraint devices the proposed calibration approach is very inexpensive compared to other techniques. Furthermore it belongs to the class of self-calibration methods [Maurine et al., 2005] and can thus be completely automated and repeated whenever necessary. Redundancy is achieved by special knowledge about singular configurations of type two which need to be passed in order to identify the kinematic parameters of a parallel kinematic manipulator. Our approach is therefore based on a technique that allows to savely guide a parallel mechanism through singularities of type two, introduced in [Helm, 2003]. Without a loss of generality the new calibration approach will be explained and validated by means of a simple 2-dof planar parallel structure, the FiveBar-robot [Sachau et al., 2002].

2. Idea of the Calibration Scheme

As mentioned in the previous section our new calibration approach relies on passing singularities of type two. Because these constitute structure configurations where two solutions of the direct kinematic problem (DKP) coincide, they are also called direct kinematic singularities. It is well known that a robot-structure is uncontrollable in this kind of configurations [Hesselbach et al., 2005] and hence particular strategies need to be applied to savely guide a manipulator through singularities of type two. With the intention of workspace enlargement Helm presented a technique to pass direct kinematic singularities, which has been experimentally proven at a planar robot-structure [Helm, 2003]. The approach has been extended to spatial parallel structures in [Budde et al., 2005]. Both methods rely on the basic idea to temporarily underactuate the robot system during passing the singular configuration and to use an additional driving force to guide the structure through the direct kinematic singularity. By means of the planar FiveBar-structure the approach is exemplarily summarized in Fig. 1. In a pose near the singular configuration (a) the structure is underactuated by releasing one actuator (b). While the second actuator is kept at a constant motor-position the endeffector-point C passes the singularity (c) driven by gravity

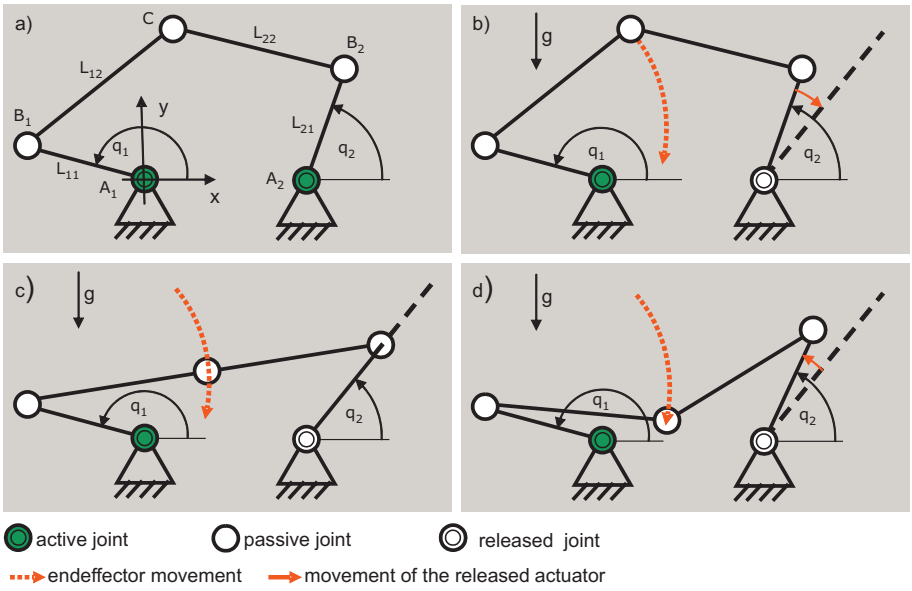

Figure 1. FIVEBAR-structure: Kinematic design (a) and basic steps while passing a singular configuration in (b)-(d).

influence until it reaches a nonsingular configuration (d) in which the released actuator can be activated again. Instead of exploiting gravity as the driving force which has been also done in [Budde et al., 2005], structure inertia may be used to pass the singularity as described in [Helm, 2003].

Mathematically singular configurations of type two can be detected by

$$\det(\mathbf{J}) = 0 \tag{1}$$

with the Jacobian matrix $\mathbf{J} = \frac{\partial \mathbf{q}}{\partial \mathbf{X}}$ relating endeffector velocities $\dot{\mathbf{X}}$ and actuator velocities $\dot{\mathbf{q}}$ [Gosseling and Angeles, 1990]

$$\dot{\mathbf{q}} = \mathbf{J}\dot{\mathbf{X}}\,. \tag{2}$$

Following the above mentioned strategy to pass the singularity one actuator needs to be released while all others remain at a constant position. In that case the systems' dof is one and $\mathbf{J}$ reduces to a scalar expression

$$J = \frac{\dot{q}}{\dot{X}}\,. \tag{3}$$

Since for scalar values

$$\det(J) = J\,, \tag{4}$$

a direct kinematic singularity is according to Eq. 1 reached under the condition

$$\dot{q} = 0 \wedge \dot{X} \neq 0\,. \tag{5}$$

Thus, in a singular structure configuration the velocity of the released actuator $\dot{q}_{released}$ is zero while the endeffector is still in motion. This corresponds to the structure in Fig. 1 where the released actuator changes its direction of movement exactly in the singular configuration (indicated by the dashed line in a,b,c). Consequently by observing the movement of the released actuator by its own encoder it is possible to identify and save the actuator coordinate $\hat{q}^{sing}_{released}$ that corresponds to a singular configuration. Furthermore, since particular geometric conditions need to be fulfilled at a singular configuration of type two, it is possible to compute the actuator coordinate $q^{sing}_{released}(\mathbf{k})$ from the kinematic model including the kinematic parameters $\mathbf{k}$. Comparing both information leads to a residual

$$r(\mathbf{k}) = \hat{q}^{sing}_{released} - q^{sing}_{released}(\mathbf{k}). \tag{6}$$

Passing the direct kinematic singularity at different locations allows for a formulation of different residual functions. These may be assembled in a vector $\mathbf{r}(\mathbf{k})$. Ideally, if the kinematic model exactly matches the real robot-structure, then $\mathbf{r}(\mathbf{k}) = \mathbf{0}$. Since we assume parameter errors, mathematical optimization methods may be applied to find $\mathbf{k}$ such that $\mathbf{r}(\mathbf{k})$ is minimized.

3. FiveBar-Robot Kinematics

In order to validate the presented approach the FiveBar-structure from Fig. 1 will be calibrated. Its kinematic model is defined by only five parameters. These are (Fig. 1a):

- 1 parameter L_0 defining the distance $\overline{A_1A_2}$ between the two actuator base points.
- 1 parameter L_{i1} for each kinematic chain $i = 1, 2$ describing the length of the crank $\overline{A_iB_i}$
- 1 parameter L_{i2} for each kinematic chain $i = 1, 2$ specifying the rod length $\overline{B_iC}$

While typical kinematic problems are concernd with relating endeffector and actuator coordinates the calibration approach presented here requires to determine the actuator coordinate $q^{sing}_{released}$ from arbitrary given fixed actuator coordinates $\mathbf{q}_{fixed}$ and a vector of kinematic parameters $\mathbf{k}$

$$q^{sing}_{released} = f_{SKP}(\mathbf{k}, \mathbf{q}_{fixed}). \tag{7}$$

We refer to this problem as the *Singular Kinematic Problem (SKP).*

The FIVEBAR-structures' SKP can be solved analytically. For brevity index f is introduced for parameters of the chain with the fixed actuator and index r for parameters of the chain whose actuator is released. We assume that $\mathbf{r}_{A_f} = [x_{A_f}, y_{A_f}]^T$ and $\mathbf{r}_{A_r} = [x_{A_r}, y_{A_r}]^T$ pointing from the base coordinate system to point A_f and A_r respectively, are given with the restriction that $|x_{A_r} - x_{A_f}| = L_0$ and consequently $y_{A_r} = y_{A_f}$. By known vector $\mathbf{r}_{B_r} = [x_{B_r}, y_{B_r}]^T$, $q_{released}$ can be solved to

$$q_{released} = q_r = atan2(y_{B_r} - y_{A_r}, x_{B_r} - x_{A_r}). \tag{8}$$

The structure is in a singular configuration under the geometric condition that the two rods of the robot build a common line. Hence $\mathbf{r}_{B_r}$ can be computed by intersecting a circle K_I with its center in B_f and radius $R_I = L_{12} + L_{22}$ and a second circle K_{II} around A_r with radius $R_{II} = L_{r1}$. With the substitutes

$$S_1 = \frac{x_{A_r}^2 + y_{A_r}^2 - (x_{A_f} + \cos q_f L_{f1})^2 - (y_{A_f} + \sin q_f L_{f1})^2 + R_I^2 - R_{II}^2}{2y_{A_r} - 2y_{A_f} - 2\sin q_f L_{f1}} \tag{9}$$

$$S_2 = \frac{x_{A_f} + \cos q_f L_{f1} - x_{A_r}}{y_{A_r} - y_{A_f} - \sin q_f L_{f1}} \tag{10}$$

$$S_3 = \frac{S_1 S_2 - S_2(y_{A_f} + \sin q_f L_{f1}) - (x_{A_f} + \cos q_f L_{f1})}{S_2^2 + 1} \tag{11}$$

$$S_4 = \frac{(S_1 - y_{A_f} - \sin q_f L_{f1})^2 + (x_{A_f} + \cos q_f L_{f1})^2 - R_I^2}{S_2^2 + 1} \tag{12}$$

two solutions

$$x_{B_{r1,2}} = -S_3 \pm \sqrt{S_3^2 - S_4}; \;\; y_{B_{r1,2}} = S_1 + S_2 x_{B_{r1,2}} \tag{13}$$

can be derived for x_{B_r} and y_{B_r}, leading to two solutions of the FIVEBAR-structures' SKP with Eq. 8.

4. Requirements and Limitations

The technique presented above is a very promising strategy to calibrate parallel mechanisms and thus to enhance their absolute accuracy. There are however several limitations:

- As there is a risk of damaging a robot-structure it is usually avoided to approach direct kinematic singularities. Due to this several parallel structures are dimensioned and designed in a way that no singular configuration of type two exist in their workspace. Obviously these manipulators cannot be calibrated by means of the proposed calibration scheme.

- Each time a singularity is passed one redundant information can be gathered. In order to identify n parameters by the calibration process at least n independent informations need to be determined. This requires that different singular configurations exist, which is for example not the case for the PARAPLACER-structure presented in [Helm, 2003].

- If only angular measurements are used for parameter calibration no unique parameter-set can be identified as each scaled version of the robot defines a possible solution to the calibration problem. Consequently one metric parameter needs to be known in advance and serves as a reference-dimension during calibration, meaning that this parameter remains constant during calibration. (This problem is the same for all calibration strategies).

- Since direct kinematic singularities for the FIVEBAR-robot occur under the geometric condition of the two rods building one line, the calibration process cannot differ between a parameter deviation of L_{12} and one in L_{22}. This however results from the particular design feature that both kinematic chains are directly connected to each other in one joint. Most parallel structures, especially those with a dof > 2 are designed in a way that the chains are not directly connected to each other but to an additonal passive platform link. In that case this problem does not occur.

The last two items limit parameter identification for the FIVEBAR-robot under consideration. In order to circumvent the scaling problem, it is assumed that L_0 is exactly known and will serve as the reference parameter during calibration. Furthermore, as it cannot be differed between parameter-deviations in L_{12} and L_{22}, $L_{12} + L_{22}$ will be handled as one parameter of the calibration procedure. In summary only three of the five parameters describing the system can be identified.

5. Simulation Studies

In order to validate the proposed calibration approach various simulation studies have been performed. For simulation purposes a vector $\mathbf{k}^{real}$ containing the actual robot geometry-parameters is generated which adds random values in the range $[\pm 1mm]$ to the nominal values of the three kinematic parameters $L_{11}, L_{21}, L_{12} + L_{22}$ that are supposed to be identified by the calibration process. Nominal parameters $\mathbf{k}^{nom}$ as well as typical real robot parameters $\mathbf{k}^{real}$ are given in Table 1.

Gathering of redundant information is simulated by application of $\hat{q}_{2,j}^{sing} = f_{SKP}(\mathbf{k}^{real}, q_{1,j})$, where j indicates a specific configuration. This

Table 1. Nominal and exemplary real dimensions for the simulation studies.

parameter	*nominal dimension [mm]*	*exemplary real dimension [mm]*
L_0	50	50
L_{11}	30	29, 1
L_{12}	50	49, 2
L_{12}	30	30, 7
L_{22}	50	50

result is compared to $q_{2,j}^{sing} = f_{SKP}(\mathbf{k}, q_{1,j})$ in a residual $r_j(\mathbf{k})$ according to Eq. 6, with $\mathbf{k}$ the current parameter set. In order to ensure that $m \geq 3$ different residuals r_j exist, $q_{1,j}$ is set to $j = 1..m$ different values. All $r_j(\mathbf{k})$ are then assembled in $\mathbf{r}(\mathbf{k}) = [r_1, .., r_j]^T$. Starting with $\mathbf{k} = \mathbf{k}^{nom}$, the idea is to find an optimal parameter set $\mathbf{k}^{opt}$ that best fits the real robot-structure by minimization of $\mathbf{r}(\mathbf{k})$. For mathematical convenience a function F is defined as $F = \mathbf{r}^T\mathbf{r}$. Minimization of F is then performed by the Levenberg Marquard algorithm [Scales, 1985] that has been proven to be successful in various calibration approaches, e.g. [Zhuang, 1997].

Figure 2 shows a typical result of our calibration studies which corresponds to the parameters from Table 1. The parameters converge to the real values within a small number of iteration steps indicating that the algorithm works successful.

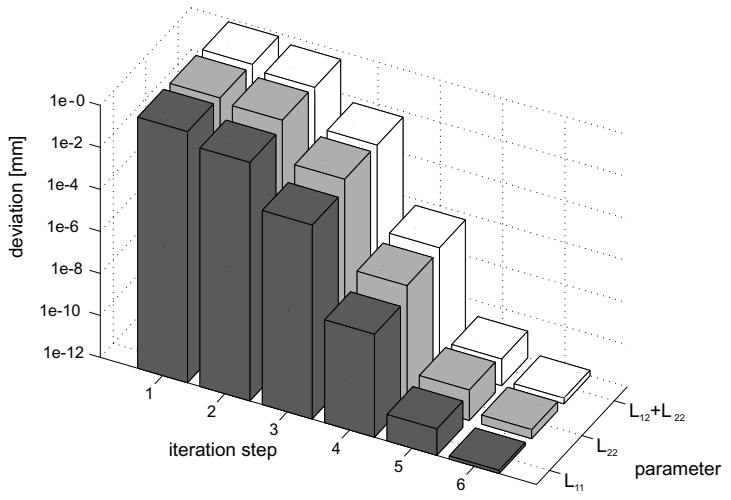

Figure 2. Simulation result corresponding to Table 1 showing the effectiveness of the presented calibration approach.

6. Conclusion

For the first time a robot calibration approach has been presented that does exclusively rely on the information delivered by the robot-system itself. Hence, as neither additional sensors nor special constraint devices are required in order to apply parameter identification methods, the proposed technique is very economical. The basic idea of the new calibration scheme has been explained and validated by means of simple planar parallel structure. Simulation results emphasize the promising potential of the approach. Future work will focus on application of the method to more complex parallel structures. In addition the effect of sensor noise in the actuator encoders will be analyzed.

7. Acknowledgements

The research work reported here was supported by the German Reserach Foundation (DFG) within the scope of the Collaborative Research Center SFB 562.

References

Budde, C., Last, P., Hesselbach, J. (2005), Workspace Enlargement of a Triglide Robot by Changing Working and Assembly Mode, *Proc. of IASTED International Conference on Robotics and Applications*, Cambridge, USA, pp. 244-248.

Gosselin, C., Angeles, J. (1990), Singularity Analysis of Closed-Loop Kinematic Chains, *IEEE Trans. on Robotics and Automation*, 6(3), pp. 281-290.

Helm, M. (2003), *Durchschlagende Mechanismen für Parallelroboter*, Dissertation, TU Braunschweig.

Hesselbach, J., Bier, C., Campos, A., Löwe, H. (2005), Direct Kinematic Singularity Detection of a Hexa Parallel Robot, *Proc. of the IEEE International Conference on Robotics and Automation, ICRA*, Barcelona, Spain, pp. 3507-3512.

Hollerbach, J. M., Wampler, C. W. (1999), The Calibration Index and Taxonomy for Robot Kinematic Calibration Methods, *International Journal of Robotics Research*, vol. 15.

Maurine, P., Liu, D. M., Uchiyama, M. (1998), Self Calibration of a New Hexa Parallel Robot, *Proc. of the 4th Japan-France Congress and 2nd Asia-Europe Congress on Mechatronics*, Kitakyushu, Japan, pp. 290-295.

Mooring, B. W., Roth, Z. S., Driels, M. R. (1991), *Fundamentals of Manipulator Calibration*, John Wiley and Sons INC.

Sachau, D., Breitbach, E., Rose, M., Keimer, E. (2001), An Adaptronic Solution to Increase Efficiency of High Speed Parallel Robots, *Proc. of the 12th Int. Conference on Adaptive Structures and Technologies*, College Park, Maryland, USA.

Scales, L. E. (1985), *Introduction to Non-Linear Optimization*, Macmillan Publishers Ltd.

Zhuang, H. (1997), Self-Calibration of Parallel Mechanisms with a Case study on Stewart Platforms, *IEEE Transaction on Robotics and Automation*, vol. 13, no. 3, pp. 387-397.

THE DYNAMIC OPTIMIZATION OF PKM

Mathias Krefft
Institute of Machine Tools and Production Technology (IWF)
Technical University Braunschweig, Langer Kamp 19b, 38106 Braunschweig, Germany
m.krefft@tu-bs.de

Juergen Hesselbach
Institute of Machine Tools and Production Technology (IWF)
Technical University Braunschweig, Langer Kamp 19b, 38106 Braunschweig, Germany
j.hesselbach@tu-bs.de

Abstract It is well known that parallel kinematic machines (PKM) have a lot of significant advantages. In recent years several machines have been developed and presented on international fairs. But up to now only a handful of machines have been transferred to industrial applications. Reasons for this lack of technical transfer are structural drawbacks and an awful design. Therefore, this paper presents a new optimization approach for the optimal design of PKM according to given application requirements. The main idea of this concept is the separation of the transmission matrices concerning translational and rotational behavior. Hence the resulting criteria allow an exact physical analysis of the kinematic and dynamic properties. To assure the practicability our approach is demonstrated by means of 6-dof Stewart-Gough platform.

Keywords: Parallel kinematics, Jacobian matrices, optimization

1. Introduction

Due to the fact that the tool center point (TCP) is supported by several guiding chains, the main advantages of PKM are high stiffness, process forces and accuracy. In addition the symmetric layout allows a modular design based on standard machine elements (Merlet, 2000). Beside the evolution of increasingly powerful machine control and sophisticated new components, the structure synthesis and optimization is one of the most important defiance's for the developing engineer. This is the starting point for several researchers dealing with the analysis and optimization of the kinematic structure. The main focus of these approaches is the optimization of two characteristics: workspace and the Jacobian matrix. In general, these first optimization strategies utilized currently look at the kinematics and dynamics of the mechanism in a successive manner. Moreover, the dynamic properties of PKM are optimized after

J. Lenarčič and B. Roth (eds.), Advances in Robot Kinematics, 339–348.

the kinematics is defined. This is a typical approach because the tools for kinematic and dynamic analysis are often not the same and the dynamic analysis is usually very difficult to perform. In this paper we will discuss new performance criteria. By integrating the kinematics and dynamics in the design process enhanced PKM can be designed.

2. Analysis

The kinematic and dynamic analysis of PKM is strongly associated with the linear transmission of the drive velocities by the Jacobian $\mathbf{J}_a$:

$$\dot{\mathbf{X}} = \mathbf{J}_a \dot{\mathbf{q}} \tag{1}$$

In literature a large number of approaches discussing this transmission behavior can be found, e.g. Ma and Angeles, 1991. Thus the standardized drive velocity $\dot{\mathbf{q}}$, which describes the surface of a F-dimensional hyper sphere in the joint space, are transmitted on a hyper ellipsoid in the Cartesian space representing the time derivates of the endeffector pose. This transmission is characterized by the extension/amplification and deformation of the hyper sphere and the phase shifting of the output vector $\dot{\mathbf{X}}$ according to the input vector $\dot{\mathbf{q}}$. The maximum amplification of an input drive velocity is given by the spectral norm of the Jacobian matrix:

$$\|\mathbf{J}_a\|_2 = \max_{\|\dot{\mathbf{q}}\|_2 \neq 0} \left(\frac{\|\mathbf{J}_a \dot{\mathbf{q}}\|_2}{\|\dot{\mathbf{q}}\|_2} \right). \tag{2}$$

In the same way $\left\|\mathbf{J}_a^{-1}\right\|_2^{-1}$ gives the minimum amplification. The spectral norm can be calculated with the square root of the maximum eigenvalue ξ_{max} of $\mathbf{J}_a\mathbf{J}_a^T$. Since $\mathbf{J}_a\mathbf{J}_a^T$ and $\mathbf{J}_a^T\mathbf{J}_a$are equal, the singular value $\sigma_{max}(\mathbf{J}_a) \equiv \|\mathbf{J}_a\|_2 = \sqrt{\xi_{max}(\mathbf{J}_a^T\mathbf{J}_a)}$ is the maximum semi half axis of the hyper ellipsoid and $\sigma_{min}(\mathbf{J}_a) \equiv \sqrt{\xi_{min}(\mathbf{J}_a^T\mathbf{J}_a)} = \sigma_{max}^{-1}\left(\mathbf{J}_a^{-1}\right)$ is the minimum semi half axis. Thus the deformation of the hyper ellipsoid can be described by the condition number κ of the Jacobian matrix:

$$\kappa(\mathbf{J}_a) = \frac{\sigma_{max}(\mathbf{J}_a)}{\sigma_{min}(\mathbf{J}_a)} = \|\mathbf{J}_a\|_2 \left\|\mathbf{J}_a^{-1}\right\|_2 \tag{3}$$

2.1 Modified Criteria

Using the inverse of the condition number the range of values can be shifted from $[1, \infty]$ to the interval $[0, 1]$ Salisbury and Craig, 1982. Even though the inverse condition number is a local value, which depends on the pose of the endeffector, a lot of authors, e.g. Ma and Angeles, 1991, use this value for the optimization of parallel robots. The aim of this

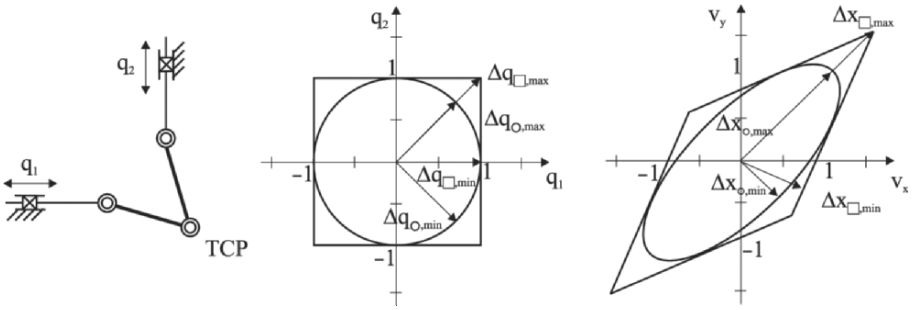

Figure 1. Exact Modeling of Independent Input Parameters.

approach is a uniform velocity transmission in all directions. If $\kappa^{-1} = 1$, the structure is called *isotropic*, irrespective of other poses. Furthermore, the general opinion that $\kappa^{-1} = 1$ means that the PKM can reach the same velocities in all directions, is completely wrong from a physical point of view. This fact has serious consequences for the use of singular values. Considering Eq. 1, the difference quotient for accuracy analysis can be derived:

$$\mathbf{J}_a = \Delta\mathbf{X}/\Delta\mathbf{q} \tag{4}$$

Fig. 1 shows the BIGLIDE-structure based on the PRRRP kinematic chain in a kinematic isotropic position (P = prismatic joint, R = rotational joint). However, considering the maximum errors of each drive, the maximum and minimum endeffector displacements differ as depicted in Table 1. The reason for this lies in the fact that the input vector $\Delta\mathbf{q}$ has to be described by a hyper square (index$_\square$) with the side length $2\Delta q_{max}$. If $\Delta q_{1,max} = \Delta q_{2,max}$, the ratio of maximum and minimum Cartesian errors is $\kappa_x = \|\Delta\mathbf{X}_{max}\|_2 \, \|\Delta\mathbf{X}_{min}\|_2^{-1} = 1,41$, which is the same as the ratio of the input drive errors $\kappa_q = \|\Delta\mathbf{q}_{max}\|_2 \, \|\Delta\mathbf{q}_{min}\|_2^{-1} = 1,41 = \kappa_x$ thus $\kappa = \kappa_x/\kappa_q = 1$ Table 1 shows the spectral norm of the errors and conditions for the PRRRP-structure as shown in Fig. 1. Thus, the extreme Cartesian errors can be calculated by

Table 1. Error Transmission of the PRRRP-Structure

input	Δq_{min}	Δq_{max}	Δx_{min}	Δx_{max}	κ_q	κ_x	κ
sphere	1.00	1.00	0.70	1.77	1.00	2.55	2.55
square	1.00	1.41	0.92	2.51	1.41	2.74	2.40

$$\Delta X_{max} = \max\left(\|\mathbf{J}_a \Delta \mathbf{q}_\square\|_2\right) \tag{5}$$

with the drive errors and permutation parameters

$$\Delta \mathbf{q}_\square = \begin{bmatrix} \mu_1 q_{1,max} & \cdots & \mu_F q_{F,max} \end{bmatrix}^T \tag{6}$$

$$\mu_i \in \{-1, 1\} \wedge \mu_j \in \{-1, 1\}, i = \{1, \ldots, F\} \setminus \{j\}\,. \tag{7}$$

2.2 Separation Approach

Considering the required accuracy of the PKM tasks, we have to guarantee a maximum deflection of the needed endeffector pose due to errors of the drive angles given by the measurement system. Hence, the drive encoders are independent and we have to consider an incremental error Δq_i of each drive. Nevertheless, we have to bear in mind that only a hypercube will accomplish this demand.

Furthermore, if we analyze a PKM with $F = 6$, e.g. the Stewart-Gough platform or a HEXAPOD in general, we will mix different physical units:

$$[\mathbf{J}_a] = \begin{bmatrix} 1 \in \Re^{3x6} \\ rad/m \in \Re^{3x6} \end{bmatrix} \tag{8}$$

In this case, each performance criterion, which is based on the Jacobian matrix, has no physical meaning. In addition the values of the two sub matrices are having different magnitudes and one sub matrix will dominate the other one. Thus some authors like Ma and Angeles, 1991 define a constant characteristic length arbitrarily. Thus, the characteristic of the mechanism performance can be manipulated without affecting the machine itself. Kirchner, 2001 uses the projection of the platform vectors on the orientation planes. But, the use of the standardized matrix is still problematic, as shown in Table 2. The table gives the six singular values of a HEXAPOD structure (6-UPS) for a given pose. As can be seen, the maximum singular values describe a combined motion, i.e. translation in y-direction and a rotation around the x- and z-axes. But what is the maximum positioning error?

The following approach using two criteria for translation and orientation will avoid this problem. The main idea is to split the Jacobian matrix into two sub matrices containing the translational (index t) and rotational (index r) transmission behavior:

$$\mathbf{J}_a = \begin{bmatrix} \mathbf{J}_{a,t}^T & \mathbf{J}_{a,r}^T \end{bmatrix}^T \tag{9}$$

Now Eq. 1 can be separated as follows

$$\mathbf{v} = \mathbf{J}_{a,t}\dot{\mathbf{q}}, \mathbf{J}_{a,t} \in \Re^3, \boldsymbol{\Omega} = \mathbf{J}_{a,r}\dot{\mathbf{q}}, \mathbf{J}_{a,r} \in \Re^3. \tag{10}$$

Table 2. Singular values and directions for different approaches

type	*singular value*	→ x	→ y	→ z	↻ x	↻ y	↻ z
standardized Jacobian							
σ_{max}	0.44	0.00	−0.36	0.00	0.28	0.00	0.04
σ_{min}	0.19	−0.02	0.00	−0.10	0.00	0.05	0.00
separated Jacobian							
Δx_{max}	0.35	0.11	−0.34	0.00	7.68	2.49	0.00
$\Delta\Phi_{max}$	9.11	−0.21	−0.23	0.00	6.75	−6.12	0.00

With regard to Eq. 4 this equation obtains the maximal translational and rotational displacements:

$$\Delta x_{max} = \max\left(\|\mathbf{J}_{a,t}\mathbf{q}_{\square}\|_2\right),\ \Delta\varphi_{max} = \max\left(\|\mathbf{J}_{a,r}\mathbf{q}_{\square}\|_2\right) \tag{11}$$

2.3 Forces and Dynamic Effects

For high speed applications the most important aim is to increase the endeffector's velocity. Therefore, most authors maximize the velocity transmission as shown in section 2.2. Nevertheless, this approach has the risk of a saturation of the drive forces since velocity and force transmission are inverse. Thus, the analysis of the drive forces $\boldsymbol{\tau}$ has to be included in the optimization approach. However, it becomes difficult to assign a physical interpretation when authors like Kirchner, 2001 and Ottaviano and Ceccarelli, 2002 mix forces and torques. Their approach yields physically inconsistent results when different units are mixed. Thus, the swiftness approach of Di Gregorio and Parenti-Castelli, 2004 is not suitable for all PKM, generally. An appropriate approach, which has been made for serial robots by Bowling and Khatib, 2005, is well suited for our task. The main idea is to separate the different force components, e.g. inertia, torques, forces, etc.

$$\boldsymbol{\tau} = \boldsymbol{\tau}_{\mathbf{f}_L} + \boldsymbol{\tau}_{\mathbf{m}_L} + \boldsymbol{\tau}_{\dot{\mathbf{v}}} + \boldsymbol{\tau}_{\dot{\boldsymbol{\Omega}}} + ... \tag{12}$$

The addition of each contribution can be represented geometrically by mapping one force ellipsoid onto every point on the surface of the other as shown in Fig. 2. To simplify the problem we firstly consider the external loads and inertia effects. The separation of the geometric Jacobian

$$\mathbf{J}_g^T = \left[\mathbf{J}_{g,t}^T \mathbf{J}_{g,r}^T\right], \tag{13}$$

which differs from the analytic Jacobian $\mathbf{J}_a$ for PKM with $F > 3$, yields

$$\boldsymbol{\tau} = \mathbf{J}_{g,t}^T \mathbf{f}_L + \mathbf{J}_{g,rot}^T \mathbf{m}_L + \mathbf{B}_t \dot{\mathbf{v}} + \mathbf{B}_r \dot{\boldsymbol{\Omega}}, \tag{14}$$

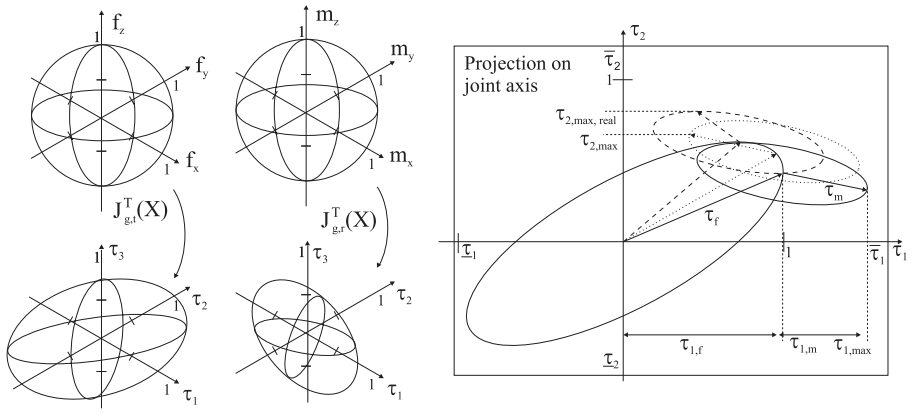

Figure 2. Addition of the single force terms and their projected contributions in the direction of each drive.

with the inertia matrix $\mathbf{B} = \left[\begin{array}{cc} \mathbf{B}_t^T & \mathbf{B}_r^T \end{array} \right]^T = \mathbf{J}_{g,t}^T \sum \left(\mathbf{J}_j^T \mathbf{M}_j \mathbf{J}_j \right)$, where $\mathbf{M}_j$ is the mass matrix of each body j. For instance the transmission ellipsoid of the external load $\mathbf{f}_L$ is given by:

$$\boldsymbol{\tau}_{\mathbf{f}_L}^T \left(\mathbf{J}_{g,t}^T \mathbf{J}_{g,t} \right)^+ \boldsymbol{\tau}_{\mathbf{f}_L} = \|\mathbf{f}_L\|_2^2 \tag{15}$$

This equation can be understood by mapping a force hyper sphere into the space of the drive forces. Here a hyper sphere can be used, because it represents a maximum force vector with constant length and arbitrary direction. These mappings are valid because we use the Moore-Penrose pseudo inverse

$$(\mathbf{J}_{g,...}^T)^+ = \left(\mathbf{J}_{g,...} \mathbf{J}_{g,...}^T \right)^{-1} \mathbf{J}_{g,...}, \tag{16}$$

since the single contributions are of a smaller dimension than the drive force vector. The difficulty of the approach by Bowling and Khatib, 2005, is the calculation of the maximum projection of each contribution on each drive axis in the space of the drive forces. Fig. 2 shows that this projection cannot be calculated by using the greatest singular values of the separated geometric Jacobian sub matrices, here $\mathbf{J}_{g,t}^T$ and $\mathbf{J}_{g,r}^T$. Instead of Bowling's numerical approach we use the maximum singular values of each row to calculate the maximum projection of each contribution.

$$\mathbf{J}_g^T(\mathbf{X}) = \left[\begin{array}{cc} \mathbf{J}_{g,t,1}^T & \mathbf{J}_{g,r,1}^T \\ \vdots & \vdots \\ \mathbf{J}_{g,t,F}^T & \mathbf{J}_{g,r,F}^T \end{array} \right] \tag{17}$$

This process is very simple and quite effective, because it gives the exact maximum force value for each drive

$$\tau_{max} = \max_i \left(\left\| \mathbf{J}_{g,t,i}^T \mathbf{f}_L \right\|_2 + \left\| \mathbf{J}_{g,r,i}^T \mathbf{m}_L \right\|_2 \right). \tag{18}$$

Notice that this equation provides the possibility to independently determine the worst case contributions of all terms in Eq. (12) without using any standardization values.

3. Modified Evolutionary Algorithm

The mentioned performance criteria are discontinuities, discrete and nonlinear functions with constraint conditions. Thus the optimization problem has no convexity properties and therefore gradient methods failed where simple stochastic methods are too time consuming. In this case evolutionary algorithms are very effective to search the global optima without any knowledge about the optimization problem itself (Zitzler et al., 2003). In contrast to some authors (Ottaviano and Ceccarelli, 2002), who used a weighted cost function as one criterion, our approach is a pareto based multi criteria evolutionary algorithm.

$$\begin{aligned} Ind_1 \succ Ind_2 : & \forall k \in \{1, \ldots, N_{Obj}\} : O_k(Ind_1) \geq O_k(Ind_2) \wedge \\ & \exists p \in \{1, \ldots, N_{Obj}\} : O_p(Ind_1) > O_p(Ind_2) \end{aligned} \tag{19}$$

To enhance the performance of the evolutionary algorithm, we modified the approach of Zitzler et al., 2003, with respect to a dynamic parameter limitation and a better initialization as well as adaptive mutation and termination functionalities (see Krefft et al., 2006). The result is an uniform distributed compromise set with all N_{Ind} solutions Ind fitting the N_{Obj} contradictory objectives O_i of the given application.

4. Optimization of a Hexapod

The performance of our optimization approach was demonstrated by means of a HEXAPOD manipulator with hydraulic drives for metal forming, which was designed at the IWF in 2002 (Fig. 3). The advantage of the hydraulic actuators is the high power to weight ratio. For the metal forming process the platform has to rotate around the pitch and roll axes with a sin-characteristics respectively, resulting in a tumbling motion with a maximum angle of 15° and 1 Hz. The process forces are 50kN in z-direction and 5kN in the xy-plane. Beside the workspace $\mathcal{W}$ the minimization of the maximum actuator forces (due to process forces) and the maximum actuator velocities (due to the tumbling motion) inside $\mathcal{W}$ are the main aims of the optimization task. However, these two aims are

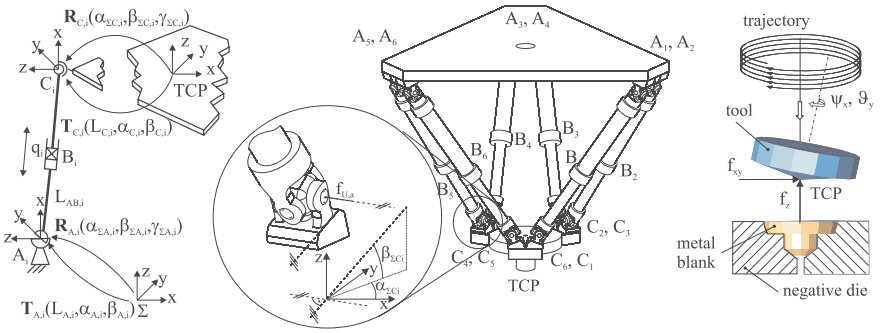

Figure 3. Parameters/Layout of the Structure and Process Parameters.

Table 3. Requirements.

no.	*requirement*	*variable*	*border in* $\mathcal{W}$	*aim*	*note*
1.	workspace radius	$r_{\mathcal{W}}$	0,05 m		shape 6D:
2.	workspace height	$h_{\mathcal{W}}$	0,05 m		cylindrical
3.	pivoting angle	ψ_x, θ_y	±15°		independent
4.	max. drive force	$\tau_{i,max}$	50kN	min	$F_z = 50$ kN, $F_{xy} = 5$kN
5.	max. drive velocity	$\dot{q}_{i,max}$	0,5 m/s	min	$\dot{\psi}_x, \dot{\theta}_y = f(\psi_x, \theta_y)$ $\dot{\psi}_{x,max}, \dot{\theta}_{y,max} = 95\,°/\mathrm{s}$
6.	max. axial bearing forces	$f_{U_a,i,max}$		min	

contradictory. Nevertheless, the separation of the translational kinetostatic and rotational kinematic aspects may help to overcome this problem. Additionally, the axial bearing forces of the universal joints have to be reduced for the sake of stiffness and accuracy (Table 3). Considering the performance of the hydraulic drives, the border values $\tau_{i,max} = 50\,\mathrm{kN}$ and $\dot{q}_{i,max} = 0.5\,\mathrm{m/s}$ have not been exceeded in any pose of $\mathcal{W}$. Using these sufficient restriction, we can guarantee that all fixed requirements are fulfilled.

In addition to the radius of the base L_{A_i} and platform L_{C_i} and the distance of the universal joint pairs L_U, the orientation $\alpha_{\Sigma C_i}, \beta_{\Sigma C_i}$ of the first joint axes in spherical coordinates are the input parameters of the optimization. So far a 60° rotation of base and platform is the optimum arrangement.

Fig. 4 shows the result of the optimization. Due to an enhanced strength pareto evolutionary algorithm (SPEA) based on Zitzler et al., 2003, the pareto set has a uniform distribution. The pareto set in the 3D objectives space is similar to a shell, which is formed by the best solutions fitting

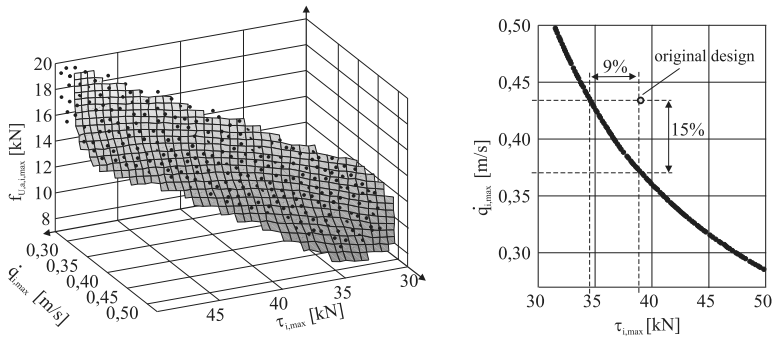

Figure 4. 3D Pareto Set (Req. 4-6) and Quality of First Design (Req. 4,5).

the requirements in Table 3. Due to the fact that all demands have to be minimized, there exists no solution on the backside of this area. It can be seen that using this evolutionary algorithm, an exact hyper surface, which is representing the best solution set, can be derived.

In comparison to the first design of the machine, which is the reference for our new approach, the pareto set offers both, minimized drive forces and drive velocities. Even if there was no suitable optimization tool up to the time of the first development, the original design offers a good overall performance (Fig. 4). The projection of the pareto solution shows the contradictory behavior of the requirements 4 and 5 (Fig. 4). The final selection out of the pareto set has to be done by the developing engineer with his expert knowledge by using weighting factors. To overcome the problem of combining different physical values in one cost function the objectives have to be standardized with the limiting objective values of the pareto set O_p.

$$\hat{O}_i = (O_i - \min(O_p))/(\max(O_p) - \min(O_p)). \tag{20}$$

In contrast to common cost function approaches, e.g. Ottaviano and Ceccarelli, 2002, this procedure has two advantages: Firstly, the optimization process must not be restarted, if one may change the weighting factors and secondly, a standardization of the objectives is very easy. As depicted in Fig. 5, different weighting factors obtain different solutions. Whereas the variants 2-4 have a better overall performance than the original design, the solutions 1 and 5 offer the best solution of one objective according to the fixed requirements. With regard to the first design the axial bearing forces are minimized with all variants.

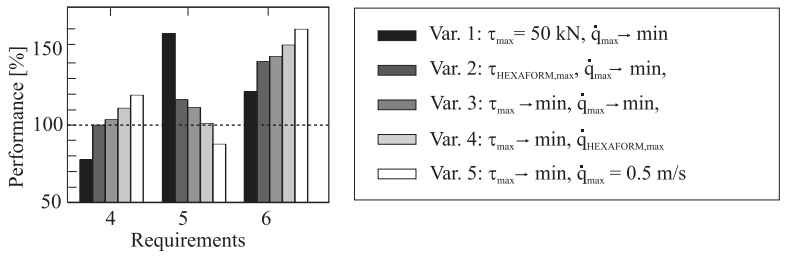

Figure 5. Enhancement of 5 Optimized Variants According to the First Design.

5. Conclusion

This article presents a new optimization approach for optimized PKM. The key feature is the separation of the Jacobian matrix and the projection of the current values with respect to translation/rotation as well as drive axes. Thus, we get performance criteria with a physical exact meaning. It is understood that this basic idea can be copied to other problems. The optimization of an existing machine shows that this new approach obtains a further performance enhancement.

References

Bowling, A., and Khatib, O. (2005), The dynamic capability equations: a new tool for analyzing robotic manipulator performance, *IEEE Trans. on Robotics and Automation*, vol. 21, no. 1, pp. 115–123.

Di Gregorio, R., and Parenti-Castelli, V. (2004), Comparison of 3-dof parallel manipulators based on new dynamic performance indices, *Proceedings of the 11th World Congress in Mechanism and Machine Science*, Tianjin, China, pp. 1684–1688.

Kirchner, J. (2001), *Mehrkriterielle Optimierung von Parallelkinematiken*, PhD-Thesis Technical University Chemnitz, Germany.

Krefft, M., Last, P., and Hesselbach, J. (2006), New Concepts to Adapt the Parallel Robot Performance to Application Requirements, *Proceedings of Chemnitzer Parallel Kinematik Seminar*, Chemnitz, Germany, in print.

Ma, O., and Angeles, J. (1991), Optimum Architecture Design of Platform Manipulators, *Proceedings of Int. Conf. on Advanced Robotics*, Pisa, Italy, pp. 1130–1135.

Merlet, J.-P. (2000), *Parallel Robots*, Dordrecht, Netherlands, Kluwer Academic Pub.

Ottaviano, E., and Ceccarelli, M. (2002), Optimum design of parallel manipulators for workspace and singularity performances, *Proceedings of the Workshop on Fundamental Issues and Future Research Directions for Parallel Mechanisms and Manipulators*, Quebec City, Canada, pp. 98–105.

Salisbury, J. K., and Craig, J. J. (1982), Articulated hands - Force control and kinematic issues, *Int. J. of Robotics Research*, vol. 1, no. 1, pp. 4–17.

Zitzler, E., Thiele, L., Laumanns, M., Fonseca, C. M., and Fonseca, V. G. (2003), Performance assessment of multiobjective optimizers, *IEEE Trans. on Evolutionary Computation*, vol. 7, no. 2, pp. 117–132.

ON NON-ASSEMBLY IN THE OPTIMAL SYNTHESIS OF SERIAL MANIPULATORS PERFORMING PRESCRIBED TASKS

J.A. Snyman
Department of Mechanical and Aeronautical Engineering
University of Pretoria, Pretoria 0002, South Africa
jan.snyman@eng.up.ac.za

Abstract In the application of optimization algorithms to the optimal synthesis of mechanical manipulators performing prescribed tasks, unique difficulties are encountered due to the fact that the optimization algorithms may drive the design to a configuration that experiences lock-up, and thus resulting non-assembly along the task path. If this happens no objective function can be evaluated for the current design, and the optimization procedure is forced to terminate prematurely. In previous work on planar serially linked manipulators, a heuristic procedure was proposed to deal with specific individual synthesis problems. Here the author presents a concise review and justification of the proposed methodology in terms of general kinematic constraint equations that may define the prescribed motion of any serially linked manipulator.

Keywords: Optimal dimensional synthesis, serial manipulator, non-assembly

1. Introduction

In the optimal synthesis of a serially linked manipulator a dimensional configuration, i.e. link lengths and base positioning, is sought that will ensure favorable performance along a prescribed task path. In particular the required dimensional design must be such that the end-effector not only executes a time-specific prescribed task path, but also does so in some optimal manner. Of course, if non-assembly or lock-up of the manipulator occurs along the task path then the configuration cannot be evaluated. In comparison to much work that has been done on the optimal synthesis of linkages [Erdman and Sandor, 1997], very little work appears to have been done on the above serial manipulator synthesis problem. This is probably due to the greater complexity of the latter problem, and particularly because of the unique complication of non-assembly during the numerical solution of the associated optimization problem. It is of interest to note that the problem of non-assembly in the optimal synthesis of linkages has also received little attention [Minnaar et al., 2001].

J. Lenarčič and B. Roth (eds.), Advances in Robot Kinematics, 349–356.

Relatively recently the author and co-worker Berner [Berner and Snyman, 1999, Snyman and Berner, 1999a, Snyman and Berner, 1999b] have addressed the above optimal synthesis problem for a specific planar manipulator performing a variety of different prescribed tasks, subject to the average absolute torque requirement being optimal. They proposed and applied an ad hoc heuristic procedure in solving the associated optimization problems for this specific manipulator, with different imposed practical constraints. The purpose of this paper is to present a concise review of the previously proposed methodology, but here in terms of general kinematic constraint equations that may define the prescribed motion of any serially linked manipulator. In doing so the basic elements of the proposed methodology for overcoming the problem of non-assembly are elucidated.

In spite of the sophistication of existing mathematical optimization algorithms, certain inhibiting difficulties remain when these algorithms are applied to real-world problems [Snyman, 2005]. This is particularly true in the field of mechanical design where unique difficulties arise that have prevented the general application of mathematical programming techniques to optimal design problems. Some typical optimization difficulties that may arise are: (i) computational expense in evaluating performance via dynamical simulations, (ii) presence of numerical noise and discontinuities in the objective function, (iii) the existence of multiple minima, and (iv) the existence of regions in the design space where the objective function is not defined, and therefore cannot be evaluated. Problems (i) – (iii) have often been addressed, and various general methods and techniques have been developed to overcome the respective problems [Snyman, 2005]. Difficulty (iv), however, has by comparison been neglected. There does not appear to be a general method for solving this particular problem. Often the nature of the system being optimized dictates the method to be adopted in overcoming this problem. Here the previous problem-specific methodology of Snyman and Berner, for overcoming difficulty (iv), is reviewed and justified in terms of general kinematic constraint equations.

2. Problem Formulation

In the optimal design of a serially linked manipulator, it may be required to minimize an objective function associated with the execution of a prescribed task path to be followed by the end-effector. In particular it may, for example, be required that for a typical planar serially linked manipulator depicted in Figure 1, where the end-effector is to follow a prescribed task path specified by the vector position $\mathbf{r}(t)$ at any instant

t, the average torque for the execution of the prescribed task path over the time interval $[0, T]$, be minimized with respect to the link lengths and base placement.

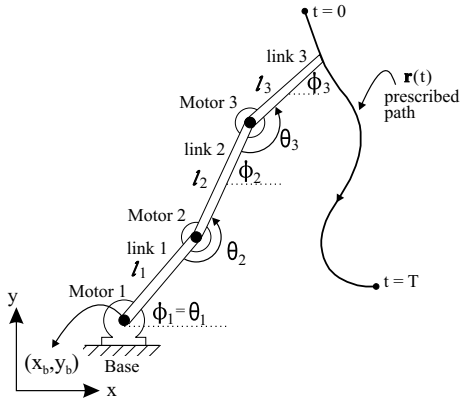

Figure 1. Representation of a planar manipulator following a prescribed path.

A major problem that may occur, corresponding to optimization difficulty (iv) mentioned in the previous section, is that during the optimization procedure the optimization algorithm, in adjusting the link lengths and base coordinates $[l_1, l_2, l_3, x_b, y_b]$, may drive the design to one where the workspace no longer fully encloses the prescribed task path. Thus, assuming that the initial point of the task path is in the workspace, the end-effector in following the prescribed task path will reach a point on the boundary of the workspace, beyond which assembly of the manipulator is no longer possible. Consequently the objective function associated with the completion of the path cannot be evaluated, i.e. difficulty (iv) is encountered, and the optimization procedure terminates prematurely and unsuccessfully. For individually specific problems Snyman and Berner proposed an ad hoc heuristic procedure, involving artificial objective function values, for overcoming this problem during optimization. Here their heuristic is reviewed with reference to the general kinematic constraint equations defining the motion of any serially linked manipulator.

3. Kinematically Driven System and Non-Assembly

In general a kinematically driven system is described by a combination of n kinematic and driving constraint equations of the form [4]:

$$\mathbf{\Phi}(\mathbf{q}, t) = \mathbf{0} \tag{1}$$

where $\mathbf{q}$ is a n-vector of generalized coordinates and t denotes the instant in time. It is assumed here that equation (1) explicitly or implicitly specifies the position vector $\mathbf{r}(t)$ of the end-effector at any instant t in the interval $[0, T]$. Suppose now that for a specific design the task path is initially ($t = 0$) inside the reachable workspace of the manipulator, but crosses the boundary at $t = t^* > 0$. This implies that assembly is lost beyond the boundary, and that for $t > t^*$ no solution to equation (1) exists. According to the definition of Haug [Haug, 1989] the configuration $\mathbf{q}^*$ at time t^* corresponds to lock-up, and further, since the solution cannot be continued beyond t^* it follows by the implicit function theorem that the Jacobian of (1) at t^*, $\mathbf{\Phi_q}(\mathbf{q}^*, t^*)$, is singular. This has an important influence on the behavior of $\dot{\mathbf{q}}$ and $\ddot{\mathbf{q}}$ as t approaches t^*.

The velocity equation obtained by taking the time derivative of (1) is

$$\mathbf{\Phi_q}(\mathbf{q}, t)\dot{\mathbf{q}} = -\mathbf{\Phi}_t \tag{2}$$

Since $\Phi_{\mathbf{q}}(\mathbf{q}, t)$ is singular at time t^*, it follows that in the situation described above, where the manipulator approaches a lock-up configuration, that the solution of (2) yields a value for the norm of $\dot{\mathbf{q}}$ that tends to infinity as t approaches t^*. Clearly the same applies to the solution of the corresponding acceleration equation obtained by differentiating (2) with respect to time. Thus the behavior of the norms of $\dot{\mathbf{q}}$ and $\ddot{\mathbf{q}}$ as t nears t^* serves as a warning that a lockup configuration and non-assembly is being approached. In the following section a simple example is presented that illustrates such a situation and shows how the behavior of the manipulator may be monitored in practice.

4. Simple Example of Lock-Up and Non-Assembly

Consider a two-link revolute manipulator ($l_1 = l_2 = 1$) with the configuration specified by link angles ϕ_1 and ϕ_2 as shown in Figure 2(a), and with the task path of the end-effector specified by $\mathbf{r}(t) = [x(t), y(t)]^T \equiv [t, \sqrt{2}]^T$ for all t in the interval $[0, 2]$. Setting $q_1 = \phi_1$ and $q_2 = \phi_2$, equation (1) assumes the form

$$\mathbf{\Phi}(\boldsymbol{\phi}, t) = \begin{bmatrix} x(t) - t \\ y(t) - \sqrt{2} \end{bmatrix} = \begin{bmatrix} \cos\phi_1 + \cos\phi_2 - t \\ \sin\phi_1 + \sin\phi_2 - \sqrt{2} \end{bmatrix} = \mathbf{0} \tag{3}$$

For any instant t equation (3) may be solved for ϕ_1 and ϕ_2. By further differentiation of (3) with respect to time, the velocity and acceleration equations may be derived, from which one may solve for $\dot{\phi}_1$, $\dot{\phi}_2$, $\ddot{\phi}_1$, and $\ddot{\phi}_2$. The values of $\dot{\phi}_1$ and $\ddot{\phi}_1$, computed at intervals of $\Delta t = 0.01$s, are plotted in Figure 2(b). The values of $\dot{\phi}_2$ and $\ddot{\phi}_2$ behave similarly

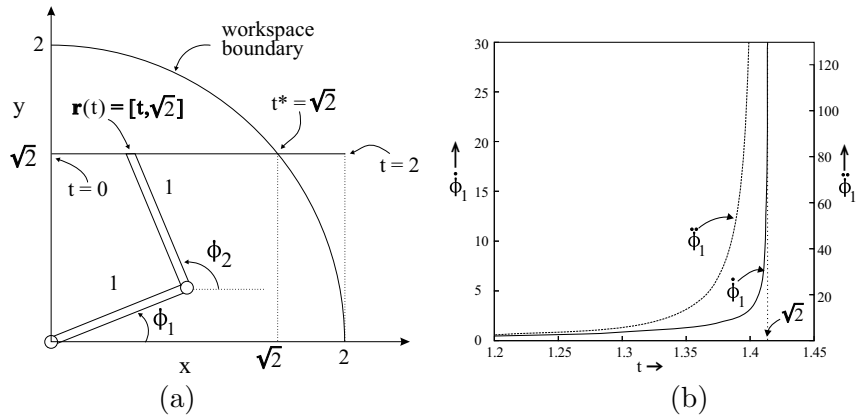

Figure 2. (a) Task path of two-link manipulator (b) Behavior of $\dot{\phi_1}$ and $\ddot{\phi_1}$ along task path.

but are negative as t approaches t^*. Clearly as t approaches $t^*=\sqrt{2}$ the velocities and accelerations increase dramatically in magnitude, as is expected from theoretical considerations, and beyond t^* no solutions exist.

If the further inverse dynamics is done, then, since the accelerations increase to infinity, the corresponding required torques τ_1 and τ_2 to be applied by the actuators on the respective links in order to maintain the prescribed motion, will also increase to infinity as t approaches t^*. The general argument in the previous section, and the evidence presented here for the simple manipulator, indicate that this behavior is in general true for a large number of practical cases where non-assembly or lock-up trajectories may be encountered. The practical significance of this behavior is discussed in the next section.

5. Evaluation of Objective Function for Lock-Up Trajectories

Consider the manipulator depicted in Figure 1 and where, for example, the objective function for a given dimensional design $\mathbf{x} = [x_1, x_2, x_3, x_4, x_5]^T = [l_1, l_2, l_3, x_b, y_b]^T$, is the average absolute torque requirement for execution of the task path given by

$$T_{av}(\mathbf{x}) = \frac{1}{T}\int_0^T (|\tau_1(t)| + |\tau_2(t)| + |\tau_3(t)|)dt \tag{4}$$

where $\tau_i(t)$ denotes the torque applied to link i. Of course, other appropriate formulations involving the torques, such as the average sum of

the squares of the torques or average energy usage over the task path, may also be considered. In practice objective function (4) is minimized subject to the imposition of constraints relating to limits on maximum deliverable absolute torque values, and upper and lower bounds on link lengths. Additionally, constraints may be specified to prevent allowable joint angle ranges from being exceeded, and to prevent violation of geometrical restrictions on the placement of the base.

Assume for the moment that it can be ensured that for all design points during the optimization procedure, the initial point and endpoint of the prescribed path lie within the workspace. If during the optimization procedure a design is obtained that results in lock-up and resultant non-assembly further along the path (between the initial and end point), then obviously the evaluation of the objective function (4) is not possible.

The behavior of the accelerations near lock-up, as discussed in the previous sections, now points to a practical strategy for obtaining a meaningful value for the objective function even if non-assembly is encountered. In practice the kinematic analysis is done at discrete time instants $t_j = j\Delta t,\ j = 1, 2, ..., N$ where Δt is an appropriately small time step and $T = N\Delta t$. The analysis starts at the initial point where assembly is assumed to be possible. Lock-up and non-assembly will therefore be detected at some discrete point along the path if a solution to equation (1) cannot be found. Non-assembly will be evident from failure of the formula for the closed form solution, if it exists, or failure of, for example, the Newton-Raphson method to converge if a numerical solution is sought. If the system is now forced through the lock-up position and the analysis continued at the discretization points for the prescribed path, the analysis will fail at intermediate steps where assembly is no longer possible. However, as assembly at the end position is guaranteed by our assumption above, a point will be reached where assembly is again possible, and the analysis can successfully be continued.

A heuristic procedure to compute a meaningful objective function value for such a lock-up trajectory was previously proposed and successfully applied to the optimal design of planar manipulators by the author and co-worker Berner. This heuristic may now be justified in terms of the theoretical argument and computational evidence presented in the previous two sections. At the integration points t_j where assembly fails, set the respective torques $\tau_i(t_j) := \tau_i(t_s)$ where t_s (close to t^*, $t_s < t^*$), corresponds to the last step at which assembly was successfully carried out and the inverse dynamics could be done. Use these artificial torque values in the numerical integration of (4) to give an associated artificial value for the objective function. This situation is depicted in Figure 3. Because t_s is close to t^*, one expects the values of $|\tau_i(t_s)|$

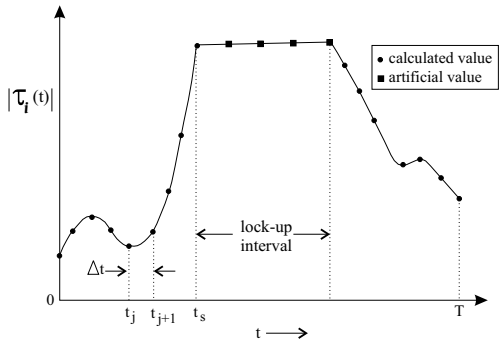

Figure 3. Numerically computed absolute torque values, $|\tau_i(t)|$, along lock-up trajectory.

to be relatively large, so that the computed value for T_{av} will be very high. Also, the longer the non-assembly time interval, the larger the expected value for the artificial objective function. Thus the objective function contains a meaningful penalty component in the case where non-assembly occurs along the task path. Any minimization procedure employing the above artificial integration procedure for evaluating the objective function, should drive the design away from lock-up trajectories with artificially high objective function values. This is indeed borne out by the work of Snyman and Berner.

6. Ensuring Assembly at Endpoints of Task Path

In the above it was assumed that for all design points occurring during the optimization procedure, assembly is at least possible at the beginning and end of the task path. If not, the evaluation of the objective function, real or artificial, corresponding to (4) is of course impossible since the integration in (4) cannot be started or completed. The conditions, that will ensure assembly in the neighbourhood of the respective extreme points, may be expressed in terms of relationships between the design variables that must be satisfied at the start and end of the time interval $[0, T]$. These two assembly conditions can be expressed in terms of inequality constraints of the general form: $g_i(\mathbf{x}) \leq 0,\ i = 1, 2.$

Thus, to overcome non-assembly at the two extreme points, the specific procedure adopted during the optimization process is to replace the objective function, corresponding to (4), by a single penalty function $P(\mathbf{x})$ containing only the assembly constraints, i.e. by $P(\mathbf{x}) = \beta_1(g_1(\mathbf{x}))^2 + \beta_2(g_2(\mathbf{x}))^2$, where $\beta_i = 0$ if $g_i(\mathbf{x}) \leq 0$ and $\beta_i = 1$ if $g_i(\mathbf{x}) > 0$, whenever one or both assembly constraints are violated. The minimization is then continued with the penalty function until the design returns

to a region where both assembly constraints are met. At this point the optimization reverts to the minimization of objective function (4) subject to the normal physical constraints. In spite of the discontinuities inherent in the switching from objective function to penalty function, it is found that the optimization can easily be performed using the robust gradient-based leap-frog algorithm [Snyman, 2005].

7. Conclusion

In an attempt to minimize the torque requirement in the optimal synthesis of a serially linked planar manipulator, an optimization algorithm is inclined to drive the design to one which can no longer be assembled at some point along the task trajectory. Here, a previously proposed ad hoc procedure for avoiding non-assembly during optimal synthesis, and which was successfully applied to specific individual synthesis problems, is reviewed and justified by considering the behavior of the general kinematic and driving constraint equations of any manipulator in the neighborhood of non-assembly. The analysis fully justifies the use of the proposed methodology in the general case. The application of this approach, in which continuation of the optimization process is ensured in order to produce a feasible optimum design, may therefore be expected to be successful in the optimal synthesis of more complicated and general three-dimensional serially linked manipulators.

References

Berner, D.F. and Snyman, J.A. (1999), The influence of joint angle constraints on the optimum design of a manipulator following a complicated path, *Computers and Mathematics with Applications*, vol. 18, pp. 111–124.

Erdman, A.G. and Sandor, G.N. (1997), *Mechanism design: analysis and synthesis*, Upper Saddle River, New Jersey, Prentice-Hall.

Haug, E.J. (1989), *Computer-aided kinematics and dynamics of mechanical systems*, Boston, Allyn and Bacon.

Minnaar, R.J., Tortorelli, D.A., and Snyman, J.A. (2001), On nonassembly in the optimal dimensional synthesis of planar mechanisms, *Structural and Multidisciplinary Optimization*, vol. 21, pp. 215–221.

Snyman, J.A. and Berner, D.F. (1999a), A mathematical optimization methodology for the optimal design of a planar robotic manipulator, *International Journal for Numerical Methods in Engineering*, vol. 44, pp. 535–550.

Snyman, J.A. and Berner, D.F. (1999b), The design of a planar robotic manipulator for optimum performance of prescribed tasks, *Structural and Multidisciplinary Optimization*, vol. 18, pp. 95–106.

Snyman, J.A. (2005), *Practical mathematical optimization: An introduction to basic optimization theory and classical and new gradient-based algorithms*, New York, NY, Springer.

Design of Mechanisms

COMPLEXITY ANALYSIS FOR THE CONCEPTUAL DESIGN OF ROBOTIC ARCHITECTURES

Waseem A. Khan, Stéphane Caro, Damiano Pasini, Jorge Angeles
Department of Mechanical Engineering, McGill University
817, Sherbrooke St. West, Montreal, QC, Canada, H3A 2K6
{wakhan, caro}@cim.mcgill.ca, damiano.pasini@mcgill.ca, angeles@cim.mcgill.ca

Abstract We propose a formulation capable of measuring the complexity of kinematic chains at the conceptual stage in robot design. As an example, two realizations of the Schönflies displacement subgroup are compared.

Keywords: Conceptual design, complexity, kinematic chains, displacement subgroups

1. Introduction

We propose here a formulation capable of measuring the complexity of the kinematic chains of robotic architectures at the conceptual-design stage. The motivation lies in providing an aid to the robot designer when selecting the best design alternative among various candidates at the early stages of the design process, when a parametric design is not yet available.

In this paper, the complexity of three lower kinematic pairs (LKPs), the revolute, the prismatic and the cylindrical pairs, is first obtained. Then, a formulation to measure the complexity of kinematic bonds (Hervé, 1978; Hervé, 1999) is introduced. Based on this formulation, the complexity of five displacement subgroups—the helical pair is left out in this paper—is established. Finally, as an application, two realizations of the Schönflies displacement subgroup (Angeles, 2004; Company et al., 2001) are compared.

2. Kinematic Pair, Kinematic Bond and Kinematic Chain

A *kinematic bond* is defined as a set of displacements stemming from the product of displacement subgroups (Hervé, 1978; Angeles, 2004), the bond itself not necessarily being a subgroup. We denote a kinematic bond by $\mathcal{L}(i, n)$, where i and n stand for the integer numbers associated

J. Lenarčič and B. Roth (eds.), Advances in Robot Kinematics, 359–368.

with the two end links of the bond. There are six basic displacement subgroups $\mathcal{R}(\mathcal{A})$, $\mathcal{P}(\mathbf{e})$, $\mathcal{H}(\mathcal{A}, p)$, $\mathcal{C}(\mathcal{A})$, $\mathcal{F}(\mathbf{u}, \mathbf{v})$ and $\mathcal{S}(O)$ (Hervé, 1978; Hervé, 1999; Angeles, 2004), each associated with a *lower kinematic pair* (LKP). In this notation, $\mathcal{A}$ stands for the axis of the kinematic pair in question; $\mathbf{e}$, $\mathbf{u}$ and $\mathbf{v}$ are unit vectors, O is a point denoting the center of the spherical pair; and p is the pitch of the helical pair.

A kinematic bond is realized by a *kinematic chain*. A kinematic chain is the result of the coupling of rigid bodies, called links, via *kinematic pairs*. When the coupling takes place in such a way that the two links share a common surface, a lower kinematic pair results; when the coupling takes place along a common line or a common point, a *higher kinematic pair* is obtained. Examples of higher kinematic pairs include gears and cams.

There are six lower kinematic pairs, namely, revolute R, prismatic P, helical H, cylindrical C, planar F, and spherical S. These pairs can be regarded as the generators of the six displacement subgroups listed above. Although the displacement subgroups can be realized by their corresponding LKPs, it is possible to realize some of their displacement subgroups by appropriate kinematic chains. A common example is that of the $\mathcal{C}(\mathcal{A})$ which, besides the C pair, can be realized by a suitable concatenation of a P and a R pair.

3. The Loss of Regularity of a Surface

In this section, we propose a measure of the complexity of a given surface. We base this measure on the concept of *loss of regularity LOR*, defined as

$$LOR \equiv \frac{||\kappa'_{rms}||_2}{||\kappa_{rms}||_2} \tag{1}$$

where κ_{rms} is the r.m.s. of the two principal curvatures at a point of the surface, κ'_{rms} is the derivative of κ_{rms} with respect to a dimensionless parameter σ. The LOR is inspired from Taguchi's *loss function* (Taguchi, 1993), and measures the diversity of the curvature distribution of the given surface, the LOR of the surfaces associated with five lower kinematic pairs, being found below.

LOR of the Surface of the R Pair. Typically, the surface associated with the revolute pair is assumed to be a cylinder. However, in order to realize the $\mathcal{R}(\mathcal{A})$ subgroup, the translation in the axial direction of the cylindrical surface must be constrained. This calls for additional surfaces, which must then be blended smoothly with the cylindrical surface in order to avoid curvature discontinuities.

The above discussion reveals that the surface associated with a revolute pair has to be a surface of revolution but cannot be an extruded surface; the cylindrical surface is both. We should thus look for a generatrix $\mathcal{G}$ other than a straight line, but with G^2-continuity everywhere. The latter would allow a shaft of appropriate diameter to be blended smoothly on both ends. The simplest realization of $\mathcal{G}$ is a 2-4-6 polynomial, namely, $P(x) = -x^6 + 3x^4 - 3x^2 + 1$.

Figure 1(a) is a 3D rendering of the surface $\mathcal{S}_\mathrm{R}$ obtained by revolving the generatrix $\mathcal{G}$ about the x-axis, so as to blend with a cylinder of unit radius.

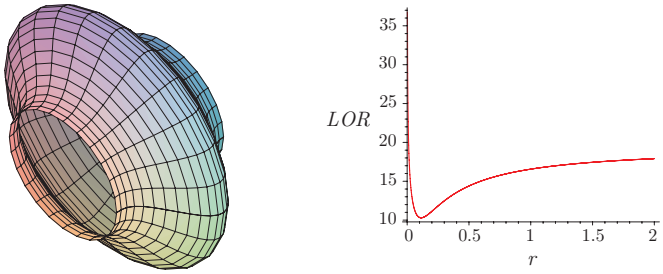

(a) (b)

Figure 1. (a) A 3D rendering of the surface of revolution $\mathcal{S}_\mathrm{R}$ and (b) its LOR vs. shaft radius r.

The two principal curvatures of $\mathcal{S}_\mathrm{R}$ are given by (Oprea, 2004)

$$\kappa_\mu = \frac{-y''}{(1+y'^2)^{3/2}}, \quad \kappa_\pi = \frac{1}{y(1+y'^2)^{1/2}} \tag{2}$$

where $y = P + r$ and r is the radius of the cylindrical shaft. The r.m.s. of the two principal curvatures, κ_μ and κ_π, can now be obtained, i.e.,

$$\kappa_{rms} = \sqrt{\frac{1}{2}(\kappa_\mu^2 + \kappa_\pi^2)} \tag{3}$$

Next, we need to choose a suitable length parameter s and a homogenizing length l. A natural choice for s is the distance traveled along $\mathcal{G}$; l can be taken as the total length of the generatrix, the dimensionless parameter being $\sigma \equiv s/l$.

The LOR of $\mathcal{S}_\mathrm{R}$ can now be evaluated by eq. (1), and depicted in Fig. 1(b). Notice that LOR_R is not monotonic in r. Further, LOR_R reaches a minimum of 10.2999 at $r = 0.1132$. We thus assign $LOR_\mathrm{R} = 10.2999$.

LOR of the Surface of the P Pair. The most common cross section of a P pair is a dovetail, but we might as well use an ellipse, a square or a rectangle. A family of smooth curves that continuously leads from a circle to a rectangle is known as Lamé curves (Gardner, 1965). In their simplest form, these curves are given by $x^m + y^m = 1$, where $m > 0$ is an even integer. When $m = 2$, the corresponding curve is a circle of unit radius, with its center at the origin of the x-y plane. As m increases, the curve becomes flatter and flatter at its intersections with the coordinate axes, becoming more like a square. For $m \to \infty$, the curve is a square of sides equal to two units of length and centered at the origin. A Fourier analysis based on the curvature of these curves confirms the intuitively accepted notion that the spectral richness, or diversity, of the curvature increases with m (Khan, Caro, Pasini and Angeles, 2006).

The LOR of the surface of the prismatic pair obtained by extruding a square or a rectangle is expected to have a very high value. A Lamé curve L with $m = 4$ is plausibly the best candidate for the cross section of the prismatic pair. This curve is shown in Fig. 2(a). Figure 2(b) is a 3D rendering of the surface $\mathcal{S}_\mathrm{P}$ obtained by extruding L along the z-axis.

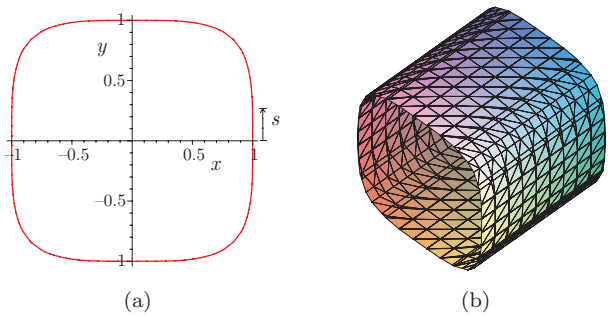

(a) (b)

Figure 2. (a) Cross section of the prismatic pair; (b) A 3D rendering of the extruded surface.

The two principal curvatures of $\mathcal{S}_\mathrm{P}$ are given by

$$\kappa_\mu = \frac{x''y' - y''x'}{(x'^2 + y'^2)^{3/2}}, \quad \kappa_\pi = 0 \tag{4}$$

The r.m.s. of the two principal curvatures, κ_μ and κ_π thus reduces to $\kappa_{rms} = \kappa_\mu$. The length parameter s and the homogenizing length l are, correspondingly, the distance traveled along $\mathcal{S}_\mathrm{P}$, depicted in Fig. 2(a), and the total length l of the Lamé curve, whence $\sigma \equiv s/l$.

The loss of regularity LOR_P of $\mathcal{S}_\mathrm{P}$, the surface associated with the P pair, is thus $LOR_\mathrm{P} = 19.6802$.

LOR of the Surface of the F Pair. The F pair is a generator of the planar subgroup $\mathcal{F}$ and requires two parallel planes, separated by an arbitrary distance. In order to avoid corners and edges, a suitable 'blending option' is the use of the quartic Lamé curve. The concept is shown in Fig. 3(a). Notice that the female element of the pair is an extruded surface $\mathcal{S}_{\mathrm{F}f}$ while the male element is a solid of revolution $\mathcal{S}_{\mathrm{F}m}$.

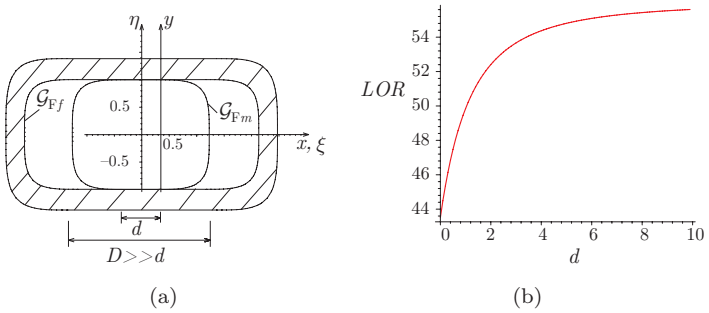

Figure 3. (a) Cross section of the simplest realization of the planar pair; (b) LOR vs. diameter d of the male element.

The LOR of the planar pair, LOR_{F}, is defined by both the male and the female elements. Further, the contribution of a flat surface to the LOR is zero, a plane being a sphere of infinite radius. We thus obtain

$$LOR_{\mathrm{plane}} = \lim_{\kappa \to 0} \frac{||\kappa'_{rms}||_2}{||\kappa_{rms}||_2} = \lim_{\kappa \to 0} \frac{0}{||\kappa_{rms}||_2} = 0 \tag{5}$$

The LOR of the female element $LOR_{\mathrm{F}f}$ is thus the same as that of the prismatic pair, that of the male element $LOR_{\mathrm{F}m}$ being evaluated below, namely,

$$\kappa_\mu = \frac{\xi''\eta' - \eta''\xi'}{(\xi'^2 + \eta'^2)^{3/2}}, \quad \kappa_\pi = \frac{1}{\xi\sqrt{1+\xi'^2}} \tag{6}$$

where, from Fig. 3(a), $\eta = y$ and $\xi = x + d/2$, and $d/2$ is the distance between the y and the η axes. The length parameter s and the homogenizing length l are, correspondingly, the distance traveled along the generatrix $\mathcal{G}_{\mathrm{F}m}$ depicted in Fig. 3(a) and its total length l, whence $\sigma \equiv s/l$.

Figure 3(b) is a graph between the LOR of $\mathcal{S}_{\mathrm{F}m}$, $LOR_{\mathrm{F}m}$, and the diameter d. Notice that $LOR_{\mathrm{F}m}$ grows monotonically with d. Further, $LOR_{\mathrm{F}m}$ reaches a limit of approximately 56.0399, whence $LOR_{\mathrm{F}m} = 56.0399$. Finally, the LOR_{F} is defined as $LOR_F \equiv (LOF_{\mathrm{F}f} + LOF_{\mathrm{F}m})/2 = 37.8601$.

LOR of the Surface of the C and S Pairs. The r.m.s. of the principal curvatures of the cylindrical and the spherical surfaces is constant. Hence, the loss of regularity is zero for the two surfaces, i.e., $LOR_{\mathrm{C}} = LOR_{\mathrm{S}} = 0$.

4. The Geometric Complexity of LKPs

We introduce here the *geometric complexity* of the LKPs based on the LOR introduced earlier: the geometric complexity $K_{G|\mathrm{x}}$ of a pair x is

$$K_{G|\mathrm{x}} \equiv \frac{LOR_{\mathrm{x}}}{LOR_{\max}} \tag{7}$$

where LOR_{x} is the loss of regularity of the surface associated with the pair x and $LOR_{\max} \equiv \max\{LOR_{\mathrm{R}}, LOR_{\mathrm{C}}, LOR_{\mathrm{P}}, LOR_{\mathrm{F}}, LOR_{\mathrm{S}}\}$. The geometric complexity of the five LKPs of interest is, in the foregoing order: 0.2721; 0; 0.5198; 1.0; and 0.

5. The Complexity of Kinematic Bonds

In this section we lay the foundations for the evaluation of the complexity of any kinematic bond. We first restrict our study to kinematic bonds that are realizable using LKPs; the study of bonds including higher kinematic pairs is as yet to be reported. Next, we define the complexity $K \in [0,1]$ of a kinematic chain as a *convex combination* (Boyd, 2004) of its various complexities:

$$K = w_J K_J + w_N K_N + w_L K_L + w_B K_B \tag{8}$$

where $K_J \in [0,1]$ is the joint-type complexity, $K_N \in [0,1]$ the joint-number complexity, $K_L \in [0,1]$ the loop-complexity, and $K_B \in [0,1]$ the bond-realization complexity, with w_J, w_N, w_L, and w_B denoting their corresponding weights, such that $w_J + w_N + w_L + w_B = 1$.

5.1 Joint-Type Complexity K_J

Joint-type complexity is that associated with the type of LKPs used in a kinematic chain. We define a *preliminary* joint-type complexity $K_{J|\mathrm{x}}$ as the geometric complexity $K_{G|\mathrm{x}}$ of the x pair, the joint-type complexity K_J of a kinematic bond $\mathcal{L}$ being defined as

$$K_{J|\mathcal{L}} = \frac{1}{n}(n_R K_{J|R} + n_P K_{J|P} + n_C K_{J|C} + n_F K_{J|F} + n_S K_{J|S}) \tag{9}$$

where n_R, n_P, n_C, n_F and n_S are the number of revolute, prismatic, cylindrical, planar and spherical joints, respectively, while n is the total number of pairs.

5.2 Joint-Number Complexity K_N

The joint-number complexity K_N is defined as that associated with a kinematic bond $\mathcal{L}$ by virtue of its number of kinematic pairs, with respect to the minimum required to realize the same set of displacements. We adopt the expression

$$K_{N|\mathcal{L}} = 1 - \exp(-q_N N); \quad N = n - m \tag{10}$$

where n is the number of joints used in the realization of the bond $\mathcal{L}$, m is the minimum number of LKPs required to produce a displacement of bond $\mathcal{L}$, and q_N is the *resolution parameter*, to be adjusted according to the resolution required. Note that $K_{N|\mathcal{L}} \in [0, 1]$.

5.3 Loop-Complexity K_L

The loop-complexity $K_{L|\mathcal{L}}$ of a kinematic bond is that associated with the number of independent loops of the kinematic chain connecting the two links, i and n, of a kinematic bond $\mathcal{L}$, with respect to the minimum required to produce the prescribed displacement set. The loop-complexity can be evaluated by means of the formula:

$$K_{L|\mathcal{L}} = 1 - \exp(-q_L L); \quad L = l - l_m \tag{11}$$

where l is the number of kinematic loops, l_m the minimum number of loops required to realize such a bond and q_L the resolution paramter.

5.4 Bond-Realization Complexity K_B

The bond-realization complexity is associated with the geometric constraints involved in the realization of a kinematic bond. The complexity of geometric constraints may be evaluated by *the number of floating-point operations (flops) required to realize a geometric constraint*. One flop is customarily defined as the combination of one addition and one multiplication. Lack of space prevents us from including the flop analysis of the geometric constraints, which is reported in (Khan, Caro, Pasini and Angeles, 2006). A summary of the results of this analysis is displayed in Table 1.

The bond-realization complexity based on the geometric constraints of its realization can now be defined as

$$K_{B|\mathcal{L}} = 1 - \exp(-q_B f) \tag{12}$$

where f is the number of floating-point operations corresponding to the constraints, q_B being the corresponding resolution parameter.

Table 1. Realization cost of some geometric constraints.

Geometric constraint	Representation	flops	total flops
Intersection of two lines	$(\mathbf{e}_1 \times \mathbf{e}_2) \cdot \mathbf{q}_{21} = 0$	$5A + 9M$	9
Angle of intersection	$\mathbf{e}_1 \cdot \mathbf{e}_2 = \cos\alpha$	$2A + 3M$	3
Parallelism b/w two lines	$\mathbf{e}_1 \times \mathbf{e}_2 = \mathbf{0}_3$	$3A + 6M$	6
Length of common normal	$\|\|\mathbf{q}_{21} - (\mathbf{q}_{21} \cdot \mathbf{e}_1)\,\mathbf{e}_1\|\|_2^2 = d^2$	$7A + 9M$	9
Intersection of three lines	$\det(\mathbf{C}) = 0$	$30A + 36M$	36
$\mathbf{e}_1$, $\mathbf{e}_2$ and $\mathbf{e}_3$ span 3D space	$\det([\,\mathbf{e}_1 \quad \mathbf{e}_2 \quad \mathbf{e}_3\,]) \neq 0$	$5A + 9M$	9

Definition of the resolution parameters. Three resolution parameters, namely q_N, q_L and q_B were introduced above. These parameters provide an appropriate resolution for the complexity at hand. Since the foregoing formulation is intended to compare the complexities of two or more kinematic chains, it is reasonable to assign a complexity of 0.9 to the chain with maximum complexity and hence evaluate the normalizing constant, i.e., for $J = B,\ L,\ N$,

$$q_J = \begin{cases} -\ln(0.1)/J_{\max}, & \text{for} \quad J_{\max} > 0; \\ 0, & \text{for} \quad J_{\max} = 0. \end{cases}$$

6. The Complexity of the Displacement Subgroups

In Section 5, we assigned the joint-type complexity of the lower kinematic pairs as the geometric complexity of the surface associated with the LKPs. The F pair requires the machining of two parallel planes, separated by an arbitrary distance. Further, the F pair poses an accessibility problem to the male element of the coupling, this pair being seldom used in practice as such. Moreover, precision spherical pairs are expensive and difficult to manufacture.

Hence, using the geometric complexity of the LKPs as the corresponding joint-type complexities is not justified. In order to solve this problem we must look at the complexity of the displacement subgroups generated by the five LKPs studied here.

The basic displacement subgroups can be realized either by their corresponding pairs or by a kinematic bond. The complexity of the displacement subgroups is defined as the complexity of the realization that exhibits the minimum kinematic bond complexity.

The complexity of the five displacement subgroups generated by the LKPs considered here can now be evaluated. In this vein, we apply the formulation introduced in the previous section to the different realizations of the displacement subgroups under study. Table 2 displays some

Table 2. Complexity of five displacement subgroups.

Subgroup	Desc.	K_J	K_N	K_B	K
$\mathcal{R}(\mathcal{A})$	R	0.2721/1	$1-e^{-q_N(0)}$	$1-e^{-q_B(0)}$	0.0907
$\mathcal{P}(\mathbf{e})$	P	0.5198/1	$1-e^{-q_N(0)}$	$1-e^{-q_B(0)}$	0.1733
$\mathcal{C}(\mathcal{A})$	C	0/1	$1-e^{-q_N(0)}$	$1-e^{-q_B(0)}$	0
	PR	0.7919/2	$1-e^{-q_N(1)}$	$1-e^{-q_B(6)}$	0.4480
$\mathcal{F}(\mathbf{u},\mathbf{v})$	PPR	1.3117/3	$1-e^{-q_N(2)}$	$1-e^{-q_B(12)}$	0.5987
	RRR	0.8163/3	$1-e^{-q_N(2)}$	$1-e^{-q_B(12)}$	0.5436
	RPR	1.0640/3	$1-e^{-q_N(2)}$	$1-e^{-q_B(9)}$	0.5412
$\mathcal{S}(O)$	RRR	0.8163/3	$1-e^{-q_N(2)}$	$1-e^{-q_B(45)}$	0.6907
$q_N = -\ln(0.1)/2 = 1.1513; \quad q_B = -\ln(0.1)/45 = 0.0512$					

Table 3. Complexity of two realizations of the Schönflies subgroup.

Description	K_J	K_N	K_L	K_B	K
McGill SMG	2.76/21	$1-e^{-q_N(21-2)}$	$1-e^{-q_L(5-0)}$	$1-e^{-q_B(258)}$	0.68
H4	16.79/22	$1-e^{-q_N(22-2)}$	$1-e^{-q_L(7-0)}$	$1-e^{-q_B(99)}$	0.79
$q_N = -\ln(0.1)/20 = 0.12; q_L = -\ln(0.1)/7 = 0.33; q_B = -\ln(0.1)/258 = 0.01$					

pertinent realizations. The minimum complexity values found for $\mathcal{R}(\mathcal{A})$, $\mathcal{P}(\mathbf{e})$, $\mathcal{C}(\mathcal{A})$, $\mathcal{F}(\mathbf{u},\mathbf{v})$ and $\mathcal{S}(O)$ are, correspondingly, 0.0907, 0.1733, 0, 0.5412 and 0.6907. Normalizing the above results so that the maximum is given a complexity of 1, we obtain the complexities of the five displacement subgroups as

$$K_{J|R} = 0.1313,\ K_{J|P} = 0.2509,\ K_{J|C} = 0,\ K_{J|F} = 0.7836 \qquad (13)$$

Notice that, although these are not the joint-type complexity defined in Section 5, which are rather based on *form* than on *function*, the above values can be used to evaluate the joint-type complexity in eq.(9).

7. Example

We apply our proposed formulation to compute the complexity of two Schönflies-motion generators. The motion capability of this subgroup includes three independent translations and one rotation about an axis of fixed orientation. Figure 4(b) shows the joint and loop graphs of the McGill SMG (Angeles, 2005) and the H4 robot (Company et al., 2001).

Table 3 displays the different complexity values associated with the topology of the two robots. Here, we note that the overall complexity of the McGill SMG is lower than that of the H4 robot.

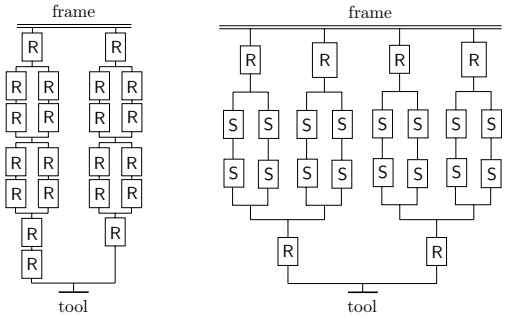

Figure 4. Joint and loop graphs of: (a) the McGill SMG; and (b) the H4 robot.

8. Conclusions

The complexity analysis of kinematic chains at the conceptual stage in robot design was proposed in this paper. To do this, the complexity of five lower kinematic pairs and a formulation of the complexity of kinematic bonds were introduced. The complexity values of two realizations of the Schönflies displacement subgroup were computed.

References

Angeles, J. (2005). The degree of freedom of parallel robots: a group-theoretic approach. *Proc. IEEE Int. Conf. Robotics and Automation,* Barcelona, 1017–1024.

Angeles, J. (2004). The qualitative synthesis of parallel manipulators. *ASME Journal of Mechanical Design*, *126*, 617–624.

Boyd, S. and Vandenberghe, L. (2004). *Convex Optimization*. Cambridge University Press, Cambridge.

Company, O., Pierrot, F., Shibukawa, T., and Koji, M. (2001). *Four-Degree-of-Freedom Parallel Robot*. European Patent EP1084802, March 21.

Gardner, M. (1965). The superellipse: a curve that lies between the ellipse and the rectangle. *Scientific American*, *213*, 222–234.

Hervé, J. (1978). Analyse structurelle des mécanismes par groupes de déplacements. *Mech. Mach. Theory*, *13*, 437–450.

Hervé, J. (1999). The Lie group of rigid body displacements, a fundamental tool for mechanical design. *Mech. Mach. Theory*, *34*, 719–730.

Khan, W.A., Caro, S., Pasini, D. and Angeles, J. (2006). *The Geometric Complexity of Kinematic Chains*. Department of Mechanical Engineering and Centre for Intelligent Machines Technical Report. CIM-TR 0601, McGill University, Montreal.

Oprea, J. (2004). *Differential Geometry and its Applications*. Pearson Prentice Hall, New Jersey.

Taguchi, G. (1993). *Taguchi on Robust Technology Development. Bringing Quality Engineering Upstream*. ASME Press, New York.

ROBUST THREE-DIMENSIONAL NON-CONTACTING ANGULAR MOTION SENSOR

Danny V. Lee
Department of Mechanical and Aeronautical Engineering
University of California Davis
dvxlee@ucdavis.edu

Steven A. Velinsky
Department of Mechanical and Aeronautical Engineering
University of California Davis
savelinsky@ucdavis.edu

Abstract For devices based on a sphere rotating in a cradle, the axis of rotation of the sphere is arbitrary and can change instantaneously. Consequently, a non-contact means of velocity sensing is desirable. For the ball wheel mechanism, which serves as the drive train for a class of omnidirectional mobile robots, most existing methods are not feasible, such as optical techniques based on surface-pattern distinction. Thus, in this paper, a robust, three-dimensional angular velocity sensor based on magnetometry is presented that tracks the orientation of ferromagnet embedded in the sphere. An algorithm based on vector orthogonality is used to approximate the angular velocity vector of the sphere from the sampled orientation data.

Keywords: Motion-tracking, sensor, spherical motion

1. Introduction

In the literature, there are a variety of devices based on a sphere rotating in a cradle. These include: spherical motors as in Chirikjian and Stein 1999, Dehez et al., 2005, spherical continuously variable transmissions as in Ostrowski 2000, Gillespie et al., 2002, and omnidirectional vehicles based on the ball wheel mechanism as in West and Asada 1997, Ferriere et al., 2001. However, according to Stein et al., 2003, there is little work on spherical encoders or other means of three-dimensional, orientation feedback without mechanical coupling.

In this paper, a non-contacting, angular velocity sensor based on magnetometry is presented. The primary application for this sensor is a ball wheel mechanism, which will serve as the drive train in a robust omnidirectional mobile platform. Designed for operation in unstructured environments, the spherical tire will be subject to contamination and

J. Lenarčič and B. Roth (eds.), Advances in Robot Kinematics, 369–376.

wear. As a result, optical encoder techniques that require surface contrast or surface patterning, as proposed by Garner et al., 2001, Stein et al., 2003, are not feasible for this application. For non-contact motion tracking in demanding environments, magnetic sensing is commonly employed. Jacobs and Nelson 2001 use magnetic sensors to track abdominal cavity deflection in crash test dummies; Donecker et al., 2003 use magnetic sensing for vehicle guidance; and Weitschies et al., 1994, Prakash and Spelman 1997 use magnetic marker tracking for non-invasive gastrointestinal transit monitoring.

Information on the configuration of a magnetic source provides a means of determining the configuration of the body to which the sources are attached. In this case, the goal is to determine the axis of rotation and angular speed of the sphere given the absolute position of a point on the sphere, which the magnetometry scheme provides. To solve this inverse problem, a method based on vector orthogonality will be employed. This approach is described in Panjabi 1979, Halvorsen et al., 1999 1999 for applications in limb motion tracking in biomechanics.

2. Magnetometry Scheme

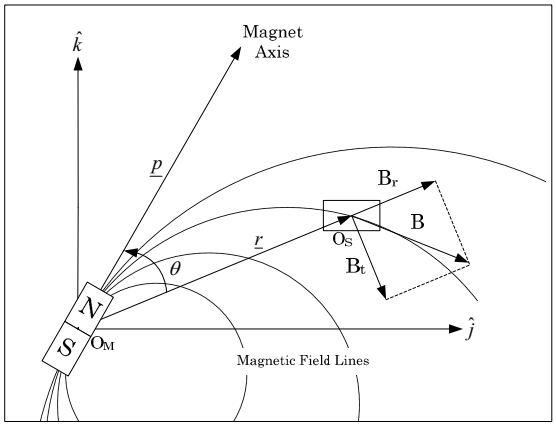

Figure 1. Schematic of field lines from magnetic dipole.

The proposed magnetometry scheme is based on tracking the magnetic flux density vector of a cylindrically-symmetric ferromagnet, which will be modeled as a magnetic dipole. Generally, the theoretical field equations are a function of six configuration variables and physical properties of the magnet. For this analysis it will be assumed that the sphere and the magnet are both fixed in translation and both are perfectly centered at the origin of an inertial reference frame.

Consider the planar case as shown in Fig. 1. The magnet is located at origin O_m and the sensor is located at point O_S. Unit vector $\hat{p}$ defines the magnet axis, $\underline{r}$ is the position vector from O_m to O_S, and θ is the relative orientation between $\underline{r}$ and $\hat{p}$. The magnetic flux density vector $\underline{B}$ is decomposed into radial and tangential components B_r and B_t, and are, respectively,

$$\left\{ \begin{array}{l} B_r = \dfrac{\mu_0 M}{2\pi r^3}\cos\theta \\ B_t = \dfrac{\mu_0 M}{4\pi r^3}\sin\theta \end{array} \right\}, \tag{1}$$

where μ_0 is the permeability and M is the dipole moment. The relationship between the field components and the configuration variables can be found in most texts on electromagnetic fields, such as Shadowitz 1975. For the three-dimensional case, the expressions in Eq. 1 can be used in the plane defined by vectors $\hat{p}$ and $\underline{r}$. It remains, then, to find the relationship between the radial and tangential field components and the the three-dimensional, measured field components. A diagram of the configuration is shown in Fig. 2.

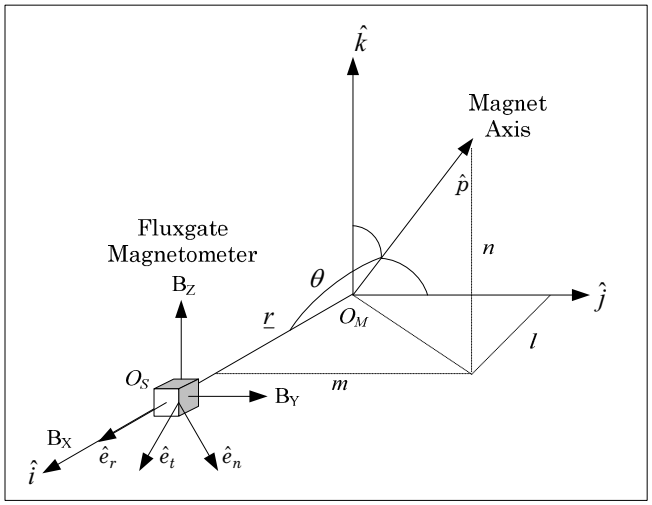

Figure 2. Sensor Diagram.

The magnetometer is positioned along the x-axis of the inertial reference frame. This significantly simplifies the geometry of the problem. {Bx,By,Bz} are the orthogonal field components from the magnetometer

and {l,m,n} are the direction cosines used to parameterize the magnet axis $\hat{p}$. Next, orthogonal triad $\{\hat{e}_r, \hat{e}_n, \hat{e}_t\}$ is positioned at O_S and defined as,

$$\left\{ \hat{e}_r = \frac{\underline{r}}{\|r\|}, \hat{e}_n = \frac{\hat{e}_r \times \hat{p}}{\|\hat{e}_r \times \hat{p}\|}, \hat{e}_t = \hat{e}_r \times \hat{e}_n \right\}. \tag{2}$$

Unit vector $\hat{e}_r$ is directed along the radial vector, $\hat{e}_n$ is a unit vector normal to the plane defined by $\hat{p}$ and $\underline{r}$, and $\hat{e}_t$ is the tangential unit vector in the $\hat{e}_n$ -plane, orthogonal to $\hat{e}_r$. Moreover, the trigonometric functions in Eq. 1 can be expressed as a function of the direction cosines of $\hat{p}$; as such,

$$\left\{ \begin{matrix} \cos\theta = l \\ \sin\theta = \sqrt{m^2 + n^2} \end{matrix} \right\}. \tag{3}$$

For an arbitrary orientation of $\hat{p}$, the theoretical magnetic flux density vector can be expressed as,

$$\underline{B}_{TH} = B_r \hat{e}_r + B_t \hat{e}_t . \tag{4}$$

Eq. 2 and Eq. 3 provide the proper sign conventions through the transformations. Substituting Eq. 1-3 into Eq. 4 results in the following expression:

$$\underline{B}_M = \begin{bmatrix} B_x \\ B_y \\ B_z \end{bmatrix}_M \cong \underline{B}_{TH} = \begin{bmatrix} \frac{\mu_0 M}{2\pi r^3} l \\ -\frac{\mu_0 M}{4\pi r^3} m \\ -\frac{\mu_0 M}{2\pi r^3} n \end{bmatrix}. \tag{5}$$

Eq. 5 states that the direction cosines of $\hat{p}$ are linearly proportional to the measured field components. In other words, this scheme directly measures the motion of vector, fixed relative to the sphere, under spherical motion. It remians to solve the inverse kinematics problem of extracting the angular velocity vector of the sphere given this data.

3. Inverse Kinematics of Spherical Motion

Calculating the angular displacement given the axis of rotation and the trajectory of a point on the body, is a straightforward matter; several techniques are shown in Murray et al., 1994. However, determining the orientation of the rotation axis and the angular displacement, given only the trajectory of a point, is not well established. A method for estimating these values can be found in Halvorsen et al., 1999. In this work, two displacements are used to locate the instantaneous axis of rotation for

limb motion. More specifically, each of these displacement vectors represent a plane; the axis of rotation is defined by the intersection of these planes. Halvorsen's method involves a quadratic optimization problem developed for post-processing. For applications in vehicle tracking, a real-time method is necessary. The scheme presented below is based on Halvorsen's concept of vector orthogonality but results from a direct calculation of the on-line sampled data.

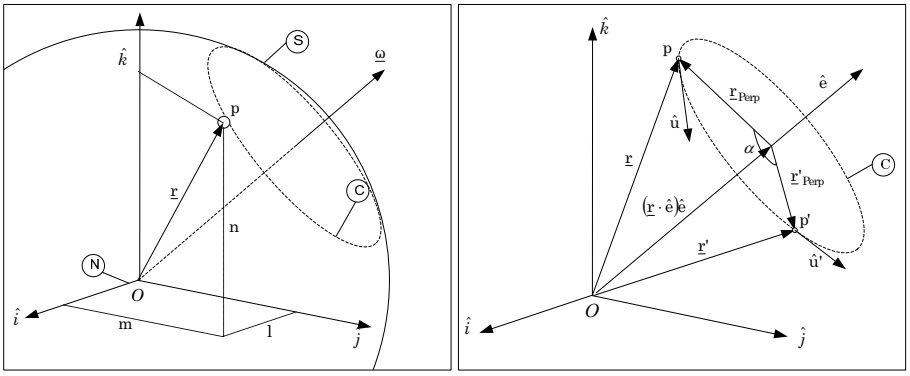

Figure 3. Diagram for (a) general system kinematics and (b) planar sub-problem.

Fig. 3(a) is a diagram for the problem formulation. The position vector $\underline{r}$ of point p on sphere S is parameterized by the direction cosines {l,m,n}, which is now a measured quantity from the magnetometry scheme. As S rotates with angular velocity $\underline{\omega}$, p follows the circular arc C. Fig. 3(b) illustrates the vector relations of this motion; $(\underline{r}.\hat{e})\hat{e}$ is the projection of position vector $\underline{r}$ along the axis of rotation, denoted by unit vector $\hat{e}$, and projection $\underline{r}_{Perp}$ is related to the other configuration variables by:

$$\underline{r}_{Perp} \times \underline{r}'_{Perp} = \left|\underline{r}_{Perp}\right|\left|\underline{r}'_{Perp}\right| \sin\alpha \, \hat{e}. \tag{6}$$

All the variables in Eq. 6 are unknown since the projections cannot be made until the axis of rotation is determined. However, following Halvorsen's work $\underline{r}_{Perp}$ can be replaced with a vector $\hat{u}$, which represents the displacement of p and calculated by normalizing its instantaneous tangential velocity p; as such,

$$\hat{u} = \frac{\underline{v}_p}{\left|\underline{v}_p\right|} = \frac{\dot{\underline{r}}}{\left|\dot{\underline{r}}\right|}. \tag{7}$$

Substituting $\hat{u}$ for $\underline{r}_{Perp}$ and making a small angle approximation, Eq. 6 becomes,

$$\hat{u} \times \hat{u}' = \alpha \, \hat{e} \, . \tag{8}$$

Eq. 8 is often called the rotation vector for α is the radian rotation of $\hat{u}$. Dividing by the period T between samples results in the approximate angular velocity vector; as such,

$$\frac{\hat{u}(t - T) \times \hat{u}(t)}{T} = \frac{\alpha(t)}{T} \hat{e} \approx \omega(t) \, . \tag{9}$$

4. Experimental Verification

To verify this scheme a rod magnet rotated by a DC motor and an Applied Physics Systems (APS) 535 fluxgate magnetometer was used to track the resulting field. The magnet was positioned 6-inches from the sensor origin. The rotation speed is stepped through a range of values for comparison with the theoretical calculation. The maximum commanded speed corresponds to a desired vehicle speed of approximately 5 mph. The raw and filtered direction cosine data is shown in Fig. 4(a) and the calculated tangential velocity components are shown in Fig. 4(b).

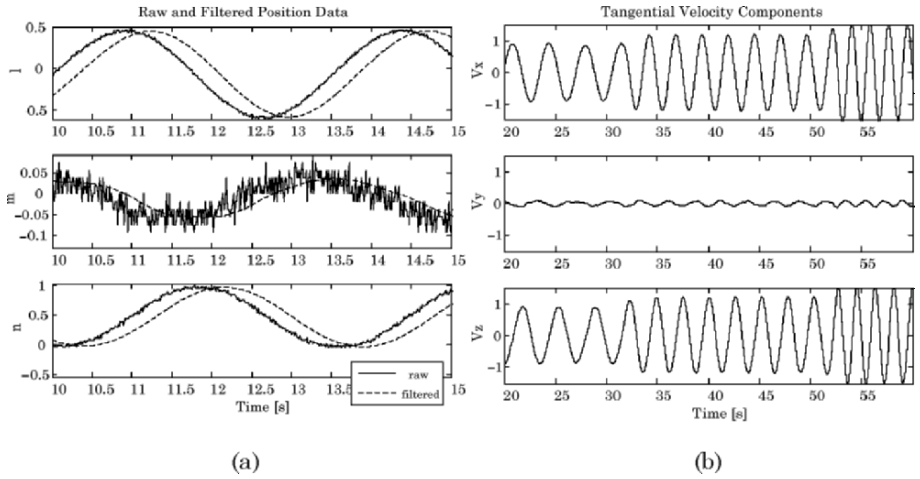

Figure 4. Experimental data for (a) position and (b) velocity.

The raw data is processed with a second order Butterworth filter and the differentiations were made using an ideal digital differentiator. While these functions were chosen for convenience, the signal is always sinusoidal in nature and therefore numerical differentiation of the on-

line sampled data is well-behaved. Fig. 5(a) is the radian rotation of the magnet about the orthogonal axes of the inertial reference frame at each sample, essentially the output of Eq. 8. The sensed speed compared to the commanded speed is shown in Fig. 5(b).

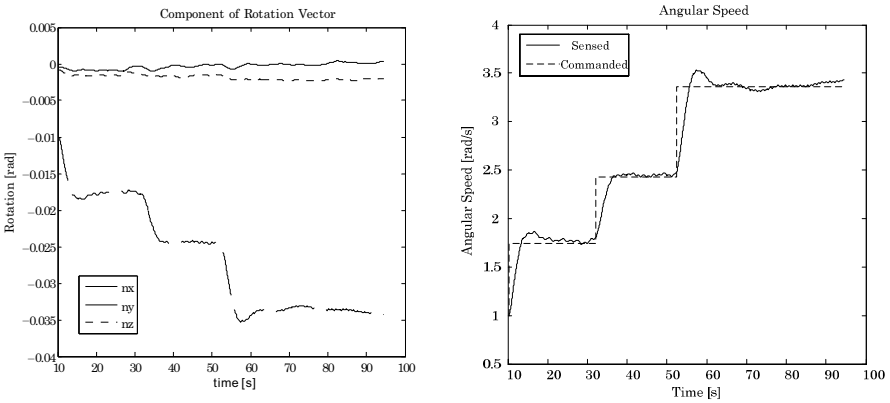

(a) (b)

Figure 5. Sensor output (a) rotation vector and (b) angular speed.

For the results presented, the axis of rotation was aligned with the y-axis of the magnetometer. Tests with the axis oriented relative to the sensor were also carried out with equally promising results. A more precise test fixture is being developed with optical encoders to track transients as the axis of rotation changes orientation relative to the sensor.

5. Conclusion

A three-dimensional, non-contacting, angular velocity sensor based on magnetometry has been presented. The sensing scheme tracks the orientation of the axis of a cylindrically-symmetric ferromagnet. A vector-orthogonality approach is used to approximate the angular velocity vector from the sampled orientation data. Initial feasibility testing has clearly shown the potential of the approach.

References

Chirikjian, G. S. and D. Stein (1999). "Kinematic design and commutation of a spherical stepper motor." *IEEE/ASME Transactions on Mechatronics* **4**(4): 342-353.

Dehez, B., V. Froidmont, D. Grenier and B. Raucent (2005). "Design, modeling and first experimentation of a two-degree-of-freedom spherical actuator." *Robotics and Computer-Integrated Manufacturing* **21**(3): 197-204.

Donecker, S. M., T. A. Lasky and B. Ravani (2003). "A Mechatronic Sensing System for Vehicle Guidance and Control." *IEEE/ASME Transactions on Mechatronics* **8**(4): 500-510.

Ferriere, L., G. Campion and B. Raucent (2001). "ROLLMOBS, A New Drive System for Omnimobile Robots." *Robotica* **19**(1): 1-9.

Garner, H., M. Klement and K. M. Lee (2001). "Design and Analysis of an Absolute Non-Contact Orientation Sensor for Wrist Motion Control." *IEEE/ ASME International Conference on Advanced Intelligent Mechatronics, AIM* 1: 69-74.

Gillespie, R. B., C. A. Moore, M. Peshkin and J. E. Colgate (2002). "Kinematic Creep in a Continuously Variable Transmission: Traction Drive Mechanics for Cobots.**"** *Transactions of the ASME Journal of Mechanical Design* **124**(4): 713-722.

Halvorsen, K., M. Lesser and A. Lundberg (1999). "New Method for Estimating the Axis of Rotation and the Center of Rotation." *Journal of Biomechanics* **32**(11): 1221-1227.

Jacobs, B. C. and C. V. Nelson (2001). *Development and Testing of a Magnetic Position Sensor System for Automotive and Avionics Applications*. Proceedings of SPIE – The International Society for Optical Engineering.

Murray, R. M., Z. Li and S. S. Sastry (1994). *A Mathematical Introduction to Robotic Manipulation*. Boca Raton, CRC Press.

Ostrowski, J. P. (2000). *Controlling more with less using nonholonomic gears.* 2000 IEEE/RSJ International Conference on Intelligent Robots and Systems, Oct. 31-Nov. 5 2000, Takamatsu, Institute of Electrical and Electronics Engineers Inc.

Panjabi, M. (1979). "Center and angles of rotation of body joints: A study of errors and optimization." *Journal of Biomechanics* **12**(12): 911-920.

Prakash, N. M. and F. A. Spelman (1997). *Localization of a Magnetic Marker for GI Motility Studies: An In Vitro Feasibility Study*. Proceedings of the 19th Annual International Conference of the IEEE Engineering in Medicine and Biology Society.

Shadowitz, A. (1975). *Electromagnetic Fields*. New York, McGraw-Hill.

Stein, D., E. R. Scheinerman and G. S. Chirikjian (2003). "Mathematical models of binary spherical-motion encoders." *IEEE/ASME Transactions on Mechatronics* **8**(2): 234-244.

Weitschies, W., J. Wedemeyer, R. Stehr and L. Trahms (1994). "Magnetic Markers as a Noninvasive Tool to Monitor Gastrointestinal Transit." *IEEE Transactions on Biomedical Engineering* **41**(2): 192-195.

West, M. and H. Asada (1997). "Design of Ball Wheel Mechanisms for Omnidirectional Vehicles with Full Mobility and Invariant Kinematics." *Transactions of the ASME Journal of Mechanical Design* **119**(2): 153-161.

SYNTHESIS OF SPHERICAL FOUR-BAR MECHANISMS USING SPHERICAL KINEMATIC MAPPING

Katrin Brunnthaler,
Hans-Peter Schröcker,
Manfred Husty
University Innsbruck, Institute of Engineering Mathematics, Geometry and Computer Science, Technikerstraße 13, A-6020 Innsbruck, Austria
katrin.brunnthaler@uibk.ac.at, hans-peter.schroecker@uibk.ac.at, manfred.husty@uibk.ac.at

Abstract Designing a spherical four-bar mechanism that guides a coupler system through five given orientations is an old and well known problem. Here we use kinematic mapping to solve the problem. We investigate the constraint surface belonging to a spherical *RR*-chain and solve the problem in the newly defined kinematic design space. The algorithm results in *RR*-chains which pairwise combined give the synthesized four-bars. It is remarkable that with this method the univariate polynomial can be computed completely general without specifying the parameters of the problem with numerical values. Furthermore for the first time an example with six real *RR*-chains is given. These can be combined to 30 real four-bars that move the coupler system through the five given precision points.

Keywords: Mechanism synthesis, spherical four-bar mechanism, five-orientations-problem

1. Introduction

A spherical four-bar mechanism is a closed chain, which consists of four bodies, linked by four revolute pairs incident with the same point. One of the four bodies is called the base and is located in the fixed system Σ_0, which is connected with two links to the coupler, the moving system Σ. Given five finitely separated orientations $\Sigma_{t_1}, \ldots, \Sigma_{t_5}$ of Σ (Fig. 1) – sometimes called precision points – one can always find a finite set of spherical RR-chains, guiding a coordinate system attached to the coupler through them. To be more precise, one can find according to Roth, 1967 at most six real RR-chains, which are essentially different. That means, that solutions with axes origin-symmetric to axes of these RR-chains are neglected. Six real RR-chains determine 30 different spherical four-bar mechanisms, if there are just four, two or zero real RR-chains,

J. Lenarčič and B. Roth (eds.), Advances in Robot Kinematics, 377–384.

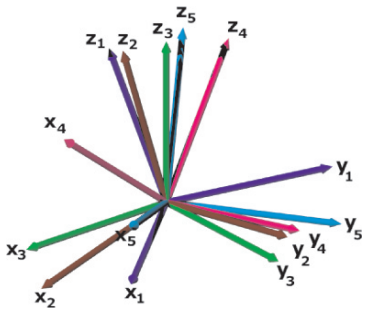

Figure 1. Given 5 orientations of a coordinate system.

one can build only 12, one or zero spherical four-bar mechanisms guiding a coordinate system attached to the coupler through the given five orientations. Note, that not all orientations necessarily have to lie in the same assembly branch of the spherical four-bar mechanism. There exist a number of solutions of this synthesis problem, most of them use kinematic properties of the motion itself. Bottema and Roth, 1979, McCarthy, 2000, Chiang, 1988, Lin, 1998, Dowler et al., 1978 solved the problem via intersecting two center point curves to obtain the centers respectively two circle point curves to obtain the circle points. These points represent the points moving on circles in the synthesized spherical four-bar motion. Bodduluri and McCarthy, 1992 solved this problem as special case of a curve fitting method by minimizing a normal distance in the image space. McCarthy, 2000 also solved this problem by using a two-step elimination procedure that yields a sixth degree polynomial in one of the coordinates of the fixed axes. In this paper the spherical four-bar mechanism synthesis is solved in the kinematic image space of spherical Euclidean displacements. We compute the constraint surface representing a spherical RR-chain in this space and define then the kinematic design space which is sort of dual to the kinematic image space. It turns out that in the kinematic design space the constraint surface representing the design problem is a quadric surface with a very special and simple structure. These geometric considerations are key to the remarkable result that the univariate polynomial of degree six that governs this design problem can be derived completely general, i.e., without specifying the coordinates of the five given orientations.

The paper is organized as follows: In Section 2 we give a brief introduction to the mathematical framework and recall especially spherical kinematic mapping. In Section 3 we derive the kinematic image of spherical RR-chains and solve the synthesis problem using this representation.

Section 4 illustrates the presented algorithm with a numerical example that presents for the first time six real RR-chains.

2. Preliminaries

Spherical Euclidean displacements $\mathcal{D}$ can be described by

$$\mathbf{X} = \mathbf{A}\mathbf{x}, \tag{1}$$

where $\mathbf{X}$ and $\mathbf{x}$ represent a point in the fixed and moving frame, respectively and $\mathbf{A} \in SO(3)$ is a 3×3 proper orthogonal matrix (Husty et al., 1997; McCarthy, 2000). For the following it is convenient to use the Euler parameters to parameterize $SO(3)$:

$$\mathbf{A} := \begin{bmatrix} x_0^2 + x_1^2 - x_3^2 - x_2^2 & -2x_0x_3 + 2x_2x_1 & 2x_3x_1 + 2x_0x_2 \\ 2x_2x_1 + 2x_0x_3 & x_0^2 + x_2^2 - x_1^2 - x_3^2 & -2x_0x_1 + 2x_3x_2 \\ -2x_0x_2 + 2x_3x_1 & 2x_3x_2 + 2x_0x_1 & x_0^2 + x_3^2 - x_2^2 - x_1^2 \end{bmatrix}. \tag{2}$$

In the matrix $\mathbf{A}$ the entries x_i have been normalized so that $x_0^2 + x_1^2 + x_2^2 + x_3^2 = 1$. The mapping

$$\begin{gathered} \kappa : \mathcal{D} \to P \in P^3 \\ \mathbf{A}(x_i) \to (x_0 : x_1 : x_2 : x_3) \neq (0 : 0 : 0 : 0) \end{gathered} \tag{3}$$

is called *spherical kinematic mapping* and maps each spherical Euclidean displacement $\mathcal{D}$ to a point P in P^3. The space P^3 is called kinematic image space and is naturally endowed with an elliptic metric (Blaschke, 1960). It should be mentioned that x_i are the components of the Hamiltonian quaternion which is associated with the corresponding element of $SO(3)$. Therefore one could also use the quaternion calculus as it is done in McCarthy, 2000. The spherical kinematic mapping is the restriction of the general spatial kinematic mapping to the orientation part of the Euclidean displacement group. In spatial kinematic mapping each Euclidean displacement $\mathcal{D}$ is mapped to a point P on a six dimensional hyper-quadric $S_6^2 \subset P^7$. The spherical kinematic mapping restricts the general one to a three dimensional subspace on S_6^2.

3. Synthesis of Spherical Four-Bar Mechanisms

The spherical four-bar mechanism is a closed $4R$-chain, where all four revolute pairs intersect in one point. For the synthesis of such a mechanism we attach two of the revolute axes to the fixed system and two axes to the moving (coupler) system. Now we prize open the coupler link and obtain two open RR-chains. We map the possible displacements of the first RR-chain into the spherical kinematic image space P^3. This

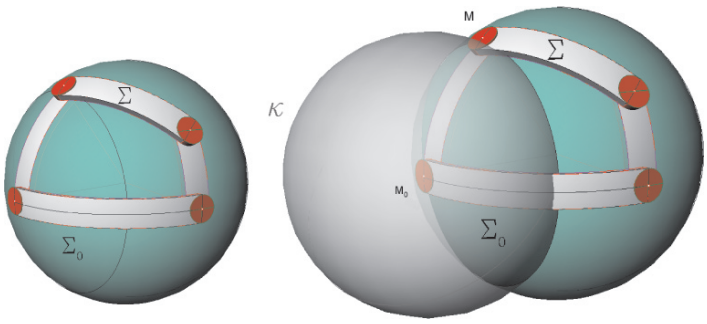

Figure 2. Four-bar and sphere.

yields the constraint manifold $\mathcal{M}_1$ of the first RR-chain in the kinematic image space. The same procedure we perform with the other RR-chain and obtain a second constraint manifold $\mathcal{M}_2$. Possible assembly modes of the two RR-chains correspond to intersection points of $\mathcal{M}_1$ and $\mathcal{M}_2$. These constraint manifolds will then be used for the synthesis algorithm.

3.1 Constraint Manifold of *RR*-Chains

In a spherical four-bar a point of the coupler revolute joint moves on a circle. In Fig. 2 this is shown for the point M. The point M is bound to this circle. When we want to model this constraint we can say that point M is constrained to be on two spheres. One is the unit sphere κ_0 the other is a sphere κ centered at piercing point M_0 of the base the revolute joint with the unit sphere and radius $r = \overline{MM_0}$. Let the vector of the fixed revolute axis be $\mathbf{v_f} = (A, B, C)^T$ and the corresponding vector of the moving revolute axis in the coupler system be $\mathbf{v_m} = (a, b, c)^T$. The endpoints of these vectors will be M_0 resp. M when we have $A^2 + B^2 + C^2 = 1$ or $a^2 + b^2 + c^2 = 1$. The path of M is now modelled as the intersection curve of the two spheres:

$$\begin{aligned}\kappa_0 &: X_1^2 + X_2^2 + X_3^2 - X_0^2 = 0\\ \kappa &: X_1^2 + X_2^2 + X_3^2 - 2AX_1X_0 - 2BX_2X_0 - 2CX_3X_0 + RX_0^2 = 0. \quad (4)\end{aligned}$$

with $R = A^2 + B^2 + C^2 - r^2$, where r is the radius of the sphere and A, B, C are the coordinates of the center. X_i are the coordinates of the moving pivot in the fixed system and can be computed via Eq. 1. Substituting $\mathbf{X} = (X_0, X_1, X_2, X_3)^T$ from Eq. 1 into Eq. 4 yields after factorization:

$$\begin{aligned}&(x_1^2 + x_0^2 + x_3^2 + x_2^2)(-2Ccx_3^2 - 2Aax_0^2 - 2Ccx_0^2 - 4Abx_0x_3 + 4Acx_0x_2\\ &\quad +4Bax_0x_3 - 4Bcx_3x_2 - 4Cax_0x_2 - 4Cbx_3x_2 + a^2x_0^2 + a^2x_3^2 + a^2x_2^2\end{aligned}$$

$$
\begin{aligned}
&+b^2x_2^2+c^2x_3^2+b^2x_0^2+b^2x_3^2+c^2x_0^2+c^2x_2^2+x_1^2c^2+x_1^2a^2+x_1^2b^2\\
&+Rx_0^2+Rx_3^2+Rx_2^2+x_1^2R+2Bbx_3^2+2Ccx_2^2+2Aax_3^2+2Aax_2^2-2Bbx_0^2\\
&-2Bbx_2^2+2x_1^2Cc-2x_1^2Aa+2x_1^2Bb-4x_1Bcx_0+4x_1Cbx_0-4x_1Abx_2\\
&-4x_1Bax_2-4x_1Acx_3-4x_1Cax_3)=0.
\end{aligned}
$$

This equation can be simplified using the normalizing condition $x_0^2+x_1^2+x_2^2+x_3^2=1$:

$$
\begin{aligned}
SCS:\ &4Acx_0x_2-4Abx_0x_3+4Bax_0x_3-4Bcx_3x_2-4Cax_0x_2-4Cbx_3x_2\\
&-2Aa-2Bb-2Cc+4Bbx_3^2+4Ccx_2^2+4Aax_3^2+4Aax_2^2+4x_1^2Cc\\
&+4x_1^2Bb-4x_1Bcx_0+4x_1Cbx_0-4x_1Abx_2-4x_1Bax_2-4x_1Acx_3\\
&-4x_1Cax_3+B^2+A^2+C^2+a^2+b^2+c^2-r^2=0. \qquad (5)
\end{aligned}
$$

SCS is a quadratic surface (a hyperboloid) in P^3 and can be conveniently used for the analysis of spherical four-bar mechanisms following the process demonstrated in Bottema and Roth, 1979 for planar four-bar mechanisms. The four-bar motion is mapped to the intersection curve of two hyperboloids in the image space and can easily be investigated using the properties of the image space curve.

For the synthesis we have to adapt a different point of view. In the synthesis some positions of a moving system are given and a mechanism has to be synthesized. Therefore in Eq. 2 x_i are known coefficients and A, B, C, a, b, c, r are unknowns. Changing the point of view we have now a seven dimensional design space $\mathcal{DS}$ having the coordinates A, B, C, a, b, c, r and Eq. 2 is again a quadratic surface but now in the seven dimensional design space. This surface is called design constraint surface DCS and has the remarkable structure:

$$
DCS: \quad \mathbf{w}^T \begin{pmatrix} \mathbf{I} & -2\mathbf{B} & \mathbf{0} \\ -2\mathbf{B} & \mathbf{I} & \mathbf{0} \\ \mathbf{0}^T & \mathbf{0}^T & -1 \end{pmatrix} \mathbf{w} = 0 \qquad (6)
$$

where the coordinates of $\mathcal{DS}$ are assembled to a vector $\mathbf{w}=(A,B,C,a,b,c,r)^T$, $\mathbf{I}$ is the three dimensional unit matrix, $\mathbf{B}$ is the right lower 3×3-matrix in matrix $\mathbf{A}$ (Eq. 1) and $\mathbf{0}$ is a 3-dimensional zero vector. From this representation we see immediately that the squared coordinates of DCS are free of the position parameters x_i. This will be crucial in the synthesis algorithm below.

3.2 Synthesis Algorithm

Given are five precision points P_1, P_2, P_3, P_4 and $P_5 \in P^3$, corresponding to five orientations of a coordinate system. The goal is to

compute the design parameters A, B, C, a, b, c, r of the spherical mechanism that guides the coupler system through these orientations. It is evident from the section before that the five precision point yield five design constraint equations $DCS_i, i = 1, \ldots, 5$. Furthermore we have two normalizing equations $N_1 : A^2 + B^2 + C^2 - 1 = 0,\ N_2 : a^2 + b^2 + c^2 - 1 = 0$. DCS_i and N_i constitute a system of seven nonlinear equations to solve the synthesis problem. N_i are free of position parameters, therefore they will be used at the very end of the the synthesis algorithm to normalize the solution vectors.

Without loss of generality we can assume that the fixed system Σ_0 coincides with one of the five given orientations. Otherwise there exists a unique Euclidean transformation, which does not change the design of the mechanism, to obtain this situation. Thus, the image space point, which represents the identity

$$(x_0 : x_1 : x_2 : x_3) = (1 : 0 : 0 : 0) \tag{7}$$

has to be on one design constraint manifold:

$$DCS_1 := -2Bb - 2Cc - 2Aa + A^2 + C^2 + B^2 + a^2 + b^2 + c^2 - r^2 = 0. \tag{8}$$

Now four simple equations are built by subtracting DCS_1 from the other four constraint equations:

$$M_{1j} = DCS_j - DCS_1, \qquad j = 2, \ldots 5.$$

The four difference equations are bilinear in the unknowns A, B, C, a, b, c and do not contain r. Note that at least one of the unknowns in (A, B, C) and (a, b, c) has to be non zero. Let us assume that C and c are nonzero. Therefore we can set for the moment $C = 1, c = 1$. We emphasize that this is no restriction of generality. Now we have four simple bilinear equations M_{1j}. Two of these equations, say $M_{1,2}$ and $M_{1,3}$ are used to solve linearly for two of the unknowns, say a, b. The solutions are substituted into $M_{1,4}$ and $M_{1,5}$. This yields two cubic equations C_1, C_2. The resultant of C_1, C_2 with respect to one of the remaining unknowns, say B yields a univariate polynomial Q^9 of degree nine in the unknown A. Q^9 factors into the solution polynomial Q^6 of degree six and in three linear factors. The linear factors are not solution of the system because they would cause the determinant of the linear system to vanish. This proposition can be proven easily by computing the resultant of the determinant polynomial of the linear system $(M_{1,2}, M_{1,3})$ and e.g. C_1. The linear factors are contained in the ideal spanned by these two equations. Therefore they have to be cancelled.

Solving Q^6 for A yields either $0, 2, 4$ or 6 real numerical solutions. Back substitution gives the other unknowns. The final step of the algorithm uses both equations N_i to normalize the solution vector.

Remark: The geometric preprocessing and the simple structure of the resulting equations allows a solution of this synthesis problem completely general, without specifying the position parameters. This is to the best of the author's knowledge for the first time that the final univariate polynomial of the spherical four-bar synthesis problem could be computed without specifying the input parameters.

4. Numerical Examples

We start with five points $P_1, P_2, P_3, P_4, P_5 \in P^3$; these points correspond to five arrays of Euler-parameters which represent the five given orientations:

Table 1. Input data for the example.

	x_0	x_1	x_2	x_3
Pose1	1	0	0	0
Pose2	0.37721	0.82336	0.38967	0.16722
Pose3	0.0078934	0.041131	0.085164	−0.99549
Pose4	0.039457	0.77456	−0.60494	−0.18041
Pose5	−0.30301	−0.36492	0.85697	0.20157

These input data yield six real RR-chains. The input data are plugged into the algorithm above and the resulting centers M_0 in the fixed system and M in the moving system are displayed below. $\mathbf{v_f}$ and $\mathbf{v_m}$ are the position vectors of the points M_0 and M in the fixed resp. moving system.

$$\mathbf{v_f}[1] = \begin{pmatrix} 0.216419 \\ -0.188593 \\ 0.957912 \end{pmatrix},\ \mathbf{v_f}[2] = \begin{pmatrix} 0.380468 \\ 0.064814 \\ 0.922520 \end{pmatrix},\ \mathbf{v_f}[3] = \begin{pmatrix} 0.254798 \\ 0.644619 \\ 0.720794 \end{pmatrix},$$

$$\mathbf{v_m}[1] = \begin{pmatrix} -0.711602 \\ 0.697874 \\ 0.081202 \end{pmatrix},\ \mathbf{v_m}[2] = \begin{pmatrix} 0.054261 \\ -0.996977 \\ 0.055603 \end{pmatrix},\ \mathbf{v_m}[3] = \begin{pmatrix} 0.900242 \\ 0.435383 \\ 0.002536 \end{pmatrix},$$

$$\mathbf{v_f}[4] = \begin{pmatrix} 0.136474 \\ -0.909345 \\ 0.393022 \end{pmatrix},\ \mathbf{v_f}[5] = \begin{pmatrix} 0.861340 \\ -0.443225 \\ 0.248284 \end{pmatrix},\ \mathbf{v_f}[6] = \begin{pmatrix} 0.791447 \\ -0.581484 \\ 0.188383 \end{pmatrix},$$

$$\mathbf{v_m}[4] = \begin{pmatrix} 0.349442 \\ -0.144163 \\ 0.925801 \end{pmatrix},\ \mathbf{v_m}[5] = \begin{pmatrix} 0.323069 \\ -0.589944 \\ 0.739995 \end{pmatrix},\ \mathbf{v_m}[6] = \begin{pmatrix} 0.242377 \\ 0.197065 \\ 0.949957 \end{pmatrix}.$$

5. Conclusion

Using spherical kinematic mapping a new method for the synthesis of spherical four-bar mechanisms was presented. It was found that the

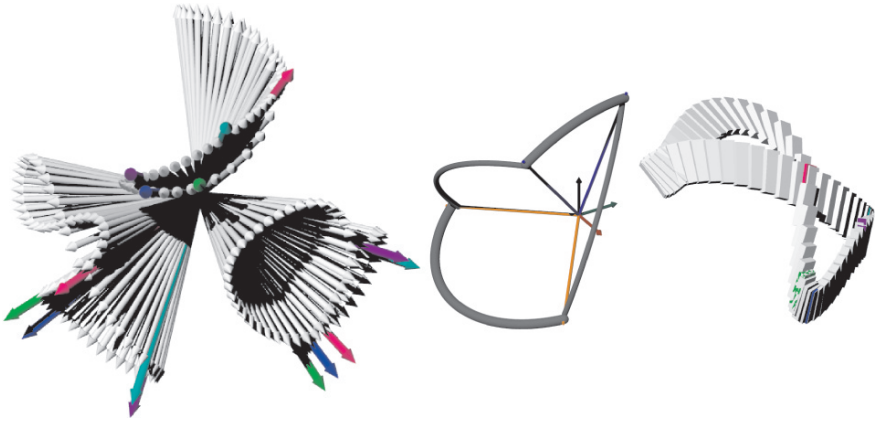

Figure 3. Motion of the coordinate frame; one of the synthesized four-bar mechanisms; corresponding motion of a body.

constraint equation describing the design constraints is a quadric surface in the seven dimensional design space of the synthesis problem. Because of the resulting simple equations the problem could be solved completely general, i.e., the univariate polynomial governing the synthesis could be computed without specifying the input parameters. Furthermore this approach allowed to find an example with six real RR-chains that can be assembled to 30 real spherical four-bar mechanisms.

References

Blaschke, W. (1960). *Kinematik und Quaternionen*. Mathematische Monographien. Springer Verlag, Berlin.

Bodduluri, R. and McCarthy, J. (1992). Finite position synthesis using the image curve of a spherical four-bar motion. *Journal of Mechanical Design*, 114:55–60.

Bottema, O. and Roth, B. (1979). *Theoretical kinematics*, volume 24 of *North-Holland Series in Applied Mathematics and Mechanics*. North-Holland Publishing Company, Amsterdam, New York, Oxford.

Chiang, C. (1988). *Kinematics of spherical mechanisms*. Cambridge Univ. Pr., Cambridge.

Dowler, H., Duffy, J., and Tesar, D. (1978). A generalised study of four and five multiply separated positions in spherical kinematics-ii. *Journal of Mechanism and Machine Theory*, 13:409–435.

Husty, M., Karger, A., Sachs, H., and Steinhilper, W. (1997). *Kinematik und Robotik*. Springer-Verlag, Berlin, Heidelberg, New York.

Lin, C.-C. (1998). Complete solution of the five-position synthesis for spherical four-bar mechanisms. *Journal of Marine Science and Technology*, 6(1):17–27.

McCarthy, J. (2000). *Geometric Design of Linkages*, volume 320 of *Interdisciplinary Applied Mathematics*. Springer-Verlag, New York.

Roth, B. (1967). Finite-position theory applied to mechanism synthesis. *Journal of Applied Mechanics*, 34:599–605. Transactions of the ASME, Series E.

SYNTHESIS OF 2-DOF SPHERICAL FULLY PARALLEL MECHANISMS

Rocco Vertechy
DIEM, University of Bologna
Viale Risorgimento, 2, 40136 Bologna, Italy
rocco.vertechy@mail.ing.unibo.it

Vincenzo Parenti-Castelli
DIEM, University of Bologna
Viale Risorgimento, 2, 40136 Bologna, Italy
Vincenzo.parenticastelli@mail.ing.unibo.it

Abstract This paper deals with the synthesis of 2-dof spherical fully parallel mechanisms with legs of type US (U and S are for universal and spherical joints, respectively). First, two analytical methods derived from the literature are used to find the conditions for the legs to fit within the desired spherical relative motion between the base and the movable platform of the mechanism. Then, these conditions are used to devise three families of mechanisms which comprise also over-constrained architectures. Finally, actuation issues and kinematic, workspace and singularity analyses are addressed.

Keywords: Parallel manipulators, Spherical motion, Over-constrained mechanisms

1. Introduction

Spherical mechanisms are used for the orientation of bodies. High-demanding applications, for instance in aerospace and automotive fields, require mechanisms which perform limited rotations about the axes of motion, but are very resistant and lightweight, have low encumbrance and desired stiffness characteristics. Closed chain architectures are well suited to devise mechanisms which match the aforementioned features.

Two-dof spherical parallel mechanisms are used in pointing systems for mirrors and antennas, steering systems of vehicles and joints for biomimetic robots. In the literature, 2-dof spherical parallel mechanisms have been proposed by Baumann et al., 1997, Gosselin and Caron, 1998, Dunlop and Johnes, 1999, Wiitala and Stanisic, 2000, Di Gregorio, 2002, Bauer, 2002, Carricato and Parenti-Castelli, 2004, Gogu, 2005.

This paper deals with the synthesis of 2-dof spherical fully parallel mechanisms with legs of US-type (US-PM for short), i.e. closed chains

J. Lenarčič and B. Roth (eds.), Advances in Robot Kinematics, 385–394.

which comprise, regardless of how their actuation is performed, a fixed base and a moving platform connected to each other through binary links of constant length and of US-type (U and S are for universal and spherical joint, respectively). From the mathematical standpoint, this study is related to the Shönflies problem, Shönflies, 1886; to the spherical motion problem, Bricard, 1906, and Borel, 1908; and to the study of architecturally singular and shaky UPS parallel manipulators, Ma and Angeles, 1992, Husty and Zsombor-Murray, 1994, Karger and Husty, 1998, Roshel and Mick, 1998, Kong, 1998, Husty and Karger, 2002, and Wohlhart, 2003.

In particular, by means of two analytical methods derived from the literature, we show that only two types of US-legs exist which fit within the desired spherical motion between the mechanism base and platform. Then, three families of mechanisms, which comprise over-constrained mechanisms too, are derived by properly combining a number of these legs. Finally, we address actuation issues and kinematic, workspace and singularity analyses.

2. Problem Definition and Methods

The synthesis of a spherical US-PM falls under the body-guidance problems. Indeed, the matter at hand amounts to finding the lengths of the US-legs and the locations of the U and S joint centers on the platform and on the base so that the assembly of a number of legs fits within the desired relative spherical motion of the platform and the base.
To this end, two analytical methods can be used:

- Method M1 (adaptation of the procedure by Karger and Husty, 1998): it is based on the closure equations of the mechanism. Upon expression of the closure equations as a function of the parameters used to describe the desired motion, the synthesis problem amounts to finding the locations of the U and S joint centers, on the base and on the platform, of a set of US-legs, with unknown and constant lengths, whose axes (defined by the centers of the U and S joints) belong to an n-system of lines and which satisfy the closure equations for every set of given values of the motion parameters.
- Method M2 (adaptation of the procedure by Wohlhart, 2003): it is based on the virtual work principle. By considering the expressions of the velocity vectors of the attachment points of the US-legs on the moving platform as functions of the motion parameters and their first time derivatives, the synthesis problem amounts to finding the locations of the U and S joint centers, on the base and on the platform, of a set of US-legs, with unknown and constant lengths, whose axes belong to an

n-system of lines which are orthogonal to the aforementioned velocity vectors for every set of given values of the motion parameters and their derivatives.

3. Synthesis of 2-dof Spherical US-PM

In this section, the methods mentioned in Section 2 are applied to the synthesis of 2-dof spherical US-PM. First, a standard parameterization of the desired spherical motion is introduced. Then, methods M1 and M2 are applied to find the conditions for the US-legs to fit within the desired spherical relative motion of the platform and the base. Finally, these conditions are used to devise the sought mechanisms.

3.1 Definition and Parameterization of the Motion

Referring to Fig. 1: frame of reference $S_0 = \{O; \mathbf{i}_0, \mathbf{j}_0, \mathbf{k}_0\}$, with origin O, and $S_1 = \{C; \mathbf{i}_1, \mathbf{j}_1, \mathbf{k}_1\}$, with origin C, are embedded in the base and in the platform, respectively. Here, $\mathbf{i}_0$, $\mathbf{j}_0$, $\mathbf{k}_0$ are the unit vectors of the axes X, Y, Z of the system S_0 and $\mathbf{i}_1$, $\mathbf{j}_1$, $\mathbf{k}_1$ are the unit vectors of the axes x, y, z of the system S_1. Point C is the center of the relative spherical motion between the base and the platform, i.e. between S_0 and S_1. Axis Z of system S_1 is taken from O to C.

We consider a 2-dof spherical motion of the platform with respect to the base defined by the two following rotations: a rotation α about Z-axis of S_0 and a rotation β about x-axis of S_1 (i.e. rotations about unit vector $\mathbf{k}_0$ and $\mathbf{i}_1$, respectively). The 3 x 3 rotation matrix $\mathbf{R}$ from S_1 to S_0 is

$$\mathbf{R} = \begin{bmatrix} c_\alpha & -s_\alpha c_\beta & s_\alpha s_\beta \\ s_\alpha & c_\alpha c_\beta & -c_\alpha s_\beta \\ 0 & s_\beta & c_\beta \end{bmatrix}, \tag{1}$$

where $c_\alpha = \cos\alpha$, $s_\alpha = \sin\alpha$, $c_\beta = \cos\beta$ and $s_\beta = \sin\beta$. Matrix $\mathbf{R}$ transforms vector components from S_1 to S_0.

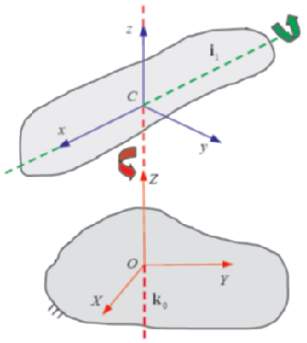

Figure 1. Base, platform and axes of rotation.

3.2 Synthesis Procedure

The synthesis of a US-PM amounts to finding the location of the U and S joints on the base and on the platform respectively, and the lengths of the connecting legs. That is, if for each leg k, we introduce the column array of components $\boldsymbol{p}_k = [p_k; q_k; r_k]$, with respect to S_1, of the point P_k which is the center of either the U or the S joint on the platform, the column array of components $\boldsymbol{B}_k = [A_k; B_k; C_k]$, with respect to a frame parallel to S_0 but centered in C, of the point B_k which is the center of either the S joint or the U joint on the base, and the length $l_k = |\mathrm{P}_k - \mathrm{B}_k|$ of the connecting leg between P_k and B_k, we have to search for N unknown arrays of geometric parameters, i.e. $\boldsymbol{Q}_k = [\,\boldsymbol{p}_k; \boldsymbol{B}_k; l_k\,]$ for $k = 1,...,N$. Use of the method M1 or M2 makes it possible to find the conditions for $\boldsymbol{Q}_k$ so that the leg $\mathrm{P}_k\mathrm{B}_k$ fits within the desired 2-dof spherical motion between platform and base.

Method M1: Assuming the description and the parameterization of the orientation introduced in Section 3.1, the length of the k-th US-leg is given by

$$l_k = \left|\boldsymbol{l}_k\right| = \left|\mathrm{P}_k - \mathrm{B}_k\right| = \left|\mathbf{R}\boldsymbol{p}_k - \boldsymbol{B}_k\right|, \tag{2}$$

which, according to Eq. 1 is a function of the motion parameters α and β. However, for the k-th US-leg to comply within the desired motion of the platform, the length l_k must not depend on α and β. This means that if one considers the expression

$$l_k = \sqrt{\boldsymbol{l}_k^2} = \sqrt{\begin{bmatrix} p_k\,\mathrm{c}_\alpha - q_k\,\mathrm{s}_\alpha\,\mathrm{c}_\beta + r_k\,\mathrm{s}_\alpha\,\mathrm{s}_\beta - A_k \\ p_k\,\mathrm{s}_\alpha + q_k\,\mathrm{c}_\alpha\,\mathrm{c}_\beta - r_k\,\mathrm{c}_\alpha\,\mathrm{s}_\beta - B_k \\ q_k\,\mathrm{s}_\beta + r_k\mathrm{c}_\beta - C_k \end{bmatrix}^2} = \sqrt{2f(\alpha,\beta)}, \tag{3}$$

where

$$f(\alpha,\beta) = \begin{pmatrix} -A_k p_k\,\mathrm{c}_\alpha + A_k q_k\,\mathrm{s}_\alpha\,\mathrm{c}_\beta - A_k r_k\,\mathrm{s}_\alpha\,\mathrm{s}_\beta - B_k p_k\,\mathrm{s}_\alpha - B_k q_k\,\mathrm{c}_\alpha\,\mathrm{c}_\beta + \\ +B_k r_k\,\mathrm{c}_\alpha\,\mathrm{s}_\beta - C_k q_k\,\mathrm{s}_\beta - C_k r_k\mathrm{c}_\beta + p_k^2 + q_k^2 + r_k^2 + A_k^2 + B_k^2 + C_k^2 \end{pmatrix}, \tag{4}$$

all the coefficients in c_α, s_α, c_β and s_β of the polynomial $f(\alpha,\beta)$ must vanish, and the length of the k-th leg must become

$$l_k = \sqrt{p_k^2 + q_k^2 + r_k^2 + A_k^2 + B_k^2 + C_k^2}\,. \tag{5}$$

Vanishing of the coefficients of Eq. 4 leads to the following conditions

$$A_k p_k = 0\,,\ A_k q_k = 0\,,\ A_k r_k = 0\,,\ B_k p_k = 0, \tag{6.1}$$

$$B_k q_k = 0\,,\ B_k r_k = 0\,,\ C_k q_k = 0\,,\ C_k r_k = 0, \tag{6.2}$$

to be satisfied simultaneously for each leg $\mathrm{P}_k\mathrm{B}_k$.

It turns out that the only non trivial solutions, i.e. $l_k \neq 0$, are obtained for the following two sets of parameters

$$^1\boldsymbol{Q}_i = \left\{ \forall A_i; \forall B_i; \forall C_i; p_i = 0; q_i = 0; r_i = 0; l_i = \sqrt{A_i^2 + B_i^2 + C_i^2} \right\}, \tag{7}$$

$$^2\boldsymbol{Q}_j = \left\{ A_j = 0; B_j = 0; \forall C_j; \forall p_j; q_j = 0; r_j = 0; l_j = \sqrt{p_j^2 + C_j^2} \right\}. \tag{8}$$

Method M2: Since for a general motion of the US-PM the parameters α and β are functions of time, based on the time derivative of the equation

$$\boldsymbol{l}_k = \mathbf{R}\boldsymbol{p}_k - \boldsymbol{B}_k = \begin{bmatrix} p_k \mathrm{c}_\alpha - q_k \mathrm{s}_\alpha \mathrm{c}_\beta + r_k \mathrm{s}_\alpha \mathrm{s}_\beta - A_k \\ p_k \mathrm{s}_\alpha + q_k \mathrm{c}_\alpha \mathrm{c}_\beta - r_k \mathrm{c}_\alpha \mathrm{s}_\beta - B_k \\ q_k \mathrm{s}_\beta + r_k \mathrm{c}_\beta - C_k \end{bmatrix}, \tag{9}$$

the relative velocity vector $\boldsymbol{v}_k$, of point P_k and point B_k, is given by

$$\boldsymbol{v}_k = \begin{bmatrix} -p_k \mathrm{s}_\alpha - q_k \mathrm{c}_\alpha \mathrm{c}_\beta + r_k \mathrm{c}_\alpha \mathrm{s}_\beta \\ p_k \mathrm{c}_\alpha - q_k \mathrm{s}_\alpha \mathrm{c}_\beta + r_k \mathrm{s}_\alpha \mathrm{s}_\beta \\ 0 \end{bmatrix} \dot{\alpha} + \begin{bmatrix} q_k \mathrm{s}_\alpha \mathrm{s}_\beta + r_k \mathrm{s}_\alpha \mathrm{c}_\beta \\ -q_k \mathrm{c}_\alpha \mathrm{s}_\beta - r_k \mathrm{c}_\alpha \mathrm{c}_\beta \\ q_k \mathrm{c}_\beta - r_\alpha \mathrm{s}_\beta \end{bmatrix} \dot{\beta}, \tag{10}$$

where $\dot{\alpha}$ and $\dot{\beta}$ are the first time derivatives of the motion parameters α and β, respectively. Since the legs $\mathrm{P}_k\mathrm{B}_k$ have constant length l_k, it must hold that, during the motion, the components of the velocity $\boldsymbol{v}_k$ in the direction of the leg axis must be zero, i.e.

$$\boldsymbol{v}_k \cdot \boldsymbol{l}_k = g(\alpha, \beta)\dot{\alpha} + h(\alpha, \beta)\dot{\beta} = 0, \tag{11}$$

where

$$g(\alpha, \beta) = p_k A_k \mathrm{s}_\alpha + q_k A_k \mathrm{c}_\alpha \mathrm{c}_\beta - r_k A_k \mathrm{c}_\alpha \mathrm{s}_\beta - p_k B_k \mathrm{c}_\alpha + q_k B_k \mathrm{s}_\alpha \mathrm{c}_\beta - r_k B_k \mathrm{s}_\alpha \mathrm{s}_\beta, \tag{12}$$

$$h(\alpha, \beta) = q_k B_k \mathrm{c}_\alpha \mathrm{s}_\beta + r_k B_k \mathrm{c}_\alpha \mathrm{c}_\beta - q_k A_k \mathrm{s}_\alpha \mathrm{s}_\beta - r_k A_k \mathrm{s}_\alpha \mathrm{c}_\beta - q_k C_k \mathrm{c}_\beta + r_k C_k \mathrm{s}_\beta. \tag{13}$$

Since this condition must hold for every configuration and motion of the platform (that is it should not depend on α, β, $\dot{\alpha}$ and $\dot{\beta}$), all the coefficients in c_α, s_α, c_β and s_β of the two polynomials $g(\alpha,\beta)$ and $h(\alpha,\beta)$ must vanish.

Vanishing of the coefficients of Eqs. 12-13 leads to the same conditions expressed by Eq. 6 and, therefore, to the non-trivial solutions represented by Eqs. 7-8.

That is, legs characterized by the set of parameters $^1\boldsymbol{Q}_i$ (type-1) and $^2\boldsymbol{Q}_j$ (type-2) are the only ones which comply with the desired 2-dof spherical motion.

In Section 3.3 we will show that a feasible mechanism requires both types of legs.

3.3 Generation of Mechanisms

Equations 7-8 provide the geometric conditions for legs of US-type to fit within the desired spherical motion between platform and base. The conditions identify two types of legs. Legs of type-1 have one joint located at point C in the platform and the other joint located anywhere in the base. Legs of type-2 have the joint in the based located on $\mathbf{k}_0$ axis and the joint in the platform located on $\mathbf{i}_1$ axis.

Generation of mechanisms amounts to combining a proper number I of legs of type-1 and a proper number J of legs of type-2. Of course, the choice of I and J clearly affects the mechanism architecture and its feasibility. In particular, certain conditions on I and J must be satisfied.

First, in order for the mechanism to have 2-dof, the axes of the legs in the set $\{ {}^1\boldsymbol{Q}_1,...,{}^1\boldsymbol{Q}_I, {}^2\boldsymbol{Q}_1,...,{}^2\boldsymbol{Q}_J \}$ must belong to a linear variety of lines with rank = 4 (Merlet, 1989), usually referred to as linear line congruence. Therefore, at least four legs with linear independent axes are needed, i.e. $I+J \geq 4$. Here, the axis of the k-th leg is defined as the line through point P_k to point B_k.

Second, since the legs (of type-1) in the set $\{ {}^1\boldsymbol{Q}_1,...,{}^1\boldsymbol{Q}_I \}$ pass through the common point C, i.e. the center of the reference frame S_1, while the legs (of type-2) in the set $\{ {}^2\boldsymbol{Q}_1,...,{}^2\boldsymbol{Q}_J \}$ lie in the plane defined by the vectors $\mathbf{k}_0$ and $\mathbf{i}_1$, the axes of the legs within each type form, at most, a linear variety of lines with rank = 3 (Merlet, 1989). Indeed, the axes of the legs within the family of type-1 generate at most a bundle of lines, while the axes of the legs within the family of type-2 generate at most a plane of lines. Therefore, in order for the set of geometric parameters $\{ {}^1\boldsymbol{Q}_1,...,{}^1\boldsymbol{Q}_I, {}^2\boldsymbol{Q}_1,...,{}^2\boldsymbol{Q}_J \}$ to define a linear variety with rank = 4, at least one leg for each type is needed, i.e. $I \geq 1$ and $J \geq 1$.

That is, in a feasible 2-dof spherical fully parallel mechanism with legs of US-type, the axes of all the legs must define a degenerate congruence, i.e. the variety of lines which lie in the plane defined by unit vectors $\mathbf{k}_0$ and $\mathbf{i}_1$ or pass through the point C of that plane.

In practice, depending on the varieties of lines spanned by the axes of the legs within a type, three families of mechanism architectures can be identified:

- Family-1 (Fig. 2): The axes of the legs in the set $\{ {}^1\boldsymbol{Q}_1,...,{}^1\boldsymbol{Q}_I \}$ define a linear variety with rank = 1, i.e. a single line passing through C but with direction different to $\mathbf{k}_0$, and the axes of the legs in the set $\{ {}^2\boldsymbol{Q}_1,...,{}^2\boldsymbol{Q}_J \}$ define a linear variety of lines with rank = 3, i.e. a plane of lines defined by $\mathbf{k}_0$ and $\mathbf{i}_1$.
- Family-2 (Fig. 3): The axes of the legs in the set $\{ {}^1\boldsymbol{Q}_1,...,{}^1\boldsymbol{Q}_I \}$ define a linear variety with rank = 2, i.e. a planar pencil of lines with center in

C but which does not contain the line through $\mathbf{k}_0$, and the axes of the legs in the set $\{ {}^2\boldsymbol{Q}_1,...,{}^2\boldsymbol{Q}_J \}$ define a linear variety of lines with rank = 2, i.e. a planar pencil of lines in the plane defined by $\mathbf{k}_0$ and $\mathbf{i}_1$.

- Family-3 (Fig. 4): The axes of the legs in the set $\{ {}^1\boldsymbol{Q}_1,...,{}^1\boldsymbol{Q}_I \}$ defines a linear variety of lines with rank = 3, i.e. a bundle of lines centered in C, and the axes of the legs in the set $\{ {}^2\boldsymbol{Q}_1,...,{}^2\boldsymbol{Q}_J \}$ define a linear variety of lines with rank = 1, i.e. a single line in the plane defined by the unit vectors $\mathbf{k}_0$ and $\mathbf{i}_1$ but which does not pass through C.

Figures 2-4 depicted the basic (non-over-constrained) mechanisms which are the generators of the three families. For convenience, in the figures, both U and S joints are represented by circles.

Moreover, addition of legs of type-1 and/or of type-2 to such basic US-PMs does not alter the mechanism kinematics but renders the systems redundant and with self-motion.

Examples of over-constrained US-PM with five and six US-legs are depicted in Fig. 5. For ease of understanding, the redundant legs are drawn in long-dash-dot lines. Note that over-constrained architectures have several advantages with respect to the basic ones. Indeed, the former make it possible to augment the mechanism stiffness-to-weight

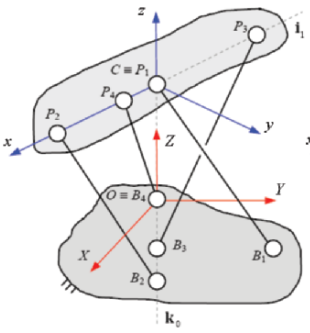

Figure 2. Family-1.

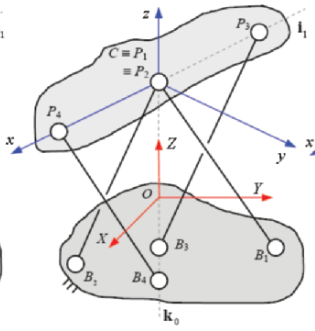

Figure 3. Family-2.

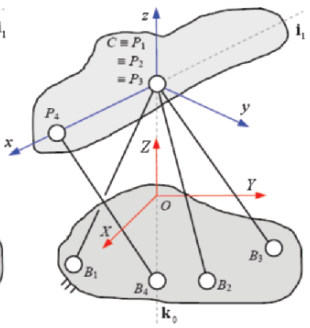

Figure 4. Family-3.

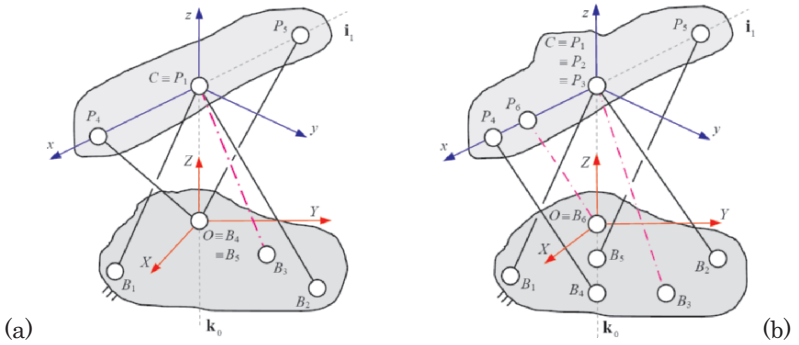

(a) (b)

Figure 5. Over-constrained mechanisms.

and -to-encumbrance ratios, the mechanism strength-to-weight and -to-encumbrance ratios, allow the mechanism to be preloaded so as to reduce system backlash, and allow the system to be built through simpler elements such as rafters and wireropes. As an example, the mechanism depicted in Fig. 5.a can be made by means of one rafter (leg drawn in long-dash-dot line) and by four wireropes (legs drawn in solid line). Besides, over-constrained architectures further limit the range of motion of the mechanism and render its assemblage more complex.

From a kinematic standpoint, note that many of the U and S joints of the mechanisms depicted in Figs. 2-5 may, in practice, be suppressed and/or replaced by simpler pairs. Indeed, joints which are not placed along the axes $\mathbf{k}_0$ and $\mathbf{i}_1$ are idle; the joints which are placed either on $\mathbf{k}_0$ or $\mathbf{i}_1$ work as simpler revolute joint with rotation axis along $\mathbf{k}_0$ or $\mathbf{i}_1$, respectively; and the joints which are placed on both $\mathbf{k}_0$ and $\mathbf{i}_1$ work as U joints with rotation axes along $\mathbf{k}_0$ and $\mathbf{i}_1$. However, from the kinetostatic standpoint, suppression of the idle degrees of freedom of the U and S joints makes the legs to bear consistent flexional loads which may cause the mechanism to be oversized. Replacement of the idle pairs with elastic hinges introduces much smaller flectional loads and, therefore, may be the most effective way to implement the mechanism.

4. Actuation

The mechanisms presented in Section 3.3 are inherently suited to be actuated in-parallel by motors with linear motion. In practice, the addition of two UPS-legs (P stands for actuated prismatic P joint), each connecting the base and the platform by means of a U joint and an S joint, provides a very simple means to fully control the mechanism throughout the desired range of motion.

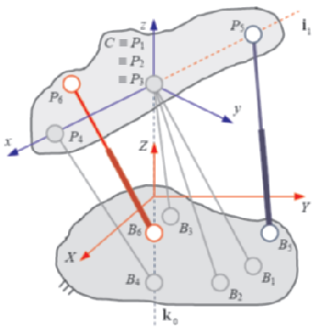

Figure 6. Actuated mechanism of family-3.

In practice, proper placements of the actuators make it possible to decouple the motion about the axes $\mathbf{k}_0$ and $\mathbf{i}_1$. Indeed, since a force is not able to generate moments about the lines it crosses, it is clear that every U<u>P</u>S-leg whose connecting joint on the base is centered in a point B_k, which lies on $\mathbf{k}_0$, makes it possible to control rotations about $\mathbf{i}_1$ only, while every U<u>P</u>S-leg whose connecting joint on the platform is centered in a point P_k, which lays on $\mathbf{i}_1$, makes it possible to control rotations about $\mathbf{k}_0$ only.

A decoupled actuated manipulator obtained from a US-PM of family-3 is represented in Fig. 6 (U<u>P</u>S-legs are drawn as telescopic legs). The actuated U<u>P</u>S-leg, P_5B_5, controls the rotation about the axis $\mathbf{k}_0$ only, while the actuated U<u>P</u>S-leg, P_6B_6, controls the rotation about the axis $\mathbf{i}_1$ only.

Note that the manipulator obtained from the mechanisms of family-3 coincides with the fully parallel spherical wrist with the <u>P</u> actuator on the leg P_4B_4 locked.

5. Kinematic, Workspace and Singularity Analyses

Due to the decoupled actuation of the rotations of the mechanism about the $\mathbf{k}_0$ and $\mathbf{i}_1$ axes, the direct kinematic, workspace and singularity analyses are very straightforward. Indeed, these problems are reduced to the study of two spatial Whitworth's quick-return mechanisms. Solutions of these problems can be accomplished as in Di Gregorio and Sinatra, 2002, Di Gregorio, 2002, and Carricato and Parenti-Castelli, 2004.

6. Conclusions

This paper presented the synthesis of 2-dof spherical fully parallel mechanisms. In particular, by means of two analytical methods derived from the literature, three families of 2-dof spherical mechanisms have been synthesized. These families comprise over-constrained mechanisms too. Actuation issues and kinematic, workspace and singularity analyses have been addressed which show that such mechanisms are very easy to analyze and control.

7. Acknowledgements

Support of this work by the Advanced Concept Team (ACT) of European Space Agency (ESA) under ESTEC/Contract No. 18911/05/ NL/MV is gratefully acknowledged.

The collaboration and discussions with Dr. Carlo Menon of the ACT are acknowledged and appreciated.

References

Shönflies, A. (1886), *Geometrie der Bewegung in Sinthetischer Darstellung*, Lipzieg.

Bricard, R. (1906), Memoire sur les Displacements a Trajectoires Spheriques, *Journal de l'Ecole Polytechnique*, vol. 11, no. 2, pp. 1-96.

Borel, E. (1908), Memoire sur les Displacements a Trajectories Spheriques, *Memoires Presentes par Divers Savants*, Paris, vol. 33, no. 2, pp. 1-128.

Merlet, J.P. (1989), Singular Configurations of Parallel Manipulators and Grassmann Geometry, *The Int. J. of Robotics Research*, vol. 8, pp. 45-56.

Ma, O. and Angeles J. (1992), Architecture Singularities of Parallel Manipulators, *Int. Journal of Robotics and Automation*, vol. 7, pp. 23-29.

Innocenti, C. and Parenti-Castelli, V. (1993), Echelon Form Solution of Direct Kinematics for the General Fully-Parallel Spherical Wrist, *Mechanism and Machine Theory*, vol. 28, pp. 553-561.

Husty, M.L. and Zsombor-Murray, P. (1994), A Special Type of Singular Stewart Gough Platform, *Advances in Robots Kinematics*, pp. 439-449.

Baumann, R., Maeder, W. Glauser, D. and Clavel, R. (1997), The PantoScope: a Spherical Remote-Center-of-Motion Parallel Manipulator for Force Reflexion, *Proc. IEEE Int. Conf. Robotics and Automation*, pp. 718-723.

Gosselin, C.M. and Caron F. (1998), Two Degree-Of-Freedom Spherical Orienting Device, US Patent #5,966,991.

Karger, A. and Husty, M. (1998), Classification of all Self-Motions of the Original Stewart-Gough Platform, *Computer-Aided Design*, vol. 30, pp. 205-215.

Roshel O. and Mick S. (1998), Charachterization of Architecturally Shaky Platforms, *Advances in Robots Kinematics*, pp. 465-474.

Kong X. (1998), Generation of Singular 6-SPS Parallel Manipulators, *Proc. of 1998 ASME Design Technical Conferences*, 98DETC/MECH-5952.

Dunlop, G.R. and Johnes, T.P. (1999), Position Analysis of a two DOF Parallel Mechanism – the Canterbury Tracker, *Mechanism and Machine Theory*, vol. 34, pp. 599-614.

Wiitala, J.M. and Stanisic, M.M. (2000), Design of an Overconstrained Dextrous Spherical Wrist, *Journal of Mechanical Design*, vol. 122, pp. 347-353.

Bauer, J.R. (2002), Kinematics and Dynamics of a Double-Gimballed Control Moment Gyroscope, *Mechanism and Machine Theory*, vol. 37, pp. 1513-1529.

Husty, M.L. and Karger, A. (2002), Self Motions of the Stewart-Gough-Platforms, an overview, *Proceedings of the Workshop on Fundamental Issues and Future Research Directions for Parallel Mechanisms and Manipulators*, Quebec, Canada, pp. 131-141.

Di Gregorio, R. and Sinatra, R. (2002), Singulariy Curves of a Parallel Pointing System, *MECCANICA*, vol. 37, pp. 255-268.

Di Gregorio, R. (2002), Analytic Determination of Workspace and Singularities in a Parallel Pointing System, *Journal of Robotics Systems*, vol. 18, pp. 37-43.

Wohlhart, K. (2003), Mobile 6-SPS Parallel Manipulators, *Journal of Robotics Systems*, vol. 20, pp. 509-516.

Carricato, M. and Parenti-Castelli, V. (2004), A Novel Fully Decoupled Two-Degrees-of-Freedom Parallel Wrist, *The Int. J. of Robotics Research*, vol. 23, pp. 661-667.

Gogu, G. (2005), Fully-Isotropic Over-Constrained Parallel Wrists with Two Degrees of Freedom, *Proc. IEEE Int. Conf. Robotics and Automation*, pp. 4025-4030.

CONSTRAINT SYNTHESIS FOR PLANAR N-R ROBOTS

Gim Song Soh
gsoh@uci.edu

J. Michael McCarthy
jmmccart@uci.edu
Robotics and Automation Laboratory
University of California, Irvine
Irvine, CA 92697

Abstract In this paper, we control the joints of a planar nR chain mechanically using RR dyads and obtain a one degree-of-freedom system that guides the end-effector smoothly through five specified task positions. To solve this problem, we specify the nR chain and determine it configurations when its end-effector is positioned in each of the five task positions. This yields a set of RR chain synthesis problems that constrain alternating links in a way that ensures that the relative joint angles required by the task positions are attained. In general, we cannot guaranteed that the resulting assembly will move smoothly between the task positions without jamming, however we present a strategy based on enforcing symmetry of the nR chain that yields useful solutions. Examples of constrained 3R, 4R, 5R and 6R are discussed. The procedure is general and can be applied to arbitrarily long serial chains.

1. Introduction

In this paper, we consider the addition of n-1 RR chains to a planar nR serial chain robot in order to mechanically prescribe its movement through five task positions. In the case of a planar 3R robot this is equivalent to the synthesis of a Watt I six-bar linkage. For a planar 4R, 5R and 6R serial chains, we obtain planar eight-bar, 10-bar and 12-bar linkages. In general, our synthesis results transform an n degree-of-freedom nR chain into a single degree-of-freedom 2n-bar linkage that has $3n - 2$ revolute joints.

Our design equations only ensure that the solution linkage can be assembled in each task position, not that it can move smoothly between the positions. Therefore, it can happen that a resulting linkage has task positions reachable from different assemblies. This is known as a circuit defect **?**. A fundamental challenge in linkage synthesis is finding

J. Lenarčič and B. Roth (eds.), Advances in Robot Kinematics, 395–402.

solutions that have the task positions on the same single circuit. In what follows, we present a synthesis strategy that yields successful constrained nR chains that have the five task positions on the same circuit.

2. Literature Review

This work is inspired by **?**, who derived synthesis equations for planar nR planar serial chains in which the n joints are constrained by a cable drive. They obtained a "single degree-of-freedom coupled serial chain" that they use to design an assistive device.

? formulated and solved the design equations for six-bar linkages, and **?** extended this to eight-bar linkages. Our approach is simpler in that we do not attempt to design the entire 2n-bar linkage, rather we assume the nR serial chain is given, and use standard dyad synthesis theory to solve for individual RR constraints, see **?**.

Once a linkage has been designed, we analyze it to determine its configuration for given values of the input crank, in order to simulate its movement. **?** presents an analysis methodology for general planar linkages using complex number loop equations and the Dixon determinant. However, the our synthesis approach yields linkages that are a series of four-bar loops and are easily analyzed individually.

3. Kinematics Equations of a Planar nR Chain

Let the configuration of an nR serial chain be defined by the coordinates $\mathbf{C}_i = (x_i, y_i)$, $i = 1, \ldots, n$ of each of its revolute joints. The distances $a_{i,i+1} = |\mathbf{C}_{i+1} - \mathbf{C}_i|$ defined the lengths of each link. Attach a frame A_i to each of these links so so its origin is located at $\mathbf{C}_i$ and its x axis is directed toward $\mathbf{C}_{i+1}$. The joints $\mathbf{C}_1$ and $\mathbf{C}_n$ are the attachments to the base frame $F = A_1$ and the moving frame $M = A_n$, respectively, and we assume they are the origins of these frames. The joint angles θ_i define the relative rotation about the joints $\mathbf{C}_i$.

Introduce a world frame G and task frame H so the kinematics equations of the nR chain are given by

$$[D] = [G][Z(\theta_1)][X(a_{12})][Z(\theta_2)][X(a_{23})] \ldots [X(a_{n-1,n})[Z(\theta_n)][H], \quad (1)$$

where $[Z(\theta_i)]$ and $[X(a_{i,i+1})]$ are the 3×3 homogeneous transforms that represent a rotation about the z-axis by θ_i, and a translation along the x-axis by $a_{i,i+1}$, repspectively. The transformation $[G]$ defines the position of the base of the chain relative to the world frame, and $[H]$ locates the task frame relative to the end-effector frame. The matrix $[D]$ defines the coordinate transformation from the world frame G to the task frame H.

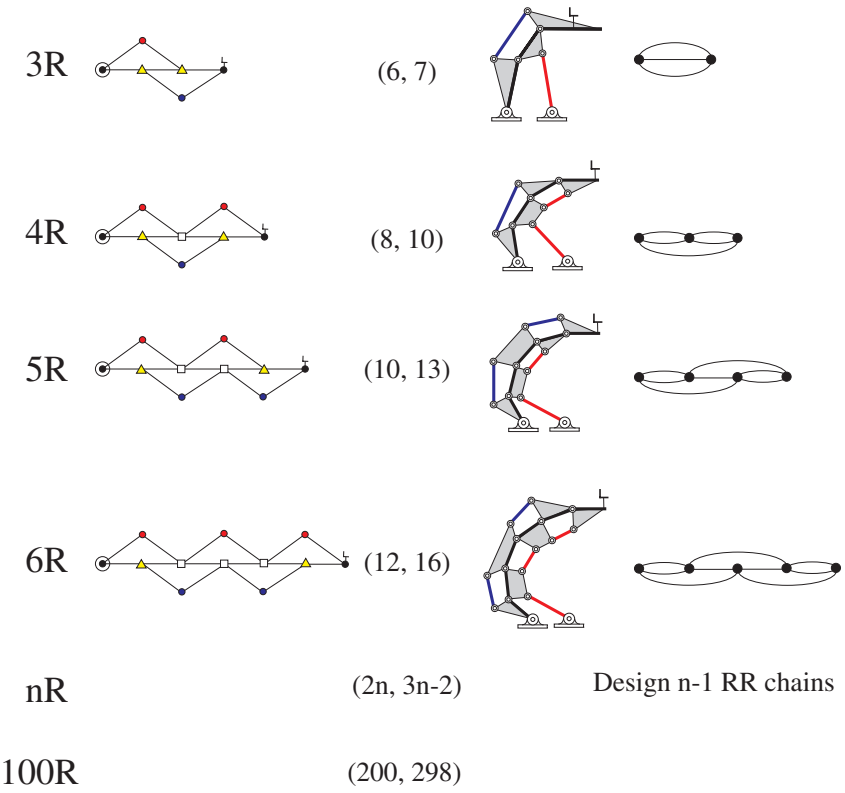

Figure 1. This shows the kinematic structure of mechanically constrained serial chains. The linkage graph is on the left, which has each link as a node and each R joint as an edge. The contracted graph on the right shows only links with three or four edges as nodes. This shows that the structure extends to any length of nR robot.

Given five task positions $[T_j], j = 1, \ldots, 5$ of the end-effector of this chain, we can solve the equations

$$[D] = [T_j], \quad j = 1, \ldots, 5, \tag{2}$$

to determine the joint parameter vectors $\vec{\theta}_j = (\theta_{1,j}, \theta_{2,j}, \ldots, \theta_{n,j})$. Because there are three independent constraints in this equation, we have free parameters when $n > 3$. In what follows, we show how to use these free parameters to facilitate the design of mechanical constraints on the joint movement so the end-effector moves smoothly through the task positions.

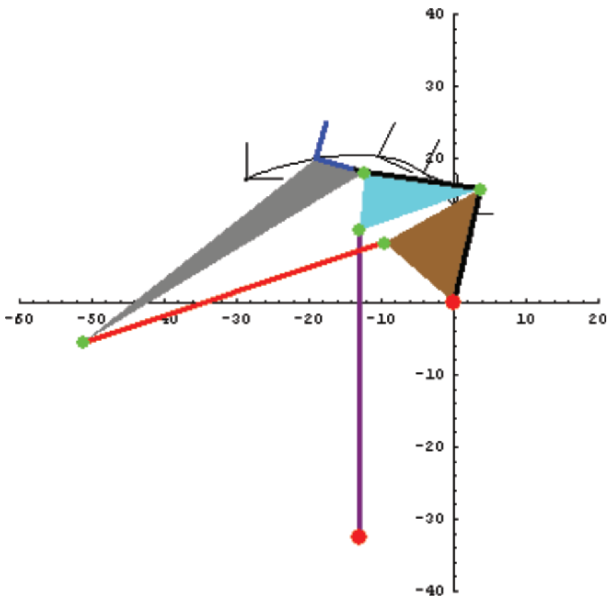

Figure 2. This six-bar chain is obtained by designing two RR chains to constrain the joint movement of a 3R robot, so its end-effector passes through the five specified positions.

4. Synthesis of RR Constraints

Assume that we have solved the inverse kinematics problem that ensures our nR chain reaches the five specified task $[T_j], j = 1, \ldots, 5$, which means we know the five joint parameter vectors $\vec{\theta}_j$. From this we can determine five positions of the link frame A_{i+1} relative to the link frame A_{i-1}. The result is n-1 sets of five relative positions that we use to synthesis an RR chain that connects link A_{i+1} to A_{i-1}.

Let $[V_{k,j}]$, $j = 1, \ldots, 5$ denote the five positions of A_{k+1} relative to A_{k-1}. Then the coordinates of the moving pivot $\mathbf{P}_k$ attached to A_{k+1} and the fixed pivot $\mathbf{B}_k$ attached to A_{k-1} must satisfy the equations,

$$([V_{k,j}]\mathbf{P}_k - \mathbf{B}_k) \cdot ([V_{k,j}]\mathbf{P}_k - \mathbf{B}_k) = R_k, \quad j = 1, \ldots, 5. \tag{3}$$

These are the well-known constraint equations for an RR chain, which can be solved algebraically to determine as many as four solutions for the coordinates of $\mathbf{P}_k$ and $\mathbf{B}_k$. For the details of this solution, please see **?** and **?**. It is useful to note that the existing RR chain $\mathbf{C}_k\mathbf{C}_{k+1}$ satisfy these design equations, which guarantees the presence of second real solution.

The RR design equations allow us to constrain an nR chain to reach five task positions. Figure **??** lists the planar linkages that this procedure allows us to design. Notice that in each the chain is a sequence of four-bar linkages extending from the base frame F to the moving frame M. Furthermore, while the base and moving frames are binary links having only two revolute joints, the links A_1 and A_{n-1} are ternary links, and the remaining links are quaternary.

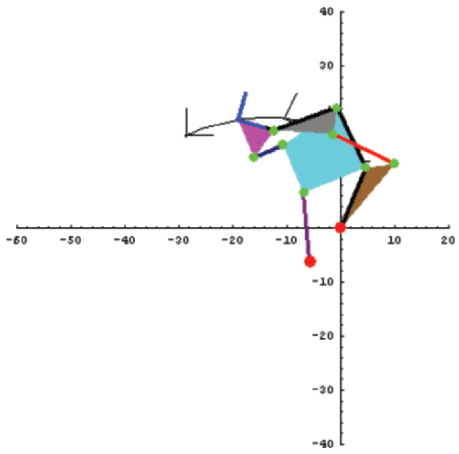

Figure 3. This eight-bar chain is obtained by constraining the joints of a 4R serial chain to pass through the same five specified task positions.

5. Synthesis for Smooth Movement

In the design or serial chain robots it is convenient to have near-equal length links to reduce the size of workspace holes. For this reason, we assume that the link dimensions of our nR chain satisfy the relationship

$$a_{12} = a_{23} = \ldots = a_{n-1,n}. \tag{4}$$

This reduces the specification of the nR chain to the location of the base joint $\mathbf{C}_1$ in G and the end-effector joint $\mathbf{C}_n$ relative to task frame H.

If the serial chain has three joints, then the inverse kinematics equations are completely prescribed and the synthesis of two RR chains yields the constrained serial chain. Figure **??** shows the results of this synthesis. In this case, though we obtained a solution that passes smoothly through the task positions, we are not able to guarantee that this will occur.

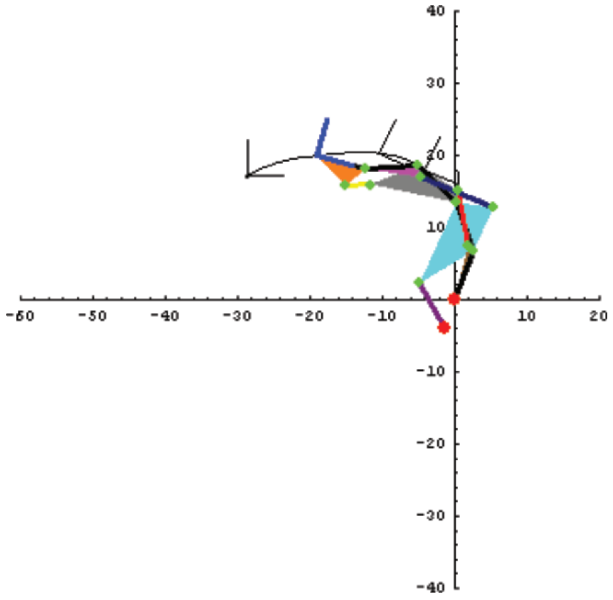

Figure 4. This 10-bar chain is obtained from a 5R that reaches the same five task positions.

If the serial chain has $n > 3$ joints, then we impose a symmetry condition

$$\theta_2 = \theta_3 = \ldots = \theta_{n-1}, \tag{5}$$

in order to obtain a unique solution to the inverse kinematics equations. This causes the design equations for the RR constraints at the joints $\mathbf{C}_2$ through $\mathbf{C}_{n-1}$ to degenerate to the multiple solutions identical to the existing links of the nR chain. In this case the design equations have four simultaneous roots.

In order to obtain useful RR constraints, we perturb the condition (**??**), so these angles are close in value but not equal. The result is a set of solutions to the design equations that are near the existing links. While this process does not guarantee a solution that does not have a circuit defect, we have been successful in finding 4R, 5R and 6R linkages that move smoothly through the five task positions, see Figures **??**, **??** and **??**.

6. Configuration Analysis

In order to evaluate and animate the movement of these linkage systems we must analyze the system to determine its configuration for each value of the input angle θ_1. Figure **??** shows that these systems consist

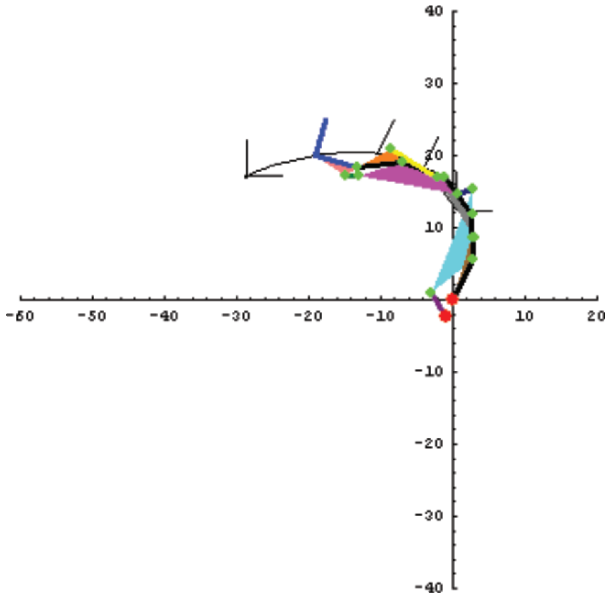

Figure 5. This 12-bar chain is a mechanically constrained 6R chain that guides the end-effector through the same five task positions.

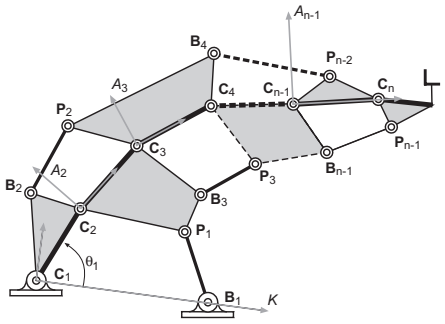

Figure 6. This shows our conventions for the analysis of a mechanically constrained nR serial chain.

of a network of interconnected four-bar linkages. This means that the entire system can be analyzed as a sequence of four-bar linkage analysis problems.

We begin the analysis with the results of the inverse kinematics analysis of the nR chain at each of the five task positions. Our approach uses the analysis procedure of 4 bar linkage from **?**. We analyze each of the n-1 4 bar linkages in the order of frame K, A_2, A_3, ..., A_{n-1}.

Starting from the first four-bar linkage in frame K, we solve for P_1 for a given θ_1. Then, we move to the second four-bar linkage in frame A_2 and solve for P_2. Next, we move to the thrid four-bar linkage in frame A_3 and solve for P_3. The procedure continues until we conclude with the $n-1$st four-bar linkage in frame A_{n-1}.

The result is a complete analysis of the mechanically constrained nR serial chain.

7. Conclusions

Our synthesis of a mechanically constrained nR chain yields a one degree-of-freedom system that guides the end-effector of the chain smoothly through five task positions. We set the size of each of the links of the chain to the same value, and specify the coordinates of its attachment to ground and to the end-effector. The inverse kinematics of the nR chain in each of the five task positions provides relative positions that enable the computation of sequence of $n-1$ RR chains. These chains combine with the nR chain back-bone to form a network of four-bar linkages which are easily analyzed to simulate the movement of the chain. A strategy of perturbation of a singular solution has yielded linkage 4R, 5R and 6R linkage systems that have all of the task positions on the same circuit.

References

Mirth, J. A., and Chase, T. R., 1993, "Circuit Analysis of Watt Chain Six-Bar Mechanisms," *ASME Journal of Mechanical Design*, 115(2):214-222.

Krovi, V., Ananthasuresh, G. K., and Kumar, V., 2002, "Kinematic and Kinetostatic Synthesis of Planar Coupled Serial Chain Mechanisms," *ASME Journal of Mechanical Design*, 124(2):301-312.

Lin, C.-S., and Erdman, A. G., 1987, "Dimensional Synthesis of Planar Triads for Six Positions," *Mechanism and Machine Theory*, 22:411-419.

Subbian, T., and Flugrad, D. R., 1994, "6 and 7 Position Triad Synthesis using Continuation Methods," *Journal of Mechanical Design*, 116(2):660-665.

Sandor, G. N., and Erdman, A. G., 1984, *Advanced Mechanism Design: Analysis and Synthesis, Vol. 2*. Prentice-Hall, Englewood Cliffs, NJ.

Perez, A., and McCarthy, J. M., 2005, "Clifford Algebra Exponentials and Planar Linkage Synthesis Equations," *ASME Journal of Mechanical Design*, 127(5):931-940, September.

Wampler, C. W., "Solving the Kinematics of Planar Mechanisms by Dixon Determinant and a Complex Plane Formulation", *ASME Journal of Mechanical Design*, 123(3), pp. 382-387.

McCarthy, J. M., 2000, *Geometric Design of Linkages*, Springer-Verlag, New York.

CALCULATING FORCE DISTRIBUTIONS FOR REDUNDANTLY ACTUATED TENDON-BASED STEWART PLATFORMS

Tobias Bruckmann, Andreas Pott and Manfred Hiller
Chair of Mechatronics
University Duisburg-Essen, Germany
{bruckmann,pott, hiller}@imech.de

Abstract Completely and redundantly restraint tendon-based Stewart platforms demand for a distribution of tendon forces to control the platform on a given trajectory. Thus, position control has to be extended by a tendon force controller which generates continuous and feasible force values. The computation of such force distributions can be formulated as a constrained optimization problem. Solving the problem is numerically expensive and requires an algorithm which is capable to be integrated into a realtime environment. In this paper, different algorithms for tendon force distribution are proposed and investigated with respect to their usability on a realtime system.

1. Introduction

At the Chair of Mechatronics, the testbed for the $n = 6$ d.o.f. tendon-based Steward-platforms SEGESTA (Seilgetriebene Stewart-Plattformen in Theorie und Anwendung) has been developed during the past few years. Presently, the SEGESTA teststand uses $m = 7$ tendons to move the platform along desired trajectories (Hiller et al., 2005b). In a future modified version of SEGESTA it is planned to add an eighth tendon.

The platform can be basically guided using position control in the domain of tendon lengths. Following a trajectory, intermediate poses for every time step are calculated. For these points, the inverse kinematics delivers the corresponding tendon lengths. Since the actual tendon lengths are available from sensors, feedback control is used to guide the platform. This basic control concept provides satisfying results at low velocities. For higher accelerations and velocities it was observed that the platform begins to "wobble" due to slack tendons. To prevent slackness and also to limit forces, tension has to be controlled within lower and upper bounds. The calculation of a force distribution is theoretically straight forward in the case of a manipulator with $m = n + 1$ tendons. In the case of $m > n + 1$, optimization is required, which is always expensive in terms of computational time. For 6 d.o.f. systems,

J. Lenarčič and B. Roth (eds.), Advances in Robot Kinematics, 403–412.

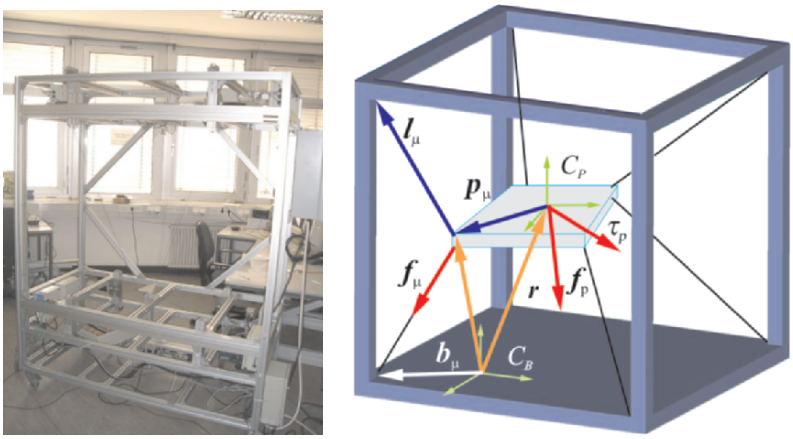

a) b)

Figure 1. SEGESTA Testbed and Symbol Definitions for a General Tendon-Based Stewart-Platform.

one cannot precalculate force distributes for all poses. Therefore, it is required to determine force distributions online. The chosen algorithm needs to be suitable with respect to calculation time and possibly fulfill deterministic realtime requirements.

The paper is structured as follows: In chapter 2, a short description of the kinematics and dynamics of SEGESTA is given. Methods for generating continuous tendon force distributions are discussed in chapter 3, including examples. Finally, in chapter 4, the conclusions are drawn and an outlook is given.

2. Kinematics and Force Equilibrium

SEGESTA consists of two main components: a frame of aluminium profile bars which carries motors, winches as well as further components like computers, measurement equipment etc. (fig. 1a). The triangular shaped platform is connected to the winches by tendons. SEGESTA is designed as an reconfigurable system by using modules which carry winches and motors and which can be installed and removed easily. Due to its lightweight structure, SEGESTA can generate high-dynamic motions (Hiller et al., 2005a).

Platform poses are calculated along a trajectory and for every step, computation of the tendon lengths (inverse kinematics) is trivial compared to the generally complicated forward kinematics. SEGESTA can be described using the following vectors and coordinate frames, with $\mu = 1, \ldots, m$ (Fang, 2005):

- The coordinate frame C_B is the base frame, while C_P is connected to the platform (fig. 1b).
- The vectors $\boldsymbol{b}_\mu$ denote the positions of the winch points, represented by the points where tendons are led through small ceramic eyes which are fixed.
- $\boldsymbol{p}_\mu$ are the platform-fixed vectors to the connecting points.
- $\boldsymbol{l}_\mu$ denote the tendon vectors from the platform to the winches.
- The forces in the tendons are described by f_μ, where $\boldsymbol{f}_P$ and $\boldsymbol{\tau}_P$ denote all other applied forces and torques acting on the platform.

Since tendons can only transmit pulling forces, tensions must always be greater than zero which leads to the requirement of at least $m = n + 1$ tendons (where n is the number of d.o.f.'s and m the number of tendons) when no external load is available to tighten the tendons. The force equilibrium for the platform can be easily expressed as (Ming and Higuchi, 1994, Verhoeven, 2003)

$$\begin{bmatrix} \boldsymbol{\nu}_1 & \cdots & \boldsymbol{\nu}_m \\ \boldsymbol{p}_1 \times \boldsymbol{\nu}_1 & \cdots & \boldsymbol{p}_m \times \boldsymbol{\nu}_m \end{bmatrix} \begin{bmatrix} f_1 \\ \vdots \\ f_m \end{bmatrix} + \begin{bmatrix} \boldsymbol{f}_p \\ \boldsymbol{\tau}_p \end{bmatrix} = 0, \quad \boldsymbol{f} > 0 \qquad (1)$$

with $\boldsymbol{\nu} = \frac{\boldsymbol{l}_\mu}{|\boldsymbol{l}_\mu|}$ or in a more compact form as

$$\boldsymbol{A}^{\mathrm{T}} \boldsymbol{f} + \boldsymbol{w} = \boldsymbol{0}, \quad \boldsymbol{f} > 0. \qquad (2)$$

3. Force Generation

Since force control is necessary to guarantee a defined tension distribution, a method to calculate tendon forces must be provided. Because we have force redundancy in the examined systems with $m \geq n + 1$ and thus at least an one-dimensional solution set for the force distributions belonging to a specific position, an optimal solution is desired. The term "optimal" has to be used with respect to the technical application (Verhoeven, 2003). In this paper, "optimal" means small forces, but it is also possible to generate high forces (for higher eigenfrequency and stiffness) or force distributions in between (for safety and robustness against parameter changes). Beside minimum tendon forces (which can be zero as smallest possible force) also maximum tendon force are of great importance since their ratio defines the workspace boundaries. To evaluate the proximity of a specific position of the platform to workspace

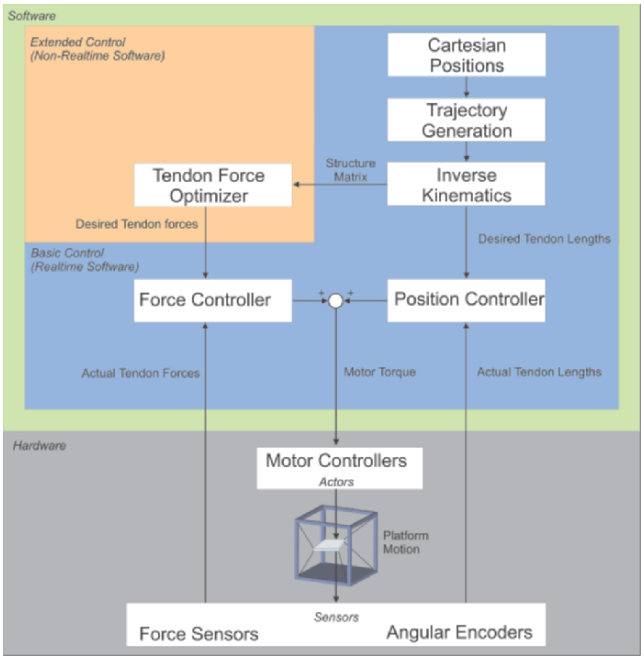

Figure 2. Combined Force- and Position Control.

boundaries, knowledge of the tendon forces is presumed. Obtaining a solution from the optimization algorithm which exceeds the tendon force boundaries means that the platform is outside the predefined workspace. So, the calculation of force distributions plays also an important role in terms of reliability and safety. In practice, it is of great importance to find continuous solutions. Non-continuous tendon forces may consist of acceptable solutions, but since those values are needed for control, they would cause steps in motor torques which leads to vibrations and high mechanical loads. Using both the results from the inverse kinematics and the force optimization makes a combined position-force-control possible, as shown in fig. 2. The position part delivers positioning precision while the force controller is responsible for positive tensions and acts as a kind of pilot control. Detailed concepts for tendon force control are also proposed in (Oh and Agrawal, 2004).

3.1 Force Distribution

For tendon-based robots with $m \geq n+1$, let $r = m - n$ denote the degree of redundancy. The tendon force distribution $\boldsymbol{f}$ has to be generated with the $m \times r$-dimensional kernel of $\boldsymbol{A}^{\mathrm{T}}$ and the pseudo inverse $\boldsymbol{A}^{+\mathrm{T}}$ as follows

$$\boldsymbol{f} = -\boldsymbol{A}^{+\mathrm{T}}\boldsymbol{w} + \boldsymbol{H}\ \boldsymbol{\lambda}. \tag{3}$$

The limits for minimum tendon force $f_{\min}$ and maximum tendon force $f_{\max}$ form a hypercube. The kernel (or nullspace) $\boldsymbol{H}$ of $\boldsymbol{A}^{\mathrm{T}}$ is defined by $\boldsymbol{A}^{\mathrm{T}}\boldsymbol{H} = 0$. All solutions for $\boldsymbol{f}$ can be represented by a r-dimensional plane. If solutions exist, the cube and the plane intersect and form a polyhedron which contains all acceptable solutions, i.e. solutions where no tendon exceeds its minimum or maximum force limits. The term $\boldsymbol{f}_{\mathrm{lsq}} = \boldsymbol{A}^{+\mathrm{T}}\boldsymbol{w}$ is a least square solution, that lies somewhere on that plane. It lies not necessarily within the cube which means that it is not acceptable in this case. On the other hand, the term $\boldsymbol{f}_{\mathrm{krn}} = \boldsymbol{H}\ \boldsymbol{\lambda}$ provides the possibility to "move" the solution on the plane since it only tenses or reliefs the tendons without violating the platform's force equilibrium.

3.2 Completely Restrained Manipulator

In case of a Completely Restrained Parallel Manipulator (CRPM), i.e. $m = n + 1$, the structure matrix $\boldsymbol{A}^{\mathrm{T}}$ has the dimension $n \times (n + 1)$. To solve (3) with respect to $\boldsymbol{f}$, a least square algorithm (pseudo inverse) is used

$$\boldsymbol{f} = \underbrace{-\boldsymbol{A}^{+\mathrm{T}}\boldsymbol{w}}_{\boldsymbol{f}_{\mathrm{lsq}}} + \underbrace{\boldsymbol{h}\lambda}_{\boldsymbol{f}_{\mathrm{krn}}}, \tag{4}$$

where $\boldsymbol{h}$ is the $m \times 1$-dimensional kernel of $\boldsymbol{A}^{\mathrm{T}}$ and λ is a scalar factor (Verhoeven, 2003, Bruckmann et al., 2006). This means that we have one d.o.f. to move on a straight line via choosing a suitable λ. Based on this, a simple algorithm can be provided:

1. Calculate the structure matrix $\boldsymbol{A}^{\mathrm{T}}$ based on a given platform pose and the kernel $\boldsymbol{h}$ of the structure matrix.
2. Get the least square solution $\boldsymbol{f}_{\mathrm{lsq}}$ and the "force offset" f_{off_μ} which has to be added to each tendon, which exceeds its lower bounds in the least squares solution $\boldsymbol{f}_{\mathrm{off}} = \boldsymbol{f}_{\min} - \boldsymbol{f}_{\mathrm{lsq}}$.
3. Compute the necessary kernel multiplication factors λ_μ for these tendons to achieve the force offset via kernel addition $\lambda_\mu = \frac{f_{\mathrm{off}_\mu}}{h_\mu}$.
4. Select the maximum multiplication factor $\lambda_{\mu_{\max}}$.
5. Correct tendon forces using kernel $\boldsymbol{h}$ and $\lambda_{\mu_{\max}}$.
6. Check if no tendon is exceeding its bounds. If at least one tendon does, there is no solution.

The algorithm has been implemented using M⃞BILE and `LAPACK` routines. The function `DGESVD` (providing singular value decomposition, SVD) was used to calculate the kernel and the function `DGELSD` (computes the minimum-norm solution to a real linear least squares problem) was chosen to get the least squares solution.

3.3 Redundantly Restrained Manipulator

In the case of a Redundantly Restrained Parallel Manipulator (RRPM) we have $m > n + 1$ and the tendon force distribution has to be generated with the $m \times r$-dimensional kernel of $\boldsymbol{A}^{\mathrm{T}}$. The SEGESTA teststand having eight drives is an example of this category.

This leads to a more complex optimization problem, since now there are $r > 1$ redundant d.o.f.. Again, it is relatively easy to find acceptable solutions, but it needs some consideration to find continuous solutions along a trajectory. In the domain of optimization, continuity depends on the cost function, which is given to the optimizer. Intuitive ideas like choosing a maximum (infinity) norm

$$\|\boldsymbol{v}\|_{\infty} = \max_{1 \le \mu \le m} |f_{\mu}| \tag{5}$$

result in non-continuous force distribution runs. A helpful choice is the p-Norm

$$\|\boldsymbol{f}\|_{p} = \sqrt[p]{\sum_{\mu=1}^{m} f_{\mu}^{p}}, \tag{6}$$

as proven by (Verhoeven and Hiller, 2002). In the paper, $p = 2$ was chosen due to common optimizer implementations, using quadratic cost functions. This leads to an optimization problem with r unbounded parameters $\lambda_{\alpha}, 1 \le \alpha \le r$, and $(2 \cdot m)$ linear constraints and a quadratic cost function. Thus, one obtains the following optimization problem

$$\text{minimize} \quad g(\boldsymbol{f}) = \quad \|\boldsymbol{f}\|_{2} = \sqrt{\sum_{\mu=1}^{m} f_{\mu}^{2}} \tag{7}$$

$$\text{s.t.} \qquad -\infty \le \lambda_{\alpha} \le \infty \tag{8}$$

$$\text{Linear Constraints} \qquad f_{\mu_{\text{off}}} \le \sum_{\alpha=1}^{m-n} H_{\mu\alpha}\, \lambda_{\alpha} \le f_{\mu_{\max}} - f_{\mu_{\text{lsq}}} \tag{9}$$

This formulation requires a two step process, first calculating the kernel $\boldsymbol{H}$ of the structure matrix and determining $\boldsymbol{f}_{\text{lsq}}$. Then the optimization is performed. An alternative idea is to use the optimizer with a different

set of linear constraints. Having the structure matrix, it is also possible to get constraints which are different from the previous ones:

$$\text{minimize} \quad g(\boldsymbol{f}) = \quad \|\boldsymbol{f}\|_2 = \sqrt{\sum_{\mu=1}^{m} f_\mu^2} \tag{10}$$

$$\text{s.t.} \qquad f_{\mu_{\min}} \leq f_\mu \leq f_{\mu_{\max}} \tag{11}$$

$$\text{Linear Constraints} \qquad w_\mu = -\sum_{\mu=1}^{m} A_{\alpha,\mu}^{\mathrm{T}} f_\mu \tag{12}$$

Although this alternative approach has to deal with m instead of r parameters, it was found to be faster in certain examples due to the good initial values, which can be reused from the last time step.

3.4 Force Distribution using Interval Analysis

Interval analysis provides a powerful algorithm to solve constrained global optimization problems (Hansen, 1992). This algorithm was successfully used for the optimization of parallel kinematic machines e.g. by Pott and Hiller, 2006. But the algorithm is also capable to deal with the problem of force distribution given by (7)-(9). This approach clearly makes use of the kernel $\boldsymbol{H}$ of the structure matrix, and thus, requires to determine $\boldsymbol{H}$ before the optimization is carried out. Generally, interval analysis can also deal with the problem given by (10)-(12), i.e. more forces are sought and the constraints are equations instead of inequalities. Nevertheless, interval based optimization guarantees to find the optimum or to reliably report, that no such force distribution exists. Furthermore, interval analysis naturally takes into account numerical round off errors. For the usage in online control, it must be assured that the force calculation can be performed within the cycle time. The worst-case calculation time of the interval based optimization can be determined but it is far beyond the required cycle time of the controller. Filtering techniques like consistency tests and interval gradient methods can drastically reduce the average calculation time but in general it is difficult to improve the worst case runtime. Thus, the interval analysis based algorithm is used as reference for the calculation of the tendon forces, where an iterative scheme is proposed for the online control.

3.5 Solution using Gradient-based Optimizers

For optimization, gradient-based optimizers are widely-used. For this purpose, the NAG library offers a variety of routines. The routine `nag_opt_lin_lsq` (solves linearly constrained linear least-squares problems using gradients) was chosen to solve the described optimization

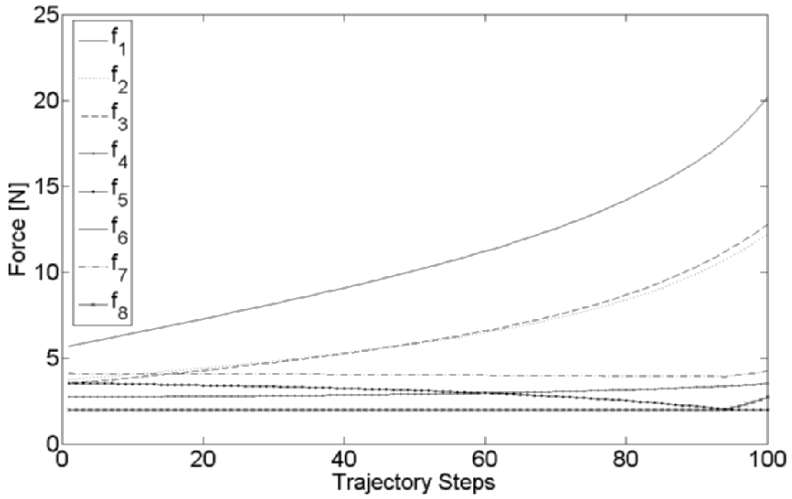

Figure 3. Force Distribution For Eight Tendons.

problem. Since the solutions for $\boldsymbol{f}$ can be represented by a plane - or, in case of the RRPM – a hyperplane, such gradient-based optimizers fit good to this kind of optimization task. Moreover, such optimizers are able to use an initial estimate of the solution. Since a trajectory in workspace is continuous, the entries of the structure matrix vary just a little bit between two force distribution calculations. Thus, the initial estimate of the next force distribution calculation is very close to the last solution which results in short calculation times. Nevertheless it is an iterative algorithm and has thus in its present implementation using the NAG libraries no hard realtime capabilities. For the future use within a hard realtime environment, a possible realtime-capable approach is to implement a gradient-based optimizer including a calculation time supervision. Since a good initial estimate can be provided, even a poor optimization which has been interrupted due to a restricted computation time may be close to the optimal result and thus usable.

3.6 Example

As a simulation example, a tendon-based Stewart platform with the frame dimensions $1000 \times 1000 \times 800$ $[mm]$ and eight tendons has to follow a straight line trajectory which starts at $100mm$ above the ground and lifts the platform for $500mm$. The platform orientation is constant with the Bryant angles $\varphi = \theta = \psi = 2.0°$ which are small resulting in a relatively large translational workspace. The minimum tension force

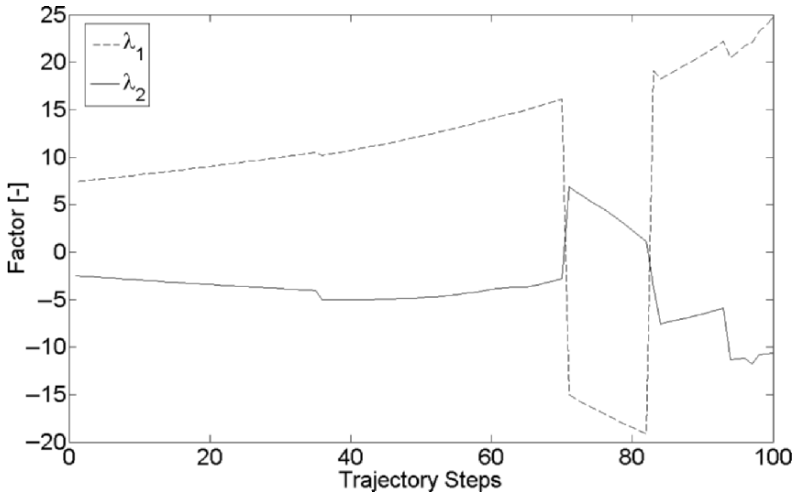

Figure 4. Parameters λ_1, λ_2 For Eight Tendons.

desired is $2N$, the maximum allowed force is $50N$. The time history of the design variables in fig. 4 is of some interest: Kernel computation is done by SVD and as an artifact of the routine used, the spanning vectors of the kernel may rotate non-continuously. Therefore, the corresponding λ_μ have to change accordingly in order to fulfill the objective function.

Thus, the algortihm generates a continuous and therefore usableforce distribution as shown in fig. 3. It is obvious that reaching the upper workspace boundaries leads to relatively high tendon forces. The force distribution is continuous and remains between the given force bounds. Thus, it is feasible for control purposes. The example was calculated both using interval analysis and gradient-based optimization. Within the required precision, no relevant differences could be figured out.

4. Conclusions and Outlook

In this paper, algorithms for generating continuous force distributions for the tendon-based Stewart-platform SEGESTA were presented. Methods for the cases of $m = n + 1$ and $m > n + 1$ tendons (in particular $m = 8$), respectively, were proposed. In the latter case, optimization algorithms have to be used, which are expensive in terms of computation time. To solve the resulting optimization problem, two algorithms using interval analysis and gradient-based optimizers were described. Interval analysis based optimization provides guaranteed solutions at the cost of a long computational time. Contrary, the gradient based optimizer

generated the identical results in average within the given cycle time. Due to its iterative approach this cannot be guaranteed in general.

Deriving realtime-capable algorithms from the methods stated here and embedding them into the controller framework will be part of future work. A more powerful PC will be set up and integrated into the modular controller to perform numerically expensive computations. The combination of force- and position control will be realized and tested, and the enhancements regarding safety and precision of movement can be verified.

Acknowledgements

This work is supported by the German Research Council (Deutsche Forschungsgemeinschaft) under HI370/24-1 and HI370/19-3.

References

Bruckmann, T., Pott, A., Franitza, D., and Hiller, M. (2006). A modular controller for redundantly actuated tendon-based stewart platforms. In Husty, M. and Schroecker, H.-P., editors, *1st European Conference on Mechanism Science*, Obergurgl, Austria.

Fang, S. (2005). *Design, modeling and motion control of tendon-based parallel manipulators*. Ph. D. dissertation, Gerhard-Mercator-University, Duisburg, Germany.

Hansen, E. (1992). *Global Optimization using Interval Analysis*. Marcal Dekker, Inc.

Hiller, M., Fang, S., Hass, C., and Bruckmann, T. (2005a). Analysis, realization and application of the tendon-based parallel robot segesta. In Last, P., Budde, C., and Wahl, F., editors, *Robotic Systems for Handling and Assembly*, volume 2 of *International Colloquium of the Collaborative Research Center SFB 562*, pages 185–202, Braunschweig, Germany. Aachen, Shaker Verlag.

Hiller, M., Fang, S., Mielczarek, S., Verhoeven, R., and Franitza, D. (2005b). Design, analysis and realization of tendon-based parallel manipulators. *Mechanism and Machine Theory*, 40.

Ming, A. and Higuchi, T. (1994). Study on multiple degree of freedom positioning mechanisms using wires, Part 1. *Int. J. Japan Soc. Prec. Eng.*, 28:235–242.

Oh, S.R. and Agrawal, S.K. (2004). Cable suspended planar robots with redundant cables: controllers with positive tensions. In *IEEE Transactions on Robotics, Accepted for Publication (SCI)*, 2004.

Pott, A. and Hiller, M. (2006). A parallel implementation for the optimization of parallel kinematic machines under process requirements. In *1st European Conference on Mechanism Science*, Obergurgl, Austria.

Verhoeven, R. (2003). *Analysis of the workspace of tendon-based Stewart-platforms*. Ph. D. dissertation, Gerhard-Mercator-University, Duisburg, Germany.

Verhoeven, R. and Hiller, M. (2002). Tension distribution in tendon-based Stewart platforms. *Proceedings of the ARK '02, 8th. International Symposium on Advances in Robot Kinematics*.

A STUDY OF MINIMAL SENSOR TOPOLOGIES FOR SPACE ROBOTS

Peggy Boning
Department of Mechanical Engineering, MIT
Cambridge, MA, USA
pboning@mit.edu

Steven Dubowsky
Department of Mechanical Engineering, MIT
Cambridge, MA, USA
dubowsky@mit.edu

Abstract Sensing in space robotic systems is expensive but necessary to compensate for imprecise actuation, disturbances, and modeling errors. It has been shown that force/torque sensors can identify actuation efforts including joint torques and reaction jet forces for multi-manipulator free-flying space robots and greatly improves system precision. This paper studies the minimum number of sensors which can identify these actuation efforts. The method uses force/torque sensors to isolate sections of the system, which are reduced to canonical elements. This allows the analysis of a small number of elements. The results of the analysis of the canonical elements are combined to determine the number of sensors needed for the original system. Configurations of one- and two-manipulator space robots are examined here and the minimal number of sensors shown.

1. Introduction

Autonomous robots will be needed for future space missions such as satellite capture and on orbit construction of large space structures including space telescopes and solar power stations (see Fig. 1) [Ueno 2003, Staritz 2001]. For these missions a space robot needs to perform precise motion and force control using its manipulators and reaction jets [Matsumoto 2002]. However, in space actuation can be imprecise and constrained by inherent nonlinearities. Sensing is necessary to compensate for torque disturbances due to joint friction, reaction jet variability and bias, thermal warping effects, and modeling errors [Breedveld 1997]. Sensing in space is limited and expensive because of hardware cost and system complexity. The objective of this work is to study the system topologies that minimize the number of sensors needed to measure joint torques and reaction jet forces for space robots.

J. Lenarčič and B. Roth (eds.), Advances in Robot Kinematics, 413–422.

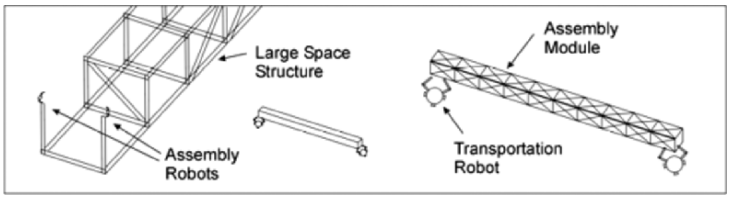

Figure 1. Construction of a large space structure by teams of robots.

Sensor-based methods to compensate for actuation nonlinearities and errors have been shown to provide precise control. Friction has proven difficult to model but control methods have been developed that use joint torque sensors to compensate successfully for friction [Vischer 1995]. However, placing a sensor at every actuator increases weight, cost, and complexity, and reduces system reliability, motivating study of minimal sensing methods to measure actuation, such as a gyro-based method for detecting faults for thruster-controlled spacecraft [Wilson 2002].

To avoid internal joint-torque sensors a method called Base Sensor Control (BSC) was developed for fixed-based terrestrial manipulators [Morel 2000]. BSC uses measurements from a six-axis force/torque sensor to estimate joint torques for closed-loop control. This method has recently been extended for space robots and it has been shown that force/torque sensors mounted between the manipulators and spacecraft can determine both the joint torques and the reaction jet forces and moments [Boning 2006]. This paper uses the method to examine the best placement and the minimum number of force/torque sensors for a given space robot to simultaneously measure joint and spacecraft actuation.

This problem could be solved by exhaustive analysis. However, varying the number of manipulators p, the number of links n, reaction jets or not, payload or not, and considering force/torque sensors at the base of the manipulator or at the end-effector, the number of cases c that need to be considered grows rapidly ($c = 16\,\mathrm{p} \times \mathrm{n}$). Here, it is shown that most cases are topologically similar and the space of possible solutions can be reduced to a small number of similar cases called canonical elements. The dynamic analysis is needed only for these elements and the results can be applied to more general systems.

2. Analytical Development

The systems studied are 3D free-flying space robots with multiple manipulators (see Fig. 2). It is assumed that the spacecraft and links are 3D rigid bodies (for example, fuel slosh is not considered). It is also assumed that the actuator forces and moments and friction at each joint and reaction jet forces are unknown. Further, it is assumed that there are no additional external loads acting on the system such as gravity

gradient effects. For this study, quantities measured are assumed to be known exactly and include accelerations. If the manipulator is holding a payload it is assumed that the end-effector makes a firm grasp.

The approach taken here is to divide the system at each six-axis force/torque sensor into subsystems. The subsystems are categorized by a small set of canonical elements. The dynamics of the canonical elements are analyzed using Newton's method to find intermediate forces and torques. Finally, the results are applied to the original system to find the minimum number of sensors required to calculate the actual net joint efforts (eliminating the effects of friction) and the actual thruster forces and reaction wheel moments.

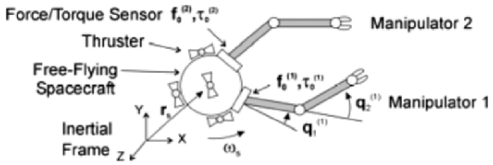

Figure 2. Space robot with sensors between spacecraft and manipulators.

2.1 Categorizing by Canonical Element

All the subsystems created by isolating sections for the space robots at force/torque sensors can be reduced to the canonical elements in Fig. 3. The force/torque sensors provide the known interface forces and moments. The canonical element for a given subsystem is determined by reducing the subsystem following rules which are shown in Fig. 4. First the system is divided at the force/torque sensors and the sensors are replaced with equal and opposite known force/torques. Next, zero end loads at the end-effectors are replaced with known force/torques, since zero loads are known loads. Adding these zero loads allows more cases to be considered as one type. Then, reaction jets are replaced with unknown force/torques. Finally, branches are replaced with chains. If a known load is applied at the end of a chain, it is equivalent to applying a known load at the branching point. The same is true for an unknown load.

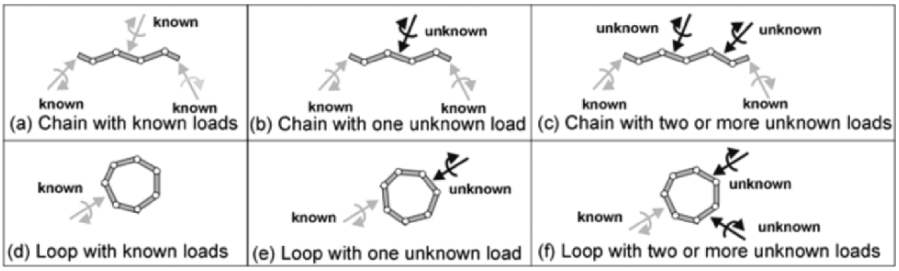

Figure 3. Canonical system elements.

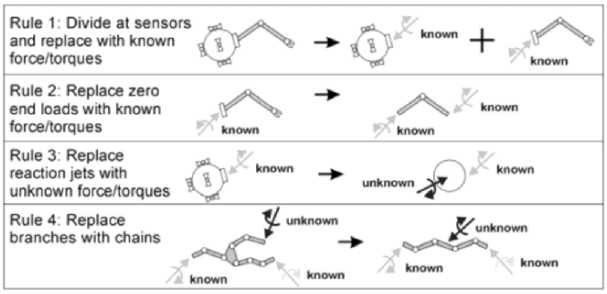

Figure 4. Reduction to canonical elements.

An example of the application of these rules is given in Fig. 5 which shows how the unknown reaction jets on a spacecraft become the canonical element chain with one unknown. More examples are shown in Fig. 6. Fig. 6(a) (Case 1) is a free-floating (no thrusters) space robot with two manipulators and a single force/torque sensor. The sensor separates the system into two canonical elements, both chains with known loads. Fig. 6(b) (Case 2) shows a free-floating robot with a single sensor at the wrist, equivalent to a chain with known loads. The sensor measures very little, since there is no payload in this case. Fig. 6(c) (Case 3) shows a free-flying space robot with a single sensor between the spacecraft and both manipulators. Fig. 6(d) (Case 4) shows a free-flying space robot that contains a closed kinematic chain or loop.

Figure 5. Reduction of unknown reaction jets to chain with one unknown.

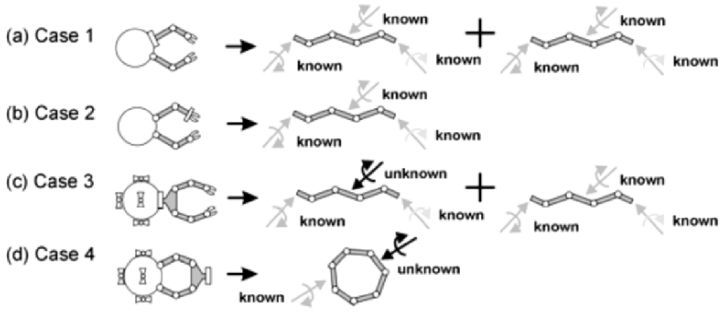

Figure 6. More reduction examples.

2.2 Dynamic Analysis

The objective of this section is to determine if there is enough sensory information for a given subsystem topology to find the net actuator forces and moments on all joints and links in the subsystem. The analysis is for a full 3D system. The friction at unactuated joints can also be measured.

A representative space system is shown in Fig. 7(a). It is assumed that for this system the spacecraft linear acceleration $\ddot{\mathbf{r}}_s$, angular velocity $\boldsymbol{\omega}_s$ and acceleration $\dot{\boldsymbol{\omega}}_s$ can be measured or estimated. For each manipulator j, the forces $\mathbf{f}_0^{(j)}$ and torques $\boldsymbol{\tau}_0^{(j)}$ at each sensor are measured along with measurements or estimates of the joint angles $\mathbf{q}^{(j)}$, velocities $\dot{\mathbf{q}}^{(j)}$, and accelerations $\ddot{\mathbf{q}}^{(j)}$. Fig. 7(b) shows a typical link. Fig. 7(c) shows a link at a branch point.

First it is noted that the positions, velocities, and acceleration of the links are known from system kinematics. To find the link's unknown actuator load, a link with only known forces and moments (given by a force/torque sensor) is located. Looking at the free body diagram in Fig. 7(b), from fundamental mechanics the unknown force $\mathbf{f}_{i+1}$ can be determined from the known force $\mathbf{f}_i$:

$$\mathbf{f}_{i+1} = \mathbf{f}_i - m_i \dot{\mathbf{v}}_{ci} \tag{1}$$

where m_i is the mass of the ith link and $\dot{\mathbf{v}}_{ci}$ is the acceleration at the ith center of mass. Similarly, the unknown torque $\boldsymbol{\tau}_{i+1}$ can be found from the known torque $\boldsymbol{\tau}_i$:

$$\boldsymbol{\tau}_{i+1} = -\mathbf{I}_i \dot{\boldsymbol{\omega}}_i - \boldsymbol{\omega}_i \times (\mathbf{I}_i \boldsymbol{\omega}_i) + \boldsymbol{\tau}_i + \mathbf{r}_{ci,i} \times f_i - \mathbf{r}_{ci,i+1} \times \mathbf{f}_{i+1} \tag{2}$$

where $\mathbf{I}_i$ is the ith inertia tensor, $\boldsymbol{\omega}_i$ is the angular velocity ith link, and $\mathbf{r}_{ci,i}$ is a vector from the center of mass of the ith link to the ith joint. Force and torque calculations can be projected along the chain by repeating the procedure.

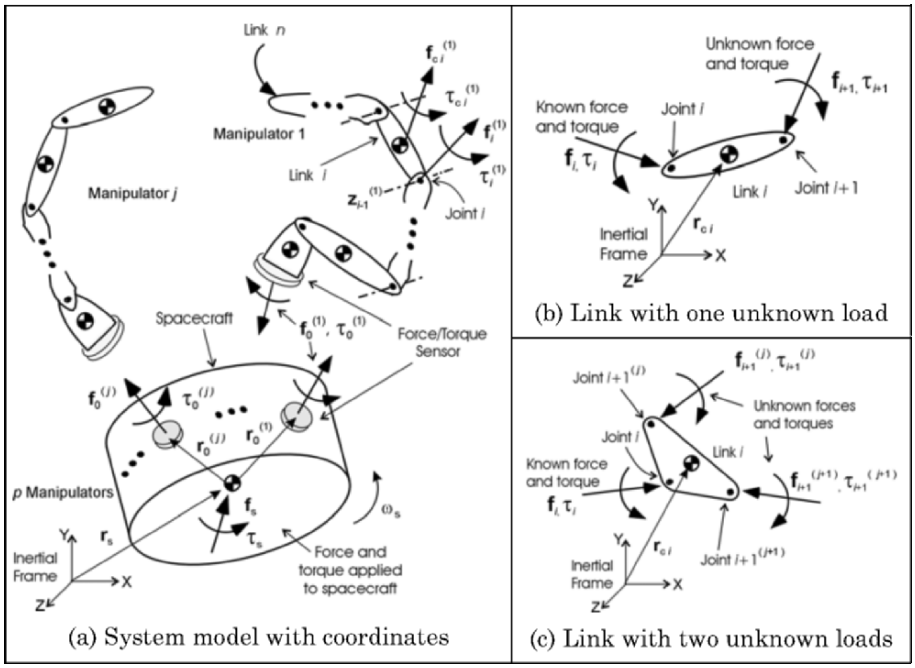

Figure 7. System models.

When there are two unknown forces (such as in Fig. 7(c)) the forces and torques cannot be calculated directly. This situation can often be solved by starting at several points in the chain and propagating the known forces and moments to a common point. In other cases additional information (such as provided by an additional force/torque sensor) is needed to permit a solution. When all of the links in the system have been visited it is possible to determine if the given set of sensors is sufficient or if additional sensors are required.

2.3 Analysis of Canonical Elements

The above analysis can be applied case by case to the canonical elements in Fig. 3. First consider the chain with known loads (Fig. 3(a)). Starting with the link on the far left, it is possible to find the actuator torques on the first joint. Continuing with the links from left to right it is possible to find forces and torques on all joints in this system. Hence there are enough sensors to completely identify all actuation efforts for this case.

The canonical element chain with one unknown load also has enough sensors, but it is necessary to work inward from both ends of the chain simultaneously so that the single unknown load at the middle link can be determined. However, for any chain that has more than one unknown load (as in Fig. 3(c)) all actuator efforts cannot be determined without adding more sensors.

Loops can be resolved into two chains joined by two branching links. Loops are analysed by starting with a link that has only known applied loads and propagating the loads in both directions around the loop until the chain rejoins. It can be shown that there are not enough sensors to determine all actuation efforts for any of the three canonical elements with loops. However, inserting a sensor in a loop converts this problem into the case of the chain with known loads (Fig. 3(a)). To summarize, for all the canonical elements, only a chain with known loads (Fig. 3(a)) and a chain with one unknown load (Fig. 3(b)) have enough sensory information to determine all actuation efforts.

Using the analysis of the canonical elements, it is straightforward to apply the results to the original system to determine sensor placement. For any given robot configuration with multiple manipulators, links, branches, etc., it is possible to enumerate potential sensor placements, divide the system into subsystems at the sensors, classify each subsystem by its canonical element, eliminate the layouts where there is not enough sensory information, and find the minimal number and placement of sensors for the system.

3. System Topologies

Systems such as Fig. 2 were studied to determine the torques at each joint and the reaction jet forces. The parameters varied are number of manipulators (p = 1, 2), number of links per manipulator (n = 1, 2, many), reaction jets or not (free-flying or free-floating), and payload or not. The primary locations for sensor placement are the manipulator wrist and the manipulator base where it joins the spacecraft. For most cases it is not necessary to enumerate all the cases where the sensor is placed at any joint in between since they are often equivalent to the cases where there are sensors at the ends of manipulator.

3.1 Minimum Sensor Configurations

The sensor placement method presented above was applied to space robots with one and two manipulators. A collection of single manipulator cases with and without thrusters is summarized in Fig. 8. In all cases with a single manipulator there was adequate sensing. Figs. 9-12 summarize the results for space robots with two manipulators. The cases in Fig. 9 do not have (or are not firing their) thrusters. The first row shows possible sensor placements when one sensor is available. It can be placed between the manipulator and the spacecraft, at the end effector, between both manipulators and the spacecraft, or at the end of both end-effectors. The second row shows placement of two sensors, the third three sensors, and the last row the only configuration with four sensors. All cases reduce to the canonical chain elements with at most one unknown load, except for the two loop cases which are crossed out. The crossed out cases do not have enough sensing to determine all actuation efforts. From the remaining cases which do have enough information it is easy to determine the minimal sensors (one) and their potential locations. These cases are outlined in bold. Fig. 10 shows the same cases as Fig. 9, except that the space robots now have thrusters. The addition of the unknown thruster loads does not change the results. There are still only two cases which do not have enough sensing, and a single force torque sensor is enough to determine actuation.

Fig. 11 shows robots which have no thrusters but carry a payload grasped by both manipulators creating a closed loop. Most of the loops are broken by a sensor so actuation can be determined but there are only two places to put a single sensor to determine actuation. Fig. 12 shows the robots from Fig. 11 with thrusters. Once again addition of unknown thruster forces does not significantly change the results.

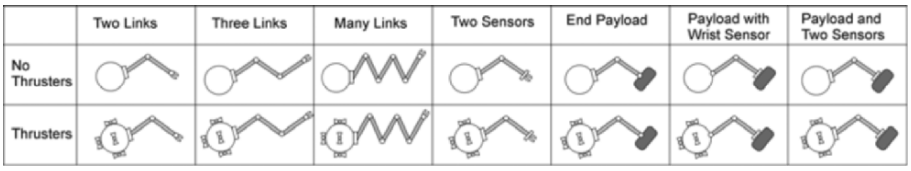

Figure 8. Space robot configurations for a single manipulator, no thrusters.

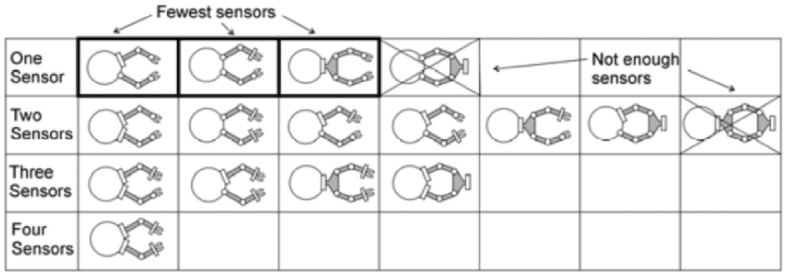

Figure 9. Space robot configurations for two manipulators and no thrusters.

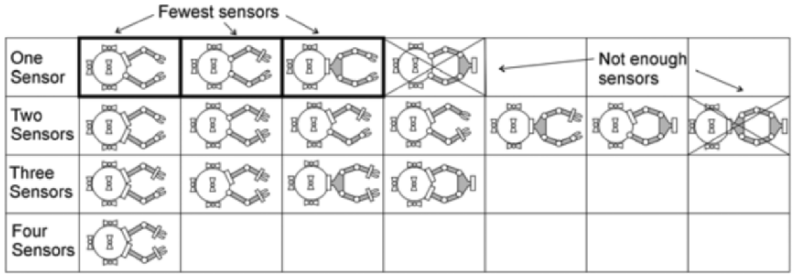

Figure 10. Space robot configurations for two manipulators and thrusters.

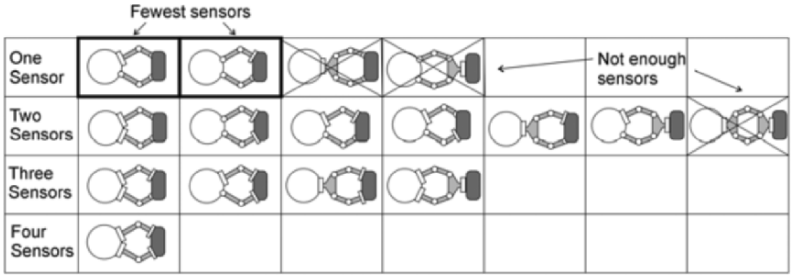

Figure 11. Space robot configurations for two manipulators and payload.

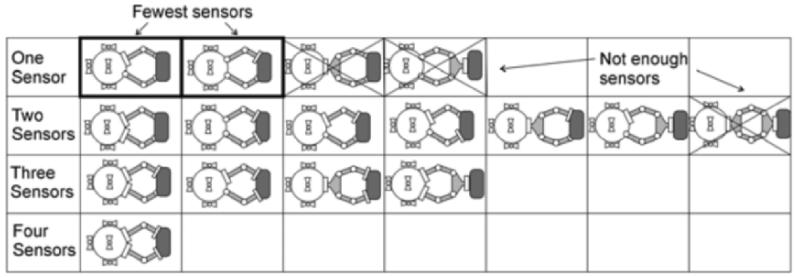

Figure 12. Space robot configurations for two manipulators, payload, thrusters.

4. Illustrative Examples

To demonstrate the validity of the basic method it is applied to the system shown in Fig. 2. One sensor could be used; however two sensors are included here to provide sensor redundancy. With failure of one sensor this system could still maintain precise control. While the above results are valid for 3D systems, for clarity 2D cases of a satellite capture task were simulated. The simulations were done in Matlab for the free-flying space robot, firing its thrusters at the same time as the manipulator end-effectors were tracking the grasp points on the satellite [Boning 2006]. Fig. 13 shows joint torques for the first manipulator. The manipulators have very high friction, 50% of their maximum capable torque. The method's torque estimate and actual applied torque agree very well even though the manipulator is unable to follow the torque command due to very large friction. In this case, a torque loop is not closed to compensate for friction. With a valid torque estimate this could be accomplished but control algorithms are beyond the scope of this paper. Fig. 14 shows the results of the same sensor measurements used to estimate the applied spacecraft reaction jet forces. The actual reaction jet forces do not match the commanded due to nonlinear effects. However the method is still able to estimate these forces.

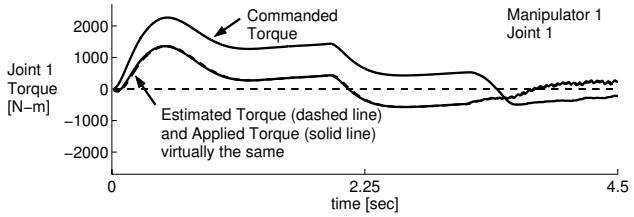

Figure 13. Manipulator 1 torques for the satellite capture task.

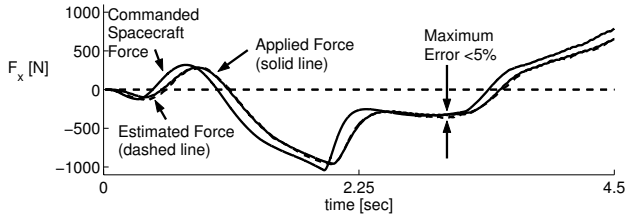

Figure 14. Continuous commanded net thruster forces, satellite capture task.

5. Conclusions

In space robots, actuator effort sensing is required for precise control. However, such sensing adds complexity, weight and cost. Hence it is important to minimize the number of sensors used. Here it is shown that there are minimum sensor configurations that are able to determine system actuation precisely. It was found that a base force torque sensor

for each manipulator can provide an estimate for friction in the joints and applied reaction jets. A wrist force torque sensor for each manipulator can also be used to estimate joint friction and applied reaction jet forces. However, additional sensors are needed for cases when there are closed kinematic loop configurations.

The methods shown here can be applied to other situations such as unknown contact forces at the end-effector, unknown payload mass, or payload gripped with pin joints (rather than rigidly grasped). Systems with reaction wheels can be considered with this methodology. The approach is useful to study redundant sensor configurations and accommodate sensor failure. Current studies are underway to consider the effects of higher order dynamics and sensor noise. An experimental validation of the method is expected to be completed shortly (in time for the ARK conference).

Acknowledgment

The support of the Japan Aerospace Exploration Agency (JAXA) is acknowledged by the authors. The authors would like to thank Prof. Ohkami, Mr. Ueno, and Mr. Ishijima for their useful comments.

References

Boning, P. and Dubowsky, S. (2006), Identification of Actuation Efforts using Limited Sensory Information for Space Robots, *Proc. of the IEEE International Conference on Robotics and Automation*, (to be published).

Breedveld, P., Diepenbroek, A., van Lunteren, T. (1997), Real-time Simulation of Friction in a Flexible Space Manipulator, *Proceedings of the 8th International Conference on Advanced Robotics*, Monterey, CA.

Matsumoto, S., Ohkami, Y., Wakabayashi, Y., Oda, M., and Ueno, H. (2002), Satellite Capturing Strategy using Agile Orbital Servicing Vehicle, Hyper-OSV, *Proc. of the IEEE Int Conf. on Robotics and Automation*, Wash. DC.

Morel, G., Iagnemma, K., and Dubowsky, S. (2000), The Precise Control of Manipulators with High Joint-Friction Using Base Force/Torque Sensing, *Automatica: The Journal of the International Federation of Automatic Control*, No. 7, vol. 36, pp. 931-941.

Staritz, P.J., Skaff, S., Urmson, C., and Whittaker, W. (2001), Skyworker: A Robot for Assembly, Inspection and Maintenance of Large Scale Orbital Facilities, *Proc. IEEE Int. Conf. on Robotics and Automation,* Seoul, Korea.

Ueno, H., Nishimaki, T., Oda, M., and Inaba, N. (2003), Autonomous Cooperative Robots for Space Structure Assembly and Maintenance, *Proc. 7th Int. Symp. on Artificial Intelligence, Robotics, and Automation in Space*, NARA, Japan.

Vischer D. and Khatib O. (1995), Design and Development of High-Performance Torque-Controlled Joints, *IEEE Trans. Robotics & Automation*, No. 4, vol. 11.

Wilson, E., Lages, C., and Mah, R. (2002), Gyro-based maximum-likelihood thruster fault detection and identification, *Proc. of the American Control Conference*, Anchorage, AK.

KINEMATICS AND OPTIMIZATION OF THE TRANSLATING 3-CCR/3-RCC PARALLEL MECHANISMS

Massimo Callegari and Matteo-Claudio Palpacelli
Polytechnic University of Marche, Department of Mechanics
Ancona, Italy
{m.callegari, m.palpacelli}@univpm.it

Abstract The paper presents the kinematics of the 3-RCC/3-CCR translating parallel mechanisms and several machines of such family are described in detail taking into account different possible kinds of actuations. They all share good kinematic properties as for instance simple closed-form relations and convex workspace, but differ for overall dimensions of the mobile platform and dynamic behaviour: therefore the concepts have been optimized and compared against common performance indices, to determine the best solutions for selected classes of applications. Based on such results, a prototype robot has been finally built.

Keywords: Parallel robots, Translating Parallel Machines, Kinematic analysis, Conceptual design, Optimization

1. Introduction

The kinematics of parallel mechanisms with full spatial mobility is usually very complex and sometimes cannot even be solved in closed form, as for example in the well-known case of the general Gough-Stewart platform (Liu and Fitzgerald, 2003). For this reason it is recently growing the interest of researchers and industry towards minor mobility mechanisms, able to perform elementary motions like pure rotations, pure translations or planar displacements: in this way the complexity of the analytical problem is greatly reduced while the advantages of closed-loop actuation are still preserved, eventually by having two parallel mechanisms mounted in series or cooperating in parallel for the accomplishment of a given task.

Many new translating parallel machines (TPMs) have been studied in the last years, including the 3-RPC mechanism by (Callegari and Tarantini, 2003) that showed good kinematic performances, e.g. simple equations, high stiffness, convex workspace, and so on. However the aforementioned concept presented also some clear weak points, such as a cumbersome moving platform, poor dynamic performances and an

J. Lenarčič and B. Roth (eds.), Advances in Robot Kinematics, 423–432.

overconstrained structure: therefore the study has been enlarged to the whole family of machines with 3-RCC/3-CCR kinematics (Callegari and Marzetti, 2003) to assess whether other mechanisms of this set show better features than the one previously identified.

The paper briefly presents three mechanisms selected among the most interesting elements of this class, develops their kinematics according to the possible different actuations and finally performs a kinematic optimization and compares the resulting performances.

2. Description of the Family of Mechanisms

A whole family of mechanisms can be defined by the functional design schematically represented in Fig. 1a: a mobile platform is connected to the fixed base by three identical limbs, that are composed by two members coupled by a cylindrical pair; the lower link of each leg is connected to the frame by a revolute joint while the upper one is connected to the platform by a cylindrical pair. Such kind of mechanisms are conventionally called 3-RCC to indicate the sequence of the joints in the three (identical) limbs, starting from the fixed frame and moving towards the platform; the 3-CCR architecture, shown in Fig. 1b, is simply obtained by kinematic inversion. It can be easily seen that the described architecture is characterized by 3 d.o.f.'s in space where in the general case spatial translations are coupled with changes of orientation of the platform. Nevertheless for particular geometrical configurations such mechanisms can provide motions of pure translation, i.e. iff (i) the axes of the revolute and outer cylindrical joint of i^{th} limb are parallel to the same unit vector $\hat{\mathbf{u}}_i$ and (ii) $\hat{\mathbf{u}}_i \neq \hat{\mathbf{u}}_j$ for $i \neq j$ ($i,j = 1,2,3$).

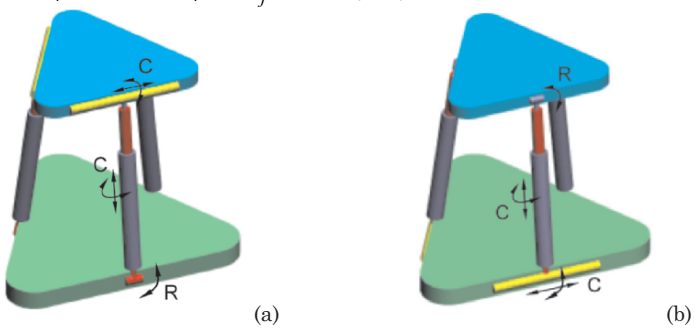

(a) (b)

Figure 1. The 3-RCC (a) and 3-CCR (b) parallel mechanisms.

It must be pointed out that in these cases the two links of each leg do not turn around the cylindrical pair, which could well be substituted by a prismatic joint, giving rise to the already mentioned 3-RPC (or 3-CPR) overconstrained mechanism.

3. Kinematics of Some Mechanisms

In this section three different mechanisms are considered. The 3-RCC architecture shown in Fig. 1a can be actuated either by driving the base revolute joints or by controlling legs' extensions: the mobile platform of such concepts turns out to be rather bulky because of the (unavoidable) length of the stroke of the cylindrical pairs mounted on the platform itself. This drawback can be possibly avoided by inverting the kinematic structure of the mechanism, Fig. 1b: in this case the legs can be actuated by directly driving the sliders running along the fixed slideways. Unfortunately a mere inversion of the mechanism is not possible because the resulting kinematics shown in Fig. 1b is singular in its entire workspace; therefore two more concepts are presented, slightly different from first mechanism but both characterized by a 3-CCR architecture.

3.1 3-RCC with Triangular Configuration

The configuration of the mechanism is symmetric, Fig. 1a, with the axes of the three revolute pairs forming an equilateral triangle on the fixed base; in the same manner, another equilateral triangle is formed on the moving platform by the axes of the cylindrical pairs; moreover, the legs are perpendicular to the joints connecting them with the two bases.

In case the machine is driven by controlling legs' lengths, IPK is characterized by a single configuration of the mechanism while DPK presents 8 different solutions that can be simply evaluated in closed-form (Callegari and Tarantini, 2003). When the unit vectors of the three limbs become linearly dependent, the manipulator gets stuck in a singular configuration: therefore the locus of all the singular points is given by a right cylinder, that however can be moved outside the workspace with a proper dimensioning of the machine. No constraint (rotation) singularities exist apart from the surface of the mentioned cylinder. This mechanism can be easily driven by means of rotary motors lumped at the end of the limbs and ball screws, see Fig. 2: such design yields very good static properties (e.g. a high thrust can be delivered since the legs are loaded only by normal forces) but the resulting dynamic behaviour is poor due to the relevant mass of the mobile platform and the high inertia of the spinning or tilting masses (Callegari et al., 2006).

Better dynamic performances can be obtained by directly powering the base revolute joints, even if the limbs are loaded by bending moments in this case. (Callegari and Marzetti, 2003) developed the complete kinematics of such mechanism: it is shown that a (very simple) unique solution exists for both direct and inverse position problem and no translation or rotation singularities are possible at all.

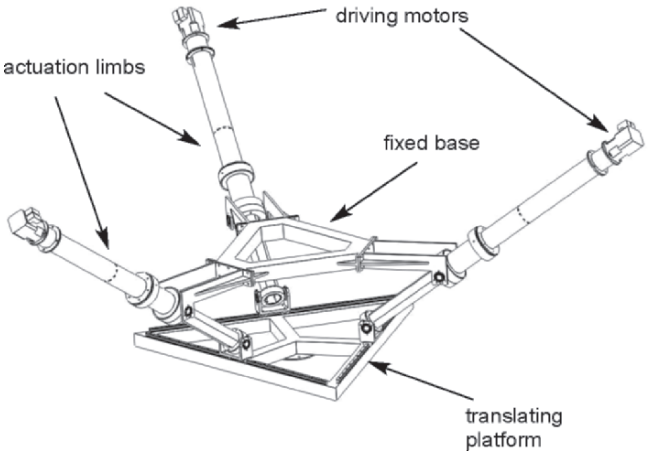

Figure 2. Sketch of the 3-RCC translational platform (actuation on legs' length).

3.2 3-CCR with Tetrahedral Configuration

The mere kinematic inversion of the 3-RCC mechanism just described is shown in Fig. 1b: (Callegari and Marzetti, 2003) proved that such mechanism is useless since all the points of its workspace are singular. As a matter of fact, in order to give full mobility to the inverted mechanism it is necessary that the direction of the axes of the three pairs connecting the limbs to the ground are linearly independent.

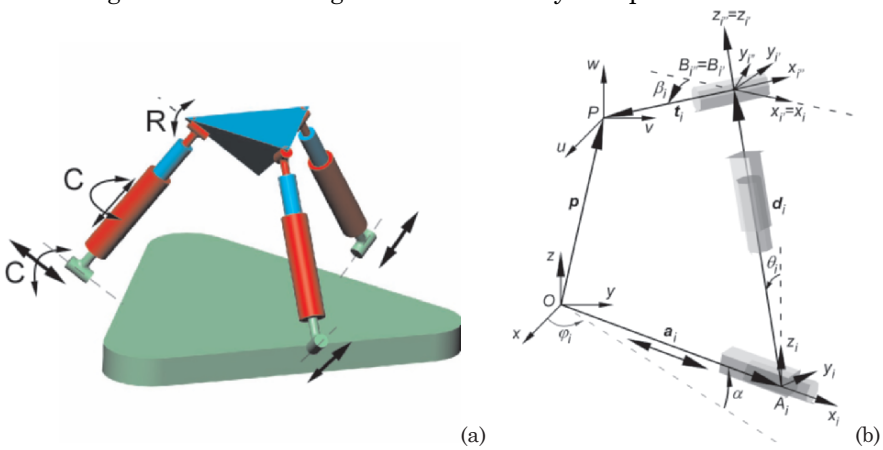

Figure 3. Sketch of the tetrahedral 3-CCR architecture and loop-closure for i^{th} limb.

For instance, in the tetrahedral configuration shown in Fig. 3a such axes stem from the origin of the fixed frame $O(\hat{x},\hat{y},\hat{z})$ and are tilted by α radians with respect to the horizontal plane. If a frame $P(\hat{u},\hat{v},\hat{w})$, parallel to $O(\hat{x},\hat{y},\hat{z})$, is attached to the mobile platform at the intersection of the

three revolute joints, the vector $\mathbf{p} = \overrightarrow{OP}$ can be taken to specify the position of the moving platform.

In order to simplify the study of the mechanism, other frames can be easily defined for each link as shown in Fig. 3b: e.g. the frame $A_i(\hat{x}_i, \hat{y}_i, \hat{z}_i)$, attached at of ith limb, is obtained by starting at the global frame $O(\hat{x}, \hat{y}, \hat{z})$, then it is rotated by φ_i around the (current) z_i axis and then by α around the (current) y_i axis, finally a translation a_i along the direction of the (current) x_i axis is performed, to allow for the variable sliding of the cylindrical pair. Moreover, the articular coordinates of the 3 joints are defined as follows: a_i and ϑ_i for the first cylindrical pair, d_i and β_i for the second one and γ_i for the revolute joint. It is also noted that the configuration of Fig. 3 is characterized by maximum symmetry, therefore $\varphi_1 = 0°, \varphi_2 = 120°, \varphi_3 = 240°$ and $t_i = t$ for *i = 1,2,3*.

The loop-closure equation of i^{th} limb is given by:

$$\mathbf{p} = \mathbf{a}_i + \mathbf{d}_i + \mathbf{t}_i \tag{1}$$

that can be expressed in the local A_i frame as:

$$\begin{bmatrix} c\varphi_i c\alpha & s\varphi_i c\alpha & s\alpha \\ -s\varphi_i & c\varphi_i & 0 \\ c\varphi_i s\alpha & -s\varphi_i s\alpha & c\alpha \end{bmatrix} \begin{bmatrix} p_x \\ p_y \\ p_z \end{bmatrix} = \begin{bmatrix} a_i \\ 0 \\ 0 \end{bmatrix} - t_i \begin{bmatrix} c\beta_i \\ c\vartheta_i s\beta_i \\ s\vartheta_i s\beta_i \end{bmatrix} - d_i \begin{bmatrix} 0 \\ s\vartheta_i \\ c\vartheta_i \end{bmatrix} \tag{2}$$

The mobility analysis developed in the Appendix shows that unfortunately such architecture is liable of constraints singularities inside its entire workspace; therefore, in order to prevent it rotating, it is necessary to turn to an overconstrained architecture by replacing limbs' internal cylindrical pairs with a prismatic pairs, resulting with a 3-CPR kinematics. The following analysis will be performed with reference to this case, where Eq. 2 still holds with $\beta_i = 0$.

Inverse position kinematics relations provide the actuated variables as functions of platform's position **p**:

$$a_i = p_x c\varphi_i c\alpha + p_y s\varphi_i c\alpha + p_z s\alpha + t_i \tag{3}$$

The same Eq. 3, written for *i=1,2,3*, is used to solve the *direct position kinematics* and find the values of p_x, p_y, p_z as functions of a_i. The direct derivation of Eq. 1 is the base for the velocity analysis:

$$\mathbf{v}_p = \dot{a}_i \cdot \hat{\mathbf{a}}_i + \dot{d}_i \cdot \hat{\mathbf{d}}_i + \boldsymbol{\omega}_i \times \mathbf{d}_i \tag{4}$$

By dot-multiplying both sides of Eq. 4 by the unit vector $\hat{\mathbf{a}}_i$ and collecting the 3 relations for *i=1,2,3* in a single expression in matrix form, $J\mathbf{v}_p = \dot{\mathbf{a}}$, the expressions of the *Jacobian matrix* is obtained:

$$J = \begin{bmatrix} \hat{\mathbf{a}}_1^T \\ \hat{\mathbf{a}}_2^T \\ \hat{\mathbf{a}}_3^T \end{bmatrix} = \begin{bmatrix} c\varphi_1 c\alpha & s\varphi_1 c\alpha & s\alpha \\ c\varphi_2 c\alpha & s\varphi_2 c\alpha & s\alpha \\ c\varphi_3 c\alpha & s\varphi_3 c\alpha & s\alpha \end{bmatrix} \tag{5}$$

The constant Jacobian shows that this mechanisms belongs to the class of the so-called Cartesian parallel robots (Kim and Tsai, 2002). It is noted that the maximum value of $\det(J) = c^2\alpha s\alpha$, granting an "optimal" manipulability, is obtained for $\alpha \approx 35.26°$ which corresponds to aligning the ground cylindrical pairs along a Cartesian frame.

3.3 3-CCR with Cartesian Configuration

The setting of the joints shown in Fig. 4 gives rise to a full Cartesian kinematics; in fact *inverse and direct position kinematics* are solved by:

$$\begin{cases} a_1 = p_x + t_1 \\ a_2 = p_x c\alpha + p_y s\alpha + t_2 \\ a_3 = p_z \end{cases} \qquad \begin{cases} p_x = a_1 - t_1 \\ p_y = \dfrac{-c\alpha \cdot a_1 + a_2 + c\alpha \cdot t_1 - t_2}{s\alpha} \\ p_z = a_3 \end{cases} \tag{6 a-b}$$

and *velocity kinematics* is expressed by the following Jacobian matrix:

$$J = \begin{bmatrix} \hat{\mathbf{a}}_1^T \\ \hat{\mathbf{a}}_2^T \\ \hat{\mathbf{a}}_2^T \end{bmatrix}^T = \begin{bmatrix} 1 & 0 & 0 \\ c\alpha & s\alpha & 0 \\ 0 & 0 & 1 \end{bmatrix} \tag{7}$$

showing that J is the identity matrix when the three ground cylindrical pairs are orthogonal one to the others ($\alpha = 90°$). Also this architecture is affected by rotation singularities inside the workspace therefore, just as before, the equivalent 3-CPR mechanism should be used instead.

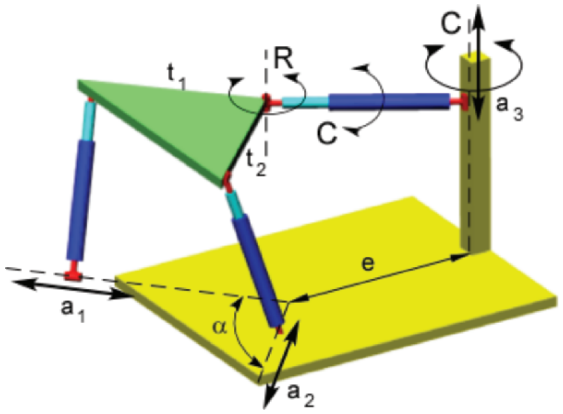

Figure 4. Sketch of the Cartesian 3-CCR architecture.

4. Optimization of the Families

The kinematic performances of the described machines strongly depend on the specific geometric parameters of the four architectures: therefore according to what has been proposed by (Carretero et al., 2000), the machines have been individually optimized and then the resulting performances have been compared. The following non-dimensional *performance index* has been used for the optimization:

$$PI = \beta_1 \cdot F_1 + \beta_2 \cdot F_2 + \beta_3 \cdot F_3 \tag{8}$$

where F_1 measures the volume of the workspace, F_2 is proportional to mobile platform's overall dimensions, F_3 quantifies the dexterity of the mechanism and β_i, $i=1,2,3$ are the weights of the 3 functions; since the functions F_i are chosen such that $0 \le F_i \le 1$ and β_i are subject to the condition: $\beta_1+\beta_2+\beta_3=1$, the performance index results bounded by $0 \le PI \le 1$.

The measure of workspace volume F_1 is chosen with reference to the Monte Carlo method proposed by (Stamper, 1997): robot's workspace is inscribed inside a cube of side $2d_{max}$ and is discretized in n_{tot} points; then a numerical procedure determines the number of n_{in} points belonging to robot's workspace and it is finally defined:

$$F_1 = n_{in} \Big/ n_{tot} \tag{9}$$

Overall dimensions of mobile platform are evaluated as:

$$F_2 = \left(t_{\max} - t\right) \Big/ t_{\max} \tag{10}$$

where t_{max} is the maximum dimension of its height and is constrained to the maximum stroke of the ground sliders. Machine's dexterity is assessed by computing the *condition number* c of the matrix J^TJ, with J Jacobian matrix, as suggested by (Gosselin and Angeles, 1991); by using the already defined discretization, it is therefore defined:

$$F_3 = \frac{\int_W \frac{1}{c^2} dW}{\int_W dW} \approx \frac{8d_{\max}^3 \frac{\sum_{i=1}^{n_{in}} \frac{1}{c_i^2}}{n_{tot}}}{8d_{\max}^3 \frac{n_{in}}{n_{tot}}} = \frac{\sum_{i=1}^{n_{in}} 1 \Big/ c_i^2}{n_{in}} \tag{11}$$

The variable parameters of the optimization are the geometric dimensions of both platforms, limbs' lengths and the incidence angle α between joint axes (or the offset distance e for the fully Cartesian machine); in order to deal with dimensionless parameters all variables are divided by maximum limbs' lenght or by the stroke of ground sliders, i.e. $d_{max} = 1$ or $a_{max} = 1$ is imposed according to the specific architecture.

If the three functions F_i are equally weighted, i.e. $\beta_1=\beta_2=\beta_3$, the optimization process yields the results collected in Table 1: it is clear that

the two 3-CPR concepts yield the best performances also when the two 3-RCC architectures present a relatively high *PI* in spite of a virtually null workspace. In fact the optimization process drove geometry variations of the 3-RCC concepts towards very small values of mobile platforms sides, therefore constraining the displacements of its cylindrical pairs.

Table 1. Comparison of robots performances (optimization with equal weights).

	RCC	**R(PR)C**	**CPR (Tetrahedral)**	**CPR (Cartesian)**
a	0.5	0.8	1	1
t	0.1	0.1	0	0
α	—	—	35.26°	90°
PI	**0.42**	**0.45**	**0.70**	**0.70**
W	1.1%	≈0%	12.5%	12.5%
e	—	—	—	0

However, also in case the only workspace is maximized for the 4 mechanisms ($\beta_1=1$, $\beta_2=\beta_3=0$) the two 3-CPR architectures still show a workspace comparable with the other concepts (see Fig. 5), that are in this case characterized by big overall dimensions and limited dexterity.

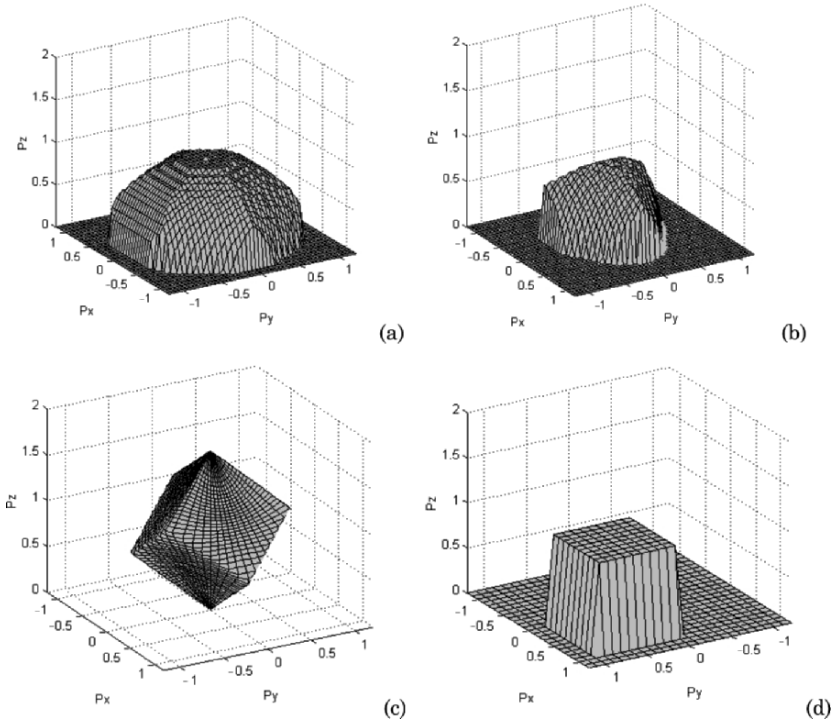

Figure 5. Optimized workspace of the 4 machines: 3-RCC with rotary (a) or linear (b) actuation, 3-CPR with tetrahedral (c) or Cartesian (d) configuration.

5. Conclusions

The paper has presented the kinematic properties of the translating platforms characterized by the 3-RCC architecture: it has been shown that also its 3-CCR kinematic inversion can be considered but, due to rotation singularities, the rotation of the inner cylindrical joint must be avoided by turning to the 3-CPR overconstrained architecture. After having optimized the mechanisms, it has been shown that the two 3-CPR concepts present quite better performances than the others: as a matter of fact they are both Cartesian parallel machines, being slightly different only due to the disposition of joint axes in the space and present a (comparably) wide workspace characterized by very high dexterity.

Moreover by still keeping the same geometry of the 3-CCR tetrahedron design of Fig. 3, but with a different disposition of the pairs, i.e. the 3-CPU architecture shown in Fig. 6a, it is possible to get rid of all singularities and obtain a non-overconstrained machine that still retains the good feature of the original concept (as a matter of fact the same kinematics equations at all). A prototype robot has been built with this structure, as described in (Callegari et al., 2005), and is shown in Fig. 6b: the first experimentations are still under way.

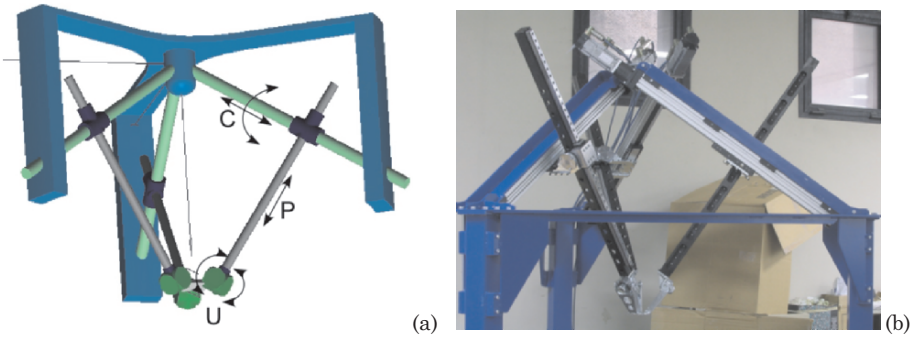

Figure 6. Concept (a) and prototype (b) of the 3-CPU translation robot.

References

Callegari, M., Marzetti, P. (2003), Kinematics of a Family of Parallel Translating Mechanisms, *Proc. Intl. Workshop on Robotics in Alpe-Adria-Danube Region*, Cassino (Italy), May 7-10.

Callegari, M., Palpacelli, M.-C., Principi, M. (2006), Dynamics Modelling and Control of the 3-RCC Translational Platform, submitted to *Mechatronics*.

Callegari, M., Palpacelli, M.-C., Scarponi, M. (2005), Kinematics of the 3-CPU parallel manipulator assembled for motions of pure translation, *Proc. Intl. Conf. Robotics and Automation*, Barcelona, April 18-22, pp. 4031-4036.

Callegari, M., Tarantini, M. (2003), Kinematic Analysis of a Novel Translational Platform, *ASME Journal of Mechanical Design*, vol. 125, pp. 308-315.

Carretero, J.A., Podhorodesky, R.P., Nahon, M.A., Gosselin, C.M. (2000), A Global Performance Index for the Kinematic Optimization of Robotic Manipulators, *ASME Journal of Mechanical Design*, vol. 122, pp. 17-24.

Gosselin, C., Angeles, J. (1991), A Global Performance Index for the Kinematic Optimization of Robotic Manipulators, *ASME Journal of Mechanical Design*, vol. 113, pp. 220-226.

Kim, H.S., Tsai, L-W. (2002), Evaluation of a Cartesian parallel manipulator. In *Advances in Robot Kinematics: Theory and Applications*, Lenarcic and Thomas Eds., Springer, pp. 21-28.

Liu, K., Fitzgerald, J.M. (2003), Kinematic Analysis of a Stewart Platform Manipulator, *IEEE Trans. Industrial Electronics,* vol. 40, pp. 282-293.

Stamper, R.E. (1997), A Three Degree of Freedom Parallel Manipulator with Only Translational Degrees of Freedom, *Ph.D. Thesis*, University of Maryland, College Park, Maryland.

Appendix. Mobility analysis of the tetrahedral 3-CCR

The angular velocity $\boldsymbol{\omega}$ of mobile platform can be expressed in function of i^{th} limb's articular coordinates as follows, see Fig. 3b:

$$\boldsymbol{\omega} = \dot{\vartheta}_i \cdot \hat{\mathbf{a}}_i + \dot{\beta}_i \cdot \hat{\mathbf{d}}_i + \dot{\gamma}_i \cdot \hat{\mathbf{t}}_i \tag{12}$$

By dot-multiplying Eq. 12 by $\hat{\mathbf{d}}_i$, it is obtained:

$$\hat{\mathbf{d}}_i^T \cdot \boldsymbol{\omega} = \dot{\beta}_i \tag{13}$$

Taking into account Eq. 13, the derivation of the first line of Eq. 2 provides:

$$c\varphi_i c\alpha \cdot \dot{p}_x + s\varphi_i c\alpha \cdot \dot{p}_y + s\alpha \cdot \dot{p}_z = \dot{a}_i + t_i s\beta_i \left(\hat{z}_{i''}^T \cdot \boldsymbol{\omega}\right) \tag{14}$$

If platform's motors are held still ($\dot{a}_i = 0$), due to the absence of translation singularities is also: $\dot{p}_x = \dot{p}_y = \dot{p}_z = 0$ and therefore from Eq. 14:

$$t_i s\beta_i \left(\hat{\mathbf{d}}_i^T \cdot \boldsymbol{\omega}\right) = 0 \tag{15}$$

Initial mounting conditions require $\beta_i = 0$, therefore it is evident that a finite angular velocity $\boldsymbol{\omega}$ can be initiated: however, since in case of pure translations the legs do not rotate around their own axes, the problem can be overcome by the introduction of prismatic pairs in place of the inner cylindrical joints (3-CPR architecture).

Motion Synthesis and Mobility

PSEUDO-PLANAR MOTION GENERATORS

Chung-Ching Lee
Dept. Tool & Die-Making Engineering,
National Kaohsiung University of Applied Sciences,
415 Chien Kung Road, Kaohsiung, 80782, Taiwan R.O.C.
E-mail: cclee@cc.kuas.edu.tw

Jacques M. Hervé
Ecole Centrale Paris,
Grande Voie des Vignes,
F-92295, Chatenay-Malabry, France
E-mail: jherve@ecp.fr

Abstract In this paper, a particular type of motion is called pseudo-planar motion and termed Y motion for brevity. A set of Y-motions having the same plane direction and the same pitch is endowed with the algebraic structure of a three-dimensional (3D) Lie group. The possible architectures of the mechanical generators of a Y subgroup are disclosed. All singular postures of Y-motion generators are described and their embodiments are graphically displayed.

Keywords: Pseudo-planar motion, Lie group, mechanical generator, singularity

1. Introduction

A special 3-dof-motion type, which includes any translation parallel to a given plane and any helical motion with a given pitch about any axis provided that the axis is perpendicular to the foregoing plane can be called pseudo-planar motion and is denoted Y-motion. A set of Y motions with a given plane direction and a given pitch is endowed with the algebraic structure of a 3D Lie group and, in other words, is a 3D displacement Lie subgroup. Hervé (1978) defined this kind of subgroup and some essential properties of the Y-motion generators together with some examples of applications were disclosed more recently (Hervé, 2004). In Angeles (2004), a subgroup of Y-motions is named a "translating-screw" group. In this paper, Y-motion generators including hinged parallelograms are introduced and the singular postures of the generators are comprehensively derived.

One can discriminate two types of singularity, namely permanent singularity and local singularity. The permanent singularity yields an inadequate chain that does never generate the desired Y motion. Local

J. Lenarčič and B. Roth (eds.), Advances in Robot Kinematics, 435–444.

singularities are specific of particular poses of the chain that generally generates the Y motion.

In any singular pose of the chain, intermediate bodies between the distal bodies of the open chain can undergo motions that are passive with respect to the relative motion between the distal bodies. Such passive motions may have finite (or full-cycle) amplitude or only infinitesimal amplitude. For brevity, these two types of singularity will be designated by the shortened locutions, infinitesimal singularity and finite singularity, respectively.

After recalling some properties of the Y motion, we enumerate all generators of Y-motion with serial arrays of 1-dof Reuleaux pairs or hinged parallelograms. The article will emphasize the singularity in the previous generators.

2. Pseudo-Planar Motion Generators

A 3D Lie group of Y displacements is denoted $\{\boldsymbol{Y}(\mathbf{w}, p)\}$ where curly brackets indicate a set, $\mathbf{w}$ is a given unit vector perpendicular to the plane Pl and p is the given pitch of the feasible helical displacements. The pitch can be any real number and, therefore, the planar displacements are the special case $p = 0$. This is reflected by the notation: $\{\boldsymbol{Y}(\mathbf{w}, 0)\} = \{\boldsymbol{G}(\mathbf{w})\}$. Furthermore, any set of helical displacements with pitch p around any axis parallel to $\mathbf{w}$ is included in $\{\boldsymbol{Y}(\mathbf{w}, p)\}$. It is straightforward to verify that any translation parallel to Pl belongs to $\{\boldsymbol{Y}(\mathbf{w}, p)\}$. Hence, $\{\boldsymbol{Y}(\mathbf{w}, p)\}$ has 3 categories of proper Lie subgroups. They are: (a) $\{\boldsymbol{H}(N, \mathbf{w}, p)\}$: any set of helical movements of axis $(N, \mathbf{w})$ with the given pitch p, $\forall N$; (b) $\{\boldsymbol{T}(\mathbf{s})\}$: any set of rectilinear translations parallel to any given vector $\mathbf{s}$ that must be perpendicular to $\mathbf{w}$, $\forall \mathbf{s} \perp \mathbf{w}$; (c) $\{\boldsymbol{T}(Pl)\} = \{\boldsymbol{T}(\perp \mathbf{w})\}$: set of planar translations parallel to the Pl-plane (or perpendicular to $\mathbf{w}$). The improper subgroups of $\{\boldsymbol{Y}(\mathbf{w}, p)\}$ are $\{\boldsymbol{E}\}$, which contains only one element, namely the identity E, and $\{\boldsymbol{Y}(\mathbf{w}, p)\}$ itself.

The set of feasible displacements of a rigid body with respect to another body of the same kinematic chain is called kinematic bond between the bodies. The serial layout of kinematic pairs generates a bond between the distal bodies, which bond is the product of the bonds generated by the serial pairs. The chains producing a given bond are called its mechanical generators. Generally, a given bond has several mechanical generators.

Because of the closure of the product in a 3D subgroup $\{\boldsymbol{Y}(\mathbf{w}, p)\}$, the product of three 1D manifolds included in $\{\boldsymbol{Y}(\mathbf{w}, p)\}$ can be equated to

$\{\boldsymbol{Y}(\mathbf{w}, p)\}$ in a neighborhood of E provided that this product is 3-dimensional. The following equalities express the 3D subgroup $\{\boldsymbol{Y}(\mathbf{w}, p)\}$ as products of three 1D subgroups, which are associated to the 1-dof Reuleaux pairs (Reuleaux, 1875), as shown in Figure 1.

$$\{\boldsymbol{Y}(\mathbf{w}, p)\} = \{\boldsymbol{H}(N_1, \mathbf{w}, p)\}\,\{\boldsymbol{H}(N_2, \mathbf{w}, p)\}\,\{\boldsymbol{H}(N_3, \mathbf{w}, p)\} \tag{1a}$$
$$= \{\boldsymbol{T}(\mathbf{u})\}\,\{\boldsymbol{H}(N_2, \mathbf{w}, p)\}\,\{\boldsymbol{H}(N_3, \mathbf{w}, p)\} \quad (\forall\, \mathbf{u} \perp \mathbf{w}) \tag{1b}$$
$$= \{\boldsymbol{H}(N_1, \mathbf{w}, p)\}\,\{\boldsymbol{T}(\mathbf{u})\}\,\{\boldsymbol{H}(N_3, \mathbf{w}, p)\} \quad (\forall\, \mathbf{u} \perp \mathbf{w}) \tag{1c}$$
$$= \{\boldsymbol{H}(N_1, \mathbf{w}\ p)\}\,\{\boldsymbol{H}(N_2, \mathbf{w}, p)\}\,\{\boldsymbol{T}(\mathbf{u})\} \quad (\forall\, \mathbf{u} \perp \mathbf{w}) \tag{1d}$$
$$= \{\boldsymbol{T}(\mathbf{u})\}\,\{\boldsymbol{H}(N, \mathbf{w}, p)\}\,\{\boldsymbol{T}(\mathbf{v})\} \quad (\forall\, \mathbf{u} \perp \mathbf{w}, \forall\, \mathbf{v} \perp \mathbf{w}, \mathbf{u} \neq \mathbf{v}) \tag{1e}$$
$$= \{\boldsymbol{H}(N, \mathbf{w}, p)\}\,\{\boldsymbol{T}(\mathbf{u})\}\,\boldsymbol{T}(\mathbf{v})\} \quad (\forall\, \mathbf{u} \perp \mathbf{w}, \forall\, \mathbf{v} \perp \mathbf{w}, \mathbf{u} \neq \mathbf{v}) \tag{1f}$$
$$= \{\boldsymbol{T}(\mathbf{u})\}\,\{\boldsymbol{T}(\mathbf{v})\}\,\{\boldsymbol{H}(N, \mathbf{w}, p)\} \quad (\forall\, \mathbf{u} \perp \mathbf{w}, \forall\, \mathbf{v} \perp \mathbf{w}, \mathbf{u} \neq \mathbf{v}) \tag{1g}$$

The serial Y-motion generators with 1-dof Reuleaux pairs are HHH, PHH, HPH, PHP and HPP. Reversing the order of joints also yields a mechanical generator of $\{\boldsymbol{Y}(\mathbf{w}, p)\}$.

The coupling of two opposite bars in a hinged parallelogram can also be used for the structural synthesis of Y motion generators. As a matter of fact, the two bars remain parallel and the motion of one bar with respect to the other bar is 1-dof translation along a circle. Replacing one or two P pairs in the generators of Figure 1 by one or two hinged parallelograms, we obtain seven Y-motion generators with hinged parallelograms, Figure 2. The planes of the parallelograms must be perpendicular to $\mathbf{w}$. Flattened parallelograms are singular and must be avoided.

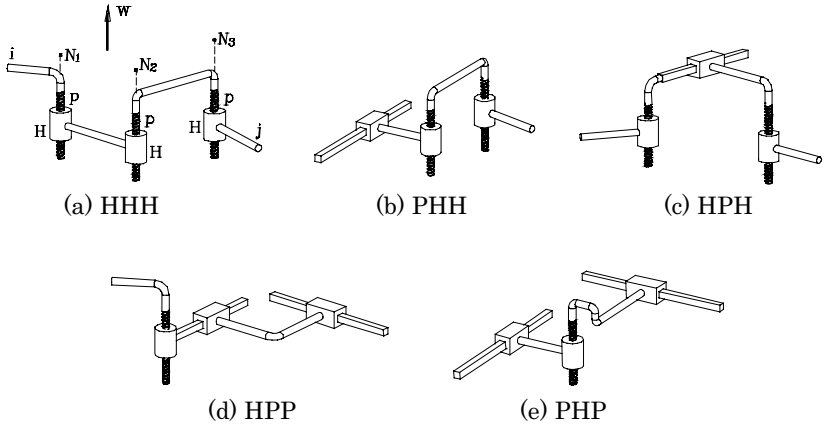

(a) HHH (b) PHH (c) HPH

(d) HPP (e) PHP

Figure 1. Y-motion generators.

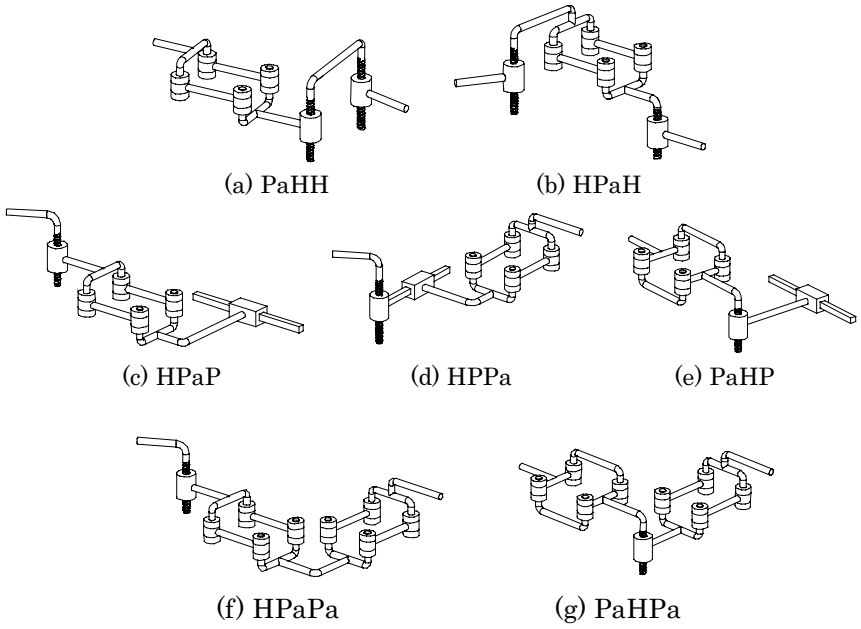

Figure 2. Y- motion generators with hinged parallelograms.

3. Finite Singularity of the Y-Motion Generators

In this section, the singularity rises from an undesired finite (or full-cycle) motion of an intermediate link in the chain aiming to generate Y motion. If the distal bodies of the chain are rigidly connected, then the resulting closed chain is movable with one or more degrees of freedom. Such a type of singularity may be permanent or local. The former does not correspond properly to a generator singularity but actually characterizes inadequate chains, which do never generate Y motion. The latter may happen in particular poses of a chain that generally generates the Y motion.

From the Delassus contribution [Delassus, 1922, Waldron, 1969, Lee, 1998], there are only "ordinary" types of movable three-bar linkages. Using Hervé's approach, the "ordinary" mobility can be explained via the group algebraic properties of the displacement set. It is straightforward to derive all the possible cases of group dependency between the subgroups of $\{\boldsymbol{Y}(\mathbf{w}, p)\}$. It is worth recalling that two subgroups are dependent iff their set intersection is not $\{\boldsymbol{E}\}$. The 2D subgroup of planar translations $\{\boldsymbol{T}(Pl)\}$ can be dependent of a subgroup of rectilinear translation parallel to Pl. A 1D subgroup of rectilinear translation or a 1D subgroup of helical displacements can be dependent only of itself.

Obviously, if the chain includes three P pairs parallel to the plane Pl, the closed chain PPP is a trivial 1-dof chain associated to the 2D subgroup of planar translations $\{\boldsymbol{T}(Pl)\} = \{\boldsymbol{T}(\perp\mathbf{w})\}$ parallel to the plane Pl

that is perpendicular to $\mathbf{w}$. Its corresponding open chain PPP generates $\{\boldsymbol{T}(\perp\mathbf{w})\}\subset\{\boldsymbol{Y}(\mathbf{w}, p)\}$ with 1-dof of passive mobility. Hence, the generators of Y-motions necessarily include one or more H pair.

In a chain with two P pairs and one H pair, an undesired motion may happen if the P pairs are parallel. Such a geometric arrangement of the P pairs may be permanent or transitory. If the P pairs are adjacent, then their common rigid link maintains the parallelism and the chain is a wrong generator of Y-motion. In a PHP array, the angle between the two P pairs can change and the chain generates Y-motion when the P pairs are not parallel and may become locally singular in a possible posture with transitory parallel P pairs. Both cases are shown in Figure 3.

(a) permanent finite singularity (b) locally finite singularity

Figure 3. Finite Singularity of PPH and PHP Y-motion generators.

In a pseudo-planar chain with two H pairs, an undesired finite motion may happen when two H pairs are coaxial. It is an inadequate chain if the coaxial H pairs are adjacent as shown in Figure 4. Otherwise, it is a local (or transitory) singularity, Figure 5.

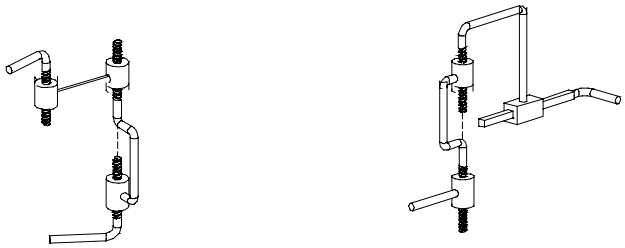

(a) permanent singularity (b) permanent singularity

Figure 4. Permanent finite singularity of chains with two coaxial H pairs.

(a) (b)

Figure 5. Finite local singularity of Y-motion generators with two coaxial H pairs.

4. Infinitesimal Singularity of HHH Generators

Through an infinitesimal displacement belonging to the $\{\boldsymbol{H}(N, \mathbf{w}, p)\}$ subgroup, a generic point M of the Euclidean affine 3D space is transformed into another point $M' = M + \mathrm{d}\mathbf{M}$, that is,

$$M \longrightarrow M' = N + (\alpha\, p/2\pi)\, \mathbf{u} + \exp(\alpha\, \mathbf{w}\times)\, (\mathbf{NM}) \tag{4}$$

where is α an infinitesimal angle. The exponential series yields $\exp(\alpha\mathbf{w}\times)(\mathbf{NM}) = (\mathbf{NM}) + \alpha\mathbf{w} \times (\mathbf{NM})$. Hence,

$$M' = M + \alpha\, [(p/2\pi)\, \mathbf{w} + \mathbf{w} \times (\mathbf{NM})] \tag{5}$$

and, the point O being any origin,

$$(\mathbf{OM}') = (\mathbf{OM}) + \alpha\, [(p/2\pi)\, \mathbf{w} + (\mathbf{ON}) \times \mathbf{w} + \mathbf{w} \times (\mathbf{OM})] \tag{6}$$

This further provides

$$\mathrm{d}\mathbf{M} = (\mathbf{OM}') - (\mathbf{OM}) = \alpha[\mathbf{w} \times (\mathbf{OM}) + (\mathbf{ON}) \times \mathbf{w} + (p/2\pi)\mathbf{w}] \tag{7}$$

The expression in Eq.(7) is usually called the twist in the H pair. Actually, the twist is a mapping, $M \rightarrow \mathrm{d}\mathbf{M}$, of the 3D Euclidean affine space in the 3D Euclidean vector space. The expression of $\mathrm{d}\mathbf{M}/\alpha$ determines what is often called the "rate of twist". The rate of twist is characterized at the origin O by the datum of two vectors, namely $\mathbf{w}$ and $\mathbf{t} = (\mathbf{ON}) \times \mathbf{w} + (p/2\pi)\, \mathbf{w}$. Conversely, the pitch p and the foot N of the perpendicular drawn from O to the screw axis can be derived from $\mathbf{w}$ and $\mathbf{t}$ by employing the two relations $k = p/2\pi = \mathbf{w}.\mathbf{t}$ and $(\mathbf{ON}) = \mathbf{w} \times \mathbf{t}$.

Consequently, the twist of any H pair, which has the axis $(N, \mathbf{w})$ and the pitch $p = 2\pi k$ can be expressed as

$$\alpha[\mathbf{w} \times (\mathbf{OM}) + (\mathbf{ON}) \times \mathbf{w} + k\mathbf{w}] = \alpha\, [\mathbf{w} \times (\mathbf{OM}) + \mathbf{t}] \tag{8}$$

In order to obtain simple expressions in what follows, without loss of the generality, the point N that can be any point belonging to the screw axis, is chosen in the plane that is perpendicular to the unit vector $\mathbf{w}$ and contains the origin O; this plane will be denoted $Pl\,(O, \perp\mathbf{w})$.

Any linear combination of two twists is a third twist, which is called resultant twist. The resultant twist is the twist of the serial array of two pairs characterized by the first two twists. Natively the resultant twist is linearly dependent on the first two twists and is an element of the linear span of the first two twists. In other words, the three twists belong to the same 2D vector subspace of the 6D vector space of all twists. If three kinematic pairs are characterized by three linearly dependent twists, then the serial array of these pairs is singular. Generally, this singularity is a local infinitesimal singularity.

Let us consider two H pairs with the same pitch $p = 2\pi k$ and parallel axes $(N_1, \mathbf{w})$ and $(N_2, \mathbf{w})$. We choose N_1 and N_2 in the plane $Pl\,(O, \perp\mathbf{w})$. Obviously, if $N_1 = N_2$, then the screw pairs are coaxial and the linear span of the two twists is made of the twists of all coaxial H pairs with the pitch p. In what follows, $N_1 \neq N_2$. The twist of the first H is $\mathrm{d}_1\mathbf{M} = \alpha[\mathbf{w} \times (\mathbf{OM}) + (\mathbf{ON}_1) \times \mathbf{w} + k\mathbf{w}]$ and the twist of the second H is $\mathrm{d}_2\mathbf{M} =$

$\beta[\mathbf{w}\times(\mathbf{OM}) + (\mathbf{ON}_2)\times\mathbf{w} + k\mathbf{w}]$; α and β denote infinitesimal angles in each of the two H pairs. The resultant twist $d_R\mathbf{M}$ of a serial array of two parallel H pairs having the same pitch p, can be expressed as

$$d_R\mathbf{M} = d_1\mathbf{M} + d_2\mathbf{M} = \alpha_R[\mathbf{w}\times(\mathbf{OM}) + (\mathbf{ON}_R)\times\mathbf{w} + k_R\mathbf{w}] = \alpha_R[\mathbf{w}\times(\mathbf{OM}) + \mathbf{t}_R] \quad (9)$$

in which

$\alpha_R = \alpha + \beta$

$\mathbf{t}_R = (\mathbf{ON}_R)\times\mathbf{w} + k_R\mathbf{w} = [\alpha(\mathbf{ON}_1) + \beta(\mathbf{ON}_2)]/(\alpha+\beta)\times\mathbf{w} + k_R\mathbf{w}$

$k_R = p_R/2\pi = (\alpha p + \beta p)/[2\pi(\alpha+\beta)] = p/2\pi = k$

N_R : a point belonging to the resultant screw axis, in $Pl(O, \perp\mathbf{w})$.

One can identify in $[\alpha(\mathbf{ON}_1) + \beta(\mathbf{ON}_2)] / (\alpha + \beta)$ the barycenter (center of mass) of the point N_1 and the point N_2 with the mass $\alpha/(\alpha+\beta)$ and the mass $\beta/(\alpha+\beta)$, respectively. Hence, N_R lies on the straight line N_1N_2. One can readily demonstrate

$$(\mathbf{N_RN_1}) = (\mathbf{ON_1}) - (\mathbf{ON_R}) = (\mathbf{ON_1}) - [\alpha(\mathbf{ON_1}) + \beta(\mathbf{ON_2})]/(\alpha+\beta)$$
$$= (\mathbf{ON_1}) - [\alpha(\mathbf{ON_1}) + \beta(\mathbf{ON_1} + \mathbf{N_1N_2})] / (\alpha+\beta)$$
$$= \beta\,(\mathbf{N_2N_1})/(\alpha+\beta) \quad (10a)$$

By the same token,

$$(\mathbf{N_RN_2}) = -\alpha\,(\mathbf{N_2N_1})/(\alpha+\beta) \quad (10b)$$

Equations (10a) and (10b) show that the coefficients $\alpha/(\alpha+\beta)$ and $\beta/(\alpha+\beta)$ can be expressed with ratios of vectors that are derived of the arrangement on a straight line of the three points N_1, N_2 and N_R, namely $\alpha/(\alpha+\beta) = (\mathbf{N_2N_R})/(\mathbf{N_2N_1})$ and $\beta/(\alpha+\beta) = (\mathbf{N_1N_R})/(\mathbf{N_1N_2})$.

The resultant twist can be identified as the twist of a H pair with the pitch p and the axis $(N_R, \mathbf{w})$. We find out the singular chain postures that are represented by the following product of three subgroups of helical displacements

$$\{\boldsymbol{H}(N_1, \mathbf{w}, p)\}\,\{\boldsymbol{H}(N_2, \mathbf{w}, p)\}\{\boldsymbol{H}(N_R, \mathbf{w}, p)\} \text{ with } N_R \in \text{line}\,(N_1N_2) \quad (11)$$

The position of N_R on the straight line N_1N_2 can be anyone. The three H pair axes lies in the same plane parallel to $\mathbf{w}$, Figure 6. Furthermore, the planar case is a special case $(p=0)$ of the pseudo-planar case. Hence, a generator RRR of planar gliding motion becomes singular iff the three R axes lies in a plane as shown in Figure 7.

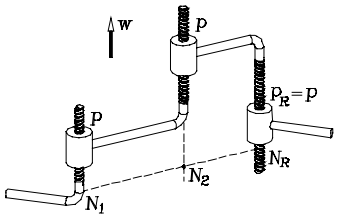

Figure 6. A HHH chain with a local infinitesimal singularity.

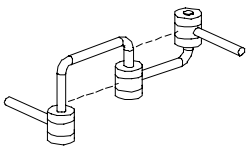

Figure 7. Infinitesimal singularity of RRR generator of planar motion.

5. Infinitesimal Singularity in Chains with One P

Let us consider a pseudo-planar chain including a P pair generating $\{\boldsymbol{T}(\mathbf{s})\}$. An infinitesimal displacement belonging to the subgroup $\{\boldsymbol{T}(\mathbf{s})\}$ is the point transformation $M \rightarrow M' = M + \beta\mathbf{s}$ where β is an infinitesimal real number. This transformation is an infinitesimal translation that has no screw axis $d\mathbf{M} = \beta\mathbf{s}$. Now, let us consider one H pair having the axis $(N, \mathbf{w})$ and the pitch $p = 2\pi k$ whose twist is $d_1\mathbf{M} = \alpha[\mathbf{w} \times (\mathbf{OM}) + (\mathbf{ON}) \times \mathbf{w} + k\mathbf{w}]$ and one prismatic P pair parallel to the unit vector $\mathbf{s}$ whose twist is $d_2\mathbf{M} = \beta\mathbf{s}$. The resultant twist of the serial array HP can be expressed as

$$d_R\mathbf{M} = d_1\mathbf{M} + d_2\mathbf{M} = \alpha[\mathbf{w} \times (\mathbf{OM}) + (\mathbf{ON}) \times \mathbf{w} + (k\mathbf{w} + \beta/\alpha\mathbf{s})] = \alpha_R[\mathbf{w} \times (\mathbf{OM}) + \mathbf{t}_R] \quad (15)$$

in which $\alpha_R (= \alpha)$ denotes the infinitesimal angle in the resultant twist. One can readily identify the twist of a H pair. The twist axis is parallel to $\mathbf{w}$. The pitch is $p_R = 2\pi\mathbf{w}.\mathbf{t}_R = 2\pi[k + \beta/\alpha(\mathbf{w}.\mathbf{s})] = 2\pi k = p$ because $\mathbf{w}.\mathbf{s} = 0$, $\mathbf{s}$ being perpendicular to $\mathbf{w}$. The axis position is determined by a point N_R belonging to the resultant screw axis. The point N_R is chosen in the plane $Pl\,(O, \perp\mathbf{w})$. $(\mathbf{ON}_R) = \mathbf{w} \times \mathbf{t}_R = \mathbf{ON} + (\beta/\alpha)\mathbf{w} \times \mathbf{s}$. The vector $\mathbf{w} \times \mathbf{s}$ is parallel to the plane $Pl\,(O, \perp\mathbf{w})$ and is perpendicular to $\mathbf{s}$. Moreover, one can verify that $\mathbf{w} \times \mathbf{s}$ is a unit vector. The number $a = \beta/\alpha$ is the abscissa of point N_R in the frame of reference $(N, \mathbf{w} \times \mathbf{s})$. The abscissa a can be any real number.

We find out the singular postures of a HPH generator of *Y*-motion. The P pair is perpendicular to the plane of the two parallel H axes as shown in Figure 8.

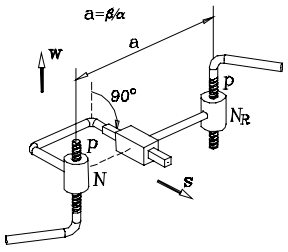

Figure 8. Local infinitesimal singularity of HPH *Y*-motion generator.

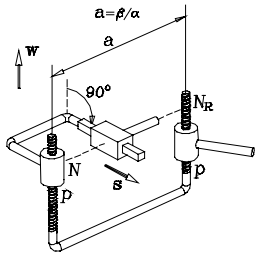

Figure 9. Local infinitesimal singularity of PHH *Y*-motion generator.

The previous resultant twist of a HP array is also the resultant twist of a PH array. Therefore, Figure 9 shows a singular pose of a PHH generator. Furthermore, Figure 10 and Figure 11 depict the singular poses in the generators RPR and PRR (or RRP) of the subgroup $\{\boldsymbol{G}(\mathbf{w})\}$ of planar gliding motions perpendicular to $\mathbf{w}$.

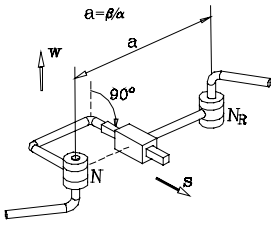

Figure 10. Infinitesimal singularity of RPR *G*-motion generator.

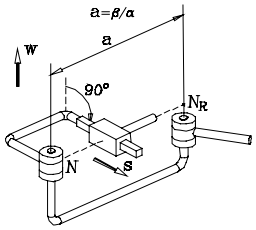

Figure 11. Infinitesimal local singularity of PRR *G*-motion generator.

To sum up, a HPH, PHH or HHP open chain aiming to be a generator of *Y*-motion has a local infinitesimal singularity iff the P pair is perpendicular to the plane of the two parallel H axes.

What is more, based on the above findings, the possible local singular postures of *Y* motion generators with hinged parallelograms are readily deduced and are displayed in Figure 12.

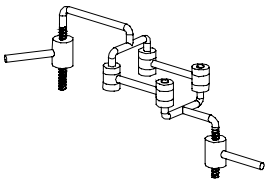

(a) deduced from Figure 8

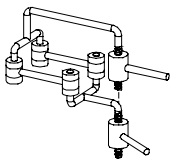

(b) deduced from Figure 5(b)

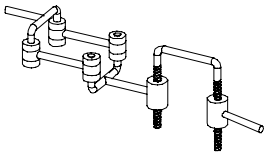

(c) deduced from Figure 9

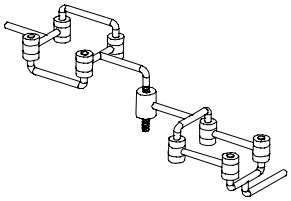

(d) deduced from Figure 3(b)

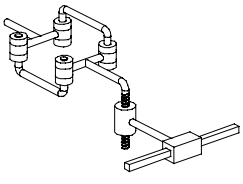

(e) also deduced from Figure 3(b)

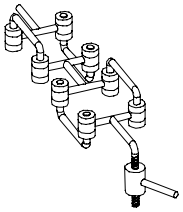

(f) deduced from Figure 3(a)

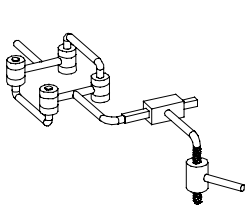

(g) also deduced from Figure 3(a)

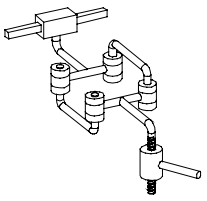

(h) also deduced from Figure 3(a)

Figure 12. Singular postures of Y-motion generators with hinged parallelograms.

6. Conclusion

Five distinct architectures of Y motion generators with Reuleaux pairs and seven ones with hinged parallelograms are enumerated and their kinematic chains are graphically displayed in order to be a tool for the selection of limb structures in the synthesis of parallel manipulators. The singular postures resulting of undesired motion with finite and infinitesimal amplitude are disclosed through the study of group dependency of displacement subsets and linear dependency of twists, respectively. It is quite clear that several novel 3-dof parallel manipulators with pseudo-planar limbs can be envisioned but this lies outside of the scope of this paper.

References

Angeles, J. (2004), The Qualitative Synthesis of Parallel Manipulators, ASME J. Mech. Design, Vol. 126, pp. 617−674.

Delassus, E. (1922), Les Chains Articulées Fermées et Déformables à Quatre Membres, Bull. Sci. Math., Vol. 46, pp. 283−304.

Hervé, J. M., (1978), Analyse Structurelle des Mécanismes par Groupe des Déplacements, In: Mechanism and Machine Theory, Vol. 13, No. 4, pp. 437−450.

Hervé, J. M. (2004), Parallel Mechanisms with Pseudo-Planar Motion Generators, On advances in Robot Kinematics, Kluwer Academic Publishers, pp. 431−440.

Lee, C.–C. (1998), An Account of Delassus Three-Bar Overconstrained Mechanisms, Proceedings of the First National Conference on the Design of Mechanisms and Machines, Tainan, Taiwan R.O.C., pp. 31−37.

Reuleaux, F. (1875), Theoretische Kinematik:Grunzüge einer Theorie des Maschinenwesens. Vieweg, Braunschweig, Reprinted as Kinematics of Machinery by Dover, New York, 1963.

Waldron, K. J. (1969), The Mobility of Linkages, Ph.D. Dissertation, Stanford University.

ON PKM WITH ARTICULATED TRAVELLING-PLATE AND LARGE TILTING ANGLES

Sébastien Krut, François Pierrot, Olivier Company
LIRMM, UMR 5506 CNRS – Université Montpellier 2
161 rue Ada, 34392 Montpellier CEDEX 5, France
<krut, pierrot, company>@lirmm.fr

Abstract This paper discusses some ways to achieve large tilting motions with PKM by resorting to articulated travelling plate. Different options are firstly presented: remote actuation, hybrid architectures, redundancy, rotation-amplification and translation-to-rotation transformation. Starting from two of those features, the aim of this paper is to go one step further and to show that it might be possible to design a 5-DoF (Degrees of Freedom) mechanism with large tilting angles about two axes.

Keywords: PKM, articulated travelling-plate, large tilting angles

1. Introduction

The idea of parallel mechanisms resorting to a non-rigid (or articulated) moving platform (traveling plate) which includes passive joints has been introduced recently and a few academic prototypes have already demonstrated the effectiveness of this principle (Pierrot et al., 1999; Krut et al., 2003). These prototypes implement Scara motions. Indeed, the 4 DoF of Scara motions are well adapted to pick-and-place tasks: 3 translations to carry an object from one point to another, plus one rotation about a given axis in world coordinates for the orientation. For efficient pick-and-place a 360-degree orientation range is expected. Robots inspired from Delta architecture (Clavel, 1985) encountered a real commercial success achieving this task because of their high dynamics (acceleration capability) that has a strong influence on cycle time. This is due to their lightweight (actuators are fixed on the base) parallel (having closed kinematics chains) design. However, the **R**UPUR central kinematic chain (R: Revolute, U: Universal, P: Prismatic, bold letter stands for actuated joint) that transmits the rotational motion from a revolute actuator fixed on the frame to the effector may become a weak point. This is particularly true for Delta with huge workspace or, even more, with linear Delta that might be used for designing machine-tools.

Most of recent researches in that field have proposed different designs to obtain Scara motions either for serving as pick-and-place robots, or for

J. Lenarčič and B. Roth (eds.), Advances in Robot Kinematics, 445–454.

being a part of a more complex machine-tool; some of them are parallel mechanisms, like Kanuk (Rolland, 1999) or H4 (Pierrot et al., 1999), some others have non-fully-parallel designs (Angeles et al., 2000). Other 4-DoF parallel mechanisms have been studied in the past, but they are dedicated to different applications such as Koevermans' flight simulator (Koevermans et al., 1975) and Reboulet's four-DoF wrist (Reboulet et al., 1991). Even more recently, a machine with a moving platform including passive prismatic joints and a "Translation-to-Rotation" transformation system has been introduced (Krut et al., 2003); in the latest paper it was shown that it was possible to get a realistic practical design for a very specific design: (*i*) four linear motors in the same plane and aligned on the same direction, (*ii*) a three-part moving platform. Moreover, it induces very simple kinematics model in closed form for both Inverse and Forward problems.

The aim of this paper is to go one step further and to propose two ideas:

1. It might be indeed possible to obtain a 4-DoF design which compares directly with commercially available Delta-based robots (e.g. the FlexPicker, an ABB Robotics piece of harware) in terms of technology, workspace, and performance while avoiding the **R**UPUR kinematic chain.
2. It might be possible to design a 5-DoF machine with large tilting angle about two axes.

To do so, we have designed the prototype of a robot (we call Eureka) by resorting to several components from the industrial FlexPicker robot. A prototype is about to be built. Its design can be seen as an "extension" of the principle of articulated travelling plate with passive linear joints. Hence, it also combines actuation redundancy so that we obtain a 5-DoF, large-tilting-angle solution.

In this paper, this prototype is described and the way to achieve the desired rotations is discussed. Then, geometrical models are derived (a nice feature for this robot is that the forward geometrical model can be written in a closed form). Afterwards, a kinematic modelling able to witness all the singularities of the robot is established. It is based on a detailed modelling of the so-called "spatial parallelograms" which are described here for what they really are: two SS chains. It shows up the geometrical condition that must be verified in order to achieve the desired motions.

2. Getting Large Tilting Angles

It is well established that PKM suffers from different types of singularities that are often said to belong to two families:

- Serial-type (or under-mobility) when the mechanism loses one (or more) degree of freedom;
- Parallel-type (or over-mobility) when the mechanism's stiffness vanishes in one (or more) direction.

In the following section, this paper will discuss this description of singularities (even explaining that additional problems exist) but it is nevertheless true that the tilting angles are often limited by parallel-type singularities. So far, different solutions have been proposed to overcome that problem and getting larger tilting angles, as described in the following sub-sections:

Remote actuation – One way to get large tilting angles is to arrange one revolute joint on the travelling plate (in a "serial" way) and, to limit the moving parts masses, to place the actuation in a fixed remote location, that is, the base. It is the option selected for most Delta robots, using a telescopic fourth chain (with an **R**UPUR arrangement) dedicated to tool rotation. This principle allows the rotation range to be as large as for serial chains (indeed, the last rotation is actually arranged in a serial way...) while keeping the moving masses low because all motors are still fixed on the base.

Hybrid architecture – Kinematic optimization is always an open option when a PKM has to be designed, and it is often feasible to select an "optimal" set of design parameters (position of actuators, length of legs, etc.) to maximize the workspace of a mechanism in terms of tilting angles range. Obviously, this optimization process is made easier if some constraints are removed, for example if the machine is designed for tilting purpose only. This solution leads to machines made with two sub-parts, each of them specialized in only a part of the task.

Redundancy – The general concept of "redundancy" applied to mechanism theory can be roughly stated as follows: installing more actuators than the number of the TCP's (Tool Control Point). For serial chains, this gives, for a given position of the TCP, and infinite number of actuated joints positions. Selecting properly a set of joint positions may help in avoiding singularities. This option (called "kinematic redundancy") exists for PKM but it has been used in a very limited number of cases. The principle is here to select among the possible joint positions, one position that is far enough from singularities.

Moreover, PKM offer the ability to create a different type of redundancy, called "actuation redundancy", that can be described as follows: for a given set of external load, an infinite number of joint force sets exist for balancing the external load. In that case, the principle is to choose among the possible sets of joint forces, one set of forces

which guarantees a good stiffness (see Ryu et al., 1998, for a good implementation of such a principle).

This type of redundancy has been studied in more details for PKM than the previous one (for kinematic redundancy most efforts had been dedicated to the serial case) and several prototypes have been built, giving researchers the opportunity to evaluate control schemes. Indeed, control is here the key issue since actuation redundancy leads to over-constrained mechanisms. Consequently internal forces may exist, and control schemes have to cope with that.

Rotation amplification – In recent years, we have studied such an option in some details, by proposing different mechanism architectures based on one key principle: designing a travelling plate which includes passive revolute joints. This was the base of H4 architecture, a mechanism for "Scara-like motions", already described. H4 is based on 4 identical elementary chains (**R**[SS]$_2$ chains) and on an articulated travelling plate equipped with 3 passive revolute joints. The last revolute joint is moved by a coupling system about a 360 degree range, which relates its motion to the motion of another passive revolute joint that has only a 90 degree range by using an additional gear-based amplification.

Translation-to-Rotation transformation – It has been shown that H4 is an architecture providing Scara motions. However, some of its limitations can be pointed out:

- When tool orientation changes, the Jacobean matrix condition number may vary a lot, leading to important changes in machine behaviour;
- It has been proved that the relative positions of the four "spatial parallelograms" must be properly selected to avoid singular cases;
- Its forward geometrical model has not been established in analytical form, except for specific arrangements.

It was proposed in Krut et al., 2003, to build travelling plates with prismatic passive joints instead of revolute joints. It is always possible to transform this translational motion into a rotational one by means of rack-and-pinion, belt or cable-and-pulley devices. This solves most difficult points due to revolute joints: models are simpler, load balance is easier to achieve, general design is simpler, etc.

3. Combining Redundancy and T-to-R Transformation

This section of the paper introduces a novel mechanical architecture which combines two of the previous features. Eureka, the proposed machine, is redundant (6 actuators for 5 DoF provides actuation redundancy) and is based on an articulated three-body travelling plate with two linear joints. The machine offers 3 translations and 2 rotations with large tilting capabilities in two directions; the first axis of rotation

has a constant direction with respect to a fixed frame, the second axis is orthogonal to the first one.

A detailed kinematic analysis is carried out and leads to geometrical conditions to be verified by the mechanism for proper functioning. Then a kinematic modelling illustrates the mechanism simplicity and provides a first evaluation of the machine's workspace. Finally, preliminary information is given regarding practical implementation of this new architecture.

3.1 General Concept

The proposed machine is a 6-actuator / 5-dof parallel mechanism. In Fig. 1, a joint-and-loop graph is depicted: grey boxes represent actuated joints; white boxes passive joints and circles express a kinematic coupling between two joints.

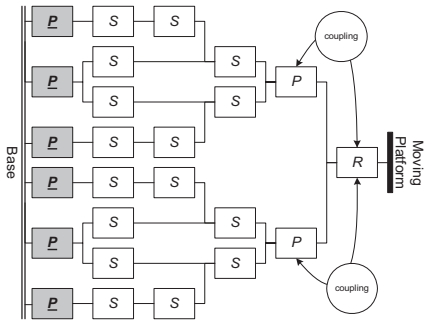

Figure 1. Joint-and-loop graph.

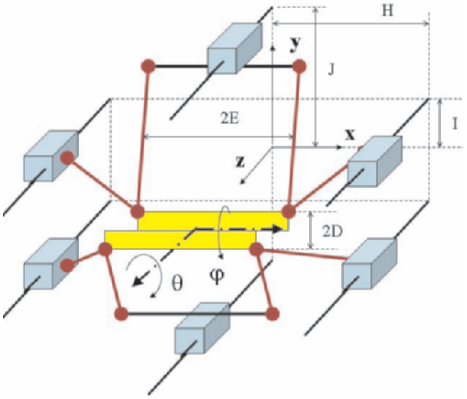

Figure 2. Kinematics scheme.

As for Delta and H4 architectures, the actuators are fixed on the base. Actuators may be rotational or linear; one S-joint per chain may be replaced by U-joint (to get rid of internal motions). One must notice the machine's symmetrical architecture: the machine's upper and lower parts are identically made of a "spatial-parallelogram" and two single rods. Each single rod is connected to the "spatial parallelogram".

Note that, in a general matter, the "spatial-parallelogram" chains (that is, the $\mathbf{P}(SS)_2$ chains) only add one constraint on a mechanism (3 translations and 2 rotations remain feasible) while a "spatial-parallelogram" made of $\mathbf{P}R(RR)_2R$ chains (as done on the Orthoglide, see Chablat et al., 2002) adds two constraints on the mechanism (3 translations and 1 rotation remain feasible).

The travelling plate is the one introduced in Krut et al., 2003, with the I4L robot: while the two sub-parts shift one relatively to the other, a mechanical device transforms this motion into a rotation. Two types of travelling plates exist (see Fig. 3): *Type 1* is made of two prismatic joints and two kinematically coupled rack-and-pinion systems. It has a symmetrical design, which is good for balancing the loads among all the parts. *Type 2* is made up with one part less, but loses *Type 1*'s symmetrical design.

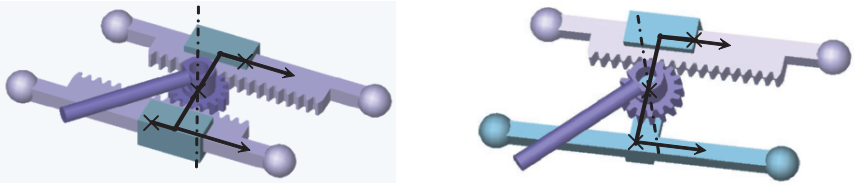

(a) Type 1 *(b) Type 2*

Figure 3. Different possibilities of travelling plate.

3.2 A Remark on Singularity Analysis

Singularities analysis is often based on the analysis of the standard Jacobean matrices $\boldsymbol{J}_x$ and $\boldsymbol{J}_q$ representing the input-output velocity relationship:

$$\boldsymbol{J}_q \dot{\boldsymbol{q}} = \boldsymbol{J}_x \dot{\boldsymbol{x}}, \tag{1}$$

where $\dot{\boldsymbol{q}}$ and $\dot{\boldsymbol{x}}$ are respectively the joint velocity vector and the operational velocity vector.

But other kind of singularities can occur (Zlatanov et al., 1998). To reveal them, a deeper analysis is required. At first, we will recall the fact that "spatial parallelograms" can be seen in two different ways. The realistic case where spherical joints are modelled as 3-DoF joints and not as 2-DoF joints is considered here. Then, two types of modelling will be given: one suggesting that the linear guide is a cylindrical joint (isostatic modelling), and another assuming that it is a prismatic joint (over-constrained modelling). In both cases, geometrical constraints, which must be fulfilled to get rid of internal singularities, will be derived.

According to Hervé's notations (see Hervé, 1999) about displacement subgroups, $\{T\}$ stands for the subgroup of spatial translations and $\{X(\mathbf{u})\}$ stands for the subgroup of Schoenflies displacements (or Scara motions), where $\mathbf{u}$ is a unitary vector collinear to the rotation axis. If a closed loop mechanism is composed of two chains producing Schoenflies displacements with $\mathbf{v} \neq \mathbf{u}$, then:

$$\{X(\mathbf{u})\} \cap \{X(\mathbf{v})\} = \{T\} \tag{2}$$

that is to say that such a mechanism will produce only three translations. The case of machines with **R**R(RR)$_2$R chains (Fig. 4-a) is easily handled with such a technique since those chains correspond to Schoenflies subgroup.

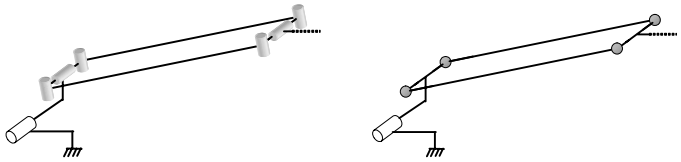

(a) **R**R(RR)$_2$R *(b)* **R**(SS)$_2$

Figure 4. Two ways to model "spatial parallelograms".

The case of machines with **R**(SS)$_2$ chains (Fig. 4-b) is more complex: each chain provides 5 DoF, 3T-2R, and does not correspond to a group. Indeed, it is possible that the union ($\cup$) of two 3T-2R chains generates a 3T-3R motion.

This implies the recourse to a more complex analysis when dealing with mechanisms based on **R**(SS)$_2$ chains: for lack of space, this is recalled here, but the reader may find relevant information in Company et al., 2006.

3.3 Workspace Analysis

In this section, the focus is given to a particular design, where the six linear motors are all collinear with vector $\mathbf{e}_z$: this guarantees a large workspace in this particular direction. The selected geometrical parameters are as follows $H = 0.45$ m, $I = 0.08$ m and $J = 0.4$ m (See Fig. 2 for geometrical parameters explanations). The travelling plate is of *type 1*. The values of geometrical parameters are: $D = 0.05$ m, $E = 0.06$ m and $k_1 = -0.05$ m/rad. Note that the amplification ratio $|k_1|$ is chosen equal to D in order to have same rotation capabilities for θ and φ (+/-90 degrees for this design). Lengths of rods are: $l_i = 0.9$ m, $i \in \{1,\ldots,6\}$. Actuators limits are: $0 \le q_i \le 1.3$m. Figure 5 presents the domain where the condition number of the normalized Jacobean matrix is smaller than 8 (note that along the Z direction corresponding to $\mathbf{z}$, the workspace is only limited by the actuators' stroke).

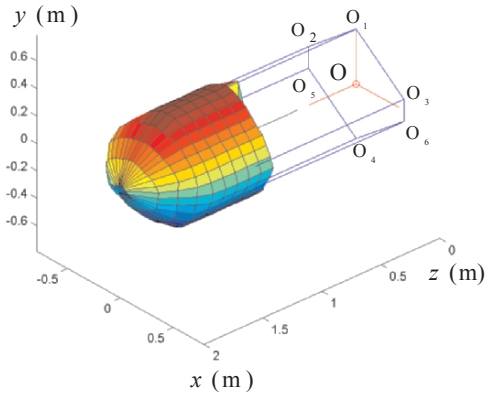

Figure 5. Workspace for cond($\mathbf{J}_q^{-1}\mathbf{J}_x\mathbf{W}_x^{-1}$) < 8

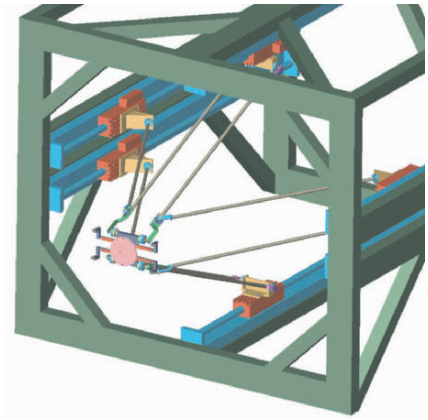

Figure 6. CAD View of the Eureka prototype.

3.4 Practical Design Considerations

It could be interesting, for simplicity purposes, to connect the "single rods" directly to the travelling plate; however, such a practical design faces too many self-collisions. The machine depicted in Fig. 7 (left) shows such a practical design. Another architecture avoiding self-collisions is shown in Fig. 7 (right). It involves curved shapes of the single rods in order to avoid self-collisions.

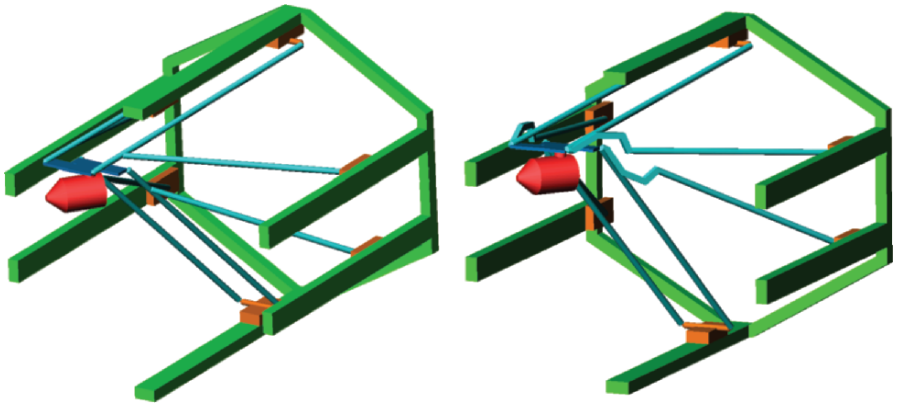

Figure 7. Self-collision-free design #1 and #2.

A prototype is about to be built. The practical design is extremely simple thanks to Linear motors (Fig. 6). Dimensions are the ones introduced for computing the workspace. Rods and travelling plate are

made of aluminium. Instead of using rack-and-pinion systems, the mobile platform has been equipped with cable-pulley devices. This kinematics provides the same displacements as those of the Tricept robot. This design is well suited for the manipulation of light objects, but other applications are still possible.

A design of a haptic master arm based on this kinematics is proposed in Fig. 8. It uses revolute actuators instead of prismatic ones, so the footprint is reduced. DD motors are used in order to reduce friction. The required range for angular displacements is +/-45 degrees. This allows the use of an articulated travelling plate based on a planar parallelogram to provide the desired rotation. The translation to rotation transformation is then suppressed and friction reduced. The Eureka base provides three Translations plus two Rotations (3T-2R). The missing rotation (to get the complete master arm) is obtained using a carried revolute axis, located directly on the ending stick. This is similar to the design of classical master arms, such as the PHANToM (SensAble Technologies).

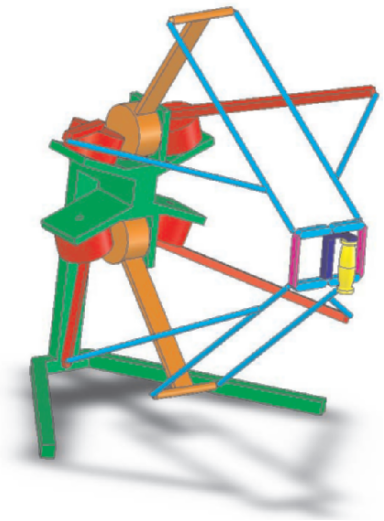

Figure 8. CAD view of the Eureka haptic arm.

4. Conclusion

In this paper, several techniques for reaching high tilting angles have been presented, with a focus on solutions related to articulated travelling plates. Even though such results are still at an early stage of development, they show that it might be possible to use (*i*) on the one hand, travelling plates embedding passive joints which allows local motion amplification, and (*ii*) on the other hand, actuation redundancy as

a way to overcome some singular positions that usually limit the range of motion.

References

Angeles, J., Morozov, A., Navarro, O., A novel manipulator architecture for the production of SCARA motions, *Proceddings of IEEE International Conference on Robotics and Automation*, San Francisco, April 24-28, 2000, pp. 2370-2375.

Chablat, D., and Wenger, P., Design of a Three-Axis Isotropic Parallel Manipulator for Machining Applications: The Orthoglide, *Proceedings of Workshop on Fundamental Issues and Future Research Directions for Parallel Mechanisms and Manipulators*, October 3-4, Québec, Québec, Canada, 2002.

Clavel, R., Une nouvelle structure de manipulateur parallèle pour la robotique légère, *APII, 23(6)*, 1985, pp. 371-386.

Company, O., Krut, S., and Pierrot, F., Internal Singularity Analysis of a Class of Lower Mobility Parallel Manipulators with Articulated Travelling Plate, *IEEE Transactions on Robotics*, 2006 (to appear).

Hervé, J.M., The Lie group of rigid body displacements, a fundamental tool for mechanism design, *Mechanism and Machine Theory*, Vol. 34, 1999, pp. 719-730.

Koevermans, W.P., Design and performance of the four dof motion system of the NLR research flight simulator*, Proceedings of AGARD Conference,* La Haye, 20-23 October 1975, pp. 17-1/17-11.

Krut, S., Company, O., Benoit, M., Ota, H., and Pierrot, F., I4: A new parallel mechanism for Scara motions, *Proceedings of IEEE International Conference on Robotics and Automation*, Taipei, Taiwan, September 14-19, 2003.

Pierrot, F., and Company, O., H4: a new family of 4-dof parallel robots, *Proceedings of IEEE/ASME International Conference on Advanced Intelligent Mechatronics*, Atlanta, Georgia, USA, September 19-22, 1999, pp. 508-513.

Reboulet, C., Rapport d'avancement projet VAP, thème 7, phase 3. Rapport de Recherche 7743, CNES/DERA, January 1991.

Rolland L., The Manta and the Kanuk: Novel 4 dof parallel mechanism for industrial handling, *Proceedings of ASME Dynamic Systems and Control Division IMECE'99 Conference*, Nashville, November 14-19, 1999, vol. 67, pp. 831-844.

Ryu, S.J., Kim, J.W., Hwang, J.C., Park C., Ho, H.S., Lee, K., Lee, Y., Cornel U., Park, F.C., and Kim, J., ECLIPSE: An Overactuated Parallel Mechanism for Rapid Machining, *Proceedings of ASME International Mechanical Engineering Congress and Exposition*, Vol. 8, USA, 1998, pp. 681-689.

Zlatanov, D., Fenton, R.G., and Benhabib, B., Identification and classification of the singular configurations of mechanisms, *Mechanism and Machine Theory*, Vol. 33, No. 6, pp. 743-760, August 1998.

MOBILITY AND CONNECTIVITY IN MULTILOOP LINKAGES

César Real Diez-Martínez
Instituto Tecnológico y de Estudios Superiores de Occidente
Guadalajara, Jal. México
creal@iteso.edu

José M. Rico, J. Jesús Cervantes-Sánchez
Facultad de Ingenieria Mecánica Eléctrica y Electrónica
Universidad de Guanajuato, Salamanca, Gto. México
jrico, jecer@salamanca.ugto.mx

Jaime Gallardo
Departamento de Ingenier'a Mecánica
Instituto Tecnológico de Celaya, Celaya, Gto. México
gjaime@itc.mx

Abstract This contribution provides new definitions of infinitesimal mobility and connectivity of kinematic chains. These definitions are straightforwardly connected with accepted definitions of finite mobility and connectivity. Further, screw theory is applied to the determination of the infinitesimal mobility and connectivity of multi-loop linkages. These results provide a guide for the determination of the finite mobility and connectivity of general topology of multiloop linkages, one of the important remaining problems in mobility theory.

Keywords: Mobility, connectivity, multiloop linkages, screw theory

1. Introduction

The last three years have seen a flurry of studies about mobility and connectivity of kinematic chains. For the most part, these analyses have been focused on single-loop kinematic chains and parallel platforms. Most of the few studies about mobility and connectivity of general multiloop linkages deal with the mobility and connectivity determined from their velocity analysis. It is well known that the information gathered via velocity analysis of any class of kinematic chains does not provide conclusive information about their mobility and connectivity. In this contribution, it is shown that higher order analyses, in particular

J. Lenarčič and B. Roth (eds.), Advances in Robot Kinematics, 455–464.

acceleration analysis, can be successfully employed in shedding light on the mobility and connectivity of general multiloop linkages. It should be noted that Wohlhart, 1999 and Wohlhart, 2000, employed higher order analyses to shed light into the characteristics of singular positions of fully parallel platforms. In contrast, in this contribution the authors are interested in general topology multiloop linkages. Further, the higher order analyses are employed, in addition, as an important aid in the determination of their mobility, a problem that remain unsolved in this general case.

2. Mobility and Connectivity

In this section, a review of the concepts of mobility and connectivity as well as new definitions of infinitesimal mobility and connectivity are presented.

Definition 1. Consider a single-loop or multiple loop kinematic chain. The **finite mobility of the chain**, denoted by M_F, in a given configuration is the number, minimum and necessary, of scalar variables required to determine the pose, with respect to a link regarded as reference, of all the remaining links of the kinematic chain.

In our approach, the finite mobility depends not only on the kinematic chain, but also of the configuration of the kinematic chain to be analyzed, and it becomes a property of the configuration of the kinematic chain and its neighborhood. This definition is motivated by the presence of kinematotropic chains, Galletti and Fanghella, 2001, and differs from the definition, usually presented in undergraduate and graduate textbooks, and adopted by Gogu, 2005.

Consider now the velocity analysis equation of the kinematic chain, in a given configuration, which can be written as follows

$$J\vec{\omega} = \vec{0}, \tag{1}$$

where, the Jacobian matrix, J, is a matrix with as many columns as screws associated with the kinematic pairs of the chain and as many rows as fundamental circuits and loops of the kinematic chain, multiplied by 6. Additionally, $\vec{\omega}$ is the vector of joint rates, translational or angular, associated with the screws of the chain, and the vector $\vec{0}$ has the same number of rows as the Jacobian matrix.

Definition 2. Consider a kinematic chain whose velocity analysis equation is given by Eq. 1. Then, the kinematic chain has first order infinitesimal mobility if there exists a vector $\vec{\omega}_1 \neq \vec{0}$ that satisfies the Eq. 1. Moreover, the number of independent components of the vector $\vec{\omega}_1$ determines the number of first order degrees of freedom, or **first**

order infinitesimal mobility, denoted by M_1, of the chain in a given configuration.

Consider now the acceleration analysis equation of the kinematic chain in the same given configuration, which can be written as follows

$$J\dot{\vec{\omega}} = -\$_L, \tag{2}$$

where, $\$_L$ is the Lie screw that contains terms of the form $[\omega_i \$_i \ \omega_j \$_j]$, where the bracket represents the dual motor product or Lie product, see Rico et al., 1999. Unlike the velocity analysis equation, the acceleration analysis equation is non-homogeneous. Further, the solution of a non-homogeneous linear system is given by the sum of the subspace solution of the associated homogeneous system and a particular solution of the non-homogeneous system, Bentley and Cooke, 1971. Thus, the associated homogeneous linear system is given by

$$J\dot{\vec{\omega}} = \vec{0}. \tag{3}$$

Therefore, a vector $\dot{\vec{\omega}}$ whose components are numerically equal to those of any of the vectors $\vec{\omega}_1$, solution of the Eq. 1, is also a solution of Eq. 3. Furthermore, a necessary and sufficient condition for the Eq. 2 to have a particular solution is given, Bentley and Cooke, 1971, by

$$Rank(J) = Rank(J, \$_L). \tag{4}$$

If $Rank(J)$ is less than the number of matrix rows, Eq. 4 frequently imposes additional conditions over the components of the vector $\vec{\omega}_1$. These additional conditions require that one or more of the independent components of $\vec{\omega}_1$ satisfy additional equations, frequently, these conditions require that one or more of the independent components of $\vec{\omega}_1$ be zero. Let $\vec{\omega}_2$ be the solution of both, the velocity and the acceleration analyses equations. This result, provides the rationale for defining the second order infinitesimal mobility of the chain.

Definition 3. Consider a kinematic chain in a given configuration, such that the velocity and acceleration analyses equations are given by Eqs. 1, 2. The chain has a second order infinitesimal mobility if there is a non-zero vector $\vec{\omega}_2$ that satisfies both equations. Furthermore, the number of independent components of the vector $\vec{\omega}_2$ determines the number of second order degrees of freedom, or **second order infinitesimal mobility**, denoted by M_2, of the chain in a given configuration.

Similarly, it is possible to define similar concepts regarding the connectivity.

Definition 4. Consider a kinematic chain in a given configuration. The **finite connectivity** between a pair of links (i, j), in the kinematic

chain is the minimum and necessary number of joint – scalar – variables that determine the pose of one link with respect to the other, and it if denoted as $C_F(i,j)$.

Consider an arbitrary kinematic chain and assume that (i,j) is an arbitrary pair of links of the chain. Further, assume that the velocity analysis of the chain has been solved and that the **unique** velocity state, ${}^i\vec{V}_1^j$, of link j with respect to link i, following all possible paths between links i and j has been determined. The velocity state ${}^i\vec{V}_1^j$ depends on independent variables that solve the velocity analysis solution, contained in $\vec{\omega}_1$. These elements are linear or angular velocities associated with the kinematic pairs of the chain. Further, ${}^i\vec{V}_1^j$ is a vector space. Then it is possible to define the first order infinitesimal connectivity.

Definition 5. Consider a kinematic chain in a given configuration and let (i,j) be a pair of links. The **first order infinitesimal connectivity** between links (i,j), denoted by $C^1(i,j)$, is defined as

$$C^1(i,j) \;=\; dim({}^i\vec{V}_1^j). \tag{5}$$

Definition 6. Consider a kinematic chain in a given configuration and let (i,j) be a pair of links. Further, assume that the velocity and acceleration analyses of the chain has been solved. The number of independent variables of the vector $\vec{\omega}_2$ might be less than the number of independent variables of the vector $\vec{\omega}_1$. Assume that the unique velocity state of link j with respect to link i, using the solution of the velocity and acceleration analyses $\vec{\omega}_2$, denoted by ${}^i\vec{V}_2{}^j$, is also known. Then, their **second order infinitesimal connectivity**, denoted by $C^2(i,j)$, is defined by

$$C^2(i,j) \;=\; dim({}^i\vec{V}_2{}^j). \tag{6}$$

Higher order mobilities and connectivities can be defined accordingly.

3. Mobility and Connectivity in Multiloop Linkages

Consider the multiloop spatial kinematic chain shown in Fig. 1, proposed by Fayet, 1995 and used by Wohlhart, 2004. The chain has two spherical pairs, four cylindrical pairs, a planar pair and three revolute pairs.

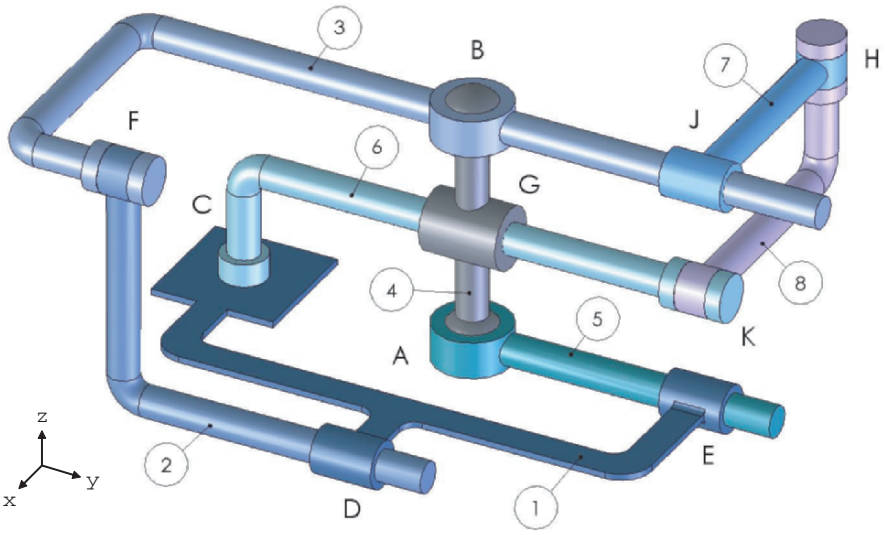

Figure 1. Kinematic chain proposed by Fayet and used by Wohlhart.

Locating the origin of the coordinate system at point A, the screws associated with the kinematic pairs are given by

$$
\begin{array}{llll}
A1 & {}^{5}\$^{5a} = (1,0,0;0,0,0), & B1 & {}^{4}\$^{4a} = (1,0,0;0,1,0),\\
A2 & {}^{5a}\$^{5b} = (0,1,0;0,0,0), & B2 & {}^{4a}\$^{4b} = (0,1,0;-1,0,0),\\
A3 & {}^{5b}\$^{4} = (0,0,1;0,0,0), & B3 & {}^{4b}\$^{3} = (0,0,1;0,0,0),\\
C1 & {}^{1}\$^{1b} = (0,0,0;1,0,0), & D1 & {}^{2}\$^{2a} = (0,0,0;0,1,0),\\
C2 & {}^{1b}\$^{1c} = (0,0,0;0,1,0), & D2 & {}^{2a}\$^{1} = (0,1,0;0,0,1),\\
C3 & {}^{1c}\$^{6} = (0,0,1;-1,0,0), & E1 & {}^{1}\$^{1a} = (0,0,0;0,1,0),\\
F & {}^{3}\$^{2} = (0,1,0;-1,0,1), & E2 & {}^{1a}\$^{5} = (0,1,0;0,0,0),\\
G1 & {}^{6}\$^{6a} = (0,0,0;0,1,0), & H & {}^{8}\$^{7} = (0,0,1;1,1,0),\\
G2 & {}^{6a}\$^{4} = (0,1,0;-1/2,0,0), & J1 & {}^{7}\$^{7a} = (0,0,0;0,1,0),\\
K & {}^{6}\$^{8} = (0,1,0;-1/2,1,0), & J2 & {}^{7a}\$^{3} = (0,1,0;-1,0,0),
\end{array}
$$

where the screws ${}^{5}\$^{5a}$, ${}^{5a}\$^{5b}$ and ${}^{5b}\$^{4}$ correspond to the spherical pair located in point A. Similarly, for the remaining kinematic pairs. Up to the velocity analysis, the approach follows that proposed by Wohlhart, 2004, see also Baker, 1981. The graph associated with the kinematic chain is shown in Fig. 2. The graph associates links with vertex and kinematic pairs with edges.

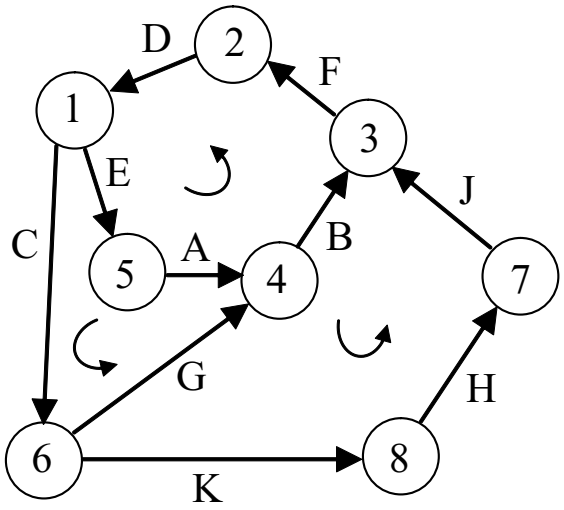

Figure 2. Graph of the kinematic chain proposed by Fayet and used by Wohlhart.

From this graph, and following the loops, it is possible to find the velocity analysis equation for the kinematic chain given, in matrix form, by

$$J\,\vec{\omega} = \vec{0} \quad \text{or} \quad \begin{bmatrix} {}^{5}\$^{5a} & -{}^{5}\$^{5a} & \$_0 \\ {}^{5a}\$^{5b} & -{}^{5a}\$^{5b} & \$_0 \\ {}^{5b}\$^{4} & -{}^{5b}\$^{4} & \$_0 \\ {}^{4}\$^{4a} & \$_0 & -{}^{4}\$^{4a} \\ {}^{4a}\$^{4b} & \$_0 & -{}^{4a}\$^{4b} \\ {}^{4b}\$^{3} & \$_0 & -{}^{4b}\$^{3} \\ {}^{3}\$^{2} & \$_0 & \$_0 \\ {}^{2}\$^{2a} & \$_0 & \$_0 \\ {}^{2a}\$^{1} & \$_0 & \$_0 \\ {}^{1}\$^{1a} & -{}^{1}\$^{1a} & \$_0 \\ {}^{1a}\$^{5} & -{}^{1a}\$^{5} & \$_0 \\ \$_0 & {}^{1}\$^{1b} & \$_0 \\ \$_0 & {}^{1b}\$^{1c} & \$_0 \\ \$_0 & {}^{1c}\$^{6} & \$_0 \\ \$_0 & {}^{6}\$^{6a} & -{}^{6}\$^{6a} \\ \$_0 & {}^{6a}\$^{4} & -{}^{6a}\$^{4} \\ \$_0 & \$_0 & {}^{6}\$^{8} \\ \$_0 & \$_0 & {}^{8}\$^{7} \\ \$_0 & \$_0 & {}^{7}\$^{7a} \\ \$_0 & \$_0 & {}^{7a}\$^{3} \end{bmatrix}^{T} \begin{bmatrix} {}^{5}\omega_{5a} \\ {}^{5a}\omega_{5b} \\ {}^{5b}\omega_{4} \\ {}^{4}\omega_{4a} \\ {}^{4a}\omega_{4b} \\ {}^{4b}\omega_{3} \\ {}^{3}\omega_{2} \\ {}^{2}\omega_{2a} \\ {}^{2a}\omega_{1} \\ {}^{1}\omega_{1a} \\ {}^{1a}\omega_{5} \\ {}^{1}\omega_{1b} \\ {}^{1b}\omega_{1c} \\ {}^{1c}\omega_{6} \\ {}^{6}\omega_{6a} \\ {}^{6a}\omega_{4} \\ {}^{6}\omega_{8} \\ {}^{8}\omega_{7} \\ {}^{7}\omega_{7a} \\ {}^{7a}\omega_{3} \end{bmatrix} = \begin{bmatrix} 0 \\ 0 \\ 0 \\ 0 \\ 0 \\ 0 \\ 0 \\ 0 \\ 0 \\ 0 \\ 0 \\ 0 \\ 0 \\ 0 \\ 0 \\ 0 \\ 0 \\ 0 \\ 0 \end{bmatrix}, \quad (7)$$

where $\$_0$ is a six dimensional vector whose elements are all equal to zero.

The solution of the velocity analysis solution, given by Eq. 7, is found to be

$$
\begin{aligned}
{}_5\omega_{5a} &= 0, & {}_{5a}\omega_{5b} &= 2\,{}_1\omega_{1b} + 2\,{}_{4b}\omega_3 - {}_{1a}\omega_5,\\
{}_{5b}\omega_4 &= -\,{}_{4b}\omega_3, & {}_4\omega_{4a} &= 0,\\
{}_{4a}\omega_{4b} &= -2\,{}_1\omega_{1b} - 2\,{}_{4b}\omega_3, & {}_3\omega_2 &= 2\,{}_1\omega_{1b} + 2\,{}_{4b}\omega_3,\\
{}_2\omega_{2a} &= -\,{}_1\omega_{1a}, & {}_{2a}\omega_1 &= -2\,{}_1\omega_{1b} - 2\,{}_{4b}\omega_3,\\
{}_{1c}\omega_6 &= -\,{}_{4b}\omega_3, & {}_6\omega_{6a} &= {}_1\omega_{1a} - {}_{1b}\omega_{1c},\\
{}_{6a}\omega_4 &= 2\,{}_1\omega_{1b} + 2\,{}_{4b}\omega_3, & {}_8\omega_7 &= {}_{4b}\omega_3,\\
{}_7\omega_{7a} &= {}_1\omega_{1a} - {}_{1b}\omega_{1c} - {}_{4b}\omega_3 - 2\,{}_1\omega_{1b}, & {}_{7a}\omega_3 &= -2\,{}_1\omega_{1b},\\
{}_6\omega_8 &= 2\,{}_1\omega_{1b},
\end{aligned}
$$

where, ${}_1\omega_{1b}$, ${}_{1b}\omega_{1c}$, ${}_1\omega_{1a}$, ${}_{1a}\omega_5$ and ${}_{4b}\omega_3$ can be selected arbitrarily. Therefore, the first order mobility is, $M_1 = 5$. Furthermore, the first order connectivity matrix is given by

$$
C^I = \begin{bmatrix}
0 & 2 & 2 & 3 & 2 & 3 & 3 & 3\\
2 & 0 & 1 & 2 & 2 & 3 & 3 & 3\\
2 & 1 & 0 & 2 & 2 & 3 & 2 & 3\\
3 & 2 & 2 & 0 & 2 & 2 & 2 & 2\\
2 & 2 & 2 & 2 & 0 & 4 & 3 & 3\\
3 & 3 & 3 & 2 & 4 & 0 & 2 & 1\\
3 & 3 & 2 & 2 & 3 & 2 & 0 & 1\\
3 & 3 & 3 & 2 & 3 & 1 & 1 & 0
\end{bmatrix}. \tag{8}
$$

The acceleration analysis equation has a solution, if and only if, the augmented matrix, J_a, obtained by augmenting the coefficient matrix, J, with the column given by $L_S = \begin{bmatrix} \$_{L1} & \$_{L2} & \$_{L3} \end{bmatrix}^T$, or

$$
J_a = \begin{bmatrix} J & L_S \end{bmatrix} \tag{9}
$$

where, $\$_{L1}$, $\$_{L2}$ and $\$_{L3}$ are the Lie screws of the three loops of the kinematic chain, satisfy the condition

$$
Rank(J_a) = Rank(J). \tag{10}
$$

This condition yields

$$
{}_{4b}\omega_3 = {}_1\omega_{1b} = 0. \tag{11}
$$

Therefore, the solution of the velocity analysis that takes into consideration the acceleration analysis condition is given by Eq. 11 and the

following additional results

$$
\begin{array}{lll}
{}_5\omega_{5a} = 0, & {}_{5a}\omega_{5b} = -{}_{1a}\omega_5, & {}_{5b}\omega_4 = 0, \\
{}_4\omega_{4a} = 0, & {}_{4a}\omega_{4b} = 0, & {}_3\omega_2 = 0, \\
{}_2\omega_{2a} = -{}_1\omega_{1a}, & {}_{2a}\omega_1 = 0, & {}_{1c}\omega_6 = 0, \\
{}_6\omega_{6a} = {}_1\omega_{1a} - {}_{1b}\omega_{1c}, & {}_{6a}\omega_4 = 0, & {}_8\omega_7 = 0, \\
{}_7\omega_{7a} = {}_1\omega_{1a} - {}_{1b}\omega_{1c}, & {}_{7a}\omega_3 = 0, & {}_6\omega_8 = 0,
\end{array}
$$

Thus, only ${}_1\omega_{1a}$, ${}_{1a}\omega_5$ and ${}_{1b}\omega_{1c}$ can be arbitrarily selected. Hence, the second order infinitesimal mobility is $M_2 = 3$. Further, the second order infinitesimal mobility matrix is given by

$$
C^{II} = \begin{bmatrix}
0 & 1 & 1 & 1 & 2 & 1 & 1 & 1 \\
1 & 0 & 0 & 0 & 1 & 1 & 1 & 1 \\
1 & 0 & 0 & 0 & 1 & 1 & 1 & 1 \\
1 & 0 & 0 & 0 & 1 & 1 & 1 & 1 \\
2 & 1 & 1 & 1 & 0 & 2 & 2 & 2 \\
1 & 1 & 1 & 1 & 2 & 0 & 0 & 0 \\
1 & 1 & 1 & 1 & 2 & 0 & 0 & 0 \\
1 & 1 & 1 & 1 & 2 & 0 & 0 & 0
\end{bmatrix}. \tag{12}
$$

Finally, it will be shown that the results obtained up to this point, allow to determine the finite mobility and connectivity of this multiloop kinematic chain. For that purpose, recent results on the mobility of parallel platforms, Rico et al., 2005, will be adapted for the task. The infinitesimal mechanical liaisons associated with all the possible four paths, I, II, III, IV, between links 1, regarded as the fixed platform, and 5, regarded as the moving platform, are the column spaces of the matrices

$${}^1V_I^5 = \left[{}^1\$^{1a}\ {}^{1a}\$^5\right], \quad {}^1V_{II}^5 = \left[{}^1\$^{1b}\ {}^{1b}\$^{1c}\ {}^{1c}\$^6\ {}^6\$^{6a}\ {}^{6a}\$^4\ {}^4\$^{5b}\ {}^{5a}\$^{5b}\ {}^5\$^{5a}\right],$$

$${}^1V_{III}^5 = \left[{}^1\$^{2a}\ {}^{2a}\$^2\ {}^3\$^2\ {}^{4b}\$^3\ {}^{4a}\$^{4b}\ {}^{4a}\$^4\ {}^{5b}\$^4\ {}^{5a}\$^{5b}\ {}^5\$^{5a}\right],$$

$${}^1V_{IV}^5 = \left[{}^1\$^{1b}\ {}^{1b}\$^{1c}\ {}^{1c}\$^6\ {}^6\$^8\ {}^8\$^7\ {}^7\$^{7a}\ {}^{7a}\$^3\ {}^{4b}\$^3\ {}^{4a}\$^{4b}\ {}^{4a}\$^4\ {}^{5b}\$^4\ {}^{5a}\$^{5b}\ {}^5\$^{5a}\right].$$

The absolute mechanical liaison is given by

$${}^1V_a^5 = {}^1V_I^5 \cap {}^1V_{II}^5 \cap {}^1V_{III}^5 \cap {}^1V_{IV}^5 = \begin{bmatrix} 0 & 1 & 0 & 0 & 0 & 0 \\ 0 & 0 & 0 & 0 & 1 & 0 \end{bmatrix}^T \tag{13}$$

It is easy to recognize ${}^1V_a^5$ as the subalgebra, of the Lie algebra of the Euclidean group, $se(3)$, associated with cylindrical displacements along the y axis. This result accounts for two of the degrees of freedom, from the three determined by the second order infinitesimal mobility. They are the finite displacements associated with the screws ${}^1\$^{1a}$ and ${}^{1a}\$^5$ located in point E. The remaining degree of freedom is related to the translational motion, along the same axis y, and produced by the screws ${}^{1b}\$^{1c}$, located in point C, and ${}^7\$^{7a}$, located in point J, while the revolute joints located between them remain inactive. This degree of freedom is passive when the fixed and moving platforms are links 1 and 5.

The conclusion is that the finite mobility of the multiloop linkage is $M_F = M_2 = 3$. Therefore, the finite connectivities among the diferent links, $C_F(i,j)$ are given by the elements of the second order infinitesimal connectivity matrix C^{II}.

4. Conclusions

This contribution has shown that it is possible to provide higher-order definitions of infinitesimal mobility and connectivity that are congruent with the usual definitions of finite mobility and connectivity. They provide a guide for the computation of finite mobility of general multiloop linkages, this is, in the opinion of the authors, the most difficult task in mobility computations. The results have been verified using Adams©.

5. Acknowledgements

The first author thank Conacyt for the support of his M. Sc. studies. The authors thank Concyteg for the support of several projects, including a thesis scholarship for the first author. This work is based on his M. Sc. thesis at the Instituto Tecnológico de Celaya.

References

Baker, J. E. (1981), On Mobility and Relative Freedoms in Multiloop Linkages and Structures, *Mechanism and Machine Theory*, vol. 16, no. 6, pp. 583-597.

Bentley, D. L., and Cooke, K. L. (1971), *Linear Algebra with Differential Equations*, New York: Holt, Rinehart and Winston.

Fayet, M. (1995), Mécanismes Multi-Boucles I. Détermination des Espaces de Torseurs Cinématiques Dans un Mécanisme Multi-Boucles Quelconque, *Mechanism and Machine Theory*, vol. 30, no. 2, pp. 201-217.

Galletti, C., and Fanghella, P. (2001), Single-Loop Kinematotropic Mechanisms, *Mechanism and Machine Theory*, vol. 36, no. 6, pp. 743-761.

Gogu, G. (2005), Mobility of Mechanisms: a Critical Review, *Mechanism and Machine Theory*, vol. 40, no. 9, pp. 1068-1097.

Rico, J. M., Gallardo, J., and Duffy, J. (1999), Screw Theory and Higher Order Analyses of Open Serial and Closed Chains, *Mechanism and Machine Theory*, vol. 34, no. 4, pp. 559-586.

Rico, J. M., Aguilera, L. D., Gallardo, J., Rodriguez, R., Orozco, H., and Barrera, J. M. (2006), A More General Mobility Criterion for Parallel Platforms, *ASME Journal of Mechanical Design*, vol. 128, no. 1, pp. 207-219.

Wohlhart, K. (1999), Degrees of Shakiness, *Mechanism and Machine Theory*, vol. 34, no. 7, pp. 1103-1126.

Wohlhart, K. (2000), Architectural Shakiness or Architectural Mobility of Platforms, *On Advances in Robot Kinematics*, Lenarčič, J. and Stanišić, eds. Dordrecht: Kluwer Academic Publishers, pp. 365-374.

Wohlhart, K. (2004), Screw Spaces and Connectivities in Multiloop Linkages, *On Advances in Robot Kinematics*, Lenarčič, J. and Galletti, C. eds. Dordrecht: Kluwer Academic Publishers, pp. 97-104.

JACOBIAN INVERSE KINEMATICS ALGORITHMS WITH VARIABLE STEPLENGTH FOR MOBILE MANIPULATORS

Krzysztof Tchoń
Institute of Computer Engineering, Control and Robotics
Wrocław University of Technology
tchon@ict.pwr.wroc.pl

Janusz Jakubiak
Institute of Computer Engineering, Control and Robotics
Wrocław University of Technology
Janusz.Jakubiak@pwr.wroc.pl

Abstract We study Jacobian inverse kinematics algorithms for mobile manipulators composed of a nonholonomic mobile platform and a holonomic onboard manipulator. In general, the Jacobian algorithms converge locally, often producing weird end effector and platform trajectories. In the paper we use the existing theory of Newton algorithms in order to improve the quality of convergence of the Jacobian algorithms. Specifically, we examine a strategy of adjusting the steplength in the Jacobian pseudoinverse algorithm that results from the affine covariant Lipschitz condition imposed on the mobile manipulator's Jacobian. The affine covariant strategy is verified by extensive computer simulations and compared with the constant length step and a simple Armijo strategies.

Keywords: Mobile manipulator, inverse kinematics, Jacobian algorithm

1. Introduction

In this paper by a mobile manipulator we call a robotic system composed of a nonholonomic mobile platform and a stationary manipulator fixed to the platform. The nonholonomic constraints imposed on the platform and the holonomic kinematics of the onboard manipulator are modelled as a driftless control system with outputs. The end-point map of this system determines the kinematics of the mobile manipulator Tchoń and Jakubiak, 2003. The Jacobian inverse kinematics algorithm for mobile manipulators are conveniently devised using the continua-

J. Lenarčič and B. Roth (eds.), Advances in Robot Kinematics, 465–472.

tion method Chitour and Sussmann, 1998; Divelbiss et al., 1998. In this framework, an inverse kinematics algorithm is determined by a dynamic system operating in an inifinite dimensional Hilbert configuration space. Computable inverse kinematics algorithms make use of a Ritz approximation of platform controls by truncated orthogonal series. The Jacobian algorithms usually have local convergence and often produce unrealistic platform and end effector trajectories Tchoń and Jakubiak, 2003. The fact that inverse kinematics algorithms for stationary manipulators and mobile platforms are of the Newton type is well known, see e.g. Isobe et al., 1992; Divelbiss et al., 1998; Duleba and Sasiadek, 2003. In particular in Divelbiss et al., 1998 the line searching has been mentioned as a method of adjusting the steplength of the inverse kinematics algorithm for a mobile platform.

Motivated by these circumstances in this paper we are attempting at improving the quality of convergence of Jacobian inverse kinematics algorithms by appropriate steplength adjustment. Our approach relies on existing results for Newton algorithms Deulfhard, 2004. We consider a general Jacobian inverse kinematics algorithm associated with a given right inverse of the Jacobian. Then we formulate the affine covariant condition and obtain a prediction-correction strategy of the steplength adjustment. This strategy is applied to a mobile manipulator composed of a kinematic car platform and an RTR onboard manipulator, driven by the inverse kinematics algorithm based on the Jacobian pseudoinverse. The affine covariant strategy is examined by computer simulations and compared with two other strategies. Our conclusions are twofold. First: the variable steplength improves both the speed and the quality of convergence of the Jacobian pseudoinverse algorithm in comparison to the case of constant steplength. Second, although generally profitable, the affine covariant strategy is sometimes overpassed by a simple Armijo choice of the steplength from among a finite set of possibilities.

The composition of this paper is the following. Section 2 recalls basic concepts of the endogenous configuration space approach. Section 3 presents the affine covariant steplength adjustment strategy for a general Jacobian inverse kinematics algorithm. This strategy is specified to the Jacobian pseudoinverse algorithm and examined by computer simulations in section 4. The paper is concluded with section 5.

2. Basic Concepts

We shall study mobile manipulators whose kinematics are represented by a driftless control system with outputs,

$$\dot{q} = G(q)u = \sum_{i=1}^{m} g_i(q)u_i, \quad y = k(q, x). \tag{1}$$

In (1) $q \in R^n$, $x \in R^p$ and $y \in R^r$ denote, respectively, generalized coordinates of the platform, joint positions of the manipulator, and the end effector location in the taskspace. The control functions $u(t)$ of the platform and joint positions x of the onboard manipulator, acting over a control time horizon $T > 0$, define the endogenous configuration space $\mathcal{X} = L^2_m[0,T] \times R^p$. The space $\mathcal{X}$ equipped with the inner product $< (u_1(\cdot), x_1), (u_2(\cdot), x_2) >= \int_0^T u_1^T(t)u_2(t)dt + x_1^T x_2$ becomes an infinitely dimensional Hilbert space with induced norm

$$||(u(\cdot), x)||^2 = <(u(\cdot), x), (u(\cdot), x) > . \tag{2}$$

An endogenous configuration $(u(\cdot), x) \in \mathcal{X}$ determines a platform trajectory $q(t) = \varphi_{q_0,t}(u(\cdot))$ and an end effector trajectory $y(t) = k(q(t), x)$. The instantaneous kinematics $K_{q_0,T} : \mathcal{X} \to R^r$ of the mobile manipulator are defined as the end-point map of (1), i.e.

$$K_{q_0,T}(u(\cdot), x) = y(T) = k(\varphi_{q_0,T}(u(\cdot)), x). \tag{3}$$

The kinematics (3) define end effector positions and orientations of the mobile manipulator steered by the control $(u(\cdot), x)$ that can be reached at T. By differentiation of the kinematics $K_{q_0,T}(u(\cdot), x)$ we obtain the analytic Jacobian

$$J_{q_0,T}(u(\cdot), x)(v(\cdot), w) = C(T, x) \int_0^T \Phi(T, s)B(s)v(s)ds + D(T, x)w. \tag{4}$$

The Jacobian may be interpreted as the output reachability map at T of the linear approximation

$$\dot{\xi} = A(t)\xi + B(t)v, \quad \eta = C(t, x)\xi + D(t, x)w, \tag{5}$$

to system (1) along the control-state trajectory $(u(t), x, q(t))$, initialized at $\xi_0 = 0$. The matrices appearing in (5) have the standard form $A(t) = \frac{\partial}{\partial q}(G(q(t))u(t))$, $B(t) = G(q(t))$, $C(t, x) = \frac{\partial k}{\partial q}(q(t), x)$, $D(t, x) = \frac{\partial k}{\partial x}(q(t), x)$, while matrix $\Phi(t, s)$ in (4) satisfies the evolution equation $\frac{\partial}{\partial t}\Phi(t, s) = A(t)\Phi(t, s)$ with initial condition $\Phi(s, s) = I_n$. Let us recall that an endogenous configuration is regular, if the analytic Jacobian $J_{q_0,T}(u(\cdot), x) : \mathcal{X} \to R^r$ is surjective. This is equivalent to the full rankness of the dexterity matrix

$$\mathcal{D}_{q_0,T}(u(\cdot), x) =$$
$$C(T, x) \int_0^T \Phi(T, s)B(s)B^T(s)\Phi^T(T, s)ds\, C^T(T, x) + D(T, x)D^T(T, x);$$

otherwise $(u(\cdot), x)$ is referred to as singular. The inverse kinematic problem for the mobile manipulator (1) consists in determining an endogenous configuration $(u_d(\cdot), x_d)$ such that for a given location y_d of the end effector $K_{q_0,T}(u_d(\cdot), x_d) = y_d$. Jacobian inverse kinematics algorithms for mobile manipulators are conveniently derived using the continuation method. Among them, the most often used is the Jacobian pseudoinverse algorithm Tchoń and Jakubiak, 2003; its alternative is the extended Jacobian algorithm Tchoń and Jakubiak, 2005. The Jacobian pseudoinverse algorithm relies on the Jacobian pseudoinverse

$$(J^{\#}_{q_0,T}(u(\cdot), x)\eta)(t) = \begin{bmatrix} B^T(t)\Phi^T(T,t)C^T(T,x) \\ D^T(T,x) \end{bmatrix} \mathcal{D}^{-1}_{q_0,T}(u(\cdot), x)\eta$$

and assumes the following form

$$\frac{d}{d\theta}\begin{pmatrix} u_\theta(t) \\ x(\theta) \end{pmatrix} = -\gamma J^{\#}_{q_0,T}(u_\theta, x(\theta))e(\theta))(t), \tag{6}$$

where $\gamma > 0$ denotes the steplength, and $e(\theta) = K_{q_0,T}(u_\theta(\cdot), x(\theta)) - y_d$ is the taskspace error. For the algorithm exploits the inversion of the dexterity matrix, it is defined only for regular configurations of the mobile manipulator. The dynamic system (6) produces a trajectory $(u_\theta(\cdot), x(\theta)) \in \mathcal{X}$ parameterized by $\theta \in R$. A solution $(u_d(t), x_d)$ to the inverse kinematic problem is computed as a limit $(u_d(t), x_d) = \lim_{\theta \to +\infty} (u_\theta(t), x(\theta))$.

3. Steplength Adjustment

Let $K = K_{q_0,T} : \mathcal{X} \longrightarrow Y$ defined by (3) describe the kinematics of a mobile manipulator. For simplicity of notation, in this section we shall denote endogenous configurations by $z = (u(\cdot), x)$ and omit subscripts. At a regular configuration $z \in \mathcal{X}$ the Jacobian (4) has a right inverse $D\,K^{\#}(z) : R^r \to \mathcal{X}$ that determines an associated Jacobian inverse kinematics algorithm

$$\frac{d\,z(\theta)}{d\,\theta} = -\gamma D\,K^{\#}(z(\theta))e(\theta), \quad z(0) = z_0. \tag{7}$$

As before, the solution of the inverse kinematic problem is obtained as a limit $z_d = \lim_{\theta \to +\infty} z(\theta)$. In particular, when $D\,K^{\#} = J^{\#}_{q_0,T}$, the algorithm (7) coincides with the Jacobian pseudoinverse algorithm (6).

After discretization the algorithm (7) becomes a Newton algorithm

$$z(k+1) = z(k) - \gamma D\,K^{\#}(z(k))e(k), \quad k = 0, 1, 2, \ldots. \tag{8}$$

The quantity $D\,K^{\#}(z(k))e(k)$ appearing in (8) is called the Newton direction at the step k. It is known that the Newton direction guarantees

a gradual decrease of the taskspace error from step to step, provided that the steplength γ is chosen properly. Relying on Deulfhard, 2004 we shall consider two strategies of the steplength choice in (8). The first strategy is called the Armijo strategy that consists in defining for a fixed integer m a set $\Gamma_m = \{1, \frac{1}{2}, \ldots, \frac{1}{2^m}\}$ of candidate steplengths and choosing at every step of the algorithm $\gamma = argmin_{\alpha \in \Gamma_m} ||K(z - \alpha DK^{\#}(z)e) - y_d||^2$.

A more sophisticated strategy may be based on the affine covariant Lipschitz condition imposed on $D\,K$,

$$||D\,K^{\#}(z)(D\,K(y) - D\,K(w))v|| \leq \omega||y - w||||v||, \tag{9}$$

where $||\cdot||$ denotes the norm (2) in $\mathcal{X}$, $v, w, y, z \in \mathcal{X}$, and $\omega > 0$ is a Lipschitz constant. It may be checked that in a singularity-free region of the endogenous configuration space the affine covariant condition is satisfied. However, for the reason that usually the Lipschitz constant ω in (9) is not available, the computation of γ relies on some estimates achieved in a prediction-correction procedure Deulfhard, 2004, culminating in the following algorithm of the steplength adjustment. The algorithm is initiated at z_0 with $\gamma_1^0 = 1$. At the step k the algorithm returns $z^0(k)$, computes $e^0(k) = K(z^0(k)) - y_d$, and makes a prediction γ_k^0. Then the predicted value of γ_k^0 is subject to a series of corrections. Suppose that after the ith correction step the algorithm proposes a steplength γ_k^i. Then the algorithm finds $z^i(k) = z^0(k) - \gamma_k^i D\,K^{\#}(z^0(k))e^0(k)$, computes $e^i(k) = K(z^i(k)) - y_d$, and accomplishes the $(i+1)$st correction as $\gamma_k^{i+1} = \min\{\gamma_k^i/2, 1/h_k^{i+1}\}$, where

$$h_k^{i+1} = \frac{2||D\,K^{\#}(z^0(k))e^i(k) - (1 - \gamma_k^i)D\,K^{\#}(z^0(k))e^0(k)||}{(\gamma_k^i)^2||D\,K^{\#}(z^0(k))e^0(k)||}.$$

These corrections are made a preassumed number of times yielding an i^* such that $\gamma_k^{i^*} = argmin_{\,i}||e^i(k)||^2$. Next, given $\gamma_k^{i^*}$ the algorithm sets $z^0 = z^0(k+1) = z^{i^*}(k)$, $e^0 = e^0(k+1) = K(z^0(k+1)) - y_d$, and computes a prediction for the step $k+1$ as $\gamma_{k+1}^0 = \min\{1, 1/h_{k+1}^0\}$, where

$$h_{k+1}^0 = \frac{||D\,K^{\#}(z^0)(D\,K(z^0) - D\,K(z^0(k)))D\,K^{\#}(z^0)e^0||}{\gamma_k^{i^*}||D\,K^{\#}(z^0(k))e^0(k)||}.$$

In the next section we shall apply the above procedure to the Jacobian pseudoinverse algorithm (6) driving a specific mobile manipulator.

4. Computer Simulations

In simulations we shall use a Ritz approximation of platform control functions by truncated Fourier series: $u_1(t) = \lambda_{10} + \sum_{j=1}^{2} \lambda_{1\,2j-1} \sin j\omega t +$

$\lambda_{1\,2j}\cos j\omega t$, $u_2(t) = \lambda_{20} + \lambda_{21}\sin\omega t + \lambda_{22}\cos\omega t$, where $\omega = \frac{2\pi}{T}$. For a suitable matrix $P(t)$ the control can be written as $u(t) = P(t)\lambda$, where the control parameters $\lambda = (\lambda_{10}\ldots,\lambda_{14},\lambda_{20},\lambda_{21},\lambda_{22}) \in R^8$. The Ritz approximation defines a finite-dimensional, band-limited endogenous configuration space $\tilde{\mathcal{X}} \cong R^{11}$, and yields the band-limited kinematics $\tilde{K}_{q_0,T}(\lambda,x)$ and the band-limited analytic Jacobian

$$\tilde{J}_{q_0,T}(\lambda,x) = \left[\tilde{C}(T,x)\int_0^T \tilde{\Phi}(T,s)\tilde{B}(s)P(s)ds,\ \tilde{D}(T,x)\right].$$

In consequence, a discrete band-limited Jacobian pseudoinverse inverse kinematics algorithm (6) will take the following form

$$\begin{pmatrix}\lambda_{k+1}\\ x_{k+1}\end{pmatrix} = \begin{pmatrix}\lambda_k\\ x_k\end{pmatrix} - \gamma\tilde{J}^T_{q_0,T}(\lambda_k,x_k)\tilde{\mathcal{D}}^{-1}_{q_0,T}(\lambda_k,x_k)\tilde{e}_k, \tag{10}$$

where $\tilde{e} = \tilde{K}_{q_0,T}(\lambda,x) - y_d$ and $\tilde{\mathcal{D}}_{q_0,T}(\lambda,x) = \tilde{J}_{q_0,T}(\lambda,x)\tilde{J}^T_{q_0,T}(\lambda,x)$.

The inverse kinematics algorithm (10) has been applied to a mobile manipulator composed of a kinematic car platform carrying an RTR manipulator, portrayed in Figure 1. The vector $q = (q_1,q_2,q_3,q_4) =$

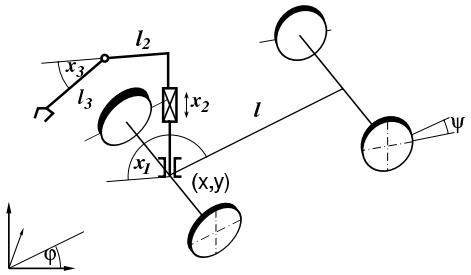

Figure 1. RTR manipulator mounted on kinematic car.

$(\mathsf{x},\mathsf{y},\varphi,\psi) \in R^4$ includes the position and the orientation of the platform and the heading angle of its front wheels. The vector $x = (x_1,x_2,x_3) \in R^3$ denotes joint positions of the onboard manipulator. Cartesian positions of the end effector $y = (y_1,y_2,y_3) \in R^3$ serve as taskspace coordinates. The representation (1) of kinematics, excluding the side-slip of platform wheels, takes the following form

$$\dot{q}_1 = u_1\cos q_3\cos q_4,\quad \dot{q}_2 = u_1\sin q_3\cos q_4,\quad \dot{q}_3 = u_1\sin q_4,\quad \dot{q}_4 = u_2,$$
$$y = (q_1 + L\cos(q_3+x_1), q_2 + L\sin(q_3+x_1), x_2 + l_3\sin x_3),$$

where $L = l_2 + l_3\cos x_3$. In simulations the length of the car $l = 1$, the link lengths of the onboard manipulator $l_2 = 0.5$, $l_3 = 1$, and the control

time horizon $T = 1$. The initial platform coordinates $q_0 = (0, 10, 0, 0)$, the initial joint positions $x_0 = (0, 2, \pi/4)$, the desired taskspace point $y_d = (0, 0, 1)$. The algorithm has been initiated at diverse λ_{10}, λ_{20} lying in a square $[-100, +100]^2$, while remaining $\lambda_{ij} = 0$. Table 1 displays the number of steps after which y_d has been reached within the accuracy of 10^{-6}. The symbol >2000 means that within 2000 iterations the convergence has not been observed. For comparison, the Jacobian pseudoinverse algorithm has been examined with constant steplength $\gamma = 1$ and with the steplength governed by the Armijo strategy with $m = 5$. Figure 2 shows platform and end effector trajectories obtained for $\lambda_{20} = -\lambda_{10} = 0.01$ using the constant step and the affine covariant strategies.

5. Conclusions

Assuming the affine covariant Lipschitz condition we have obtained a strategy of steplength adjustment in Jacobian inverse kinematics algorithms for mobile manipulators. This strategy has been implemented for the Jacobian pseudoinverse algorithm and examined by computer simulations. The examination has demonstrated that using a variable steplength improves both the speed and the quality of convergence of

Table 1. Convergence of the Jacobian pseudoinverse algorithm

λ_{10}	λ_{20}	$\gamma = 1$	*Arm*	*cov*	λ_{10}	λ_{20}	$\gamma = 1$	*Arm*	*cov*
100	100	136	14	13	–100	100	17	22	16
10	10	11	11	11	–10	10	37	70	40
1	1	100	27	29	–1	1	276	132	94
0.1	0.1	295	25	113	–0.1	0.1	249	331	65
0.01	0.01	152	28	52	–0.01	0.01	1307	211	59
0.001	0.001	40	32	57	–0.001	0.001	830	33	58
–100	–100	126	160	>2000	–100	0	90	27	62
–10	–10	26	1158	117	–10	0	90	334	145
–1	–1	138	60	20	–1	0	91	302	26
–0.1	–0.1	241	22	47	–0.1	0	101	30	89
–0.01	–0.01	115	86	54	–0.01	0	205	40	58
–0.001	–0.001	177	427	46	–0.001	0	332	29	55
100	–100	509	310	344	100	0	189	360	62
10	–10	78	573	142	10	0	353	29	167
1	–1	75	26	1538	1	0	194	76	79
0.1	–0.1	801	61	78	0.1	0	64	70	90
0.01	–0.01	318	40	58	0.01	0	171	90	58
0.001	–0.001	120	30	62	0.001	0	207	247	56

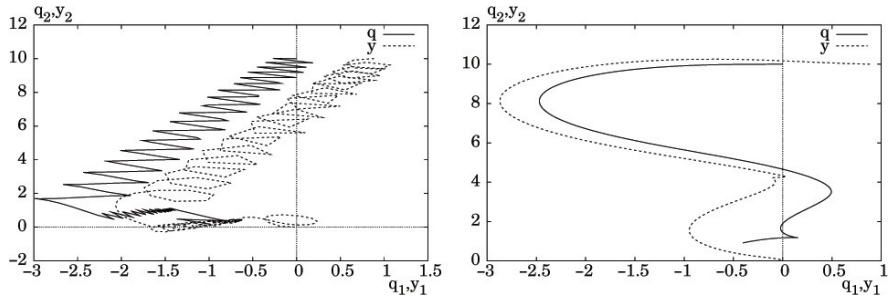

Figure 2. Trajectory for constant steplength (left) vs. affine covariant (right).

the algorithm in comparison to the case of constant steplength. When the prediction-correction procedure produces very small steplenghts the affine covariant strategy may be overpassed by a simple Armijo strategy. The fact that no lost of convergence has been observed along with the result of Chitour and Sussmann, 1998 on global convergence of the Jacobian pseudoinverse algorithm for the mobile platform from Figure 1 may suggest that the examined algorithm also converges globally.

6. Acknowledgements

This research was supported by the Foundation for Polish Science.

References

Chitour, Y., and Sussmann, H. J. (1998), Motion planning using the continuation method, In: *Essays on Mathematical Robotics*, ed. by J. Baillieul, S. S. Sastry and H. J. Sussmann, Springer-Verlag, New York, pp. 91-125.

Deuflhard, P. (2004), *Newton Methods for Nonlinear Problems*, Springer-Verlag, Berlin, 2004.

Divelbiss, A., Seereeram, S., and Wen, J.T. (1998), Kinematic path planning for robots with holonomic and nonholonomic constraints. In: *Essays on Mathematical Robotics*, ed. by J. Baillieul, S. S. Sastry and H. J. Sussmann, Springer-Verlag, New York, pp. 127-150.

Duleba, I., and Sasiadek, J. Z. (2003), Nonholonomic motion planning based on Newton algorithm with energy optimization, *IEEE Trans. Contr. Syst. Technology*, vol. 11, no. 3, pp. 355-363.

Isobe, T., Nagasaka, K., and Yamamoto, S. (1992), A new kinematic control of simple manipulators, *IEEE Trans. Syst., Man, Cybernet.*, vol. 22, no. 5, pp. 1116-1124.

Tchoń, K., and Jakubiak, J. (2003), Endogenous configuration space approach to mobile manipulators: a derivation and performance assessment of Jacobian inverse kinematics algorithms, *Int. J. Control*, vol. 76, no. 14, pp. 1387-1419.

Tchoń, K., and Jakubiak, J. (2005), A repeatable inverse kinematics algorithm with linear invariant subspaces for mobile manipulators, *IEEE Trans. Syst., Man, Cybernet., – Part B Cybernetics*, vol. 35, no. 5, pp. 1051-1057.

KINEMATICS AND GRASPING USING CONFORMAL GEOMETRIC ALGEBRA

Julio Zamora-Esquivel and Eduardo Bayro-Corrochano
Center of research and advanced studies of IPN, Unit Guadalajara
Geovis Laboratory. Jalisco, Mexico
jzamora,edb@gdl.cinvestav.mx

Abstract In this paper we introduce the conformal geometric algebra in the field of robot grasping. It help us to tackle problems of object modelling, hand kinematics and vision system using a unifying geometric language. We present an grasp algorithm using velocity control.

1. Introduction

As the technology advances new mechanisms emerge that enable us interact with a wider variety of objects, in this way new challenges related to object grasping planning arises. There are many approaches to deal with this kind of problems based in shape primitives [Miller, 2003], forces equilibrium [Borst, 1999] for cite two examples. We are working in how to obtain the optimal grasping points by means of mathematical modelling of the object and the manipulator. In this manner we also obtain the hand (manipulator) pose. Conformal geometric Algebra has been used in this work due to its powerful geometric representation and algebraic richness of which helps greatly in the process of modelling mechanical structures like the Barrett Hand^{TM}.

2. The Geometric Algebra of n-D Space

In this paper we will specify a geometric algebra $\mathcal{G}_n$ of the n dimensional space by $\mathcal{G}_{p,q,r}$, where p, q and r stand for the number of basis vector which squares to 1,–1 and 0 respectively and fulfill $n = p+q+r$.

We will use e_i to denote the vector basis i. In a Geometric algebra $G_{p,q,r}$, the geometric product of two basis vector is defined as

$$e_i e_j = \begin{cases} 1 & for \quad i = j \in 1, \cdots, p \\ -1 & for \quad i = j \in p+1, \cdots, p+q \\ 0 & for \quad i = j \in p+q+1, \cdots, p+q+r. \\ e_i \wedge e_j & for \quad i \neq j \end{cases}$$

Geometric algebra $G_{4,1}$ can be used to treat conformal geometry in a very elegant way. In this geometry an Euclidean vector space $\mathbb{R}^3$

J. Lenarčič and B. Roth (eds.), Advances in Robot Kinematics, 473–480.

is represented in $\mathbb{R}^{4,1}$. This space has orthonormal vector basis given by $\{e_i\}$ and $e_{ij} = e_i \wedge e_j$ are bivectorial basis where e_{23}, e_{31} and e_{12} correspond to the Hamilton basis. The unit Euclidean pseudo-scalar $I_e := e_1 \wedge e_2 \wedge e_3$, a pseudo-scalar $I_c := I_e E$ and the bivector $E := e_4 e_5$. The conformal geometry is related to a stereographic projection in Euclidean space. A stereographic projection is a mapping taking points lying on a hypersphere to points lying on a hyperplane. In this case, the projection plane passes through the equator and the sphere is centered at the origin. To make a projection, a line is drawn from the north pole to each point on the sphere and the intersection of this line with the projection plane constitutes the stereographic projection. The points are mapped to a point of conformal geometry by $x = x + \frac{1}{2}\|x\|^2 e_\infty + e_o$. More information about the conformal geometry in [Hestenes, 2001].

3. Barrett Hand Forward Kinematics

The direct kinematics involves the computation of the position and orientation of the robot end-effector given the parameters of the joints. The direct kinematics can be easily computed provided that the lines of the axes of screws are given for more information [Bayro, 2000].

In order to introduce the kinematics of the Barrett Hand^{TM}, we show the kinematic of one finger, in this example we will assume that the finger is totally extended. Note that such an hypothetical position is not reachable in normal operation.

We points x_{1o}, x_{2o} and x_{3o} to describe the position of each union and the end of the finger in the Euclidean space, see the figure 1. Here we use A_w, $A_{1,2,3}$ and D_w as the dimension of the finger's components.

$$x_{1o} = A_w e_1 + A_1 e_2 + D_w e_3, \quad (1)$$

$$x_{2o} = A_w e_1 + (A_1 + A_2) e_2 + D_w e_3, \quad (2)$$

$$x_{3o} = A_w e_1 + (A_1 + A_2 + A_3) e_2 + D_w e_3. \quad (3)$$

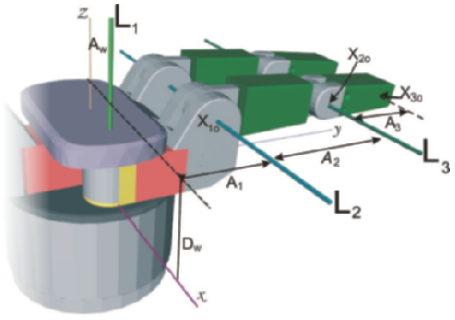

Figure 1. Barrett hand hypothetical position.

Once we have defined these points it is quite simple to calculate the axes $L_{1o,2o,3o}$, which will be used as motor's axis. as you can see at the figure 1.

$$L_{1o} = -A_w(e_2 \wedge e_\infty) + e_{12}, \quad (4)$$
$$L_{2o} = (x_{1o} \wedge e_1 \wedge e_\infty)\, I_c, \quad (5)$$
$$L_{3o} = (x_{2o} \wedge e_1 \wedge e_\infty)\, I_c. \quad (6)$$

when the hand is initialized the fingers moves away to the home position, this is the angle $\Phi_2 = 2.46°$ by the joint two and the angle $\Phi_3 = 50°$ degrees by the joint three. In order to move the finger from this hypothetical position to its home position the appropriate transformation is as follows:

$$M_{2o} = cos\,(\Phi_2/2) - sin(\Phi_2/2)L_{2o}, \quad (7)$$
$$M_{3o} = cos\,(\Phi_3/2) - sin(\Phi_3/2)L_{3o}. \quad (8)$$

Once we have gotten the transformations, then we apply them to the points x_{2o} and x_{3o} in order to get the points x_2 and x_3 that represents the points in its home position, also the line L_3 is the line of motor axis in home position.

$$x_2 = M_{2o}x_{2o}\widetilde{M}_{2o}, \quad (9)$$
$$x_3 = M_{2o}M_{3o}x_{3o}\widetilde{M}_{3o}\widetilde{M}_{2o}, \quad (10)$$
$$L_3 = M_{2o}L_{3o}\widetilde{M}_{2o}. \quad (11)$$

The point $x_1 = x_{1o}$ is not affected by the transformation, the same for the lines $L_1 = L_{1o}$ and $L_2 = L_{2o}$ see figure 2. Since the rotation

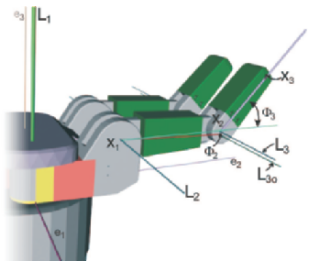

Figure 2. Barrett hand at home position

angles of both axis L_2 and L_3 are related, we will use fractions of the angle q_1 to describe their individual rotation angles. The motors of each joint are computed using $\frac{2}{35}q_4$ to rotate around L_1, $\frac{1}{125}q_1$ around L_2 and

$\frac{1}{375}q_1$ around L_3, these specific angle coefficients where taken from the Barrett Hand user manual.

$$M_1 = cos(q_4/35) + sin(q_4/35)L_1, \quad (12)$$
$$M_2 = cos(q_1/250) - sin(q_1/250)L_2, \quad (13)$$
$$M_3 = cos(q_1/750) - sin(q_1/750)L_3. \quad (14)$$

The position of each point is related to the angles q_1 and q_4 as follows:

$$x'_1 = M_1 x_1 \widetilde{M}_1, \quad (15)$$
$$x'_2 = M_1 M_2 x_2 \widetilde{M}_2 \widetilde{M}_1, \quad (16)$$
$$x'_3 = M_1 M_2 M_3 x_3 \widetilde{M}_3 \widetilde{M}_2 \widetilde{M}_1. \quad (17)$$

4. Grasping the Objects

In our example considering that the cameras can only see the surface of the observed objects, thus we will consider them as bi-dimensional surfaces which are embedded in a 3D space, and are described by the function

$$\vec{H}(s,t) = h_x(s,t)e_1 + h_y(s,t)e_2 + h_z(s,t)e_3 \quad (18)$$

where s and t are real parameters in the range $[0,1]$. Such parameterization allows us to work with different objects like points, conics, quadrics, or even more complex objects like cups, glasses, etc. The table 1 shows some parameterized objects.

Table 1. Parameterized Objects

Particle	$\vec{H}= 3e_1 + 4e_2 + 5e_3$
Cylinder	$\vec{H}= cos(t)e_1 + sin(t)e_2 + se_3$
Plane	$\vec{H}= te_1 + se_2 + (3s + 4t + 2)e_3$

Due to that our objective is to grasp such objects with the Barrett Hand, we must consider that it has only three fingers, so the problem consists in finding three "touching points" for which the system is in equilibrium during the grasping; this means that the sum of the forces equals to zero, and also the sum of the moments. For this case, we consider that there exists friction in each "touching point".

If the friction is being considered, we can claim that over the surface $H(s,t)$ a set of forces exist which can be applied. Such forces are inside a cone which have the normal $N(s,t)$ of the surface as its axis (as shown in Fig. 3). Its radius depends on the friction's coefficient $\|F - F_n\| \leq$

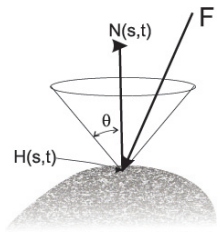

Figure 3. The friction cone.

$-\mu(|F_n|)$, where $F_n = (F \cdot N(s,t))N(s,t)$ is the normal component of F. The angle θ for the incidence of F with respect to the normal can be calculated using the wedge product, and should be smaller than a fixed θ_μ

$$\frac{\|F \wedge N(s,t)\|}{F \cdot N(s,t)} \leq tan(\theta_\mu) \tag{19}$$

We know the surface of the object, so we can compute its normal vector in each point using

$$N(s,t) = \left(\frac{\partial \vec{H}(s,t)}{\partial s} \wedge \frac{\partial \vec{H}(s,t)}{\partial t} \right) I_e \tag{20}$$

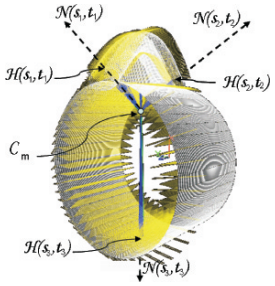

Figure 4. Object and his normal vectors.

In surfaces with lower friction, the angle θ is very small, then the value of F tends to its projection over the normal ($F \approx F_n$). To maintain equilibrium, the sum of the forces must be zero ($\sum_{i=1}^{3} \|F_n\| N(s_i,t_i) = 0$). This fact restricts the points over the surface in which it can be applied the forces. This number of points is even more reduced if we are confronted with the case when considering the unit normal ($\sum_{i=1}^{3} N(s_i,t_i) = 0$) the forces over the object are equal. Additionally, to maintain the equilib-

rium, it must be accomplished that the sum of the moments is zero

$$\sum_{i=1}^{3} H(s,t) \wedge N(s,t) = 0 \tag{21}$$

The points on the surface having the same directed distance to the center of mass of the object fulfill $H(s,t) \wedge N(s,t) = 0$. Due to the normal in such points crosses the center of mass (C_m), it does not produce any moment. Before determining the external and internal points, we must compute the center of mass as follows

$$C_m = \int_0^1 \int_0^1 \overrightarrow{H}\,(s,t) ds dt \tag{22}$$

Once that C_m is calculated we can establish next constraint

$$(H(s,t) - C_m) \wedge N(s,t) = 0 \tag{23}$$

The values s and t satisfying (23) form a subspace called *grasping space*. They accomplish that the points represented by $H(s,t)$ are critical on the surface (being maximums, minimums or inflections). In this work we will not consider other grasping cases like when they do not utilize extreme points other when friction cones are being considered. This issues will be treated in future work. The equation (23) is hard to fulfill due to the noise, and it is necessary to consider a cone of vectors. So, we introduce an angle called α,

$$\frac{\|(H(s,t) - C_m) \wedge N(s,t)\|}{(H(s,t) - C_m) \cdot N(s,t)} \leq tan(\alpha) \tag{24}$$

We use equation (24) instead of (23), because it allows us to deal with errors or data lost. The constraint imposing that the three forces must be equal is hard to fulfill because it implies that the three points must be symmetric with respect to the mass center. When such points are not present, we can relax the constraint to allow that only two forces are equal in order to fulfill the hand's kinematics equations. Then, the normals $N(s_1,t_1)$ and $N(s_2,t_2)$ must be symmetric with respect to $N(s_3,t_3)$.

$$N(s_3,t_3)N(s_1,t_1)N(s_3,t_3)^{-1} = N(s_2,t_2) \tag{25}$$

Once the three grasping points ($P_1 = H(s_1,t_1), P_2 = H(s_2,t_2), P_3 = H(s_3,t_3)$) are calculated, it is really easy to determine the angles at the joints in each finger. To determine the angle of the spread ($q_4 = \beta$) for example we use

$$\cos\beta = \frac{(p_1 - C_m) \cdot (C_m - p_3)}{|p_1 - c_m|\,|C_m - p_3|},\ \sin\beta = \frac{|(p_1 - C_m) \wedge (C_m - p_3)|}{|p_1 - c_m|\,|C_m - p_3|}, \tag{26}$$

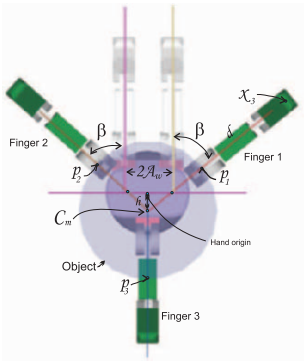

Figure 5. Object relative position

or it is possible to implement a control law which will allow to move the desired finger without the need of solving any kind of inverse kinematics equations C. Canudas, G. Bastin, B. Siciliano. Given the the differential kinematics equation

$$\dot{X}'_3 = \begin{bmatrix} \frac{1}{125}X'_3 \cdot L'_2 + \frac{1}{375}X'_3 \cdot L'_3 & -\frac{2}{35}X'_3 \cdot L'_1 \end{bmatrix} \begin{bmatrix} \dot{q_1} \\ \dot{q_4}, \end{bmatrix} \tag{27}$$

If we want to reach the point $H(s_1, t_1)$, we require that the suitable velocity at the very end of the finger should be proportional to the error at each instance $V_i = -0.7(X'_3 - H(s_1, t_1))$. This velocity is mapped into the phase space by means of using the Jacobian inverse. Here we use simply the pseudo-inverse. with $j_1 = \frac{1}{125}X'_3 \cdot L'_2 + \frac{1}{375}X'_3 \cdot L'_3$ and $j_2 = -\frac{2}{35}X'_3 \cdot L'_1$

$$\begin{bmatrix} \Delta q_1 \\ \Delta q_4 \end{bmatrix} = (j_1 \wedge j_2)^{-1} \cdot \begin{bmatrix} V_i \wedge j_2 \\ j_1 \wedge V_i \end{bmatrix} \tag{28}$$

Applying this control rule, one can move any of the fingers at a desired position above an object, so that an adequate grasp is accomplish.

5. Results

In this section we present the experimental results of our grasping algorithm. In Figure 6, the inferior images correspond to the simulated scenario and the other ones are real. In this experiment the object was suspended manually above the grasping hand, simply to check whether the has been opened correctly or not. We can see that for each object the algorithm manages to find the singular grasp points, so that the object is hold properly and in equilibrium. Note that the found points correspond to the expected grasping points.

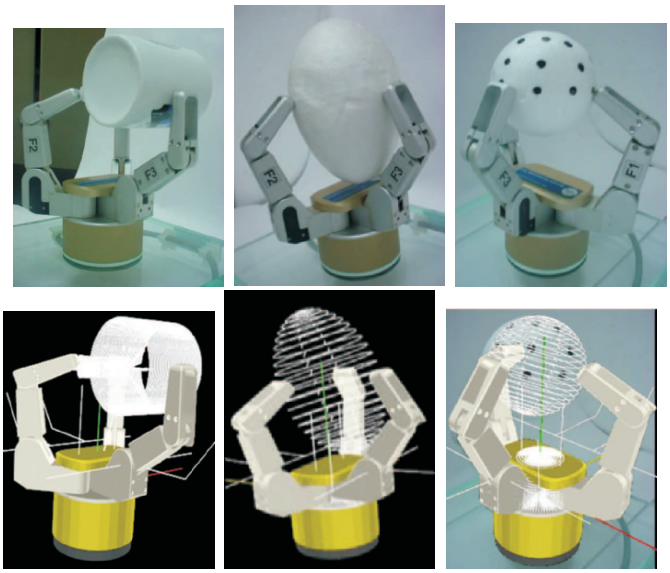

Figure 6. Grasping some objects.

6. Conclusion

Using conformal geometric algebra we show that it is possible to find three grasping points for each kind of object, based on the intrinsic information of the object. The hand's kinematic and the object structure can be easily related to each other in order to manage a natural and feasible grasping where force equilibrium is always guaranteed.

References

Li, H., Hestenes, D., Rockwood A. (2001). "Generalized Homogeneous coordinates for computational geometry". G. Somer, editor, *Geometric Computing with Clifford Algebras*, pages 27-52. Springer-Verlag Heidelberg.

Bayro-Corrochano, E. and Kähler, D. (2000). Motor Algebra Approach for Computing the kinematics of robot manipulators. *Journal of Robotics Systems*, 17(9):495-516.

Carlos Canudas de Wit, Georges Bastin, Bruno Siciliano. (1996). Theory of Robot Control, Springer.

Ch Borst, Fischer, M. and Hirzinger, G. (1999). *A Fast and Robust Grasp Planner for Arbitrary 3D Objects*. ICRA, pages 1890-1896. Detroit, Michigan.

Andrew T. Miller, Steffen Knoop, Peter K. Allen, Henrik I. Christensen. (2003). "Automatic Grasp Planning Using Shape Primitives," In Proceedings of the IEEE International Conference on Robotics and Automation, pp. 1824-1829.

APPLICATION OF KINEMATICS TOOLS IN THE STUDY OF INTERNAL MOBILITY OF PROTEIN MOLECULES

Raghavendran Subramanian
Graduate Student
Dept. of Mechanical Engineering
University of Connecticut
Storrs, CT – 06268
raghavendran@engr.uconn.edu

Kazem Kazerounian
Professor
Dept. of Mechanical Engineering
University of Connecticut
Storrs, CT – 06268
kazem@engr.uconn.edu

Abstract In this paper, we present a new methodology to identify the rigid domains in a protein molecule. This procedure also identifies the flexible domains as well as their degree of flexibility. Identification of rigid domains significantly simplifies the motion modeling procedures (such as molecular dynamics) that use geometric features of a protein as variables.

Keywords: Kinematics, mobilities, functions, graph theory, nano machines, closed loops

1. Introduction

Proteins are the building blocks that play an essential role in a variety of basic biological functions such as signal transduction, ligand binding, catalysis, regulation of activity, transport of metabolites, formation of larger assemblies and cellular locomotion. Its internal motions results in conformational transitions and often relate structure to its function. Hence, comprehending the protein internal motion is the key to the understanding of the structural relationship of these natural machines to their function. Protein molecules have always been observed with rigid domains connected by flexible portions as shown in the figure 1. Kinematics serial chain model of proteins has been established and justified in few of our previous works (Kazerounian 2004; Kazerounian, Latif et al., 2005; Kazerounian, Latif et al., 2005; Subramanian 2005; Kazerounian June 2002). As the long snake type serial linkage folds, new bonds are created between atoms of the residues that are not

J. Lenarčič and B. Roth (eds.), Advances in Robot Kinematics, 481–488.

neighbors. These bonds transform the open loop linkage to a linkage with some relatively large links (rigid body domains) and closed kinematic loops. These bonds are generally categorized as follows: 1) Hydrogen Bonds (main chain to main chain, main chain to Side chain and side chain to side chain), and 2) Disulphide bonds.

To gain insight into a protein function, we must understand the kinematics and the mobility of the internal motion of the protein. There are five different computational methods reported in literature to identify rigid domains of the protein. Two of the methodsalso attempt to establish the mobility of the chain. First method (Nichols, Rose et al., 1995) involves comparison of two conformations of a protein to identify the rigid domains in a molecule. The second method (Wriggers and Schulten 1997) also compares two different conformations of the same protein. It uses a least square technique to best fit the two conformations. Third method (Levitt, Sander et al., 1985) is based on the dynamics of a protein molecule. The procedure creates an equivalent elastic network model with atoms as masses serially connected one after the other by springs. This mathematical treatment yields vibrational frequency modes of all the atoms. An atom for which all frequency modes are computed to be zero, will be considered as a part of a rigid domain. This method is computationally, a very expensive procedure even with a network of just C_α atoms. Fourth method is a variant of the third method. In this method normal mode analysis coupled with molecular dynamics (Doruker, Bahar et al., 2002) and Monte Carlo simulation is used to form the trajectory of all the atoms. This method too requires unreasonably excessive computation. Fifth method (Jacobs, Rader et al., 2001) is based on the graph theory. This method requires only one conformation to identify the rigid domains in a protein molecule. It uses the distance constraints between atoms due to the presence of covalent and the hydrogen bonds between them. It develops a rigidity matrix which on further manipulation based on the set of rules defined under the rigidity theory, one can find rigid domains. This method disregards the presence of disulphide bonds in a protein molecule which also reduces the mobility of atoms in proteins.

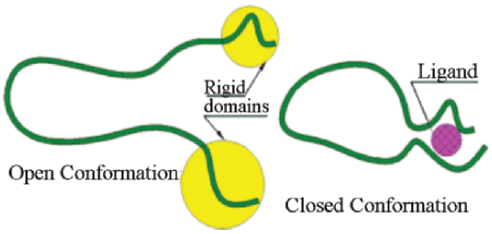

Figure 1. Ribbon view of a peptide chain in its open and closed conformation.

The methodology presented in this paper treats the protein molecule as a kinematic chain that has open as well as closed loops. In the recent

past, many kinematicians (Crossley 1965; Woo 1967; Manolescu 1973; Mruthyunjaya and Raghavan 1979) have extensively used graph theory for type synthesis of mechanisms especially to identify non-isomorphic mechanisms and to enumerate mechanisms. This method also uses graph theory based on the primary (linear) structure of the protein, and uses the atom coordinates to detect the hydrogen and disulphide bonds. The resulting graph maintains the information on the connectivity of links in the protein mechanism and thereby identifies all the loops formed by hydrogen and disulphide bonds. The loops that are kinematically over-constrained form rigid structures. This is an iterative process that results in the identification of all the rigid domains.

2. Identification of the Hydrogen Bonds

Hydrogen bonds occur when two electronegative atoms interact with the same hydrogen. The hydrogen atom is covalently attached to one atom (commonly called donor), and interacts electrostatically with the other atom (commonly called acceptor). This interaction is due to the dipole effect between the electronegative atoms and the proton (hydrogen). Hydrogen bond possesses some degree of orientational preference and has the characteristics of a covalent bond (although it is weak). Several fine works in the literature have focused on this directional behavior of hydrogen bonds (Baker and Hubbard 1984; Eswar and Ramakrishnan 2000). These works have established generalized geometric characteristics for identification of the hydrogen bonds when the positional coordinates of the electronegative atoms and the hydrogen atoms are known. Protein Data Bank (PDB) (Berman, Westbrook et al., 2000) offers the coordinate position of all the atoms in a protein configuration. A shortfall of these data files is that the hydrogen atom positions are usually not recorded.

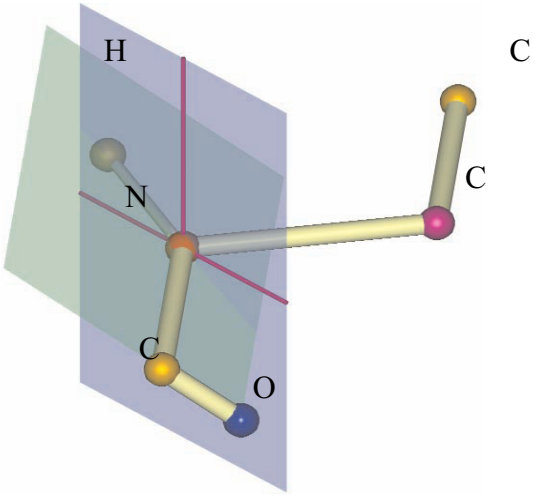

Figure 2. Location of Hydrogen atom with respect to the neighboring atoms.

2.1 Hydrogen Atom Position Calculation

The chemical (directional) nature of the covalent bonds leads to a unique relative position of a hydrogen atom with respect to the positional coordinate of its neighboring atoms. Hence the coordinates of a hydrogen atom can be established theoretically using coordinates of its neighbor atoms (figure 2). The detailed procedure and formulation based on figure 2 is included in Rigid body assumption in proteins has been established and justified in few of our previous works (Subramanian 2005).

2.2 Criteria to Establish Hydrogen Bonds

There are predominantly three types of hydrogen bonds observed in the protein structures. They are main chain to main chain, main chain to side chain and side chain to side chain hydrogen bonds. The majority of the main chain to main chain hydrogen bonds are local in nature involving less than six consecutive residues in the primary sequence of a protein. As mentioned earlier, the directional nature of the hydrogen bond results in a set of geometric criteria to be established to identify the presence of hydrogen bonds. These geometric criteria solely depend on the coordinate positions of two electronegative atoms and a hydrogen atom. These geometric criteria are different for different sets of the electronegative atoms and the geometric conditions for identification of the hydrogen bonds are quite extensive. Reference (Subramanian 2005) and the exhaustive conditions for selecting each one of the three possible hydrogen bonds, as developed by the authors.

3. Identification of the Disulphide Bonds

A disulphide bridge is formed between two cysteine residues by the oxidation of their sulfur atoms to form a double bond. Thus two cysteine residues connect through their sulphur atoms and form loops in the open chain. In proteins disulphide bridges contribute significantly to the stability of proteins.

Two parameters have been established (Sowdhamini, Srinivasan et al., 1989) to identify the presence of disulphide bonds between two cysteine residues in a protein molecule. They are based on the geometric features that exist between the two test residues. The distance parameters include the distance between the two alpha carbon atoms and the distance between the two beta carbon atoms of two cysteine residues in the primary sequence. The two geometric conditions are that the first distance mentioned lies within 3.8Å to 6.5Å and the second distance lies within 3.4Å to 4.5Å. These criteria are checked for all the possible

combinations of any two cysteines in a protein molecule. Those combinations that meet the above requirements are assumed to form the disulphide bonds.

4. Application of the Graph Theory to Loop Detection in a Protein Chain

The internal mobility of a protein chain is a function of how various links in the open chain model connect by means of hydrogen and disulphide bonds. These bonds transform the open loop linkage to more complex multi closed loop system. The size of the protein molecule and the large number of such bonds demands a sophisticated method of accounting for connections within the molecule. Graph theory is an ideal tool for this purpose

The equivalent linkage mechanisms to protein chains can be described as a graph with links as edges and joints as vertices and is a very useful tool to represent the connectivity between links. A two dimensional matrix (commonly called as connectivity matrix) mathematically represent the connectivity between all the links. Prior to the detection of the over-constrained loops from the given connectivity matrix, all the side chain links which do not participate in the loop formation will be eliminated from the connectivity matrix. This will reduce the computational complexity of the problem of detecting the over-constrained closed loops.

As a first step, we will eliminate all those side chain links which do not participate in the loop formation. This process starts from the end link of all the side chains. If the end link has only one joint, then it does not form a loop. Consequently the link preceding the removed end link becomes the end link itself. This procedure iteratively eliminates all the links of the side chains that do not form closed loops except the first link of the side chains (that is connected to the two main chain links).

The graph after the previous step will have only one side chain link for all the side chains which are not involved in the loop formation. As mentioned earlier, these side chains will be connected only to two main chain links and no side chain links. In the second step the procedure eliminates all such first links of the side chains. This requires that the side chain links be differentiated from main chain links by their index numbers. This can be done by storing the index numbers of all the main chain links and all the side chain links in two different vectors. This information is readily available from Protein Data Bank (PDB) files. Note that in the above two stages the size and the values in the connectivity matrix changed while eliminating all the side chain links that were not part of any closed loops. This will leave the graph with

none of the open ended side chain branches off the main chain. Thus the complexity involved with maintaining the information of the un-influencing side chain links is avoided. This also reduces the computational needs for solving the problem of detecting all the over constrained loops.

The procedure we have developed to detect all the over-constrained loops involves finding all the closed loops with two links, three links, four links, five links and six links respectively, until all the over-constrained loops are detected. The steps to detect loops with m links (m = 2 to 6) are briefly explained as follows. The detailed algorithm for this detection process is included in reference(Subramanian 2005). The search starts with any link and through the detection of a "1" in the row corresponding to that link in the connectivity matrix, we follow the trail of the links connected until we arrive back on the link we started the search with. This indicates that the loop is closed and a counter keeps track of the number of links in that closed loop.

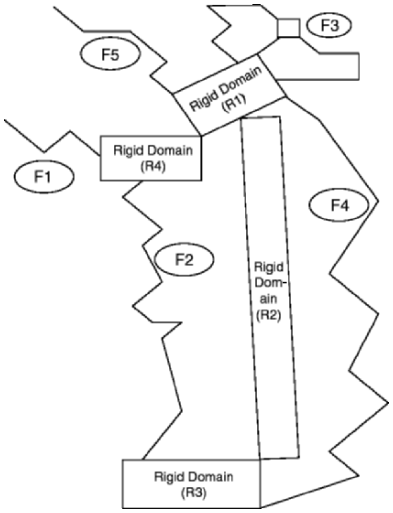

Figure 3. Kinematic Sketch of the protein BPTI (1K6U) with its rigid and flexible domains.

In the repeated local search for all the over-constrained loops, we change the connectivity matrix every time an over-constrained loop is found. The changes are as follow: all the links of an over-constrained loop is replaced by a single new link, thus the rows and columns corresponding to these links are dropped from the connectivity matrix and a new row and column is appended to the connectivity matrix to represent this new link. All the connections to all the links of this over-constrained loop will now be the connections to this new link.

5. Results and Discussion

The methodology developed in this work was succesfully applied to numerous protein molecules to identify their rigid domains and flexible portions. One such numerical experiment was on the protein BPTI (PDB

ID: 1K6U). Bovine Pancreatic Trypsin Inhibitor (PDB ID: 1K6U) is a 58 residue long protein. We identified a total of 26 hydrogen bonds in the protein molecule of which 19 were main chain to main chain hydrogen bonds and the rest of the hydrogen bonds were between main chain and side chains. This protein molecule was identified with 3 disulphide bonds.

The protein molecule had 4 rigid domains (R1 to R4) and 5 flexible portions (F1 to F5). The kinematic sketch for this protein is shown in figure 3 (kinematic arrangement) and a 3-D illustration in Figure 4. The alpha helices and beta sheets as expected formed rigid domains or part of rigid domains. Among all the flexible chains, 3 of them were closed loops. The degrees of freedom for such constrained closed loops are also reported. These are as follow: 7 for F2, 1 for F3 and 5 for F4. These results were compared visually with the motion of the protein molecules available in the website: http://molmovdb.mbb.yale.edu/molmovdb/ (Echols, Milburn et al., 2003). The results were observed to be consistent with these motion pictures for each of the three protein molecules.

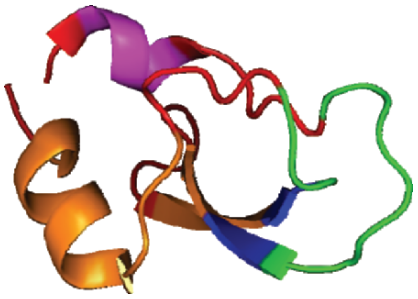

Figure 4. Color code based distinction between the rigid domains and flexible portions of the protein, BPTI (PDB ID: 1K6U). Red portions are the flexible regions and other colors (pink, green, orange and blue) represent the different rigid domains in the protein.

6. Conclusion

We have developed a computationally efficient methodology to identify all the rigid domains in a protein identified in a PDB type format (and contact). The coordinate value of all the atoms in the protein is used only to establish the location of hydrogen and disulphide bonds. It also finds all the flexible portions of a protein molecule and calculates its degrees of freedom, a numerical value as a flexibility measure, for each of these flexible portions. This methodology has been successfully tested on several proteins from PDB.

7. References

Baker, E. N. and R. E. Hubbard (1984). "Hydrogen bonding in globular proteins." Prog Biophys Mol Biol 44(2): 97-179.

Berman, H. M., J. Westbrook, et al. (2000). "The Protein Data Bank." Nucleic Acids Res 28(1): 235-42.

Crossley, F. R. E. (1965). "The permutations of Kinematic Chains of Eight Members or Less from Graph Theoretic Viewpoint." Developments in Theoretical and Applied Mechanics 2: 467-487.

Doruker, P., I. Bahar, et al. (2002). "Collective deformations in proteins determined by a mode analysis of molecular dynamics trajectories." POLYMER 43(2): 431-439.

Echols, N., D. Milburn, et al. (2003). "MolMovDB: analysis and visualization of conformational change and structural flexibility." Nucleic Acids Research 31(1): 478-482.

Eswar, N. and C. Ramakrishnan (2000). "Deterministic features of side-chain main-chain hydrogen bonds in globular protein structures." Protein Eng 13(4): 227-38.

Jacobs, D. J., A. J. Rader, et al. (2001). "Protein flexibility predictions using graph theory." Proteins 44(2): 150-65.

Kazerounian, K. (2004). "From mechanisms and robotics to protein conformation and drug design." Journal of Mechanical Design 126(1): 40-45.

Kazerounian, K. (June 2002). Is Design of New Drugs a Challenge for Kinematics? Proceedings of the 8th Int. Conf. on Advance Robot Kinematics - ARK, Caldes de Malavalla, Spain.

Kazerounian, K., K. Latif, et al. (2005). "Protofold: A successive kinetostatic compliance method for protein conformation prediction." Journal of Mechanical Design 127(4): 712-717.

Kazerounian, K., K. Latif, et al. (2005). "Nano-kinematics for analysis of protein molecules." Journal of Mechanical Design 127(4): 699-711.

Levitt, M., C. Sander, et al. (1985). "Protein normal-mode dynamics: trypsin inhibitor, crambin, ribonuclease and lysozyme." J Mol Biol 181(3): 423-47.

Manolescu, N. I. (1973). "A Method based on Barnov Trusses, and using Graph Theory to find the set of Planar Jointed Kinematic Chains and Mechanisms." mechanism and machine theory 8(1): 3-22.

Mruthyunjaya, T. S. and M. R. Raghavan (1979). "Structural Analysis of Kinematic Chains and Mechanisms based on Matrix Representation." ASME Journal of Mechanical Design 101: 488-494.

Nichols, W. L., G. D. Rose, et al. (1995). "Rigid Domains in Proteins - an Algorithmic Approach to Their Identification." Proteins-Structure Function and Genetics 23(1): 38-48.

Sowdhamini, R., N. Srinivasan, et al. (1989). "Stereochemical modeling of disulfide bridges. Criteria for introduction into proteins by site-directed mutagenesis." Protein Eng 3(2): 95-103.

Subramanian, R. (2005). Calibration of Structural Variables and Mobility Analysis of Protein molecules. Mechanical Engineering Department. Storrs, University of Connecticut. MS.

Woo, L. S. (1967). "Type Synthesis of Plane Linkages." ASME Journal of Engineering for Industry: 159-172.

Wriggers, W. and K. Schulten (1997). "Protein domain movements: Detection of rigid domains and visualization of hinges in comparisons of atomic coordinates." Proteins-Structure Function and Genetics 29(1): 1-14.

MOTION PATTERN SINGULARITY IN LOWER MOBILITY PARALLEL MANIPULATORS

Oscar Altuzarra, Charles Pinto, Victor Petuya, Alfonso Hernandez
Department of Mechanical Engineering
University of the Basque Country, Alameda de Urquijo s/n 48013 Bilbao, Spain
[oscar.altuzarra, charles.pinto, victor.petuya, a.hernandez]@ehu.es

Abstract Many procedures to detect singularities in manipulators have been described in the literature up to now. Singularities are often defined as an instantaneous or permanent modification in the number of degrees of freedom (DOF), either affecting certain links or the whole mechanism. However, the motion of the end-effector of a parallel manipulator is not only given by the number of DOF but also by the nature of them (rotational or translational). There are poses in which, being no quantitative alteration of the DOF of the platform, there are changes in this nature. This is also a singularity, and produces, as other singularities do, a mathematical deficiency in the velocity equations of the manipulator. This type of singularity affects only the so called lower mobility parallel manipulators. In this contribution the authors define this new type of singularity, called motion pattern singularity, and present a procedure to analyze it.

Keywords: Motion Pattern, Parallel Manipulators, Platform Twist, Singularities

1. Introduction

In robot design, knowing the possibilities of motion of the end-effector is the key to a proper choice of the application. The motion possibilities of the parallel manipulator's end-effector are not only determined by the number of DOF, but also by the nature of these freedoms. This nature has a qualitative aspect (translational or rotational) and a quantitative one: the directions of possible translation or rotation at each pose. Both features define the motion pattern of the platform. This denomination has been previously used for parallel manipulators in Kong and Gosselin, 2005. The motion pattern is specially important in lower mobility parallel manipulators because it determines the possible task to be performed. In addition, a proper design looks for constant directions of the DOF inside the workspace. Unfortunately, in many of the lower mobility parallel manipulators there is a variation of the translational and rotational directions with the pose. This does not imply a singularity,

J. Lenarčič and B. Roth (eds.), Advances in Robot Kinematics, 489–496.

but it does condition the kinematic characteristics of the manipulator such as its manipulability.

The nature of the DOF of the moving platform is usually unaltered by the motion of the manipulator, the same with the number of DOF. Nevertheless, it is possible that, in certain poses of the platform, some of the DOF change in nature, e.g. some rotational DOF becomes translational. Obviously, this alters substantially the motion pattern of the platform and hence, it can be considered as a singularity. In fact, it generates a mathematical deficiency as it will be explained later. In these circumstances, it is possible that the robot were unable to accomplish with the intended task, at least instantaneously at that pose. It must be highlighted that such a condition is independent of the coexistence with any other type of singularity. Anyway, it is necessary to have a procedure to detect those variations in the nature of the DOF of the platform along its motion.

A wide bibliography on singularities in robots has been issued in the past. We bring notice to some well known references as Freudenstein, 1962, Hunt, 1978, Sugimoto et al., 1982, Merlet, 1989, Gosselin and Angeles, 1990, Zlatanov et al., 1994, and Park and Kim, 1999. These works and some others have stated fundamental concepts as direct kinematic singularity, inverse kinematic singularity, or increased mobility configuration. Some more specific concepts have also been issued, such as constraint singularity Zlatanov et al., 2002, architecture singularity Ma and Angeles, 1992, internal singularities Company et al., 2006 or cuspidal manipulator Wenger, 2004. In all these works the singularity is understood as an alteration in the number of DOF, either globally in the mechanism as a whole, or locally at some part of it (preferably at input or output). However, to our best knowledge, such singularity as the one described in this paper has not been discussed. In fact, the latest references on parallel manipulator singularities as Thomas et al., 2005, Huang and Cao, 2005, or Liu et al., 2005 go over the quantitative modification of the number of DOF again.

2. Motion Pattern Singularity

In this section the authors present the definition and procedure to obtain the motion pattern of the manipulator's platform as well as the singularity associated to that concept.

2.1 Motion Pattern

The motion pattern of a parallel manipulator represents the platform's capacity of motion. The number of degrees of freedom, their

nature (traslational or rotational) and directions define this characteristic. Although this is an instantaneous feature, the number and nature of the DOF are, generally, permanent in the workspace. In fact, when they change in some pose, is because it is a singular configuration. Against, the directions of translation and rotation of the platform's DOF are often variable in parallel manipulators.

The motion pattern is obtained with a procedure that starts with a velocity equation that maps joint velocities to the platform's twist:

$$\dot{\mathbf{x}} = \mathbf{J}\ \dot{\mathbf{q}} \tag{1}$$

where $\dot{\mathbf{x}} = \left[\dot{\mathbf{p}}^T \boldsymbol{\omega}^T\right]^T$ is the twist of the moving platform, being $\dot{\mathbf{p}}$ the velocity of a point P in the platform and $\boldsymbol{\omega}$ the platform's angular velocity, $\mathbf{J}$ is a Jacobian matrix and $\dot{\mathbf{q}}$ is the vector of input joint rates. This Jacobian matrix is not always easy to find analytically. It will be often found numerically, and in those occasions the motion pattern is analyzed pose by pose.

This Jacobian can be divided into two submatrices $\mathbf{J}_T$ and $\mathbf{J}_R$, corresponding to terms that affect linear and angular velocity respectively. If the full cycle mobility, Hunt, 1978, of a non-redundant manipulator is F Eq. 1 is

$$\left\{ \begin{array}{c} \dot{\mathbf{p}} \\ \boldsymbol{\omega} \end{array} \right\}_{6\times 1} = \left[\begin{array}{c} \mathbf{J}_T \\ \mathbf{J}_R \end{array} \right]_{6\times F} \dot{\mathbf{q}}_{F\times 1} \tag{2}$$

The rotational motion space is analyzed extracting the equations corresponding to angular components from that system:

$$\boldsymbol{\omega} = \mathbf{J}_R\ \dot{\mathbf{q}} \tag{3}$$

The number of rotational DOF of the platform F_R is the rank of matrix $\mathbf{J}_R$ and the corresponding directions $\boldsymbol{\omega}_r$ are obtained in Eq. 3 with a basis $\dot{\mathbf{q}}_r$ of the rangespace of that matrix:

$$\boldsymbol{\omega}_r = \mathbf{J}_R\ \dot{\mathbf{q}}_r \qquad r = 1 \ldots F_R \tag{4}$$

The number of translational DOF of the platform F_T is $(rank\,(\mathbf{J}) - F_R)$, and the corresponding directions $\dot{\mathbf{p}}_t$ are solved in the translational part of Eq. 2 upon substitution of a basis $\dot{\mathbf{q}}_t$ of the null space of matrix $\mathbf{J}_R$:

$$\dot{\mathbf{p}}_t = \mathbf{J}_T\ \dot{\mathbf{q}}_t \qquad t = 1 \ldots F_T \tag{5}$$

Therefore, the platform's motion pattern is defined by the number of rotational DOF, $F_R = rank\,(\mathbf{J}_R)$, and translational DOF, $F_T = rank\,(\mathbf{J}) - rank\,(\mathbf{J}_R)$, along with the rotational and translational directions, $\boldsymbol{\omega}_r$ and $\dot{\mathbf{p}}_t$ respectively.

2.2 Singularity

A motion pattern singularity occurs in a pose where, being no alteration in the number of DOF of the moving platform, some DOF change in nature, e.g. a rotational DOF becomes translational or vice versa. Note that this singularity does not make reference to variations in the directions of possible translation or rotation of the platform. In fact, this latter is quite usual in lower mobility parallel manipulators although constant directions are desirable in design. Obviously, this type of singularity is only possible in lower mobility parallel manipulators.

Other type of singularities affecting the moving platform, and already described in the references, are the constraint singularity defined in Zlatanov et al., 2002 and the so called Impossible Output introduced in Zlatanov et al., 1994. The former implies a gain while the latter means a loss in the DOF of the end-effector.

The rank of Jacobian $\mathbf{J}_R$ has to be checked to detect mathematically the motion pattern singularity. As this Jacobian is homogeneous in terms of units, the first singular value not null of that Jacobian serves well as an indicator of closeness to singularity. The Singular Value Decomposition technique applied to $\mathbf{J}_R$ provides both the range and null spaces, and the motion pattern of the platform at the singularity is obtained with them.

3. Example

A 3 DOF parallel manipulator with rotational motion is shown in Fig. 1. A passive limb with 3 revolute joints (R) constrains the desired motion while three linear actuators (SPS) provide the control of the end-effector. A fixed frame is defined with origin at point O and a moving frame is attached to the platform with origin at point P. The loop-closure position equation is stated for every limb relating vector $\mathbf{p}$ that positions point P with: vectors $\mathbf{a}_i$ that locate the fixed S joints A_i of the linear actuators, vectors that go from A_i to B_i (being $\mathbf{s}_i$ a unit vector in the direction of actuators and ρ_i the length of the actuator), and vectors ${}^p\mathbf{b}_i$ that place points B_i with respect to point P in the platform and are best expressed in the moving frame:

$$\mathbf{p} = \mathbf{a}_i + \rho_i \mathbf{s}_i - {}^p\mathbf{b}_i \quad i = 1, 2, 3 \tag{6}$$

Differentiating Eq. 6 with respect to time yields

$$\dot{\mathbf{p}} = \dot{\rho}_i \cdot \mathbf{s}_i + \boldsymbol{\omega}_i \times \rho_i \mathbf{s}_i - \boldsymbol{\omega} \times {}^p\mathbf{b}_i \quad i = 1, 2, 3 \tag{7}$$

where $\dot{\rho}_i$ is the actuator's rate, $\boldsymbol{\omega}_i$ are the angular velocities of the actuators, and $\boldsymbol{\omega}$ is the angular velocity of the platform. If now we dot

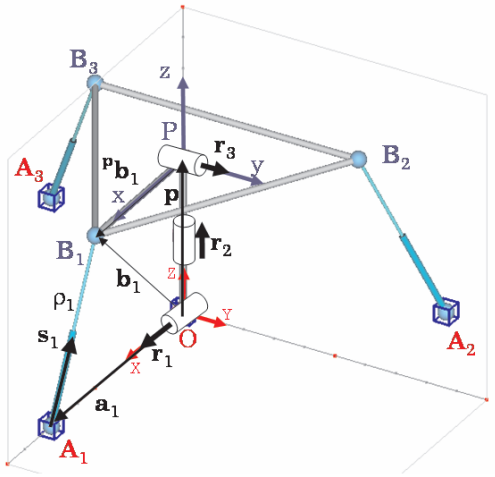

Figure 1. Kinematic Model of a Rotational Platform.

multiply Eq. 7 by $\mathbf{s}_i$ and simplify wherever possible we get

$$\mathbf{s}_i \cdot \dot{\mathbf{p}} + [{}^p\mathbf{b}_i \times \mathbf{s}_i] \cdot \boldsymbol{\omega} = \dot{\rho}_i \quad i = 1, 2, 3 \tag{8}$$

The revolute joints of the passive limb constrain the platform to a 3 DOF rotational motion. Let's consider the geometrical constraints imposed by each of the revolute joints in the passive limb. These can be formulated taking into account the fixed orientation of the position vector $\mathbf{p}$ with respect to each of the R joints' axes $\mathbf{r}_i$, namely

$$\mathbf{r}_1 \cdot \mathbf{p} = 0 \tag{9}$$

$$\mathbf{r}_2 \cdot \mathbf{p} = p \tag{10}$$

$$\mathbf{r}_3 \cdot \mathbf{p} = 0 \tag{11}$$

Differentiating Eq. 9 to 11 with respect to time yields

$$\mathbf{r}_1 \cdot \dot{\mathbf{p}} = 0 \tag{12}$$

$$\mathbf{r}_2 \cdot \dot{\mathbf{p}} = 0 \tag{13}$$

$$\mathbf{r}_3 \cdot \dot{\mathbf{p}} + [\mathbf{r}_3 \times \mathbf{p}] \cdot \boldsymbol{\omega} = 0 \tag{14}$$

Compiling Eq. 8 and Eqs. 12 to 14 in matrix form gives

$$\begin{bmatrix} \mathbf{r}_1^T & \mathbf{0}^T \\ \mathbf{r}_2^T & \mathbf{0}^T \\ \mathbf{r}_3^T & [\mathbf{r}_3 \times \mathbf{p}]^T \\ \mathbf{s}_1^T & [{}^p\mathbf{b}_1 \times \mathbf{s}_1]^T \\ \mathbf{s}_2^T & [{}^p\mathbf{b}_2 \times \mathbf{s}_2]^T \\ \mathbf{s}_3^T & [{}^p\mathbf{b}_3 \times \mathbf{s}_3]^T \end{bmatrix} \begin{Bmatrix} \dot{\mathbf{p}} \\ \boldsymbol{\omega} \end{Bmatrix} = \begin{bmatrix} \mathbf{0} \\ \mathbf{I} \end{bmatrix} \dot{\boldsymbol{\rho}} \tag{15}$$

This is a velocity equation that maps the twist of the platform to the inputs of the manipulator. A rank deficiency in the first Jacobian in Eq. 15, called $\mathbf{J}_x$, imply a direct kinematic singularity. A rank deficiency of the second Jacobian, called $\mathbf{J}_q$, is not possible in this manipulator, and hence no singularity in the inverse problem exists.

The Jacobian $\mathbf{J}_x$ must be inverted and postmultiplied by the second Jacobian to get the following expression of the twist

$$\left\{ \begin{array}{c} \dot{\mathbf{p}} \\ \boldsymbol{\omega} \end{array} \right\} = \frac{1}{|\mathbf{J}_x|} \left[\begin{array}{ccc} \boldsymbol{\delta}_1 & \boldsymbol{\delta}_2 & \boldsymbol{\delta}_3 \\ \boldsymbol{\alpha}_1 & \boldsymbol{\alpha}_2 & \boldsymbol{\alpha}_3 \end{array} \right] \dot{\boldsymbol{\rho}} = \left[\begin{array}{c} \mathbf{J}_T \\ \mathbf{J}_R \end{array} \right] \dot{\boldsymbol{\rho}} \tag{16}$$

where the translational Jacobian $\mathbf{J}_T$ is formed by vectors $\boldsymbol{\delta}_i$ multiplied by $\frac{1}{|\mathbf{J}_x|}$:

$$\boldsymbol{\delta}_1 = [\mathbf{n}_3 \cdot (\mathbf{m}_3 \times \mathbf{m}_2)] \cdot (\mathbf{r}_1 \times \mathbf{r}_2) \tag{17}$$

$$\boldsymbol{\delta}_2 = [\mathbf{n}_3 \cdot (\mathbf{m}_1 \times \mathbf{m}_3)] \cdot (\mathbf{r}_1 \times \mathbf{r}_2) \tag{18}$$

$$\boldsymbol{\delta}_3 = [\mathbf{n}_3 \cdot (\mathbf{m}_2 \times \mathbf{m}_1)] \cdot (\mathbf{r}_1 \times \mathbf{r}_2) \tag{19}$$

being

$$\mathbf{n}_3 = \mathbf{r}_3 \times \mathbf{p} \tag{20}$$

$$\mathbf{m}_1 = {}^p\mathbf{b}_1 \times \mathbf{s}_1 \tag{21}$$

$$\mathbf{m}_2 = {}^p\mathbf{b}_2 \times \mathbf{s}_2 \tag{22}$$

$$\mathbf{m}_3 = {}^p\mathbf{b}_3 \times \mathbf{s}_3 \tag{23}$$

And the rotational Jacobian $\mathbf{J}_R$ is formed by vectors $\boldsymbol{\alpha}_i$ multiplied by $\frac{1}{|\mathbf{J}_x|}$:

$$\begin{aligned} \boldsymbol{\alpha}_1 = &- [\mathbf{r}_3 \cdot (\mathbf{r}_1 \times \mathbf{r}_2)] \cdot (\mathbf{m}_3 \times \mathbf{m}_2) - [\mathbf{s}_2 \cdot (\mathbf{r}_1 \times \mathbf{r}_2)] \cdot (\mathbf{n}_3 \times \mathbf{m}_3) \\ &- [\mathbf{s}_3 \cdot (\mathbf{r}_1 \times \mathbf{r}_2)] \cdot (\mathbf{m}_2 \times \mathbf{n}_3) \end{aligned} \tag{24}$$

$$\begin{aligned} \boldsymbol{\alpha}_2 = &- [\mathbf{r}_3 \cdot (\mathbf{r}_1 \times \mathbf{r}_2)] \cdot (\mathbf{m}_1 \times \mathbf{m}_3) - [\mathbf{s}_1 \cdot (\mathbf{r}_1 \times \mathbf{r}_2)] \cdot (\mathbf{m}_3 \times \mathbf{n}_3) \\ &- [\mathbf{s}_3 \cdot (\mathbf{r}_1 \times \mathbf{r}_2)] \cdot (\mathbf{n}_3 \times \mathbf{m}_1) \end{aligned} \tag{25}$$

$$\begin{aligned} \boldsymbol{\alpha}_3 = &- [\mathbf{r}_3 \cdot (\mathbf{r}_1 \times \mathbf{r}_2)] \cdot (\mathbf{m}_2 \times \mathbf{m}_1) - [\mathbf{s}_1 \cdot (\mathbf{r}_1 \times \mathbf{r}_2)] \cdot (\mathbf{n}_3 \times \mathbf{m}_2) \\ &- [\mathbf{s}_2 \cdot (\mathbf{r}_1 \times \mathbf{r}_2)] \cdot (\mathbf{m}_1 \times \mathbf{n}_3) \end{aligned} \tag{26}$$

Then, the procedure to analyze the motion pattern can be applied and possible singularities in the motion pattern found.

In a nonsingular position the rangespace of the rotational Jacobian $\mathbf{J}_R$ has a dimension of 3, and hence the platform has 3 rotational DOF. The rank of $\mathbf{J}$ is also 3, and the nullspace of $\mathbf{J}_R$ has a zero dimension, therefore the platform has 0 translational DOF.

However, in any pose where the revolute axis $\mathbf{r}_3$ is parallel to the joint axis $\mathbf{r}_1$ (see Fig. 2) the rank of the rotational Jacobian $\mathbf{J}_R$ decreases. Vectors $\boldsymbol{\alpha}_i$ are

$$\boldsymbol{\alpha}_1 = -\left[\mathbf{s}_2 \cdot (\mathbf{r}_1 \times \mathbf{r}_2)\right] \cdot (\mathbf{n}_3 \times \mathbf{m}_3) - \left[\mathbf{s}_3 \cdot (\mathbf{r}_1 \times \mathbf{r}_2)\right] \cdot (\mathbf{m}_2 \times \mathbf{n}_3) \quad (27)$$

$$\boldsymbol{\alpha}_2 = -\left[\mathbf{s}_1 \cdot (\mathbf{r}_1 \times \mathbf{r}_2)\right] \cdot (\mathbf{m}_3 \times \mathbf{n}_3) - \left[\mathbf{s}_3 \cdot (\mathbf{r}_1 \times \mathbf{r}_2)\right] \cdot (\mathbf{n}_3 \times \mathbf{m}_1) \quad (28)$$

$$\boldsymbol{\alpha}_3 = -\left[\mathbf{s}_1 \cdot (\mathbf{r}_1 \times \mathbf{r}_2)\right] \cdot (\mathbf{n}_3 \times \mathbf{m}_2) - \left[\mathbf{s}_2 \cdot (\mathbf{r}_1 \times \mathbf{r}_2)\right] \cdot (\mathbf{m}_1 \times \mathbf{n}_3) \quad (29)$$

Note that the three of them are perpendicular to $\mathbf{n}_3$ and hence dependent. The dimension of the rangespace is 2, the possible rotation has 2 DOF and its direction is on the plane perpendicular to $\mathbf{n}_3$.

The nullspace is one dimensional, and upon substitution into the translational Jacobian $\mathbf{J}_T$ the direction of translation is obtained. In view of Eqs. 17 to 19 is easy to note that every vector $\boldsymbol{\delta}_i$ that form the translational Jacobian $\mathbf{J}_T$ is parallel to vector $\mathbf{r}_1 \times \mathbf{r}_2$. Therefore this is the only direction of possible translation. Adequate inputs can produce a finite motion with this motion pattern.

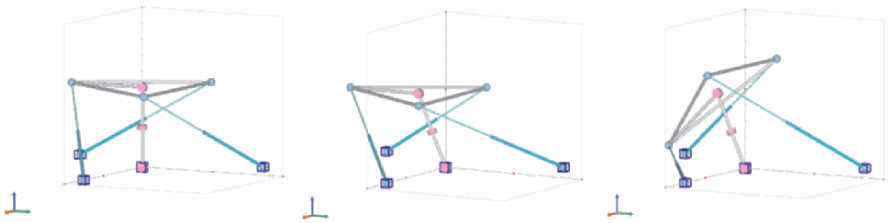

Figure 2. Sequence of motion in a Motion Pattern Singularity ($\mathbf{r}_1 = \mathbf{r}_3$).

4. Conclusions

This paper describes a singularity that affects the moving platform of lower mobility parallel manipulators. As far as the authors know, this type of singularity has not been defined in the references on this subject. This singularity does not cause an increment or reduction of the DOF of the end-effector, but a change in their nature (transforming from rotational to translational or vice versa). Regarding the manipulator performance, this singularity may produce problems with the control or the actuators. If the manipulator approaches a pose where there is a motion pattern singularity, it is evident that the desired twist in the end-effector may require very high inputs. In practice this produces abrupt increments of the inputs that can damage the machine, or simply not move the platform at all. As with other types of singularities, the

motion pattern singularity is generally instantaneous, i.e. dependent on the pose. However, there are many cases where the singularity becomes permanent for certain inputs.

5. Acknowledgements

This research work was supported in part by the Spanish Ministerio de Ciencia y Tecnologia (Project DPI2005-02207), and the University of the Basque Country (Project 9/UPV00145.345-14494/2002).

References

Kong X. and Gosselin C. M. (2005), Type Synthesis of 3-DOF PPR-Equivalent Parallel Manipulators Based on Screw Theory and the Concept of Virtual Chain, *ASME Journal of Mechanical Design*, vol. 127, pp. 1113-1121.

Freudenstein F. (1962), On the variety of motions generated by mechanisms, *Trans. ASME. J. Eng. Ind.*, pp. 156-160.

Hunt K.H. (1978), *Kinematic geometry of mechanisms*, Clarendon Press.

Sugimoto K., Duffy J. and Hunt K.H. (1982), Special configurations of spatial mechanisms and robot arms, *Mechanism and Machine Theory*, vol. 17, no. 2, pp. 119-132.

Merlet J.-P. (1989), Singular configurations of parallel manipulators and Grassmann geometry, *Int. J. of Robotics Res.*, vol. 8, no. 5, pp. 45-56.

Gosselin C. and Angeles J. (1990), Singularity analysis of closed-loop kinematic chains, *IEEE Trans. Robot. Autom.*, vol. 6, no. 3, pp. 281-290.

Zlatanov D., Fenton R.G. and Benhabib B. (1994), Singularity analysis of mechanisms and robots via velocity-equation model of the instantaneous kinematics, *IEEE Int. Conf. Rob. Autom.*, vol. 2, pp. 986-991.

Park F.C. and Kim J.W. (1999), Singularity analysis of closed kinematic chains, *ASME Journal of Mechanical Design*, vol. 121, pp. 32-38.

Zlatanov D.S., Bonev I.A. and Gosselin C.M. (2002), Constraint singularities of parallel mechanisms, *Proc. IEEE Int. Conf. Rob. Autom.*, Washington DC, USA.

Ma O. and Angeles J. (1992), Architecture singularities of parallel manipulators, *Int. J. Robot. Automt.*, vol. 7, no. 1, pp. 23-29.

Company O., Krut S. and Pierrot F. (2006), Internal singularity analysis of a class of lower mobility parallel manipulators with articulated traveling plate, *IEEE Tran. on Robotics*, vol. 22, no. 1, pp. 1-11.

Wenger P. (2004), Uniqueness Domains and Regions of Feasible Paths for Cuspidal manipulators, *IEEE Tran. on Robotics*, vol. 20, no. 4, pp. 745-750.

Thomas F., Ottaviano E., Ros Ll. and Ceccarelli M. (2005), Performance Analysis of a 3-2-1 Pose Estimation Device, *IEEE Tran. on Robotics*, vol. 21, no. 3, pp. 288-297.

Huang Z. and Cao Y. (2005), Property Identification of the Singularity Loci of a Class of Gough-Stewart Manipulators, *The Int. J. Robotics Research*, vol. 24, no. 8, pp. 675-685.

Liu X.-J.,Wang J. and Pritschow G. (2005), Kinematics, singularity and workspace of planar 5R symmetrical parallel mechanisms, *Mechanism and Machine Theory*, In press.

Author Index